

Measurement of Cross Sections and Polarisation Observables in η Photoproduction from Neutrons and Protons Bound in Light Nuclei

Inauguraldissertation
zur
Erlangung der Würde eines Doktors der Philosophie
vorgelegt der
Philosophisch-Naturwissenschaftlichen Fakultät
der Universität Basel
von
Lilian Witthauer
aus Basel, BS

Basel, 2015

Genehmigt von der Philosophisch-Naturwissenschaftlichen Fakultät
auf Antrag von

Prof. Dr. B. Krusche
Prof. Dr. V. Metag

Basel, den 13.10.2015

Prof. Dr. Jörg Schibler
Dekan

Abstract

The structure of matter, i.e. the binding of nucleons to nuclei and the formation of quarks to nucleons or other hadrons, is governed by the strong interaction. The underlying Gauge theory, Quantum Chromodynamics (QCD), is well established and has a characteristic property: the coupling constant is decreasing as a function of the momentum transfer (energy). In high-energy reactions, quarks and gluons behave as free particles and the coupling constant is small. This regime of QCD, where quarks and gluons interact only weakly, is called asymptotic freedom and perturbative calculations can be used to predict interactions. However, at small energies, the quarks interact strongly and virtual gluons can produce gluon-gluon pairs and confine quarks in colorless hadrons. Due to the large coupling constant, perturbative calculations of QCD are unreliable at low energies and cannot explain the confinement. In this low-energy range, only phenomenological models such as quark models or numerical calculations (lattice QCD) can be used to solve QCD. To verify QCD models at low energies, the excitation spectrum of the nucleon is of particular interest. Comparison of the model predictions and the experimentally observed states have shown a large discrepancy in number and ordering of the levels. Many more states are predicted than have been experimentally observed, which is known as the *problem of missing resonances*. This mismatch may either originate from the effective degrees of freedom of the models or from experimental bias.

In the beginning of hadron spectroscopy, most results have been obtained from pion-nucleon scattering experiments. However, since the intermediate nucleon resonance depends on the production mechanism, only resonances that couple to πN have been observed. In the last decades, these results have been supplemented with data on unpolarised cross sections obtained from meson photoproduction at various acceleration facilities. These results could clarify the situation to some extent. Nevertheless, the problem of missing resonances persists, which is mainly caused by the fact that many resonances are broad and overlapping. Thus, current experiments focus on the measurement of single and double polarisation observables, which may improve the situation since observables are sensitive to interference terms and thus can enhance weak contributions from resonances.

In this work, η photoproduction from quasi-free protons and neutrons has been studied. Photoproduction of η mesons is of particular interest since former results of different collaborations have shown an unusual narrow structure in the cross section on the neutron, which is not visible on the proton. Various theoretical models exist that try to explain this effect, but no conclusive solution has been found yet. Thus, to get a final interpretation of this effect, unpolarised cross sections, the double polarisation observable E and the helicity dependent cross sections $\sigma_{1/2}$ and $\sigma_{3/2}$ have been extracted in this work.

Unpolarised total and differential cross sections have been determined for protons and neutrons bound in light nuclei, i.e. deuterium and ^3He . Data have been measured with the CBELSA/TAPS experiment at the Electron Stretcher Accelerator (ELSA) in Bonn (deuterium, December 2008) and with the A2 experiment at the Mainzer Microtron (MAMI) in Mainz (^3He , November 2008). Both setups used energy-tagged photon beams to produce η mesons from cryogenic liquid targets. The target was surrounded by an almost 4π covering detector setup. At CBELSA/TAPS the combined setup of Crystal Barrel (CBB) and MiniTAPS was used, at A2 the main detectors were Crystal Ball (CB), TAPS.

Furthermore, experiments aiming at the extraction of the double polarisation observable E , have been run at both acceleration facilities. A circularly polarised photon beam and a longitudinally polarised deuterated butanol (dButanol) target have been used.

The results obtained in this work give input to new partial wave analysis and help to straighten out the situation of η photoproduction from the neutron.

Acknowledgements

I would like to express my appreciation and thanks to my advisor Prof. Dr. Bernd Krusche for guiding me through all the years and letting me grow as a research scientist. This work has only been possible with his supervision and continuous support. I would also like to thank the committee member, Prof. Dr. Volker Metag for serving as my co-referee.

Special thanks to Irakli Keshelashvili with his tremendous scientific knowledge and emotional support since the first day of my research work. I am grateful for the successful collaboration with Manuel Dieterle during all the analysis and experimental work. Thanks for your brilliant suggestions and invaluable discussions. Thanks to Dominik Werthmüller for supporting me with his experience, programming skills, and for encouraging me on the last lap of my PhD work. Many thanks also to Natalie Walford for reviewing my thesis and for her good advice.

Thanks to all past and present group members for the professional and personal time, I. Jaeglé, R. Trojer, F. Pheron, Y. Maghrbi, T. Rostomyan, M. Oberle, A. Käser, T. Strub, S. Garni, and S. Lutterer. I have appreciated the productive meetings, preparation and realisations of the experiments with all the associates of the CBELSA/TAPS and A2 collaborations.

Finally, I would like to thank my family and close friends for their patience and unconditional support through the challenges of my PhD and of my life.

Contents

1	Introduction	1
1.1	The Structure of the Nucleon	1
1.1.1	Nucleon Resonances	2
1.1.2	Model Descriptions	4
1.2	Formalism of η Meson Photoproduction	8
1.2.1	Kinematics	9
1.2.2	Electromagnetic Multipoles	10
1.2.3	Amplitude Representation	12
1.3	Observables	18
1.3.1	The Complete Experiment	20
1.3.2	Extraction of Resonance Parameters	21
1.4	Current Experimental Data	22
1.4.1	Narrow Structure on the Neutron	23
1.4.2	Double Polarisation Observable E	29
2	Experimental Setup	31
2.1	Acceleration Facilities	31
2.1.1	MAMI	31
2.1.2	ELSA	33
2.2	Generation of Photon Beams	35
2.2.1	Bremsstrahlung Process	35
2.2.2	Circularly Polarised Photons	36
2.2.3	Photon Tagging	38
2.3	Targets	40
2.3.1	Liquid Deuterium Target	40
2.3.2	^3He Target	41
2.3.3	Frozen Spin Target	41
2.3.4	Carbon Target	44
2.4	Detectors Setup	45
2.4.1	A2 Detector Setup	45
2.4.2	CBELSA/TAPS Detector Setup	49
2.5	Trigger	53
2.5.1	A2 Trigger	53
2.5.2	CBELSA/TAPS Trigger	56

CONTENTS

3 Data Sets and Polarisation Values	59
3.1 Data Sets	59
3.2 Electron Polarisation	61
3.2.1 Mott Measurement	61
3.2.2 Møller Measurement	63
3.3 Photon Polarisation	66
3.4 Target Polarisation	67
3.4.1 D-Wave Admixture	69
3.4.2 Issue with the A2 Target Polarisation Values	70
4 Software	73
4.1 A2 Software	73
4.1.1 AcquRoot	73
4.1.2 A2 Geant	74
4.1.3 PLUTO	74
4.1.4 OSCAR	75
4.2 CBELSA/TAPS Software	75
4.2.1 EXPLORA, MyAnalysis and libTOCB	75
4.2.2 CBGEANT	76
5 Event Reconstruction	79
5.1 A2 Event Reconstruction	79
5.1.1 Tagger	79
5.1.2 Crystal Ball	79
5.1.3 TAPS	80
5.2 CBELSA/TAPS Event Reconstruction	82
5.2.1 Tagger	82
5.2.2 Crystal Barrel and Forward Plug	83
5.2.3 MiniTAPS	87
6 Calibration	91
6.1 Energy Calibration	91
6.1.1 A2 Energy Calibration	91
6.1.2 CBELSA/TAPS Energy Calibration	97
6.2 Time Calibration	98
6.2.1 A2 Time Calibration	98
6.2.2 CBELSA/TAPS Time Calibration	101
7 Reaction Selection	105
7.1 Event Classes	105
7.2 Reconstruction of the η Meson	106
7.2.1 Energy and Angular Resolutions	108
7.2.2 Confidence Levels	110
7.3 Time Cuts	113

7.3.1	Coincidence Cuts	113
7.3.2	Random Background Subtraction	114
7.4	Background Rejection	115
7.4.1	Pulse Shape Analysis	116
7.4.2	Coplanarity	117
7.4.3	Missing Mass	120
7.4.4	Invariant Mass	121
7.4.5	Polar Angle Cuts	124
7.5	Further Checks	125
7.5.1	Time of Flight	125
7.5.2	ΔE versus E	127
7.5.3	Cluster Multiplicity	128
7.5.4	Fermi Momentum	128
8	Extraction of Observables	133
8.1	Unpolarised Cross Section	133
8.2	Double Polarisation Observable E	134
8.2.1	<i>Version 1</i> - Carbon Subtraction Method	134
8.2.2	<i>Version 2</i> - Direct Method	136
8.3	Helicity Dependent Cross Sections $\sigma_{1/2}$ and $\sigma_{3/2}$	136
8.3.1	<i>Version 1</i>	136
8.3.2	<i>Version 2</i>	137
8.3.3	<i>Version 3</i>	137
8.4	Target Surface Density	137
8.5	W-Reconstruction	138
8.6	Photon Flux	141
8.6.1	A2 Photon Flux	141
8.6.2	CBELSA/TAPS Photon Flux	143
8.6.3	E - and W - Dependent Flux	146
8.6.4	Helicity Dependent Photon Flux	147
8.7	Extraction of the Yields	148
8.8	Detection Efficiency	148
8.8.1	Nucleon Detection Efficiency Correction	149
8.8.2	Software Trigger	152
8.8.3	Summary of Efficiencies	154
8.9	Empty Target Subtraction	158
8.10	Carbon Subtraction	159
8.11	Data Merging	166
8.12	Systematic Uncertainties	166
8.12.1	Unpolarised Cross Sections	166
8.12.2	Double Polarisation Observable E and Helicity Dependent Cross Sections	171

9 Results and Conclusions	173
9.1 Unpolarised Cross Section from ${}^3\text{He}$ (A2)	173
9.1.1 Incident Photon Energy E_γ	174
9.1.2 Final State Energy W	177
9.2 Unpolarised Cross Section from LD_2 (CBELSA/TAPS)	183
9.2.1 Incident Photon Energy E_γ	183
9.2.2 Final State Energy W	186
9.3 Polarisation Observable E from CBELSA/TAPS Data	192
9.3.1 Consistency Checks	192
9.3.2 Results	195
9.4 Polarisation Observable E from A2 Data	200
9.4.1 Consistency Checks	200
9.4.2 Results as a Function of the Incident Photon Energy E_γ	208
9.4.3 Results as a Function of the Final State Energy W	210
9.5 Discussion of the Polarisation Observables	214
9.5.1 Angular Distributions	214
9.5.2 Cross Sections for Different Polar Angles	223
9.5.3 Comparison of A2 and CBELSA/TAPS Results	224
9.6 Conclusions	226
Appendix	228
A Hadron Multiplets	229
A.1 Meson Multiplets	229
A.2 Baryon Multiplets	230
A.3 Antidecuplet of Pentaquarks	230
B Polarisation Observables	233
B.1 General Form of the Cross Section	233
B.2 Complete Set of Observables	234
C Efficiencies	235
D Systematic Uncertainties for the ${}^3\text{He}$ Cross Sections	239
E Angular Distributions for the Polarisation Observables	243
F Data Tables	251
F.1 Unpolarised Cross Sections from ${}^3\text{He}$ (A2)	252
F.1.1 $\gamma N \rightarrow \eta(N)$ as a Function of E_γ	252
F.1.2 $\gamma p \rightarrow \eta p$ as a Function of E_γ	256
F.1.3 $\gamma n \rightarrow \eta n$ as a Function of E_γ	260
F.1.4 $\gamma p \rightarrow \eta p$ as a Function of W	264
F.1.5 $\gamma n \rightarrow \eta n$ as a Function of W	268
F.2 Unpolarised Cross Sections from LD_2 (CBELSA/TAPS)	272

F.2.1	$\gamma N \rightarrow \eta(N)$ as a Function of E_γ	272
F.2.2	$\gamma p \rightarrow \eta p$ as a Function of E_γ	276
F.2.3	$\gamma n \rightarrow \eta n$ as a Function of E_γ	279
F.2.4	$\gamma n \rightarrow \eta(n)$ as a Function of E_γ	282
F.2.5	$\gamma p \rightarrow \eta p$ as a Function of W	285
F.2.6	$\gamma n \rightarrow \eta n$ as a Function of W	288
F.3	Polarisation Observable E and Helicity Dependent Cross Sections from CBELSA/TAPS Data	291
F.3.1	E for $\gamma p \rightarrow \eta p$ as a Function of E_γ	291
F.3.2	Helicity Dependent Cross Sections for $\gamma p \rightarrow \eta p$ as a Function of E_γ	291
F.3.3	E for $\gamma n \rightarrow \eta(n)$ as a Function of E_γ	292
F.3.4	Helicity Dependent Cross Sections for $\gamma n \rightarrow \eta(n)$ as a Function of E_γ	292
F.3.5	E for $\gamma p \rightarrow \eta p$ as a Function of W	293
F.3.6	Helicity Dependent Cross Sections for $\gamma p \rightarrow \eta p$ as a Function of W	293
F.4	Polarisation Observable E and Helicity Dependent Cross Sections from A2 Data	294
F.4.1	E for $\gamma p \rightarrow \eta p$ as a Function of E_γ	294
F.4.2	Helicity Dependent Cross Sections for $\gamma p \rightarrow \eta p$ as a Function of E_γ	296
F.4.3	E for $\gamma n \rightarrow \eta n$ as a Function of E_γ	299
F.4.4	Helicity Dependent Cross Sections for $\gamma n \rightarrow \eta n$ as a Function of E_γ	301
F.4.5	E for $\gamma p \rightarrow \eta p$ as a Function of W	304
F.4.6	Helicity Dependent Cross Sections for $\gamma p \rightarrow \eta p$ as a Function of W	306
F.4.7	E for $\gamma n \rightarrow \eta n$ as a Function of W	309
F.4.8	Helicity Dependent Cross Sections for $\gamma n \rightarrow \eta n$ as a Function of W	311

Chapter 1

Introduction

In this chapter, a short introduction to the underlying theory of this work is given. Section 1.1 gives an overview of experimental and theoretical knowledge of the structure of the nucleon and the corresponding excitation spectrum. Section 1.2 introduces the formalism used to describe η photoproduction including kinematical considerations and amplitude representations. In Sec. 1.3, several aspects of polarisation observables are discussed. Finally, Sec. 1.4 summarises the currently available data.

1.1 The Structure of the Nucleon

Nucleons (protons and neutrons) are the basic elements of atomic nuclei. The way the nucleon is composed of quarks and gluons directly affects the properties of the nuclei. Hence, understanding the internal structure of the nucleon is one of the most crucial and challenging tasks of modern nuclear physics.

Already in 1933, R. Frisch and O. Stern showed [1] that their measurements of the magnetic moment of the nucleon are not compatible with the results found for point-like spin-1/2-particles. Like the electron, the proton was expected to have a magnetic moment of $\mu_N = e\hbar/2m_p c$, where e is the electron charge, \hbar is the reduced Planck constant, m_p is the proton mass, and c is the speed of light. Hence, in this formula, μ_N corresponds to a rotating charge with an angular momentum of $\hbar/2$. Even more, the magnetic moment of the neutron was supposed to be zero. The current CODATA [2] values are $\mu_p = 2.792\mu_N$ and $\mu_n = -1.913\mu_N$ and thus are in clear contradiction to a structure-less nucleon.

Electron scattering experiments in the mid 1950s by Hofstadter *et al.* [3] confirmed the extended structure of the nucleon by measuring the charge radius of the proton $\sqrt{r_p^2} = (0.74 \pm 0.24) \text{ fm}$.

Some years before, the research group of E. Fermi published results on pion-proton scattering [4] and found an excessive increase in the cross section at a pion energy of 195 MeV, the first excited state of the nucleon ($\Delta(1232)$). Ongoing experiments showed that this rise is only the first of several excited states of the nucleon, known as the nucleon resonances.

1.1.1 Nucleon Resonances

At first glance, the excitation spectrum of an atom and a nucleon may look very similar, but there are crucial differences. A first very obvious difference is that the density of states of the excitation spectrum of the nucleon is much higher than that seen for the atoms. Furthermore, the energy differences between the various states of the nucleon spectrum are similar to the nucleon mass and therefore orders of magnitude larger than for the spectra of atoms. The resonances have a decay width of 100-200 MeV and decay via the strong interaction by the emission of mesons (compared to the emission of \sim eV photons for the excited states of atoms). Resonances have different quantum numbers and thus emit different mesons. This is illustrated in Fig. 1.1, where the total photoabsorption cross section and its decomposition into the different final states is shown. The cross section for each meson (double meson) final state has its own characteristic shape. This shape is a result of single nucleon resonances, their interference and the contribution of non-resonant background terms (Fig. 1.7 shows the contributing Feynman diagrams in the case of η photoproduction). As already mentioned, the nucleon resonances are in general very broad, meaning they have a large width, and thus overlap with other nearby resonances. Therefore, it can be quite challenging to disentangle different resonance contributions. However, this is crucial for the comprehension of the internal structure of the nucleon. The situation is highlighted in Fig.

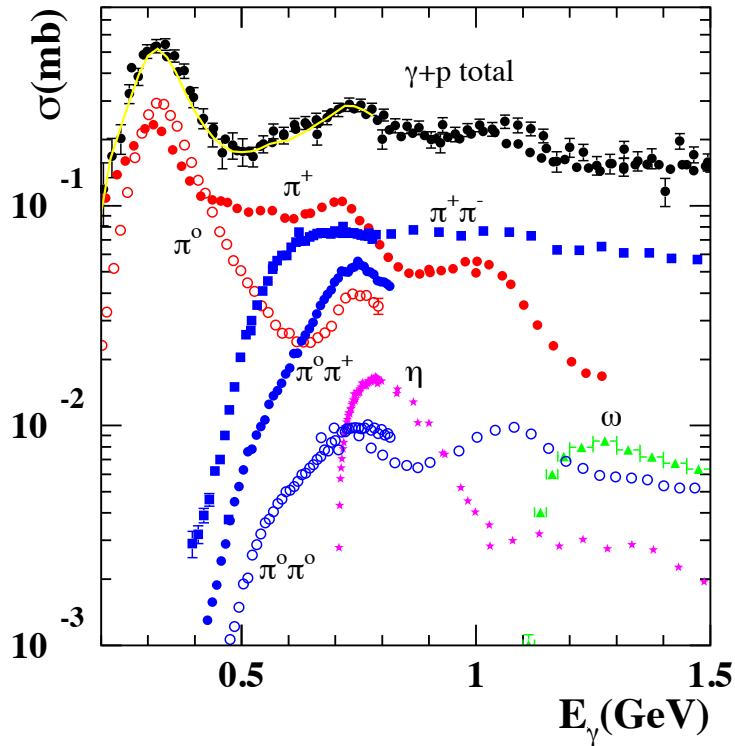


Figure 1.1: Total photoabsorption cross section and the decomposition into the different meson final states for the reaction on the free proton. Figure taken from [5].

1.1. THE STRUCTURE OF THE NUCLEON

1.2, where the individual resonance contributions for two certain final states ($p\pi^0$ and $p\eta$) are shown. The following notation is used for nucleon resonances:

$$L_{2I2J}(W), \quad (1.1)$$

where L is the orbital angular momentum of the nucleon-meson pair from the decay of the resonance, I is the isospin, J is the total angular momentum of the resonance, and W is the mass of the resonance in MeV/c^2 . L is usually written in the spectroscopic notation where $L = 0, 1, 2, 3$ and corresponds to the atomic orbital levels S, P, D, F . This notation is somehow outdated, as the newest *Review of Particle Physics by the Particle Data Group (PDG)* [6] lists the resonances according to their isospin and total angular momentum:

$$I(W)J^P, \quad (1.2)$$

where I is either N for $I = \frac{1}{2}$ resonances or Δ for $I = \frac{3}{2}$ resonances, J^P is the angular momentum and parity of the state, and W is the mass of the resonance.

As can be seen from Fig. 1.2, in single pion photoproduction on the proton, the N resonance $S_{11}(1535)$ (PDG $N(1535)1/2^-$) is almost invisible because of the dominating Δ resonance $P_{33}(1232)$ (PDG $\Delta(1232)3/2^+$) and the N^* resonances $D_{13}(1520)$ (PDG $N(1520)3/2^-$) and $F_{15}(1680)$ (PDG $N(1680)5/2^+$). On the contrary, the $S_{11}(1535)$ is the dominating resonance in η photoproduction. One reason for this situation is that in η photoproduction, only N ($I = \frac{1}{2}$) resonances can contribute since the η meson has isospin zero and therefore serves as an isospin filter. This is illustrated in Fig. 1.2 on the right-hand side, where the excited states of the nucleon and their decay modes are illustrated.

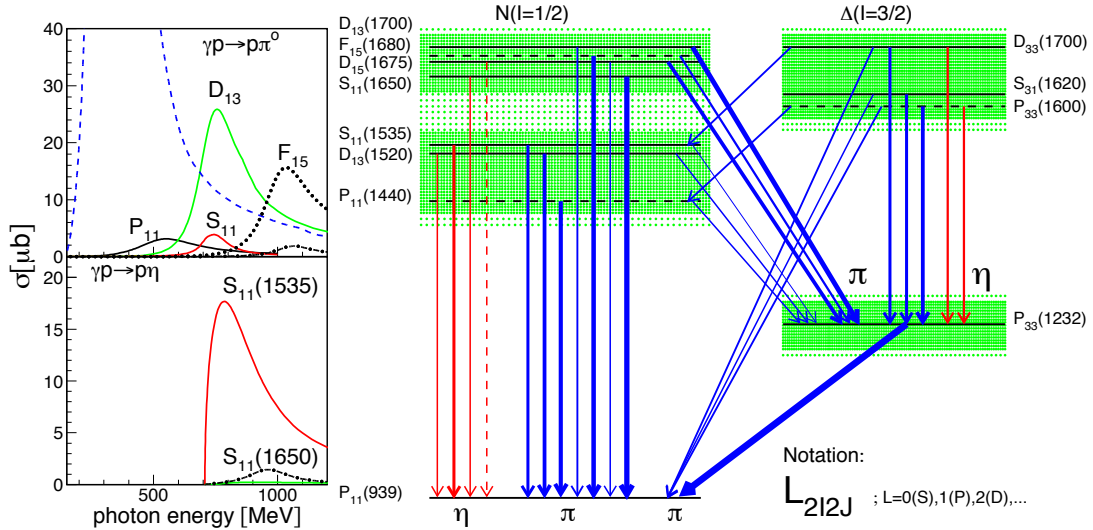


Figure 1.2: Left: resonance contribution to single pion and η photoproduction. Right: low lying states of the nucleon and their decay modes via the emission of mesons. The η meson serves as an isospin filter (red lines) and hence only populates resonances with $I = 1/2$. Figure taken from [7].

1.1.2 Model Descriptions

The precise measurement of the excitation spectrum of the nucleon and the comparison to model predictions allows to gain fundamental information about the underlying strong interaction. However, due to the large coupling constant at low energies (see Fig. 1.3), perturbative methods are not straightforward and quark model and lattice QCD calculations have to be used to solve Quantum Chromodynamics (QCD). These models shall be briefly explained in this section.

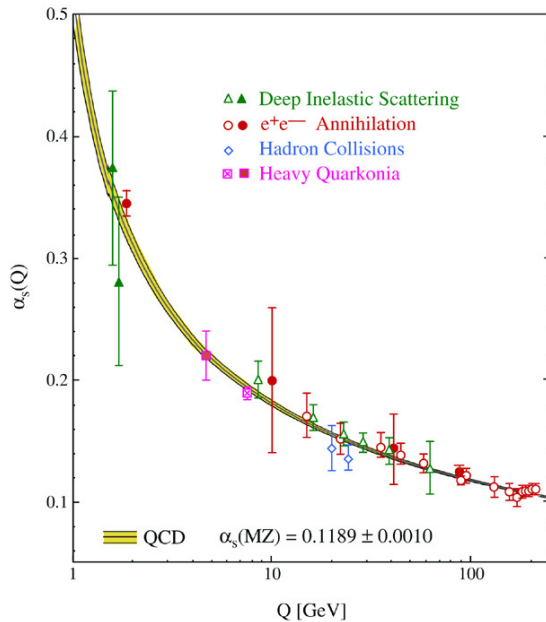


Figure 1.3: Results on the coupling constant of the strong interaction, α_s as a function of the energy scale Q , obtained from different experiments. Next-to-leading order QCD calculations are shown as open symbols. Next-next-to-leading order calculations are given as closed symbols. The yellow band is the QCD prediction for the combined world average value of α_s on a common energy scale $Q \equiv M_{Z^0}$, where M_{Z^0} is the mass of the Z^0 boson. Figure taken from [8].

Quark Models

The simple quark model was originally proposed by Gell-Mann [9, 10] and Zweig [11] in the 1960s. Their model suggested that hadrons can be arranged in a multiplet structure, as seen in Appendix A, and are composed of constituents, the quarks, that belong to the representation of $SU(3)$, a Lie group of three dimensional unitary matrices with determinant one. Gell-Mann wrote: "A simpler and more elegant scheme can be constructed if we allow non-integral values for the charges. We can dispense entirely with the basic baryon b if we assign to the triplet t the following properties: spin $1/2$, $z = -1/3$, and baryon number $1/3$. We then refer to the members $u^{2/3}$, $d^{-1/3}$ and $s^{-1/3}$ of the triplet as "quarks" q and the members of the anti-triplet as anti-quarks \bar{q} . Baryons can now be constructed from quarks by using the combinations (qqq) , $(qqq\bar{q})$, etc., while mesons are made

out of $(q\bar{q})$, $(qq\bar{q}\bar{q})$, etc. It is assuming that the lowest baryon configuration (qqq) gives just the representations **1**, **8**, and **10** that have been observed, while the lowest meson configuration $(q\bar{q})$ similarly gives just **1** and **8**.”[10]

Hence, the quark model of Gell-Mann only accounted for the three lightest quarks, whereas the *Standard Model* of particle physics contains six quarks (flavours) that belong to three generations, as seen in Table 1.1.

generation	quark	charge	mass
I	u	$2/3$	~ 2.3 MeV
	d	$-1/3$	~ 4.8 MeV
II	c	$2/3$	~ 1.2 GeV
	s	$-1/3$	~ 95 MeV
III	t	$2/3$	~ 173 GeV
	b	$-1/3$	~ 4.6 GeV

Table 1.1: The six quarks are grouped into three generations. Numbers taken from [6].

With only three quarks, the model of Gell-Mann and Zweig was able to classify all known particles at that time and even predict the quantum numbers of the missing member of the baryon-3/2 decuplet, the Ω^- , which was experimentally observed in 1964. Furthermore, the model explained the mass splitting between mesons and baryons, magnetic moments and even predicted scattering cross section ratios. However, their model could not answer a fundamental question: what holds the quarks together in hadrons? A very puzzling fact was that the symmetric wave function of the Δ^{++} -baryon violated the Pauli principle. The latter problem was solved when O.W. Greenberg [12] introduced the quark property of colour charge (one year later M.Y. Han and Y. Nambu introduced colour as a gauge symmetry [13]) [14]. These questions and the fact that quarks had never been observed were the reason that the quark model was seen as highly doubtful for several years.

In 1968, R. Feynman [15] concluded from results on high-energy hadron collisions that protons are composed of point like spin-1/2 *partons*, but never specified what these partons were. Bjorken and Paschos [16] further developed this model in means of deep inelastic electron-proton scattering (DIS) and suggested the Bjorken scaling, which means that in the limit of infinite momentum transfer Q^2 , the structure functions should only depend on the dimensionless scaling variable $x = Q^2/(M\nu)$, where ν is the energy transferred to the nucleon by the scattering electron and M is the mass of the proton. Bjorken scaling implies that at large Q^2 , the electron is scattered off free point-like constituents. The experimental observation of the Bjorken scaling in DIS and the construction of QCD [17], the gauge theory of interacting quarks and gluons, together with the idea of asymptotic freedom in QCD by D. Gross, F. Wilczek and D. Politzer [18, 19], led to the justification of the constituent quark model and the formulation of the Standard Model, which contains the quantum field theories for the strong and the electroweak interactions.

The original quark model by Gell-Mann and Zweig, which was purely a symmetry based classification, was able to explain the masses of the ground state baryons with

simple formulas, but could not do so for excited states of the baryons. For this purpose, non-relativistic harmonic oscillator models were developed by Greenberg [12], Dalitz [20], Faiman and Hendry [21]. De Rujula *et al.* [22] then refined this model and introduced a spin-dependent hyperfine potential due to the one-gluon exchange between two quarks to account for the mass splitting between the baryon octet and decuplet. However, to reproduce the observed N - Δ ground state splitting, this model implied an unexpected large coupling constant, α_s , and spin-orbit splittings that were not previously seen [23]. Isgur and Karl [24] accounted for the latter issue by neglecting spin-orbit interaction with the argument that it would cancel out with the confining potential. Their model was quite successful in reproducing the nucleon and Δ members of the octet and the decuplet states, supporting the idea that the nucleon and the Δ only differ by the arrangement of the quark spins.

In the subsequent years, many different quark models have been developed to get a better understanding of the excitation spectrum. The spectrum generated by the models is affected by the number of degrees of freedom and the residual quark-quark interaction. The degrees of freedom determine the number of excited states, whereas the ordering of states and their decay properties are related to the residual quark-quark interaction [6].

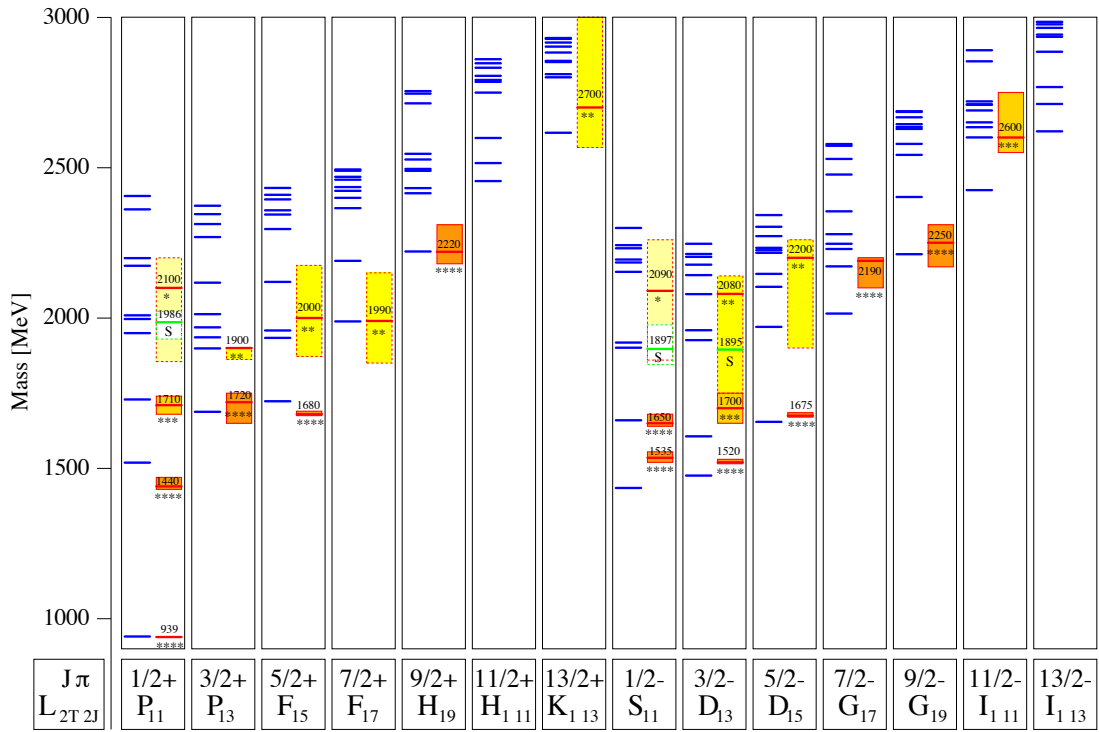


Figure 1.4: Positive and negative parity nucleon resonances predicted by the quark model by Löring *et al.* The model results (blue lines) are compared to experimentally observed states (yellow, orange and red boxes). The box size is showing the uncertainty of the mass measurement. Especially at higher energies, large discrepancies between experimentally observed and predicted states are visible. Figure taken from [25].

In the classic constituent quark model, the degrees of freedom are three constituent quarks. Constituent quarks are valence quarks consisting of current quarks, which are surrounded by gluons and quark-antiquark pairs. All the complex aspects of their interaction are subsumed into the effective constituent quark masses. For the two light quarks, u and d, this effective mass is of the order of 340 MeV (compared to the current quark masses of 2-5 MeV, as seen in Table 1.1). To get more predicted excited states, the number of degrees of freedom can be increased. This is done in so-called flux tube models, which were pioneered by Isgur and Paton [26], and Iachello *et al.* [27]. The string picture (quarks are connected by gluonic strings, so-called *flux tubes*) for the confinement mechanism is motivated from the fact that certain baryon states lie on a $M^2 \sim J$ trajectory, so called Regge trajectories, where M is the baryon mass, and J is the corresponding spin. A more recent relativistic quark model approach, which uses flux tubes was developed by Löring *et al.* [25]. In their quark model, confinement is a linearly rising three-body string potential. This model uses instanton interactions to describe the potential between quarks. Fig. 1.4 shows the remarkable results of this model on the nucleon resonances up to total spin $J = 13/2$. At low energies, the number of predicted states (blue lines) are in agreement with the experimentally observed states (coloured boxes). However, the predicted position of the resonances is not always consistent with the experimental results. At higher energies, huge discrepancies in numbering and ordering of states occurs. The issue is commonly known as the *problem of missing resonances*. To account for the mismatch, quark models that include less degrees of freedom have been developed. One example is the diquark model [28], which describes the nucleon as a closely bound diquark and quark and, hence, reduces the number of degrees of freedom and also the number of states. Diquark models reproduce the low lying states quite well and even predict form factors that are in agreement with experimental data. However, lattice QCD calculations have found evidence that diquarks do not form [29].

Lattice QCD

Besides quark models, numerical methods, such as lattice QCD calculations, can be used to predict the low energy excitation spectrum of the nucleon. Lattice QCD is a gauge theory, which is formulated in discrete spacetime on a grid with lattice spacing a . Quarks are represented as fields that are defined on lattice sites, whereas gluon fields are defined on the links connecting the sites. Lattice QCD approaches continuous QCD in the limit of vanishing lattice spacing. Results from lattice QCD are obtained by repeated calculations with different grid spacings and hence, are computational expensive. Recent computations for the nucleon excitation spectrum up to $J = 7/2$ by Edwards *et al.* [30] are shown in Fig. 1.5. The pattern of the predicted low-lying states is similar to the ones obtained from the quark models. The $N = 1$ oscillator band (negative parity) consists of two states for $J = 1/2$ and $J = 3/2$ each, followed by one single state in $J = 5/2$. No state is predicted for $J = 7/2$. The states of $N = 2$ (positive parity) oscillator band follow the pattern 4-5-3-1, the same pattern is predicted by the quark model shown in Fig. 1.4.

Similar to quark models, lattice QCD predicts numerous states at higher energies, which have not been experimentally observed. Furthermore, since the calculations are in an early stage (the pion mass used in this calculation was $m_\pi = 396$ MeV, whereas the nominal mass of the pion is $m_\pi \simeq 140$ MeV), the predicted position of the resonances are far away from experimental results. In summary, the calculations by quark models and lattice QCD still show large discrepancies if one compares them to experimental results. However, the question arises whether this is coming from inadequate degrees of freedom in the models or from experimental bias. This work should give additional input to this discussion.

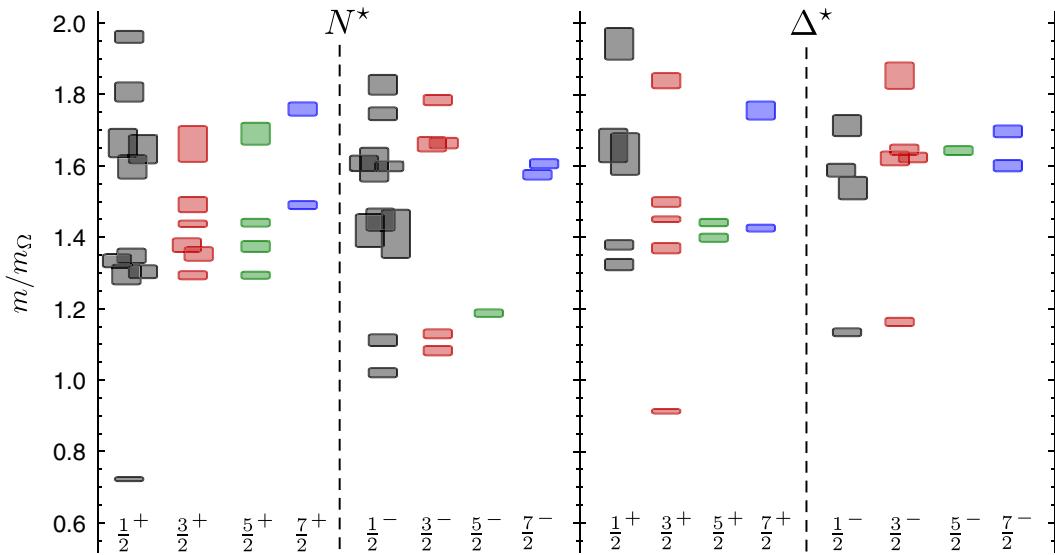


Figure 1.5: N^* and Δ resonances predicted by lattice QCD calculations by Edwards et al. for $m_\pi = 396$ MeV. Figure taken from [30].

1.2 Formalism of η Meson Photoproduction

One possible cause for the *problem of missing resonances* may originate from the fact that many of the resonances listed (at least until 2010) in the *Review of Particle Physics* [6] have been found in πN scattering experiments. Hence, resonances that couple only weakly to this channel may have not been observed. Thus, different production mechanisms, such as reactions induced by real photons (photoproduction), are a good way to find new nucleon resonances.

This work focuses on the photoproduction of η mesons, which is one of many possible channels. The Feynman diagram of η photoproduction via the intermediate excitation of a nucleon resonance is shown in Fig. 1.6. In the left vertex, the photon interacts electromagnetically with the nucleon to produce a resonance N^* . This resonance decays via the strong interaction (right vertex) into the nucleon ground state by the emission of a pseudoscalar η meson.

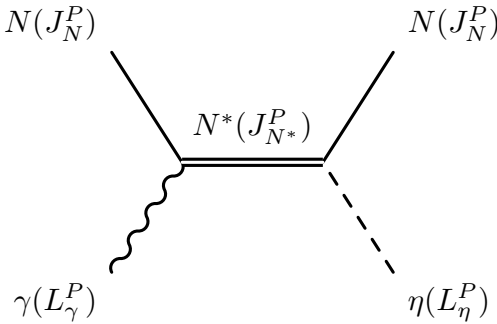


Figure 1.6: Photoproduction of the η meson via the excitation of a nucleon resonance with electromagnetic (left) and hadronic (right) vertex as given in Ref. [31].

1.2.1 Kinematics

For η meson photoproduction, the following reaction equation applies [32]:

$$\gamma(k) + N(p_i) \rightarrow \eta(q) + N(p_f), \quad (1.3)$$

where $k = (k_0, \vec{k})$ and $q = (\omega, \vec{q})$ are the four-vectors of the photon and the η meson in the center of mass (cm) frame, respectively, $p_i = (E_i, -\vec{k})$ is the four-vector of the initial state nucleon, and $p_f = (E_f, -\vec{q})$ is the four-vector for the final state nucleon.

For such a two particle scattering process, three Lorentz-invariant quantities can be defined, known as the Mandelstam variables s, u and t :

$$\begin{aligned} s &= (k + p_i)^2 = (q + p_f)^2, \\ u &= (k - p_f)^2 = (q - p_i)^2, \\ t &= (q - k)^2 = (p_i - p_f)^2. \end{aligned} \quad (1.4)$$

The sum of the Mandelstam variables is equal to the sum of the squared masses of the participant particles:

$$s + u + t = 2M_N^2 + M_\eta^2 + k^2. \quad (1.5)$$

Physical reactions are characterised as s -, t - or u -channels. The depiction of these channels as Feynman diagrams is done in a way such that the incoming particles enter from the left side, whereas the scattered particles exit on the right-hand side. The interaction is mediated through a virtual particle (between two vertices) that carries the momentum transfer equal to the corresponding Mandelstam variable.

For η photoproduction, the contributing channels are shown in Fig. 1.7. In the s -channel, a resonant term and a non-resonant Born term contribute. The non-resonant Born term exists also in the u -channel, as well as a slowly varying non-resonant background term with an intermediate resonance. Furthermore, a vector meson can be exchanged in the t -channel at high photon energies. In η photoproduction, the sum of the background terms is small. According to the MAID model [33], this is caused by the fact that the Born terms and t -channel contributions compensate each other.

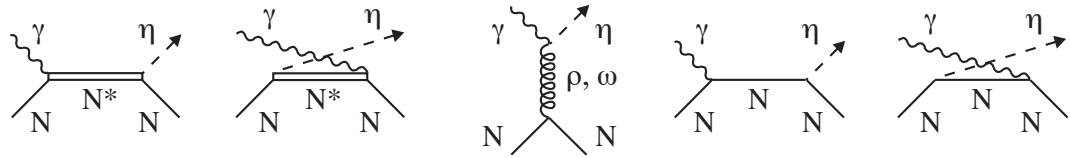


Figure 1.7: Feynman diagrams for η meson photoproduction: Resonant contribution from s -channel, non-resonant background in u -channel, vector meson exchange term in t -channel and non-resonant Born terms in s - and u -channel (from left to right). Figure taken from [31].

1.2.2 Electromagnetic Multipoles

The photon with spin \vec{s} ($s_\gamma = 1$) and angular momentum \vec{l} relative to the initial state nucleon has total angular momentum $\vec{L}_\gamma = \vec{l} + \vec{s}_\gamma$. The initial state nucleon has spin $\vec{J}_N (J = \frac{1}{2})$ and parity $P_N = +1$ and it couples electromagnetically to the photon. An intermediate resonance N^* with spin \vec{J}_{N^*} and parity P_{N^*} is excited. The selection rules define the spin and the parity of this nucleon resonance:

$$\begin{aligned} |L_\gamma - J_N| &\leq J_{N^*} \leq |L_\gamma + J_N| \\ |L_\gamma - \frac{1}{2}| &\leq J_{N^*} \leq |L_\gamma + \frac{1}{2}| \end{aligned} \quad (1.6)$$

and

$$P_{N^*} = P_N \cdot P_\gamma = P_\gamma. \quad (1.7)$$

As mentioned, such a resonance decays to the ground state via the strong interaction by the emission of light mesons, in the current case the pseudoscalar η meson with $J_\eta = 0, P_\eta = -1$, and relative orbital angular momentum $l = L_\eta$. Analogous to the initial state one can use the selection rules to get spin and parity of the resonance:

$$\begin{aligned} |L_\eta - J_N| &\leq J_{N^*} \leq |L_\eta + J_N| \\ |L_\eta - \frac{1}{2}| &\leq J_{N^*} \leq |L_\eta + \frac{1}{2}| \end{aligned} \quad (1.8)$$

and

$$P_{N^*} = P_N \cdot P_\eta \cdot (-1)^{L_\eta} = (-1)^{L_\eta + 1}. \quad (1.9)$$

Combining Eqs. 1.6 and 1.8 yields:

$$|L_\gamma \pm \frac{1}{2}| \leq J_{N^*} \leq |L_\gamma \pm \frac{1}{2}|, \quad (1.10)$$

where both signs are independent of each other. Consequently, Eqs. 1.7 and 1.9 can be combined to find the corresponding parity:

$$P_\gamma = P_{N^*} = (-1)^{L_\eta + 1} \quad (1.11)$$

To excite resonances of a certain spin and parity, electromagnetic multipole transitions of the photon in the initial state are necessary. Due to parity and angular momentum conservation, magnetic multipoles ML , i.e. $P_\gamma = (-1)^{L_\gamma+1}$, are only allowed with:

$$ML: L = L_\eta . \quad (1.12)$$

On the contrary, electric multipoles EL , i.e. $P_\gamma = (-1)^{L_\gamma}$ are possible for:

$$EL: L = L_\eta \pm 1 . \quad (1.13)$$

For multipoles of pseudoscalar photoproduction, the notation $E_{l\pm}$ and $M_{l\pm}$ is used, where E and M stands for electric and magnetic multipoles, respectively, $l = L_\eta$ is the relative orbital angular momentum of the final state meson-nucleon system and \pm indicates whether the nucleon spin has to be added to or subtracted from l to obtain the total angular momentum J_{N^*} in the intermediate state. As a consequence, resonances with $J_{N^*} > 1/2$ can be excited by one electric and one magnetic multipole and are given in Table 1.2. States with $J_{N^*} = 1/2$ can only be excited by one multipole, E_{0+} for negative parity and M_{1-} for positive parity.

photon M-pole	initial state (L_γ^P, J_N^P)	interm. state $J_{N^*}^P$	final state (J_N^P, L_η^P)	multi-pole	$(k^*/q^*)d\sigma/d\Omega$
E1	$(1^-, \frac{1}{2}^+)$	$\frac{1}{2}^-$	$(\frac{1}{2}^+, 0^-)$	E_{o+}	$ E_{o+} ^2$
		$\frac{3}{2}^-$	$(\frac{1}{2}^+, 2^-)$	E_{2-}	$\frac{1}{2} E_{2-} ^2(5 - 3x^2)$
M1	$(1^+, \frac{1}{2}^+)$	$\frac{1}{2}^+$	$(\frac{1}{2}^+, 1^+)$	M_{1-}	$ M_{1-} ^2$
		$\frac{3}{2}^+$	$(\frac{1}{2}^+, 1^+)$	M_{1+}	$\frac{1}{2} M_{1+} ^2(5 - 3x^2)$
E2	$(2^+, \frac{1}{2}^+)$	$\frac{3}{2}^+$	$(\frac{1}{2}^+, 1^+)$	E_{1+}	$\frac{9}{2} E_{1+} ^2(1 + x^2)$
		$\frac{5}{2}^+$	$(\frac{1}{2}^+, 3^+)$	E_{3-}	$\frac{9}{2} E_{3-} ^2(1 + 6x^2 - 5x^4)$
M2	$(2^-, \frac{1}{2}^+)$	$\frac{3}{2}^-$	$(\frac{1}{2}^+, 2^-)$	M_{2-}	$\frac{9}{2} M_{2-} ^2(1 + x^2)$
		$\frac{5}{2}^-$	$(\frac{1}{2}^+, 2^-)$	M_{2+}	$\frac{9}{2} M_{2+} ^2(1 + 6x^2 - 5x^4)$

Table 1.2: Lowest order multipole amplitudes for pseudoscalar meson photoproduction. In the last column, the differential cross sections are shown, where k^* and q^* are the photon and the meson four-momenta in center of mass frame, respectively. A pair of multipoles always have the same angular distributions, $d\sigma/d\Omega(M_{l+1,-}) \sim d\sigma/d\Omega(E_{l,+})$ and $d\sigma/d\Omega(M_{l-1,+}) \sim d\sigma/d\Omega(E_{l,-})$, which is known as the Minami ambiguity. Figure taken from [31].

1.2.3 Amplitude Representation

According to scattering theory, the process described in Eq. 1.3 can be expressed in terms of the scattering matrix S , which denotes the probability P to move from the initial $|i\rangle$ to the final state $|f\rangle$:

$$P(i \rightarrow f) = |S_{fi}|^2. \quad (1.14)$$

The S -matrix includes all the aspects of the scattering, i.e. the reaction phase space, the four-momentum conservation, and the interaction. The elements S_{fi} can be expressed in terms of the invariant matrix element iM_{fi} [32]:

$$S_{fi} = \frac{1}{(2\pi)^2} \delta^4(p_f + q - p_i - k) \sqrt{\frac{M_N^2}{2\omega k E_i E_f}} iM_{fi}. \quad (1.15)$$

The invariant matrix element iM_{fi} of Eq. 1.15 is a product of the current operator of the hadronic interaction O^μ and the photon polarisation operator ϵ_μ :

$$iM_{fi} = \bar{U}(p_f) \epsilon_\mu O^\mu U(p_i), \quad (1.16)$$

where $U(p_i)$ and $\bar{U}(p_f)$ are the Dirac spinors of the initial and final state nucleon, respectively. For photoproduction the invariant matrix element can be expressed in terms of four independent amplitudes:

$$iM_{fi} = \bar{U}_f(p_f) \sum_{j=1}^4 A_j(s, t, u, k^2) M_j U_i(p_i), \quad (1.17)$$

where the invariant amplitudes A_j contain the dynamics of the transition and the matrices M_j are given by:

$$\begin{aligned} M_1 &= -\frac{1}{2} \gamma_5 \gamma_\mu \gamma_\nu F^{\mu\nu} \\ M_2 &= +2\gamma_5 P_\mu \left(q_\nu - \frac{1}{2} k_\nu \right) F^{\mu\nu} \\ M_3 &= -\gamma_5 \gamma_\mu q_\nu F^{\mu\nu} \\ M_4 &= -2\gamma_5 \gamma_\mu P_\nu F^{\mu\nu} - 2M_N M_1 \end{aligned} \quad (1.18)$$

where $P^\mu = \frac{1}{2} (p_i + p_f)^\mu$, γ_5 are the Dirac matrices, and $F^{\mu\nu}$ is the electromagnetic field tensor:

$$F^{\mu\nu} = \epsilon^\mu k^\nu - \epsilon^\nu k^\mu. \quad (1.19)$$

Finally, the differential cross section can be deduced using the following equation [34]:

$$\frac{d\sigma}{d\Omega} = \frac{1}{2} \frac{q}{k} \sum_{spins} |M_{fi}|^2 = \frac{1}{2} \frac{q}{k} \text{Tr}(M^\dagger M). \quad (1.20)$$

CGLN Amplitudes

The matrix elements in Eq. 1.17 can be written in a two-component form by expressing the γ matrices and the Dirac spinors in terms of the two component spinors and Pauli matrices [32]:

$$U_{i,f}(p_{i,f}, s_{i,f}) = \sqrt{\frac{E_{i,f} + M_N}{2M_N}} \begin{pmatrix} 1 \\ \vec{\sigma} p_{i,f} \\ \hline E_{i,f} + M_N \end{pmatrix} \chi_{i,f}, \quad (1.21)$$

where $i, f = \pm \frac{1}{2}$ and

$$\chi_{+\frac{1}{2}} = \begin{pmatrix} 1 \\ 0 \end{pmatrix} \text{ and } \chi_{-\frac{1}{2}} = \begin{pmatrix} 0 \\ 1 \end{pmatrix}. \quad (1.22)$$

Thus, it follows that

$$M_{fi} = \frac{4\pi W}{M_N} \chi_f^\dagger \mathcal{F} \chi_i, \quad (1.23)$$

where $W = \sqrt{s}$ is the center of mass (cm) energy. A widely used form of \mathcal{F} is given by the Chew-Goldberger-Nambu-Low (CGNL) parametrisation for photoproduction [35]:

$$\mathcal{F} = iF_1 \cdot \vec{\sigma} \cdot \vec{\epsilon} + F_2(\vec{\sigma} \cdot \hat{q})(\vec{\sigma} \cdot (\hat{k} \times \vec{\epsilon})) + iF_3(\vec{\sigma} \cdot \hat{k})(\hat{q} \cdot \vec{\epsilon}) + iF_4(\vec{\sigma} \cdot \hat{q})(\hat{q} \cdot \vec{\epsilon}), \quad (1.24)$$

where \mathcal{F} is a two-dimensional matrix with the unity vectors $\hat{k} = \vec{k}/|\vec{k}|$ and $\hat{q} = \vec{q}/|\vec{q}|$, $\vec{\epsilon}$ is the polarisation vector of a real photon with helicity $\lambda_\gamma = \pm 1$, and $\vec{\sigma}$ are the nucleon's spin matrices. The four complex CGLN amplitudes, F_i , are the structure functions and depend on the cm energy W and θ is the polar angle of the meson in the cm system.

The CGLN amplitudes can be used to parametrise the differential cross section for an unpolarised target and beam [31]:

$$\begin{aligned} \frac{k}{q} \frac{d\sigma}{d\Omega} = & [|F_1|^2 + |F_2|^2 + \frac{1}{2}|F_3|^2 + \frac{1}{2}|F_4|^2 + \text{Re}(F_1 F_3^*)] \\ & + [\text{Re}(F_3 F_4^*) - 2\text{Re}(F_1 F_2^*)] \cos \theta \\ & - [\frac{1}{2}|F_3|^2 + \frac{1}{2}|F_4|^2 + \text{Re}(F_1 F_4^*) + \text{Re}(F_2 F_3^*)] \cos^2 \theta \\ & - [\text{Re}(F_3 F_4^*)] \cos^3 \theta. \end{aligned} \quad (1.25)$$

Furthermore, the CGLN amplitudes can be expanded in terms of derivatives of the Legendre polynomials for angular dependence $P'_l(\cos \theta)$ and $P''_l(\cos \theta)$ and the multipole amplitudes $M_{l\pm}$, $E_{l\pm}$ for energy dependence:

$$\begin{aligned} F_1(W, \theta) &= \sum_{l=0}^{\infty} [lM_{l+} + E_{l+}] P'_{l+1}(\cos \theta) + [(l+1)M_{l-} + E_{l-}] P'_{l-1}(\cos \theta) \\ F_2(W, \theta) &= \sum_{l=0}^{\infty} [(l+1)M_{l+} + lM_{l-}] P'_l(\cos \theta) \end{aligned} \quad (1.26)$$

$$F_3(W, \theta) = \sum_{l=0}^{\infty} [E_{l+} - M_{l+}] P''_{l+1}(\cos \theta) + [E_{l-} + M_{l-}] P''_{l-1}(\cos \theta)$$

$$F_4(W, \theta) = \sum_{l=0}^{\infty} [M_{l+} - E_{l+} - M_{l-} - E_{l-}] P''_{l-1}(\cos \theta) .$$

Hence, using the $E_{l\pm}$ and $M_{l\pm}$ from the multipole expansion, one gets direct access to the spin and parity information of the resonance. However, to determine the multipoles one has to measure the four complex amplitudes F_i and thus seven real numbers for all energies and angles (apart from an arbitrary phase).

Helicity Amplitudes

Another form of the matrix elements \mathcal{F} is the parametrisation in terms of the initial and final state helicities. The helicity λ is defined as projection of the spin \vec{s} onto the direction of the momentum \vec{p} :

$$\lambda = \frac{\vec{s} \cdot \vec{p}}{|\vec{p}|} \quad (1.27)$$

which implies a helicity $\lambda_\gamma = \pm 1$ for photons, $\nu_{i,f} = \pm 1/2$ for initial and final state nucleons and $\lambda_\eta = 0$ for pseudoscalar mesons. For the reaction given in Eq. 1.3, this yields $2 \times 2 \times 2 = 8$ matrix elements, $H_{\nu_f, \mu = \nu_i - \lambda_\gamma} = \langle \nu_f | T | \lambda_\gamma \nu_i \rangle$ where $\mu = \nu_i - \lambda_\gamma$ is convention. Considering parity conservation, only four complex amplitudes remain [31]:

$$H_1 = H_{+1/2, +3/2} = +H_{-1/2, -3/2} \quad H_2 = H_{+1/2, +1/2} = -H_{-1/2, -1/2} \quad (1.28)$$

$$H_3 = H_{-1/2, +3/2} = -H_{+1/2, -3/2} \quad H_4 = H_{+1/2, -1/2} = +H_{-1/2, +1/2}, \quad (1.29)$$

where H_2 is the non-spinflip amplitude, H_1 and H_4 are the single spin flip amplitudes, and H_3 is the double-spinflip amplitude.

The helicity amplitudes can be expanded in terms of the partial waves [34]:

$$H_1(\theta, \phi) = \frac{1}{\sqrt{2}} e^{i\phi} \sin \theta \cos \frac{\theta}{2} \sum_{l=0}^{\infty} [B_{l+} - B_{(l+1)-}] [P''_l(\cos \theta) - P''_{l+1}(\cos \theta)]$$

$$H_2(\theta, \phi) = \sqrt{2} \cos \frac{\theta}{2} \sum_{l=0}^{\infty} [A_{l+} - A_{(l+1)-}] [P'_l(\cos \theta) - P'_{l+1}(\cos \theta)] \quad (1.30)$$

$$H_3(\theta, \phi) = \frac{1}{\sqrt{2}} e^{2i\phi} \sin \theta \sin \frac{\theta}{2} \sum_{l=0}^{\infty} [B_{l+} - B_{(l+1)-}] [P''_l(\cos \theta) + P''_{l+1}(\cos \theta)]$$

$$H_4(\theta, \phi) = \sqrt{2} e^{i\phi} \sin \frac{\theta}{2} \sum_{l=0}^{\infty} [A_{l+} + A_{(l+1)-}] [P'_l(\cos \theta) - P'_{l+1}(\cos \theta)] .$$

The helicity elements $A_{l\pm}$ describe the transition from the γN initial state with helicity $1/2$ to the final state with total angular momentum $J = l \pm 1/2$ and meson relative orbital angular momentum l . $B_{l\pm}$ is the same for the helicity $3/2$ initial state.

In contrast to the coefficients of the CGLN amplitudes, which are the multipoles themselves, the helicity elements $A_{l\pm}$ and $B_{l\pm}$ contain different multipoles and thus

components of different resonances are seen in the following equations [31]:

$$\begin{aligned} A_{l+} &= \frac{1}{2}[(l+2)E_{l+} + lM_{l+}] & B_{l+} &= E_{l+} - M_{l+} \\ A_{(l+1)-} &= \frac{1}{2}[-lE_{(l+1)-} + (l+2)M_{(l+1)-}] & B_{(l+1)-} &= E_{(l+1)-} + M_{(l+1)-}. \end{aligned} \quad (1.31)$$

Helicity amplitudes are important, since they yield a direct connection to the electromagnetic couplings in the transition from γN to the resonance N^* , as seen in the following equations [31]:

$$\begin{aligned} A_{1/2} &= \sqrt{2\pi\alpha/k} \langle N^*, J_z = +\frac{1}{2} | J_{em} | N, S_z = -\frac{1}{2} \rangle \\ A_{3/2} &= \sqrt{2\pi\alpha/k} \langle N^*, J_z = +\frac{3}{2} | J_{em} | N, S_z = +\frac{1}{2} \rangle. \end{aligned} \quad (1.32)$$

Assuming a Breit-Wigner shape for the resonances, the following equations apply [31]:

$$\begin{aligned} A_{1/2} &= \mp(1/C_{Nm}) \sqrt{(2J+1)\pi} \frac{q}{k} \frac{M_R}{m_N} \frac{\Gamma_R^2}{\Gamma_m} \text{Im}[A_{l\pm}(W = M_R)] \\ A_{3/2} &= \pm(1/C_{Nm}) \sqrt{(2J+1)\pi} \frac{q}{k} \frac{M_R}{m_N} \frac{\Gamma_R^2}{\Gamma_m} \sqrt{(2J-1)(2J+3)/16} \text{Im}[B_{l\pm}(W = M_R)], \end{aligned} \quad (1.33)$$

where J is the spin of the resonance, M_R and Γ_R are resonance position and width, respectively, Γ_m is the partial width for the current decay channel, and C_{Nm} is the isospin Clebsch-Gordan coefficient for the decay of the resonance and is equal to -1 for η photoproduction. Eq. 1.33 implies that a nucleon resonance with spin $J = 1/2$ has only a $A_{1/2}$ electromagnetic coupling, whereas a $J = 3/2$ resonance has both a $A_{1/2}$ and a $A_{3/2}$ coupling.

A very simple parametrisation for the unpolarised cross section can be found with the following equation [34]:

$$\frac{d\sigma}{d\Omega} = \frac{1}{2} \frac{q}{k} \sum_{i=1}^4 |H_i|^2. \quad (1.34)$$

The cross section can be split into the two helicity components $1/2$ (anti-parallel photon and nucleon spin) and $3/2$ (parallel photon and nucleon spin), as seen in Fig. 1.8:

$$\frac{d\sigma_{1/2}}{d\Omega} \propto (|H_2|^2 + |H_4|^2) \quad (1.35)$$

and

$$\frac{d\sigma_{3/2}}{d\Omega} \propto (|H_1|^2 + |H_3|^2). \quad (1.36)$$

Thus, resonances with $J = 1/2$ are only visible in the $\sigma_{1/2}$ cross section, whereas $J = 3/2$ resonances contribute to both $\sigma_{1/2}$ and $\sigma_{3/2}$.

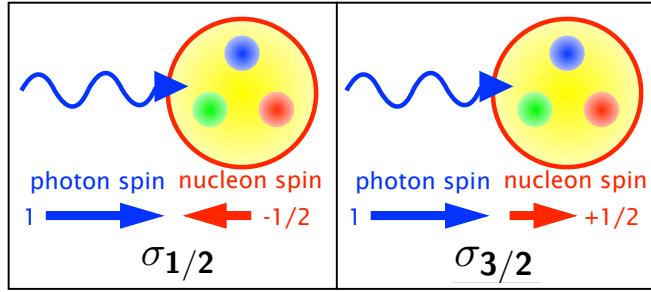


Figure 1.8: The two possible helicity states: $1/2$ state for anti-parallel alignment of photon and nucleon spin and $3/2$ state for parallel alignment.

Isospin Decomposition

A very important aspect has not yet been discussed, namely the isospin decomposition of the invariant amplitudes A_j in Eq. 1.17. As already mentioned in Section 1.1.1, only N^* ($I = 1/2$) resonances are allowed as intermediate states in η photoproduction since the isospin (total isospin I and third component I_3) is conserved in the strong interaction (hadronic vertex in Fig. 1.6), as seen in the following equation:

$$\langle I_f, I_{3f} | \mathcal{O}_S | I_i, I_{3i} \rangle = 0 \quad \text{if } I_f \neq I_i \text{ or } I_{3f} \neq I_{3i}. \quad (1.37)$$

Furthermore, the strong interaction is independent of the I_3 component (equal for proton and neutron). Thus, the following two matrix elements are equal:

$$\langle I, I_3 | \mathcal{O}_S | I, I_3 \rangle = \langle I, I'_3 | \mathcal{O}_S | I, I'_3 \rangle \quad (1.38)$$

On the contrary, in electromagnetic interaction, only the third component of the isospin I_3 is conserved and not the total isospin I . Thus, the interaction can depend on I_3 :

$$\mathcal{O}_{em} = \mathcal{S} + \mathcal{V}, \quad (1.39)$$

where S is the isoscalar ($\Delta I = 0$) component of the electromagnetic current and is independent of I_3 and V the isovector part $\Delta I = 0, \pm 1$ [31]. Hence, for the photoproduction of isovector ($I = 1$) mesons (π, ρ) off nucleons, this leads to three independent matrix elements in the notation $\langle I_f, I_{3f} | \hat{A} | I_i, I_{3i} \rangle$, where $| I_i, I_{3i} \rangle$ stands for the initial state γN system and $\langle I_f, I_{3f} |$ for the final state πN system [31]:

$$\begin{aligned} A_j^{IS} &= \langle \frac{1}{2}, \pm \frac{1}{2} | \hat{S} | \frac{1}{2}, \pm \frac{1}{2} \rangle \\ \mp A_j^{VS} &= \langle \frac{1}{2}, \pm \frac{1}{2} | \hat{V} | \frac{1}{2}, \pm \frac{1}{2} \rangle \\ A_j^{V3} &= \langle \frac{3}{2}, \pm \frac{1}{2} | \hat{V} | \frac{1}{2}, \pm \frac{1}{2} \rangle, \end{aligned} \quad (1.40)$$

which yields the following amplitudes for pion photoproduction:

$$\begin{aligned}
 A_j(\gamma p \rightarrow \pi^+ n) &= -\sqrt{\frac{1}{3}} A^{V3} + \sqrt{\frac{2}{3}} (A^{IV} - A^{IS}) \\
 A_j(\gamma p \rightarrow \pi^0 p) &= +\sqrt{\frac{2}{3}} A^{V3} + \sqrt{\frac{1}{3}} (A^{IV} - A^{IS}) \\
 A_j(\gamma n \rightarrow \pi^- p) &= +\sqrt{\frac{1}{3}} A^{V3} - \sqrt{\frac{2}{3}} (A^{IV} + A^{IS}) \\
 A_j(\gamma n \rightarrow \pi^0 n) &= +\sqrt{\frac{2}{3}} A^{V3} + \sqrt{\frac{1}{3}} (A^{IV} + A^{IS}) .
 \end{aligned} \tag{1.41}$$

For isoscalar ($I = 0$) mesons as the η meson, $V3$ ($\Delta I = 1$) cannot contribute and the amplitudes therefore are [31]:

$$A_j(\gamma p \rightarrow \eta p) = A_j^{IS} + A_j^{IV} \quad \text{and} \quad A_j(\gamma n \rightarrow \eta n) = A_j^{IS} - A_j^{IV}. \tag{1.42}$$

A direct consequence of the isospin amplitudes is that the coupling for the N resonances are different for protons and neutrons, but equal for Δ resonances. Taking into account the isospin and the helicity coupling, one can deduce the electromagnetic couplings for a resonance with isospin I and spin J , as seen in Table 1.3.

I	J	
	1/2	3/2
1/2 (N^*)	$A_{1/2}$ proton $A_{1/2}$ neutron	$A_{1/2}, A_{3/2}$ proton $A_{1/2}, A_{3/2}$ neutron
3/2 (Δ)	$A_{1/2}$	$A_{1/2}, A_{3/2}$

Table 1.3: Electromagnetic couplings for N^* and Δ resonances with spin $J = 1/2$ and $J = 3/2$.

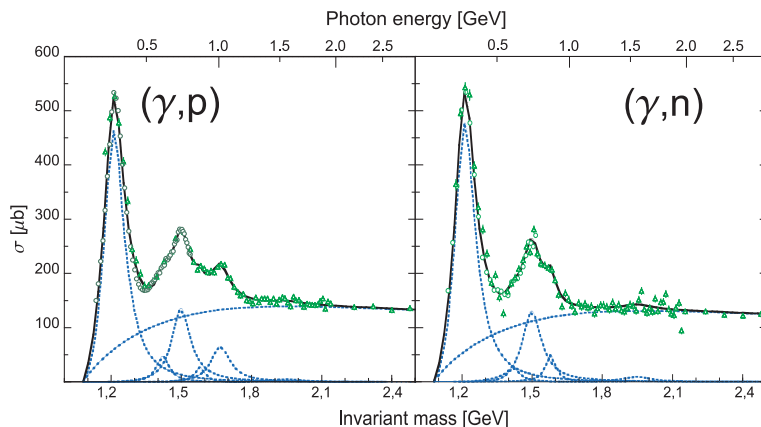


Figure 1.9: The electromagnetic excitation of the nucleon is isospin dependent, hence, different for proton (left) and neutron (right). Figure taken from [36].

1.3 Observables

As seen in Eq. 1.34, the cross section can be written as a sum of squares of the helicity amplitudes, with the latter further expanded in terms of multipoles. Therefore, the multipoles also appear as squares. For that reason, the cross section will be mainly affected by dominating multipoles and multipoles with small contributions will be suppressed. Hence, other observables that include interference terms would be more favourable. Besides the unpolarised cross section, additional observables can be measured when the photon, target, or recoil nucleon is polarised.

A real photon can be either circularly or linearly polarised. Circularly polarised photons consists of two plane waves that have the same amplitude, but have a 90° difference in phase. Thus, the electric field vector is rotating around the direction of travel. For linearly polarised photons, this electric field vector is confined in a plane and hence, is composed of only one plane wave. The target (such as proton or neutron) can be polarised in three different directions (x, y, z) as well as the recoil (such as proton or neutron) in x', y', z' , which can be seen in Fig. 1.10.

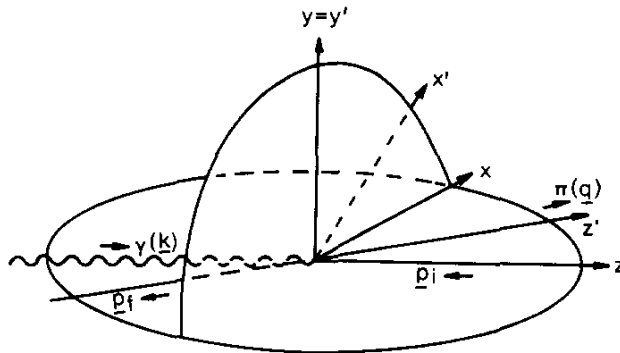


Figure 1.10: Coordinate system used for the definition of the polarisation observables: $z = k/|k|$, $y = k \times q/|k \times q|$, $x = y \times z$, $z' = q/|q|$, $y' = y$, $x' = y \times z'$ with the photon momentum k and the meson momentum q (in cm system). Figure taken from [37].

Thus, in total, $2 \times 3 \times 3 = 18$ double polarisation observables are theoretically possible. However, this number is reduced to only 12 observables since some combinations do not yield additional information. Together, with the S-type observables, one can measure 16 polarisation observables in total. S-type observables are the unpolarised cross section σ , the beam asymmetry Σ , the target asymmetry T , and the recoil polarisation P . The double polarisation observables can be divided into three groups of four observables and are given in Table 1.4 [37]:

Beam-Target (\mathcal{BT})	Beam-Recoil (\mathcal{BR})	Target-Recoil (\mathcal{TR})
G, H, E, F	O_x, O_z, C_x, C_z	T_x, T_z, L_x, L_z

Table 1.4: The double polarisation observables can be divided into three groups of four observables.

1.3. OBSERVABLES

The \mathcal{BT} observables require a polarised beam and target, the \mathcal{BR} observables a polarised beam and recoil nucleon, and the \mathcal{TR} observables a polarised target and polarised recoil nucleon. An overview of all observables and the required polarisation is given in Table 1.5.

photon		target			recoil			target + recoil			
		x	y	z	-	-	-	x	z	x	z
		-	-	-	x'	y'	z'	x'	x'	z'	z'
-	σ	-	T	-	-	P	-	$T_{x'}$	$-L_{x'}$	$T_{z'}$	$L_{z'}$
linearly	Σ	H	-P	-G	$O_{x'}$	-T	$O_{z'}$	-	-	-	-
circularly	-	F	-	-E	$-C_{x'}$	-	$-C_{z'}$	-	-	-	-

Table 1.5: Overview of the 16 polarisation observables.

The most general form of the cross section includes all polarisation observables and can be written as [38]:

$$d\sigma \propto \left(d\sigma_0 + \hat{\Sigma}[-P_L^\gamma \cos(2\phi)] + \hat{T}[P_y^T] + \hat{P}[P_{y'}^R] \right. \\ \left. + \hat{E}[-P_c^\gamma P_z^T] + \hat{G}[P_L^\gamma P_z^T \sin(2\phi)] + \hat{F}[P_c^\gamma P_x^T] + \hat{H}[P_L^\gamma P_x^T \sin(2\phi)] \right. \\ \left. + \hat{C}_{x'}[P_c^\gamma P_{x'}^R] + \hat{C}_{z'}[P_c^\gamma P_{z'}^R] + \hat{O}_{x'}[P_L^\gamma P_{x'}^R \sin(2\phi)] + \hat{O}_{z'}[P_L^\gamma P_{z'}^R \sin(2\phi)] \right. \\ \left. + \hat{L}_{x'}[P_z^T P_{x'}^R] + \hat{L}_{z'}[P_z^T P_{z'}^R] + \hat{T}_{x'}[P_x^T P_{x'}^R] + \hat{T}_{z'}[P_x^T P_{z'}^R] \right) , \quad (1.43)$$

where P^T and P^R are the degree and direction of the target and recoil polarisation, respectively, defined in the coordinate frame of Fig. 1.10, P_c^γ is the degree and direction of circular photon polarisation, P_L^γ is the degree of linear photon polarisation, ϕ is the angle of the transverse polarisation with respect to the reaction plane, and σ_0 is the integrated cross section over all initial state polarisations and then summed over all final state polarisations [38]. In this notation the hat indicates that not the asymmetries themselves, but the product of them with σ_0 , the profile function $\hat{A} = A\sigma_0$, have been used.

As can be seen in Appendix B.1, each asymmetry also has contributions from higher order terms, e.g. including recoil polarisations that do not appear here since those degrees of freedom were not measured in this work. Thus, it is generally possible to measure all single polarisation observables in a double polarisation setting and all double polarisation observables in a triple polarisation setting. However, this yields no additional information and therefore is not further discussed here.

For this work, only the unpolarised cross section $d\sigma_{unpol}$ and the double polarisation observable E are of interest. The double polarisation observable E is accessed via a longitudinally polarised target and a circularly polarised beam. Hence, the \mathcal{BT} part of Eq. 1.43 can be reduced to [37]:

$$d\sigma = d\sigma_{unpol} \cdot [1 - P_c^\gamma P_z^T E] . \quad (1.44)$$

The double polarisation observable E is a helicity dependent asymmetry and can be

described as:

$$E = \frac{\sigma_{1/2} - \sigma_{3/2}}{\sigma_{1/2} + \sigma_{3/2}}, \quad (1.45)$$

where $\sigma_{3/2}$ is the helicity dependent cross section for the parallel configuration of photon and nucleon spin and $\sigma_{1/2}$ the cross section for anti-parallel photon and nucleon spin. Using Eq. 1.35 and Eq. 1.36, one can find the representation of E in terms of the helicity amplitudes [37]:

$$\hat{E} = \frac{1}{2} (-|H_1|^2 + |H_2|^2 - |H_3|^2 + |H_4|^2). \quad (1.46)$$

The parametrisation of E using the CGLN representation is [38]:

$$\hat{E} = \Re e \{ F_1^* F_1 + F_2^* F_2 - 2 \cos \theta F_1^* F_2 + \sin^2 \theta (F_2^* F_3 + F_1^* F_4) \} \rho, \quad (1.47)$$

where $\rho = q/k$ is the phase space factor.

1.3.1 The Complete Experiment

As mentioned in the Section 1.2.3, to determine the four complex amplitudes one has to measure seven real values as a function of two kinematical variables (W and θ), neglecting the overall phase. The definition of the number of required observables to find the four complex amplitudes is not straightforward since ambiguities have to be avoided.

The discussion about how one can determine the amplitudes from a complete set of experiments started already in the 1970s. In their paper on *Complete Experiments in Pseudoscalar Photoproduction*, Barker, Donnachie and Starrow [37] stated that one can unambiguously determine all amplitudes by measuring five double polarisation observables and all four S-type observables, on a condition that less than four double polarisation observables are of the same group \mathcal{BT} , \mathcal{BR} , \mathcal{TR} , known as the BDS-rule. However, Keaton and Workman [39] showed that the BDS rule is not sufficient to reject all ambiguities, but did not provide updated conditions for a complete experiment. The paper by Chiang and Tabakin [40] states that in general, measuring the four S-type observables yields the magnitude of the amplitudes. When in addition three double polarisation observables are measured, the relative phases between the amplitudes can be determined. However, ambiguities remain since the observables are non-linearly dependent of each other. Thus, Chiang and Tabakin suggested that eight appropriately selected observables (instead of nine according to the BDS rule) are necessary where the eight measurements include the four S-type observables and four carefully chosen double polarisation observables. The selection rules are very complicated and an overview of the possible complete sets of observables is given in Appendix B.2. Furthermore, since the electromagnetic excitation is isospin dependent, the eight observables have to be measured as a function of the energy for both proton and neutron targets.

1.3.2 Extraction of Resonance Parameters

Having a complete set of observables (eight according to Chiang and Tabakin [40]), a partial wave analysis (PWA) can be performed, i.e. the observable can be decomposed into the partial waves, where the multipoles $E_{l\pm}$ and $M_{l\pm}$ contain contributions from resonant and background terms (see Fig. 1.7). In a second step, the resonant contributions can be extracted by parametrising the resonant and background terms. Usually, the resonance terms are modelled by relativistic Breit-Wigner curves [6]:

$$A = \frac{\Gamma_R W_R}{W_R^2 - W^2 - iW_R \cdot \Gamma_R}, \quad (1.48)$$

where W_R is the resonance position, Γ_R is its width, and W is the cm energy. Alternatively, one can use the non-relativistic version:

$$A = \frac{\Gamma_R/2}{W_R^2 - W - i \cdot \Gamma_R/2}. \quad (1.49)$$

The resonance parameters are then found by fitting the resonance parametrisations to the partial waves.

In contrast to the proper PWA, Isobar models parametrise the resonant and background terms in the multipoles already in the beginning by Breit-Wigner distributions and Lagrangians, respectively. These parametrisations are then directly fitted to the data. The less complete an experiment is, the more assumptions have to be put into the parametrisation.

The most common PWA for η photoproduction, SAID [41], and the two Isobar models MAID [42], and Bonn-Gatchina (BnGa) [43] shall be described now.

SAID

SAID (*Scattering Analysis Interactive Dial-in*) was developed by the CNS Data Analysis Centre at the George Washington University in Washington DC, USA. It is a database for πN scattering, and electro- and photoproduction data, and provides multipoles from PWA. For η photoproduction, the information available from SAID is very limited. Differential cross sections and data for the polarisation observable E are only available for the proton target. Their results on η photoproduction for the proton are based on a coupled-channel fit to pion-nucleon and η nucleon data, more information can be found in Ref. [44].

MAID

The Mainz Isobar model (MAID) [42], developed at the Johannes Gutenberg Universität in Mainz, Germany, uses differential photoproduction cross sections from MAMI, GRAAL and Jefferson Lab (JLab) data. The non-resonant background Born and vector meson exchange terms are constructed using effective Lagrangians. Resonances are parametrised as energy dependent Breit-Wigner shapes. N^* resonance contributions

from $D_{13}(1520)$, $S_{11}(1650)$, $D_{15}(1675)$, $F_{15}(1680)$, $D_{13}(1700)$, $P_{11}(1710)$, and $P_{13}(1720)$ are considered. Besides the standard η -MAID model (t -channel exchanges are described by ρ and ω poles) [33], a Reggeized η MAID model exists [45, 46], in which the vector meson exchanges are modelled by Regge trajectories. This model leads to better results at higher energies than the standard η MAID. The MAID model provides data for differential cross sections as well as for the double polarisation observable E on proton and neutron targets.

Bonn-Gatchina

The Bonn-Gatchina model (BnGa) [43], developed at the Rheinische Friedrich-Wilhelms-Universität Bonn, Germany, and the Petersburg Nuclear Physics Institute in Gatchina, Russia, is a coupled channel analysis. The model is fitted simultaneously to all available data of baryon spectroscopy, including πN scattering and photoproduction experiment of various final states (single and multi-meson final states). Unpolarised cross sections and polarisation observables as a function of energy and angle are considered in their analysis. The BnGa PWA uses a K-matrix approach at low energies and relativistic multi-channel Breit-Wigner amplitudes at high energies to parametrise the resonances. Non-resonant reggeized t - and u - channel amplitudes have been added to the resonant amplitudes [47]. The BnGa models for the differential cross sections and the double polarisation observable E are used to compare to the current experimental results. For this purpose, the most recent published BnGa model, as given in Ref. [48], was used.

1.4 Current Experimental Data

Thanks to an extensive investigation of the excitation spectrum of the nucleon in the past years via photoproduction experiments, the number of the resonances has increased significantly. The current status of the N^* ($I = 1/2$) resonances is shown in Table 1.6 (the $I = 3/2$ Δ -resonances are not shown here since they cannot contribute to η photoproduction). The PDG star-rating indicates how well a certain resonance is established. One star stands for poor evidence of the resonance and four stars stands for a well-established resonance. Many of the listed resonances are three or four star resonances due to new photoproduction data on differential cross sections and polarisation observables. However, one resonance is more noteworthy, the new tentative resonance $N(1685)$ (red marked line in Table 1.6), which is the main motivation for this work. The listing of this speculative state is based on experimental results by Kuznetsov *et al.* [49, 50], Jaegle *et al.* [51], and Werthmüller *et. al.* [52]. A part of the results of this work was published in the latter publication. All these studies have reported a narrow structure at a cm energy of approximately 1.68 GeV in the cross section of the neutron, which is not visible in the cross section of the proton.

1.4. CURRENT EXPERIMENTAL DATA

Particle	J^P	Status			Status as seen in —						
		overall	πN	γN	$N\eta$	$N\sigma$	$N\omega$	ΛK	ΣK	$N\rho$	$\Delta\pi$
N	$1/2^+$	****									
$N(1440)$	$1/2^+$	****	****	****	***				*	***	
$N(1520)$	$3/2^-$	****	****	****	***				***	***	
$N(1535)$	$1/2^-$	****	****	****	****				**	*	
$N(1650)$	$1/2^-$	****	****	***	***			***	**	**	***
$N(1675)$	$5/2^-$	****	****	***	*		*		*	***	
$N(1680)$	$5/2^+$	****	****	****	*	**			***	***	
$N(1685)$?	*									
$N(1700)$	$3/2^-$	***	***	**	*			*	*	*	***
$N(1710)$	$1/2^+$	***	***	***	***	**	***	**	*	**	
$N(1720)$	$3/2^+$	****	****	***	***		**	**	**	*	
$N(1860)$	$5/2^+$	**	**						*	*	
$N(1875)$	$3/2^-$	***	*	***		**	***	**		***	
$N(1880)$	$1/2^+$	**	*	*		**		*			
$N(1895)$	$1/2^-$	**	*	**	**		**	*			
$N(1900)$	$3/2^+$	***	**	***	**	**	***	**	*	**	
$N(1990)$	$7/2^+$	**	**	**					*		
$N(2000)$	$5/2^+$	**	*	**	**		**	*	**		
$N(2040)$	$3/2^+$	*									
$N(2060)$	$5/2^-$	**	**	**	*				**		
$N(2100)$	$1/2^+$	*									
$N(2150)$	$3/2^-$	**	**	**			**			**	
$N(2190)$	$7/2^-$	****	****	***		*	**		*		
$N(2220)$	$9/2^+$	****	****								
$N(2250)$	$9/2^-$	****	****								
$N(2600)$	$11/2^-$	***	***								
$N(2700)$	$13/2^+$	**	**								

**** Existence is certain, and properties are at least fairly well explored.

*** Existence is very likely but further confirmation of quantum numbers and branching fractions is required.

** Evidence of existence is only fair.

* Evidence of existence is poor.

Table 1.6: Overview of the status of the N^* ($I = 1/2$) resonances. The tentative $N(1685)$ resonance is marked red, which this work is based on. Table taken from [6].

1.4.1 Narrow Structure on the Neutron

A narrow structure was first observed by the GRAAL Collaboration in η photoproduction on the quasi-free neutron bound in deuterium [49]. The $\eta \rightarrow 2\gamma$ decay was detected in coincidence with recoil nucleons. The setup consisted of a bismuth germanate (BGO) ball ($25^\circ \leq \theta \leq 155^\circ$) and a time of-flight (TOF) hodoscope wall

($\theta \leq 23^\circ$). Charged particles were rejected with plastic scintillators and two cylindrical multi-wire proportional chambers (MWPC). A clean identification was achieved by an invariant mass analysis and subsequent kinematical cuts. Cross sections have been determined as a function of the initial state energy and thus are smeared out by Fermi motion. The results are shown in Fig. 1.11 (a). The position of the structure in the neutron cross sections was determined to be 1.68 GeV (no error was given). The corresponding width was comparable to the experimental resolution and was estimated to be $\Gamma \leq 30$ MeV. Also by the GRAAL Collaboration, a similar behaviour was later observed in quasi-free Compton scattering on the neutron [50]. The extracted

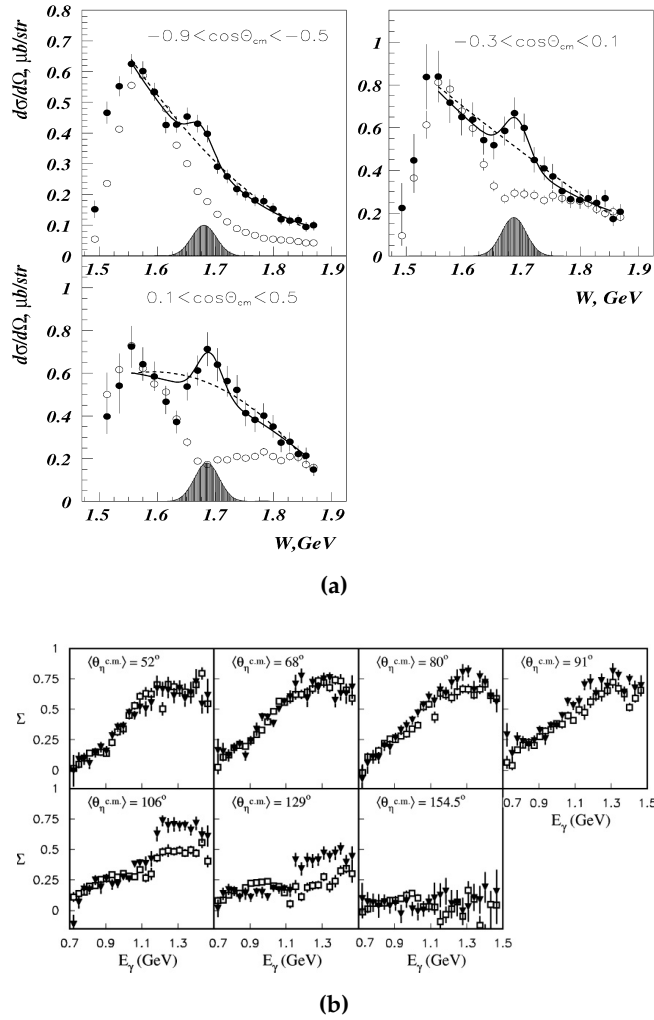


Figure 1.11: (a) Narrow structure observed in η photoproduction on the neutron. Cross section for different angular bins for the quasi-free proton (open circles) and neutron (filled circles) target obtained by the GRAAL collaboration. The distribution was fitted with a polynomial of third order and a Breit-Wigner line shape. [49] (b) GRAAL beam asymmetry Σ for η photoproduction on the proton (open circles) and neutron (filled circles). Proton and neutron data start to deviate at $E_\gamma \sim 1.05$ GeV for backward angles. Figure taken from [53].

1.4. CURRENT EXPERIMENTAL DATA

position and width of the structure $W = (1686 \pm 7_{\text{stat}} \pm 5_{\text{sys}})$ MeV and $\Gamma \simeq (28 \pm 12)$ MeV are in agreement with the results from η photoproduction. However, this analysis is more challenging, since the reaction is dominated by π^0 background. GRAAL has also published first results on the beam asymmetry Σ for η photoproduction on the neutron [53]. The beam asymmetry Σ is interesting, since it contains interference terms of multipoles and thus can enhance weak resonances. The results are shown in Fig. 1.11 (b). The asymmetries for proton and neutron look similar up to energies of $E_\gamma = 1.05$ GeV. At backward angles, the distributions on the neutron show a rapid rise at a cm energy of $W = 1.715$ GeV. Model calculations could not correctly describe this behaviour.

Further evidence for a narrow structure in η photoproduction was found at LNS in Sendai [54]. Their detector setup consisted of four blocks of 74 caesium iodide (CsI) crystals each, two blocks in the forward direction ($15^\circ \leq \phi \leq 72^\circ$ and $17^\circ \leq \phi \leq 77^\circ$) and two blocks in the backward direction ($95^\circ \leq \phi \leq 125^\circ$ and $-12^\circ \leq \phi \leq 12^\circ$). Charged particles have been identified with 5 mm thick plastic scintillators mounted in front of the crystals. The η meson was reconstructed from two decay photons via an invariant mass analysis. In contrast to GRAAL, an inclusive measurement was performed and the neutron cross section was determined by subtracting the Fermi-folded η MAID predictions [33] for the proton from the inclusive measurement ($\sigma_n = \sigma_{\text{incl}} - \sigma_p$). The parameters of the narrow structure on the neutron have been extracted by fitting a Breit-Wigner function to the data. A position of $W = (1666 \pm 5)$ MeV and a width of $\Gamma \leq 40$ MeV were found. Hence, these results are in agreement with the previous observations by the GRAAL Collaboration.

In 2011, the CBELSA/TAPS collaboration published η photoproduction cross sec-

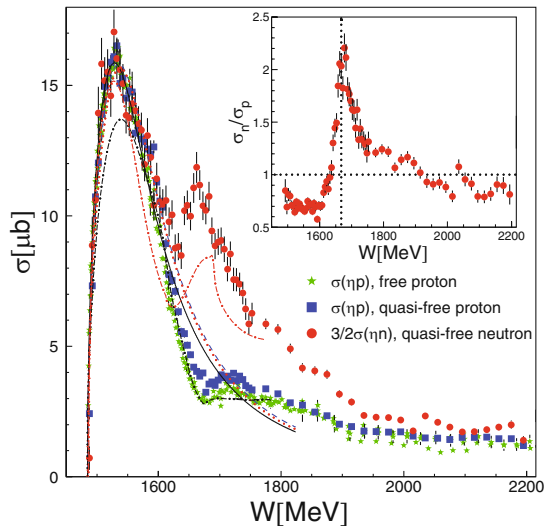


Figure 1.12: Total cross section for η photoproduction on the neutron as a function of the final state energy W for the quasi-free proton (blue) and neutron (red) by the CBELSA/TAPS collaboration. The cross section ratio of neutron and proton shows a steep rise around 1.68 GeV. Figure taken from [51].

tions [51] that exhibit an analogous behaviour as seen by the other experiments. This time, the $\eta \rightarrow 3\pi^0 \rightarrow 6\gamma$ channel was analysed. The decay photons have been detected in coincidence with recoil protons and neutrons.

The settings were similar to the ones used for this work as the detector setup provided an angular coverage of almost 4π steradian. The cm energy was reconstructed from the final state by determining the energy of the recoil nucleon via a kinematical reconstruction or via a TOF measurement. The latter restricted the cross sections to $\cos\theta > -0.1$, but allowed to see the narrow structure without the effects of Fermi motion. A combined fit of two Breit-Wigner functions yielded $W = 1683$ MeV and $\Gamma = (60 \pm 20)$ as parameters for the narrow state. The results for the total cross section are shown in Fig. 1.12. In addition, angular distribution have been extracted, but are not shown here.

Parallel to the analysis done for this work, η photoproduction experiments for protons and neutrons bound in deuterium have been performed by the A2 Collaboration at MAMI [55, 56]. The same setup as for this work and an analogous analysis have been used to extract high statistics data of differential and total cross sections as a function of the final state energy. The cross sections for different $\cos\theta_\eta^*$ (polar angle of η meson in cm frame) bins are shown in Fig. 1.13. The narrow structure is visible on a wide angular range, but disappears at very forward and backward angles.

In summary, all experimental results on this narrow structure in η photoproduction on the neutron are in reasonable agreement. The structure has unusual properties for a nucleon resonance, for example, the width is only about 30 MeV, which is very small compared to the $S_{11}(1535)$ resonance ($\Gamma \sim 125$ MeV [6]).

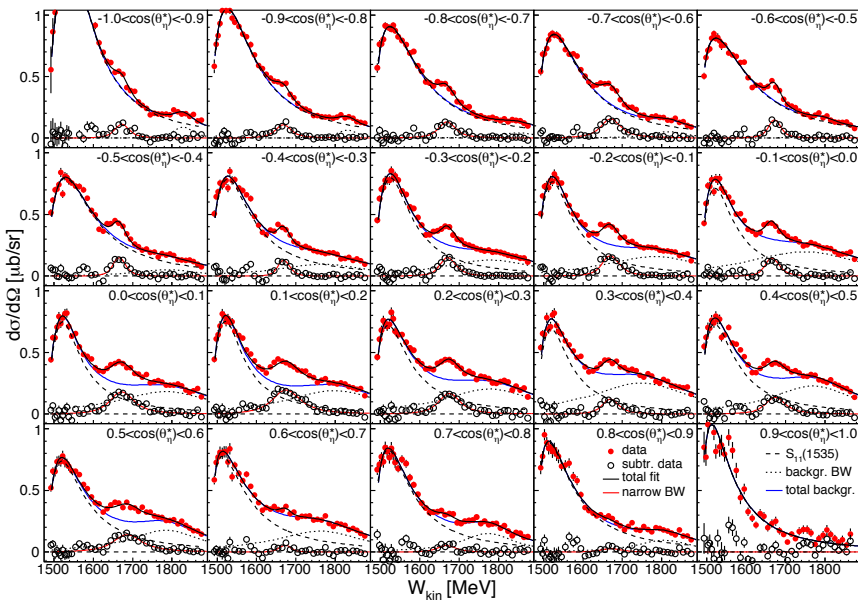


Figure 1.13: High statistics η photoproduction cross sections on the neutron by the A2 Collaboration. The results are shown for different angular ranges and a Breit-Wigner fit is indicated. The narrow structure is nicely visible, but vanishes at very forward and backward angles. Figure taken from [55].

Theoretical Explanations

Various theoretical explanations exist that claim to be able to describe the observed narrow structure on the neutron, which is not visible on the proton. They can be divided into three groups: effects by known resonances, coupled channel effects, and the existence of a new narrow resonance. An overview of the most interesting model descriptions shall now be given.

1. Effects by known resonances:

- η -MAID (Chiang *et al.* [33]): the MAID model (explained in Sec. 1.3.2) describes the narrow structure in the cross section on the neutron by a large contribution of the $D_{15}(1675)$ resonance. This state is Moorhouse suppressed [57] on the proton, and thus only visible on the neutron. The Moorhouse selection rule states that "...transition amplitudes for γp to all resonances of representation [70, 48], such as $D_{15}(1675)$, must be zero due to the vanishing transition matrix element for the charge operator." [58]. On the neutron, such resonances can contribute. However, this prediction yields an unexpected large value for the branching ratio to ηN for this state $\Gamma_{\eta N}/\Gamma_{tot} \sim 17\%$, while the PDG value is almost zero.
- Giessen Model (Shklyar *et al.* [59]): the Giessen model is a coupled channel effective Lagrangian approach and uses πN and γN data, including the preliminary CBELSA/TAPS results on η photoproduction on the neutron [51]. Their model explains the bump structure on the neutron by the contributions of the $S_{11}(1650)$ and $P_{11}(1710)$ resonances. The resulting differential cross sections show a rise at backward angles. Furthermore, they showed that the shape of the cross section in the region of the narrow structure is extremely sensitive to variations in the electromagnetic coupling $A_{1/2}$.
- Chiral quark model (Zhong *et al.* [60]): the chiral quark model uses an effective chiral Lagrangian to describe the quark-pseudoscalar-meson coupling. The two major features of this model are that it requires only one parameter to couple all resonances to the pseudoscalar mesons and it treats all resonances equally. Their analysis includes six resonances, the $S_{11}(1535)$, $S_{11}(1650)$, $D_{13}(1520)$, $D_{13}(1700)$, $D_{15}(1675)$ and $P_{13}(1720)$. The chiral quark model yields a good description of the differential cross sections, total cross sections, and the beam asymmetry. The bump structure on the neutron is explained by a constructive interference between the $S_{11}(1535)$ and the $S_{11}(1650)$ resonances. On the contrary, a destructive interference between the latter two produces a dip on the proton at $W \sim 1.68$ GeV. In addition, they found that the u -channel contribution is not negligible and the $D_{13}(1520)$ resonance is very important, since it is responsible for the deviations from an s -wave in the differential cross sections.
- BnGA (Anisovich *et al.* [48, 61]): the basic properties of the BnGa model are mentioned in Section 1.3.2. Similar to the Giessen model, their newest

fit shows that the bump structure on the neutron can be explained by an interference between the $S_{11}(1535)$ and the $S_{11}(1650)$ resonances. However, it introduces a sign change of the electromagnetic $A_{1/2}$ helicity coupling of the $S_{11}(1650)$ resonance with respect to the current PDG value ($A_{1/2}^n = (-0.050 \pm 0.020) \text{ GeV}^{-1/2}$ [6]) and previous fits. Their fitted value is $A_{1/2}^n = (0.019 \pm 0.006) \text{ GeV}^{-1/2}$. Introducing a new narrow spin- $1/2$ $N(1685)$ resonance drastically decreased the quality of the fit.

2. Coupled channel effects:

- *s*-wave model (Döring *et al.* [62]): The *s*-wave model was developed for the simultaneous description of pion-photoproduction and πN scattering. ηN , $K\Lambda$ and $K\Sigma$ final states have been included as coupled channels. This model describes the narrow structure as a result of intermediate strangeness states. The absence of this structure on the proton is explained by the presence of πN , $K\Sigma$, and $K^+\Lambda$ intermediate states. The latter are only existent in the reaction on the proton and their contribution cancels with the first two (π^+n and $K^+\Sigma^0$). For more details of this model, see Ref. [62].

3. New narrow resonance:

- Chiral quark soliton model (χ QSM) (Diakonov *et al.* [63–66]): The chiral symmetry breaking in QCD implies that quarks interact with the light Goldstone-mesons, the pions, and thus produce chiral fields. In χ QSM, baryons are seen as solitons of this chiral fields. *"Different baryons are realized by different (quantized) rotational excitations of the same classical soliton. ... A baryon in the χ QSM is a bound state (by the chiral mean-field) of three constituent quarks put on the valence level together with the whole constituent quark Dirac-sea. The presence of the chiral-field distorts the Dirac-sea producing additional $q\bar{q}$ pairs..."* [67] χ QSM not only predicts the known baryon octet and decuplet, but also suggests the higher lying exotic baryon antidecuplet (see Fig. A.4). It is exotic, because it contains members with strangeness $S = +1$. The latter can only be explained by assuming bound states of five quarks, i.e. pentaquarks. The non-strange member N of the baryon antidecuplet was first related to the $J^p = 1/2^+$ $N(1710)$ [63] and later by other calculations to the $N(1680)$ or $N(1730)$ or by a mixed state of the two [64]. Furthermore, it was shown that the photoexcitation of the non-exotic members of the baryon antidecuplet is strongly suppressed for protons [65]. Even more, the members of the antidecuplet are thought to be very narrow states. Hence, the structure in η photoproduction on the neutron exhibits all the properties predicted for the baryon antidecuplet N by the χ QSM.
- Reggeized η -MAID (Fix *et al.* [46]): This model was already shortly described in Sec. 1.3.2. The model Reggeized η -MAID was fit to the preliminary CBELSA/ TAPS results on η photoproduction on the neutron [51]. In

addition to the standard MAID model, it contains a new narrow $P_{11}(1670)$ to explain the narrow structure on the neutron.

1.4.2 Double Polarisation Observable E

Experimental results for the double polarisation observable E for η photoproduction from the neutron are not yet available. Results for the free proton have been recently published [68]. The data stems from a measurement with the CEBAF Large Acceptance Spectrometer (CLAS) in Hall B at JLab. Charged particles were tracked with drift chamber systems and matched to hits in a scintillator-based time-of-flight system and a start counter array. A frozen butanol (C_4H_9OH) target with an average polarisation of $(84 \pm 1)\%$ was used. The electron polarisation was measured with a Møller polarimeter and was $(82 \pm 5)\%$.

Since CLAS is specialised for the detection of charged particles the $\gamma p \rightarrow \eta p$ reaction was identified by the detection of the recoil proton and a subsequent missing mass reconstruction of the neutral η meson. The decay of the η into $\pi^+ \pi^- \pi^0$ was identified by detecting at least one of the two charged pions. The background was reduced by fits in the missing mass spectra.

The double polarisation observable E was extracted for energies from threshold up to $W = 2.1$ GeV for a wide angular range. The resulting asymmetry is shown in Fig. 1.14. At low energies, the determined asymmetry is unity within the given uncertainties. This is expected from the dominance of the $S_{11}(1535)$ resonance. At higher energies, additional resonance contributions introduce a W -dependent modulation of E . The results are compared to fits obtained by the SAID [69], the ANL-Osaka [69], and the Jülich [70] groups. The inclusion of the new CLAS data into the Jülich model induces quite significant changes, as seen in Fig. 1.14. The fit shows that the structure around $W \sim 1.7$ GeV and $\cos \theta_{cm} = 0.2$ can be explained by the interference of an E_0^+ and a M_1^+ multipole from the $N(1650)^{1/2-}$ and $N(1720)^{3/2+}$ resonances. Together with a slowly varying E_2^- multipole, the experimental data can be described without requiring a narrow resonance at $W = 1.68$ GeV.

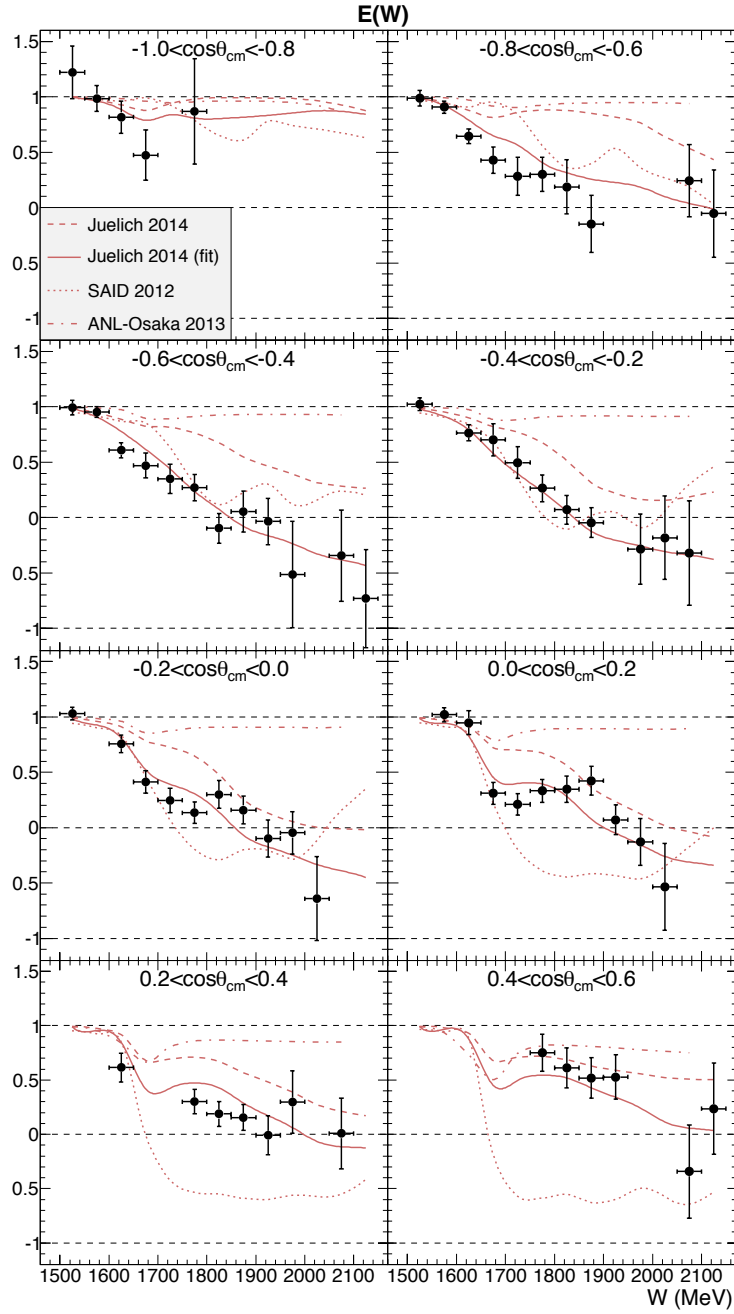


Figure 1.14: Double polarisation observable E for the free proton for various angular ranges obtained with the CLAS setup at JLab. The lines indicate different phenomenological fits. Figure taken from [68].

Chapter 2

Experimental Setup

As previously mentioned, the subject of this work was to determine unpolarised cross sections and the double polarisation observable E for η photoproduction on quasi-free protons and neutrons. To collect the data for this analysis, experiments were carried out at two different acceleration facilities in Germany, the Electron Stretcher Accelerator (ELSA) in Bonn and the Mainzer Microtron (MAMI) in Mainz. The corresponding experiments are called CBELSA/TAPS (Bonn) and A2 (Mainz). Both are fixed target experiments and use electron beams to produce real photons for the purpose of photoproduction experiments. Data were taken using a circularly polarised photon beam in combination with an unpolarised or longitudinally polarised target. The two different acceleration facilities, as well as the experimental setups are explained in the next sections in detail.

2.1 Acceleration Facilities

2.1.1 MAMI

MAMI is operated at the Institut für Kernphysik at the Johannes Gutenberg Universität Mainz, and provides a high-duty continuous wave (cw) electron beam with beam currents up to $100 \mu\text{A}$ (unpolarised electrons). Electron energies of up to 1.6 GeV can be reached by a series of different sub-accelerator systems. An overview of the acceleration facility is given in Fig. 2.1.

Production of the Electron Beam

MAMI has two different electron guns to produce either polarised or unpolarised electrons. The unpolarised electrons are generated with a thermionic electron gun, EKAN, by releasing electrons from the surface of a hot cathode. Longitudinally polarised electrons are generated by the optical pumping of a gallium arsenide phosphor (GaAsP) semiconductor with a pulsed titanium sapphire laser. The optical pumping requires circularly polarised light. Thus, the linearly polarised laser light is converted to circularly polarised light by the use of a quarter-wave plate. A quarter-wave plate is a birefringent material (different index of refraction for different light orientations),

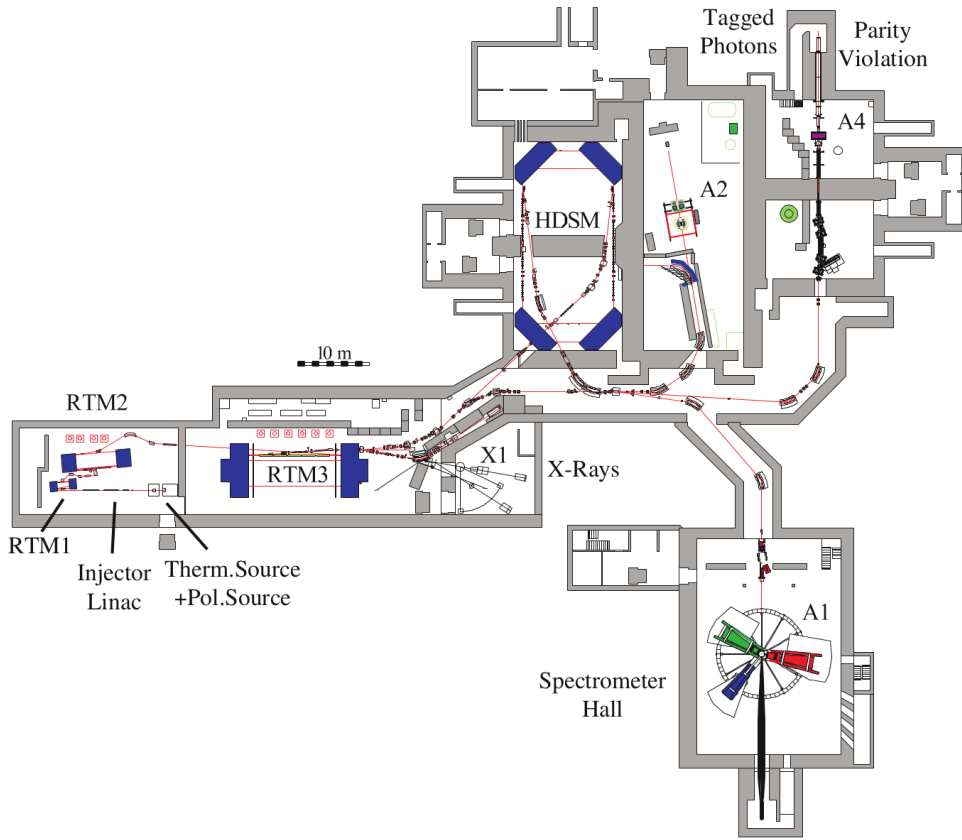


Figure 2.1: Floorplan of MAMI. Shown are the different sub-acceleration systems, linac, RTM1 to RTM3 and the HDSM. The different experimental halls X1, A1, A4 and A2 are indicated. The latter is used to perform the photoproduction experiments used for this work. The A1 collaboration is specialised in electron scattering experiments, A4 in parity violating experiments, and X1 focusses on the development of brilliant novel radiation sources. Figure taken from [71].

which shifts the phase by 90° with respect to the light transmitted perpendicular to it. When the quarter-wave plate has an angle of 45° with respect to the optical axis, the amplitude of transmitted perpendicular and parallel light is equal, resulting in circular polarisation. A Pockels cell is used as birefringent material, which allows the beam helicity to be switched by flipping the voltage polarity. The beam helicity is flipped with a frequency of 1 Hz. For the current data, an electron polarisation degree of approximately 80 percent was achieved. [72–74]

Acceleration of the Electron Beam

The acceleration of electrons with MAMI is a five-step process. The injector linear accelerator (linac) accelerates the electrons from the gun up to 3.97 MeV and then injects them into the first of three Racetrack Microtrons (RTM1 to RTM3, bottom left of Fig. 2.1), where they reach an energy of 14.86 MeV. A RTM is a microtron, which is comprised of two D-shaped magnets and one linac. The uniform field in the dipole

2.1. ACCELERATION FACILITIES

magnets deflect the electrons by 180° . The linacs of the RTMs have radio-frequency (rf) cavities of 2.45 GHz to accelerate the electrons. The *MAMI-B* acceleration part is completed by the RTM3 with an energy of 855 MeV. In 2006, MAMI was upgraded with the harmonic double sided microtron (HDSM, top middle of Fig. 2.1), reaching its final energy of 1.6 GeV in the *MAMI-C* stage. The HDSM has two linacs and in total four 90° bending magnets. Compared to the RTM setup, the magnet size in the HDSM setup can be drastically reduced due to the smaller bending angle and the two linacs.

Whereas the acceleration of unpolarised electrons is straightforward, the acceleration of longitudinally polarised electrons reveals some challenges. In the MAMI acceleration subsystems, the magnetic fields used to guide the beam are perpendicular and the accelerating electric fields are parallel to the direction of the motion of the electrons. According to the Thomas-BMT equation [75], spin precession occurs with a frequency [76]:

$$\omega_s = (1 + a\gamma)/\omega_c, \quad (2.1)$$

where $a = (g - 2)/2$ is the anomalous magnetic moment of the electron, $\gamma = (1 + T)/m$ with the kinetic energy T and mass m of the electron, and ω_c is the cyclotron frequency. Hence, to ensure that the polarisation of the electrons is purely longitudinal on the bremsstrahlung target in the A2 hall, a spin rotator (Wien filter) was installed in the injection beam line. All other possible depolarising effects are negligible at MAMI. [74, 76]

2.1.2 ELSA

The ELSA electron accelerator is located at the Physics Institute of the Rheinische Friedrich-Wilhelms-Universität in Bonn. ELSA uses three acceleration stages to reach a final beam energy of 3.5 GeV: the injector linear accelerators (linac1 and linac2), the booster synchrotron, and the stretcher ring, as seen Fig. 2.2.

Production of the Electron Beam

Similar to MAMI, ELSA has a polarised and an unpolarised electron source. As at MAMI, the longitudinally polarised electrons are produced by striking a GaAs photocathode with circularly polarised laser light. The production of polarised electron for ELSA is explained in detail in Ref. [78].

Acceleration of the Electron Beam

Having generated the electrons with one of the two electron guns, the electrons are accelerated with a linac up to 26 MeV and then injected into the booster synchrotron where they reach an energy of 1.6 GeV. The last step is the stretcher ring, which can be used in three different ways to generate energies of up to a maximum of 3.5 GeV:

- Pure stretcher mode: the pre-accelerated electrons from the booster ring are injected into the stretcher ring with a repetition rate of 50 Hz. By slow extraction,

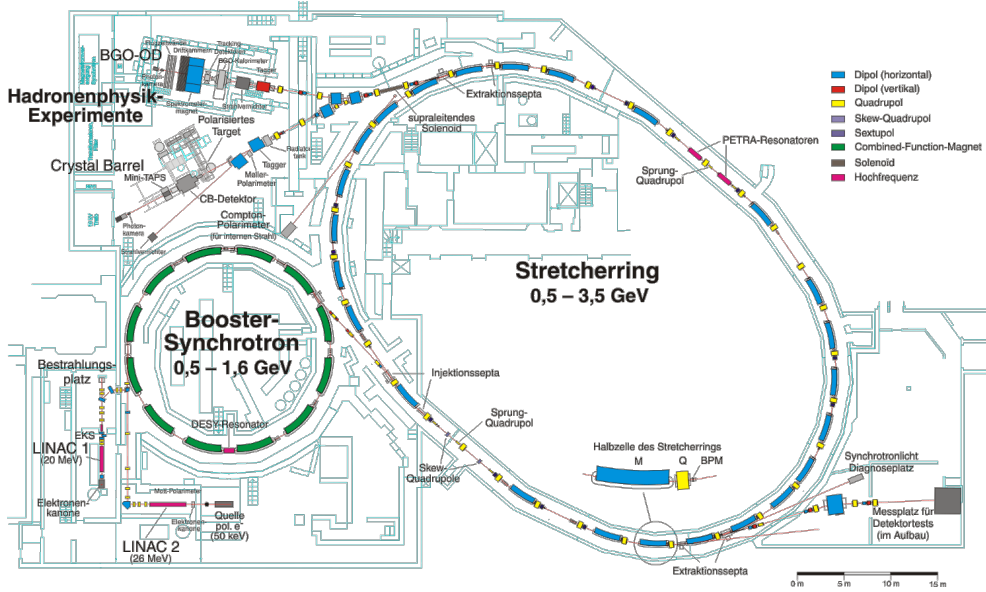


Figure 2.2: The electron accelerator ELSA with the two injector linacs, booster synchrotron, and stretcher ring. The energies reached with the different subsystems are indicated as in the figure. Figure taken from [77].

the pulsed beam is converted into a continuous beam. The maximum energy is 1.6 GeV.

- Post-accelerator mode: in this mode, the stretcher ring is used with higher fields for the ramping magnets to increase the electron energy up to 3.5 GeV. For the present work, the post-accelerator mode has been used to extract energies of 2.4 GeV (since the linear polarised electrons are only available up to this energy, as explained below).
- Storage mode: this mode is mainly used for synchrotron radiation experiments. Large currents are accumulated in the ring and accelerated to the desired energy. The bending magnets of the ring cause the electrons to emit synchrotron radiation.

As for MAMI, the spin of the longitudinally polarised electrons precesses around the magnetic field vectors of the dipole magnets. However, to reduce depolarisation in circular accelerators, the electron spin has to be rotated into the perpendicular position with respect to the flight path (transversal polarisation) by deflecting the beam about 90°. In addition, the focussing solenoid lenses of the linac cause Larmor precessions, which are corrected with the help of double solenoids in the injection beamline. Right after extraction, the spin is again turned into the longitudinal direction by a superconducting magnet. In contrast to MAMI, additional depolarising effects due to the imperfect magnetic fields in the circular accelerator, can not be neglected [78, 79]:

- imperfection resonances: the depolarisation is caused by imperfect positting and fields of the magnets.

- intrinsic resonances: depolarisation caused by the vertical betatron oscillation of the electrons around the desired path.

These resonances can be satisfactorily compensated with correction magnets and by changing the operating point, up to 2.4 GeV electron energy, and can be seen in Fig. 2.3.

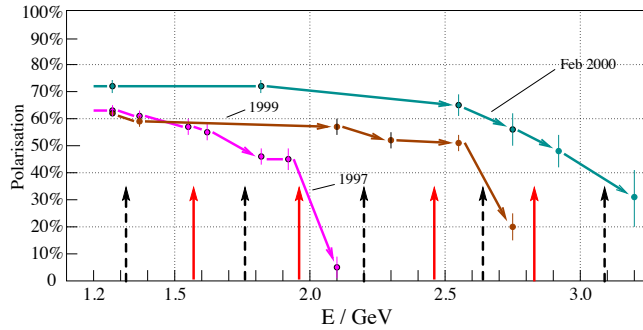


Figure 2.3: Achieved longitudinal electron polarisation values in dependence of the extracted electron energy since 1997. The imperfection resonances are indicated by black dashed arrows and the intrinsic resonances by red arrows. The improvement from 1997 to 1999 is mainly caused by compensation of the intrinsic resonance at ~ 1.9 GeV by pulsed quadrupole magnets. For the measurement in 2000, a new 50 keV electron source has been used and the correction of the equilibrium position has been improved. Figure taken from [78].

2.2 Generation of Photon Beams

For the purpose of photoproduction experiments, the electrons, delivered by the acceleration facilities ELSA and MAMI, have to be converted to real photons. This is done with the help of a thin radiator foil by producing bremsstrahlung photons. The scattered electrons are afterwards energy tagged in dedicated detectors (known as the tagger). The bremsstrahlung process itself and the necessary detector components shall now be explained in the following section.

2.2.1 Bremsstrahlung Process

Bremsstrahlung occurs when electrons (or other charged particles) slow down in matter due to the Coulomb interaction of the electrons with the nucleus. The breaking causes the electrons to emit a photon of the energy E_γ . A typical Feynman diagram for the bremsstrahlung process is shown in Fig. 2.4. Requiring four-momentum conservation, one can derive the following equation:

$$\begin{pmatrix} E_0 \\ \vec{p}_0 \end{pmatrix} = \begin{pmatrix} T \\ \vec{q} \end{pmatrix} + \begin{pmatrix} E \\ \vec{p} \end{pmatrix} + \begin{pmatrix} E_\gamma \\ \vec{k} \end{pmatrix}, \quad (2.2)$$

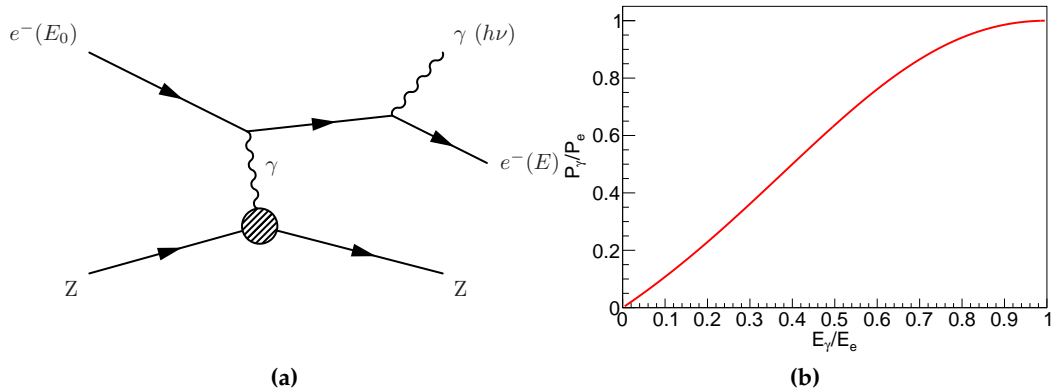


Figure 2.4: (a) Possible Feynman diagram for the bremsstrahlung process. (b) Polarisation transfer from the longitudinally polarised electron with energy E_e to the circularly polarised photon with energy E_γ described by Eq. 2.6.

where (E_0, \vec{p}_0) is the four-momentum of the incoming electron, (E_γ, \vec{k}) is the four-momentum of the bremsstrahlung photon, (E, \vec{p}) is the momentum of the scattered electron, and (T, \vec{q}) is the recoil to the nucleus. Due to the large mass of the nucleus, the recoil energy T can be neglected, but not the recoil momentum.

2.2.2 Circularly Polarised Photons

For incoherent bremsstrahlung with relativistic electrons, the Bethe-Heitler cross section can be derived [80]:

$$d\sigma_{B-H} = 4Z^2 \alpha a_0^2 \frac{dE_\gamma}{E_\gamma} \frac{E}{E_0} \left[\frac{E_0}{E} + \frac{E}{E_0} - \frac{2}{3} \right] \left[\ln \left(\frac{2EE_0}{E_\gamma} \right) - \frac{1}{2} \right] \quad (2.3)$$

where α is the fine structure constant, Z is the atomic number, and a_0 is the Bohr radius. Hence, the distribution of the photons is mainly depending on the inverse photon energy $1/E_\gamma$. The distribution is forward peaking and independent of the energy transfer. The following mean photon opening angle can be deduced:

$$\sqrt{\langle \theta_\gamma^2 \rangle} \simeq \frac{m_e}{E_0}, \quad (2.4)$$

where m_e is the mass of the electron. However, the scattering angle of the electrons is depending on the energy transferred to the photon:

$$\sqrt{\langle \theta_e^2 \rangle} \simeq \frac{E_\gamma}{E} \sqrt{\langle \theta_\gamma^2 \rangle}. \quad (2.5)$$

For the electron energies used at MAMI and ELSA, the scattering angle of electrons and photons is of the order of mrad and is negligible in comparison with the angles of electron-electron scattering [81]. Electron-electron scattering is used for the purpose of the Møller measurement, as described in Sec. 3.2.2.

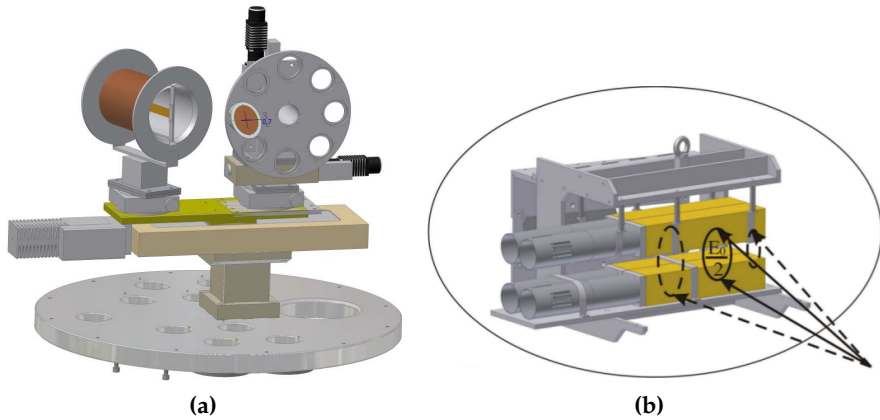


Figure 2.5: (a) The CBELSA/TAPS goniometer consisting of several radiators: copper radiators of different thickness, a diamond radiator to produce linear polarised photons, and of a Møller foil with a pickup coil. Additionally, the goniometer contains tools for beam diagnostics. Figure taken from [82]. (b) The CBELSA/TAPS Møller polarimeter with four lead glass detectors. The case of symmetric Møller scattering, where the two electron energies E_1 and E_2 are equal $E_1 = E_2 = \frac{E_0 + m_e}{2}$ is indicated by solid arrows (dashed arrows: asymmetric scattering). Figure taken from [83].

The incoherent bremsstrahlung process can be used to either produce unpolarised or circularly polarised photons. Whereas the scattering of unpolarised electrons on an amorphous radiator results in unpolarised photons, circularly polarised photons are produced by scattering of longitudinally polarised electrons on an amorphous radiator. The helicity transfer from the electron to the photon in this process is described by the following formula [84]:

$$\frac{P_\gamma}{P_e} = \frac{3 + (1 - x)}{3 + 3(1 - x)^2 - 2(1 - x)} \cdot x, \quad (2.6)$$

where $x = E_\gamma / E_0$ is the energy transfer from the electron to the photon and P_e and P_γ are the electron and photon polarisation degrees, respectively. According to Eq. 2.6, the polarisation of the photon is proportional to the electron polarisation. Hence, a high electron polarisation is needed to get a high photon polarisation. Furthermore, the helicity transfer is increasing with increasing photon energy, as seen in Fig. 2.4 (b).

The CBELSA/TAPS and A2 experiment are equipped with several amorphous radiators, which are mounted in a goniometer, as seen in Fig. 2.5 (a). To generate unpolarised electrons, thin (10-200 μm) copper foils are used. However, when running with circularly polarised photons, the Møller radiator is the best choice, since it allows to simultaneously measure the electron polarisation via Møller scattering. The Møller radiator is made of Vacoflux50, an alloy with 49% iron, 49% cobalt, and 2% vanadium. The CBELSA/TAPS Møller radiator has a thickness of 20 μm ($3.61 \cdot 10^{-3} X_0$) [85], and the Møller radiator of the A2 experiment has a thickness of 10 μm [86]. The radiator is surrounded by a coil to polarise the Møller foil. To detect the Møller scattered electrons, the CBELSA/TAPS experiment has a Møller polarimeter, as seen in Fig. 2.5 (b).

It consists of four lead glass detectors with the dimension of $64 \times 64 \times 300 \text{ mm}^3$. By building a coincidence signal between the lower and upper bar, the Møller asymmetry is measured, as explained in Sec. 3.2. In contrast to the CBELSA/TAPS experiment, the A2 experiment has no actual Møller polarimeter. However, the counters of the tagger in A2, explained in Sec. 2.2.3, can be used in combination with the Møller foil and a FPGA based trigger using VME Universal Processing Modules (VUPROM) to determine the polarisation of the electron beam. More detailed information can be found in the diploma thesis of P. Otte [86]. Since depolarisation effects during acceleration can be neglected at MAMI, the Møller measurement is not that important in Mainz, and the electron polarisation can be determined using the Mott measurement close to the electron source.

Besides the possibility to produce circularly polarised photons, both experiments A2 and CBELSA/TAPS, provide the possibility to produce linearly polarised photons via coherent bremsstrahlung. For this purpose, unpolarised electrons are scattered off a diamond radiator. The process of coherent bremsstrahlung is explained in detail in Ref. [87].

2.2.3 Photon Tagging

For photonuclear experiments, it is important to know the exact energy of the emitted bremsstrahlung photons. As discussed, the electron transfers a part of its initial energy, E_0 , to the photon. Neglecting the recoil to the nucleus, the energy of the photon is given by energy conservation:

$$E_\gamma = E_0 - E, \quad (2.7)$$

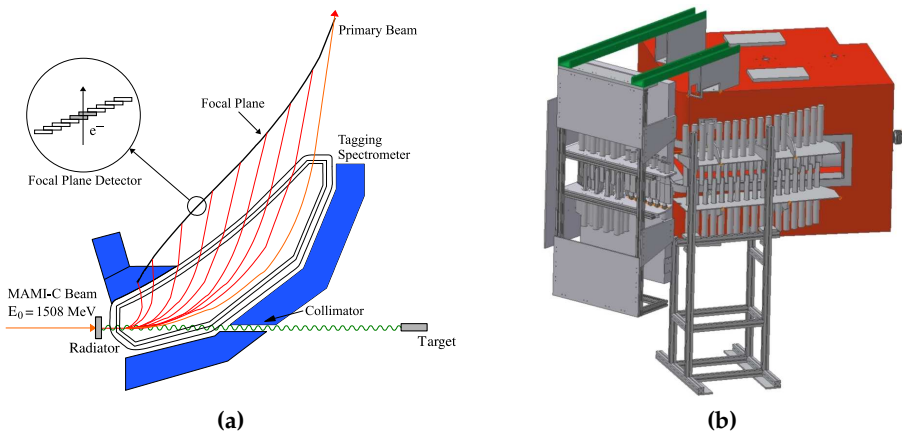


Figure 2.6: (a) Sketch of the Glasgow-Mainz photon tagger. The electrons produce bremsstrahlung photons in the radiator and exit the tagger on the right (green), while the scattered electrons are deflected (red) in the dipole magnet (blue). Figure taken from [88]. (b) The CBELSA/TAPS photon tagger with the dipole magnet (red) and the scintillating bars (gray). The scintillating fibres (left) are situated between the bars and the dipole magnet. Figure taken from [82].

where E_0 is the extraction energy of the electron beam and E the energy of the scattered electron, which is measured in the photon tagger. The tagger of both experiments, shown in Fig. 2.6, mainly consists of a dipole magnet which deflects the electrons depending on their energy. High energy electrons (a low bremsstrahlung photon energy) are deflected less than low energy electrons (a high bremsstrahlung photon energy). The deflected electrons are registered in the tagger ladder made of scintillation detectors, which are read out via photomultiplier tubes (PMTs).

The Glasgow-Mainz photon tagger (A2 experiment) [89], as seen in Fig. 2.6 (a), consists of a 1.9 T magnetic field, which is produced by a 40 ton heavy dipole magnet. Electrons that did not interact with the radiator are deflected by 79° and guided to the beam dump where the beam current is measured with a Faraday cup. The scattered electrons are registered in the tagger ladder installed in the focal plane. This ladder consists of 353 scintillation bars varying from 9 to 32 mm in thickness. The scintillation bars are overlapping such that a coincidence analysis between two adjacent bars builds in total 352 logic tagger channels. The tagger covers an energy range of 5 – 93% of the electron beam energy with a resolution of 2 to 5 MeV (see Fig. 2.7). Due to very high rates in the tagger at low photon energies ($1/E_\gamma$ dependence), the highest tagger channels (281-352) were switched off for the experiment of this work, such that only photon energies in the range between 400-1450 MeV have been tagged. Additional information on the Glasgow-Mainz photon tagger can be found in Ref. [89].

The composition of the CBELSA/TAPS tagger (see Ref. [85] for details), shown in Fig. 2.6 (b), is slightly more complex. The high-energy part ($0.166E_0 - 0.871E_0$) of the CBELSA/TAPS tagger is equipped with 480 scintillating fibres with 2 mm diameter. Sixteen fibres build one of the 30 modules, having an energy resolution of $0.1\%E_0$ for the lower electron energies and $0.4\%E_0$ for the higher energies. Additionally, 96 scintillating bars cover an energy range from $0.021E_0$ to $0.825E_0$. The bars have a thickness of 1.4 – 5 cm and a relative energy resolution of $0.1 - 6\%E_\gamma$ (see Fig. 2.7). Due to space conditions, they are mounted in three difference geometrical sets, in such a way that

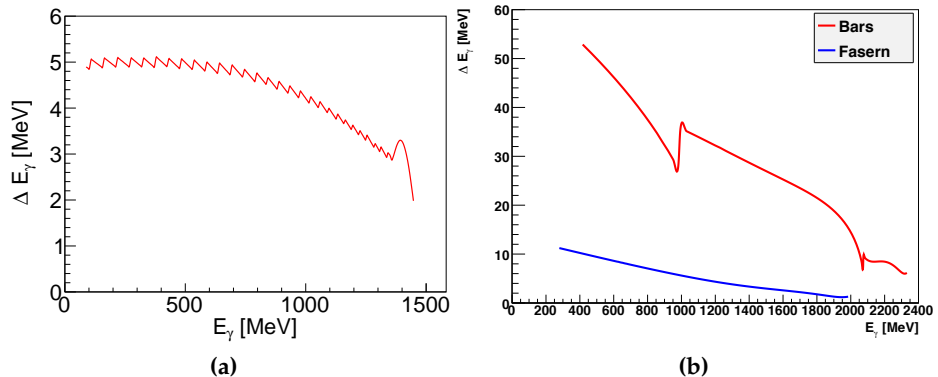


Figure 2.7: (a) Energy resolution for the Glasgow-Mainz photon tagger. (b) Energy resolution achieved by the CBELSA/TAPS tagger bars (red) and fibres (blue) for an extraction energy of 2.4 GeV. Figure (b) taken from [90].

an electron always hits two bars. By building the difference of the trigger time and the tagger time of the electron, a certain photon can be matched with the corresponding event. The photon tagger of the CBELSA/TAPS experiment is explained in more detail in Ref. [83]. After the tagger, the photon beam is collimated by lead collimators. For the current polarised target experiments, a 2 mm (A2) and 4 mm (CBELSA/TAPS) collimator were used, leading to a beam diameters of 0.9 and 0.8 mm, respectively.

2.3 Targets

The main goal of this work was to determine cross sections and the polarisation observable E for η photoproduction on the neutron. However, due to the non-existence of a free neutron target, quasi-free nucleons bound in light nuclear targets were used. The most straightforward choice is to use deuterium, which contains one proton and one neutron per nucleus. Other light nuclei are less frequently used for such measurements. Nevertheless, two other nuclei have certain advantages. Tritium ^3H , composed of one proton and two neutrons, has the most favourable neutron/proton ratio, however, the handling of this material is not very practicable due to its radioactivity. Another possible candidate is ^3He , containing two protons and one neutron. Due to an advantageous spin structure, ^3He is often used for polarisation experiments. The main component in the wave function is given by the state where the two protons are coupled with anti-parallel spin such that the net spin of the nucleus is identical with the spin of the neutron. For the present work, experiments on liquid deuterium and ^3He targets have been used to extract the unpolarised cross section on quasi-free neutrons and protons. To extract the double polarisation observable E , a frozen spin target with deuterated butanol (dButanol) was used. Furthermore, a carbon foam target was used to determine the unpolarised background.

2.3.1 Liquid Deuterium Target

The A2 liquid deuterium (LD_2) target container [91], shown in Fig. 2.8 (a), is made of 125 μm thick Kapton, is (3.02 ± 0.03) cm long, and has a diameter of 4 cm. The unpolarised cross sections, determined by D. Werthmüller [56], which have been used for the normalisation of the helicity asymmetry, have been extracted using this target and a slightly longer LD_2 target with a length of (4.72 ± 0.05) cm. To liquefy the deuterium, the target was cooled down to approximately 20 K and was wrapped in isolating foil (8 μm Mylar plus 2 μm aluminium) [91].

The container of the CBELSA/TAPS LD_2 target had a diameter of 3 cm and a length of (5.258 ± 0.1) cm (at a target cell pressure of 1350 mbar). Like the A2 target, the CBELSA/TAPS target container is made of Kapton (80 μm front/back and 125 μm on the sides). A heat exchanger was used to cool the target, which was connected to the target cell via two tubule, as seen in Fig. 2.8 (b) [90].

Both the A2 and the CBELSA/TAPS target containers can also be filled with hydrogen. Experiments with such targets have been used to extract the nucleon detection efficiency correction, as explained in Sec. 8.8.1.

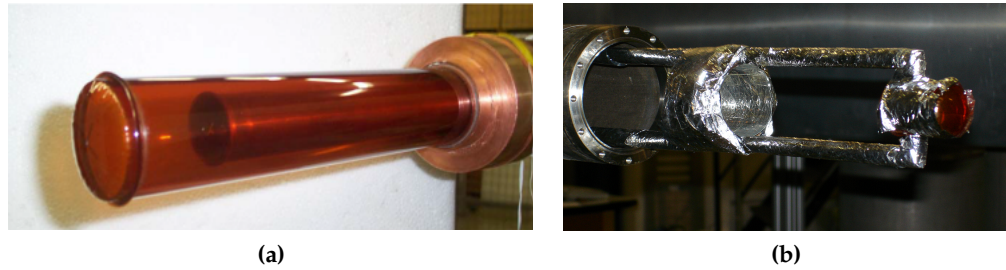


Figure 2.8: (a) The target container of the A2 LD₂ target. Figure taken from [92]. (b) The CBELSA/TAPS LD₂ target cell. Figure taken from [90].

2.3.2 ³He Target

As previously mentioned, unpolarised cross sections have also been extracted for quasi-free protons and neutrons bound in ³He. The target cell [93] was cylindrically shaped, (5.08 ± 0.02) cm long and had a diameter of (3.04 ± 0.02) cm. Since Kapton is not helium-tight, the cell was made of 175 μm Mylar.

To increase the density of ³He, the target was cooled to approximately 2.4 K with the help of a ³He/⁴He dilution refrigerator, as seen in Fig. 2.9. The density at this temperature was determined to be (74.48 ± 1) kg/m³. [94, 95].

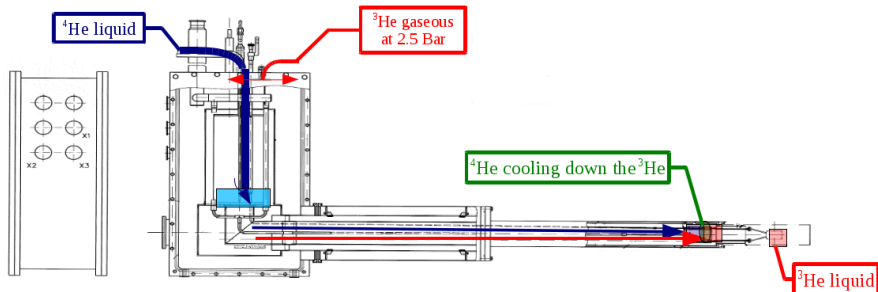


Figure 2.9: Technical drawing of the ³He target cell as used in the A2 experiment. Figure taken from [93].

2.3.3 Frozen Spin Target

In order to determine the double polarisation observable E , a target containing longitudinally polarised nucleons (protons and neutrons) is required. The theory on polarised targets will now be shortly outlined and further information can be found in Ref. [96].

When an ensemble of particles with spin s is exposed to a magnetic field \vec{B} , the energy levels split into $2s + 1$ sub-levels according to the Zeeman effect. The energy spacing of the levels is given by [97]:

$$\Delta E = -g\mu_m m B_z, \quad (2.8)$$

where $m = -s, -s+1, \dots, +s$, g is the Landé factor, and μ_m is the magneton. Hence, for protons and neutrons with spin 1/2 this leads to only two levels, whereas for deuterons three levels occur (Zeeman levels). In thermal equilibrium, the levels are occupied according to the Boltzmann distribution:

$$\frac{N(E + \Delta E)}{N(E)} = e^{\left(\frac{-\Delta E}{kT}\right)}, \quad (2.9)$$

where N is the occupation number, ΔE is the level spacing, k is the Boltzmann constant, and T is the lattice temperature. The polarisation degree P_T of the target with spin- s particles is defined by:

$$P_T = \frac{1}{s} \frac{\sum_{m=-s}^s m \cdot e^{\frac{g\mu_m B}{kT}}}{\sum_{m=-s}^s e^{\frac{g\mu_m B}{kT}}}, \quad (2.10)$$

where the g-factor and the magnetic moment μ are given in Table 2.1.

	g-factor	μ
electrons	-2.0023	μ_B
protons	5.5857	μ_N
neutrons	-3.8261	μ_N
deuterons	0.8574	μ_N

Table 2.1: *g-factor and magnetic moment of different particles with the Bohr magneton $\mu_B = 5.7883 \times 10^{-11} \text{ MeV T}^{-1}$ and the nuclear magneton $\mu_N = 3.1524 \times 10^{-14} \text{ MeV T}^{-1}$. Values taken from [2].*

From Eq. 2.10 and the values of Table 2.1, one can directly follow that deuterium alone can only be polarised to a reasonable degree at very low temperatures and high magnetic fields ($B \simeq 20 \text{ T}$, $T \simeq 10 \text{ mK}$ [97]). Thus, a different target material than deuterium has to be used. Requirements for such a material are a high maximum polarisation degree, a long relaxation time, and a short build-up time. A material which exhibits this features is deuterated butanol (dButanol) with the chemical formula $\text{C}_4\text{D}_9\text{OD}$. It is an ideal material since the residual carbon and oxygen nuclei are spinless and cause no polarised background (former experiments used ND_3 targets, which had the disadvantage that the nitrogen atoms were polarised as well).

The deuterons inside dButanol were polarised with the *Dynamic Nuclear Polarisation* (DNP) technique. DNP in dButanol can be described by the spin temperature theory, see Ref. [97]. During the DNP process, a microwave field is used to induce spin flips between the different Zeeman bands, which leads to a high electron polarisation of paramagnetic radicals. Due to their small mass and high magnetic momentum, it is much easier to polarise electrons than nucleons, as seen in Table 2.1. Already at a temperature of 1 K and a magnetic field of 2 Tesla, electrons have a polarisation degree of more than 90% [98]. The transfer of the electron polarisation to the nucle-

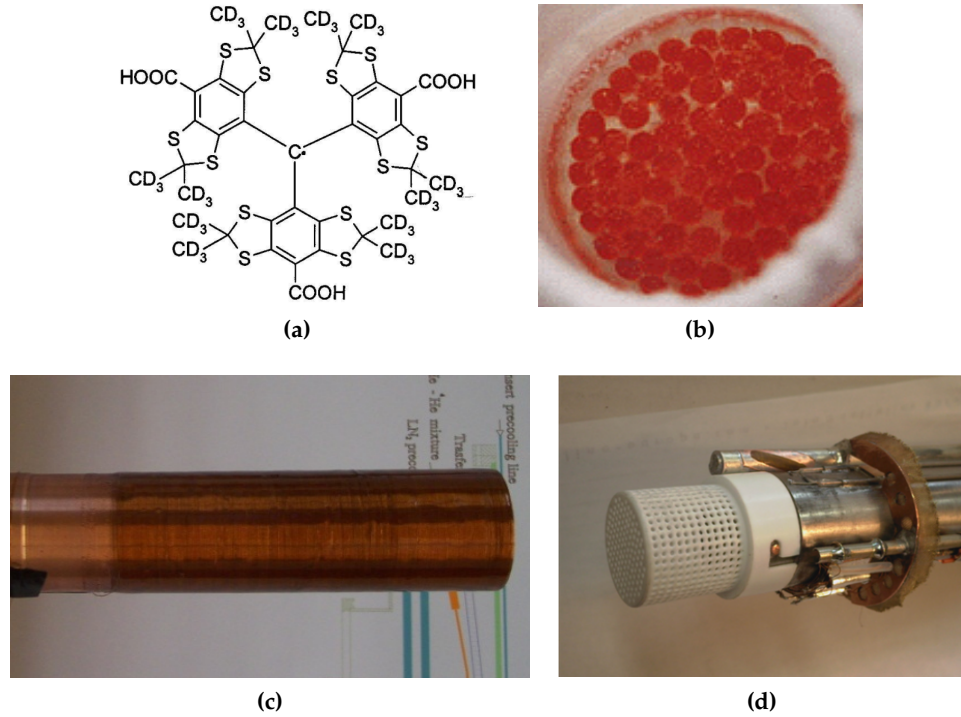


Figure 2.10: (a) Trityl radical Finland. The free electron is indicated as a point (center). Figure taken from [97]. (b) The dButanol material was frozen in small beads. (c) Longitudinal holding coil (solenoid) and (d) target container of the A2 Frozen Spin target. Figures (b) and (c) taken from [92].

ons happens via *thermal mixing*, a simultaneous transition of two electrons (flip-flop) with coincident nucleon-Zeeman transition. Depending on the frequency of the microwave field, the nucleons can be polarised in a parallel or anti-parallel direction to the magnetic field. The realisation of DNP during the experiment was done in the following way: before data taking, a superconducting magnet with a magnetic field of ~ 2.5 T was placed around the dButanol target to polarise the electrons in the paramagnetic radicals. Simultaneously, microwave frequencies were used to transfer the polarisation from the electrons to the nucleons. A certain microwave frequency range was hereby driven through to find the correct position to induce transition between the Zeeman levels. Having reached the maximum polarisation degree, the polarising magnet was removed from the target and replaced by a small longitudinal holding coil, as seen in Fig. 2.10 (c), with a magnetic field of $B_H \simeq 0.6$ T for both experiments. Then, the target was put into the frozen spin mode. For this purpose, the A2 [99–101] and CBELSA/TAPS targets [98] have been equipped with a $^3\text{He}/^4\text{He}$ dilution refrigerator, as seen in Fig. 2.11, to cool down the dButanol material to a temperature of $T \simeq 25$ mK (A2) or $T \simeq 60$ mK (CBELSA/TAPS). Under these conditions the polarisation undergoes a slow exponential decay. After several hours or days the target had to be repolarised in order to ensure a high as possible nucleon polarisation.

For the current experiments, the dButanol was doped with triphenylmethyl (short

trityl) Finland radicals, shown in Fig. 2.10 (a). The target material, shown in Fig. 2.10 (b), was shock frozen to spherical beads of 1.8 mm in diameter and brought into the target container. When cooled down, the Teflon target container (see Fig. 2.10 (c)) had a length of 2 cm (A2) and 1.88 cm (CBELSA/TAPS). The fraction of the volume covered with dButanol (filling factor) was determined to be 60% (A2) and 59% (CBELSA/TAPS) [102, 103].

The polarisation of the target was measured with a Nuclear Magnetic Resonance (NMR) technique, and is further described in Sec. 3.4.

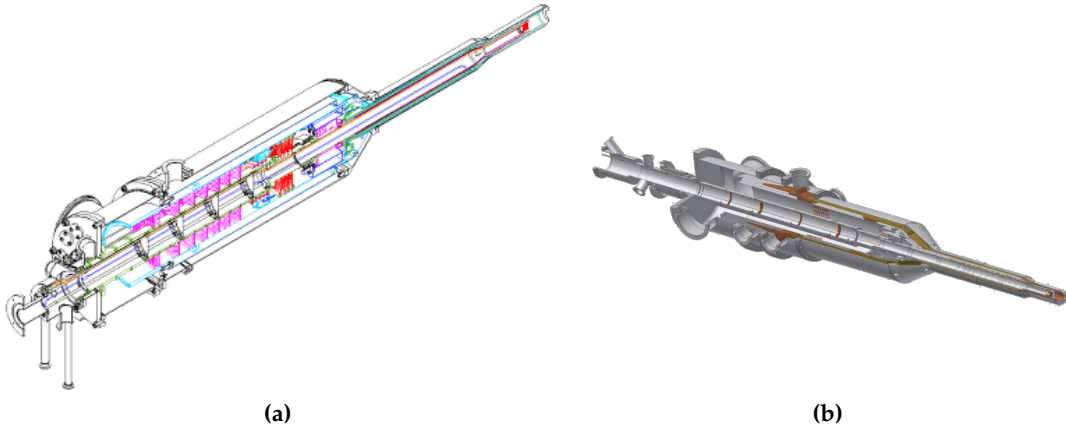


Figure 2.11: Technical drawings of the frozen spin targets used at the A2 (a) and CBELSA/TAPS experiment (b), respectively. The main part of the target is compromised of the $^3\text{He}/^4\text{He}$ dilution refrigerator, the dButanol material is situated in the tip of the target. Figures taken from [102] and [104].

2.3.4 Carbon Target

To understand the unpolarised background contributions inside dButanol, additional measurements with a carbon foam target, shown in Fig. 2.12, are necessary. The density of the carbon target has been chosen in such a way that the number of carbon nuclei matches the number of carbon nuclei inside the dButanol material. The A2 carbon foam target had a density of 0.57 g/cm^3 and the one of the CBELSA/TAPS experiment 0.50 g/cm^3 . To create similar experimental conditions as for the dButanol target, the carbon foam target was placed inside the cryostat. For the CBELSA/TAPS experiment, the carbon target was cooled down with the same $^3\text{He}/^4\text{He}$ mixture as was used for the dButanol target. However, this was not possible in the A2 experiment as serious target damages were feared and the carbon target was therefore not cooled.

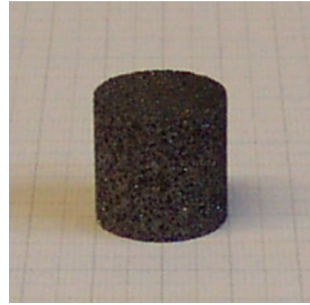


Figure 2.12: The carbon foam target as it was used for the measurement of the unpolarised carbon background in the A2 experiment. Figure taken from [92].

2.4 Detectors Setup

The detector setups of both experiments are very similar. The experiments consist of several electromagnetic calorimeters that are optimised for the detection of photons. Furthermore, charge sensitive detectors are installed to identify charged particles. The setups will now be explained in more detail.

2.4.1 A2 Detector Setup

The setup of the A2 experiment consist of the Crystal Ball (CB) calorimeter [105], the Particle Identification Detector (PID) [106], and the TAPS detector [107, 108]. An overview of the A2 experiment is depicted in Fig. 2.13.

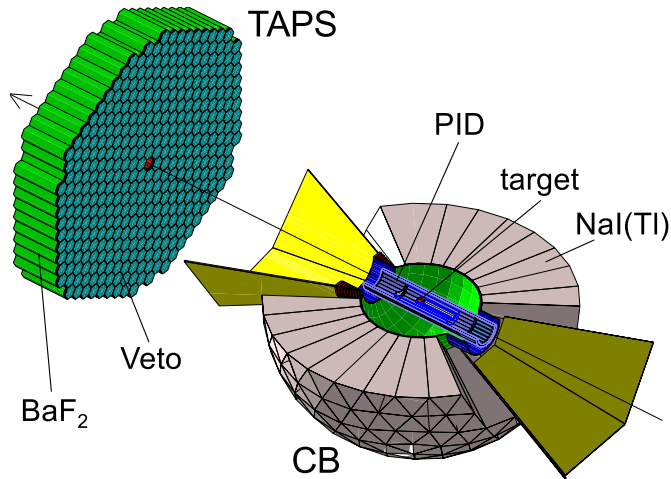


Figure 2.13: A2 setup consisting of the Crystal Ball (CB) and the TAPS detectors. The Particle Identification Detector (PID) and the veto detectors in front of TAPS are used to identify charged particles. The target is located in the center of the CB. Figure taken from [109].

Crystal Ball

The Crystal Ball (CB) [105] is the main icosahedron-shaped calorimeter covering 93% of 4π steradians. It is composed of two hemispheres with inner and outer radii of 25 and 66 cm, respectively. Each of the 672 thallium doped sodium iodide (NaI(Tl)) crystals are 41 cm ($15.7X_0$) long truncated pyramids, as seen in Fig. 2.14, and are read out with PMTs. Because of the beam line, the CB detector has a hole for polar angles smaller than 20° and larger than 160° .

Since NaI(Tl) crystals are hygroscopic, both hemispheres are under vacuum. Furthermore, the vacuum has stabilising effects. The most important properties of NaI(Tl) crystals are summarised in Table 2.2.

density	3.67 g/cm ³
X_0	2.59 cm
r_m	4.13 cm
dE/dx	4.8 MeV/cm
primary decay time	245 ns
emission max. wavelength	410 nm

Table 2.2: Properties of NaI(Tl) crystals used in the CB detector. The radiation length X_0 is defined as the characteristic distance at which the energy of an electron is reduced to $1/e$ via bremsstrahlung. The Molière radius r_m accounts for lateral spread. r_m is defined as the distance in which 90% of the energy is deposited. Values taken from [6].

The high light output of NaI(Tl) permits a good relative energy resolution $\frac{\sigma_E}{E}$ [110]:

$$\frac{\sigma_E}{E} = \frac{2\%}{E^{0.36} [GeV]}, \quad (2.11)$$

where E is the deposited energy in GeV. The polar angular resolution for photons is $\sigma_\theta = 2 - 3^\circ$ and the resolution in the azimuthal angle ϕ is given by $\sigma_\phi = \sigma_\theta / \sin \theta$ [110].

Particle Identification Detector

The Particle Identification Detector (PID) [106], as seen in Fig. 2.14 (c), is a cylindrical detector, which is situated inside the CB and surrounds the target with an inner diameter of 116.5 mm. It is composed of 24 EJ-204 plastic scintillation counters with a length of 500 mm and a thickness of 4 mm, which gives a ϕ -angle resolution of 15° and a θ -angle coverage of $15^\circ - 159^\circ$.

Due to the small thickness of the scintillation bars, the PID is ideally suited to veto charged particles, since neutral particles do not deposit energy. In addition, one can separate charged pions from protons and electrons by plotting the amount of energy deposited in the PID against the energy deposited in CB, as seen in Fig 7.20.

In addition to the PID, a multi-wire proportional chamber (MWPC) is installed. However, it was not used for the current experiment [106].

2.4. DETECTORS SETUP

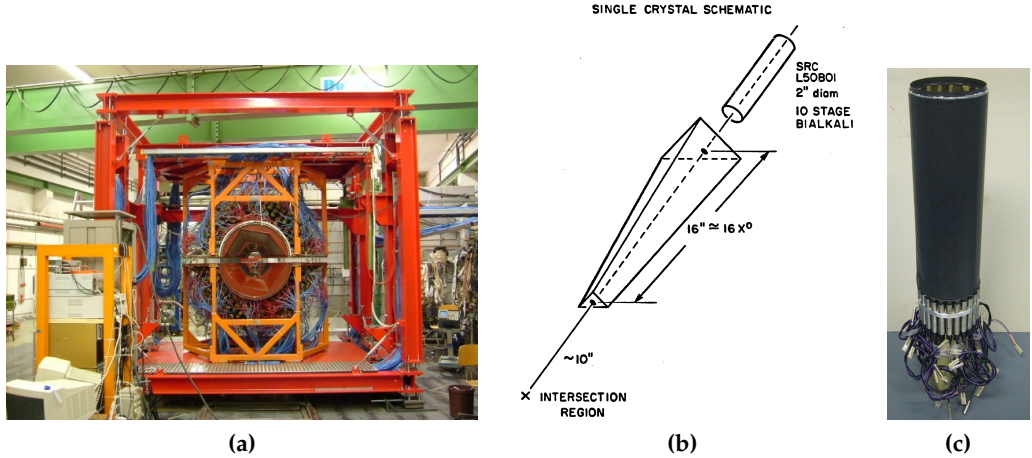


Figure 2.14: (a) Picture of the CB detector. Figure taken from [111]. (b) One of the pyramid-shaped NaI(Tl) crystals of the CB. Figure taken from [112]. (c) PID detector made of plastic scintillation bars. Figure taken from [113].

TAPS

The forward region ($5^\circ \leq \theta \leq 20^\circ$) of the A2 setup is covered by the TAPS detector [107, 108]. Before 2008, the TAPS detector consisted of 384 BaF₂ modules. The BaF₂ crystals are hexagonally shaped and 25 cm long. Each crystal is connected to a Hamamatsu R2059-01 PMT. A 5 mm thick plastic scintillator, serving as charged particle veto, is mounted in front of every crystal, as illustrated in Fig. 2.15. In 2008, the most inner ring was replaced by PbWO₄ crystals and in 2009 the same was done for the second ring. The PbWO₄ crystals are trapezoidal shaped, such that always one BaF₂ crystal was replaced by four PbWO₄ crystals. The crystals have a length of 20 cm ($12X_0$) and are connected to Photonis XP 1911 PMTs. The fast decay time, high density, small radiation length and small Molière radius of PbWO₄ (see Table 2.3) lead to a higher rate resistivity and better angular resolution. Hence, the current setup of TAPS consists of 366 BaF₂ crystals and 72 PbWO₄ crystals. For the trigger decision (see Sec. 2.5), the TAPS detector is divided into six logical subunits, as seen by the different coloured areas in Fig. 2.16 (a).

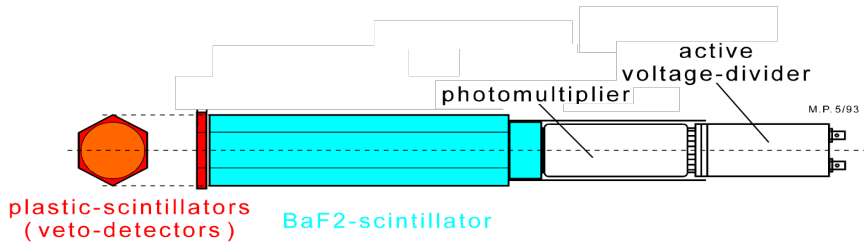


Figure 2.15: A single BaF₂ module consisting of BaF₂ crystal, a 5 mm thick plastic veto, and a PMT. Figure adapted from [114].

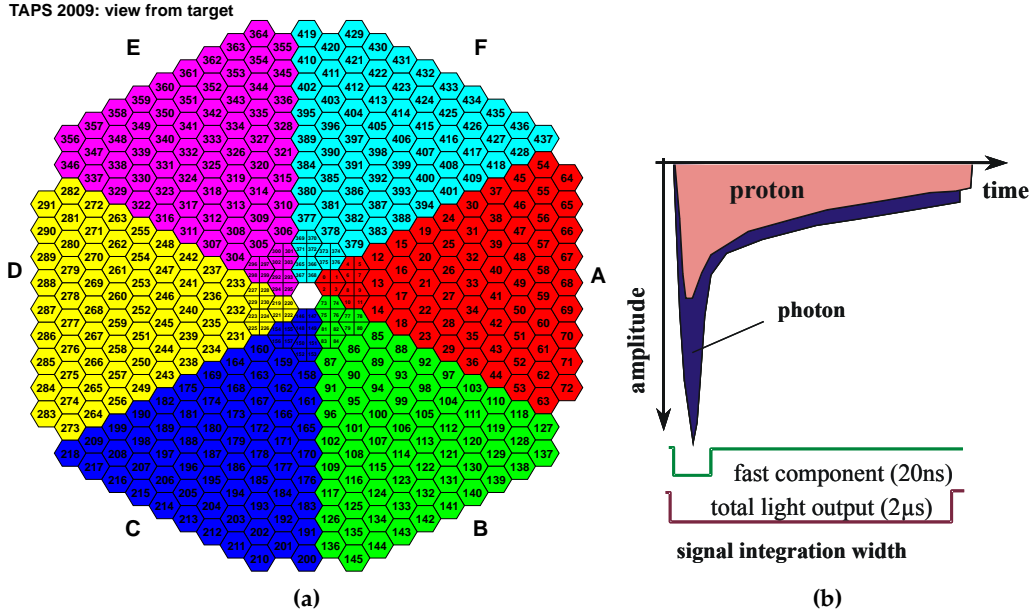


Figure 2.16: (a) TAPS crystal layout from target view with its six logical subunits (coloured triangles). Figure taken from [56]. (b) The two scintillation components of BaF_2 are integrated over two different gates for the purpose of PSA. Figure taken from [115].

One characteristic of the BaF_2 crystal is the fact that it has a fast ($\tau = 0.9$ ns) and a slow ($\tau = 650$ ns) scintillation component. This property can be used in a Pulse Shape Analysis (PSA, explained in Sec. 7.4.1) to discriminate photons from nucleons when the signal is integrated over two different time scales, as seen in Fig. 2.16 (b).

The fast scintillation component in combination with the PMT readout provides a good time resolution of TAPS ($\Delta\tau = 170$ ps for a single detector [56]), whereas the slow component is responsible for the good energy resolution. Gabler *et al.* [108]

	BaF_2	PbWO_4
density	4.89 g/cm^3	8.3 g/cm^3
X_0	2.03 cm	0.89 cm
r_m	3.1 cm	2.00 cm
dE/dx	6.5 MeV/cm	10.1 MeV/cm
fast decay time	0.9 ns	10 ns
emission max. wavelength	220 nm	420 nm
slow decay time	650 ns	30 ns
emission max. wavelength	300 nm	425 nm

Table 2.3: Properties of BaF_2 and PbWO_4 crystals used in the TAPS detector. Values taken from [6].

2.4. DETECTORS SETUP

determined the energy resolution σ_E for a collimated photon beam of energy E :

$$\frac{\sigma_E}{E} = \frac{0.79\%}{\sqrt{E[GeV]}} + 1.8\%. \quad (2.12)$$

Flux Monitoring

Behind the TAPS detector, an ionisation chamber, referred to as P2, was mounted to detect the photons that did not interact with the target material (most photons did not interact due to the low hadronic cross section in the target). The ratio of the count rates in the P2 and the tagger can be used to continuously monitor the quality of the beam. The ratio of these count rates is proportional to the tagging efficiency (number of energy tagged photons reaching the target divided by the number of registered electrons in the tagger). Furthermore, a lead glass detector was moved into the beam line during low intensity tagging efficiency runs. This lead glass detector has an efficiency of approximately 100 % at low intensities. The determination of the tagging efficiency is further explained in Sec. 8.6.

2.4.2 CBELSA/TAPS Detector Setup

Fig. 2.17 shows an overview of the CBELSA/TAPS experiment with its various detectors. In this section, all detectors components are shortly explained. More detailed information can be found in the cited references.

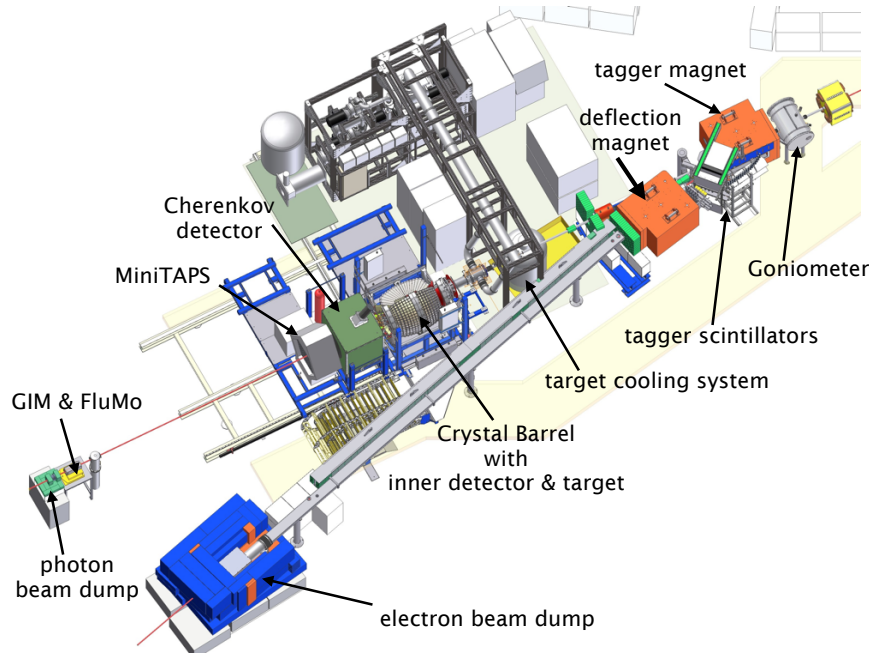


Figure 2.17: Overview of the CBELSA/TAPS experiment with all detector components.
Figure adapted from [82].

Crystal Barrel

The Crystal Barrel (CBB) detector [116], shown in Fig. 2.18, is the main electromagnetic calorimeter. It consists of 1230 thallium doped caesium-iodide crystals (CsI(Tl) properties are given in Table 2.4) arranged in a barrel-like shape around the target region. It has an angular coverage of $\theta = 30 - 156^\circ$ in polar angle and the full azimuthal range $\phi = 0 - 360^\circ$. Twenty out of the 21 azimuthal symmetric rings are made of 60 crystals each, having an angular coverage of $\Delta\theta = \Delta\phi = 6^\circ$. The 21st ring covers $\Delta\theta = 6^\circ$ and $\Delta\phi = 12^\circ$ [117]. The crystals have a length of 30 cm, corresponding to $16.1X_0$ [116]. By determining the center of gravity of the shower, an angular resolution of 1.5° is achieved. The relative energy resolution σ_E/E is given by [116] :

$$\frac{\sigma_E}{E} = \frac{2.5\%}{\sqrt[4]{E[GeV]}}. \quad (2.13)$$

The deposited energy E is proportional to the signal read out by photodiodes of the CBB crystals. Preamplifiers are used to amplify the signal of the photodiodes. The output signal of the preamplifiers is shaped and forwarded to the Fast Cluster Encoder (FACE) [118]. Since the signals of the preamplifiers are very long, the time information of the CBB can not be used. FACE is cellular logics based and is used as a part of the online trigger, as explained in Sec. 2.5.

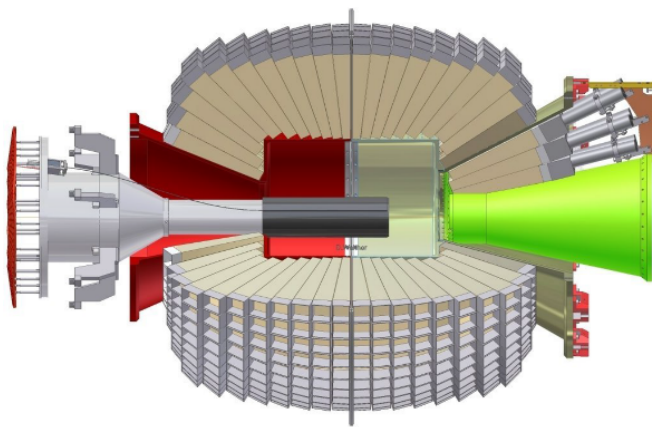


Figure 2.18: The CBB detector together with the FP (right-hand side) and the inner detector (left-hand side). Figure taken from [119].

Forward Plug

Similar to the CBB detector, the Forward Plug (FP) [120] also consists of CsI(Tl) crystals. Sixty modules are arranged in three rings to cover the front part of the CBB up to an angle of $\theta = 11.18^\circ$. In contrast to the CBB, the detectors are read out over light-guides and PMTs, which makes it possible to use them in the first-level trigger due to the faster signals. The FP has a time resolution of approximately 1.3 ns [117].

Charged particle vetoes, made of 3 mm thick plastic scintillators, are mounted in

2.4. DETECTORS SETUP

front of the crystals. The vetoes build two layers with the second layer shifted about 6° with respect to the crystals. By requiring two coincident hits in overlapping vetoes, a detection efficiency of around 95% can be achieved for charged particles [117]. More details can be found in Ref. [120].

density	4.51 g/cm ³
X_0	1.86 cm
r_m	3.57 cm
dE/dx	5.6 MeV/cm
primary decay time	0.9 μ s
emission max. wavelength	550 nm

Table 2.4: Properties of CsI(Tl) crystals used in the CBB and the Forward Plug. Values taken from [6] and [116].

Inner Detector

The inner detector [121], shown in Fig. 2.18, is an approximately 40 cm long cylindrical charged particle detector. It is made up of three layers of 513 cylindrical fibres. The fibres of the most outer layer are orientated in the direction of the beam, whereas the other two layers are turned by 25.7° and -24.5° , respectively. With the help of this setup, a hit of a charged particle in the inner detector can be reconstructed by an intersection of at least two layers, which yields an angular resolution of $\Delta\theta = 0.4^\circ$ and $\Delta\phi = 0.1^\circ$. To allow for charged particle identification, the position from the intersection of at least two fibres in the inner detector can be matched to hits in the CBB comparing the angular position. Since the scintillating fibres do not allow a decent energy determination, only the timing signal of the inner detector can be used. [122]

MiniTAPS

The MiniTAPS detector [107, 108], shown in Fig. 2.19 (a), closes the hole in the CBB in the forward direction between $\theta = 2^\circ - 12^\circ$. The modules of the MiniTAPS detector, shown in Fig. 2.15, are the same as used for the A2 TAPS detector. However, MiniTAPS is much smaller, consisting of only 216 modules. Similar to the A2 TAPS detector, MiniTAPS is divided into four logical subunits for the trigger decision (coloured sectors in Fig. 2.19).

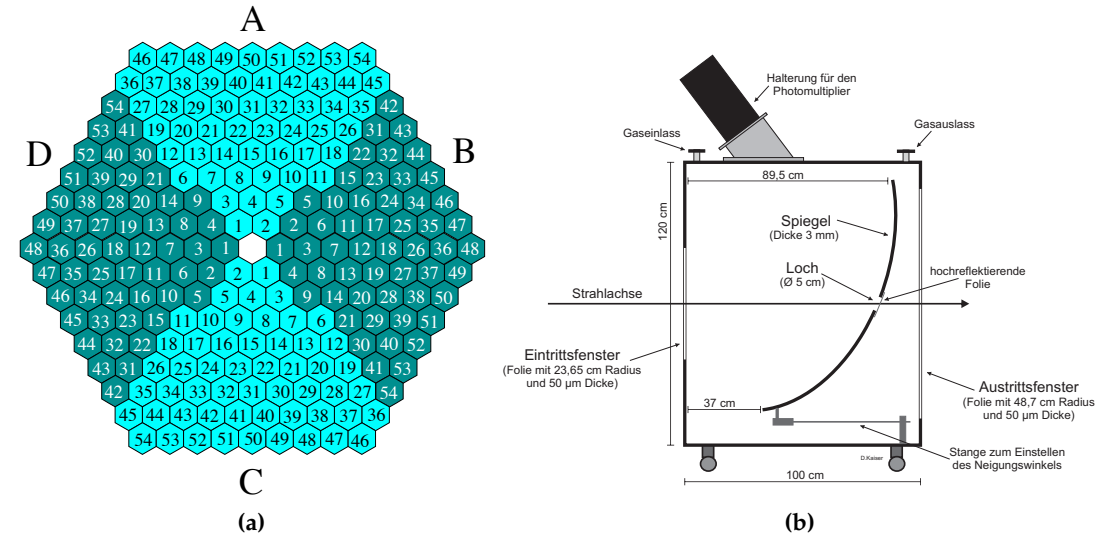


Figure 2.19: (a) MiniTAPS front view with its logical sectors (color coded). Figure taken from [123]. (b) Gas Cherenkov detector as it was used for the experiments with a polarised target in the CBELSA/TAPS experiment. Figure taken from [124].

Cherenkov Detector

In the CBELSA/ TAPS experiment a Cherenkov detector [124] is used to reduce electromagnetic background. In the A2 experiment, the available Cherenkov detector was not used, since, due to the geometrical constellations, it reduces the angular acceptance of the detector setup. In experiments with a polarised target, the electromagnetic background coming from Compton effect $\propto Z$ (atomic number) and pair production $\propto Z^2$ is strongly increased due to the high Z of the dButanol target material. In addition, the magnetic field of the holding coil can focus the particles (mostly electrons and positrons) to the forward direction. However, this effect is not that strong, since the magnetic field is small.

The Cherenkov detector at ELSA is situated between the FP and MiniTAPS, as seen in Fig. 2.17, and consists of a carbon dioxide (CO_2) filled aluminium container with an entrance and exit window. The Cherenkov light produced by the particles in the CO_2 gas is focused by a mirror and detected by a PMT, which is mounted on the top of the container, as seen in Fig. 2.19 (b). CO_2 is especially suited to produce Cherenkov light since its refractive index of 1.00043 sets the threshold energy for electrons to produce Cherenkov light to 17.4 MeV, which is below the trigger threshold of MiniTAPS. Additionally, charged pions do not produce Cherenkov light below pion energies of 4.7 GeV, which is clearly above the energies reached at the CBELSA/TAPS experiment. The Cherenkov detector has a detection efficiency of $99.72 \pm 0.45\%$ [124].

Flux Monitoring

The detectors to monitor the photon flux were situated at the end of the photon beamline. The Gamma Intensity Monitor (GIM), made of 4×4 PbF_2 crystals, was used to

monitor the photon intensity behind the MiniTAPS detector. The impinging photons produce electrons and positrons in the crystals by the pair production process. The created electrons and positrons produce Cherenkov light, which is detected by a PMT. At high rates ($\simeq 5$ MHz), the GIM signal shows saturation effects, thus an additional detector was installed to monitor the flux (FluMo). The FluMo contained a conversion target (an aluminium plate) where only a fraction of the photons were converted to electrons and positrons. These particles are coincidentally detected in two plastic scintillators. A third scintillator was mounted in front of the aluminium plate to serve as a veto to reduce the background contributions [125].

2.5 Trigger

During the experiment, the trigger decides which events will be recorded to a file for offline analysis or which events will be discarded. The trigger selects events which are of major interest and suppresses background events. In the analysis, the software trigger, applied to experimental and simulated data, mimics the settings of the hardware trigger, as explained in Sec. 8.8.2. To get a correct reproduction of the experiment in the simulation, it is important to choose the settings of the software trigger at least as stringent as the conditions of the hardware trigger.

The structure and the settings of the triggers used for the A2 and CBELSA/TAPS experiment are different and will now be described.

2.5.1 A2 Trigger

In order to speed up the data acquisition of the A2 experiment, the trigger was upgraded in 2013, the corresponding trigger scheme is shown in Fig. 2.20 (an overview of the old trigger can be found in Ref. [56]).

Due to the long rise-time of the signal from the NaI(Tl) crystals, the trigger is divided into a Level-1 and Level-2 trigger. The Level-1 trigger is based on the total energy deposited in CB. For this purpose, the analogue sum of all the CB signals is built and discriminated by a Leading Edge Discriminator (LED). A LED is a discriminator, which produces a logical output pulse, at the time when the input signal reaches a certain threshold voltage (energy). Hence, this leads to different trigger times when the signals have different amplitudes, referred to as time walk.

For the experiment of the present work, the CB energy sum threshold was set to approximately 300 MeV to reject events from single pion production. Thus, only events with more than 300 MeV deposited energy in the CB have been recorded.

In addition to the CB energy sum, a multiplicity trigger can contribute in the Level-2 trigger. Each crystal in the CB is assigned to a group of 16 adjacent channels. When at least one of these crystals registers an energy above a certain threshold (for example 30 MeV), the group adds to the total multiplicity. As mentioned in Sec. 2.4.1, the TAPS detector is divided into six logical segments of 64 modules, as seen in Fig. 2.16 (a). As for the CB detector, the energy of at least one crystal of a segment has to be larger than the LED1 threshold to contribute to the total multiplicity. Furthermore, the

A2 experiment provides the possibility to trigger only in the forward direction. This is done by using only the TAPS multiplicity trigger with an LED2 threshold (TAPS alone).

A M2+ trigger is a trigger which requires at least a multiplicity of two in the combined setup of CB and TAPS and was used for the current work. TAPS alone, i.e. without a contribution from CB, could not trigger. Furthermore, the first inner two rings of TAPS could not contribute to the trigger decision. The used trigger thresholds are summarised in Table 2.5. They have been determined separately for each detector module and the given thresholds are only typical values.

CB LED	10-30 MeV
CB Energy Sum	250-360 MeV
TAPS LED	35-45 MeV

Table 2.5: *Software trigger thresholds used for the experiments with the dButanol target at A2. The energy sum trigger was set to 250-360 MeV to reduce background from single pion photoproduction. The multiplicity counter is incremented when one of the crystals of a sector in the CB or TAPS is higher than the corresponding LED threshold.*

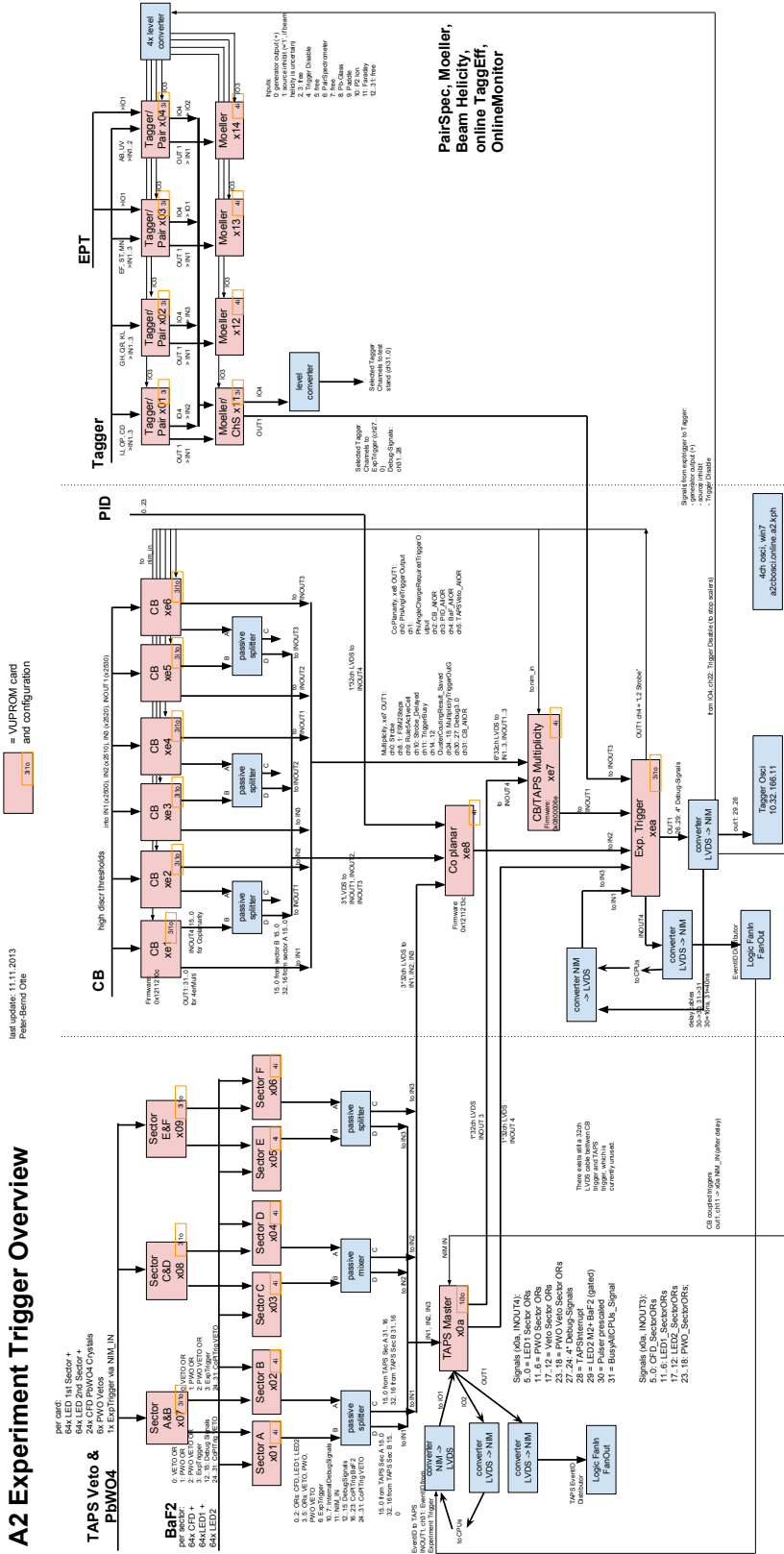


Figure 2.20: A2 experimental trigger scheme. Figure taken from [126].

2.5.2 CBELSA/TAPS Trigger

In Bonn, the trigger was done by a FPGA module, which used the information from all the detectors, for more information see Ref. [127].

The trigger decision was done in two steps. In the first step referred to as the First-Level trigger, only information from the detectors that deliver their signal faster than 400 ns is used. These detectors are the FP, Inner Detector, MiniTAPS and Cherenkov detector:

- FP: for the trigger decision in the FP, a dedicated Cluster Finder (CF) algorithm was developed. The algorithm recognises accumulations of neighbouring fired crystals and combines them into a cluster. The deposited energy in the corresponding crystal has to lie above a certain crystal threshold. For further information, see Ref. [128].
- Inner Detector: for the Inner Detector a layer trigger is used. For this purpose, the number of fired fibres per layer are counted. Since it acts only on charged particles, this trigger was not used for the current experiment. Further information can be found in Ref. [122].
- MiniTAPS: the MiniTAPS detector is divided into four logical sectors. The trigger multiplicity of MiniTAPS corresponds to number of fired sectors. Analogous to the TAPS trigger in the A2 experiment, a sector is seen as fired when the energy deposited in one crystal is above a certain LED threshold.

If the requirements of the First-Level trigger are satisfied, the Second-Level trigger was deployed. For the Second-Level trigger decision, the number of clusters (cluster multiplicity) in the CBB is counted by the Fast Cluster Encoder (FACE), as mentioned in Sec. 2.4. FACE is capable to determine the number of clusters in the CBB in the time range of only 6 μ s. The working principle of FACE is explained in more detail in Ref. [118].

Since the aim of the current work was to analyse the decay of the η meson into six photons, it was decided to use a four-particle-trigger for the dButanol experiment, known as the *eta4* trigger. More information can be found in Table 2.6 (a). The LD₂ experiment additionally used a three-particle-trigger, known as the *eta3* trigger, explained in Table 2.6 (b). Table 2.7 shows the conditions for the more open trigger, known as the *trig42c*. This trigger was used for the hydrogen beamtime and required only two or more hits.

The used trigger thresholds are summarised in Table 2.8. FACE required 15 MeV per crystal and at least 20 MeV in one element of the cluster. The FP thresholds were set to 30 MeV. For the MiniTAPS detector, two different thresholds were used: *LED High* for events with one fired segment and *LED Low* when more than two segments were fired. Due to the high particle rate close to the beam axis, the first ring of MiniTAPS could not contribute to the trigger and the threshold in the second ring was 120 MeV and thus higher than for the others (80 MeV). To make the different beamtimes

2.5. TRIGGER

as comparable as possible, the trigger thresholds in the software were set to the same values.

First Level	FACE	First Level	FACE
Taps1	≥ 2	Taps1	≥ 3
CF2 & Taps1	bypass	CF2 & Taps1	≥ 1
CF1 & Taps1	≥ 1	CF1 & Taps1	≥ 2
CF2	≥ 1	CF2	≥ 2
CF1	≥ 2	CF1	≥ 3
Taps2	≥ 1	Taps2	≥ 2
CF1 & Taps2	bypass	CF1 & Taps2	≥ 1
CF2 & Taps2	bypass	CF2 & Taps2	bypass

(a) η_3 trigger

(b) η_4 trigger

Table 2.6: Triggers used for the d Butanol and LD_2 beamtime at Bonn. All conditions are connected via a logical AND, which means that all columns have to be fulfilled. The following abbreviations are used: CF1: exactly one cluster in the FP, CF2: at least two clusters in the FP, Taps1: exactly one sector in MiniTAPS, Taps2: at least two sectors in MiniTAPS, Inner: at least two layers in the Inner Detector. FACE: the number of clusters is indicated.

First Level	FACE
Inner	≥ 2
CF1	≥ 1
CF2	bypass
CF1 & Taps1	bypass
Taps1	≥ 1
Taps2	bypass

Table 2.7: Trigger $trig42c$ at Bonn, which was used for the hydrogen beamtime. The same abbreviations as defined in Fig. 2.6 are used.

CB (FACE)	15 MeV (20 MeV)
FP LED (CF1/2)	30 MeV
TAPS LED Low (Taps 2)	120 MeV (2nd ring), 80 MeV (others)
TAPS LED High (Taps 1)	100 MeV (first ring was not in trigger)

Table 2.8: Trigger thresholds that have been applied in the analysis for all CBELSA/TAPS beamtimes. The same abbreviations as defined in Fig. 2.6 are used.

Chapter 3

Data Sets and Polarisation Values

In this chapter, the different data sets used for the present work are summarised. Furthermore, the extraction of the polarisation values for the electron and photon beam, as well as for the target, is explained in this chapter.

3.1 Data Sets

A first part of the present work was to extract unpolarised cross sections of η photo-production from quasi-free protons and neutrons. For this purpose, CBELSA/TAPS deuterium data, taken in December 2008, and A2 ^3He data taken in November 2008 were analysed. In addition, as explained in Sec. 8.8.1, to get a correct nucleon detection efficiency, hydrogen data were analysed. The experiment with a hydrogen target was performed in November 2008 (CBELSA/TAPS) and April 2009 (A2). The analysis of the ^3He data is fully explained in Ref. [129] and [109]. Only selected information and the final results are shown in the present work. The main object of this work were the two dButanol and the one carbon experiments, which were performed at the ELSA in Bonn, to measure the double polarisation observable E . Unfortunately, the second of these dButanol beamtimes in June 2011 was terminated due to a fire in a 2 m high power supply, as seen in Fig. 3.1. However, the double polarisation measurement could be continued at the A2 experiment in Mainz in July 2013. Two additional dButanol data sets were collected in Mainz in February 2014 and in March 2015. The corresponding carbon background measurement was taken in February 2014. In addition, deuterium data from May 2009 were analysed to extract cut positions and determine the contribution of carbon and deuterium in dButanol, as explained in Sec. 8.10. An overview of all these data sets can be found in Table 3.1.

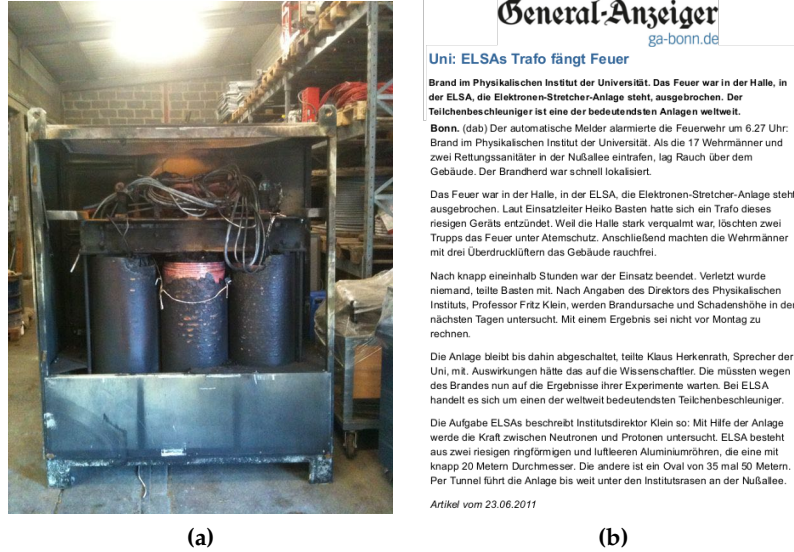


Figure 3.1: (a) Photo of the burned power supply of the CBELSA/TAPS experiment. (b) Article published in the local newspaper General-Anzeiger because of the power failure caused by the fire. Due to the fire, the Frozen Spin target was destroyed and the experiment could not be continued in Bonn. During the subsequent weeks, the whole experimental hall had to be cleaned from the acid caused by the extinguishing water. Article taken from [130].

	beamtime	target material	length [cm]	E_e - [GeV]	radiator	collimator [mm]	current [nA]	trigger	hours [h]
CBELSA/TAPS	29.11-15.12.2008	LD ₂	5.258	2.35	20 μ m Vacoflux50	4	0.32	eta3	45
	07.11.-27.11.2008	LH ₂	5.262	2.35	20 μ m Vacoflux50	7	0.32	eta3	120
	02.03.-22.04.2011	dButanol	1.88	2.35	20 μ m Vacoflux50	4	0.19	trig42	220
	08.06.-21.06.2011	dButanol	1.88	2.35	20 μ m Vacoflux50	4	0.70	eta4	550
	04.12.-10.12.2011	carbon	1.88	2.35	20 μ m Vacoflux50	4	0.70	eta4	190
A2	28.10-17.11.2008	³ He	5.08	1.508	10 μ m Cu	4	8.0	M2+ 300 MeV	250
	31.03-30.04.2009	LH ₂	10.0	1.558	10 μ m Cu	4	10.0	M3+ 360 MeV	240
	08.05-25.05.2009	LD ₂	3.02	1.558	10 μ m Vacoflux50	4	4.5	M2+ 300 MeV	190
	15.07.-24.07.2013	dButanol	2.0	1.558	10 μ m Vacoflux50	2	8.3	M2+ 250 MeV	145
	23.02.-28.02.2014	dButanol	2.0	1.558	10 μ m Vacoflux50	2	9.0-10.0	M2+ 250 MeV	80
	28.02.-03.03.2014	carbon	2.0	1.558	10 μ m Vacoflux50	2	9.0	M2+ 250 MeV	55
	24.03.-30.03.2015	dButanol	2.0	1.558	10 μ m Vacoflux50	2	10.0	M2+ 250 MeV	75

Table 3.1: Overview of the data sets used for this work. The following items are listed (from left to right): beamtime dates, target material, target length, beam electron energy, radiator type, collimator diameter, electron current, trigger condition, and effective hours.

3.2 Electron Polarisation

As mentioned in Sec.2.2.2, the electron polarisation was determined using Mott and Møller scattering. While the Mott measurement was done in the beginning of the acceleration chain, the Møller measurement was done with the accelerated electrons, which hit the Møller radiator directly in front of the tagger. Furthermore, for the Mott measurement, the production data taking had to be stopped, whereas the Møller measurement ran in parallel to the experiment.

3.2.1 Mott Measurement

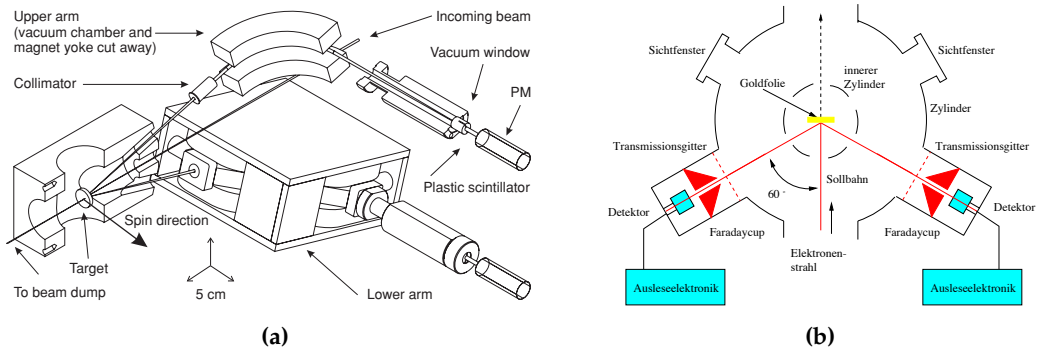


Figure 3.2: Sketch of the Mott polarimeters used at MAMI (a) and ELSA (b). The main components are two identical detector systems, a vacuum chamber, and different gold foils (Mott target). Figures taken from [131] and [78], respectively.

During the Mott measurement, transversely polarised electrons were scattered on a thin unpolarised gold foil. For this purpose, the original longitudinal polarisation of the electrons was flipped to transversal polarisation. The scattering of a polarised electron beam on atomic nuclei is described by the following cross section [132]:

$$\frac{d\sigma}{d\Omega} = \frac{d\sigma_M}{d\Omega} \cdot [1 + P_e \cdot S(\theta, E) \sin \phi], \quad (3.1)$$

where θ is the scattering angle, E the scattering energy, $\frac{d\sigma_M}{d\Omega}$ is the polarisation independent Mott cross section, P_e is the transversal electron polarisation, S is the analysing power or Sherman function, and ϕ is the azimuthal angle. S is depending on the scattering angle, energy, and the atomic number Z of the target material and can be determined by calculation for single elastic scattering. However, since in foils of finite thickness multiple scattering occurs, S has to be extrapolated. More details can be found in Ref. [132] and [133]. Hence, the spin-orbit interaction induces a scattering angle dependent Mott asymmetry A :

$$A(\theta) = \frac{\frac{d\sigma}{d\Omega}(\phi_1) - \frac{d\sigma}{d\Omega}(\phi_2)}{\frac{d\sigma}{d\Omega}(\phi_1) + \frac{d\sigma}{d\Omega}(\phi_2)} = \frac{N_L - N_R}{N_L + N_R}, \quad (3.2)$$

where N_L and N_R is the number of elastic scattered electrons to left- or right-hand angles with respect to the incoming electron beam, respectively. Combining Eq. 3.1 and 3.2, one finds that the asymmetry is directly proportional to the transversal polarisation of the electron:

$$A(\theta) = P_e \cdot S(\theta). \quad (3.3)$$

In order to eliminate instrumental asymmetries, the asymmetry was measured for electrons with positive and negative helicity [78] :

$$A = \frac{\sqrt{N_L^+ N_R^-} - \sqrt{N_R^+ N_L^-}}{\sqrt{N_L^+ N_R^-} + \sqrt{N_R^+ N_L^-}}. \quad (3.4)$$

To perform this measurement, the Mott polarimeter was used. The setup consisted of two identical detector systems, and a vacuum chamber with gold foils of different thickness, as shown in Fig. 3.2.

MAMI Mott Measurement

At MAMI, the Mott measurement was performed after the linac, where the electrons had an energy of 3.65 MeV and the Mott scattering angle was 164° (angle of the wien filter) [134]. For an extraction electron energy of 1.557 GeV, an additional correction factor $k = 1.0551$ had to be introduced since the longitudinal polarisation (before flipping) had an admixture of 2.07% transversal polarisation at the site of the A2 radiator ($\delta\theta = 11.8^\circ$ spin angle) [134].

The error of the electron polarisation at the site of the A2 radiator is compromised of the following factors [131, 134, 135]:

- 1.1% from electron spin angle ($\pm 3.1^\circ$ at 1.557 GeV) due to beam bending before the A2 hall
- 2.2% from the admixture of the transversal electron polarisation
- 1.0% from the Mott measurement itself because of the finite thickness of the Mott radiator (radiative effects during the determination of the Sherman function S_0 , extrapolation uncertainties and target induced background)
- 0.2% statistical error

This leads to a total uncertainty of the electron polarisation of approximately 2.7%.

The electron polarisations determined with Mott scattering for the three different dButanol experiments are shown in Fig. 3.3 as a function of the run number. Mott measurements have been performed approximately every day. The average electron polarisation was 84.9% (July 2013), 81.0% (February 2014), and 83.2% (March 2015).

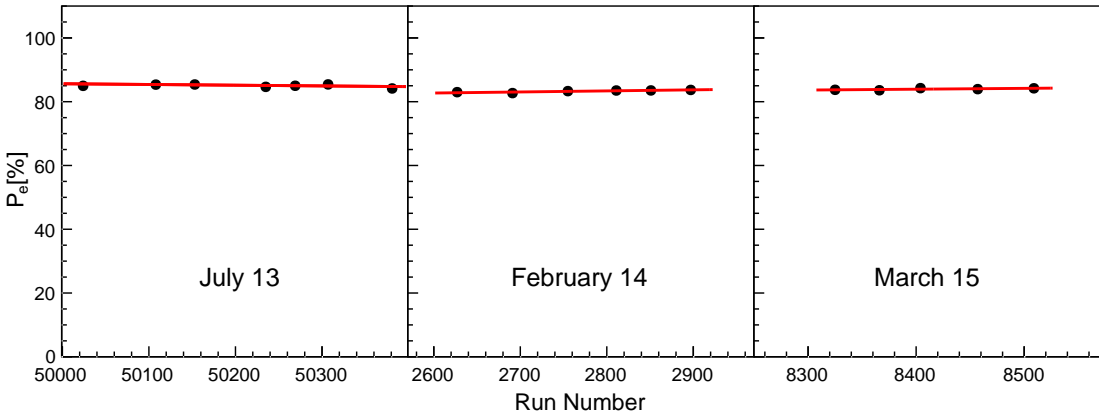


Figure 3.3: Electron polarisation P_e per run extracted from the Mott measurement at MAMI. The values for all three dButanol experiments, July 2013, February 2014, and March 2015 (from left to right) are shown. The measurement have been interpolated with a linear fit.

ELSA Mott Measurement

At ELSA in Bonn, the Mott polarimeter was situated after the polarised source at an electron energy of 50 keV and a scattering angle of 120° was used [136].

However, as mentioned in Sec. 2.1.2, the acceleration of longitudinally polarised electrons at ELSA is involving significant polarisation losses due to depolarising resonances and beam transfer. Hence, the polarisation values obtained from the Mott measurement are not reflecting the electron polarisation on the position of the Møller radiator and are thus not used. Instead, only the values obtained from Møller scattering, as explained in the next section, are used for the final calculation of the photon polarisation.

3.2.2 Møller Measurement

In addition to the Mott measurement, the Møller measurement was done to know the polarisation at the stage of the tagger and to monitor the time stability of the polarisation. The Møller measurement was done with the Møller polarimeters described in Sec. 2.2.2. The electron spins in the Møller target MT (Møller radiator) were aligned to a field, which was created by the surrounding Møller coil. Hence, inducing a Møller target polarisation of [137]:

$$P_{MT} = 2 \frac{g - 1}{g} \frac{M}{N_e \mu_B}, \quad (3.5)$$

where g is the gyromagnetic ratio, N_e number of electrons and μ_B the Bohr magneton. The magnetisation M of the target was measured with a pickup coil. When scattering longitudinally polarised electrons on the polarised Møller target, the electrons are emitted in a cone shape to forward directions. In the cm frame, a fixed relation between the scattering angle θ and energy E of the two Møller electrons $i = 1, 2$ can be

derived as:

$$E_i = m_e + (E_0 - m_e) \cos^2 \left(\frac{\bar{\theta}_i}{2} \right), \quad (3.6)$$

where E_0 is the energy of the incoming electron, m_e is the mass of the electron, and $\bar{\theta}$ is the scattering angle in the cm frame. Hence, the scattering angle decreases with increasing energy:

$$\bar{\theta} \sim \frac{1}{\sqrt{E}}. \quad (3.7)$$

The scattering angle for Møller electrons is in general much larger than the one of bremsstrahlung photons, as seen in Eq. 2.4.

Using the asymmetry coefficients a_{jj} and the beam and target electron polarisation P_i^B and P_j^T , the following cross section can be deduced [138]:

$$\frac{d\sigma}{d\bar{\Omega}}(\bar{\theta}) = \frac{d\sigma_0}{d\bar{\Omega}}(\bar{\theta}) \left\{ 1 + \sum_{j=x,y,z} a_{jj}(\bar{\theta}) P_j^B P_j^{MT} \right\}, \quad (3.8)$$

where $\frac{d\sigma_0}{d\bar{\Omega}}(\bar{\theta})$ is the cross section for the unpolarised electrons. Since the asymmetry coefficient a_{zz} is bigger than a_{xx} and a_{yy} , a large asymmetry A is measurable for parallel and anti-parallel spins of electron beam and target, respectively:

$$A = \frac{N_{\uparrow\uparrow} - N_{\uparrow\downarrow}}{N_{\uparrow\uparrow} + N_{\uparrow\downarrow}}, \quad (3.9)$$

where $N_{\uparrow\uparrow}$ and $N_{\uparrow\downarrow}$ are the number of Møller scattered electrons with parallel and anti-parallel spin orientation, respectively. The asymmetry is at maximum for symmetric Møller scattering ($a_{xx} = -a_{yy} = -1/9$ and $a_{zz} = -7/9$ at $\bar{\theta} = 90^\circ$ [139]). This can be explained by the Pauli principle, which states that the total wave function of two electrons has to be antisymmetric. When having parallel electron spins and therefore a symmetric spin wave function, the spatial wave function has to be antisymmetric. However, the even coefficients of a Legendre polynomial expansion of an antisymmetric wave function cancel out. In addition, when having symmetric scattering with $\bar{\theta} = 90^\circ$, the odd coefficients are also zero. Hence, this causes that anti-parallel spin configurations have a higher scattering rate.

By knowing the Møller target polarisation and the asymmetry coefficients a_{jj} , the beam polarisation P_j^B can be extracted [138]:

$$P_j^B = \frac{A}{\sum_{j=x,y,z} a_{jj} \cdot P_j^{MT}} \quad (3.10)$$

3.2. ELECTRON POLARISATION

A2 Møller Measurement

In the A2 experiment, the Møller foil had an angle of $\alpha = 25 \pm 0.1^\circ$ with respect to the beam direction, thus the electron beam polarisation is given by [86]:

$$P_e = \frac{A}{P_{MT} \cdot \cos \alpha \cdot a_{zz}}, \quad (3.11)$$

where the Møller target polarisation was $P_{MT} \simeq 8.08 \pm 0.21\%$. For relativistic energies, one can derive [86]:

$$a_{zz} \simeq -\frac{\sin^2 \bar{\theta} \cdot (8 - \sin^2 \bar{\theta})}{(4 - \sin^2 \bar{\theta})^2} \quad \text{and} \quad \bar{\theta} = 2 \arctan \frac{E_0 - E_i}{E_i - m_e}, \quad (3.12)$$

where E_0 is the beam energy, E_i the energy of the scattered electron $i = 1, 2$, and m_e is the electron mass.

For the dButanol experiment in July 2013, the Møller polarimeter could only be used to determine relative values, which had to be scaled to the absolute polarisation values taken with the Mott measurement. As seen in Fig. 3.4 (a), Mott and Møller measurements show a similar time behaviour. However, Møller measurements show some fluctuations. In January 2014, the Møller measurement was optimized in a way that absolute values could also be extracted. The corresponding Møller values are compared in Fig. 3.4 (b) to Mott measurements. The extracted Møller polarisation is approximately 3-4% lower than the Mott values. However, the deviations are within the systematic uncertainties. The systematic error of the Møller measurement is mainly originating from the uncertainty of the polarisation of the Møller foil and was estimated to be of the order of 3% [140].

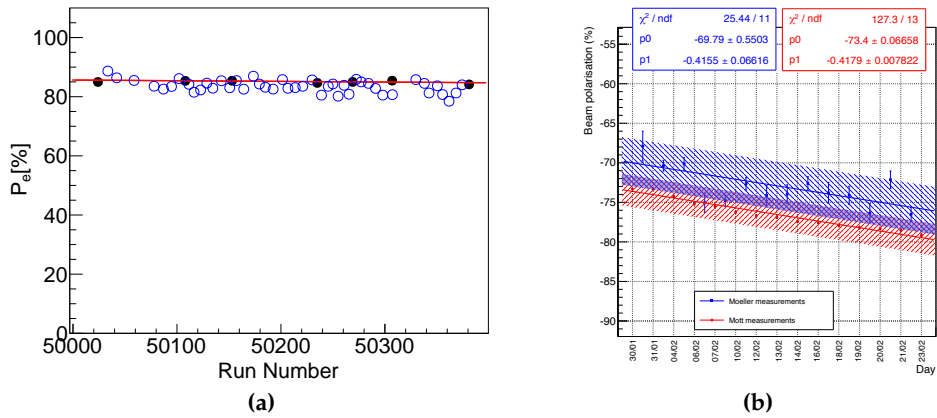


Figure 3.4: (a) Electron polarisation P_e per run extracted from the Møller measurement (blue open circles) at the A2 experiment. An overall factor has been used to scale the Møller values to the Mott polarisation (black dots). (b) Absolute polarisation extracted from Møller (blue) and Mott measurement for the dButanol experiment in January 2014 at A2 by Costanza et al. [140]. The hatched areas show the systematic uncertainties.

CBELSA/TAPS Møller Measurement

At ELSA, the electron polarisation is not perfectly longitudinal at the position of the Møller foil and a transversal component remains. Hence, one has to measure the asymmetry for two angles of the Møller foil $\alpha \sim \pm 20^\circ$ [141], which leads to a beam electron polarisation of:

$$P_e = \frac{A(\alpha) + A(-\alpha)}{2a_{zz}P_{MT} \cos \alpha}, \quad (3.13)$$

where $P_{MT} \simeq 8\%$ and the asymmetry coefficient a_{zz} is given by Eq. 3.12 [138].

The extracted polarisations from the Møller measurement of both dButanol experiments at ELSA are shown in Fig. 3.5 as a function of the run number.

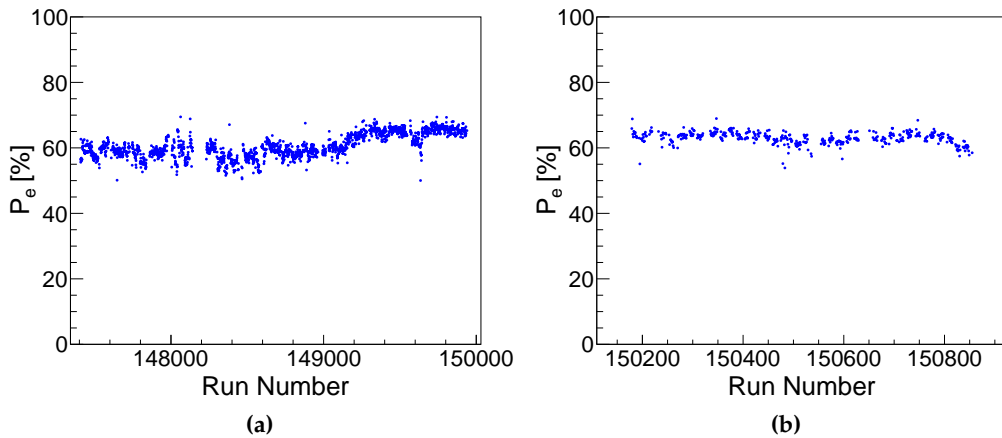


Figure 3.5: Electron polarisation P_e per run extracted from the Møller measurement for the January 2011 (a) and the June 2011 (b) dButanol experiments.

3.3 Photon Polarisation

Having measured the electron polarisation, the photon polarisation for each tagger hit can be determined via the helicity transfer using Eq. 2.6. For the A2 data, the Mott electron polarisation values and for the CBELSA/TAPS data, the Møller values, were used to extract the photon polarisation.

3.4 Target Polarisation

As mentioned in Sec. 2.3.3, the target polarisation was measured with an NMR technique. The NMR system consisted of a RCL (resistor, capacitor, inductor) series circuit with a small coil with a few windings, which surrounded the target. By switching on a radio-frequency (rf) field with a frequency close to the Larmor frequency, a level transition with $\Delta m = \pm 1$ is induced in a certain part of the target material.

As mentioned in Sec. 2.3.3, deuterons exhibit three different Zeeman levels with $m = -1, 0, +1$ when exposed to an external magnetic field. As seen in Fig. 3.6, the transition with $\Delta m = +1$ and $\Delta m = -1$ have the same resonance frequencies ω_0 (Larmor frequency). However, in dButanol, additional electric field gradients occur, which interact with the quadrupole moment of the deuteron. This effect changes the energy of the levels dependent on the angle θ between the electric field gradient and the outer magnetic field, as seen in Fig. 3.6 on the right-hand side. Thus, different resonance frequencies are necessary to induce transitions $|0\rangle \leftrightarrow |+1\rangle$ and $|0\rangle \leftrightarrow |-1\rangle$ [97]:

$$\omega_+ = \omega_0 + 3\omega_q \quad \text{and} \quad \omega_- = \omega_0 - 3\omega_q, \quad (3.14)$$

where ω_q is displacement frequency caused by the interaction of the field gradient with the quadrupole moment. Hence, the corresponding NMR signal shows two peaks at a resonance frequency of ω_{\pm} , as seen in Fig. 3.7. The peaks are broadened due to dipole effects and higher order terms.

The asymmetry method can be used to extract the target polarisation out of the NMR spectra. Using the Boltzmann distribution from Eq. 2.9, one can derive a relation between the target polarisation P_T and the ratio of the occupation number of the levels

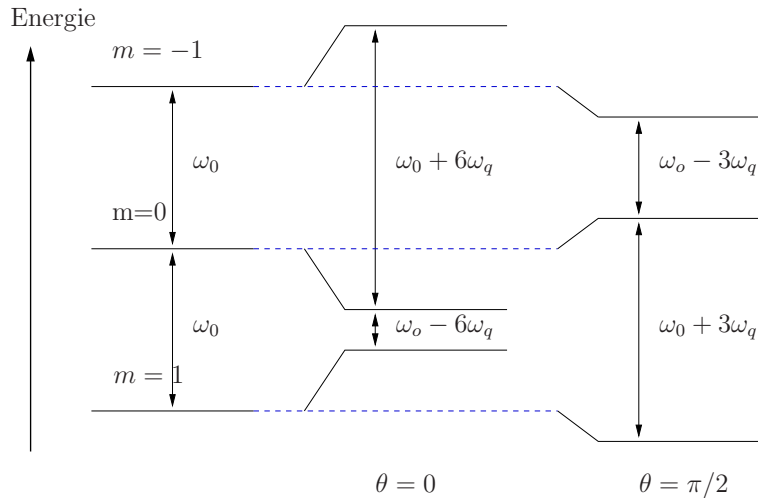


Figure 3.6: Level splitting induced in deuterons by an outer magnetic field (left-hand side). The level spacing changes in dButanol due to electric field gradients (right-hand side) depending on the angle between the electric field and the magnetic field. Figure taken from [97].

with $m = \pm 1$ [97]:

$$P_T = \frac{r^2 - 1}{r^2 + r + 1}, \quad (3.15)$$

where $r = \sqrt{N_1/N_{-1}}$ can be found from the height of the two peaks in the NMR spectrum. If the asymmetry method is used during the DNP process (see Sec. 2.3.3) to measure the target polarisation, an additional calibration factor has to be applied, since then, the signals are not in equilibrium. The calibration factor is determined from the slope when plotting the polarisation from the asymmetry measurement versus the area of the peaks (units of area), as seen in Fig. 3.7 (b). A detailed explanation of the target polarisation measurement of the dButanol target can be found in Ref. [97].

At the A2 experiment, the target polarisation was always measured before and after data taking and when changing the direction of polarisation. On the contrary, in the CBELSA/TAPS experiment, the target polarisation had to be measured every two days, when the target was repolarised. This was caused by the fact that at A2, longer relaxation times could be achieved than at CBELSA/TAPS due to the lower temperature of the A2 target. The relaxation time of the A2 target was approximately 2000 hours, whereas for the CBELSA/TAPS target a relaxation time of only 340 hours could be reached.

The target polarisation between the measurements $P_T(t)$ was determined assuming an exponential decay:

$$P_T(t) = P_T(0) \cdot e^{-t/\Delta\tau}, \quad (3.16)$$

where $P_T(0)$ is the initial target polarisation, $P_T(t)$ the target polarisation at time t , and $\Delta\tau$ the relaxation time. The relaxation time was determined from the measured initial and final polarisation. The resulting target polarisation values as a function of the run number are shown in Figs. 3.8 and 3.9 for the A2 and CBELSA/TAPS experiments, respectively.

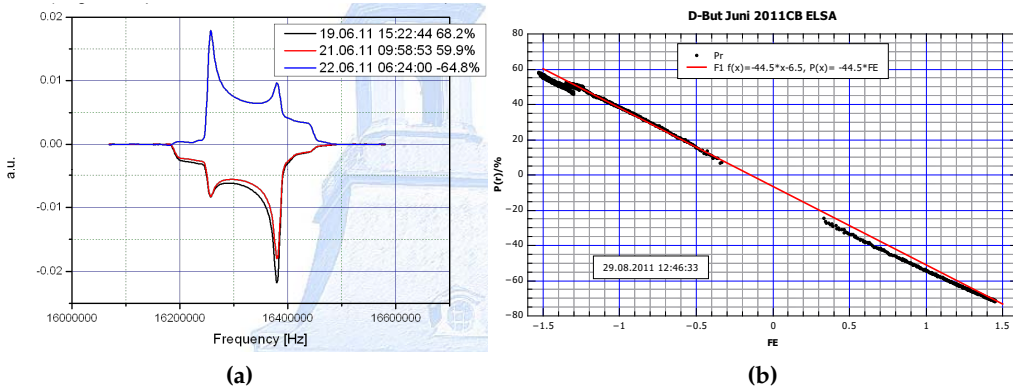


Figure 3.7: (a) NMR signal from the June 2011 dButanol experiment at ELSA. The two peaks originating from the transitions with $\Delta m = \pm 1$ are clearly visible. (b) Extraction of the calibration factor by plotting the target polarisation versus the units of area. Figures taken from [104].

3.4. TARGET POLARISATION

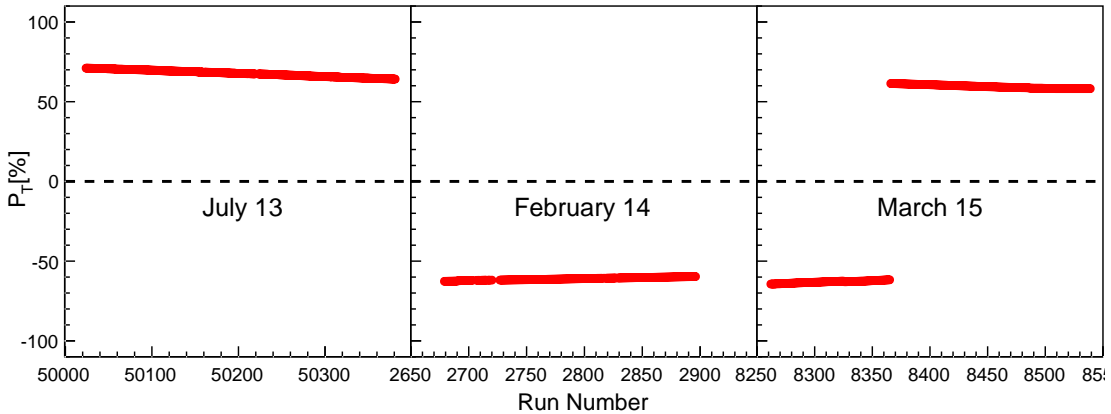


Figure 3.8: A2 target polarisation values for all three dButanol experiments during production data taking versus the run number. In February 2014 and March 2015, the direction of the target polarisation was changed in order to account for systematic effects.

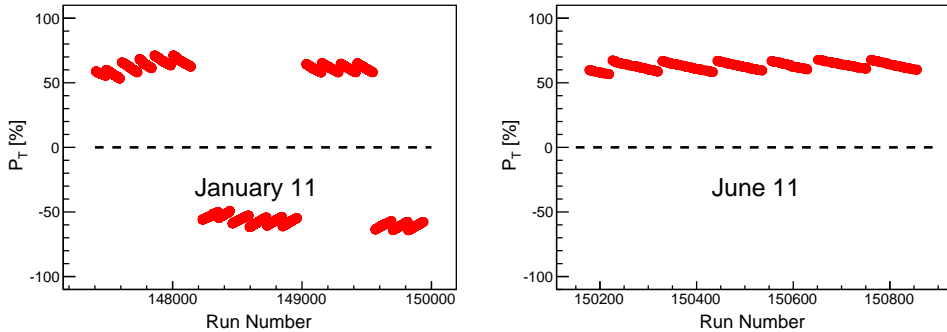


Figure 3.9: CBELSA/TAPS target polarisation values for the two dButanol experiments. As visible in the graph, the target had to be repolarised several times. Furthermore, the direction of the target polarisation was changed three times in the first of the two experiments [103].

3.4.1 D-Wave Admixture

As previously mentioned, the deuteron is composed of a proton and a neutron and has total spin $J = 1$ and positive parity $\pi = +1$, with $J = s_p + s_n + L$, where s_p and s_n are the spin of the proton and neutron, respectively, and L is the orbital angular momentum. Hence, $J^\pi = 1^+$ is possible for parallel proton and neutron spins and $L = 0$. However, the sum of the magnetic momenta of proton and neutron is smaller than the one of the deuteron, $\mu_p + \mu_n = 0.88\mu_K$, as can be deduced from Table 2.1. Thus, the deuteron is not a pure S -state ($L = 0$) and an admixture of a state with $L > 0$ is needed. Due to the positive parity of the deuteron, the state with $L = 1$ is clearly forbidden. Hence, the deuteron wave function has a contribution from the D -state with $L = 2$ and anti-parallel proton and neutron spin with respect to the angular momentum. The average probability to form a deuteron in D -state according to Rondon is $4.90 \pm 1.04\%$ [142]. The D -wave admixture in the wave function causes a deviation from the spherical shape of the nucleus and hence induces a quadrupole

moment. As mentioned earlier in this section, the quadrupole moment has an influence on the deuteron polarisation, which is measured using the NMR technique. With the help of Clebsch-Gordan coefficients, it can be shown that this leads to a reduction in the nucleon polarisation in deuterium by approximately 8% [142]:

$$\gamma = 0.926 \pm 0.016. \quad (3.17)$$

3.4.2 Issue with the A2 Target Polarisation Values

Preliminary results on the double polarisation observable E from the A2 experiments for this work have shown that there is some issue with the target polarisation. The magnitude of E was significantly smaller than unity in the energy range of the $S_{11}(1535)$ resonance, as it is expected from model predictions. Extensive analysis checks, as explained in Sec. 9.4.1, have excluded possible causes other than the target polarisation values.

Essentially, there are two possible reasons for wrong target polarisation values. The first possibility is that the target polarisation is destroyed during the measurement because of beam heating. This was excluded by several measurements of the target polarisation during data taking. The second possibility is that the target material is inhomogeneously polarised due to field inhomogeneities of the polarising magnet. The inhomogeneities would cause a position dependent splitting of the Zeeman levels of the deuterons inside the target and lead to different polarisation frequencies, as

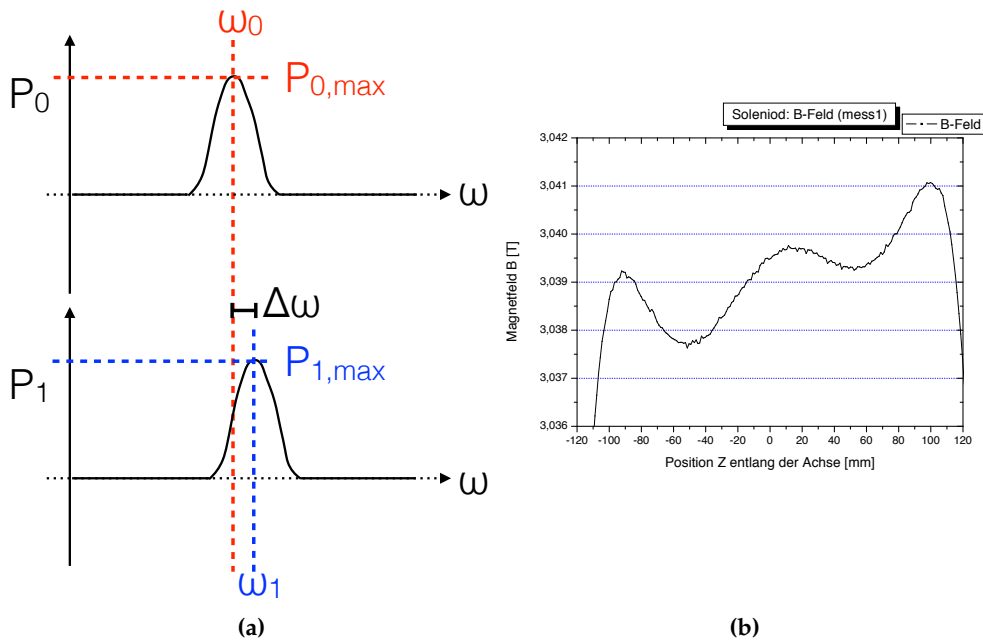


Figure 3.10: (a) The frequency ω_1 to reach a maximum possible polarisation $P_{1,max}$ (at site 1) is shifted by $\Delta\omega$ compared to the frequency ω_0 (at site 0) due to magnetic field inhomogeneities. (b) Magnetic field inhomogeneities for the A2 Frozen Spin target in z-direction measured in 2002. Figure (b) taken from [143].

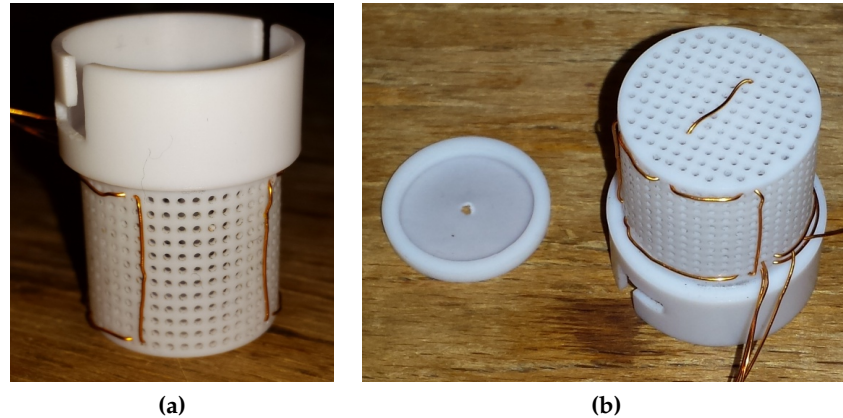


Figure 3.11: The new NMR coils installed in March 2015 to achieve position sensitivity. (a) Surface anti-Helmholtz coil, which produces a constant field gradient and no high frequency field in the center. (b) One-loop in-beam coil, produces a maximum high frequency field in the center. Figures taken from [144].

shown in Fig. 3.10 (a).

Hence, to check for inhomogeneities, the standard NMR coil was replaced by two new coils (see Fig. 3.11) for the experiment in March 2015. The surface coil (anti-Helmholtz coil) produced a constant field gradient in the target cell and no high frequency field in the center of the target. The second coil (in-beam coil) was a one-loop coil producing a maximum high frequency field in the center of the target and thus was monitoring the region of the beam spot on the target.

Measurements with these two NMR coils have shown significant differences between the target polarisation in the central and the outer region of the target, as shown in Table 3.2. By tuning the frequency during the DNP process, the polarisation in the center of the target could be significantly increased. Higher frequencies lead to a higher polarisation in the outer region of the target, hence it can be concluded that the magnetic field on the surface of the target is larger than in the center.

With the frequency shift $\Delta\omega \simeq 50$ MHz and $\gamma_e = 176085.9708$ MHz/T, the inhomogeneities of the magnetic field can be estimated via the following formula [145]:

$$\Delta B = \frac{\Delta\omega}{\gamma_e/(2\pi)} \simeq (1.78 \pm 0.36) \text{ mT}. \quad (3.18)$$

This value is slightly higher than the inhomogeneity determined in 2002, which is shown in Fig. 3.10 (b). Hence, a remeasurement of the field inhomogeneities is desirable.

If the target polarisation issue is caused by field inhomogeneities one would first expect that the same problem should be present for the HButanol target. However, the doping of HButanol and dButanol is different and the electron spin resonance (ESR) line (frequency range for the polarisation) is much broader in the case of HButanol and thus it is less sensitive to magnetic field inhomogeneities.

In the CBELSA/TAPS experiment, this issue was not observed, however, the used polarising magnet is of superior quality with respect to the A2 magnet.

In summary, the extracted target polarisation values for all experiments at A2 using the dButanol target have to be checked carefully by a monitor reaction, where models have a clear prediction of observables. The investigation of this issue is still ongoing.

date	ω [GHz]	$P_{surface}$	$P_{in-beam}$	$P_{surface}/P_{in-beam}$
24.03.15	70.032	-74.76 ± 0.65	-53.24 ± 0.54	1.40
25.03.15	70.032	-76.11 ± 0.25	-51.60 ± 0.15	1.47
25.03.15	70.030	-62.55 ± 0.08	-65.98 ± 0.25	0.94
26.03.15	70.030	-62.91 ± 0.07	-63.03 ± 0.23	0.99
26.03.15	70.026	-56.16 ± 0.30	-68.38 ± 0.10	0.82
27.03.15	70.026	-56.42 ± 0.95	-66.35 ± 0.50	0.85
27.03.15	69.978	57.07 ± 0.16	64.37 ± 0.11	0.89
30.03.15	69.978	53.66 ± 0.20	62.26 ± 0.10	0.86

Table 3.2: Polarisation values measured with the surface coil and the in-beam coil for different polarising frequencies ω . Values taken from [145].

Chapter 4

Software

The analysis of raw data files of the CBELSA/TAPS and the A2 experiment has been done using different software frameworks. The tool used to presort A2 data was AcquRoot, while EXPLORA in combination with an additional plugin was used for CBELSA/TAPS data. The presorted data was further processed with the help of OSCAR (A2 data) or libTOCB (CBELSA/TAPS data), a library derived from OSCAR. The final evaluation was done using ROOT macros. ROOT is a software framework developed at CERN [146].

4.1 A2 Software

The main software components used for the A2 experiment are AcquRoot, A2 Geant and OSCAR. A short description of every tool is given in the following subsections.

4.1.1 AcquRoot

AcquRoot is the software framework used for data acquisition, data analysis and Monte Carlo (MC) event generation by the A2 collaboration [147]. AcquRoot, written in C++, is based on ROOT. It consists of the AcquRoot analyser, AcquDAQ, and AcquMC. The latter, AcquMC, is a MC event generator and was not used for the current work. AcquDAQ was used for the data acquisition during the experiment.

The AcquRoot analyser was used to process the binary raw files from the experiment and the files created by A2 Geant. In AcquRoot, all the detector components are implemented in dedicated classes, which are derived from base classes. The TA2MyPhysics class combines all the information from the different detector subsystems and handles them over to the main presort class TA2MyPreAnalysis. During pre-selection, all calibrations are applied and a very rough event selection is done. This preselection procedure speeds up the further analysis of the data. Standard AcquRoot uses ASCII files for the configuration of detector dependent settings and calibration values. For this work, a software framework called CaLib was developed. CaLib was used to calibrate all detector systems and to store the calibration values in a MySQL database. Further information about CaLib can be found in Ref. [56].

4.1.2 A2 Geant

MC simulations have been done using the A2 Geant simulation package [148]. The A2 Geant toolkit contains the whole setup of the A2 experiment. It is based on Geant4 [149], which is being developed at CERN. Geant is an acronym for *geometry and tracking* and is used to model the passage of particles through matter. It describes the energy loss due to hadronic and electromagnetic interactions of the particles with the experimental setup.

All detector components and targets are implemented as precisely as possible to enable realistic tracking of the particle from the target to the detectors. Geant4 provides different physics lists to model the particle interactions in different energy ranges. Investigations of the cluster size and neutron detection efficiencies have shown [56] that the Bertini cascade models (QGSP_BERT) in combination with the high precision neutron package (_HP) lead to better results than the Binary cascade models (QGSP_BIC). The different physics lists are explained in detail in Ref. [150].

The output of A2 Geant was used for the determination of the detection efficiency and is described in Sec. 8.8.

4.1.3 PLUTO

For this work, the MC event generator PLUTO was used. PLUTO [151] is based on ROOT and was developed by the HADES collaboration (GSI, Darmstadt) for hadronic and heavy ion reactions. It can be used to generate particles, i.e., Lorentz vectors, using different mass and momentum sampling methods. Simple reaction channels can be combined to construct complex reactions. The needed particle properties and decay modes are read out from a PLUTO internal data base.

Different output formats can be chosen, such as ASCII and ROOT (NTUPLE) files. The PLUTO output was used as input in Geant to produce secondary particles in the detector system.

A special tool (*NucleusFermiPlugin*) was implemented for this work to use PLUTO for quasi-free nucleons that carry a Fermi momentum. The momentum of the initial state nucleons have been sampled from the corresponding Fermi distribution. Calculations from the Paris potential [152] for deuterium and Argonne potential [153] for ^3He nuclei have been used. In addition, Fermi distribution for the ^7Li [154] and ^{12}C [154] have been implemented. Some of the implemented Fermi distributions are shown in Fig. 4.1.

The PLUTO algorithm constructs the intermediate state four-vector from the beam photon and the participant nucleon, and the decay into the final state nucleon and η meson, as it is described by the participant-spectator model (see Sec. 7.5.4). At this stage, all decays were calculated using pure phase space distributions. Later, in the analysis, the events were weighted according to angular distribution extracted from experimental data.

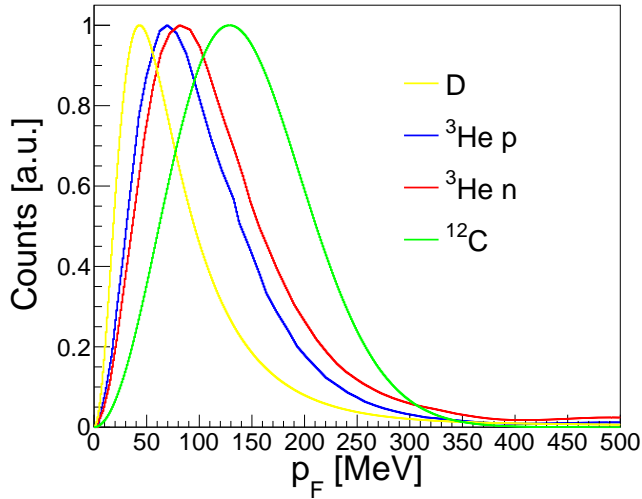


Figure 4.1: Fermi momentum distributions for deuterium [152], helium [153] and carbon [154], which have been implemented in PLUTO.

4.1.4 OSCAR

OSCAR is a C++ class library based on ROOT and was mostly developed by D. Werthmüller [56]. OSCAR stands for OSCAR Simplifies Coding and Analysing with ROOT and was intensively used for this work. It contains several different modules, for example [56]:

- A2: provides basic classes for the meson reconstruction, which are used by Ac-quRoot
- analysis: contains all analysis classes to process the presorted files
- graph and math: contain basis functions and plotting features
- utils: enables the storing of cross section data and simplifies the reading of files
- MC: provides the possibility to generate MC events

4.2 CBELSA/TAPS Software

The analysis of CBELSA/TAPS experimental data and simulation was done with the EXPLORA software in combination with a class collection similar to OSCAR, called libTOCB. Instead of Geant4, the CBELSA/TAPS experiment uses Geant3, since major parts have not yet been translated from Fortran to C++.

4.2.1 EXPLORA, MyAnalysis and libTOCB

EXPLORA [155] is an analysis software which was developed at Bonn especially for the CBELSA/TAPS experiment. EXPLORA stands for Extended Plugable Object oriented Root Analysis and is written in C++ and based on ROOT. Due to the modular

structure using plugins, EXPLORA is a very flexible tool. It uses data in the *zebra* format as input files and can be controlled via XML files. This work only used the very basic classes of EXPLORA for the readout of the data files, application of calibration, and the reconstruction of clusters. The software trigger decision, assignment of the neutral or charged particles and particle identification has been done with a plugin, especially developed for this work, called *MyAnalysis*. *MyAnalysis* is constructed in a similar way as *AcquRoot* to simplify the analysis of CBELSA/TAPS data for future students. *MyAnalysis* contains a presort analysis class, which is derived from a physics class called *MyPhysics*. As in *AcquRoot*, the *MyPhysics* class handles all the information from the different detector subsystems. *MyAnalysis* uses the same meson reconstruction algorithms and presort format as OSCAR. However, some OSCAR classes had to be slightly changed due to the different detector setup. The new classes are combined in a library called *libTOCB*.

4.2.2 CBGEANT

MC simulations with CBGEANT [156] were used for the detection efficiency correction. CBGEANT is based on Geant3 [157]. Geant3 is the older version of the CERN Geant4 and is written in Fortran.

As in A2, the whole detector setup of the CBELSA/TAPS experiment is implemented in CBGEANT. This is mainly done in the *dbio* tool of CBGEANT, which contains information about the geometry, materials, and tracking media of the whole experiment. In contrast to the rest of CBGEANT, the *dbio* is written in C. This is helpful for a future upgrade to Geant4, which is the completely renewed, object-oriented C++ programmed version of Geant3.

CBGEANT uses different interaction models for a thorough description of the interaction processes. However, especially for neutron simulations, it is important to use an additional Geant package, the GCALOR. GCALOR contains three parts:

- "*HETC: the High-Energy-Transport-Code is transporting charged hadrons up to an energy of 10 GeV through the materials of the setup.*" [158]
- "*FLUKA: the FLUKA fragmentation model is utilized for interactions above the HETC limit.*" [158] (Though, FLUKA is not of interest for this work, since it contains only higher energies.)
- "*MICAP: the neutron code from the Monte-carlo-Ionization-Chamber-Analysis-Program is called for neutrons with a kinetic energy below 20 MeV. The simulation of interactions is based on measured/calculated cross sections and secondary particle energy/angular distributions.*" [158]

CBGEANT is controlled via *crd* files, where one can select between different detectors and targets. The output of CBGEANT is a *zebra* file with energy and timing informations for each sensitive detector element of the setup. This MC output file can then be analysed with the same EXPLORA analysis that is used for the experimental data.

4.2. CBELSA/TAPS SOFTWARE

For similar reasons as discussed in Sec. 4.1.2, the detection efficiency determined from simulations with CBGEANT were corrected using hydrogen data, as explained in Sec. 8.8.

Chapter 5

Event Reconstruction

In this section, the reconstruction of events is explained. The event reconstruction uses all the available information from the involved detector elements to determine the spatial position, time, energy, and type of detected particles.

When a photon hits a detector, an electromagnetic shower is produced, which spreads over several neighbouring crystals. Therefore, all hit elements have to be combined to a cluster to be able to assign the energy and impact position to the current event. For all detectors, very similar reconstruction methods were used, but they are not identical and are explained in more detail in this chapter.

5.1 A2 Event Reconstruction

5.1.1 Tagger

A real clustering algorithm was not used for the tagger, instead, as explained in Sec. 2.2.3, the electronics required a coincident signal in two adjacent tagger scintillators. Depending on the magnetic field, the tagger energy calibration assigns the mean value and width of the corresponding electron energy to each tagger channel. The calibration is implemented in a small Fortran program called `ugcalv2ua` [89]. It calculates the correct channel assignments from the average magnetic field and the electron beam energy of the current experiment with the help of a uniform magnetic field map. The field map of the tagger magnet has been determined in several measurements. The energy assignment of the tagger channels is based on a measurement where the tagger was scanned with a very low electron current from MAMI. The energy of the MAMI electron beam has an accuracy of 140 keV [89]. The photon energy for each tagger channel was then calculated using Eq. 2.7.

5.1.2 Crystal Ball

The event reconstruction in the CB was done with a dedicated cluster algorithm. The cluster algorithm first goes through the list of all hit crystals and orders them according to their energy. The crystal with the maximum deposited energy is set to the cluster center and the time of this crystal was set as the time of the cluster. By going through

all 12 neighbouring (directly adjacent) crystals, the cluster was formed. The cluster algorithm only used the directly adjacent crystals since in the CB, as explained in Ref. [106], 98% of the energy of a photon is deposited in 13 crystals. The energy of all the cluster members E_i , where $i = 1, \dots, n$, was added to the cluster energy $E_{cluster}$, when it was bigger than the crystal threshold of approximately 2 MeV:

$$E_{cluster} = \sum_{i=1}^n E_i, \quad (5.1)$$

where n is the number of hit elements (13 in maximum). One crystal was only allowed to belong to one cluster, and overlapping clusters were not split. The maximum number of clusters was limited to 12 clusters in the CB, whereas each cluster was required to have a total energy of more than 20 MeV in order to reduce split-off effects. A split-off is an energy deposit, which is not connected to the main cluster. Most often split-offs are induced by showers of secondary particles.

By energy weighting the individual crystal positions, \vec{r}_i , the cluster position was determined with:

$$\vec{r}_{cluster}^{CB} = \frac{\sum_{i=1}^n \sqrt{E_i} \cdot \vec{r}_i}{\sum_{i=1}^n \sqrt{E_i}}. \quad (5.2)$$

After all clusters in the CB were found, the clusters were compared to hits in the PID in order to determine whether it was a charged particle or not. For this purpose, the minimum difference in azimuthal angle $\Delta\phi$ of a CB cluster and a hit PID element was calculated. Since each of the 12 PID elements covered $180^\circ/12 = 15^\circ$ in azimuthal angle, hits with $\Delta\phi < 15^\circ$ were assigned to the charged particle list and the energy deposited in the PID was weighted according to the polar angle θ :

$$E^{PID} = E_{element}^{PID} \cdot \sin \theta_{cluster}^{CB}. \quad (5.3)$$

Hence, since the PID had no θ angle information, it could have happened that a particle was wrongly identified as a charged particle when the CB cluster had a similar azimuthal angle, but different polar angle as the corresponding PID hit. This effect played a bigger role when multiple hits were in CB. It was seen [56] that the detection efficiency for the $\eta \rightarrow 3\pi^0 \rightarrow 6\gamma$ was significantly reduced by this misidentification, since such events have been rejected. However, the overall normalisation should not be affected, since the simulation exhibits the same behaviour.

To assure that the PID signal was not caused by electronic noise, a low energy threshold of 350 keV was set per PID element.

5.1.3 TAPS

In the TAPS detector, each signal goes through a Constant Fraction Discriminator (CFD), which applies an energy threshold of about 3 – 5 MeV. As for the CB, the cluster algorithm makes an energy ordered list of all hit TAPS crystals and assigns the

element with the maximum deposited energy to the logical center. Again, the time of this element is set to the cluster time. The cluster algorithm checks all the hit crystals and adds the energy to the cluster energy when the crystal is a neighbour of a cluster member (Eq. 5.1). In contrast to the CB, not only adjacent neighbours of the central element are taken into account. The cluster threshold was set to 20 MeV and the maximum number of clusters to eight. To account for the exponential energy distribution, the position was logarithmically weighted :

$$\vec{r}_{cluster}^{TAPS} = \frac{\sum_{i=1}^n W_i \cdot \vec{r}_i}{\sum_{i=1}^n W_i} \quad \text{with} \quad W_i = \max \left\{ 0, P + \ln \frac{E_i}{E_{cluster}} \right\}, \quad (5.4)$$

where the parameter $P = 5$ was determined by Molenaar *et al.* [159] with the help of MC simulations.

Since TAPS is a flat detector and the crystals are not radially mounted as in the case of the CB, a polar angle dependent correction on the position has to be applied. Fig. 5.1 shows the situation in two dimensions. Due to the shower depth $d = X_0 \cdot \ln \frac{E_{cluster}}{E_{crit}}$ ($E_{crit} = 12.7$ MeV and $X_0 = 2.05$ cm for BaF₂), the reconstructed position (x, y) with flight path s is shifted by Δx and Δy . The correct position (x', y') can be calculated according to [160]:

$$\frac{x - x'}{x} = \frac{y - y'}{y} = \left(\frac{s}{d} + 1 \right)^{-1}. \quad (5.5)$$

Since many particles have a tilted trajectory with respect to the beam axis, it can also happen that a charged particle does not deposit energy in the central element, but in a neighbouring crystal. Therefore, not only the veto in front of the central element, but also the vetoes of all adjacent neighbours of the central element and the vetoes of all cluster elements were checked. The LED threshold of the vetoes was set to 150 – 300 keV, so that only events above this energy were treated as charged.

Table 5.1 summarises the software thresholds used for all detectors in the A2 setup.

	CB	TAPS	PID	TAPS Vetoes
crystal	2 MeV	3-5 MeV	350 keV	150-300 keV
cluster	20 MeV	20 MeV	-	-

Table 5.1: Typical software thresholds used for the detectors of the A2 setup.

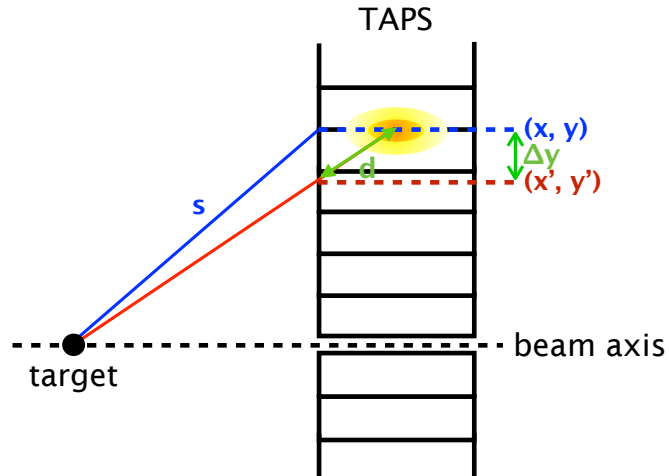


Figure 5.1: Shower depth correction for the TAPS detector as explained in Eq. 5.5.

5.2 CBELSA/TAPS Event Reconstruction

At the CBELSA/TAPS experiment, the philosophy of the clusters in the two main calorimeters CB and MiniTAPS is slightly different.

A cluster, i.e. a series of hit neighbouring crystals, can consist of several Particle Energy Deposits (PEDs). The cluster algorithm first builds clusters and then looks for local maxima and accordingly subdivides the cluster into PEDs. For this work, the number of PEDs per clusters was limited to two.

5.2.1 Tagger

As explained in Sec. 2.2, the tagger consisted of scintillating bars and scintillating fibres. An electron hit in the tagger usually caused a signal in at least two bars and additionally in the overlapping part in up to three fibres, as shown in Fig. 5.2. Thus, the reconstruction of the tagger hits was much more complex than in the case of the Mainz photon tagger. In a first step, the algorithm built clusters of hit scintillation bars using a neighbouring list. Then, the time signals were checked for coincidence. The time difference between the first and last hit of a cluster had to be smaller than 6 ns. The same was done for the scintillating fibres. Since their time resolution was slightly worse, a coincident signal of 7 ns was required. Due to inefficiencies of the fibres, gaps in the cluster of one fibre were allowed. In the next step, the clusters in the fibres and bars were combined to so-called *beam photons*, where at least one fibre was overlapping with the corresponding bar cluster. Additionally, the time difference of both clusters had to be less than 4 ns. Bar clusters that could not be combined could occur in the range where the bars and fibres were not overlapping or due to inefficiencies and were left as they are. Pure fibre clusters were not used for further analysis. To calculate the time of a *beam photon*, the average time of all fibres t_i and bars t_j were

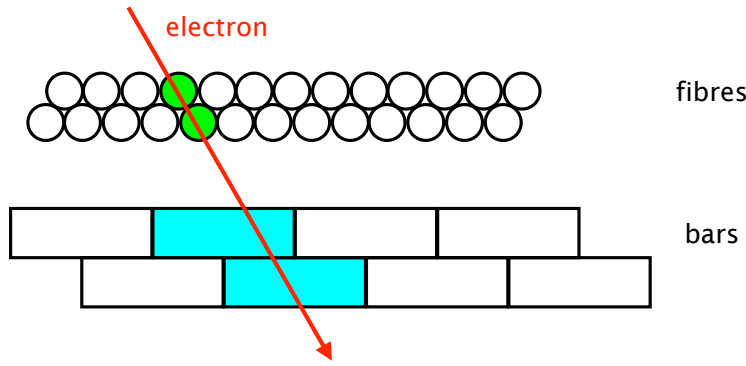


Figure 5.2: In the CBELSA/TAPS tagger, an electron hits at least two bars and in the overlapping part up to three fibres. Adapted from [119].

weighted with the corresponding resolution $w = 1/FWHM^2$ [125]:

$$t = \frac{w_{fibre} \cdot \sum_{i=1}^{n_{fibre}} t_i + w_{bar} \cdot \sum_{j=1}^{n_{bar}} t_j}{w_{fibre} \cdot n_{fibre} + w_{bar} \cdot n_{bar}}, \quad (5.6)$$

where n_{fibre} and n_{bar} is the number of hit fibres and bars, respectively.

The mapping of fibres and bars to energy was done with the help of the tagger polynomials (three for the bars and one for the fibres). These polynomials have been extracted from a calibration measurement where electrons with a known energy have been directed to the tagger ladder [83]. In order to get the beam photon energy, the average value of all hit fibres and/or bars was used:

$$E_\gamma = \frac{1}{n_{fibre/bar}} \cdot \sum_{i=1}^{n_{fibre/bar}} E_i, \quad (5.7)$$

where E_i is the energy of the tagger fibre or bar i . Due to the geometrical acceptance, the tagger fibres provide a better energy resolution and thus whenever possible, the energy was determined from the fibres and not the bars.

5.2.2 Crystal Barrel and Forward Plug

Since the crystals of the CBB and the FP are identical, the clustering for these two detectors was done simultaneously. However, the main difference between the CBB and the FP is that the FP provides a time signal, whereas the CBB does not. Therefore, the clustering was done without time information. For PEDs in the FP, the time was taken from the time of the central element.

The cluster algorithm first made a list of all hit crystals. A crystal energy threshold of 1 MeV was applied in order to get rid of signal noise. Then, as for the CB at A2, the crystal with the maximum deposited energy was set as the logical center of the cluster and all connected hit clusters were added to it. To reduce split-offs, the energy of the whole cluster, as well as the central energy of the cluster, had to be above 20 MeV. In

a second step, the cluster algorithm searched for local maxima in the cluster. Each of these local maxima elements was set as center of a PED, when its energy was above 20 MeV.

When there was only one PED in a cluster, the energy of the PED was given by the cluster energy and thus the sum over all (not only adjacent to the central element, as in the A2 CB) n crystals with deposited energy $E_i > 1$ MeV can be expressed as [161]:

$$E_{PED} = E_{cluster} = \sum_{i=1}^n E_i. \quad (5.8)$$

When two PEDs, PED1 and PED2, were in the same cluster, it was assumed that a part of the energy deposited in PED1 was coming from PED2 and vice-versa. Thus, the energy of every crystal in the PED was weighted with the Molière radius $r_m = 3.57$ cm [162]. The weight is defined as:

$$w_{12} = E_2^{max} \cdot e^{-|r_1 - r_2|/r_m}, \quad (5.9)$$

where E_2^{max} is the maximum crystal energy of PED2 and $|r_1 - r_2|$ is the distance between the current crystal in PED2 and a certain crystal in PED1. The distance was corrected for the shower depth [162]:

$$d = X_0 \cdot \left(\ln \left(\frac{E_2^{max}}{E_{crit}} \right) + 2 \right). \quad (5.10)$$

where $X_0 = 1.86$ cm is the radiation length, and $E_{crit} = 11.04$ MeV is the critical energy of CSI(Tl). The critical energy is the energy at which the energy loss by ionisation and bremsstrahlung are equal.

The whole weighting algorithm is complex and more detailed information can be found in Ref. [162]. Having weighted the energies, the energies of the central crystal and the eight adjacent neighbours of the PED are summed up. However, since the CBB has some insensitive areas where the energy cannot be detected, such as holding structures and titanium crystal wrappings, the PED energy had to be corrected with a function that was determined with MC simulations [161]:

$$E_{PED}^{corr}(\theta, E) = E_{PED} \cdot \left(f_{\text{Landau}}(E_{PED}) + k_1 \cdot \left(1 - e^{-E_{PED}^{k_2}/k_3} \right) + k_4 \cdot E_{PED} \right), \quad (5.11)$$

where E_{PED} is the energy of the PED, f_{Landau} is the Landau function [161], and the coefficients k_1, \dots, k_4 have been determined for 133 polar angle bins, as explained in Ref. [161].

To reconstruct the spatial position of the event, a logarithmic weighting was used:

$$\vec{r}_{PED}^{CBB} = \frac{\sum_{i=1}^n W_i \cdot \vec{r}_i}{\sum_{i=1}^n W_i} \quad \text{with} \quad W_i = \max \left\{ 0, P + \ln \frac{E_i}{E_{PED}} \right\}, \quad (5.12)$$

where E_i is the energy of the crystal i and \vec{r}_i the corresponding position. MC simulations have shown that the most accurate reconstruction (resolution of 2° for θ and ϕ) could be achieved with the parameter $P = 4.25$ [163].

As explained in Sec. 2.4.2, the inner detector consisted of three layers of scintillating fibres. First, the cluster algorithm combined nearby hit fibres to a group, as shown in Fig. 5.3 (b) 1.) After that, the time signals of the hits in one cluster were compared and when the difference was larger than 14 ns, the fibres were assigned to a new cluster, as shown in Fig. 5.3 (b) 2.) This second step could induce a gap in a cluster and thus a second spatial clustering was performed, as seen in Fig. 5.3 (b) 3.) The maximum number of clusters per layer was limited to 20. When having the clusters in each layer, the crossing point of two coincident fibres (<14 ns) was calculated and a θ and ϕ angle could be assigned for the current cluster. When a charged particle hit all three layers of the inner detector, three clusters would have been registered: one for coincident fibres in layers one and two, a second for layers two and three, and a third for layers three and one. When these clusters had an average time difference of less than 14 ns and an angular difference of less than 10° in θ and ϕ , these were combined to a so-called *route*. A reconstruction quality l_q was assigned to these routes according

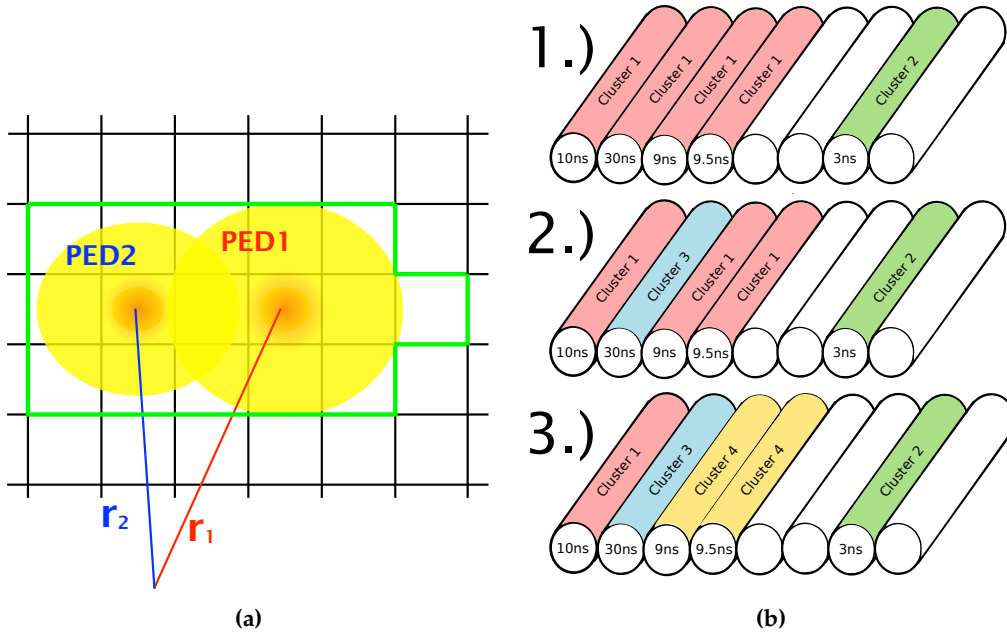


Figure 5.3: (a) Clustering in the CBB and in MiniTAPS at CBELSA/TAPS: two overlapping PEDs (yellow) form a parent cluster (green). (b) Three steps of the clustering of the inner detector: 1.) Neighbouring hit fibres are assigned to clusters. 2.) The clusters are split when the time difference is bigger than 14 ns. 3.) Second spatial clustering. Figure (b) taken from [119].

to the number of hit layers:

layers per cluster	l_q	
1	1/3	
2	2/3	
3	1	

(5.13)

Since the energy resolution of the scintillating fibres is poor, the energy information of the inner detector could not be used. However, to reduce noise, a hardware threshold of ~ 150 keV per fibre was applied.

Similar to the reconstruction in the inner detector, the clustering for the FP vetoes was subdivided into three parts: spatial clustering, time clustering, and a second spatial clustering. Since, as mentioned in Sec. 2.4.2, the vetoes were overlapping, a charged particle should always fire two vetoes. A maximum time difference of 20 ns was required for these veto clusters, as seen in Fig. 5.5. This cut is a standard EX-PLORA cut and is chosen quite broad to not cut off real events.

A reconstruction quality l_q for the resulting vetoes routes was set:

veto per cluster	l_q	
1	0.45	
2	1	
3	0.75	
> 3	0.5	

(5.14)

The time and angular information of the route was calculated by averaging the values of the corresponding vetoes.

Having θ and ϕ of the hits in the inner detector and the FP vetoes, they could be compared to the one in the CBB and FP crystals, respectively. As shown in Fig. 5.4, a hit was assigned to the charged list in the CBB, when:

$$\begin{aligned} \text{CBB: } & \Delta\phi \leq 12^\circ \text{ & } \Delta\theta \leq 30^\circ , \\ \text{FP: } & \Delta\phi \leq 14^\circ \text{ & } \Delta\theta \leq 15^\circ . \end{aligned} \quad (5.15)$$

Additionally, it was required that at least two FP vetoes or two layers of the inner detector have hit:

$$\begin{aligned} \text{CBB: } & l_q > 1/3 , \\ \text{FP: } & l_q > 0.45 . \end{aligned} \quad (5.16)$$

Therefore, clusters with only one hit in the FP vetoes or only one hit layer in the inner detector were assigned to the neutral list. However, to achieve a proper separation of protons from neutrons, events with a single hit in the FP veto or one layer hits in the inner detector were rejected from the analysis of the neutron channel.

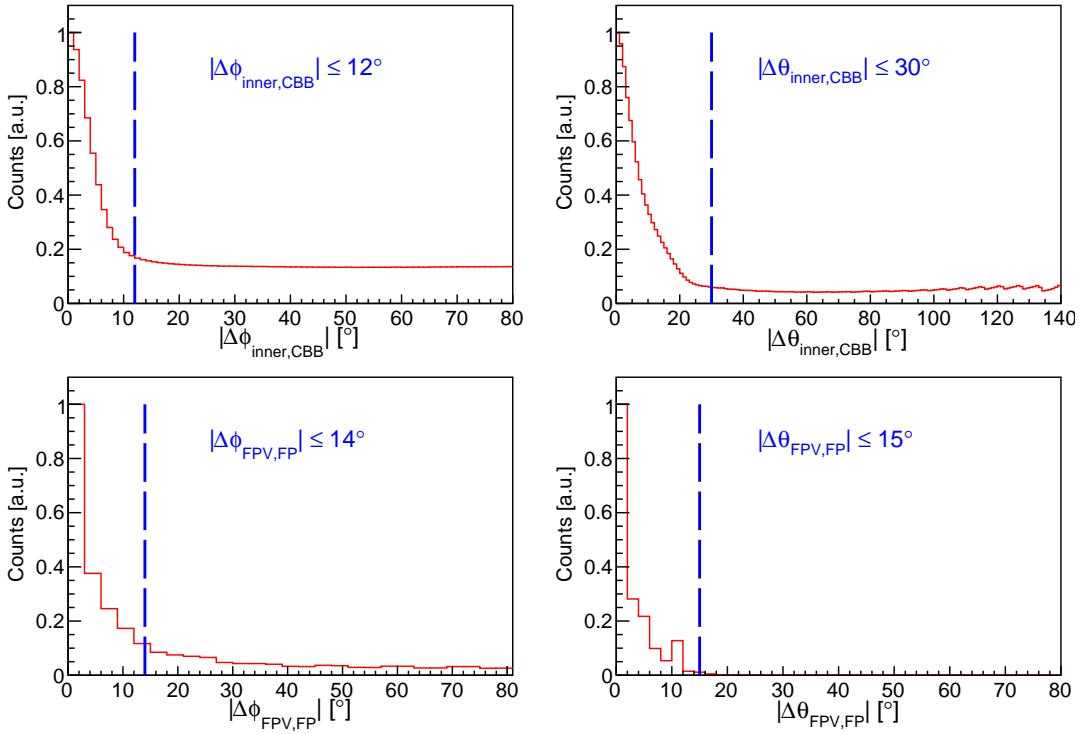


Figure 5.4: Polar and azimuthal angular difference between hits in the charge sensitive detectors and the corresponding calorimeters for all registered events (no reaction selection). The top row shows the angular difference between a cluster in the CBB and hit in the inner detector (at least two layers). The lower row shows the angular difference between a cluster in the FP and a hit in the FP vetos (FPV).

5.2.3 MiniTAPS

As for the CBB, the cluster algorithm in MiniTAPS combined connected hit crystals to a cluster. The crystal energy threshold was set to 17 MeV for the inner two rings and 13 MeV for the other rings, since the inner ring receives more electromagnetic background. The cluster energy threshold was set to 25 MeV and the crystal with the maximum energy of the cluster had to have more than 20 MeV. In addition, a time difference of less than 5 ns was required, as seen in Fig. 5.5. This cut is a standard EXPLORA cut and is chosen quite broad to not cut off real events. Up to two local maxima were considered and the cluster was then split into two PEDs. The lower limit for the deposited energy in the local maxima crystals and the total PED was set to 20 MeV. With only one PED per cluster, the energy was simply given by the sum over all crystal energies, as given in Eq. 5.8. In the case of two PEDs, the PED energy was weighted with the ratio of the two PED energies. However, since MiniTAPS had a better angular resolution than the CBB, as seen in Fig. 7.3, overlapping PEDs were very rare.

To calculate the cluster position, a logarithmic weighting was done, as given in Eq. 5.4. The parameter $P = 4$ was determined by MC simulations [164]. As for the

A2 TAPS detector, the crystals were not radially mounted in MiniTAPS and hence a shower depth correction, as shown in Fig. 5.1 was necessary. For MiniTAPS, this was done with a linear correction function that has been extracted from MC simulations [165]. Furthermore, a fine correction diminished effects coming from the hexagonally shaped crystal structure. In addition to the angular correction, shower losses due to geometrical and material effects had to be corrected for. For this purpose, a correction function was established [165]:

$$E_{PED}^{corr} = E_{PED} \cdot \left(k_0 \cdot e^{-\frac{1}{2} \cdot \left(\frac{E-k_1}{k_2} \right)^2} - k_3 \cdot e^{-k_4 \cdot E^{k_5}} + k_6 \cdot E + k_7 \right), \quad (5.17)$$

where E_{PED} is the PED energy and the coefficients k_0, \dots, k_7 have been determined from simulations and were different for each crystal and dependent on the deposited energy. As for the CBB, the time of the central element was taken as the PED time.

The charged identification in MiniTAPS was done in exactly the same way as it was explained for the TAPS detector in Mainz, see Sec. 5.1.3. A MiniTAPS PED was identified as charged when at least one veto of all cluster members had hit. A veto threshold of approximately 100 keV was applied.

Table 5.2 summarises the software thresholds used for the detectors of the CBELSA/TAPS setup.

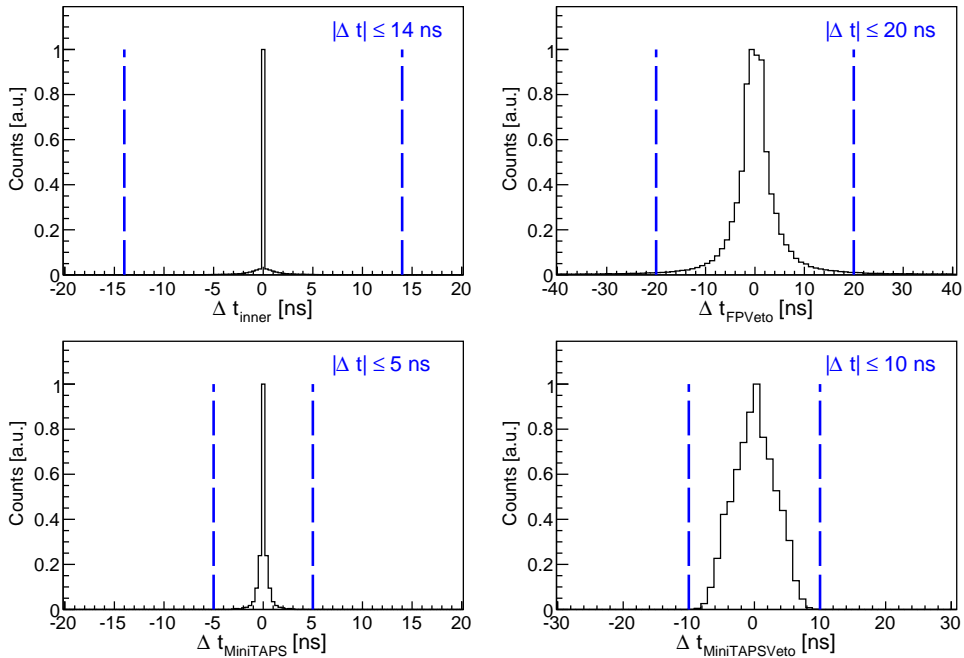


Figure 5.5: Standard EXPLORA time cuts used for the clustering (blue lines). Top left: time difference between two fibres in the same layer of the inner detector. Top right: time difference between two hit FP vetoes. Bottom: time difference between two hit crystals in MiniTAPS (left-hand side) and two hit MiniTAPS vetoes (right-hand side). All cuts are chosen quite broad to not cut off real events.

	CB / FP	MiniTAPS	Inner	FP Vetoes	MiniTAPS Vetoes
crystal	1 MeV	17/13 MeV	~150 keV	-	50 keV
cluster/PED	20 MeV	20 MeV	-	-	-
cluster time	-	5 ns	14 ns	20 ns	10 ns

Table 5.2: *Typical software thresholds used for the detectors of the CBELSA/TAPS experiment.*

Chapter 6

Calibration

In both experiments, the signal processing was done with the help of Time-to-Digital Converters (TDC) and Analogue-to-Digital Converters (ADC). TDCs enable the digitalisation of time, whereas ADCs provide digital values for a continuous physical quantity, usually voltage or energy. To convert the digital information to a physical quantity, a calibration of detector components is necessary. Sec. 6.1 explains the calibration used to extract the energy and Sec. 6.2 explains how to extract the time information. Each crystal has its own electronics and has a different time and temperature dependence. Thus, the calibration was split into different run sets and done separately for each detector module.

6.1 Energy Calibration

When particles deposit energy in the scintillating materials of the detectors, light is produced. This light is then collected and amplified with the associated PMTs or photo diodes and guided to the ADC. As mentioned in the introduction of this chapter, the energy information is stored as digital values using ADCs. The ADCs produce a digital signal c_{ADC} , which is in first order proportional to the deposited energy:

$$E_{dep} = g \cdot (c_{ADC} - p), \quad (6.1)$$

where p is the pedestal position and g is the conversion gain. The pedestal is the digital value which is registered in the ADC when no energy is deposited in the corresponding crystal. The purpose of the calibration procedure is to find both the pedestal and gain values.

6.1.1 A2 Energy Calibration

A short overview about the calibration procedure used in the A2 experiment is given in this section.

Crystal Ball

The first step in the calibration procedure of the CB energy is the rough calibration using a $^{241}\text{Am}/^{9}\text{Be}$ source and is done before data acquisition. $^{241}\text{Am}/^{9}\text{Be}$ emits neutrons with a continuous energy between 0 and 10 MeV and 4.438 MeV photons. The photons were used to adjust the conversion gain of the PMTs in a way that the response of each crystal to the 4.438 MeV photons results in approximately the same ADC channel, see Fig. 6.1. Having adjusted the conversion gains, the pedestal values were measured and then the hardware thresholds were set above these values to suppress the pedestals during the data acquisition. The procedure is explained in more detail in Ref. [166].

The gain calibration achieved by the latter procedure is only valid for very low photon energies. It must be improved by a more accurate method, namely by comparing the position of the π^0 peak in the 2γ invariant mass to the nominal π^0 mass. For this purpose, the invariant mass of two photon hits in CB was calculated:

$$\begin{aligned} m_{\gamma\gamma} &= \sqrt{(p_{\gamma_1} + p_{\gamma_2})^2} \\ &= \sqrt{(E_{\gamma_1} + E_{\gamma_2})^2 - (\vec{p}_{\gamma_1} + \vec{p}_{\gamma_2})^2} \\ &= \sqrt{2E_{\gamma_1}E_{\gamma_2} \cdot (1 - \cos(\psi_{\gamma_1\gamma_2}))}, \end{aligned} \quad (6.2)$$

where $E_{\gamma_{1/2}}$ are the photon energies, $\vec{p}_{\gamma_{1/2}}$ are the corresponding momenta, and $\psi_{\gamma_1\gamma_2}$ is the opening angle between the two photons.

The invariant mass has a better signal-to-background ratio when it was required that both photon clusters are neutral, i.e. no corresponding PID element had fired. For a correct assignment of neutral and charged hits in the CB, the correlation of the PID with the CB in the azimuthal angle has to be determined for each experiment. This is necessary, since the PID is sometimes dismounted between beamtimes for MWPC maintenance purposes.

The invariant mass was filled into a two-dimensional histogram versus the central element of the cluster. Due to the large π^0 photoproduction cross section and the dominant decay ($\Gamma = 98.823\%$ [6]) into two photons, this resulted in a clear peak. However, since the initial gain g_0 is not calibrated, the position of the peak is not equal to the pion mass $m_{\pi^0} = 134.9766$ MeV [6]. Thus, the peak has to be shifted to the nominal pion mass by calculating a new gain g :

$$g = g_0 \cdot \frac{m_{\pi^0}}{m_{\gamma\gamma}}. \quad (6.3)$$

The invariant mass $m_{\gamma\gamma}$ is determined for every crystal with a fit function consisting of a Gaussian function and a polynomial background. A typical spectrum is shown in Fig. 6.1 (b). The determination of the gain is an iterative procedure since the invariant mass not only contains the energy which is deposited in the central crystal, but also neighbouring elements.

The result of the CB energy gain calibration is that the $m_{\gamma\gamma}$ invariant mass is

6.1. ENERGY CALIBRATION

aligned at the nominal π^0 mass for each crystals and all run sets. However, since the photons of the $\eta \rightarrow 2\gamma$ decay have usually higher energies than the photons from the pion decay, the invariant mass of the η meson is not yet at the nominal η mass. This is mainly caused by angle and energy dependent shower losses, i.e., a part of the deposited energy is not detected due to insensitive material as holding structures, crystal wrapping, edge crystals, or threshold effects. At higher photon and hence η energies, less energy relative to the total energy is lost due to threshold effects, thus after calibration of the pion peak, the invariant mass of the η meson is higher than the nominal η mass. Therefore, a crystal dependent second order correction was applied to the deposited energy E using a quadratic function of the form:

$$E' = k_0 \cdot E + k_1 \cdot E^2, \quad (6.4)$$

where E' is the corrected energy and the coefficients k_1 and k_2 have been extracted from the data by shifting the invariant mass of both the η and π^0 meson to the correct position.

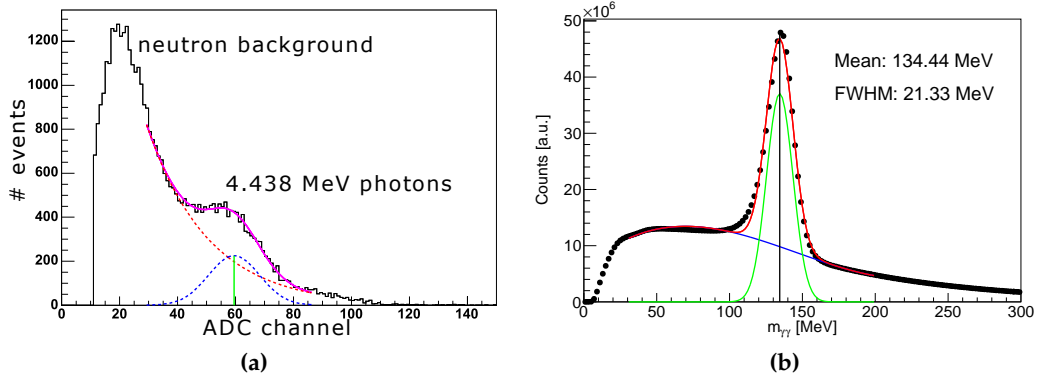


Figure 6.1: (a) ADC response of a single NaI crystal to an $^{241}\text{Am}/^9\text{Be}$ source (black). The neutron background has been fitted with an exponential function (red) and the contribution of the 4.438 MeV photons with a Gaussian distribution (blue). The mean position of the Gaussian is indicated by a green line. The sum of the background and the signal is shown in magenta. Figure adapted from [166]. (b) Invariant mass distribution of two neutral hits in CB after calibration: shown are the data points (black) and the total fit function (red) compromising of the Gaussian function (green) and the polynomial background (blue). The mean position of the pion peak is indicated by a black line.

TAPS

As for the CB detector, the procedure consists of a rough and a fine calibration part. The rough calibration is very important in order to accurately set the hardware thresholds. It is done before and after each experiment using a cosmic radiation measurement. Cosmic radiation comprises mainly of minimum ionising muons. Minimum ionising muons are situated at the minimum of the Bethe-Bloch equation and thus deposit always the same energy. The Bethe-Bloch equation describes the energy loss

$-\frac{dE}{dx}$ due to ionisation and is [167]:

$$-\frac{dE}{dx} = \frac{4\pi}{m_e c^2} \frac{nz^2}{\beta^2} \left(\frac{e^2}{4\pi\epsilon_0} \right)^2 \left[\ln \frac{2m_e c^2 \beta^2}{I \cdot (1 - \beta^2)} - \beta^2 \right], \quad (6.5)$$

where $\beta = v/c$, v is the velocity and ze is the charge of the particle, n is the electron density, I is the average ionisation potential of the atoms, m_e is the mass of the electron, and ϵ_0 is the vacuum permittivity. Hence, the energy loss decreases with $1/v^2$ at low velocities and has a minimum at $p/m_0c \simeq 4$ and increases logarithmically at relativistic particle momenta p . For BaF₂ crystals, the minimum energy is approximately 37.7 MeV per crystal [168]. The corresponding ADC spectrum is shown in Fig. 6.2. The pedestal position from Eq. 6.1 can be directly extracted from the plot (big peak on the left). The calibration gain was determined by fitting the spectrum with a Gaussian function (blue) and an exponential background (red). As mentioned in Sec. 2.4, the energy deposited in the BaF₂ crystals was integrated over a long and a short gate to allow for a Pulse Shape Analysis (PSA). Thus, for the TAPS detector, both energy components were calibrated.

The first step of the offline calibration was the determination of the pedestal positions from the data runs. The pedestals have been extracted from the long gate and the short gate separately. To account for time-dependent shifts of pedestal positions, the data runs have been assigned to run sets. Since 2014, the pedestal was suppressed during normal data taking runs to speed up the data acquisition, but dedicated pedestal runs were recorded every day. The precise calibration of the long gate was done by shifting the $m_{\gamma\gamma}$ invariant mass to the correct position at m_π as it was done for the CB. To improve statistics, events with one cluster in TAPS and one in the CB have been used for the calibration procedure. Thus, an accurate calibration of the TAPS energy

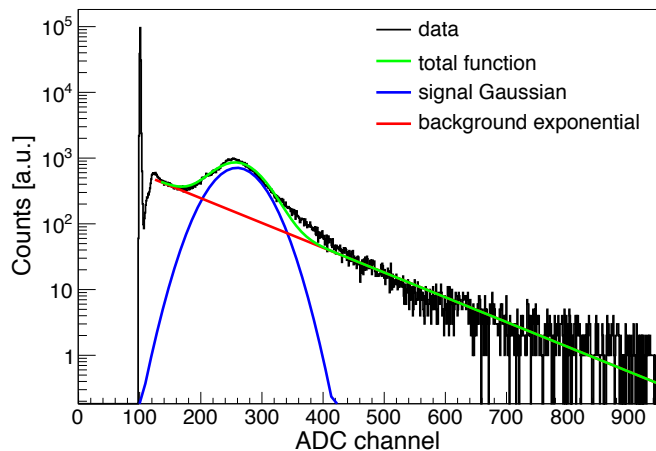


Figure 6.2: Raw ADC spectrum obtained from a cosmics measurement with the TAPS detector. Shown is the response of the crystal (black), the exponential background (red), the Gaussian signal (blue) and the total fit function (green). The peak energy of 37.7 MeV corresponds to approximately 150 ADC channels. Figure taken from [56].

6.1. ENERGY CALIBRATION

was only possible when the CB energy had already been calibrated before. Furthermore, as for the CB, a quadratic energy correction was applied. Due to statistics, the coefficients in Eq. 6.4 were not determined for every single crystal, but for each TAPS ring separately to account for θ dependent shower loss. The resulting invariant mass is shown in Fig.6.3 (a).

Having finished the calibration of the long gate component, the short gate was calibrated next. For this purpose, a typical PSA spectrum was created by plotting the PSA radius r_{PSA} versus the PSA angle ϕ_{PSA} :

$$r_{PSA} = \sqrt{E_l^2 + E_s^2} \quad (6.6)$$

$$\phi_{PSA} = \arctan \frac{E_s}{E_l}, \quad (6.7)$$

where E_l and E_s are the energies deposited in the long and short gate, respectively. The ϕ_{PSA} position of the photon band was determined at two different positions r_{PSA} ($0 \text{ MeV} < r_{PSA} < 50 \text{ MeV}$ and $500 \text{ MeV} < r_{PSA} < 600 \text{ MeV}$) by fitting a Gaussian function to the projected photon band. With the obtained values, the corresponding short gate energy was calculated and the new values for pedestal and the gain were extracted in a way that the photon band afterwards lied at $\phi_{PSA} = 45^\circ$. Fig.6.3 (b) shows a PSA spectrum for one TAPS crystal. The inserts show the projection and the extracted positions are indicated with a cross. The photon band lies at approximately 45° , while the nucleon band is situated at lower PSA angles and shaped as a banana. This is caused by the fact that nucleons deposit a smaller amount of their energy in the short gate, as seen in Fig. 2.16 (b).

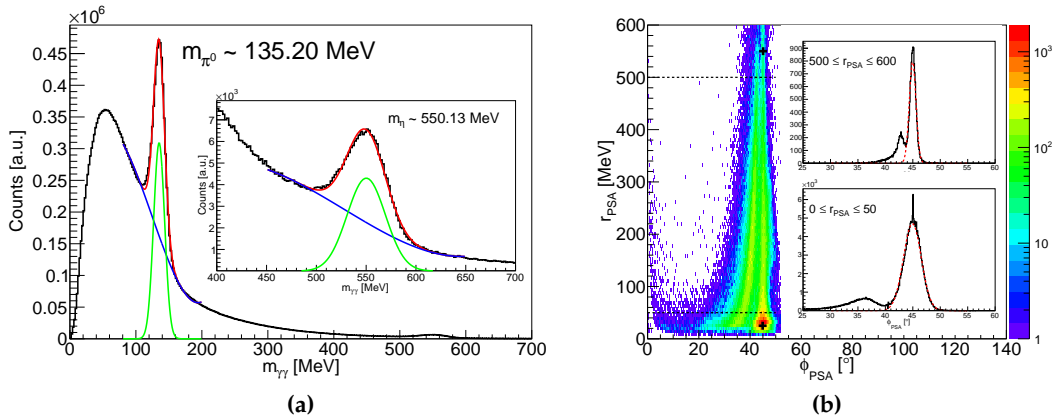


Figure 6.3: (a) Invariant mass for one neutral cluster in TAPS and one neutral cluster in the CB after the quadratic correction. The π^0 and η peak are fitted with a Gaussian (green) and a background polynomial (blue). The total fit function is shown in red. The resulting positions are indicated in the figure. (b) Short gate energy calibration: the position of the photon band is determined by fitting two projections (inserts) with a Gaussian function (red). The extracted positions are marked by a black cross in the two dimensional PSA histogram. The black dashed line indicates the area, which was used for the projection.

PID

The PID energy was calibrated with the method described in the PhD thesis of T. Jude [169]. For all hits in the CB, a raw ADC signal of the PID, ΔE , was plotted against the energy deposited in the CB, E . The proton band, as seen in Fig. 6.4, was fitted for energy bins of widths ~ 40 MeV with a Gaussian (red). The obtained mean position was then plotted against the value given by the MC simulation and fitted with a linear function. The pedestal value and gain have then been found from the y-intercept and the slope of the fit function.

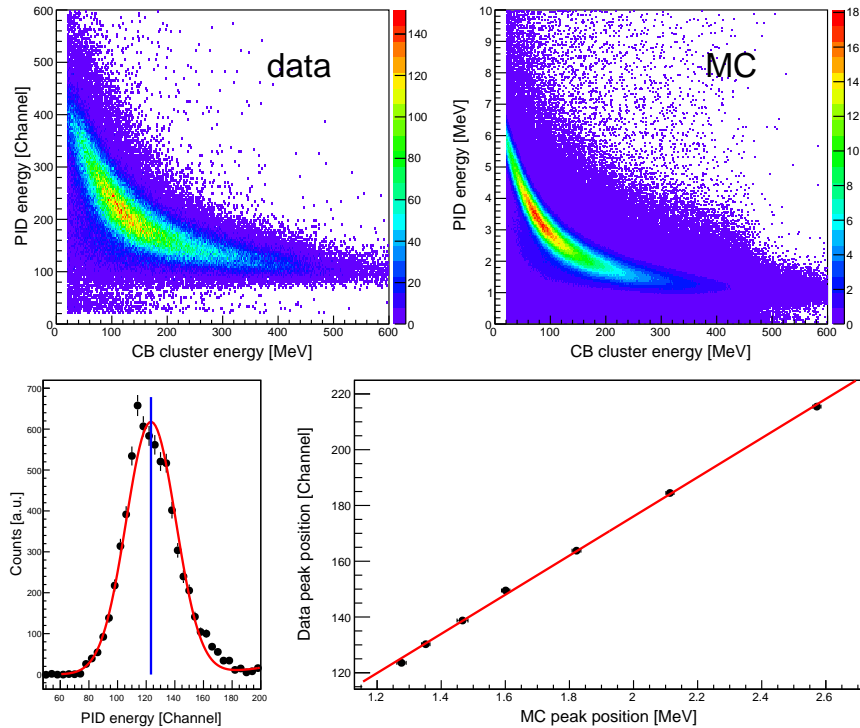


Figure 6.4: PID energy calibration. Top: the energy deposited in the PID versus the energy deposited in the CB for data and simulation. Bottom left: a projection of the two dimensional data histogram around an energy of 340 MeV with the corresponding Gaussian fit (red) and the mean position (blue line) is shown. Bottom right: the extracted position from data is plotted against the MC position and fitted with a linear function (red).

TAPS Veto

As for the energy calibration of the TAPS crystals, the pedestal position was directly extracted from the raw spectra of the data runs. For the gain calibration, ΔE (energy in the vetoes) versus E (energy in the BaF₂ crystals) histograms were produced. Similar to the PID energy calibration, the position of the proton band was shifted to the correct position using MC simulation. However, due to the poor energy resolution of the plastic vetoes, a ΔE versus E plot from TAPS is not very useful for particle identification. Nevertheless, the energy calibration of the vetoes is quite important to set the correct veto thresholds.

6.1.2 CBELSA/TAPS Energy Calibration

In contrast to Mainz, where the calibration for each experiment is done by the group which has proposed the experiment, the CBELSA/TAPS collaboration has experts for each detector subsystem.

Crystal Barrel and Forward Plug

The calibration of the CBB detector is fully explained in Ref. [163], but a short overview is given here.

The ADCs of the CBB are not able to detect energies over the full energy range up to 2 GeV with appropriate energy resolution. Thus, the ADC has two ranges, a low energy range for energies below 130 MeV and a high energy range for energies up to 2 GeV. The signal of the high range is attenuated by a factor of eight compared to the low range.

The first step in the energy calibration was the determination of the pedestal positions of the low energy range with the help of the data runs. Afterwards, the gain calibration was performed using a similar $\pi^0 \rightarrow 2\gamma$ method as it was used for the CB and the TAPS detector at Mainz. To correct for shower losses, an energy correction function as described in Sec. 5.2.2 was applied, as opposed to using a quadratic energy correction. The monitoring of time-dependent changes and the determination of the attenuation factor of the high range was done using light pulser measurements. The light pulser uses different filters to produce a spectrum which is similar to the signal produced by the CsI(Tl) crystals and covers both the high and low range of the ADCs. Several light pulser measurements were taken during each experiment. More information can be found in Ref. [170].

The energy information of the inner detector and the FP vetoes were not read out by the data acquisition and thus did not require a calibration.

MiniTAPS

Since MiniTAPS and TAPS are made of the same modules, as explained in Sec 2.4.2, the calibration is analogous to the one described in Sec. 6.1.1. Before each experiment, the cosmics measurement was performed to get a rough calibration of the thresholds. For the precise calibration, the $\pi^0 \rightarrow \gamma\gamma$ invariant mass for one cluster in MiniTAPS and one cluster in the CBB was used to determine the conversion gain. As for the CBB, no quadratic energy correction was applied, but a dedicated function, as explained in Eq. 5.17 was used to correct for shower loss.

Since usually the short gate information and the veto energy are not used in Bonn, it had to be calibrated especially for this work. The calibration procedure was analogous as the procedure presented in Sec. 6.1.1 for the TAPS detector at Mainz.

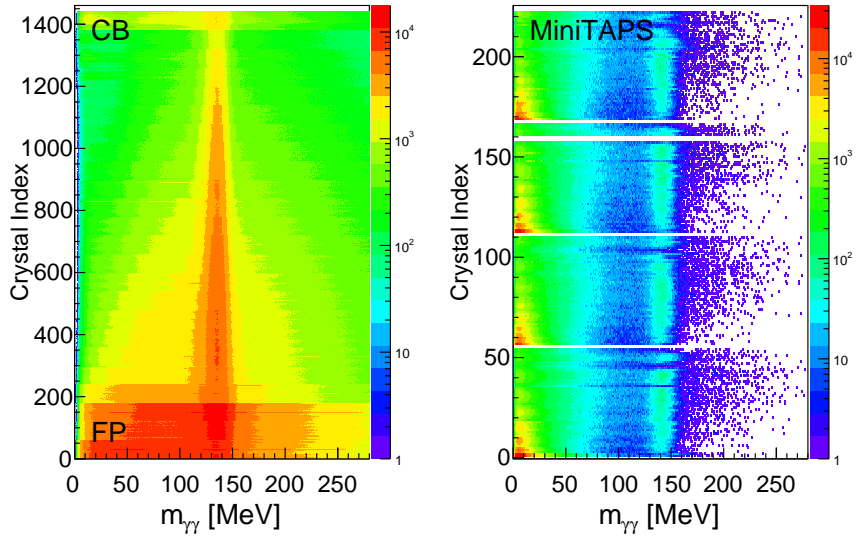


Figure 6.5: Invariant mass of two photons detected in CBB/FP (left) and MiniTAPS (right) as per crystal index. The FP consists of 60 crystals, thus, between crystal index 0 and 180 only the even numbers have a signal. In all detector elements a clear pion peak is visible at $m_{\gamma\gamma} \simeq 135$ MeV.

6.2 Time Calibration

The A2 experiment and the CBELSA/TAPS experiment use both Single-Hit-TDCs and Multi-Hit-TDCs. Single-Hit-TDCs can only record one time signal per recorded event, while Multi-Hit-TDC are able to convert several time signals. Similar to ADCs, TDCs store information as channels. Time t and TDC channels c_{TDC} can be expressed by the following formula:

$$t = g \cdot (c_{TDC} - o), \quad (6.8)$$

where g is a gain factor and o is the offset value. In contrast to the pedestal position, the offset value can be chosen freely. The time signal T of a detector is given as the difference of the real time t of the detector and the trigger time t_{trig} :

$$T = t - t_{trig}. \quad (6.9)$$

Hence, to remove jitter from the trigger timing, one has to build a time difference between the detector signal T_1 and a reference time T_2 :

$$T_1 - T_2 = (t_1 - t_{trig}) - (t_2 - t_{trig}) = t_1 - t_2, \quad (6.10)$$

where t_1 and t_2 are the times of two different detector modules.

6.2.1 A2 Time Calibration

All the detectors in Mainz have a time signal and therefore have to be calibrated. The procedure is shortly explained in this section.

Crystal Ball

The CB has CATCH TDCs with a fix conversion gain of 0.117 ns per channel. CATCH TDC are free running Multi-Hit-TDCs. They use oscillator counters and a reference TDC to measure the time.

Even though only the offset of each crystal had to be determined, the calibration procedure consisted of three steps. First, the time difference between all clusters in the CB was filled for each central element. By fitting a Gaussian to the histogram of each element the new offset was calculated [56]:

$$o'_i = o_i + \frac{\bar{t}_i}{g_i}, \quad (6.11)$$

where \bar{t}_i is the mean time, o_i is the old offset, and $g_i = 0.117\text{ns/ch}$ is the gain. To reduce background, it was required that the clusters are neutral. This calibration was done in an iterative way until the time peaks were aligned at zero.

Due to the slow rise time of the NaI(Tl) crystals and the leading edge discriminators (LED), the time strongly depended on the amplitude of the signal. This time walk effect is shown in Fig. 6.6 and had to be corrected. To reach a better signal-to-background ratio, a rough invariant and missing mass cut have been applied to select events from the $\pi^0 \rightarrow 2\gamma$ reaction. The time correction was then determined by looking at the CB time relative to the tagger time in dependence of the deposited energy for each crystal and fitting it with the following function [56]:

$$t(E) = p_0 + \frac{p_1}{(E + p_2)^{p_3}}, \quad (6.12)$$

where E is the deposited energy, and p_0, \dots, p_3 are free fit parameters. The parameters were individually determined for each crystal. The time of the CB was then corrected

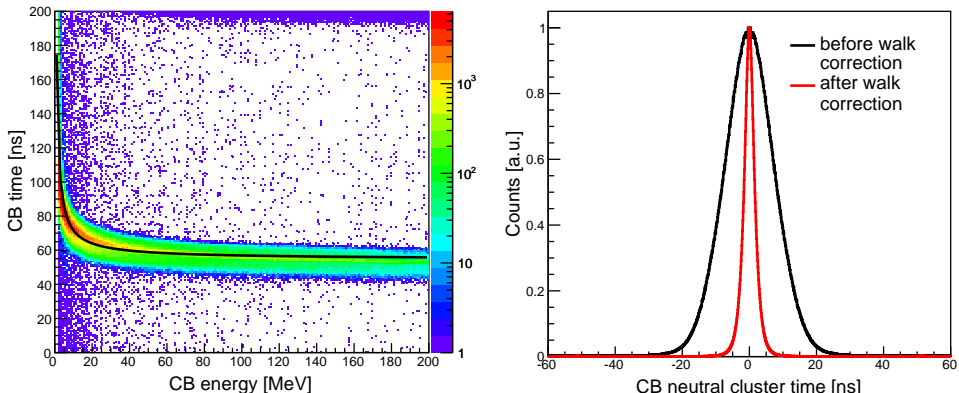


Figure 6.6: Left-hand side: CB-Tagger time versus the deposited energy, fitted with the function of Eq. 6.12 (black line). Right-hand side: CB coincidence time of two neutral clusters before (black) and after (red) the time walk correction.

by subtracting $t(E)$ from the original time t :

$$t_{corr} = t - t(E) \quad (6.13)$$

Since the tagger time was used as reference, the tagger time had to be calibrated first. The time walk correction drastically improved the time resolution of the CB, as seen in Fig. 6.6 (b).

To get an even better resolution, the coincidence time was aligned again to zero after the time walk correction by applying an additional offset.

TAPS

In contrast to the NaI(Tl) crystals of the CB, the BaF₂ crystals of the TAPS detector have a fast risetime. In addition, TAPS was situated at a relative long distance from the target (~ 1.5 m). Both the long distance and the good time resolution make TAPS ideally suited for a Time-of-Flight (TOF) measurement. Hence, a good time calibration is needed.

The first step in the time calibration was the TDC gain calibration. It is usually done before every experiment. For this purpose, the common stop signal of all TAPS elements was delayed by inserting different cables of known length. With the help of the TAPSMaintain software [56] the position of the pedestal pulser was extracted. By comparing the differences of the delays and the differences of the pedestals, the TDC gain was found for each individual detector module. The TDC offsets for the BaF₂ and PbWO₄ elements were determined in an analogous way as it was done for the CB. The time difference of two neutral clusters was plotted against the central element of the cluster. By fitting a Gaussian distribution to each time spectrum and by using Eq. 6.11, the final offset was iteratively found.

Due to the fast risetime of the BaF₂ crystals and the CFD (instead of the LED used in the CB), no time walk correction is necessary.

Tagger

The tagger was equipped with CATCH TDCs with a fixed conversion gain of 0.117 ns per channel to measure the time. Thus, as for the CB, only the TDC offsets had to be calibrated. This was done by plotting the time difference of a hit in the tagger and all neutral clusters in TAPS for every tagger channel. The tagger time calibration therefore required that the TAPS time was fully calibrated. Since the timing of one tagger channel does not depend on any other channel, this calibration was a one-step procedure.

PID and TAPS Veto

The PID and Veto time were not used for the analysis. However, since the ADC spectra were only filled when a hit in the corresponding TDC was registered, a rough calibration was necessary, to ensure that the coincidence peak lay well within the accepted

time window.

Achieved Time Resolution

Table 6.1 summarises typical time resolutions after the calibration procedure.

FWHM [ns]	
CB-CB	2.95
CB-TAPS	1.16
TAPS-TAPS	0.47
CB-Tagger	1.49
TAPS-Tagger	0.97

Table 6.1: *Typical time resolutions (FWHM) for the detectors used in the A2 setup.*

6.2.2 CBELSA/TAPS Time Calibration

The techniques for the calibration of the CBELSA/TAPS detectors are very similar to the ones used in Mainz. The diploma thesis of J. Hartmann [125] contains detailed information about the time calibration of detector components of the CBELSA/TAPS experiment. A short description is given here.

As explained in Sec. 2.4, the CsI(Tl) crystals of the CBB were read out over photo diodes. The signal of the photo diodes have a long risetime of $10 - 15 \mu\text{s}$, which means that a time measurement in the CBB was not possible.

Since the scintillating bars of the tagger had a good time resolution (FWHM = 1.438 ns [125]), their signal was used as reference to calibrate the time of all the other detectors. Therefore, the first step in the time calibration process was the tagger time calibration.

Tagger

The CATCH TDC of the 97 tagger bars were synchronised to an external reference frequency and thus had a fixed gain of $g = 0.05721 \text{ ns per channel}$ [125]. In a first rough calibration, the tagger bar offset was determined by shifting the prompt peak of every TDC spectrum to zero. However, since the resolution of this prompt peak was limited by the uncertainty of the trigger timing, an additional precise calibration was done, which was independent of the trigger time (Eq. 6.10). For this purpose, the signal of the Cherenkov detector was taken as reference time for a first rough alignment. However, the time resolution of the Cherenkov detector was worse (FWHM > 1 ns [125]) than that of the tagger and the MiniTAPS detector. Thus, an additional fine calibration of the time signals was necessary. During an iterative procedure, the tagger time was used as a reference to calibrate the MiniTAPS time followed by the MiniTAPS reference time used to calibrate the tagger time.

Forward Plug

Having calibrated the tagger time, it was used as reference signal for the calibration of the FP time. To reach a good time resolution, only clusters originating from the $\pi^0 \rightarrow \gamma\gamma$ decay were used to align the time peaks for every element. Due to the use of discriminators, the time peak was broadened by a time walk effect, which was corrected. Analogous to the procedure explained in Sec. 6.2.1, the time difference between the tagger and the CsI(Tl) crystals of the FP was plotted in dependence of the energy and fitted with a corresponding function. Using the tagger time as reference, a time resolution of $FWHM \simeq 1.99$ ns was reached, as seen in Table 6.2.

MiniTAPS

As for the TAPS detector in Mainz, the TDC gains had to be found for every single MiniTAPS element. However, the calibration was not done before the experiment, but after the data taking using the production run data. This calibration is fully explained in Ref. [125]. To calculate the individual gains, a mean gain $g_{mean} \simeq 0.1$ ns was assumed first. Then the time difference Δt between a hit in the tagger and a hit in MiniTAPS was plotted against the tagger time for one specific MiniTAPS element. This spectrum showed a vertical band at $t_{tagger} = 0$ from the tagger prompt peak, a diagonal band from the MiniTAPS prompt peak, and a horizontal band at $\Delta t = 0$ from coincident hits in the tagger and MiniTAPS. When using a fixed gain of $\simeq 0.1$ ns, the latter band was not vertical. The new conversion gain g was then found with the slope m of the band [125]:

$$g = g_{mean} + (1 + m). \quad (6.14)$$

The change of the conversion gain calculated with the help of the method was only in the range of 1 – 2%.

As in Mainz, CFDs are used in the MiniTAPS detector to record time information and thus a time walk effect is not visible and did not require a correction.

Inner Detector, Foward Plug Veto and MiniTAPS Veto

As mentioned in Sec. 5.2, the cluster algorithm used very loose cuts on the timing signals of the inner detector and FP Veto, but not for the MiniTAPS vetoes. For further analysis, the time of the charge sensitive detectors was not used. However, as for the other detectors, the time was calibrated using the tagger as time reference.

Due to the long scintillating fibres (40 mm) of the inner detector and the thin plastic vetoes of the FP and the MiniTAPS detectors, respectively, the time resolution was limited to 2.1 ns (inner detector), 4.4 ns (Forward Plug vetoes) and 3.1 ns (MiniTAPS vetoes) [125].

Achieved Time Resolutions

The typical time resolution for the CBELSA/TAPS detectors is summarised in Table 6.2.

	FWHM [ns]
FP-FP	3.28
FP-MiniTAPS	2.19
MiniTAPS-MiniTAPS	0.51
FP-Tagger	2.50
MiniTAPS-Tagger	1.25

Table 6.2: *Typical time resolutions (FWHM) for the detectors used in the CBELSA/TAPS experiment.*

Chapter 7

Reaction Selection

Having finalised all calibrations, each cluster in an event has now been assigned its energy, space, and time. This chapter will explain how this information was used to extract the η photoproduction events. All the necessary steps to reconstruct the desired reaction, as well as all applied cuts to reject background contributions, will be explained in full detail.

7.1 Event Classes

For the present work, the following two reactions were of interest:

- reaction on the quasi free proton bound in deuterium/ ^3He :

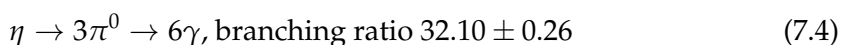
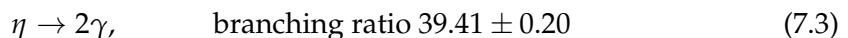


- reaction on the quasi free neutron bound in deuterium/ ^3He :



The reactions have been analysed exclusively (with the detection of the recoil nucleon) and inclusively (without requiring the recoil nucleon to be detected). Due to the detection of the recoil nucleon, the analysis of the exclusive reaction allows for additional cuts and identification possibilities compared to the inclusive reaction. However, in the first stage of the analysis, this additional information is not used.

For the A2 data, both decay channels of the η meson have been analysed [6]:



Due to the use of high multiplicity trigger conditions in Bonn, only the $\eta \rightarrow 6\gamma$ decay channel could be extracted from the CBELSA/TAPS data.

The first step in the analysis procedure was the assignment of the particles to a charged and neutral list according to the criteria explained in Chapter 5. Depending on the number of charged and neutral particles, the events were assigned to event

classes, as seen in Table 7.1. For the exclusive reaction on the proton, one charged cluster and two neutral clusters were required for $\eta \rightarrow 2\gamma$ or six neutral clusters for $\eta \rightarrow 6\gamma$. The event class for the exclusive reaction on the neutron consisted of three neutral clusters for $\eta \rightarrow 2\gamma$ and seven neutral clusters for $\eta \rightarrow 6\gamma$. Due to lack of the statistics for the CBELSA/TAPS dButanol data, the neutron was analysed inclusively by allowing events with only six neutral clusters, i.e., without the cluster of the neutron. However, to ensure a good rejection of charged particles in the inclusive reaction, it was required that no single fibre of the inner detector and no single veto of the FP saw a signal.

As seen in Table 7.1, for the quasi-free inclusive (either proton or neutron) detection of the reaction, the event class was built from events where the recoil nucleon was not detected (two or six neutral clusters), and events with recoil nucleon (the two exclusive event classes). To reduce background originating from $\eta\pi$ pairs, events with additional hits were discarded.

Hence, in the first stage, only very basic detector information was used to assign the clusters to event classes. This simple technique may not be very efficient since one might lose events when charged and neutral particles were misidentified or events with additional clusters were detected. However, it allowed for a sound reproduction of the experimental data with simulation, which was especially important for the exclusive reactions, where not only photons, but also protons and neutrons were detected.

	exclusive proton	exclusive neutron	inclusive neutron	quasi-free inclusive proton or neutron
$\eta \rightarrow 2\gamma$	2n & 1c	3n	-	2n or 3n or (2n & 1c)
$\eta \rightarrow 6\gamma$	6n & 1c	7n	6n	6n or 7n or (6n & 1c)

Table 7.1: Selected event classes: n and c stands for neutral and charged clusters in the calorimeter (defined by the criteria described in Chapter 5).

7.2 Reconstruction of the η Meson

Having classified the events, the η meson was reconstructed via an invariant mass technique. The details of the reconstruction depend on the number of detected neutral clusters.

Two neutral clusters were detected and were directly assigned to the decay photons of the η meson and the corresponding four-vector (E_η, \vec{p}_η) was calculated by combined energy and momentum conservation:

$$\begin{pmatrix} E_\eta \\ \vec{p}_\eta \end{pmatrix} = \begin{pmatrix} E_{\gamma_1} \\ \vec{p}_{\gamma_1} \end{pmatrix} + \begin{pmatrix} E_{\gamma_2} \\ \vec{p}_{\gamma_2} \end{pmatrix}, \quad (7.5)$$

where $(E_{\gamma_1}, \vec{p}_{\gamma_1})$ and $(E_{\gamma_2}, \vec{p}_{\gamma_2})$ are the four-vectors of the two decay photons, respectively.

If two neutral and one charged clusters were detected, the charged cluster was directly assigned to the proton and the η meson was reconstructed as explained in Eq. 7.5.

The situation is more complicated when three or more neutral particles were detected. In that case, the decay photons were found via a χ^2 -test by comparing the invariant mass of two clusters to the nominal η mass. For tentative $\eta \rightarrow 2\gamma$ events with three neutral clusters, the χ^2 was calculated with the following formula:

$$\chi_{ij}^2 = \left(\frac{m_{\gamma_i \gamma_j} - m_\eta}{\Delta m_{\gamma_i \gamma_j}} \right)^2, \quad (7.6)$$

where the indices i and j are from one to three under the condition $i \neq j$, $m_{\gamma_i \gamma_j}$ is the invariant mass of the current pair of neutral clusters, m_η is the nominal mass $m_\eta = 547.862$ MeV [6], and $\Delta m_{\gamma_i \gamma_j}$ is the corresponding error of the invariant mass, which depends on the error of the deposited energy ΔE , and the error of the azimuthal and the polar angle of the two photons, $\Delta\phi$ and $\Delta\theta$, respectively, as explained in Sec. 7.2.1. The exact formula and the derivation of $\Delta m_{\gamma_i \gamma_j}$ is given in Ref. [129]. Thus, in the case of three neutral hits, three different values for the χ^2 -test (as given in Eq. 7.6) were calculated. The photons belonging to the combination with the smallest χ^2 were assigned to the η meson, whereas the remaining particle was the candidate for the recoil neutron. Simultaneously, to reject events from $\pi^0 \rightarrow 2\gamma$ decay, a χ^2 for the combination of two hits to a pion was performed. When the corresponding χ^2 value was smaller than the χ^2 of the η meson, the event was rejected.

For the event classes of $\eta \rightarrow 6\gamma$, the best assignment had to be found to combine six or seven neutral hits to three π^0 mesons. Hence, the calculation of the χ^2 was:

$$\chi_{ijklmn}^2 = \left(\frac{m_{\gamma_i \gamma_j} - m_{\pi^0}}{\Delta m_{\gamma_i \gamma_j}} \right)^2 + \left(\frac{m_{\gamma_k \gamma_l} - m_{\pi^0}}{\Delta m_{\gamma_k \gamma_l}} \right)^2 + \left(\frac{m_{\gamma_m \gamma_n} - m_{\pi^0}}{\Delta m_{\gamma_m \gamma_n}} \right)^2, \quad (7.7)$$

where the same labelling as for Eq. 7.6 was used and $m_{\pi^0} = 134.9766$ MeV [6] is the nominal mass of the pion. Having one charged and six neutral clusters, the indices i, j, k, l, m, n are from one to six and the charged cluster was assigned to the proton. In the case of seven neutral clusters, the indices run from one to seven and the remaining cluster from the χ^2 test was identified as the neutron candidate. As for the 2γ decays, the η meson was reconstructed with the help of four-momentum conservation:

$$\begin{pmatrix} E_\eta \\ \vec{p}_\eta \end{pmatrix} = \sum_{i=1}^3 \begin{pmatrix} E_{\pi_i} \\ \vec{p}_{\pi_i} \end{pmatrix} = \sum_{i=1}^6 \begin{pmatrix} E_{\gamma_i} \\ \vec{p}_{\gamma_i} \end{pmatrix}, \quad (7.8)$$

where $(E_{\pi_i}, \vec{p}_{\pi_i})$ and $(E_{\gamma_i}, \vec{p}_{\gamma_i})$ are the four-vectors of the pions and decay photons, respectively.

7.2.1 Energy and Angular Resolutions

The resolutions ΔE , $\Delta\theta$, and $\Delta\phi$ used to calculate the χ^2 were obtained from MC simulations. Isotropic photons with energies up to 1 GeV have been simulated for both the A2 and the CBELSA/TAPS setup and all different targets used for the present work. The deposited energy in the simulation was smeared with a Gaussian distribution to match the measured resolutions given in Eq. 2.11-2.13. The generated energy was filled versus the detected energy E and the resolution ΔE was determined by fitting a tailed Gaussian function $f(E)$ to the projections:

$$f(E) = p_0 \cdot \left[e^{\frac{-4 \cdot \log p_4 \cdot (E-p_1)^2}{p_2^2}} + e^{\frac{(E-p_1)^2}{p_3^2}} \cdot \left(1 - e^{\frac{-4 \cdot \log p_4 \cdot (E-p_1)^2}{p_2^2}} \right) \right], \quad (7.9)$$

where p_0, \dots, p_4 are free fit parameters. In Fig. 7.1, the experimental energy resolution for the different detectors is compared to the resolution obtained from simulations after Gaussian smearing. The energy of the photons was only slightly affected by the target material and hence the energy resolution for the different targets was almost identical. Therefore, only the resolution for the dButanol target is shown in Fig. 7.1. The agreement between MC and experimental resolution for the CB and CBB is very good. The resolutions for the MiniTAPS and the TAPS detector show slight differences, which is most likely caused by the measurement technique used to determine the resolution from Eq. 2.12. As described in Ref. [108], the experimental resolution was measured using a collimated photon beam, which impinged on the center of the crystal. Since

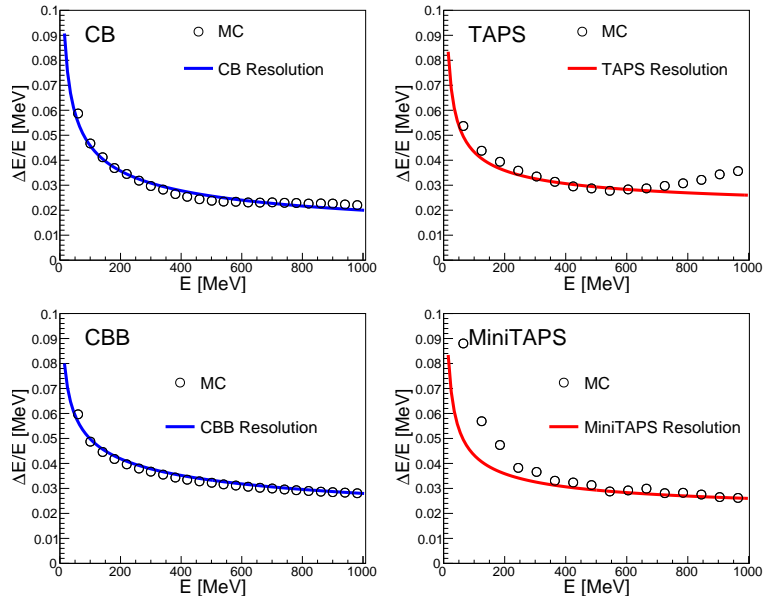


Figure 7.1: Energy resolution $\Delta E/E$ of simulation compared to the experimentally determined function. Top row: CB (left) and TAPS (right). Bottom row: CBB (left) and MiniTAPS (right). The resolution is very similar for the different targets, therefore the dButanol target is shown only.

in the simulation (and the real experiment), the photons are not collimated and distributed all over the crystal, the resolution may be different than the one obtained by Gabler *et al.* [108].

Figs. 7.2 and 7.3 show the obtained angular resolutions for the A2 and the CBELSA/TAPS setup, respectively. Simulations have been done for all different targets used for the present work. It is clearly visible that the θ resolution for the CB and CBB is dramatically better for shorter targets than for longer, whereas the ϕ and energy resolution stay approximately the same. This is caused by the fact that the vertex position is distributed over the entire target cell. Since the target is aligned in the z-direction, a longer target cell means that the vertex is distributed over a larger z-distance. Hence, causing a worse θ resolution, but similar ϕ resolution. On the other hand, the target size has only a small effect on the resolution of the TAPS and MiniTAPS detectors, since these detectors are situated at forward angles and do not surround the target. For the TAPS and MiniTAPS, the angular resolution gets worse for the most inner and most outer rings, which is caused by the fact that close to the border, some part of the shower gets lost and is not assigned to a cluster. For the same reason, the crystals at the smallest and largest θ angles of the CB and the CBB have worse angular resolution. The ϕ resolution of the CB has the shape of a horseshoe, which is a direct consequence of the spherical shape of the detector. At $\theta = 90^\circ$, more crystals cover the ϕ range than at smaller and larger polar angles. In contrast to the CB, the CBB has a barrel-like shape, hence the ϕ resolution is more flat and only gets worse at the very edges. For the θ resolution of the CBB, as seen in Fig. 7.3, a discontinuity is visible at $\theta \sim 30^\circ$.

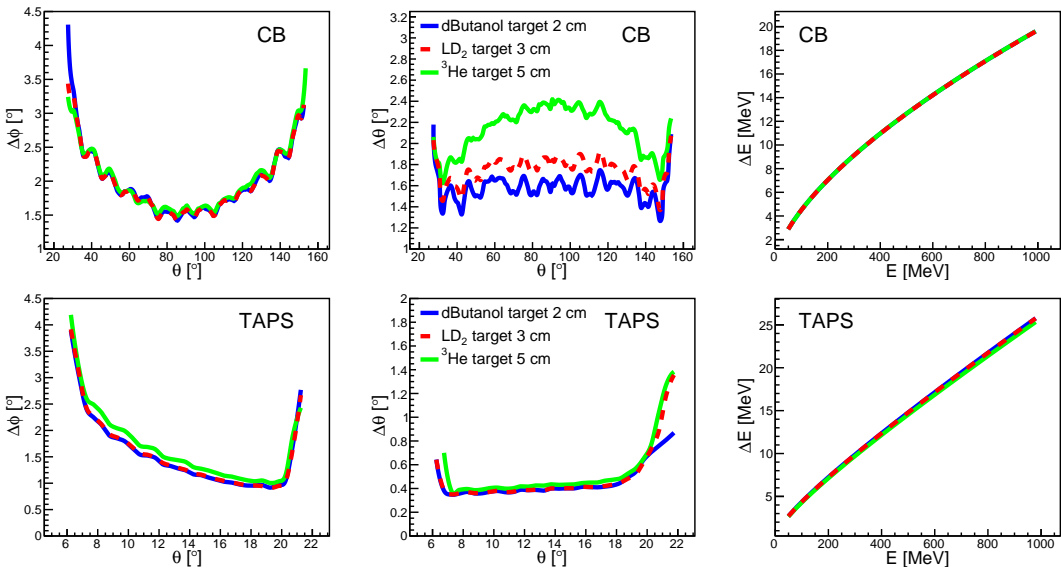


Figure 7.2: Energy and angular photon resolutions for the A2 experiment for the three different targets: dButanol (blue), LD₂ (red), and ³He (green). The top row shows the resolutions for the CB, the bottom row shows the resolution for TAPS. The resolution for the azimuthal angle (left column) and polar angle (middle column) is shown as a function of the polar angle.

This is the transition region between the CBB and the FP where additional material is mounted, and hence shower loss may occur. The periodic modulation of the θ resolution of the CBB must come from the ϕ -symmetric rings of the CBB. In contrast to the relative energy resolution, seen in Fig. 7.1, the absolute energy resolution gets worse for higher energies for all detectors, as shown in Figs. 7.2 and 7.3.

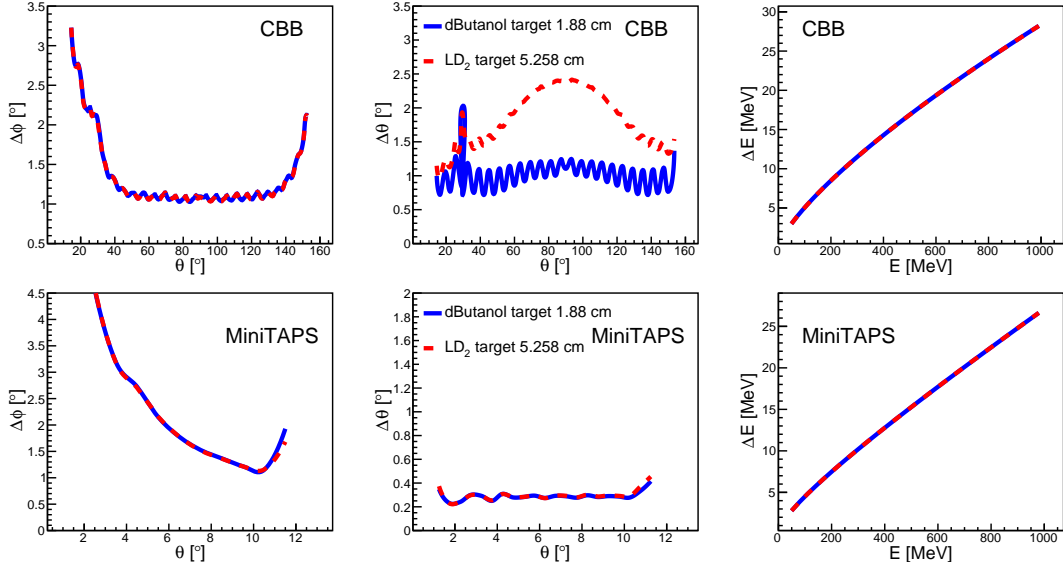


Figure 7.3: Energy and angular photon resolutions for the CBELSA/TAPS experiment for the two different targets: dButanol (blue) and LD₂ (red). The top row shows the resolutions for the CBB, the bottom row shows the resolution for MiniTAPS. The resolution for the azimuthal angle (left column) and polar angle (middle column) is shown as a function of the polar angle.

7.2.2 Confidence Levels

The quality of the reconstruction is reflected in the resulting χ^2 distribution. In general, the χ^2 for k independent standard normal random variables x_i can be calculated according to [171]:

$$\chi^2 = \frac{\sum_{i=0}^k (x_i - e_i)^2}{\sigma_i^2}, \quad (7.10)$$

where e_i are the expected values, and σ_i is the standard deviation of the random variables. The corresponding probability density function $f(\chi^2, k)$ is given by the following equation:

$$f(\chi^2, k) = \frac{(\chi^2)^{k/2-1} \cdot e^{-\chi^2/2}}{2^{k/2} \Gamma(k/2)}, \quad (7.11)$$

where $\Gamma(k/2)$ denotes the Gamma function and k is a positive integer and corresponds to the degrees of freedom. Therefore, the χ^2 distribution obtained in the reconstruction of the η meson should be close to the function given in Eq. 7.11 with one degree of

freedom for $\eta \rightarrow 2\gamma$ and three degrees of freedom for $\eta \rightarrow 6\gamma$.

However, instead of looking only at the χ^2 distribution, it is more convenient to look at the confidence level. The confidence level $W(\chi^2)$ is defined as the probability that a random number ξ^2 , which is distributed according to $f(\chi^2, k)$, is smaller than a certain χ^2 [171]:

$$W(\chi^2) = P(\xi^2 \leq \chi^2). \quad (7.12)$$

Thus, a small χ^2 corresponds to a high confidence level and vice-versa. As seen in Fig. 7.4, a confidence level distribution of an ideal χ^2 distribution is flat for all degrees of freedom.

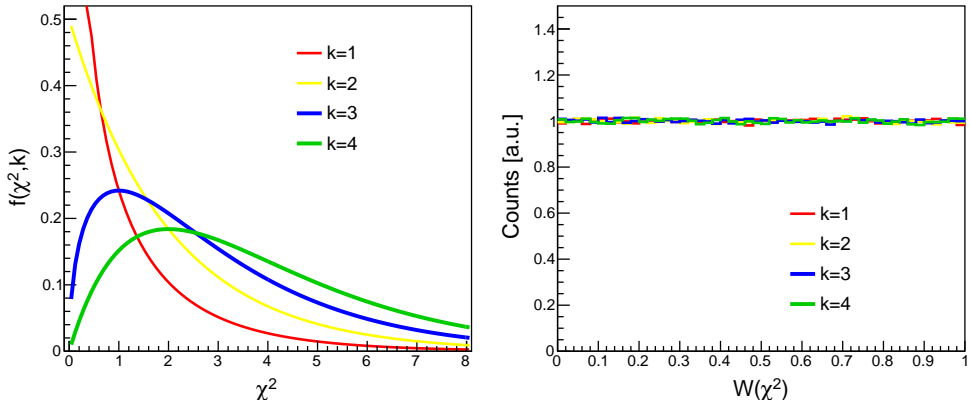


Figure 7.4: Sampled χ^2 and confidence level distributions for one to four degrees of freedom. The distributions have been normalised to their integrals.

The confidence level distributions extracted from the experimental data and MC are shown in Fig 7.5 for A2 data and in Fig. 7.6 for CBELSA/TAPS data. The confidence levels of the accepted events in blue (smallest χ^2) are compared to the ones of the rejected combinations (red). In addition, the confidence level distributions for the events that have survived all applied analysis cuts are shown in black for experimental data and green dashed line for simulation. For the rejected combinations most of the events are located at very low confidence levels (< 0.01), the distribution for accepted combinations is basically flat. Due to combinatorics, the separation between accepted and rejected combinations is less clear for the events with seven clusters than for the ones with three or six neutral clusters. Furthermore, the confidence level of data and simulation are in good agreement, which shows that the resolutions of the χ^2 test of this work, shown in Fig. 7.2 and Fig. 7.3, were realistically chosen.

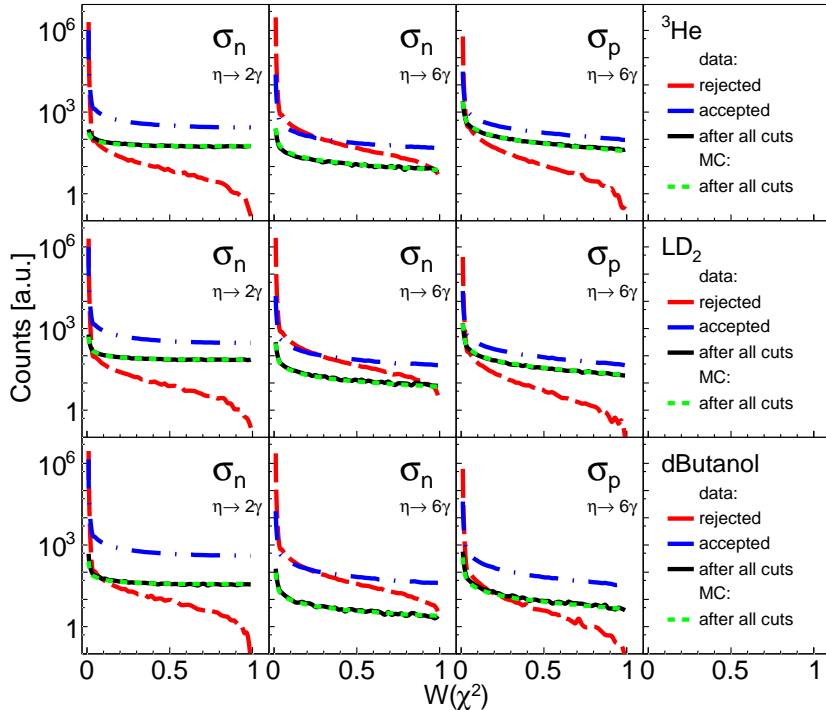


Figure 7.5: A2 confidence level distributions of the χ^2 -test for the different event classes: $\eta \rightarrow 2\gamma$ on the neutron (left column), $\eta \rightarrow 6\gamma$ on the neutron (middle column) and $\eta \rightarrow 6\gamma$ on the proton (right column). The distributions for the ${}^3\text{He}$ (first row), LD_2 (second row), and dButanol (third row) target used in this work are shown.

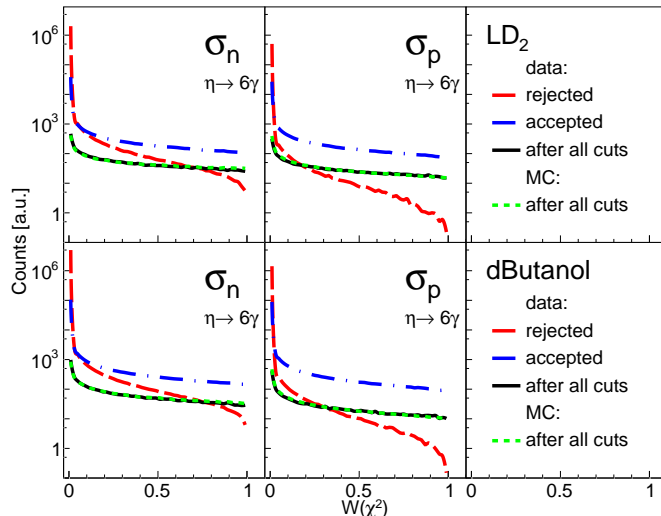


Figure 7.6: CBELSA/TAPS confidence level distributions of the χ^2 -test for the different event classes: $\eta \rightarrow 6\gamma$ on the neutron (left column) and $\eta \rightarrow 6\gamma$ on the proton (right column). The distributions for the LD_2 (first row) and the dButanol (second row) target are shown.

7.3 Time Cuts

As mentioned in Chapter 5, all detectors, except the CBB, are providing time information. The time information was mainly used to ensure coincidence of all events (see Sec. 7.3.1) and to subtract the random background in the tagger, which will be explained in Sec. 7.3.2.

7.3.1 Coincidence Cuts

To ensure that all events occurred at the same time, timing cuts have been applied to the coincidence time between two photon hits in the detectors. Since protons and neutrons have a different response characteristics, only the time of the decay photons of the meson have been used for coincidence cuts. The corresponding histograms and the coincidence cuts are shown in Fig. 7.7 for events right after the χ^2 selection (black) and after all analysis cuts (red dashed histograms). The electromagnetic background in the FP causes a broadening of the coincidence peak, which is not seen to that extent in the other detectors. This may come from the fact that events with single veto hits were assigned to the neutral list and hence could contaminate the photon candidates. However, the background events are sufficiently rejected by the analysis cuts, as can be seen from the red histogram. The coincidence cut positions are indicated by a blue line. The cuts were chosen to be quite broad to ensure that no real events were cut out. No coincidence cut was possible for events in the CBB, since no time information is available in this detector, as described in Sec. 5.2.2.

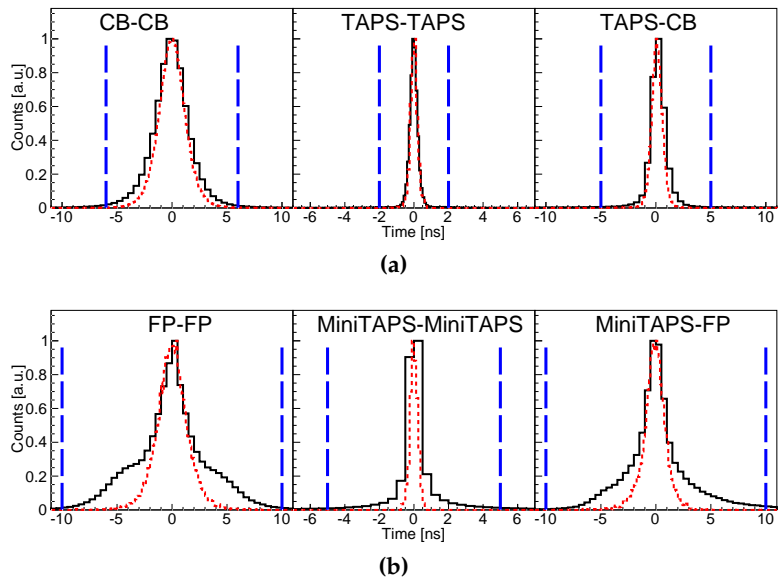


Figure 7.7: Coincidence time between two photons right after the χ^2 selection (black) and after all analysis cuts (red dashed histograms). The cut positions are indicated with a blue line. (a) Time distributions for the A2 experiment. From left to right: time difference for two photons in TAPS, one photon in CB and one in TAPS. (b) Same for the CBELSA/TAPS data: two photons in the FP (left), two photons in MiniTAPS (mid), one photon in MiniTAPS and one in the FP (right).

7.3.2 Random Background Subtraction

Due to the high intensity electron beams used at MAMI and ELSA, several electrons are usually registered in the tagger during the trigger window. However, only one of these electrons produced the bremsstrahlung photon and is correlated with the current event. The other electrons are random and have to be discarded by statistical weighting. An event-by-event correction is not possible since the number of coincident but uncorrelated hits changes with the beam intensity. This can be seen in Fig. 7.8, where the number of tagger hits in the prompt window (tagger hit multiplicity) for A2 and CBELSA/TAPS data for two different beam currents are shown.

A sideband subtraction (random background subtraction) using the coincidence time between the tagger and a hit in one of the calorimeters (CB or TAPS and FP or MiniTAPS) was done to remove the random background. The calorimeter time was averaged over all the times of the decay photons from the η meson. When one or several photons were registered in TAPS or MiniTAPS, the time was taken only from those particles, since these detectors provide a better time resolution. The corresponding time spectra are shown in Fig. 7.9. Assuming that the uncorrelated tagger hits are purely random and therefore flat, the amount of random hits in the prompt window (red) was calculated using the background windows (blue). For this purpose, all events in the analysis were weighted. The weight was chosen to be $w_P = 1$ for hits in the prompt window. For the two background windows, the weight was negative and proportional to the window size:

$$w_R = -\frac{\Delta t_P}{\Delta t_{R1} + \Delta t_{R2}}, \quad (7.13)$$

where Δt_{R1} and Δt_{R2} are the widths of the two background windows, respectively, and Δt_P is the width of the prompt window. Tagger hits not belonging to the prompt or the two background windows were rejected. Thus, the number of correlated events was given by:

$$N_C = N_P + \sum_{i=1}^{N_R} w_R^i = N_P + w_R N_R, \quad (7.14)$$

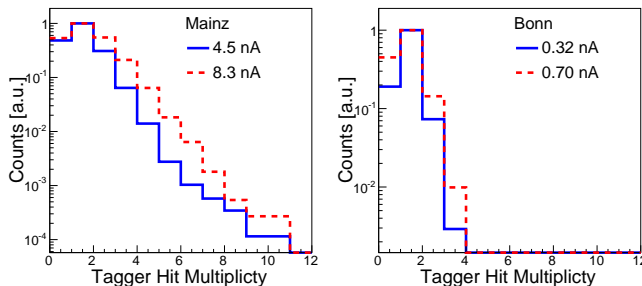


Figure 7.8: Tagger hit multiplicity: number of tagger hits in the prompt window for A2 (left) and CBELSA/TAPS (right) data. The histograms have been normalised to unity in the maximum. The number of prompt tagger hits increases with increasing beam current.

7.4. BACKGROUND REJECTION

where N_P is the number of prompt hits and N_R is the number of random hits with weight w_R . Since the error is given by:

$$\Delta N_C = \sqrt{N_P + w_R^2 N_R}, \quad (7.15)$$

the statistical uncertainty was small when having a small weight, i.e., large background windows. The background windows indicated in Fig. 7.9 are only illustrative since otherwise the peak region would not be visible. In the real analysis, the background windows were chosen much wider.

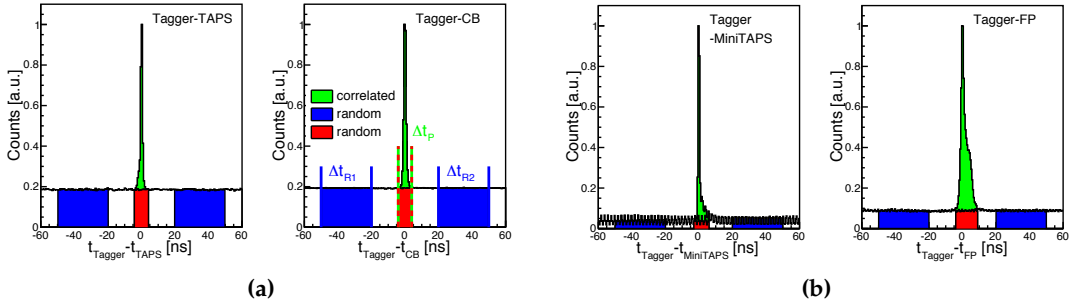


Figure 7.9: Random background subtraction for A2 (a) and CBELSA/TAPS (b) data: the random windows (blue) are used to subtract the random background in the prompt window (red), such that only the correlated (green) events remain. The random background for the CBELSA/TAPS data exhibits a 2 ns modulation coming from the 500 MHz alternating acceleration field of ELSA. The prompt peaks in the CBELSA/TAPS spectra are slightly asymmetric due to contamination from charged particles, which is rejected by the subsequent analysis cuts.

7.4 Background Rejection

Having found the possible candidates for the nucleon and the decay photons of the η meson, Pulse Shape Analysis (PSA) cuts were applied to ensure a clean separation of photons from nucleons. The used cuts are explained in Sec. 7.4.1 in more detail.

Subsequently, the complete reaction was identified and possible background from other contaminating reaction channels was rejected. Such contamination originates from other reactions that fit the same event class, i.e., have the same number of charged and neutral particles or reactions where one or several particles have not been detected. In addition, neutral and charged particles can be mixed up due to inefficiencies of the charged particle detectors. Furthermore, combinatorial background can occur due to the χ^2 test. The cuts used to discard these background contributions without eliminating too many good events are described in the next subsections. The sequence of the explained cuts is the same as it was used in the analysis procedure.

7.4.1 Pulse Shape Analysis

As mentioned in Secs. 2.4.1 and 6.1.1, the PSA can be used to distinguish nucleons from photons in TAPS and MiniTAPS. To do so, the PSA angle is plotted against the PSA radius, as explained in Eq. 6.6 and 6.7. With a proper calibration, the photons are aligned at 45° , while the nucleons form a banana at smaller PSA angles. Since each BaF_2 module of TAPS exhibits a slightly different pulse form, the PSA was done separately for each crystal. The cut position was determined by fitting a Gaussian distribution to projections of the photon band.

Having assigned the charged and neutral events to event classes and having identified the η meson and the recoil nucleon via the χ^2 test, the PSA cut was applied. To ensure reproducibility in the simulation (the PSA information is not available in the simulation), non-stringent cuts were chosen. Each of the decay photons was required to lie in a band of $\pm 3\sigma$ with respect to the mean position of the photon band, as seen in Figs. 7.10 and 7.11. The $\pm 3\sigma$ cut position for the photons (dashed line in the left two columns of Figs. 7.10 and 7.11) was chosen since the contamination of the photons with background was marginal and to ensure that only a small amount of real photons will be cut away. Since high-energetic nucleons slightly overlap with the photon band in the PSA spectrum, even less stringent cuts were chosen for the nucleons, as shown in the third and fourth column of Figs. 7.10 and 7.11. An exclusion zone was defined for the PSA radius of nucleons between 85 and 380 MeV. Only nucleon candidates with a PSA radius smaller than 85 MeV or larger than 380 MeV were cut away when lying closer than the 3σ line to the photon band. The PSA spectra of Figs. 7.10 and 7.11 shows the events after the χ^2 test and all additional analysis cuts. The contribution of photons to protons and vice-versa is minimal. However, slightly

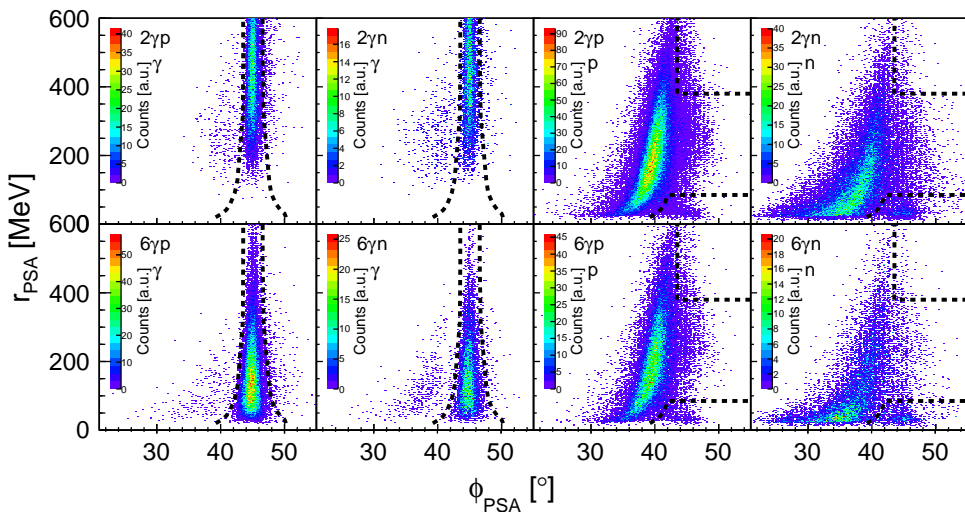


Figure 7.10: PSA spectra with all further analysis cuts applied for A2 data. The top row shows the photon and nucleon PSA spectra for the $\eta \rightarrow 2\gamma$ decay, the bottom row shows the same for the $\eta \rightarrow 6\gamma$ decay. The cut position is indicated with a dashed line. For the nucleons, the PSA cut was not applied between 85 MeV and 380 MeV.

7.4. BACKGROUND REJECTION

more background events are visible for the neutral channel where neutrons can be misidentified as photons during the χ^2 test. The influence of these events, even without cutting on the PSA, is negligible. Nevertheless, when the cut for PSA radius of the nucleon below 85 MeV was not applied, some background remains (such as electrons that have not been rejected by the vetoes), which is visible in the Time of Flight (TOF) versus energy plot, as shown in Fig. 7.12.

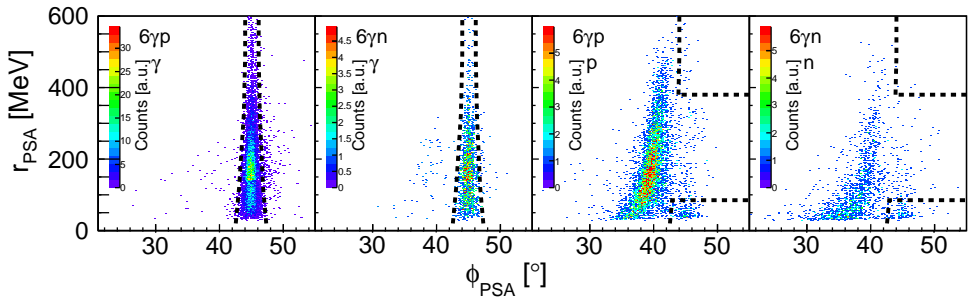


Figure 7.11: PSA spectra with all further analysis cuts applied for CBELSA/TAPS data for the photons (left two figures) and the nucleons (right two figures). The cut position is indicated with a dashed line. For the nucleons, the PSA cut was not applied between 85 MeV and 380 MeV.

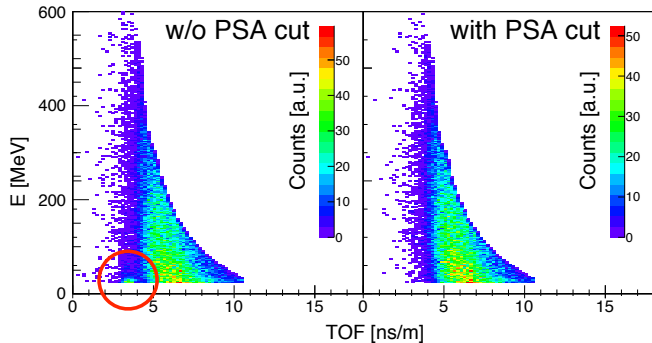


Figure 7.12: TOF versus energy plot for neutrons in TAPS without (left) and with (right) PSA cut on the nucleons. Without the PSA cut, a small background contribution is visible around 3.5 ns/m (red circle).

7.4.2 Coplanarity

Having detected the recoil nucleon (exclusive channel), the coplanarity condition was used to get a cleaner identification of the reaction. Since momentum conservation applies, the η meson is emitted in the reaction plane of the beam photon and the recoil nucleon, as seen in Fig. 7.13. Thus, the azimuthal angle difference between the recoil nucleon, ϕ_N , and the η meson, ϕ_η , is always 180° in the cm frame:

$$\Delta\phi = \begin{cases} \phi_\eta - \phi_N, & \text{if } \phi_\eta - \phi_N \geq 0 \\ 2\pi - |\phi_\eta - \phi_N|, & \text{if } \phi_\eta - \phi_N < 0. \end{cases} \quad (7.16)$$

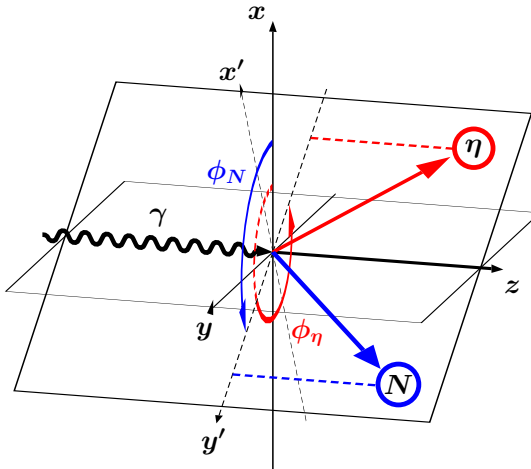


Figure 7.13: Coplanarity: the η meson (red) and the nucleon (blue) lie in the reaction plane and are separated by $\Delta\phi = 180^\circ$.

The system can be transformed via a Lorentz-Boost in the z -direction to the laboratory frame, where Eq. 7.16 applies as well since the ϕ -angle is independent of z . However, for quasi-free nucleons, the Fermi motion causes a smearing of the coplanarity angle. Fig. 7.14 shows the corresponding coplanarity spectra right after the χ^2 selection and the PSA cut, other cuts were not applied. Since the width and the position of the peak depends on the underlying kinematics, the cut position was determined for different bins of the beam energy and $\cos\theta_\eta^*$, where the star stands for the cm frame. For illustrative reasons, Fig. 7.14 shows spectra that have been integrated over the whole $\cos\theta_\eta^*$ range. The poor angular resolution at low photon energies is caused by the fact that near threshold, the η mesons have small kinetic energies and thus the Lorentz-boost has a big influence on their four momenta.

A symmetric cut of $\pm 2\sigma$ with respect to the mean position of the peak was chosen to ensure an appropriate background suppression. Separate cut positions have been determined for data and simulation to account for small differences in position and width of the peak close to threshold. Only the cut position extracted from simulation is indicated (dashed lines) in the figure. In general, the deuterium data (red and blue dots) and simulation (solid black line) are in good agreement. However, in the $\eta n \rightarrow 2\gamma n$ channel the experimental data shows an enhancement at low and high angular differences, which is not reproduced by the simulation. Investigations have shown that this structure is originating from the $\pi^0 n \rightarrow 2\gamma n$ reaction where one of the decay photons was misidentified as the recoil neutron. For the reactions on the proton, the small deviation of the experimental data from simulation is coming from $\eta\pi$ contribution. Especially at higher energies in the CBELSA/TAPS data, the contribution from charged pions increases, which is caused by the large cross section of charged pion photoproduction. Most of this background is later removed by the missing mass cut, which was not applied to these histograms. Some background is visible in experimental data and simulation, which is due to combinatorics and well understood. In

7.4. BACKGROUND REJECTION

addition to the signal on the deuterium target (blue and red circles), the distribution on the dButanol target (open black circles) is shown. The influence of the much larger Fermi momenta in the carbon nuclei, as seen in Fig. 4.1, introduces a broadening of the peak structure.

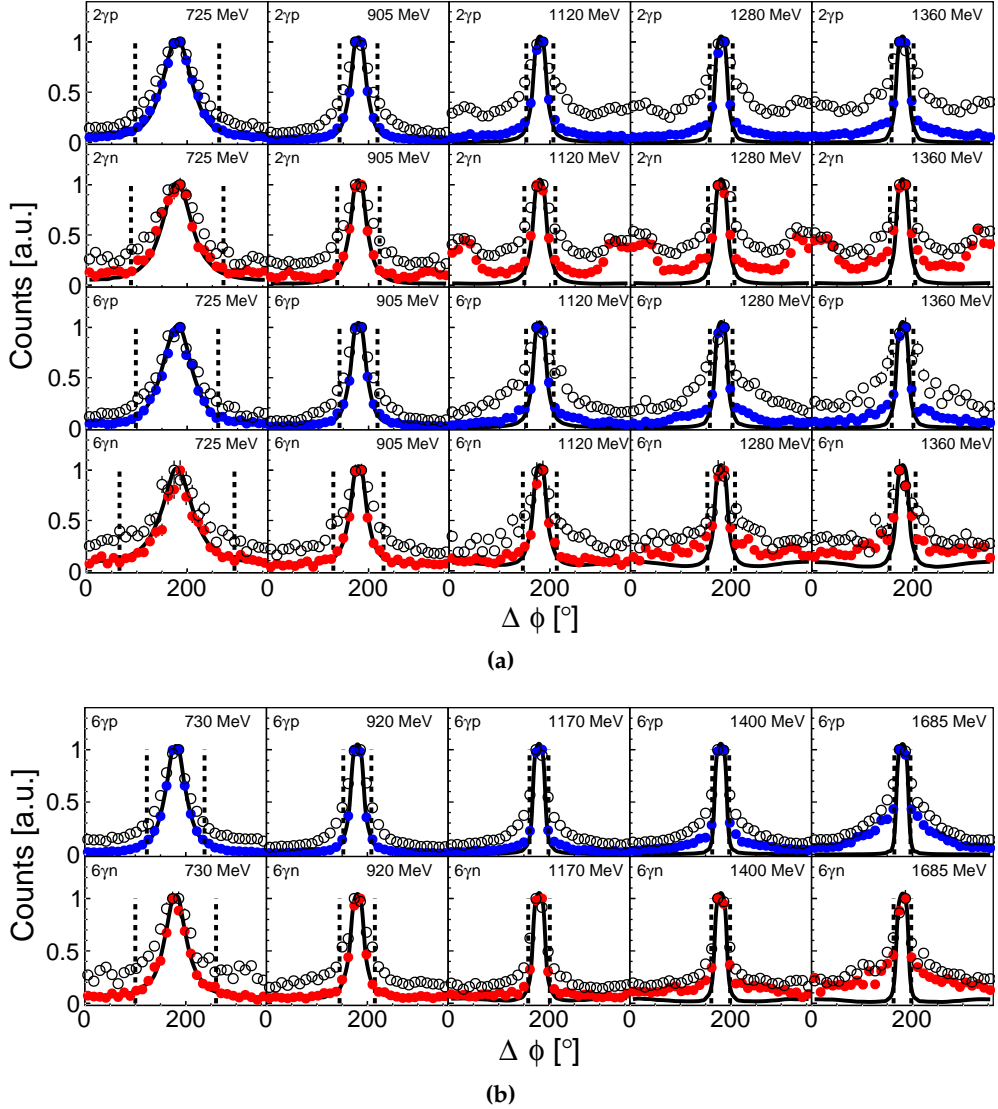


Figure 7.14: The angular difference $\Delta\phi$ between the recoil nucleon and the η meson for five different bins of incident photon energy. The spectra are integrated over the whole angular range and were filled right after the χ^2 selection, the PSA and the invariant mass cut were applied. Shown are the results for the A2 data in (a) for the $\eta \rightarrow 2\gamma$ (first two rows) and $\eta \rightarrow 6\gamma$ decay (last two rows). The spectra for the CBELSA/TAPS data are shown in (b) ($\eta \rightarrow 6\gamma$). The results for the deuterium target are shown in colors (red and blue circles) and the results for the dButanol target are shown as open black circles. The simulation is shown as solid black line. The dashed lines show the 2σ cut position determined from the simulation.

7.4.3 Missing Mass

Another method to reject background in the desired reaction channel is the determination of the missing mass. The missing mass requires only the reconstruction of the η meson and the recoil nucleon is treated as missing. Thus, the mass M of the nucleon can be calculated from the initial state and the detected final state particles:

$$M = \sqrt{\left(\sum_i p_i^{IS} - \sum_j p_j^{FS} \right)^2} = \sqrt{\left(\sum_i E_i^{IS} - \sum_j E_j^{FS} \right)^2 - \left(\sum_i \vec{p}_i^{IS} - \sum_j \vec{p}_j^{FS} \right)^2}, \quad (7.17)$$

where $p_i^{IS} = (E_i^{IS}, \vec{p}_i^{IS})$ and $p_j^{FS} = (E_j^{FS}, \vec{p}_j^{FS})$ are the four momenta of the i -th initial and j -th final state particles, respectively. For η photoproduction on the nucleon and assuming that the nucleon in the initial state is at rest, Eq. 7.17 simplifies to:

$$M = \sqrt{(E_\gamma + m_N - E_\eta)^2 - (\vec{p}_\gamma - \vec{p}_\eta)^2}, \quad (7.18)$$

where E_γ and \vec{p}_γ are energy and momentum of the incident photon beam, E_η and \vec{p}_η are the energy and momentum of the η meson, and m_N is the nucleon mass. With a correct identification of the reaction, the corresponding spectra should have a clear peak at the nucleon mass m_N . Thus, the nucleon mass was directly subtracted to get the missing mass:

$$\Delta M = M - m_N. \quad (7.19)$$

The missing mass spectra are shown in Fig. 7.15 for the deuterium target (blue and red points), the corresponding simulation (black line), and the dButanol target (open black circles). The influence of the much larger Fermi momenta in the carbon nuclei and hence in dButanol, is even more pronounced than for the coplanarity spectrum. The Fermi motion does not only broaden the peak, but also induces an asymmetric distribution at low beam energies. This is mainly caused by the fact that close to threshold, Fermi momenta in negative z-direction are favoured since they lead to a higher cm energy and reach the η production threshold more quickly.

At low incident photon energies, the deuterium data and simulation are in good agreement. Above $E_\gamma \simeq 800$ MeV, the contribution from $\eta\pi^0$ background events significantly increases. Furthermore, the channels $\gamma p \rightarrow \eta\pi^+ n$ and $\gamma n \rightarrow \eta\pi^- p$ can contribute when the neutron or the charged pion is not detected. All these background contributions induce an enhancement at larger missing masses since not all particles have been detected in the final state. However, applying energy and $\cos\theta_\eta$ dependent cuts of $\pm 1.5\sigma$ with respect to the mean peak value ensured a clean background rejection from $\eta\pi$ events while not reducing the signal too much.

7.4. BACKGROUND REJECTION

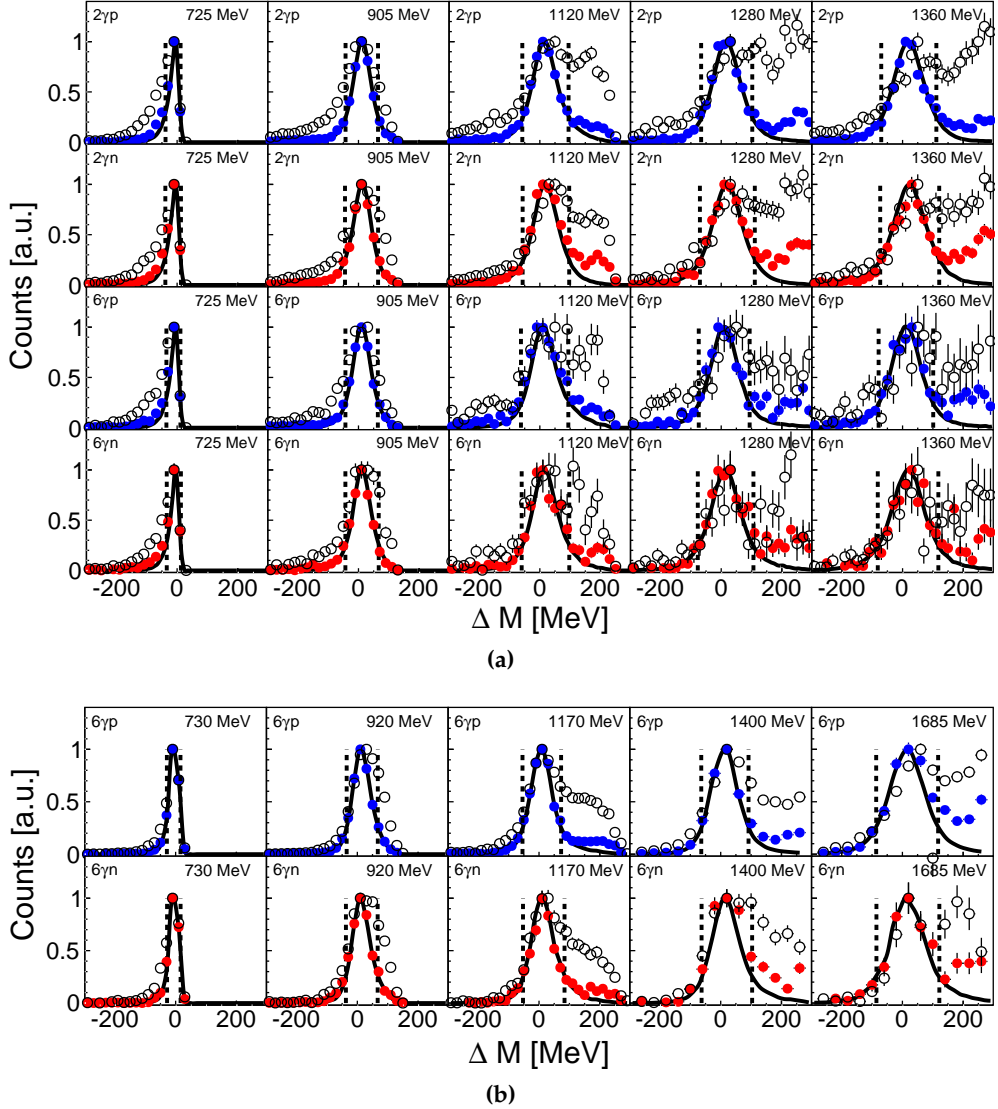


Figure 7.15: Missing mass ΔM for five different bins of incident photon energy. The spectra are integrated over the whole angular range and were filled after the χ^2 selection, the PSA, the coplanarity and the invariant mass cut were applied. Shown are the results for the A2 data in (a) for the $\eta \rightarrow 2\gamma$ (first two rows) and $\eta \rightarrow 6\gamma$ decay (last two rows). The spectra for the CBELSA/TAPS data are shown in (b) ($\eta \rightarrow 6\gamma$). The results for the deuterium target are shown in colors (red and blue circles) and the results for the dButanol target are shown as open black circles. The cut position of $\pm 1.5\sigma$ is indicated by the dashed line.

7.4.4 Invariant Mass

Having applied all previous cuts, the invariant mass of the potential η meson was investigated. For the $\eta \rightarrow 2\gamma$ decay, the invariant mass can be calculated from the four-vectors of the two decay photons respectively:

$$m_{2\gamma} = \sqrt{E_\eta^2 - \vec{p}_\eta^2} = \sqrt{(E_{\gamma_1} + E_{\gamma_2})^2 - (\vec{p}_{\gamma_1} + \vec{p}_{\gamma_2})^2}, \quad (7.20)$$

where E_{γ_1} , E_{γ_2} and \vec{p}_{γ_1} , \vec{p}_{γ_2} are the energy and momenta of the two decay photons, respectively. Using the opening angle between the two photons $\phi_{\gamma_1\gamma_2}$, this equation can be simplified to:

$$m_{2\gamma} = \sqrt{E_{\gamma_1} \cdot E_{\gamma_2} \cdot (1 - \cos \phi_{\gamma_1\gamma_2})}. \quad (7.21)$$

For the six photon decay channel, the pions with four momenta $p_{\pi_1^0}, \dots, p_{\pi_6^0}$ have to be reconstructed from the four momenta of the decay photons $p_{\gamma_1}, \dots, p_{\gamma_6}$ first:

$$p_{\pi_1^0} = p_{\gamma_1} + p_{\gamma_2} \quad (7.22)$$

$$p_{\pi_2^0} = p_{\gamma_3} + p_{\gamma_4} \quad (7.23)$$

$$p_{\pi_3^0} = p_{\gamma_5} + p_{\gamma_6}. \quad (7.24)$$

Subsequently, the η four-vector p_η can be extracted:

$$p_\eta = \sum_{i=1}^3 p_{\pi_i^0}. \quad (7.25)$$

Thus, the corresponding invariant mass is then given by:

$$m_{6\gamma} = \sqrt{E_\eta^2 - \vec{p}_\eta^2} = \sqrt{\left(\sum_{i=1}^3 E_{\pi_i^0}\right)^2 - \left(\sum_{i=1}^3 \vec{p}_{\pi_i^0}\right)^2} = \sqrt{\left(\sum_{i=1}^6 E_{\gamma_i}\right)^2 - \left(\sum_{i=1}^6 \vec{p}_{\gamma_i}\right)^2}. \quad (7.26)$$

The invariant mass spectra for both decay channels are shown in Fig. 7.16 for five energy bins. The data is in good agreement with the simulation and thus essentially background free because the background has already been rejected by the χ^2 anti-cut on the π^0 , as seen in Sec. 7.2 and the other cuts. Therefore, only broad cuts of approximately $\pm 4\sigma$ have been applied to collect as much statistics as possible. Since the width and position of the peak is more or less constant over the whole energy and angular range, fix cuts have been chosen:

$$2\gamma : \quad (450 - 620) \text{ MeV} \quad (7.27)$$

$$6\gamma : \quad (500 - 600) \text{ MeV} \quad (7.28)$$

For the inclusive reaction, a slightly more stringent cut between 510 and 590 MeV was chosen since the coplanarity, which rejects the most background, could not be applied.

As seen in Fig. 7.16, the resolution of the invariant mass of $\eta \rightarrow 6\gamma$ is better than the one of $\eta \rightarrow 2\gamma$. This is simply because the invariant mass of the three pions has been constrained to the nominal mass m_{π^0} by neglecting the angular resolution:

$$E'_{\gamma_1, \gamma_2} = \frac{m_{\pi^0}}{m_{\gamma_1 \gamma_2}} \cdot E_{\gamma_1, \gamma_2}. \quad (7.29)$$

However, the constraining of the nominal mass is only correct if one assumes that both decay photons carry approximately the same energy. The same procedure was done

7.4. BACKGROUND REJECTION

for the η meson to improve the resolution of the missing mass spectra.

In contrast to the coplanarity and missing mass spectra, the invariant mass on the dButanol target has exactly the same shape as the one on the deuterium target. This is caused by the fact that only the information of the detected decay photons was used for the calculation of the invariant mass and hence no influence of the Fermi motion is visible.

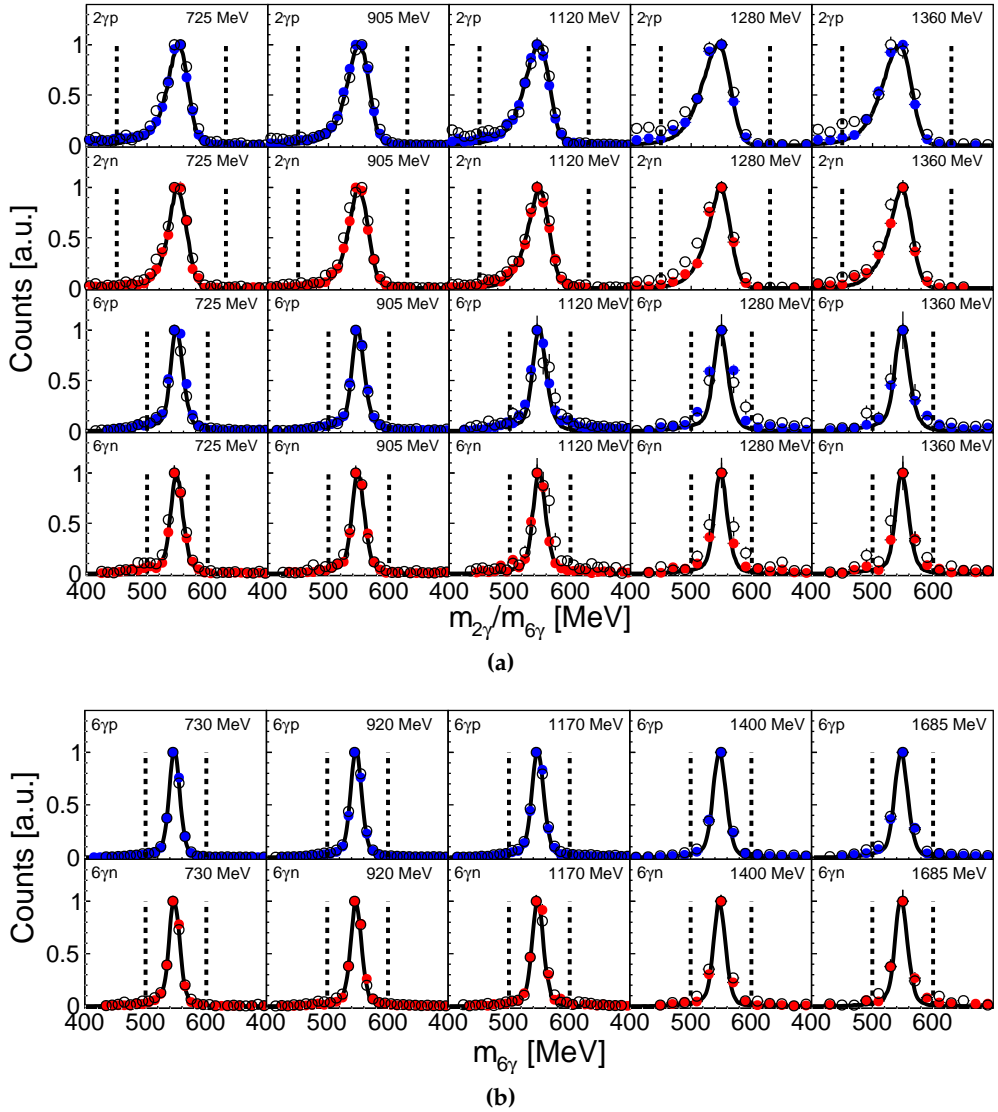


Figure 7.16: Invariant mass for bins of incident photon energy. The spectra are integrated over the whole angular range and were filled after all analysis cuts (PSA, coplanarity, missing mass) were applied. Shown are the results for the A2 data in (a) for the $\eta \rightarrow 2\gamma$ (first two rows) and $\eta \rightarrow 6\gamma$ decay (last two rows). The spectra for the CBELSA/TAPS data are shown in (b) ($\eta \rightarrow 6\gamma$). The results for the deuterium target are shown in colors (red and blue circles) and the results for the dButanol target are shown as open black circles. The simulation is shown as solid black line. The fixed cut position is indicated as a dashed line.

7.4.5 Polar Angle Cuts

Assuming quasi-free kinematics for η photoproduction on the nucleon (neglecting high Fermi momenta), the polar angle θ of the recoil nucleon in the lab frame is limited by kinematics. Figs. 7.17 and 7.18 show the corresponding spectra. The cut position (dashed line) was set to the θ angle where the experimental data starts to deviate from simulation at approximately 60° . Due to the small cluster size of nucleons, the segmentation of the detector is clearly visible.

For the A2 data, no nucleons were detected below $\theta = 5^\circ$ because this region belongs to the beam hole and the inner two rings of TAPS that have been switched off. The gap between CB and TAPS induces an acceptance hole at $\theta = 22^\circ$, which can be nicely seen in the spectra. For the CBELSA/TAPS spectra, the situation is similar and the efficiency hole between MiniTAPS and FP is clearly visible around $\theta = 12^\circ$. On the other hand, the transition between the FP and the CBB around $\theta = 30^\circ$ is quite smooth. The segmentation of the CBB is more distinct than for the CB, which is mainly caused by the higher granularity of the CBB and the perfect azimuthal symmetry of the rings.

Due to the higher Fermi momenta present in dButanol (coming from the carbon background), the corresponding spectra (blue) deviates a bit more from simulation than the deuterium data.

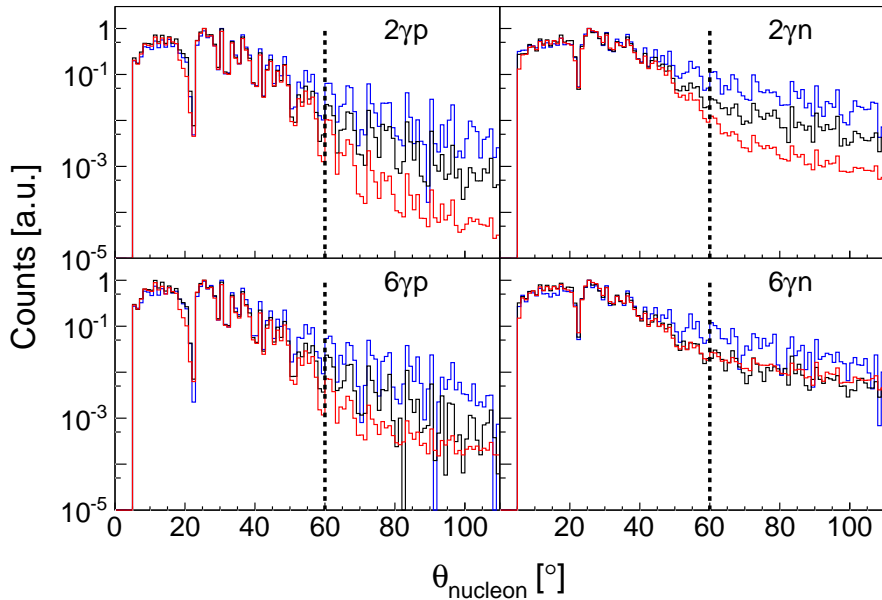


Figure 7.17: Polar angle of the nucleon in the lab frame for the A2 data after all analysis cuts were applied (PSA, coplanarity, missing mass, invariant mass). The experimental spectrum from the deuterium target is shown in black, the corresponding simulation in red. The experimental distribution for the dButanol target is shown in blue. A logarithmic y-axis is used. The spectra are normalised to unity in the maximum. The cut position is indicated by the dashed line.

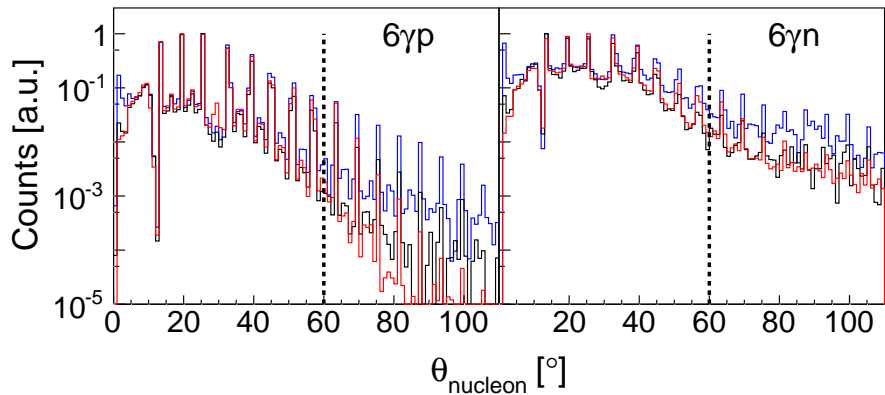


Figure 7.18: Polar angle of the nucleon in the lab frame for the CBELSA/TAPS data after all analysis cuts were applied (PSA, coplanarity, missing mass, invariant mass). The experimental spectrum from the deuterium target is shown in black, the corresponding simulation in red. The experimental distribution for the d-Butanol target is shown in blue. A logarithmic y-axis is used. The spectra are normalised to unity in the maximum. The cut position is indicated by the dashed line.

7.5 Further Checks

Not all the available information provided by the detector setup was used to reject background since the reaction identification was already sufficiently accurate. However, they have been used to check the event selection as shown in the next subsections.

7.5.1 Time of Flight

As explained in Sec. 2.4.1, due to the properties of BaF₂ and the large distance from the target (approximately 1.5 m in Mainz and 2.1 m in Bonn), TAPS and MiniTAPS are ideally suited to perform a Time of Flight (TOF) measurement. The TOF analysis exploits that particles with the same kinetic energy but different masses have different TOF since heavier particles are generally slower. Since the flight path s of every detected particle is different, the TOF was normalised to one meter:

$$\text{TOF} = \frac{\Delta t}{s} + \frac{1}{c} \text{ [ns/m]}, \quad (7.30)$$

where Δt is the time difference between a hit in TAPS or MiniTAPS and the tagger. The tagger was used as reference because it provides a better time resolution than the CB or FP. During the calibration procedure all photon times were aligned to zero, so an additional offset of $1/c$ had to be added. The TOF was plotted versus the deposited energy E in TAPS or MiniTAPS. As can be seen in Fig. 7.19, photons have an energy independent TOF of around 3.3 ns/m. On the other hand, the TOF of low energetic nucleons is larger than the TOF of nucleons with more energy. Protons deposit all their energy in the crystals, at least up to the punch-through limit and thus build a

banana-like structure. The TOF-versus-energy spectrum is completely uncorrelated for the neutrons due to different interactions that occur in the crystals. Whereas protons mainly interact via ionisation, neutrons make elastic or inelastic scattering on nuclei and nuclear reactions producing secondary particles such as photons, protons, deuterons, and α -particles.

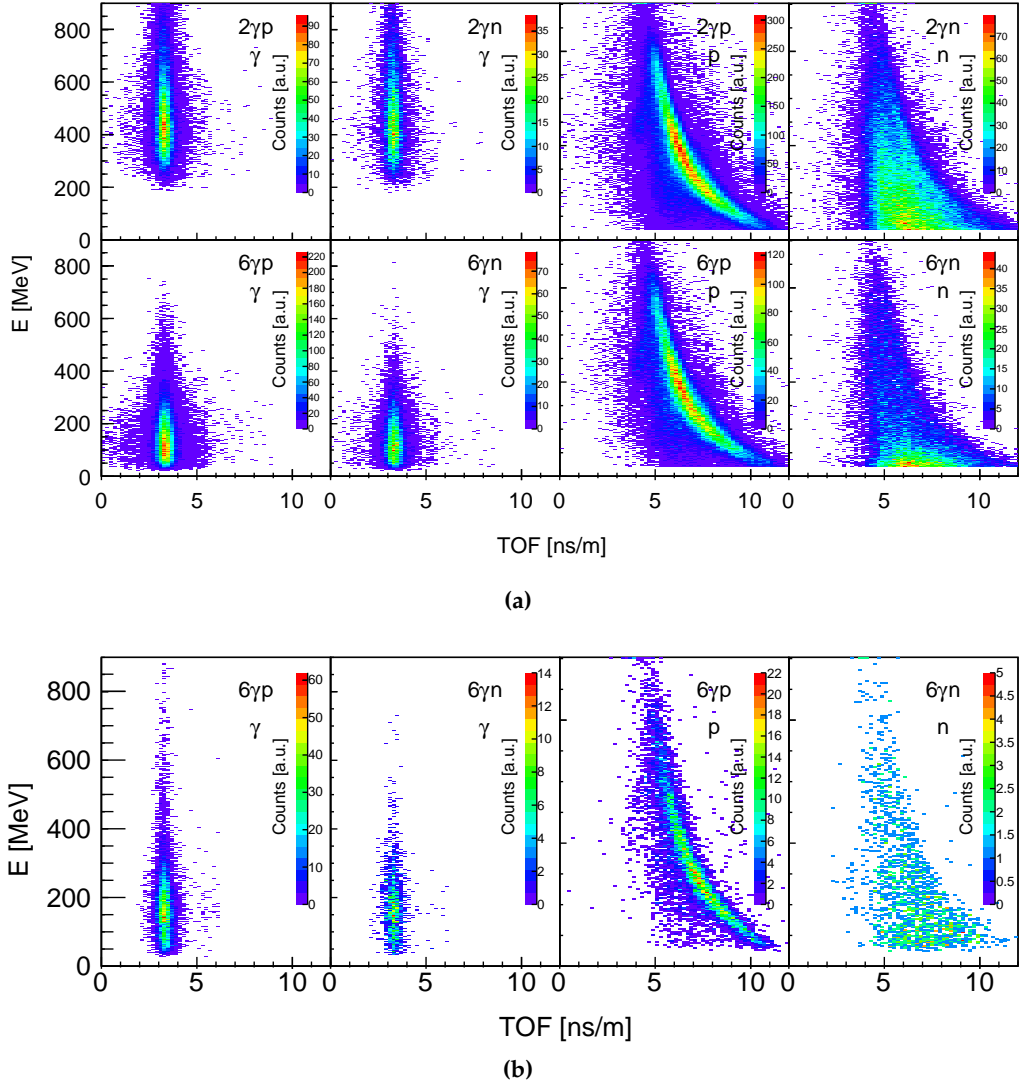


Figure 7.19: The TOF versus energy plot for TAPS (A2 data) for events that have passed all analysis cuts is shown in (a). The top row shows the photon and nucleon PSA spectra for the $\eta \rightarrow 2\gamma$ decay, the bottom row shows the same for the $\eta \rightarrow 6\gamma$ decay. (b) shows the TOF versus energy plot for MiniTAPS (CBELSA/TAPS data).

7.5.2 ΔE versus E

Another possibility to check the event selection is the ΔE versus E plot, where the energy deposited in the charge sensitive detectors (PID or vetoes) is plotted against the energy deposited in the corresponding calorimeter (CB, TAPS, and MiniTAPS). For protons, the energy deposited in the charge sensitive detectors, is strongly dependent on the energy deposited in the crystals and thus building a banana-like structure. On the other hand, charged pions are minimum ionising most of the time and thus are situated at lower energies exhibiting less energy dependence. Electrons are situated at even smaller energies ΔE and E .

In the A2 data, one can look at the energy deposited in the PID, ΔE , versus the energy deposited in CB, E . In addition, the energy deposited in the vetoes, ΔE , against the energy deposited in TAPS, E , can be used for particle identification purposes. Due to the fact that the signals of the TAPS vetoes were read out via long light guides, the energy resolution for TAPS ΔE versus E was significantly worse than for the CB, as seen in Fig. 7.20. Since in Bonn neither the inner detector nor the FP vetoes provide energy information (because of the very bad resolution, the energy was not read out on the hardware side), ΔE versus E can only be used for MiniTAPS, as seen in Fig. 7.21. Since the construction of the MiniTAPS vetoes was the same as for the TAPS vetoes, the energy resolution was poor here as well. In both A2 and CBELSA/TAPS data, the initially present background coming from electrons and charged pions was

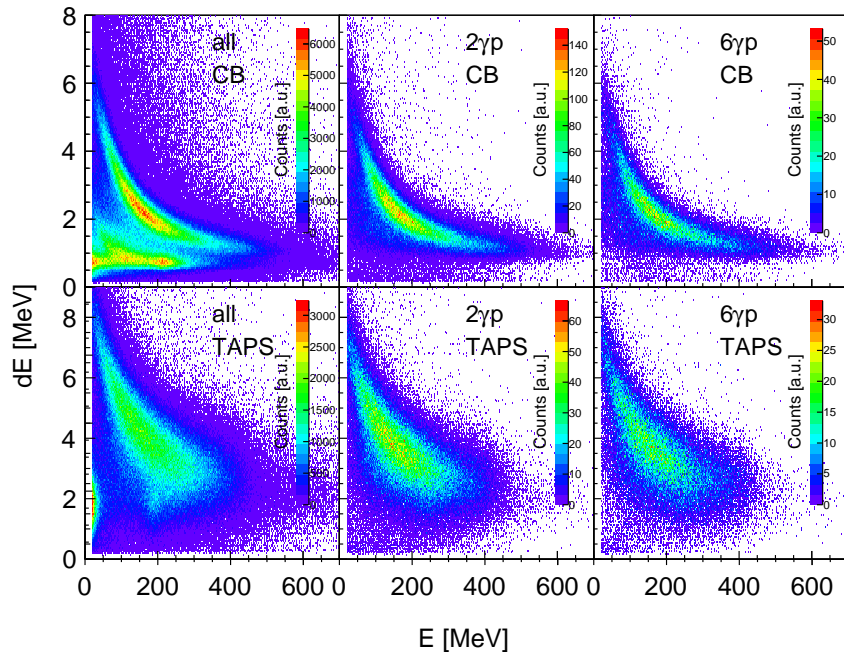


Figure 7.20: ΔE versus E for CB (top row) and TAPS (bottom row) for A2 data. Left column: spectrum for events that have been assigned to the $\eta p \rightarrow 2\gamma p$ event class, no further analysis cuts were applied. Middle column: spectra for the $\eta p \rightarrow 2\gamma p$ event class after all cuts were applied. Right column: same for $\eta p \rightarrow 6\gamma p$

satisfactorily removed by the other analysis cuts and no TOF versus energy cut was necessary.

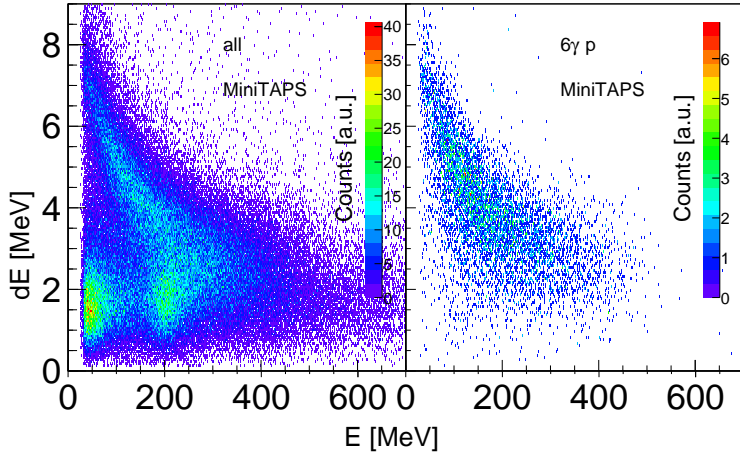


Figure 7.21: ΔE versus E for MiniTAPS (CBELSA/TAPS data). The spectrum was filled directly after the event selection (left) and is compared to the spectrum, which was filled after all analysis cuts were applied (right).

7.5.3 Cluster Multiplicity

As explained in Sec. 7.4.1, the BaF_2 crystals provide the possibility to disentangle neutrons from photons via PSA. In the CB, CBB, and FP, such a method does not exist and one has to rely on the χ^2 selection criteria. However, this is not satisfactory and the identification of the assigned photons and neutrons via the χ^2 test can be checked using the cluster multiplicity (the number of fired crystals per cluster). Since neutrons and photons interact in different ways with the scintillating material, the cluster multiplicity distributions are different, as seen in Fig. 7.22. The photon distributions peak at higher values than the one of the neutron. In addition, the distributions are different for the photons originating from the $\eta \rightarrow 2\gamma$ and $\eta \rightarrow 6\gamma$ decay since the latter photons on average have smaller energies. The validity of the neutron identification is clearly visible since the distribution for the neutrons from both decay channels exhibit the same shape. Nevertheless, due to an overlap region, this criterion should not be used for the event selection and no cut is made.

7.5.4 Fermi Momentum

The participant-spectator model is ideally suited to describe the quasi-free kinematics. In this framework, the reaction takes place on the participant nucleon, whereas the spectator remains unaffected. In the initial state, both nucleons carry a momentum p_F (with opposite sign), thus:

$$p_A = p_S + p_P = \begin{pmatrix} E_P \\ \vec{p}_P \end{pmatrix} + \begin{pmatrix} E_S \\ \vec{p}_S \end{pmatrix} = \begin{pmatrix} E_P \\ \vec{p}_F \end{pmatrix} + \begin{pmatrix} E_S \\ -\vec{p}_F \end{pmatrix} = \begin{pmatrix} m_A \\ 0 \end{pmatrix}, \quad (7.31)$$

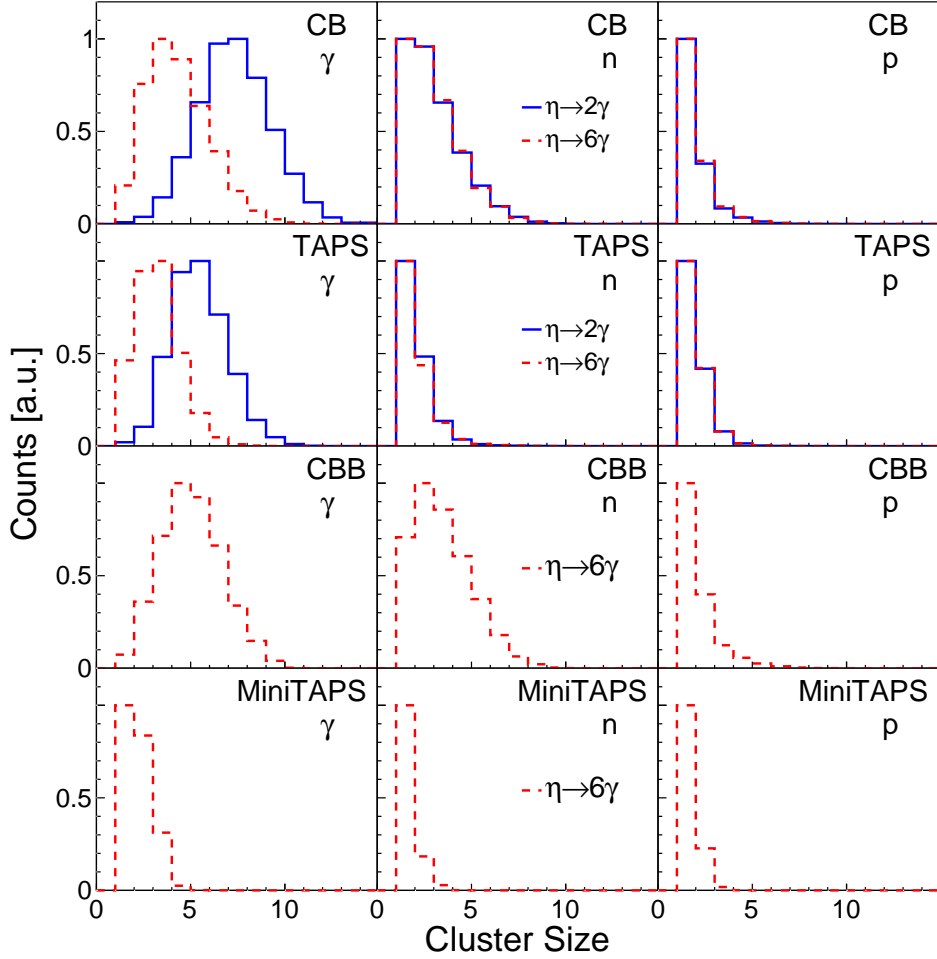


Figure 7.22: Cluster multiplicity for events that have passed all analysis cuts for the CB (first row), TAPS (second row), CBB and FP (third row) and MiniTAPS (fourth row). The first column shows the cluster multiplicity for the photon, the middle column shows the spectra for the neutron. In the right column the same is shown for the proton. For the CBELSA/TAPS data, only the $\eta \rightarrow 6\gamma$ decay channel was analysed.

where $p_A = (m_A, 0)$ is the four-momentum of the nucleus, m_A is the mass of the nucleus and $p_P = (E_P, \vec{p}_P)$ and $p_S = (E_S, \vec{p}_S)$ are the four momenta of participant and spectator nucleons, respectively. Since the spectator remains in this initial state configuration, the final state (FS) momentum distribution of the spectator nucleons should reflect the initial state (IS) momentum distributions of the participant nucleons, i.e., the Fermi momentum distribution inside the atomic nucleus. Using momentum conservation one finds that:

$$\vec{p}_\gamma + \vec{p}_P^{IS} + \vec{p}_S^{IS} = \vec{p}_\eta + \vec{P}_P^{FS} + \vec{p}_S^{FS}. \quad (7.32)$$

Since in the participant-spectator model $\vec{p}_S^{IS} = \vec{p}_S^{FS}$ applies, it follows:

$$\vec{p}_F = \vec{p}_P^{IS} = \vec{p}_P^{FS} + \vec{p}_\eta - \vec{p}_\gamma, \quad (7.33)$$

where \vec{p}_η and \vec{p}_γ is the four-momentum of the η meson and incident photon beam, respectively. Having detected all final state particles, the Fermi momentum can be calculated according to Eq. 7.33. As mentioned in Sec. 7.5.1, nucleons interact differently with the scintillating material than photons. This, in combination with the fact that the energy calibration was done for photons, causes that the deposited energy of the participant (recoil) nucleon to be not equal to its kinetic energy. Though, for a reaction with nucleus A , participant P and spectator S :



the kinetic energy can be extracted from kinematical considerations [56]:

$$\begin{pmatrix} E_\gamma \\ \vec{p}_\gamma \end{pmatrix} + \begin{pmatrix} m_A \\ 0 \end{pmatrix} = \begin{pmatrix} E_\eta \\ \vec{p}_\eta \end{pmatrix} + \begin{pmatrix} E_P \\ \vec{p}_P \end{pmatrix} + \begin{pmatrix} E_S \\ \vec{p}_S \end{pmatrix} \quad (7.35)$$

The kinetic energy T_P of the participant nucleon is then given by:

$$T_P = \frac{-(bc - 2a^2 m_P) + \sqrt{(bc - 2a^2 m_P)^2 - c^2(b^2 - a^2)}}{2(b^2 - a^2)}, \quad (7.36)$$

where

$$\begin{aligned} a &= p_{\eta,x} \sin \theta_P \cos \phi_P + p_{\eta,y} \sin \theta_P \sin \phi_P + (p_{\eta,z} - E_\gamma) \cos \theta_P, \\ b &= E_\eta - E_\gamma - m_A, \\ c &= (b + M_P)^2 - (m_S^2 + p_\eta^2 + E_\gamma^2 - 2E_\gamma p_{\eta,z}), \end{aligned} \quad (7.37)$$

and m_P is the mass of the participant nucleon, $p_{\eta,x}$, $p_{\eta,y}$, $p_{\eta,z}$ are the x, y, and z components of the η momentum, respectively, and θ_P and ϕ_P are the polar and azimuthal angles of the participant nucleon. The full derivation of this expression is given in [172].

Since the participant and spectator are simply the proton and the neutron or vice-versa, the calculation is straightforward for the deuterium nucleus. The corresponding spectator momentum distributions for participant protons and neutrons are shown in Fig. 7.23. The distributions are compared to a parametrisation of the deuteron wave function of the Paris NN potential (solid line) [152]. For large Fermi momenta, η photoproduction may be kinematically forbidden (depending on the relative orientation of the Fermi momentum with respect to the direction of the photon beam), thus the dashed curve shows only the kinematically allowed events based on the model predictions of the Paris N-N potential. The overall shape of the distributions are in quite good agreement with the model predictions. The most probable value is slightly shifted to higher spectator momenta, which is mainly caused by the experimental resolution. In addition, the high momenta tails fall off faster in data compared to simulation, but this is only a very small effect. The situation is more complicated in the case of ${}^3\text{He}$, which is composed of two protons and one neutron. Therefore, one has to assume that the two spectator nucleons in the final state can be treated as a di-nucleon without relative momentum. This simplification seems to be quite realistic, since the

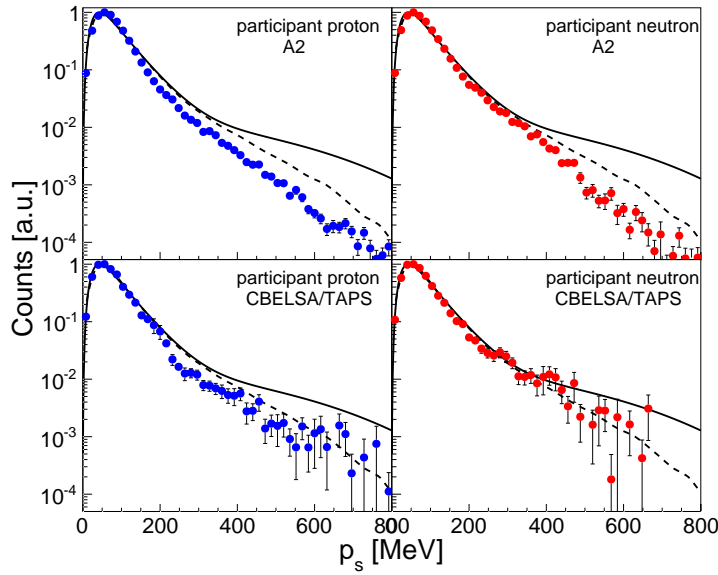


Figure 7.23: Spectator momentum distribution for participant proton and neutron in deuterium. The distributions extracted from A2 and CBELSA/TAPS data (dots) are compared to calculations using the Paris N-N potential (solid line) [152] and the corresponding kinematically allowed distribution for η photoproduction (dashed line). The y-axis is shown logarithmically.

extracted spectator momentum distributions are in nice agreement with the theoretical predictions using the Argonne potential [153], as seen in Fig. 7.24. The peak of the distribution is at the same position as for the model calculations, therefore, in better agreement as for the deuterium data. This may be caused by the less steep rise in the ^3He distribution compared to deuterium and thus the distribution is less affected by the experimental resolution. In general, the shape of the high momentum tail is similar to the one of the deuterium distribution. According to Hen *et al.* [173], this is a sign for short range correlations (SRC), i.e., a pair of nucleons with high relative and low cm momentum. This can be further investigated by looking at the ratio of the proton and neutron distribution, which is shown in the second part of Fig. 7.24. Normalising the ratio of the integrals of the distributions to the nucleon ratio in ^3He ($N/Z = 1/2$) results in a nearly perfect agreement with the model predictions. At small momenta ($p_S < 300$ MeV), the situation is dominated by long range interactions, and thus the average ratio is approximately $N/Z = 0.5$. In contrast, at larger momenta ($300 \text{ MeV} < p_S < 600 \text{ MeV}$), the ratio approaches unity (as for deuterium) and SRC (tensor interactions) dominate. Also the shape of the high momentum tail in the spectator momentum distribution is similar to the one of deuterium. Thus, one can conclude that high Fermi momenta are exclusively generated by isospin-singlet pairs [153]. Recent high energy electron scattering experiments in Hall B of the Thomas Jefferson National Accelerator Facility [173] have observed *np-dominance of SRC pairs in heavy imbalanced nuclei* [173].

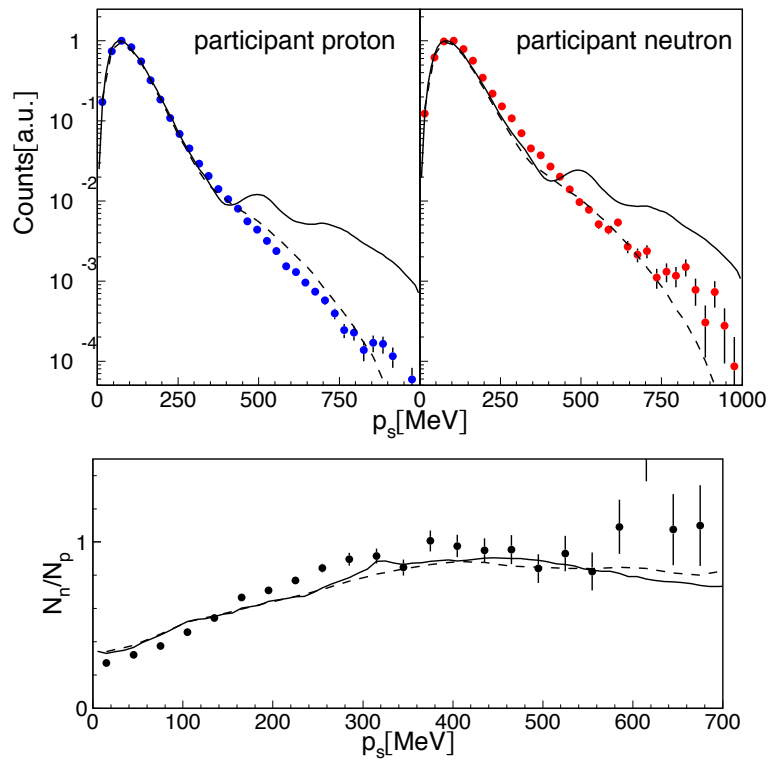


Figure 7.24: Fermi momentum distributions for ${}^3\text{He}$ extracted from the experimental data and compared to calculations by Arrington et al. [153] (solid line) and the corresponding kinematically allowed distribution for η photoproduction (dashed line). The y-axis for the Fermi momentum distribution is shown logarithmically.

Chapter 8

Extraction of Observables

In this chapter, all required quantities and the extraction procedure to obtain the unpolarised cross section, the double polarisation observable E , and the helicity dependent cross sections $\sigma_{1/2}$ and $\sigma_{3/2}$ will be explained in detail.

8.1 Unpolarised Cross Section

The unpolarised differential cross section as a function of the energy E and $\cos \theta_\eta^*$, the cosine of the polar angle of the η meson in the cm frame, was determined via:

$$\frac{d\sigma}{d\Omega} \Big|_{\text{unpol}} (E, \cos \theta_\eta^*) = \frac{N(E, \cos \theta_\eta^*)}{\epsilon(E, \cos \theta_\eta^*) \cdot N_\gamma(E) \cdot n_T \cdot \Gamma_i / \Gamma \cdot \Delta\Omega}, \quad (8.1)$$

where the following nomenclature was used:

E	energy: incident photon energy E_γ or final state energy W
θ_η^*	polar angle of the η meson in the cm frame
$N(E, \cos \theta_\eta^*)$	yields as a function of the energy E and $\cos \theta_\eta^*$
$\epsilon(E, \cos \theta_\eta^*)$	detection efficiency
$N_\gamma(E)$	incoming photon flux
n_T	target surface density in $[\text{b}^{-1}]$
Γ_i / Γ	branching ratio for the final state [6]
	$\eta \rightarrow 2\gamma: 39.41 \pm 0.20 \%$
	$\eta \rightarrow 6\gamma: 32.10 \pm 0.26 \%$
$\Delta\Omega$	solid angle coverage of the $\cos \theta_\eta^*$ -bin in $[\text{sr}]$

The determination of the differential cross sections as a function of the cosine of the polar angle and instead of the polar angle itself is more convenient since the solid angle coverage of each $\cos \theta_\eta^*$ -bins remains then constant, as can be seen in the following equation:

$$\Delta\Omega = \frac{4\pi}{N_{CT}}, \quad (8.2)$$

where N_{CT} is the number of $\cos \theta_\eta^*$ -bins and was chosen according to the available statistics.

By integrating the differential cross section over the solid angle, the total cross section $\sigma(E)$ can be deduced:

$$\sigma(E) = \int \frac{d\sigma}{d\Omega} \Big|_{\text{unpol}} (E, \theta_\eta^*) d\Omega. \quad (8.3)$$

For N_{CT} angular bins, the integral can be approximated by a sum over all angular bins:

$$\sigma(E) \simeq \frac{4\pi}{N_{CT}} \sum_{i=1}^{N_{CT}} \frac{d\sigma}{d\Omega} \Big|_{\text{unpol}} (E, \theta_\eta^*) . \quad (8.4)$$

Alternatively, the angular distribution can be fitted with a series of Legendre polynomials P_i of N -th degree:

$$f_L(E, \cos \theta_\eta^*) = \frac{q^*(E)}{k^*(E)} \sum_{i=0}^N A_i(E) P_i(\cos \theta_\eta^*) , \quad (8.5)$$

where A_i are the Legendre coefficients, $q^*(E)$ and k^* are the momenta of the η meson and the incident photon beam in the cm frame, respectively, and $q^*(E)/k^*$ is the phase-space factor. By integrating the Legendre series, the total cross section can be found from the zeroth Legendre coefficient A_0 :

$$\sigma(E) = \int_{-1}^1 f_L(E, \cos \theta_\eta^*) d\cos \theta_\eta^* = 4\pi \frac{q^*(E)}{k^*} A_0(E) . \quad (8.6)$$

8.2 Double Polarisation Observable E

The double polarisation observable E , introduced in Sec. 1.3, was extracted using two different methods, which will be explained in detail in the next sections.

8.2.1 Version 1 - Carbon Subtraction Method

As mentioned in Sec. 1.3, the double polarisation observable E is defined as the asymmetry between the two helicity states $\sigma_{1/2}$ (anti-parallel photon and nucleon spin) and $\sigma_{3/2}$ (parallel photon and nucleon spin):

$$E = \frac{\sigma_{1/2} - \sigma_{3/2}}{\sigma_{1/2} + \sigma_{3/2}} = \frac{\sigma_{\text{diff}}}{\sigma_{\text{sum}}} , \quad (8.7)$$

Plugging Eq. 8.1 in Eq. 8.7, and considering that the polarisation observable E was measured on a dButanol target, yields the following expression:

$$E^{dB} = \frac{1}{p_\gamma p_T} \cdot \frac{\frac{N_{1/2}^{dB}}{\epsilon_{1/2}^{dB} N_\gamma^{1/2}} - \frac{N_{3/2}^{dB}}{\epsilon_{3/2}^{dB} N_\gamma^{3/2}}}{\frac{N_{1/2}^{dB}}{\epsilon_{1/2}^{dB} N_\gamma^{1/2}} + \frac{N_{3/2}^{dB}}{\epsilon_{3/2}^{dB} N_\gamma^{3/2}}}, \quad (8.8)$$

where p_γ and p_T are the degrees of photon and target polarisations, respectively, $N_{1/2}^{dB}$ and $N_{3/2}^{dB}$ are the yields on the dButanol target with helicity $1/2$ and helicity $3/2$, respectively, and $N_\gamma^{1/2}$ and $N_\gamma^{3/2}$ are the corresponding photon fluxes. It was assumed that the branching ratio and the target surface density cancel out in Eq. 8.8 since they appear in the numerator and the denominator.

Eq. 8.8 can be simplified if one assumes that the efficiency is equal for both helicity states, $\epsilon_{1/2}^{dB} = \epsilon_{3/2}^{dB} = \epsilon^{dB}$. Furthermore, assuming that the photon fluxes are equal as well, $N_\gamma^{1/2} = N_\gamma^{3/2} = N_\gamma^{dB}/2$, E can be simply determined from the difference of the yields:

$$E^{dB} = \frac{1}{p_\gamma p_T} \cdot \frac{(N_{1/2}^{dB} - N_{3/2}^{dB})/N_\gamma^{dB}/2}{(N_{1/2}^{dB} + N_{3/2}^{dB})/N_\gamma^{dB}/2}. \quad (8.9)$$

Knowing that dButanol contains polarised deuterons but also unpolarised background from carbon and oxygen, one deduces for the numerator:

$$N_{1/2}^{dB} - N_{3/2}^{dB} = N_{1/2} + (N^0/2) - N_{3/2} - (N^0/2) = N_{1/2} - N_{3/2}, \quad (8.10)$$

where N^0 are the yields on the unpolarised carbon and oxygen in the dButanol target. $N_{1/2}$ and $N_{3/2}$ are the yields on the polarised deuterium with helicity $1/2$ and $3/2$, respectively. In an analogous way, one can derive the following expression for the denominator:

$$N_{1/2}^{dB} + N_{3/2}^{dB} = N_{1/2} + (N^0/2) + N_{3/2} + (N^0/2) = N_{1/2} + N_{3/2} + N^0. \quad (8.11)$$

Hence, whereas the unpolarised carbon background cancels out in the numerator, it remains in the denominator. To extract the polarisation observable E , one has to subtract the unpolarised background in σ_{sum} . As mentioned in Sec. 2.3.4, the contribution of the unpolarised carbon background was determined with the help of a measurement with a carbon target.

For the carbon subtraction, the following equation applies:

$$E = \frac{1}{p_\gamma p_T} \cdot \frac{(N_{1/2} - N_{3/2})(N_\gamma^{dB}/2)}{(N_{1/2} + N_{3/2} + N^0)/(N_\gamma^{dB}/2) - D \cdot (N^C/N_\gamma^C/2)}, \quad (8.12)$$

where N^C are the yields from the carbon target and D is known as the dilution factor, with its determination explained in Sec. 8.10. In the following, the method to extract the polarisation observable E via subtraction of the unpolarised carbon background, as shown in Eq. 8.12, is referred to as *version 1* (carbon subtraction method). The main

advantage of this method is that all possible efficiency and flux uncertainties cancel out directly. However, the carbon contribution must be known exactly.

8.2.2 Version 2 - Direct Method

Starting from Eq. 8.7 and knowing that $\sigma_{1/2} + \sigma_{3/2} = 2\sigma$ applies, one can derive the following equation:

$$E = \frac{\sigma_{1/2} - \sigma_{3/2}}{2\sigma} = \frac{\sigma_{diff}}{2\sigma}, \quad (8.13)$$

where σ is the unpolarised cross section. Hence, the double polarisation observable E cannot only be extracted using the carbon subtraction method, but also by normalising σ_{diff} with twice the unpolarised cross section.

Using Eqs. 8.1 and 8.13 one finds the following formula:

$$E = \frac{1}{p_\gamma p_T} \cdot \frac{\frac{N_{1/2}^{dB} - N_{3/2}^{dB}}{e^{dB(N_\gamma/2)} n_T^{dB} \Gamma_i / \Gamma}}{2\sigma} = \frac{1}{p_\gamma p_T} \cdot \frac{\frac{N_{1/2} - N_{3/2}}{e^{dB(N_\gamma/2)} n_T^{dB} \Gamma_i / \Gamma}}{2\sigma}, \quad (8.14)$$

where n_T^{dB} is the target surface density of the dButanol target (number of deuteron nuclei per barn), and σ is the unpolarised cross section given by Eq. 8.1.

In the following, the method to determine the polarisation observable E by normalising the difference of the two helicity states with twice the unpolarised cross section, as seen in Eq. 8.14, is called *version 2* (direct method). The unpolarised cross section was taken from the measurement by Werthmüller *et al.* [55] for the normalisation of the A2 data. For the normalisation of the CBELSA/TAPS data, the cross section, which was extracted in this work for the CBELSA/TAPS data (see Sec. 9.2) was used.

This method (*version 2*) has the advantage that it does not require a carbon subtraction. However, since the numerator and denominator stem from different experiments using different targets, the efficiency and photon flux must be taken into account.

8.3 Helicity Dependent Cross Sections $\sigma_{1/2}$ and $\sigma_{3/2}$

In Sec. 8.2, two different methods were described to extract the double polarisation observable E , *version 1*, where the carbon was subtracted, and *version 2*, where the unpolarised cross section was used for normalisation purposes. To extract the helicity dependent cross sections, three methods were used that will be explained in the following subsections.

8.3.1 Version 1

Having determined the double polarisation observable E with the carbon subtraction method (*version 1*), as described in Sec. 8.2.1, the helicity dependent cross sections can be extracted. With the help of Eq. 1.44, one finds the following expression for an anti-parallel photon and target spin:

$$\sigma_{1/2} = \sigma(1 + E), \quad (8.15)$$

8.4. TARGET SURFACE DENSITY

where σ is the unpolarised cross section and E was determined from Eq. 8.2.1 (*version 1*). On the other hand, for a parallel configuration of the spins one finds:

$$\sigma_{3/2} = \sigma(1 - E). \quad (8.16)$$

Hence, in *version 1*, the polarisation observable E was determined using carbon subtraction, then, the unpolarised cross section was used to determine the helicity dependent cross section $\sigma_{1/2}$ and $\sigma_{3/2}$.

8.3.2 Version 2

In *version 2*, the double polarisation observable E was determined by normalisation with the unpolarised cross section. The same can be done for the helicity dependent cross sections. The helicity $1/2$ cross section is then given by the following formula:

$$\sigma_{1/2} = \sigma(1 + E) = \frac{2 \cdot \sigma + \sigma_{diff}}{2}, \quad (8.17)$$

and the $3/2$ cross section is given by:

$$\sigma_{3/2} = \sigma(1 - E) = \frac{2 \cdot \sigma - \sigma_{diff}}{2}. \quad (8.18)$$

Hence, in *version 2*, both the double polarisation observable E and the helicity dependent cross sections were extracted using the unpolarised cross section, which means that *version 2* is independent of the carbon subtraction.

8.3.3 Version 3

A third method, *version 3*, can be used to calculate the helicity dependent cross sections. Using $\sigma_{diff} = \sigma_{1/2} - \sigma_{3/2}$ and $\sigma_{sum} = \sigma_{1/2} + \sigma_{3/2}$, one can directly deduce the following two expressions:

$$\sigma_{1/2} = \frac{\sigma_{sum} + \sigma_{diff}}{2}, \quad (8.19)$$

$$\sigma_{3/2} = \frac{\sigma_{sum} - \sigma_{diff}}{2}. \quad (8.20)$$

Hence, for *version 3*, only the counts from the polarised target are used and a carbon subtraction is necessary.

8.4 Target Surface Density

The target surface density n_t can be calculated by the following equation:

$$n_t = \frac{\rho_t \cdot f \cdot N_A \cdot L_t}{M_{mol}}, \quad (8.21)$$

where ρ_t is the target density in g/cm^3 , L_t is the target length, M_{mol} is the molar mass in g/mol , $N_A = 6.02214 \times 10^{23}$ is the Avogadro constant, and f is the filling factor. As explained in Sec. 2.3.3, the polarised target is filled with dButanol beads, therefore the target volume is only covered to a certain extent by dButanol, this amount is given by the filling factor f . The target surface densities for all different targets are summarised in Table 8.1.

		L_t [cm]	ρ_t [g/cm ³]	f	M_{mol} [g/mol]	N_t [b ⁻¹]
A2	³ He	5.08	0.07448	1	3.016	0.00756
	LD ₂	3.02	0.16324	1	2.014	0.14741
	C ₄ D ₉ OD	2	1.1	0.6	84.1923	0.09442
	C	1.98	0.57	1	12.011	0.05659
CBELSA/TAPS	LD ₂	5.258	0.169	1	2.014	0.26570
	C ₄ D ₉ OD	1.88	1.1	0.59	84.1923	0.08727
	C	1.88	0.5	1	12.011	0.04713

Table 8.1: Target surface density for all different targets used for the present work.

8.5 W-Reconstruction

The most straightforward way to extract cross sections is the extraction as a function of the incident photon energy E_γ . However, looking at cross sections as a function of the incident photon energy is not ideal in the case of quasi-free reactions. As bound nucleons in a nucleus have a certain Fermi momentum p_F , as seen in Fig. 4.1, the $W = \sqrt{s}$ can only be approximated in the initial state by assuming that the nucleons are at rest. This leads to a smearing of structures in the cross section and the determination of the intrinsic width of resonances is not possible. Fermi motion effects are apparent in η photoproduction close to threshold due to the steep slope of the $S_{11}(1535)$ resonance, as will be explained in Sec. 9.1. Consequently, it is a better solution to calculate W from the final state particles, i.e. as the invariant mass of the η meson and the recoil nucleon. This implies the detection of both the recoil nucleon and the decay photons of the η meson, and requires the determination of the corresponding four-momenta. The reconstruction of nucleons, especially the neutron, has a larger systematic uncertainty due to several reasons. One cause is that the detector setup is optimised for the detection of photons and thus having a lower detection efficiency for nucleons. Another reason is that the position determination for nucleons is less precise than for photons due to different cluster sizes, as seen in Fig. 7.22. Furthermore, as explained in Sec. 7.5.1, the neutron kinetic energy cannot be determined from the deposited energy and the kinetic energy of the proton can only be found by applying several corrections. This problem can be solved by a kinematical reconstruction of the participant nucleon, for which Eq. 7.36 was used. As explained in Sec. 7.5.4, one has to make some

assumptions to apply Eq. 7.36 for nucleons bound in ${}^3\text{He}$. Thus, an additional method was used to extract the cross sections as a function of the cm energy W using the TOF measurement in TAPS in the case of the ${}^3\text{He}$ target. This reconstruction method is only possible when the recoil nucleon is detected in TAPS, which corresponds to events where the η meson is emitted in backward angles, i.e. $\cos(\theta_\eta^*) < -0.4$ in the photon-nucleon cm frame. Using the TOF technique, the kinetic energy of the recoil nucleon is determined with the following formula:

$$T_P = M_P(\gamma - 1), \quad (8.22)$$

where M_P is the mass of the participant nucleon, $\gamma = 1/\sqrt{1-\beta^2}$, and $\beta = v/c = 1/(t_{\text{TOF}} \cdot c)$.

To determine the width of the narrow structure in the η meson cross section on the neutron, it is necessary to exactly know the resolution of both reconstruction methods. This was determined by simulating the response of the detectors and the analysis of photoproduction events with an intermediate state of a fixed mass (δ -function with W -energies of 1515, 1535, 1608, 1640, 1671, 1700, and 1750 MeV) decaying in a η meson and a nucleon. For this purpose, the `TOMCGenResDecay` class [56] of the OSCAR library, as explained in Sec. 4.1.4, was used. The resulting resolution of the kinematical and the TOF method is shown in Fig. 8.1 for the ${}^3\text{He}$ target of the A2 setup. Even though, the kinematical reconstruction is only an approximation for the three body final state, it leads to a better resolution than the TOF reconstruction. The resolution of the TOF reconstruction is dominated by the time resolution and decreases with rising W . This effect comes from the fact that the TOF versus energy distribution is almost flat for high energetic nucleons, as seen in Fig. 7.19.

In general, the W resolution is decreasing with increasing cm energy W . For the kinematical reconstruction, this is caused by the poor reconstruction of the four-momentum measurement of the η meson at high energies and the poor direction measurement of the recoil nucleon. High energetic photons produce larger clusters than low energetic photons and hence allow a better position determination. However, the quality of the reconstruction of the η meson is dominated by stronger shower losses occurring at higher energies. In contrast to photons, the accuracy of the position determination for nucleons is only slightly dependent on the nucleon energy itself. At high cm energies, due to kinematics the nucleons are mainly detected in the CB/CBB, where the angular resolution $\Delta\theta$ and hence the direction measurement is worse compared to the TAPS/MiniTAPS resolution ($\Delta\phi$ is similar).

The simulated response of the CBELSA/TAPS and the A2 setup for the kinematical reconstruction using the LD₂ target is shown in Fig. 8.2. The line shape is slightly asymmetric, but was approximated by a Gaussian distribution to extract the cm energy dependent resolution ΔW (right-hand side). The resolution of the CBELSA/TAPS experiment is superior than for the A2 experiment, which is a direct consequence of the resolutions shown in Sec. 7.2.1.

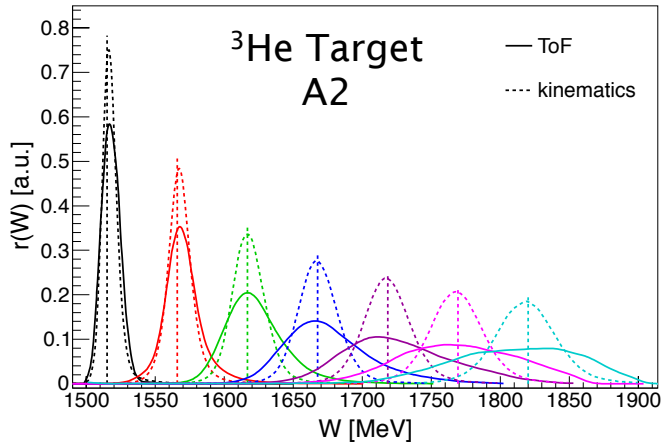


Figure 8.1: Simulated detector resolution distributions $r(W)$ for the cm energy W of the final state. The $\eta \rightarrow 2\gamma$ decay was simulated for the reaction on the neutron. The resolution from the kinematical reconstruction (dashed curves) is compared to the TOF measurement (solid curves) for the ^3He experiment (A2). The resolutions for the W -energies of 1515, 1535, 1608, 1640, 1671, 1700, and 1750 MeV (black to blue) are indicated in the figure.

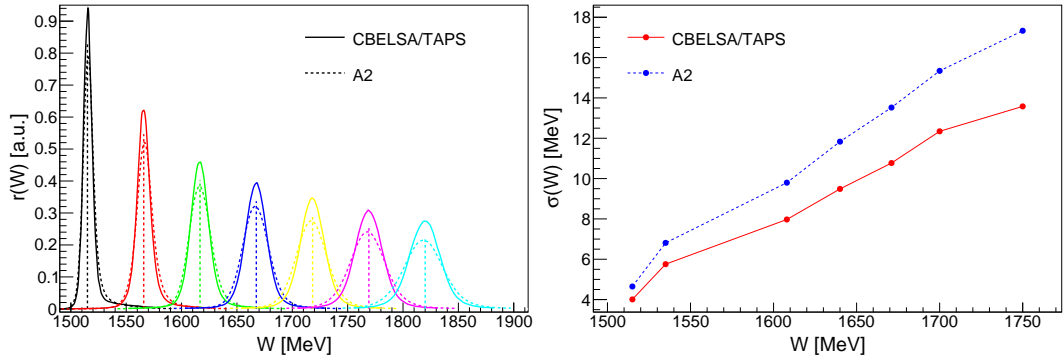


Figure 8.2: Simulated detector resolution $r(W)$ for the cm W of the final state for the kinematical reconstruction. The $\eta \rightarrow 6\gamma$ decay was simulated for the reaction on the neutron. Left: the simulated line shapes for the CBELSA/TAPS (solid line) LD₂ target is compared to the A2 LD₂ target (dashed line, resolution taken from [56]). The resolutions for the W -energies of 1515, 1535, 1608, 1640, 1671, 1700, and 1750 MeV (black to blue) are indicated in the figure. Right: the resolution $\sigma(W)$ as a function of the cm energy for both experiments.

8.6 Photon Flux

In order to get a correct normalisation of the cross sections, it is crucial to know exactly the flux of the incident photons on the target during the time of the data acquisition (DAQ). The photon flux N_γ is given by the number of electrons registered in the tagger, N_{e^-} , multiplied with the tagging efficiency ϵ_{tagg} :

$$N_\gamma = N_{e^-} \cdot \epsilon_{tagg}. \quad (8.23)$$

The tagging efficiency is mainly influenced by the collimation of the beam and thus sensitive to the beam quality and the beam position.

8.6.1 A2 Photon Flux

In the A2 experiment, the number of electrons is counted for each tagger channel using scaler modules. Before August 2013, the tagger scalers were inhibited when the tagger DAQ was busy ($1 - \Gamma_{tagg}$, with the tagger live time Γ_{tagg}). However, the DAQ of the other detectors had a different live time Γ_{det} , such that a correction had to be applied for these data sets:

$$N'_{e^-} = N_{e^-} \frac{\Gamma_{det}}{\Gamma_{tagg}}. \quad (8.24)$$

Since the live time of the detectors was approximately $\Gamma_{det} \simeq 44\%$ and the live time of the tagger was $\Gamma_{tagg} \simeq 57\%$, the correction factor was around 23%.

For the newer experiments, the old scaler modules have been replaced by VUPROM scalers. These scalers are no more live time gated and thus have to be corrected for dead time during the offline analysis. Simultaneously, the DAQ was upgraded in a way that the tagger DAQ and the DAQ of the other detectors have a common live time Γ_{all} . Thus, the number of electrons for the new data was calculated according to the following equation:

$$N'_{e^-} = N_{e^-} \cdot \Gamma_{all}. \quad (8.25)$$

The live time Γ_{all} was determined by the ratio of an inhibited scaler and a free clock scaler.

The resulting number of electrons per tagger channels is shown in the first row of Fig. 8.3. In addition to the well known inverse energy dependence coming from the bremsstrahlung process (low channel numbers correspond to high photon energies), some tagger channels with very high or very low counts are visible. These have been identified as malfunctioning channels and were rejected from the analysis.

The tagging efficiency ϵ_{tagg} was periodically (typically once per day) measured during dedicated low intensity runs. As mentioned in Sec. 2.4, a lead glass detector with an efficiency of about 100% at the low beam intensities during the tagging efficiency runs (~ 10 kHz), was used to register the incident photon beam behind the TAPS detector. In order to account for tagger hits caused by cosmic rays and nuclear decays due to activated material, runs without beam have been taken before and after each low intensity run. These runs were used to subtract the background and obtain

the correct tagging efficiency values. Since the tagging efficiency is only slightly dependent on the beam intensity, this efficiency can be directly applied to the data runs (high intensity). However, since the beam quality, and hence the tagging efficiency, changed over time, the tagging efficiency had to be extrapolated between the tagging efficiency measurements. This was done by counting the number of detected $\pi^0 + X$ events (inclusive pion production) for each run. For this purpose, the average tagging efficiency over all tagger channels N_{tc} was calculated for each low intensity run j :

$$\langle \bar{\epsilon}_j \rangle = \frac{1}{N_{tc}} \sum_{i=1}^{N_{tc}} \epsilon_i, \quad (8.26)$$

where ϵ_i is the tagging efficiency per tagger channel. The $\pi^0 + X$ counts for each

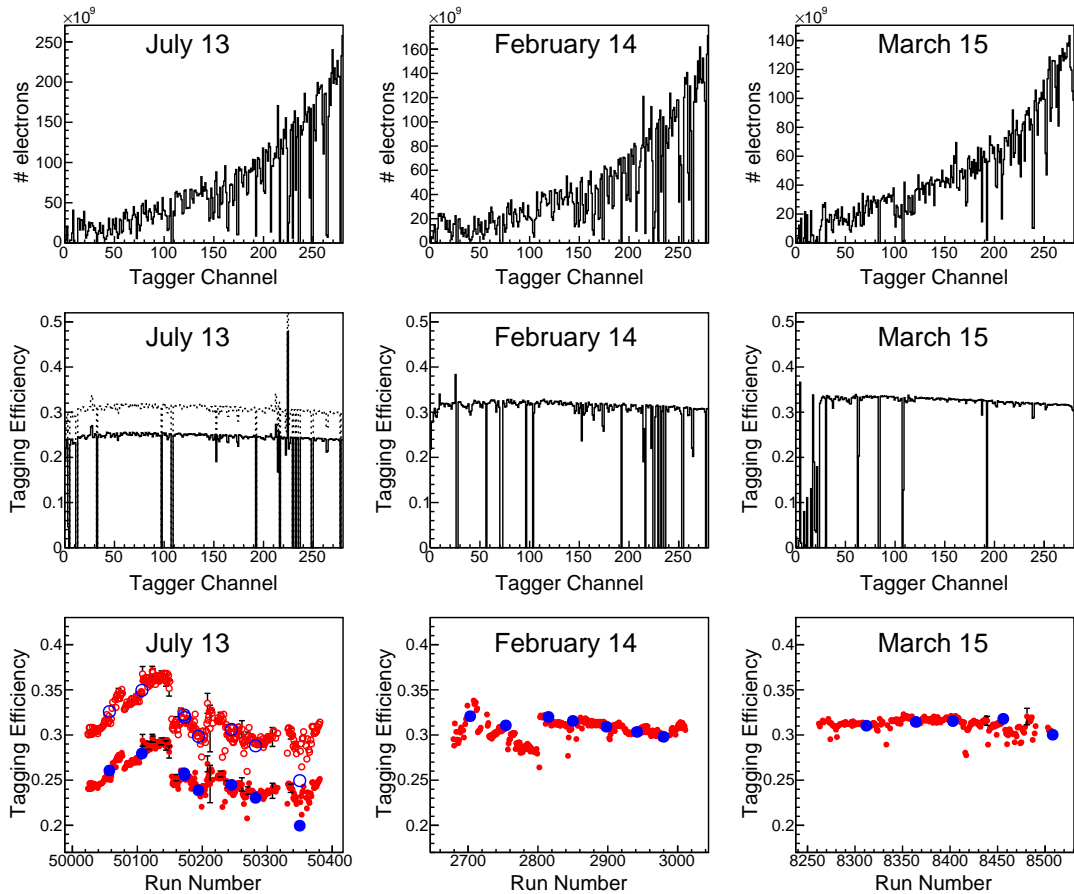


Figure 8.3: First row: number of electrons per tagger channel registered by the scaler modules. Second row: mean tagging efficiency as a function of the tagger channels. Third row: average tagging efficiency extracted from the low intensity measurements (blue), compared to the count rate per run (red) for each *d*Butanol experiment (columns). The tagging efficiency of the July 2013 beamtime was corrected with a factor of 1.25 (second row: dashed histogram, third row: open symbols). In the March 2015 beamtime, the lowest tagger channels were malfunctioning.

run, $\langle \bar{N}_k \rangle$, were then overall scaled to the average tagging efficiency values given in Eq. 8.26. The tagging efficiency for each data run k and tagger channel i was then extracted with the following formula:

$$\epsilon_k^i = \frac{\langle \bar{\epsilon}_i \rangle}{\sum_{j=1}^{N_{tc}} \langle \bar{\epsilon}_j \rangle} \cdot \langle \bar{N}_k \rangle, \quad (8.27)$$

where $\langle \bar{\epsilon}_i \rangle$ is the average tagging efficiency per channel of all tagging efficiency measurements N_{meas} :

$$\langle \bar{\epsilon}_i \rangle = \frac{1}{N_{meas}} \sum_{j=1}^{N_{meas}} \epsilon_i, \quad (8.28)$$

Fig. 8.3 shows the resulting tagging efficiencies for the three separate dButanol beamtimes. The second row of Fig. 8.3 shows that the tagging efficiency per channel is almost flat, only a small energy dependence is visible. As can be seen in the third row, the normalised counts (red), which were extracted from the data runs, nicely describe the shape given by the tagging efficiency measurements (blue).

Even though the same collimator was mounted in all dButanol experiments, the determined tagging efficiency in July 2013 was roughly 5% smaller on the absolute scale than for the other two dButanol experiments. This difference comes from an issue with the scalers during the tagging efficiency measurement in July 2013, which caused wrong live time values and was corrected by applying a scaling factor of 1.25 to the tagging efficiency. The corrected tagging efficiency is indicated in Fig. 8.3 by the dashed line (second row) and by the open symbols (third row). The correction factor was verified by comparing the unpolarised cross section of the different dButanol beamtimes.

The tagging efficiency values, which were determined for the LD₂ and ³He experiment can be found in Ref. [56] and Ref. [129], respectively.

8.6.2 CBELSA/TAPS Photon Flux

The CBELSA/TAPS photon flux was calculated according to the technique described in Ref. [125]. As explained in Sec. 5.2, the construction of the CBELSA/TAPS tagger is much more complicated since it consists of overlapping bars and fibres. Thus, the number of electrons, i.e. the number of reconstructed bar and fibre clusters, known as *beam photons*, N_γ^{rec} , and the tagging efficiency was not determined for single tagger channels, but for bins of incident photon energy. To determine N_γ^{rec} , when the DAQ is ready, first, the number of reconstructed photons was counted in a certain interval Δt . The interval Δt was chosen as wide as possible and outside of the trigger window to reduce the influence of the trigger to the energy distribution of the electrons. For this work, the following interval was chosen: (-450 ns to -50 ns) and (50 ns to 350 ns). The first row in Fig. 8.4 shows the number of reconstructed photons, $N_\gamma^{rec}(\Delta t)$, in the time interval Δt for the deuterium and the dButanol beamtimes. The distribution exhibits the typical $1/E_\gamma$ bremsstrahlung decrease. Similar to the A2 data, some malfunction-

ing bins can be seen. The spectra of the January and June 2011 beamtimes do not start before 500 MeV since the tagger channels corresponding to the lowest photon energies were switched off to achieve higher trigger rates.

As mentioned, $N_{\gamma}^{rec}(\Delta t)$ is the number of reconstructed photons in the time interval Δt . However, the number of photons during the entire live time t_{live} is of interest. Thus, in an ideal case, $N_{\gamma}^{rec}(\Delta t)$ has to be scaled by the following factor:

$$c_{live} = \frac{t_{live}}{\Delta t}. \quad (8.29)$$

Since the electron flux provided by ELSA is not constant, the scaling factor cannot be determined as shown in Eq. 8.29. Alternatively, the number of registered events in the tagger bar coincidence counters $N_{Scaler}(t_{live})$ and the number of coincident TDC hits in the data $N_{TDC}(\Delta t)$ can be used to determine the scaling factor c_{live} :

$$c_{live} = \frac{N_{Scaler}(t_{live})}{N_{TDC}(\Delta t)}. \quad (8.30)$$

The scaling factor for the LD₂ experiment was approximately 4300 ($\Gamma_{live} \sim 77\%$) and 2500 ($\Gamma_{live} \sim 44\%$) for the dButanol experiments.

As for the A2 experiment, a tagging efficiency was determined to find the number of photons on the target from the electrons in the tagger. For this purpose, the number of coincident events in the GIM and the tagger $N_{Tagger \wedge GIM}$ was used [125]:

$$\epsilon_{Tagg} = \frac{N_{Tagger \wedge GIM}}{N_{Tagger}}, \quad (8.31)$$

where N_{Tagger} is the number of hits in the tagger. The occurring random coincident events had to be subtracted. The resulting tagging efficiency is shown in Fig. 8.4 in the second row as a function of the incident photon energy. The structure around an incident photon energy of 2050 GeV and the steep falloff towards higher energies is caused by different background contributions and noise (the scintillation bars for the high energies are older than the one for low energies). The steep falloff at low photon energies is caused by the threshold of the GIM discriminators, which yields a lower efficiency for low energetic photons, as shown in the third row of Fig. 8.4. A second cause which decreases the efficiency of the GIM is the dead time of the used electronics, especially the discriminators. The GIM efficiency ϵ_{GIM} is rate dependent and was determined using the FluMo, as described in Ref. [125]:

$$\epsilon_{GIM}(\dot{N}_{\gamma}) = \epsilon_{FluMo} \frac{\dot{N}_{GIM}}{\dot{N}_{FluMo}}, \quad (8.32)$$

where ϵ_{FluMo} is the efficiency of the FluMo, \dot{N}_{FluMo} is the rate in the FluMo, and \dot{N}_{GIM} is the rate in the GIM. The calibration of the FluMo is done at low rates, where the efficiency is approximately 100%. The GIM efficiency is less flat for the January and June 2011 beamtimes than for the December 2008 beamtime. This originates from the

fact that the GIM threshold had to be increased in 2011 due to radiation damages of the GIM crystals.

Furthermore, a Cherenkov deadtime correction of 8% for the LD₂ and 5% for the dButanol experiment was applied.

Whereas this flux yielded a correct normalisation for the deuterium experiments, the flux was a factor 1.6 too large for the dButanol and carbon experiments. This is most likely due the fact that before the dButanol experiments, the scaler read out was changed, which could have lead to a wrong flux determination. Hence, for this work, the flux of the CBELSA/TAPS dButanol and carbon experiments was scaled down by a factor of 1.6. The factor was verified by a comparison of the total unpolarised cross section from the dButanol target, which was determined from A2 and CBELSA/TAPS data. Furthermore, the factor was checked in the carbon subtraction, where this factor was needed to scale the dButanol and carbon spectra to be consistent with the correctly normalised deuterium spectra.

Further information about the flux determination for the CBELSA/TAPS experiment can be found in Ref. [125].

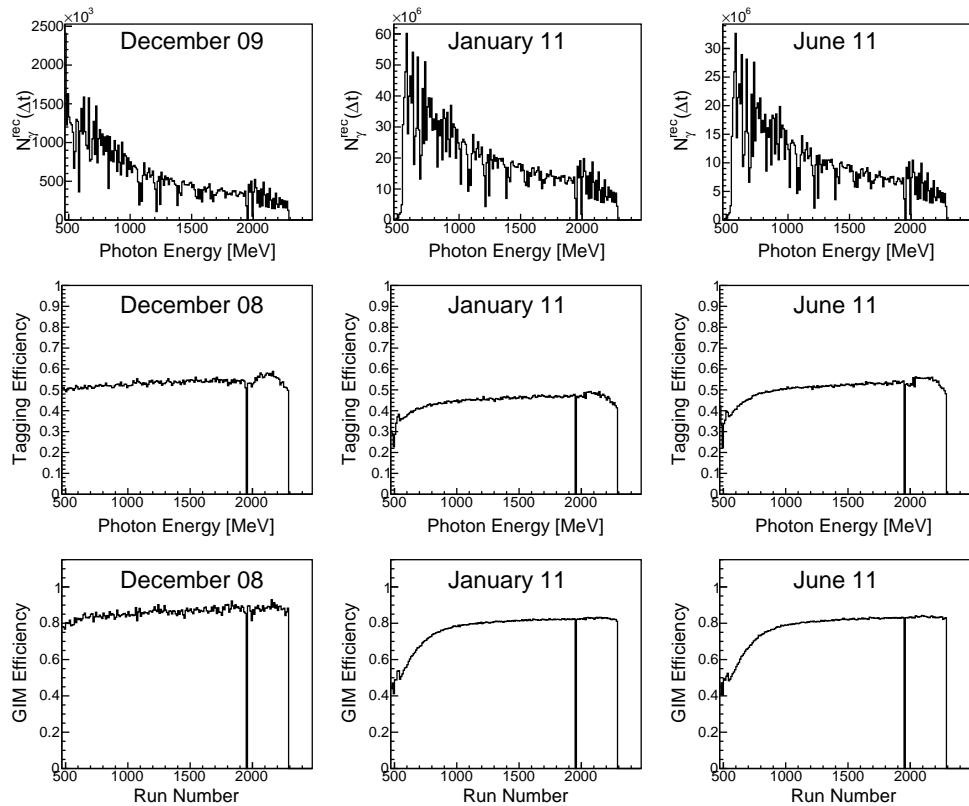


Figure 8.4: Quantities used to extract the CBELSA/TAPS photon flux for the LD₂ (left column) and the dButanol (right two columns) experiment. First row: number of reconstructed photons $N_{\gamma}^{\text{rec}}(\Delta t)$. Second row: tagging efficiency extracted from the data runs. Third row: GIM efficiency as defined in Eq. 8.32. The drop in the GIM efficiency towards low photon energies is caused by the thresholds of the used discriminators.

8.6.3 E_γ - and W-Dependent Flux

Having extracted the number of electrons, the tagging efficiency, and all other necessary quantities, the photon flux as a function of the incident photon energy E_γ can be extracted. For the A2 analysis, the tagger channels were converted to energy bins using a bin overlap method as it is described in Ref. [56]. For the CBELSA/TAPS analysis, the same bin overlap method was used to convert the energy bins of fixed width (10 MeV) to bins of desired width that were used for the extraction of the observables. This method speeds up the recalculation of the photon flux when changing to a different energy binning.

The determination of the flux as a function of the final state energy W is slightly more complex since the energy of one single tagger channel or E_γ -bin is distributed over several W -bins. The used algorithm calculates the W -distribution for each tagger channel or energy bin by sampling $n = 10^6$ W -values for each bin. Every single value was then filled into the W -dependent flux histogram with the weight from the photon flux of the current bin and the number of sampled values n . Again, the bin-overlap method was used to fill this histogram. The resulting flux histograms are shown in Fig. 8.5 for A2 and CBELSA/TAPS data.

A calculation in the participant-spectator model was used to extract the energy W . In the participant-spectator model, the energy of the spectator E_S is given by the following equation:

$$E_S = \sqrt{M_S^2 + \vec{p}_F^2}, \quad (8.33)$$

where M_S is the mass of the spectator nucleon, and \vec{p}_F is the corresponding Fermi momentum. Using Eq. 7.31 and neglecting the binding energy E_b (deuteron: $E_b = 2.2$ MeV, ${}^3\text{He}$ $E_b = 8.5$), one finds the energy E_P of the participant nucleon:

$$E_P = M_A - E_S = M_A - \sqrt{M_S^2 + |\vec{p}_F|^2}, \quad (8.34)$$

where M_A is the mass of the nucleus. Eq. 8.34 implies that the participant is off-shell ($E_P \neq \sqrt{M_P^2 + \vec{p}_P^2}$). Hence, $s = \sqrt{W}$ is given by:

$$s = (p_\gamma + p_P)^2, \quad (8.35)$$

where $p_\gamma = (E_\gamma, \vec{p}_\gamma)$ is the four-momentum of the beam photon and $p_P = (E_P, \vec{p}_F)$ is the four-momentum of the participant nucleon. Thus, it follows that:

$$s = E_\gamma^2 + 2E_\gamma E_P + E_P^2 - (\vec{p}_\gamma + \vec{p}_F)^2. \quad (8.36)$$

Inserting Eq. 8.34, the final state energy W can be deduced:

$$W = \sqrt{M_A^2 + M_S^2 + 2E_\gamma(M_A - E_S) - 2M_A E_S - 2E_\gamma p_F^z}, \quad (8.37)$$

where p_F^z is the z component of the Fermi momentum of the spectator nucleon. The absolute value of the Fermi momentum was chosen randomly according to the distri-

bution of the nucleus, i.e. ^3He [153] or deuterium [152]. The x, y and z directions were sampled isotropically.

For a nucleon at rest with mass M_N (free nucleon), the latter equation reduces to:

$$W = \sqrt{2E_\gamma M_N + M_N^2}. \quad (8.38)$$

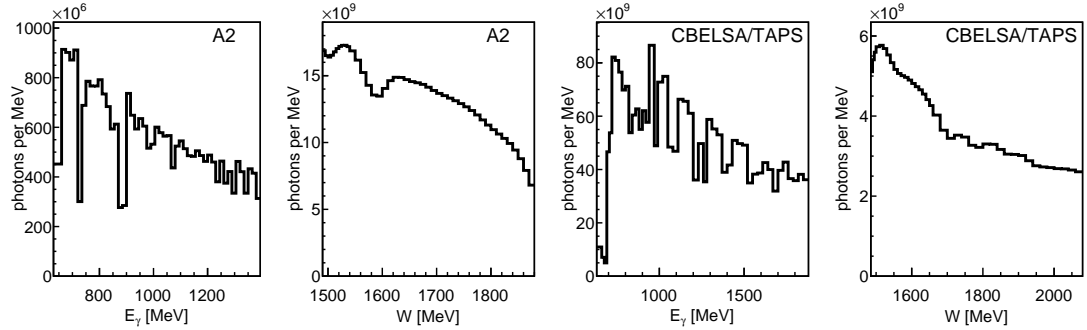


Figure 8.5: Photon flux as a function of E_γ and W for the deuteron target of the A2 and CBELSA/TAPS experiments for the proton as participant. The spikes in the E_γ fluxes are caused by malfunctioning tagger channels, as well as the dip in the W -dependent A2 flux around 1.6 GeV.

8.6.4 Helicity Dependent Photon Flux

To get a correct asymmetry, it is crucial to know the number of photons with positive and negative helicity. The helicity of the electron and thus of the photon beam was flipped with a rate of 1 Hz at MAMI and once per spill (approximately 4 seconds) at ELSA. Hence, the number of photons with positive, N_+ , and negative helicity, N_- , should be approximately half of the total photon flux. To check whether this assumption holds true, the helicity asymmetry of the incident photon beam was calculated:

$$A = \frac{N_+ - N_-}{N_+ + N_-}. \quad (8.39)$$

For this calculation, it was important to count all incident beam photons and not only the ones that were correlated with a trigger event, since the trigger could bias the event selection and induce an additional asymmetry.

Table 8.2 summarises the average helicity asymmetry values for the different dButanol beamtimes of the A2 experiment. For the CBELSA/TAPS experiment the average asymmetry was approximately $A \simeq -0.000234$. These factors were used to scale the photon fluxes of the helicity $1/2$ and $3/2$ states. However, for η photoproduction, these numbers have almost no influence, since the expected asymmetry E is large over the whole energy range.

beamtime	A
July 2013:	0.0044747
February 2015:	-0.0022007
March 2015	-0.0000320

Table 8.2: Helicity asymmetry A of the incident photon beam for the different dButanol beamtimes at the A2 experiment.

8.7 Extraction of the Yields

The yields for the calculation of the cross sections and the polarisation observable E were extracted from the invariant mass histograms shown in Fig. 7.16. The invariant mass histograms were filled as a function of the energy (incident photon energy E_γ or final state energy W) for $\cos(\theta_\eta^*)$ -bins of fixed width. The number of energy and $\cos(\theta_\eta^*)$ -bins were chosen according to the available statistics. Eight $\cos(\theta_\eta^*)$ -bins were chosen for the CBELSA/TAPS deuterium data, whereas only one $\cos(\theta_\eta^*)$ bin was used for the dButanol data since the statistics was very limited. For the A2 dButanol data, five $\cos(\theta_\eta^*)$ -bins were used and for the unpolarised ^3He ten bins were used.

The cuts described in Sec. 7.4 were able to reject the background from contaminating channels nearly completely. This can be seen in Fig. 7.16, where the experimental data for the deuterium and dButanol target are compared to the simulated signal. The corresponding spectra for ^3He can be found in Ref. [129]. Hence, no additional background subtraction was necessary in the invariant mass spectra and the yields were extracted by integrating the invariant mass spectra in the range of the invariant mass cut, which is given in Eqs. 7.27 and 7.28.

8.8 Detection Efficiency

As mentioned in Secs. 4.1.2 and 4.2.2, the Geant software packages A2 and CBGEANT were used to simulate the detection efficiency correction for the total normalisation of the cross sections and polarisation observable E . The reactions were generated using the Pluto event generator (see Sec. 4.1.3). For both the LD_2 and the dButanol target, the events were generated for nucleons bound in deuterium, i.e. with a momentum distribution according to the Fermi momentum distribution of deuterium. For the ^3He target, the Fermi momentum distribution of ^3He was used. To model the energy loss inside the target, the target container in the Geant simulation was filled with corresponding target material (deuterium, ^3He , or dButanol). Furthermore, as explained in Secs. 4.1.2 and 4.2.2, the MC simulation contained the whole detector setup of the corresponding experiment.

The reaction vertex was chosen randomly inside the whole target volume; the beam spot had a diameter of 1.3 cm for the LD_2 and ^3He of the experiment for the A2 setup and 0.8 cm for the CBELSA/TAPS setup. As mentioned in Sec. 7.2.1, the energy obtained from the simulation was smeared to reproduce the resolution expected from

the experimental data. To be consistent with the experimental data, the same detector and trigger thresholds were used in the simulation. In addition, the same malfunctioning detector elements were rejected from the event selection in experimental data and simulation.

The output of the simulation was analysed with the same analysis which was used for the experimental data. The simulated events were weighted with an inverse E_γ dependence to account for the experimental bremsstrahlung distribution and an additional event weight was taken from angular distribution from former measurements. Data from the SAID database [41, 44] were used to weight the events for η photoproduction on the proton and former results by Werthmüller [56] were used for the reaction on the neutron.

The detection efficiency was determined separately for each reaction channel given in Table 7.1 by dividing the number of detected events N_{det} by the generated events N_{gen} :

$$\epsilon(E, \cos \theta_\eta^*) = \frac{N_{det}(E_{det}, \cos(\theta_{\eta,det}^*))}{N_{gen}(E_{gen}, \cos(\theta_{\eta,gen}^*))}. \quad (8.40)$$

Eq. 8.40 yields an effective efficiency and the corresponding values may be larger than unity since the detected energy E_{det} and $\cos \theta_{\eta,det}^*$ are not necessarily equal to the generated values E_{gen} and $\cos \theta_{\eta,gen}^*$. Especially at low energies close to threshold, resolution effects were found to play an important role [56].

8.8.1 Nucleon Detection Efficiency Correction

Despite an accurate implementation of materials and interaction models, tests have shown that a convincing detection efficiency correction for nucleons was only achieved by applying corrections to the simulation, which were obtained with experimental hydrogen data. For the A2 data, the experiment from April 2009 and for the CBELSA/TAPS data, the November 2008 beamtime was used to determine a relative nucleon detection efficiency correction. With such a nucleon detection efficiency, inefficiencies of the charge sensitive detectors (PID and Veto) or deviations in the geometry of the detector setup from simulation experiment are corrected. To avoid effects coming from the different detector thresholds of the experiments, the software thresholds were set to a common maximum value of all beamtimes for the TAPS CFD, Veto LED, and PID thresholds. The following reaction were analysed to extract the nucleon efficiency correction:



The choice of the first reaction is apparent, since it exhibits similar systematic uncertainties as the η photoproduction on the quasi-free proton. However, for the neutron case, the selection of a suitable reaction is not as simple. The most straightforward choice, the $\gamma p \rightarrow \pi^+ n$ channel could not be used for the A2 data, since the hydrogen data was taken with an M3+ trigger, and this reaction has only two particles in the

final state. In addition, the cross section is quite small, and the background contribution from misidentified protons is not trivial. Furthermore, this channel has no photon in the final state, which deteriorates the random background subtraction in the tagger due to a worse time resolution. Hence, the reaction given in Eq. 8.42 was taken to extract the nucleon detection efficiency correction for the neutron.

The reactions were identified with stringent cuts on the coplanarity angle and the missing mass ($\pm 1.5\sigma$) to ensure a good background rejection. For the reaction on the neutron, TOF versus energy cuts were applied to identify the charged pion in TAPS/MiniTAPS. To reject proton contamination in the A2 data, the energy in the PID of the charged pion candidate was required to be less than 2.5 MeV (see in Fig. 7.20). Since the inner detector of the CBELSA/TAPS experiment does not provide energy information, the identification of the charged pion in the CBB remains unclear. This is the reason why it was decided to not apply the neutron detection efficiency correction for the CBELSA/TAPS data.

For both experimental and simulated data, the nucleon detection efficiency was determined by building the ratio between the events where the nucleon was registered and all events:

$$\epsilon_p(T_p, \theta_p) = \frac{N(\gamma p \rightarrow p\eta)}{N(\gamma p \rightarrow p\eta) + N(\gamma p \rightarrow \eta X)}, \quad (8.43)$$

and

$$\epsilon_n(T_n, \theta_n) = \frac{N(\gamma p \rightarrow \pi^+ \pi^0 n)}{N(\gamma p \rightarrow \pi^+ \pi^0 n) + N(\gamma p \rightarrow \pi^+ \pi^0 X)}. \quad (8.44)$$

The kinetic energy T_N and the polar angle θ_N of the nucleon in the lab frame were calculated from kinematics as described in Sec. 7.5.4.

Subsequently, a correction for the efficiency determined from simulation was calculated:

$$f^{corr} = \frac{\epsilon_N^{MC}(T_N, \theta_N)}{\epsilon_N^{data}(T_N, \theta_N)}, \quad (8.45)$$

where ϵ_N^{MC} is the nucleon efficiency determined from simulation and ϵ_N^{data} is the nucleon detection efficiency, which was extracted from experimental data.

The correction factors obtained for the proton and the neutron are shown in Fig. 8.6. Especially at low kinetic energies and smaller angles (TAPS/MiniTAPS), the correction factors deviate significantly from unity. Values larger than one mean that the efficiencies in the simulation are overestimated, values smaller than one are correlated with an underestimation of the efficiency. Entries are also visible for $\theta_N < 5^\circ$, where no detector is mounted, since the polar angle was reconstructed.

For the proton in the A2 data, the largest inconsistency between data and simulation comes from the angular range in which the nucleon goes in the forward direction, i.e. in TAPS ($\theta_N < 20^\circ$) or the forward part of the CB ($\theta_N < 25^\circ$). It was shown [56] that the simulation of the proton efficiency is extremely sensitive to the material and geometry of this tunnel region of the CB and the transition from the CB to TAPS ($15^\circ < \theta_N < 25^\circ$). In this region, the proton efficiency from simulation is overesti-

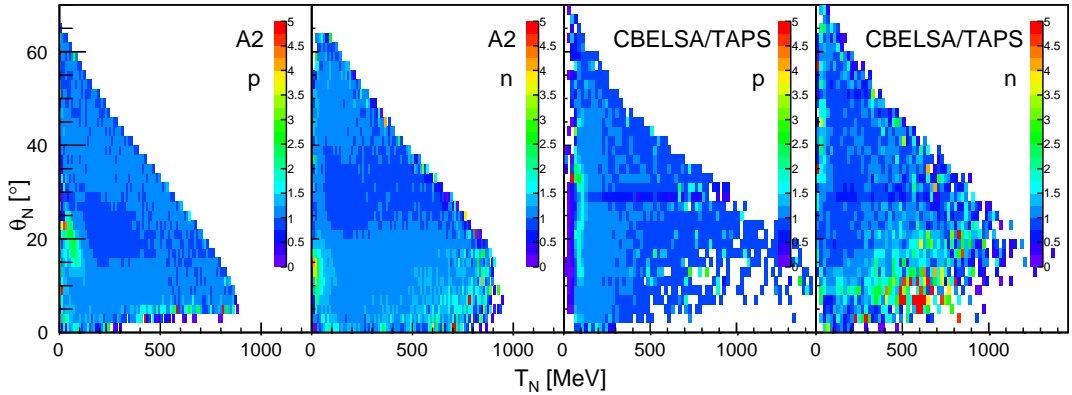


Figure 8.6: Nucleon detection efficiency correction f^{corr} as a function of the kinetic energy T_N and the reconstructed polar angle θ_N of the recoil nucleon in the lab frame. The neutron detection efficiency for the CBELSA/TAPS data was not applied due to unknown contamination of protons in CBB.

mated for low kinetic energies. For the neutron, the angular region where the neutron is detected in TAPS is more critical since the signal shapes of photons and neutrons differ stronger in BaF_2 crystals than in $\text{NaI}(\text{Tl})$ crystals. This leads to a different response of the applied thresholds for neutrons and photons and an overestimation of the neutron efficiency from simulation for low energetic neutrons.

For the proton in the CBELSA/TAPS data, the FP ($12^\circ < \theta_N < 30^\circ$) and the transition from the CBB to the FP around $\theta_N \sim 30^\circ$ seems to be most critical. In that angular region, the proton efficiency from simulation is overestimated for low energetic protons. This may be caused by geometrical inconsistencies between data and simulation, since in that region the nucleons have to pass through many of different materials. A part of the problem may also originate from the fact that no exact thresholds for the Inner Detector and the FP vetoes could be determined since neither of them provides energy information. The detection efficiency correction was also determined for the neutron in the CBELSA/TAPS data and is shown in the fourth figure of Fig. 8.6. However, as mentioned, the neutron efficiency correction was not applied due to a insufficient identification of charged pions.

The nucleon detection efficiency correction was evaluated at the angle θ_N and the kinetic energy T_N , which have been determined by kinematical reconstruction. When no correction factor was available for the current θ_N and T_N values, the factor from the closest filled bin was taken (with a maximum distance of two bins), otherwise the value was set to unity.

The influence of the nucleon detection efficiency correction for the quasi-free proton data from the CBELSA/TAPS experiment can be seen in Fig. 8.7. The most drastic improvements could be achieved in the region of the $S_{11}(1535)$, whereas the contribution is negligible for energies above $W = 1.6$ GeV. After the correction, the obtained cross section is in good agreement with former results on the free proton target by McNicoll *et al.* [110] in most parts of the energy range. However, in the top of the

$S_{11}(1535)$ small deviations persist, which are coming from the most forward and the second $\cos(\theta_\eta^*)$ bin in the differential cross section, as shown in the right part of Fig. 8.7. This indicates that the nucleon detection efficiency correction is not perfect for these points. Corresponding spectra for the A2 deuterium data can be found in Ref. [56].

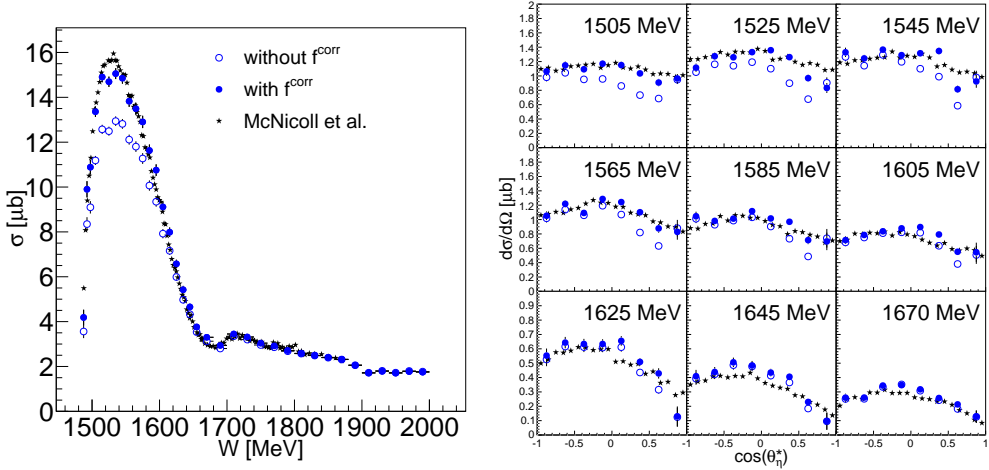


Figure 8.7: Total and differential cross section for $\gamma p \rightarrow \eta p$ on the deuterium target with (solid blue points) and without (open blue points) nucleon detection efficiency correction for the CBELSA/TAPS data. The results are compared to former MAMI-C data by McNicoll *et al.* on the free proton target [110].

8.8.2 Software Trigger

To get correct detection efficiencies, it is crucial to apply the conditions of the experimental trigger to the simulated events. The used triggers have already been explained in Sec. 2.5. The software trigger was implemented in a way that only the decay photons from the η meson could contribute to the trigger decision, the nucleon was not considered. The idea behind this implementation is that the protons and neutrons have a very different detector response, which can lead to different trigger decisions and thus induce systematic effects. Hence, this software trigger allows for the comparison of proton and neutron cross sections.

The multiplicity trigger was modelled in the same way as the decision was done in the hardware. The crystals of the CB, TAPS and MiniTAPS were assigned to logical units with a corresponding threshold. For the CBB and the FP, the number of clusters were counted as it was done online by FACE, see Sec. 2.5.2. To reduce electromagnetic background, the inner two rings of TAPS/MiniTAPS were not allowed to contribute to the trigger decision.

The CB energy sum trigger for the A2 experiment required a more precise implementation. As mentioned in Sec. 2.5, the experimental trigger checked the analogue sum of all NaI(Tl) crystals, which had to be above a certain threshold. In the software trigger, the analogue sum was realised by first de-calibrating the energy of each crystal of the experimental and simulated data with the help of an average conversion

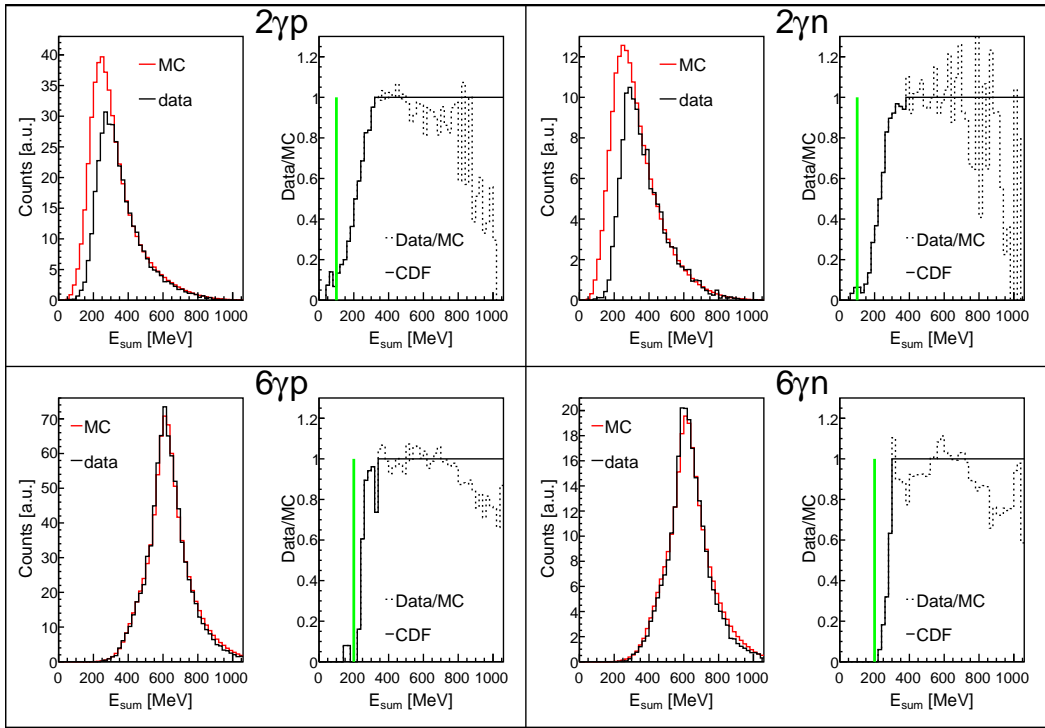


Figure 8.8: CB energy sum (left side) for the different event classes of experimental data (black) and simulation (red) for the July 2013 beamtime. The data were normalised to the simulation between 400–700 MeV for the $\eta \rightarrow 2\gamma$ decay and 600–900 MeV for the $\eta \rightarrow 6\gamma$. The ratio of data and simulation (dashed histogram) is shown on the right together with the determined CDF (solid line). To reduce statistical fluctuations at low energies, a lower threshold of 100 MeV for $\eta \rightarrow 2\gamma$ and 200 MeV $\eta \rightarrow 6\gamma$ (green line) was applied.

gain and then summing up the energies of the decay photons in the CB. The energy sum was calculated for the data and the simulation. Since the energy sum depends on the energy and angular distribution of the η meson, the corresponding distributions are slightly dependent on the reaction channel. Fig. 8.8 shows the corresponding CB energy sum distributions for the July 2013 beamtime (dButanol), the distributions for the ${}^3\text{He}$ data can be found in Ref. [129], and the distributions for the deuterium data are shown in Ref. [56]. The histogram from experimental data (black) was normalised to the simulation (red) in the descending slope and the ratio of both was calculated (dashed line, right picture). For the experimental data, events with a low energy sum are clearly suppressed compared to the simulated events for the $\eta \rightarrow 2\gamma$ decay due to the hardware trigger. As expected, the energy sum trigger had basically no influence on the $\eta \rightarrow 6\gamma$ events, since the hardware trigger was always fulfilled due to the six photons final state.

To account for fluctuations in the tail of the distribution, the ratio of the experimental and simulated data was set to one after it first crosses unity. The corresponding function is referred to as cumulative distribution function (CDF) and is shown as the solid line in Fig. 8.8. In addition, a lower threshold of 100 MeV ($\eta \rightarrow 2\gamma$) or 200 MeV

$(\eta \rightarrow 6\gamma)$ was set to reduce the scattering at low CB energy sums. The energy sum trigger was applied to the simulation by sampling a weighting factor f_{MC} according to the CDF.

8.8.3 Summary of Efficiencies

Having applied all cuts, the nucleon detection efficiency correction, and the software trigger, the detection efficiency was determined as given in Eq. 8.40. The same variable energy bins and number of $\cos(\theta_\eta^*)$ bins as for the extraction of the yields were used: five $\cos(\theta_\eta^*)$ bins were used for the polarised (dButanol) A2 efficiencies and eight $\cos(\theta_\eta^*)$ bins were used for the unpolarised (LD_2) CBELSA/TAPS efficiencies. For the polarised (dButanol) CBELSA/TAPS data total (angle independent) efficiencies were determined to have the same binning as in the experimental data. To check whether the efficiency correction is enough accurate in that case, the unpolarised cross sections were also determined by applying total efficiency and were compared to the standard binning. The results were in agreement, demonstrating that the an angular correction was not necessary. The efficiencies for the 3He target are not shown here, but can be found in Ref. [129].

To get a more clear comparison, Figs. 8.9 and 8.10 show detection efficiencies, which were integrated over the full angular range. Efficiencies on the LD_2 target are shown as closed circles, open circles indicate the efficiencies on the dButanol target. The same software thresholds and cuts were applied to the analysis of both targets (LD_2 and dButanol) to be able to compare the efficiencies. The efficiencies for the LD_2 target are a factor ~ 1.4 to ~ 1.6 larger than the efficiencies for the dButanol target. This difference mainly comes from the conversion and loss of photons, protons, and

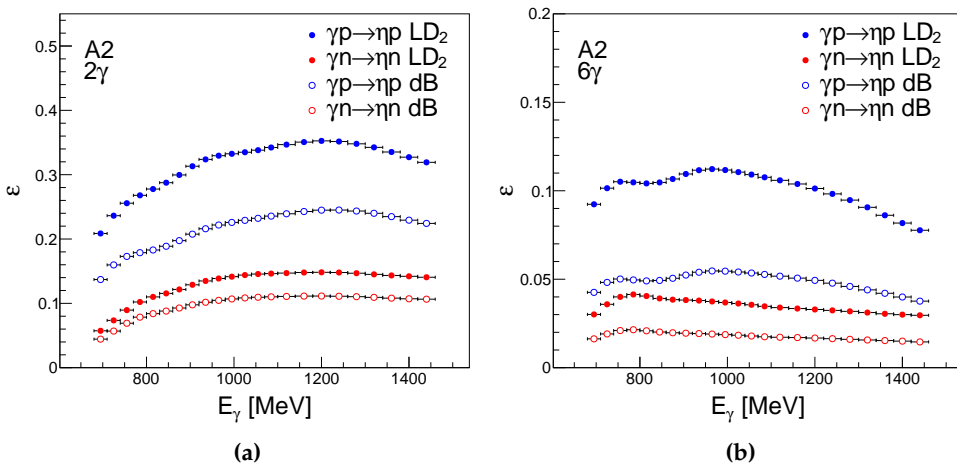


Figure 8.9: Detection efficiencies for the A2 experiment for the LD_2 target (closed symbols) and the dButanol target (open symbols). (a) shows the efficiencies for the $\eta \rightarrow 2\gamma$ decay channel and (b) for the $\eta \rightarrow 6\gamma$ decay channel as a function of the incident photon energy E_γ .

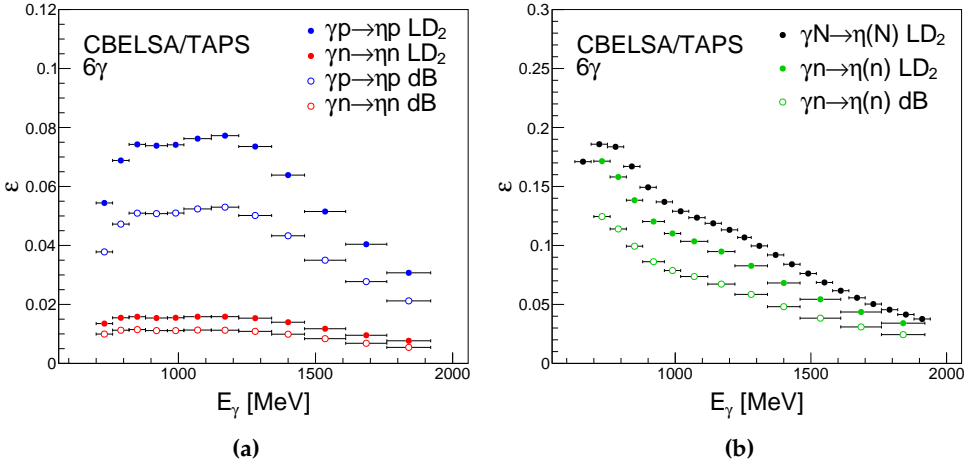


Figure 8.10: Detection efficiencies as a function of the incident photon energy E_γ for the CBELSA/TAPS experiment. The efficiencies for the LD₂ target are shown as closed symbols and the efficiencies for the dButanol target as open symbols. (a) shows the efficiencies for the exclusive channels and (b) shows the efficiencies for the quasi-free inclusive ($\gamma N \rightarrow \eta(N)$) and the inclusive neutron channel ($\gamma n \rightarrow \eta(n)$).

neutrons inside the dButanol target, which has a high density and contains material with high atomic number Z . In addition to the efficiencies for the exclusive reactions, Fig. 8.10 shows efficiencies for the inclusive reactions, which were only examined in the CBELSA/TAPS data.

In general, the efficiencies rise from threshold to a near constant value between 900 and 1400 MeV. The efficiencies for the CBELSA/TAPS setup decrease for energies above 1400 MeV. This is most likely caused by the experimental trigger, which is not a 4π trigger as in the A2 experiment, but strongly forward directed (three or four clusters in FP and MiniTAPS). At higher energies, more photons go in the backward direction and hence such events do not always fire the experimental trigger.

The efficiencies for the $\eta \rightarrow 6\gamma$ decay are smaller than for the $\eta \rightarrow 2\gamma$ reaction. The detection efficiency of a photon is approximately 98%, thus inducing only a decrease of $\sim 7.5\%$ in total efficiency for $\eta \rightarrow 6\gamma$ compared to $\eta \rightarrow 2\gamma$. The remaining part can be explained by combinatorics and increased cluster overlap for higher multiplicities.

The corresponding angular efficiencies in the cm system of the incident photon and the nucleon are shown in Appendix C. The angular efficiencies in the cm system of the final state nucleon and the η meson are shown in Fig. 8.11 for the A2 LD₂ target, in Fig. 8.12 for the A2 dButanol target, and in Fig. 8.13 for the CBELSA/TAPS LD₂ target. A strong decrease in the efficiency is visible when the η meson goes in the forward direction in the cm system. This corresponds to nucleons with small kinetic energies. Hence, the nucleons do not deposit enough energy in the detectors to be registered.

As mentioned before, only total efficiencies were determined for the CBELSA/TAPS dButanol beamtimes. The corresponding efficiencies as a function of the final state en-

ergy W are shown in Fig. 8.14.

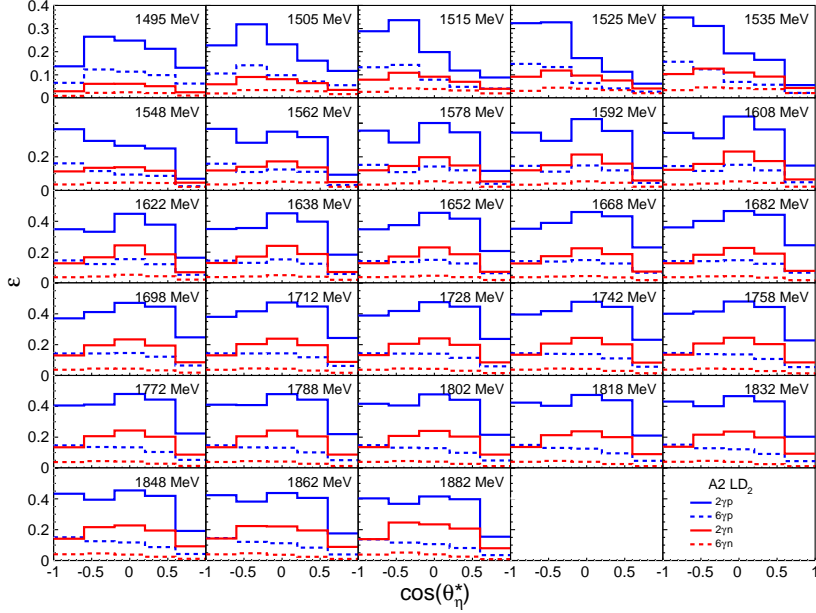


Figure 8.11: Angular detection efficiency as a function of the final state energy W for the A2 LD₂ target. The distributions are shown for both decay channels, $\eta \rightarrow 2\gamma$ (solid lines) and $\eta \rightarrow 6\gamma$ (dashed lines), and for the proton (blue) and the neutron (red). Five $\cos(\theta_\eta^*)$ bins and a variable energy binning (mean energy indicated) were used.

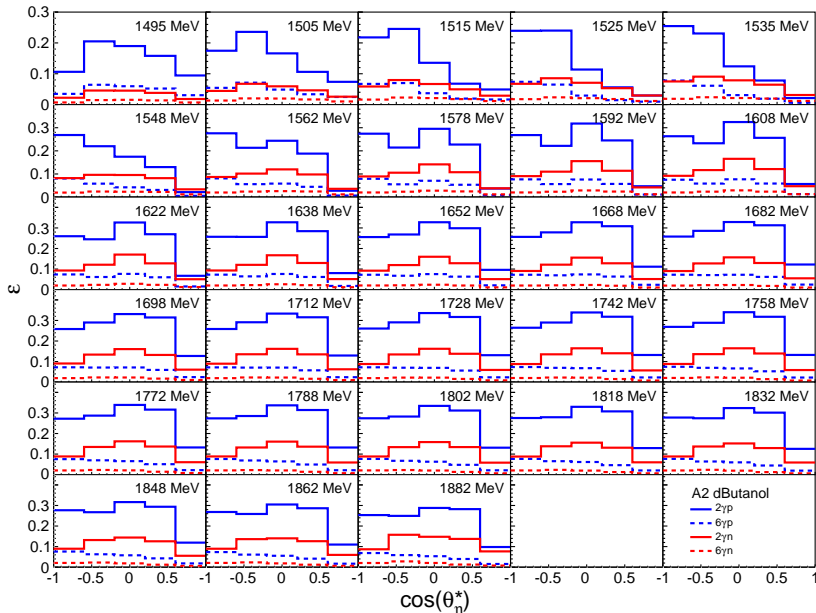


Figure 8.12: Angular detection efficiency as a function of the final state energy W for the A2 dButanol target. The distributions are shown for both decay channels, $\eta \rightarrow 2\gamma$ (solid lines) and $\eta \rightarrow 6\gamma$ (dashed lines), and for the proton (blue) and the neutron (red). Five $\cos(\theta_\eta^*)$ bins and a variable energy binning (mean energy indicated) were used.

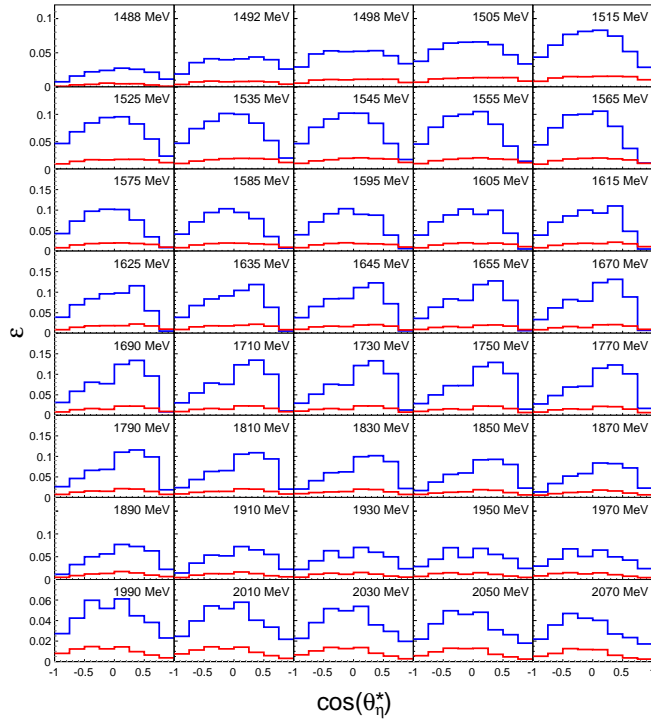


Figure 8.13: Angular detection efficiency as a function of the final state energy W for the CBELSA/TAPS LD_2 target. The distributions are shown for the proton (blue) and the neutron (red) ($\eta \rightarrow 6\gamma$). Eight $\cos(\theta_\eta^*)$ bins and a variable energy binning (mean energy indicated) were used.

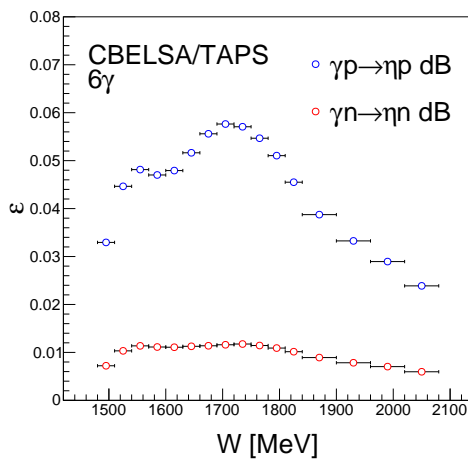


Figure 8.14: Detection efficiency for $\gamma p \rightarrow \eta p$ (blue) and $\gamma n \rightarrow \eta n$ (red) for the CBELSA/TAPS dButanol target. The distributions are shown as a function of the cm energy W for the $\eta \rightarrow 6\gamma$ decay. Only one $\cos(\theta_\eta^*)$ was used.

8.9 Empty Target Subtraction

For the determination of cross sections, it is crucial to subtract the events that were generated on the nuclei of the target container (mainly carbon nuclei) and not inside the target material (LD_2 , ${}^3\text{He}$). Usually one measures this contribution in dedicated runs using an empty target container. Such measurements were done for the A2 deuterium and ${}^3\text{He}$ experiments, as explained in Ref. [56] and Ref. [129]. Unfortunately, such a measurement was not available for the CBELSA/TAPS deuterium beamtime. However, the carbon background measurement for the dButanol experiment could be used to estimate the empty target contribution. The cross section on the carbon target was simply scaled to the number of carbon nuclei inside the target windows of the deuterium target. According to Table 8.1, the number of carbon nuclei inside the carbon target is $n_T^C \simeq 0.047130 \text{ b}^{-1}$. The two windows of the target cell were made of Kapton, which has the chemical formula $\text{C}_{22}\text{H}_{10}\text{N}_2\text{O}_5$ and hence a molar mass of:

$$M_K = 22 \cdot M_C + 10 \cdot M_H + 2 \cdot M_N + 5 \cdot M_O = 382.33 \text{ g/mol}, \quad (8.46)$$

where the following molecular masses were used [174]:

$$M_C = 12.011 \text{ g/mol} \quad (8.47)$$

$$M_H = 1.008 \text{ g/mol} \quad (8.48)$$

$$M_N = 14.0067 \text{ g/mol} \quad (8.49)$$

$$M_O = 15.999 \text{ g/mol}. \quad (8.50)$$

With the density of Kapton, $\rho = 1.42 \text{ g/cm}^3$, and the window thickness $d = 0.0125 \text{ cm}$, the number of Kapton molecules dK per barn can be calculated:

$$dK = \frac{2 \cdot d \cdot \rho \cdot N_A}{M_K} = 0.0000559 \text{ b}^{-1}. \quad (8.51)$$

Treating the hydrogen nuclei inside Kapton like deuterons, the number of carbon nuclei dC can be estimated:

$$dC = 22 + 2(M_N/M_C)^{2/3} + 5(M_O/M_C)^{2/3} = 30.27, \quad (8.52)$$

where it was assumed that the η photoproduction cross section scales like $A^{2/3}$, i.e. with the nuclear surface of the nuclei, as it was seen in previous results [109]. This leads to the number of carbon nuclei inside the target windows:

$$n_W = dK \cdot dC = 0.00163 \text{ b}^{-1}. \quad (8.53)$$

Since the carbon target has the same target window thickness as the deuterium target, the scaling factor to scale the cross section to the carbon target with target surface

density n_C to the windows with n_W is given by:

$$f_{WC} = \frac{n_W}{n_W + n_C} = 0.033440. \quad (8.54)$$

The resulting relative empty target contribution percentage to the total cross section is shown in Fig. 8.15. This ratio was used to scale down the energy and angle dependent yields.

For the determination of the polarisation observable E and the helicity dependent cross section, the empty target contribution did not need a separate subtraction, since its contribution is already contained in the carbon subtraction method explained in Sec. 8.10.

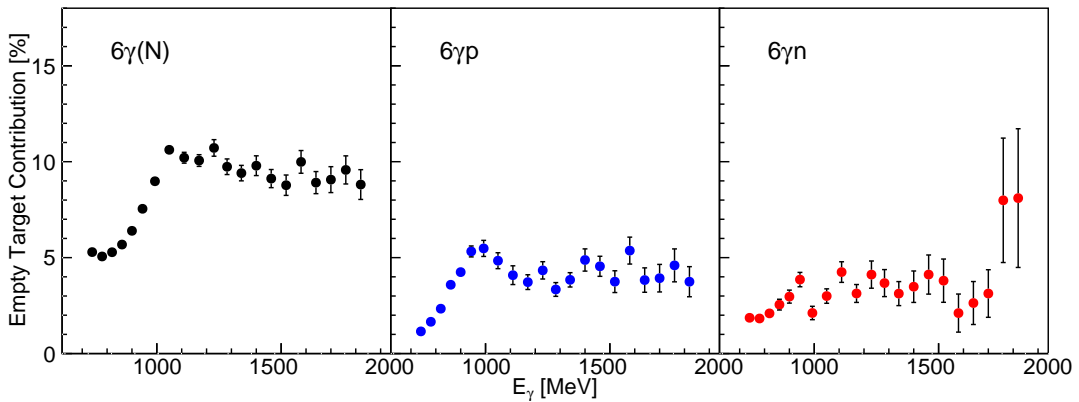


Figure 8.15: Empty target contribution for the quasi-free inclusive (left), the exclusive proton (middle), and exclusive neutron (right) cross section for the LD₂ target of the CBELSA/TAPS setup.

8.10 Carbon Subtraction

As illustrated in Fig. 8.16, the dButanol molecule has the chemical formula C₄D₉OD. It was previously mentioned that only the deuterium nuclei in the dButanol molecule are polarised, the spinless carbon and oxygen nuclei are unpolarised and thus dilute the polarised deuterons. In Sec. 8.2, it was shown that the carbon contribution cancels out in the difference of the two helicity states, whereas it has to be subtracted from the

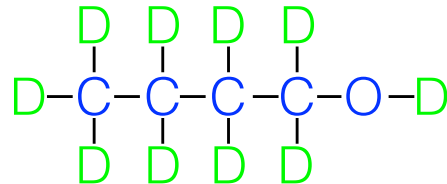


Figure 8.16: The structural formula for the dButanol molecule. The polarised deuterons are labelled as green D, the unpolarised carbon and oxygen nuclei are indicated in blue.

sum, as shown in the following equation:

$$E = \frac{1}{p_\gamma p_T} \cdot \frac{(N_{1/2} - N_{3/2}) N_\gamma^{dB}/2}{(N_{1/2} + N_{3/2} + N^0) / N_\gamma^{dB}/2 - D \cdot (N^C / N_\gamma^C)/2}, \quad (8.55)$$

where $N_{1/2}$ and $N_{3/2}$ are the yields for the two helicity states, $N_\gamma^{dB}/2$ is the corresponding photon flux, N^C are the yields on the carbon target, $N_\gamma^C/2$ is the corresponding photon flux, and D is the dilution factor.

An ideally suited method to check the carbon contamination is to look at the missing mass spectra. There, the contribution from the different nuclei are well separated due to the different Fermi momentum distributions. The missing mass spectra for the sum and the difference of the two helicity states are shown in Fig. 8.17. The first and third column shows the sums of the counts. In these figures, the broadening due to the Fermi motion of carbon is clearly visible. On the contrary, the difference of the two helicity states (second and fourth column) show no signs of carbon and are in agreement with the simulated signals (black lines).

To subtract the unpolarised carbon, it is necessary to know its contribution to the whole target, i.e. the dilution factor. The dilution of carbon and oxygen nuclei inside dButanol can be directly found by a simple calculation of the numbers of nucleons. According to Eq. 8.21, one can find the number of dButanol molecules, K_{dB} , inside the

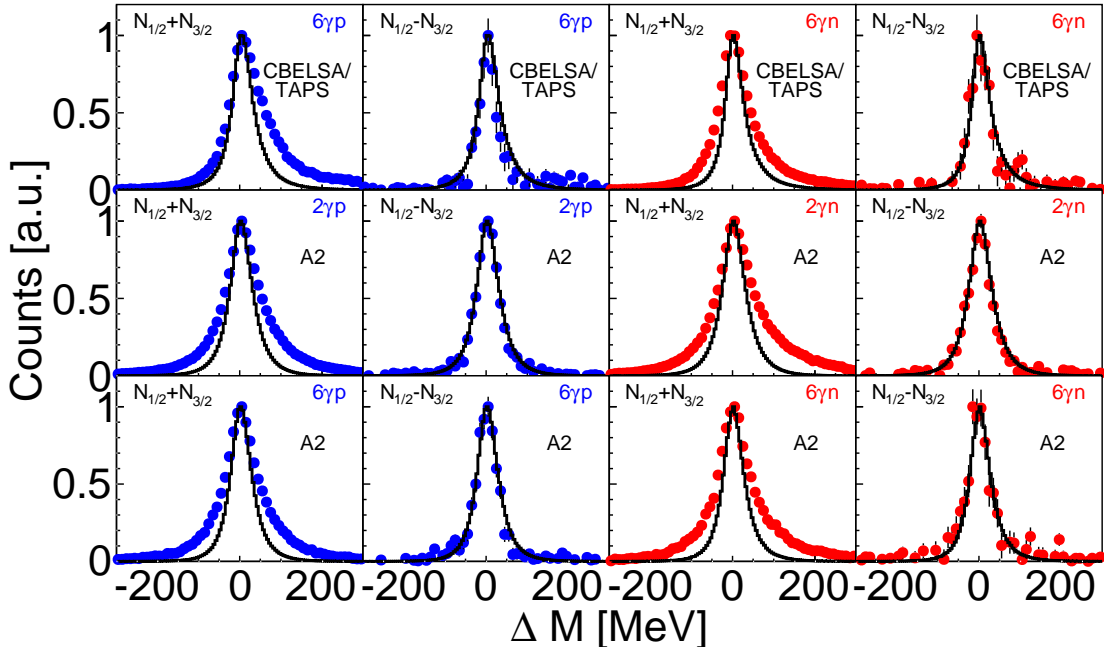


Figure 8.17: Missing mass ΔM for dButanol for the difference, $N_{1/2} - N_{3/2}$, and the sum, $N_{1/2} + N_{3/2}$, of the two helicity states for the reaction on the proton (blue) and the neutron (red). First row: $\eta \rightarrow 6\gamma$ reaction for CBELSA/TAPS data. Second row: $\eta \rightarrow 2\gamma$ reaction for A2 data. Third row: $\eta \rightarrow 6\gamma$ for A2 data. The line shape of the simulation is shown as black line. The influence of the carbon is clearly visible in the sum, whereas for the difference, the simulation and the experimental data are in agreement.

target:

$$K_{dB} = \frac{\rho_{dB} \cdot f \cdot L_{dB} \cdot N_A}{M_{mol}^{dB}}, \quad (8.56)$$

where ρ_{dB} is the density of dButanol, f is the filling factor, L_{dB} is the length of the dButanol target, N_A is the Avogadro constant, and M_{mol}^{dB} is the molar mass of dButanol. The corresponding values can be found in Table 8.1. Hence, the number of deuterons in the dButanol target n_T^{dB} can be deduced:

$$n_T^{dB} = 10 \cdot K_{dB}, \quad (8.57)$$

where the factor 10 comes from the fact that each dButanol molecule contains 10 deuterons. Assuming that the cross section scales with $A^{2/3}$ [109], the number of carbon and oxygen nuclei K_{CO} in one dButanol molecule is given by the following expression:

$$K_{CO} = 4 + (M_O/M_C)^{2/3}, \quad (8.58)$$

where M_O and M_C are the molar masses of oxygen and carbon, respectively. Thus, the number of carbon and oxygen nuclei n_{CO} inside the dButanol target can be found:

$$n_{CO} = K_{dB} \cdot K_{CO}. \quad (8.59)$$

In addition, one has to account for the ^3He - ^4He mixture inside the target, which surrounded the dButanol beads to cool down the target. The helium has a density of $\rho_{He} = 0.14 \text{ g/cm}^3$, thus, the number of helium nuclei n_{He} inside the target is given by the following equation:

$$n_{He} = K_{He} \frac{\rho_{He} \cdot [(1-f)L_{dB} + L_{end}] \cdot N_A}{M_{mol}^{He}}, \quad (8.60)$$

where L_{end} is the size of the end caps of the targets and helium can be approximated by carbon with $K_{He} = (M_{He}/M_C)^{2/3}$.

As mentioned before, to get the line-shape of the carbon contribution, dedicated carbon background measurements were taken. For this purpose, the carbon foam target, described in Sec. 2.3.4, was used, which had an almost equal target surface density as the one given in Eq. 8.59.

The yields from the deuterium N_D and dButanol target N_{dB} were scaled to the corresponding photon flux N_γ , the efficiency ϵ , the number of deuterons n_T inside the target, and the branching ratio Γ_i/Γ :

$$\sigma_D = \frac{N_D}{n_T^D \epsilon_D N_\gamma^D \Gamma_i / \Gamma} \quad (8.61)$$

and

$$\sigma_{dB} = \frac{N_{dB}}{n_T^{dB} \epsilon_{dB} N_\gamma^{dB} \Gamma_i / \Gamma}. \quad (8.62)$$

The normalisation of the carbon data of the A2 and CBELSA/TAPS experiment was slightly different. In the case of the CBELSA/TAPS data, the helium mixture was inside both targets, carbon and dButanol, whereas for the A2 experiment, the helium was not inside the carbon target, as mentioned in Sec. 2.3.4. Thus the following cross sections can be derived:

$$\sigma_C^{CBELSA/TAPS} = \frac{N_C}{(n_T^C + n_{He})\epsilon_{dB}N_\gamma^C\Gamma_i/\Gamma} \cdot \frac{n_{CO} + n_{He}}{n_T^{dB}} \quad (8.63)$$

and

$$\sigma_C^{A2} = \frac{N_C}{n_T^C\epsilon_{dB}N_\gamma^C\Gamma_i/\Gamma} \cdot \frac{n_{CO} + n_{He}}{n_T^{dB}}, \quad (8.64)$$

where n_T^C is the target surface density of the carbon target as given in Table 8.1, N_C are the yields on the carbon target, and N_γ^C is the corresponding flux.

Having properly normalised the data, the spectra obtained on the deuterium target and the carbon target should add up to the line shape measured with the dButanol target. The missing mass spectra for the A2 experiment are shown in Fig. 8.18 and 8.19 for $\eta \rightarrow 2\gamma$ and $\eta \rightarrow 6\gamma$, respectively. The contribution from the carbon target is shown in blue and the contribution from the deuterium is shown in green. These two spectra add up to the red histograms, which are more or less in agreement with the spectra from the A2 dButanol target (black dots). For $\eta \rightarrow 2\gamma$, shown in Fig. 8.18, above 1 GeV incident photon energy, additional background occurs at positive missing mass values in the spectra on the dButanol target (black dots). This background cannot be reproduced by the sum of carbon and deuterium (red). A possible explanation for this behaviour may originate in the fact that the A2 carbon target was not operated at identical conditions as the dButanol target. As mentioned in Sec. 2.3.4, the carbon target was not cooled down with ^3He - ^4He and the magnetic field was not switched on. Hence, the additional background may originate from events on the helium nuclei, which have a different Fermi momentum distribution or from charged particle background due to the magnetic field. Due to the bad statistics, it is hard to tell whether the same problem is present in the $\eta \rightarrow 6\gamma$ spectra in Fig. 8.19. For the reactions on the proton, seen in Figs. 8.18 (a) and 8.19 (a), one can see an additional inconsistency in the energy range up to 850 MeV, where the sum of the carbon and deuterium contribution is slightly higher than the measured dButanol distribution. As it will be explained in Sec. 9.4.1, this issue can be assigned to an imperfect nucleon detection efficiency for the frozen spin target. However, for energies above 850 MeV, the agreement between the dButanol spectrum and the sum of deuterium and carbon is good within the missing mass cut positions (black vertical lines).

The corresponding missing mass spectra for the CBELSA/TAPS data are shown in Fig. 8.20. The measured dButanol distributions (black points) and the sum of the deuterium and carbon contributions (red) are in almost perfect agreement, demonstrating that the contribution of the carbon in dButanol is well understood. However, as explained in Sec. 8.6.2 it was necessary to scale the photon flux of the dButanol and carbon beamtime by a factor of 1.6 due to an issue with the tagger scalers.

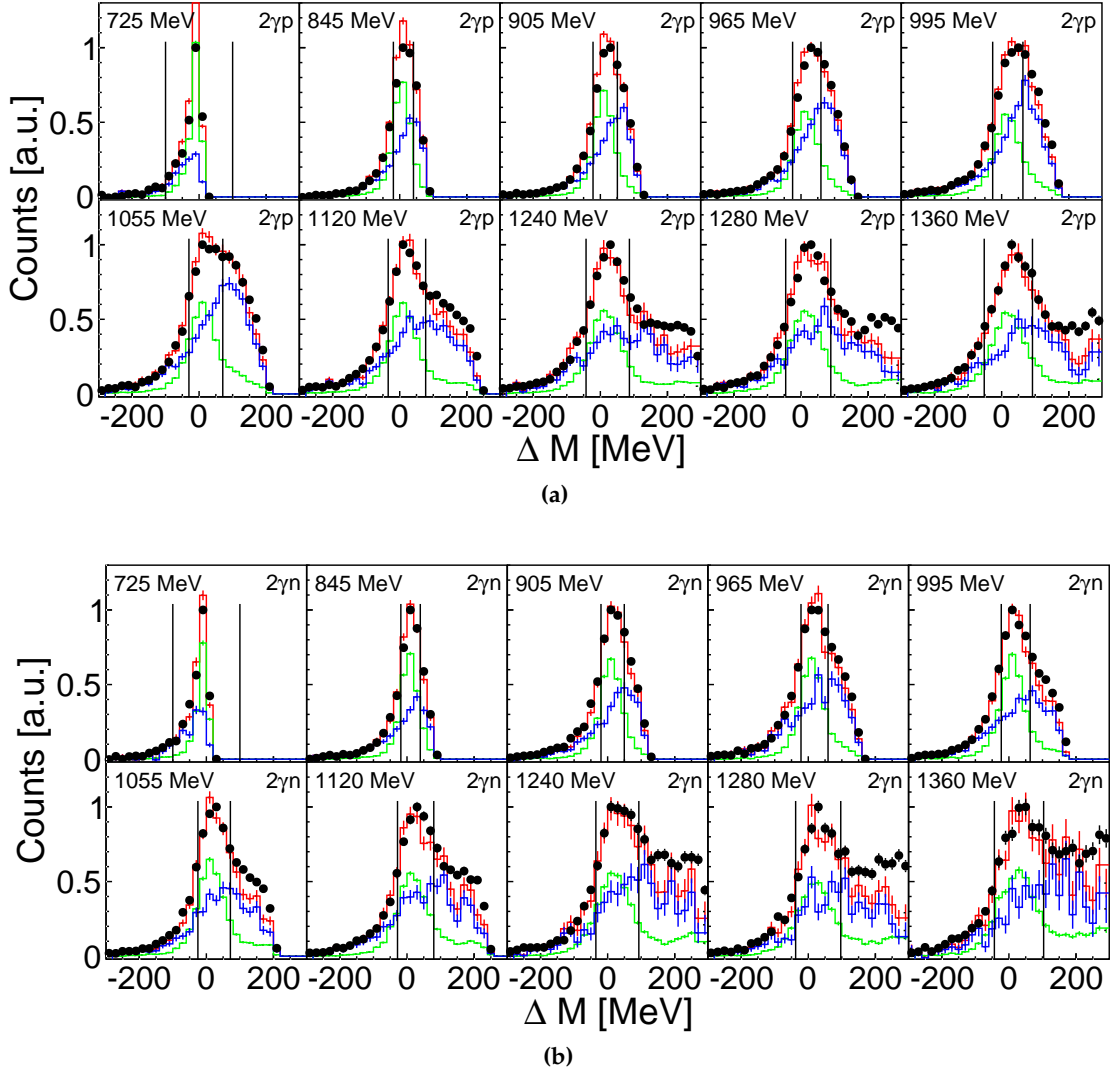


Figure 8.18: Missing mass spectra for the $\eta \rightarrow 2\gamma$ decay for the proton (a) and for the neutron (b) reaction for A2 data: the contribution from the deuterium target is shown in green, the contribution from the carbon target in blue, and the dButanol distribution is shown as black dots. The sum of the deuterium and the carbon is shown in red. The counts were normalised as described in the text. A variable energy binning was used (mean value indicated) and only a selection of bins is shown here.

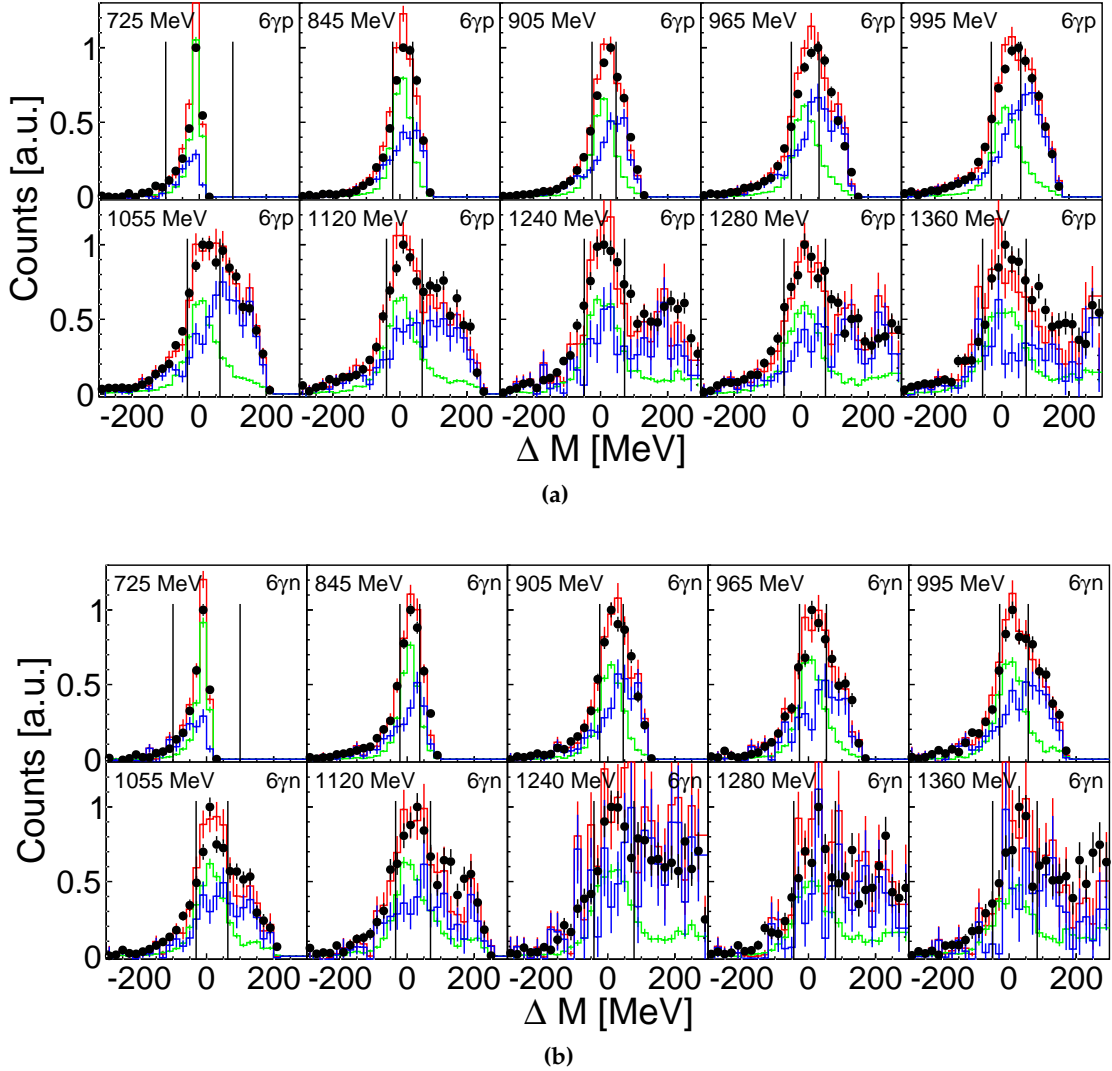


Figure 8.19: Missing mass spectra for the $\eta \rightarrow 6\gamma$ decay for the proton (a) and for the neutron (b) reaction for A2 data: the contribution from the deuterium target is shown in green, the contribution from the carbon target in blue, and the dButanol distribution is shown as black dots. The sum of the deuterium and the carbon is shown in red. The counts were normalised as described in the text. A variable energy binning was used (mean value indicated) and only a selection of bins is shown here.

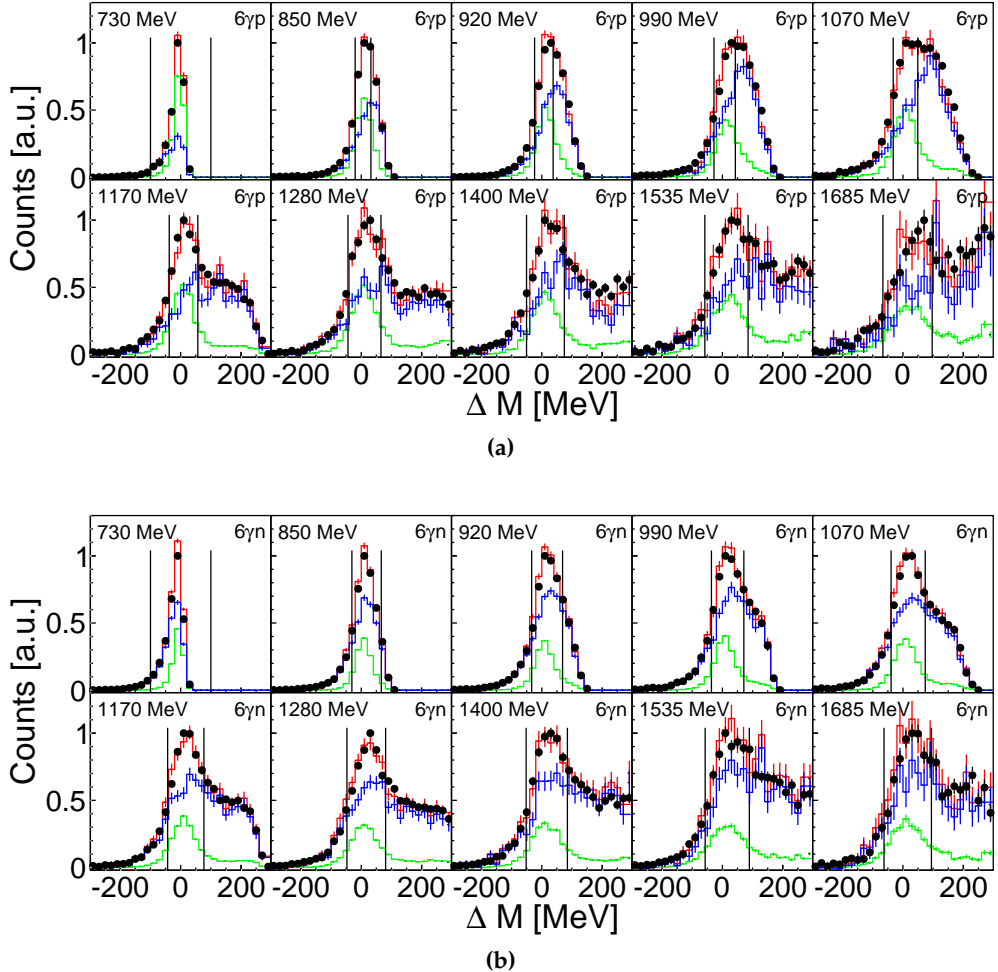


Figure 8.20: Missing mass spectra for the $\eta \rightarrow 6\gamma$ decay for the proton (a) and the neutron (b) reaction for CBELSA/TAPS data: the contribution from the deuterium target is shown in green, the contribution from the carbon target in blue, and the dButanol distributions are shown as black dots. The sum of the deuterium and the carbon is shown in red. The counts were normalised as described in the text, an additional normalisation factor of 1.6 was necessary for the dButanol and carbon data. A variable energy binning was used (mean value indicated) and only a selection of bins is shown here.

8.11 Data Merging

The final results for the present work are statistical averages of several beamtimes. In addition, the two decay channels of the η meson, $\eta \rightarrow 2\gamma$ and $\eta \rightarrow 6\gamma$, were merged (only A2 data) to get results with the smallest available statistical error.

The statistical average was calculated on the cross section level. In particular, for the polarised data the weighted average was determined separately for the sum σ_{sum} and the difference σ_{diff} of the two helicity states. For this purpose, the weighted average $\langle \sigma \rangle$ of n cross sections and the corresponding statistical error $\langle \Delta \sigma \rangle$ was calculated according to the following formula:

$$\langle \sigma \rangle = \frac{\sum_{i=1}^n \sigma_i / \Delta \sigma_i^2}{\sum_{i=1}^n 1 / \Delta \sigma_i^2} \quad \langle \Delta \sigma \rangle = \frac{1}{\sqrt{\sum_{i=1}^n 1 / \Delta \sigma_i^2}}, \quad (8.65)$$

where $\Delta \sigma_i$ is the statistical error of the cross section σ_i .

8.12 Systematic Uncertainties

Systematic uncertainties are important to judge the quality of the extracted observables and hence were determined for the unpolarised cross sections, as well as for the double polarisation observable E and the helicity dependent cross sections. Sec. 8.12.1 describes how the systematic uncertainties were determined for the unpolarised cross sections, whereas Sec. 8.12.2 describes the determination of the systematic uncertainties for the double polarisation observable E and the helicity dependent cross sections.

8.12.1 Unpolarised Cross Sections

The systematic uncertainties of the unpolarised cross sections can be divided into two groups. The first group contains uncertainties of the target surface density, the photon flux, the empty target subtraction, and the η branching ratio. These errors are all independent of the energy and angle. The second group of uncertainties was determined as a function of the energy (E_γ and W) and $\cos(\theta_\eta^*)$. The uncertainties of the analysis cuts, the nucleon efficiency correction, and the CB energy sum trigger (only A2 data) were assigned to that group.

Target Surface Density

The systematic uncertainty of the target surface density originates from the uncertainty of the target length and the target density. The latter has a specific pressure and temperature dependence. The systematic uncertainty for the deuterium target was estimated to be around 4% [55]. The uncertainty of the ^3He target was slightly larger due to the measurement of the target temperature and a possible deformation of the target cell. A value of 7% was estimated in Ref. [109].

Photon Flux

The systematic uncertainty of the A2 photon flux is clearly dominated by the determination of the tagging efficiency. As explained in Sec. 8.6.1, the time dependent tagging efficiency was determined by scaling the π^0 count rate per run to the tagging efficiency measurement. Thus, to find the uncertainty of this determination, the count rate was scaled in a way that it either fitted the minimum or maximum tagging efficiency values. Doing this, a systematic uncertainty of the flux of 5% [55] was found for the A2 ^3He experiment.

The main systematic uncertainty in the CBELSA/TAPS flux determination is coming from the GIM efficiency, which was estimated to be 7% [125]. Additionally, an error of 3.8% was estimated [125] coming from the trigger electronics. Adding them in quadrature, leads to a total systematic uncertainty of approximately 8%.

Empty Target

The systematic uncertainty for the empty target subtraction for the determination of the unpolarised cross sections, was very conservatively estimated to be in the order of half the empty target contribution, i.e. 3.5% for the CBELSA/TAPS deuterium target and 2.5% for the A2 ^3He target.

η -Decay Branching Ratio

The systematic uncertainties for the branching ratios are given in the very beginning of this Sec. 8.1. The values are 0.2% of 39.41% for the $\eta \rightarrow 2\gamma$ and 0.26% of 32.10% for the $\eta \rightarrow 6\gamma$ decay. Thus, of the systematic uncertainty for the branching ratio a maximum value of 0.8% can be assumed.

Analysis Cuts

A different choice of the analysis cut positions can possibly change the event selection significantly. Choosing loose cuts can allow more background to enter the desired reaction channel. On the other hand, more stringent cuts can select certain kinematical constellations. In general, cuts may also have a different influence on simulation and data, when the line shapes are not exactly identical. In addition, statistical fluctuations in the determination of the cut position can induce changes in the cross sections.

Hence, to account for the uncertainty induced by the applied cuts, cross sections were calculated by varying the most important cut positions by a value of $\pm 3\%$. The $\pm 3\%$ variation was seen as a reasonable change. Two analyses were done, one with a loose coplanarity, missing mass and invariant mass cut, a second one with strict cuts. The systematic uncertainty was then calculated from the difference of the obtained cross sections as a function of the energy and $\cos(\theta_\eta^*)$.

Nucleon Detection Efficiency

For the exclusive analysis, the accuracy of the detection efficiency of the nucleon is an important contribution to the total systematic uncertainty. To get a feeling for the corresponding systematic uncertainty, the quasi-free inclusive channel, $\gamma N \rightarrow \eta(N)$, was analysed. In an ideal case, neglecting coherent contribution, see Sec. 7.1, the obtained cross section should be equal to the sum of the exclusive cross section of the proton and of the neutron:

$$\sigma(\gamma N \rightarrow \eta(N)) = \sigma(\gamma p \rightarrow \eta p) + \sigma(\gamma n \rightarrow \eta n) \quad (8.66)$$

Since in the inclusive case, no recoil nucleon is required in the final state, the deviation of the inclusive cross section from the sum of the two exclusive cross sections is due to the uncertainty of the nucleon detection. Thus, half of this difference was assigned to the systematic uncertainty of the proton detection efficiency and the other half to the uncertainty of the neutron detection efficiency.

CB Energy Sum Trigger

The A2 CB energy sum trigger was explained in Sec. 8.8.2. The applied CDF had a major influence on the cross sections at CB energy sums below 400 MeV. For higher energies, no change was seen for the cross section. Hence, to determine the induced systematic uncertainty, cross sections were produced with applying the CDF shown in Fig. 8.8 and by using a fixed cut at $E_{CB} > 400$ MeV. The induced deviations were in the order of 2 – 3% percent depending on the energy and $\cos(\theta_\eta^*)$.

Combining the Systematic Uncertainties

The various systematic uncertainties $\Delta\sigma_i(E, \cos\theta_\eta^*)$, where E is either the incident photon energy E_γ , or the final state energy W , were combined to a total systematic uncertainty $\Delta\sigma(E, \cos\theta_\eta^*)$. This calculation was done individually for each reaction channel.

The energy and angle independent errors from the empty target $\Delta\sigma_{e.t.}$, the branching ratio $\Delta\sigma_{b.r.}$, the photon flux $\Delta\sigma_f.$, and the target surface density $\Delta\sigma_{t.d.}$, were added quadratically to an overall uncertainty, since it was assumed that the individual errors are independent:

$$\Delta\sigma_{tot} = \sqrt{\Delta\sigma_{e.t.}^2 + \Delta\sigma_{b.r.}^2 + \Delta\sigma_f.^2 + \Delta\sigma_{t.d.}^2} \quad (8.67)$$

The corresponding values for the A2 ^3He and CBELSA/TAPS LD_2 experiments are summarised in Table 8.3.

	$\Delta\sigma_{e.t.}$	$\Delta\sigma_{b.r.}$	$\Delta\sigma_f.$	$\Delta\sigma_{t.d.}$	$\Delta\sigma_{tot}$
^3He (A2)	2.5%	0.8%	5%	7%	~ 9%
LD_2 (CBELSA/TAPS)	3.5%	0.8%	8%	4%	~ 10%

Table 8.3: The energy and angle independent systematic uncertainties for the A2 ^3He and CBELSA/TAPS deuterium experiments.

The remaining systematic uncertainties, namely the uncertainty of the cuts $\Delta\sigma_{cuts}$, the nucleon efficiency $\Delta\sigma_{n.e.}$, and the uncertainty from the CB energy sum trigger $\Delta\sigma_{CBE}$ (only A2 data) were added to an energy and angle dependent value:

$$\Delta\sigma(E, \cos(\theta_\eta^*)) = \sqrt{\Delta\sigma_{cuts}^2 + \Delta\sigma_{n.e.}^2 + \Delta\sigma_{CBE}^2} \quad (8.68)$$

The quadratic addition is motivated by the fact that the two uncertainties are independent and hence cancellation effects may play a role.

The relative systematic uncertainties for the analysis cuts and the nucleon efficiency for the unpolarised cross section on the deuterium target from CBELSA/TAPS experiment are shown in Fig. 8.21 and Fig. 8.22. The corresponding systematic un-

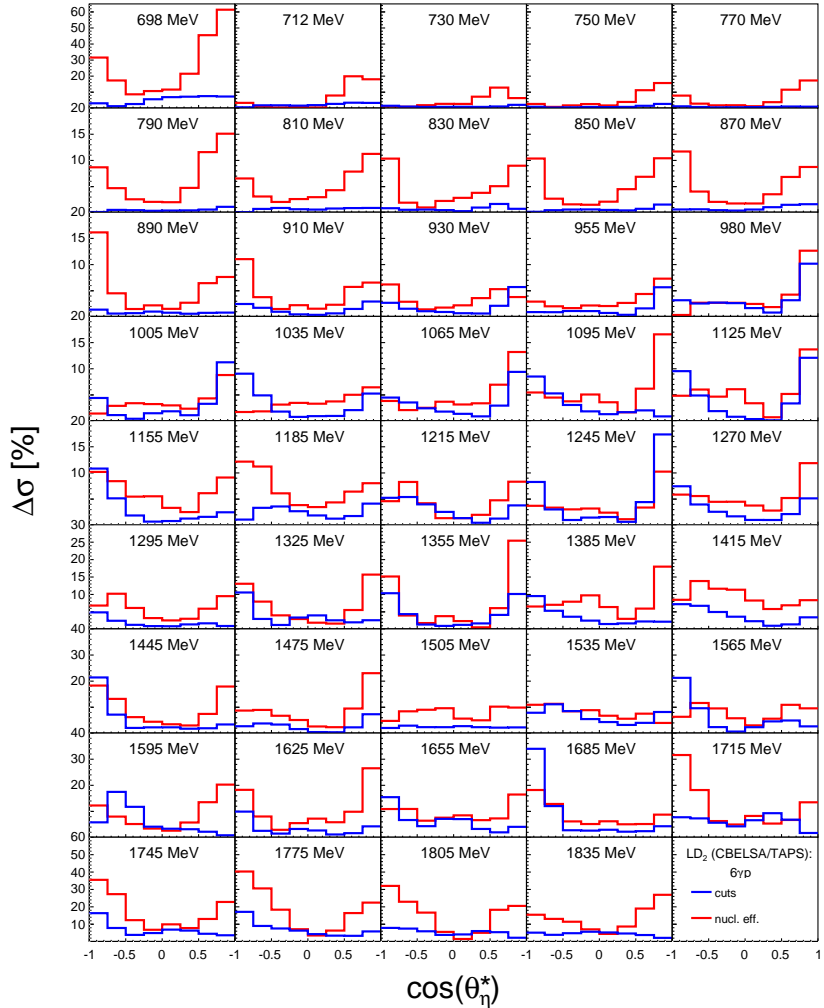


Figure 8.21: Relative systematic uncertainties from the analysis cuts (blue) and the nucleon efficiency (red) for the $\gamma + p \rightarrow \eta + p$ cross section for the CBELSA/TAPS LD₂ target (only $\eta \rightarrow 6\gamma$). The systematic uncertainties were determined as described in the text. The same variable energy binning as for the cross sections and eight $\cos(\theta_\eta^*)$ -bins were used (mean value indicated).

certainties for the for the A2 ${}^3\text{He}$ cross sections are shown in Appendix D and the uncertainties for the A2 LD_2 cross sections can be found in Ref. [56].

The error bands given in the final results of Chapter 9 are only the energy and angle dependent systematic uncertainties $\Delta\sigma(E, \cos(\theta_\eta^*))$. To get the total uncertainty, $\Delta\sigma_{\text{tot}}$ has to be added.

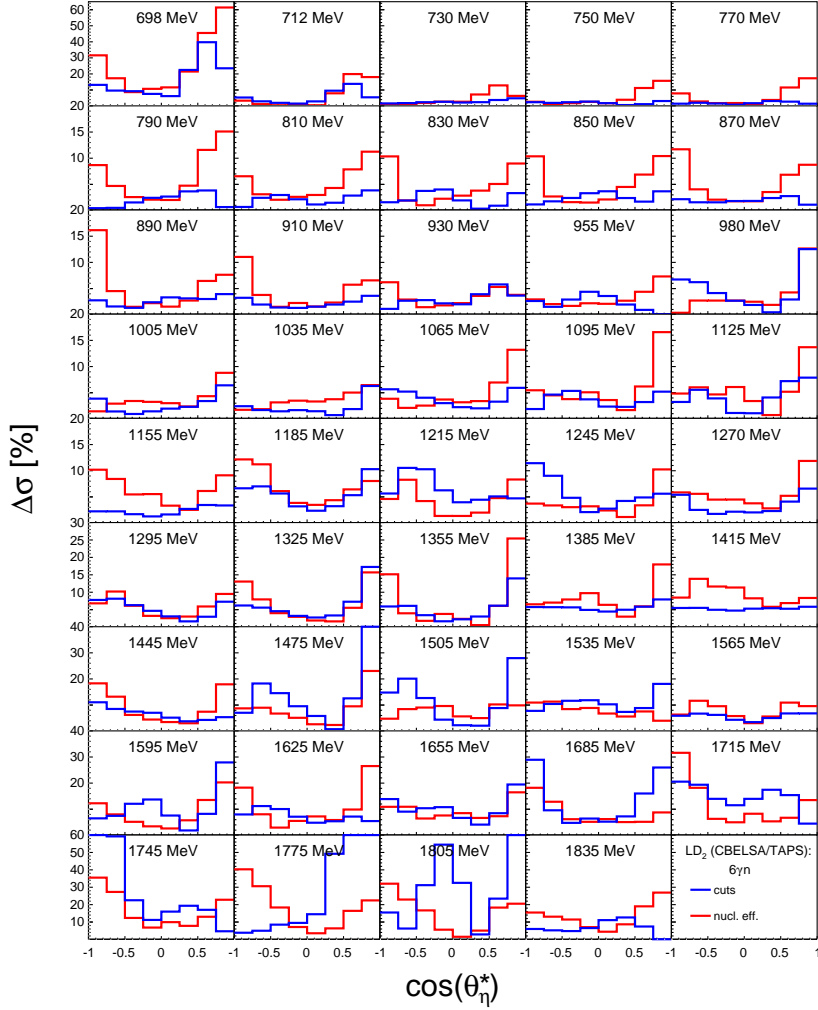


Figure 8.22: Relative systematic uncertainties from the analysis cuts (blue) and the nucleon efficiency (red) for the $\gamma + n \rightarrow \eta + n$ cross section for the CBELSA/TAPS LD_2 target (only $\eta \rightarrow 6\gamma$). The systematic uncertainties were determined as described in the text. The same variable energy binning as for the cross sections and eight $\cos(\theta_\eta^*)$ -bins were used (mean value indicated).

8.12.2 Double Polarisation Observable E and Helicity Dependent Cross Sections

The systematic uncertainties described in Sec. 8.12.1 also affect the polarised experiments. However, in the determination of E , most of these systematic uncertainties, such as the uncertainty coming from the flux and the analysis cuts, cancel out since they appear in the numerator and denominator of the fraction. Systematic uncertainties, which do not cancel out, such as the uncertainties coming from the carbon subtraction and different nucleon detection efficiencies of the polarised and unpolarised experiments, were estimated by simply building the difference between the two extraction versions for the double polarisation observable E :

$$\Delta E = |E^{\text{vers } 1} - E^{\text{vers } 2}|. \quad (8.69)$$

For the helicity dependent cross sections, the systematic uncertainty of the unpolarised cross section was neglected and the systematics were found by building the maximum difference between the three extraction versions:

$$\Delta\sigma_{1/2} = \text{Max} \left(\Delta\sigma_{1/2}^1, \Delta\sigma_{1/2}^2, \Delta\sigma_{1/2}^3 \right), \quad (8.70)$$

where $\Delta\sigma_{1/2}^1 = |\sigma_{1/2}^{\text{vers } 1} - \sigma_{1/2}^{\text{vers } 2}|$, $\Delta\sigma_{1/2}^2 = |\sigma_{1/2}^{\text{vers } 2} - \sigma_{1/2}^{\text{vers } 3}|$, and $\Delta\sigma_{1/2}^3 = |\sigma_{1/2}^{\text{vers } 3} - \sigma_{1/2}^{\text{vers } 1}|$. The systematic uncertainties for $\sigma_{3/2}$ were determined analogously:

$$\Delta\sigma_{3/2} = \text{Max} \left(\Delta\sigma_{3/2}^1, \Delta\sigma_{3/2}^2, \Delta\sigma_{3/2}^3 \right), \quad (8.71)$$

where $\Delta\sigma_{3/2}^1 = |\sigma_{3/2}^{\text{vers } 1} - \sigma_{3/2}^{\text{vers } 2}|$, $\Delta\sigma_{3/2}^2 = |\sigma_{3/2}^{\text{vers } 2} - \sigma_{3/2}^{\text{vers } 3}|$, and $\Delta\sigma_{3/2}^3 = |\sigma_{3/2}^{\text{vers } 3} - \sigma_{3/2}^{\text{vers } 1}|$. This systematic uncertainty accounts for uncertainties due to the carbon subtraction, differences in the nucleon detection efficiency, flux, and analysis cuts compared to the unpolarised measurement. In addition, the uncertainties coming from the polarisation degrees of target and incident photon beam have to be considered.

Photon Polarisation

The systematics for the electron polarisation extracted from the Mott measurement at MAMI were discussed in Sec. 3.2.1. A total relative systematic uncertainty of 2.7% was estimated.

The systematic uncertainty of beam polarisation extracted from the Møller measurement in the CBELSA/TAPS experiment is explained in detail in [81]. The error consists of the uncertainties in the Møller target polarisation (main contribution), the angle of the Møller foil, the count rate asymmetry and the error of the asymmetry coefficient. In total this yields to a most probable relative systematic uncertainty of 0.99% and a maximum possible uncertainty of 2.89%.

Target Polarisation

As mentioned in Sec. 3.4, a problem with the target polarisation of the A2 dButanol experiments was observed. The corresponding systematic uncertainty was estimated from the re-normalisation of the double polarisation E to unity in $S_{11}(1535)$ under the assumption that FSI can be neglected (as it was seen in the CBELSA/TAPS results). The double polarisation observable E was scaled to the maximum and minimum possible height to match unity in the region of the $S_{11}(1535)$ and the difference was taken as the systematic uncertainty. With this procedure, a systematic uncertainty of $\pm 10\%$ was found.

The systematic uncertainty of the target polarisation of the CBELSA/TAPS dButanol target was estimated to be 5% [175]. The uncertainty mainly comes from determination of the fit parameters of the deuteron signals, as shown in Fig. 3.7.

Combining the Systematic Uncertainties

The systematic uncertainties of the degree of the target polarisation, ΔP_T , and of the photon polarisation, ΔP_γ , were added in quadrature to get the total polarisation uncertainty:

$$\Delta P = \sqrt{\Delta P_T^2 + \Delta P_\gamma^2} \quad (8.72)$$

Hence, the systematic uncertainty of the polarisation for A2 data is given by:

$$\Delta P_{A2} = \sqrt{0.1^2 + 0.027^2} \simeq 10.4\% \quad (8.73)$$

For the CBELSA/TAPS data the following value for the systematic uncertainty of the polarisation can be determined:

$$\Delta P_{CBELSA/TAPS} = \sqrt{0.05^2 + 0.0289^2} \simeq 6\% \quad (8.74)$$

The systematic uncertainties from the different extraction versions and the uncertainties of the polarisation were combined to a common uncertainty by adding them in quadrature:

$$\Delta E^{tot} = \sqrt{\Delta E^2 + \Delta P^2}, \quad (8.75)$$

where ΔE is defined in Eq. 8.69 and ΔP is given by Eq. 8.73 or Eq. 8.74, respectively.

The uncertainties for the helicity dependent cross sections were determined analogously by the following equations:

$$\Delta \sigma_{1/2}^{tot} = \sqrt{\Delta \sigma_{1/2}^2 + \Delta P^2}, \quad (8.76)$$

$$\Delta \sigma_{3/2}^{tot} = \sqrt{\Delta \sigma_{3/2}^2 + \Delta P^2}, \quad (8.77)$$

where $\Delta \sigma_{1/2}$ and $\Delta \sigma_{3/2}$ are given by Eqs. 8.70 and 8.71, respectively

Chapter 9

Results and Conclusions

In this chapter, the final results that were obtained in this work will be presented. The first two sections will concentrate on the results on the unpolarised cross sections for η photoproduction from quasi-free nucleons bound in ${}^3\text{He}$ (A2 data) and deuterium (CBELSA/TAPS data). Sections 9.3 and 9.4 summarise the results of the double polarisation observable E and the helicity dependent cross sections $\sigma_{1/2}$ and $\sigma_{3/2}$ for CBELSA/TAPS and A2 data. Results as a function of the incident photon energy E_γ and the final state energy W were extracted. The cm frame for the results as a function of the incident photon energy was constructed under the assumption that the initial state nucleon was at rest, which leads to a smearing of narrow structures. Especially close to threshold, effects from Fermi motion are not negligible, as explained in Sec. 8.5. For the results as a function of the final state energy, the cm frame was constructed event-by-event from the invariant mass of the η meson and the reconstructed nucleon. As explained in Sec. 8.5, the nucleon momentum was determined either via kinematical reconstruction or a TOF measurement. Thus, cross sections as a function of the final state energy are dominated by the resolution of this reconstruction, as seen in Figs. 8.1 and 8.2. Sec. 9.5 gives a summary of all polarised results and discusses some important information deduced from the results. Finally, Sec. 9.6 gives a conclusion of all the obtained results in the present work.

9.1 Unpolarised Cross Section from ${}^3\text{He}$ (A2)

η photoproduction was measured for quasi-free protons and neutrons bound in ${}^3\text{He}$ from threshold ($E_\gamma \simeq 608$ MeV) up to $E_\gamma = 1.4$ GeV. The experiment was performed by the A2 collaboration at MAMI in Mainz. Both decay channels, $\eta \rightarrow 2\gamma$ and $\eta \rightarrow 3\pi^0 \rightarrow 6\gamma$, were analysed for the two exclusive reactions on the proton (σ_p) and neutron (σ_n) and for the quasi-free inclusive reaction (σ_{incl}). Results have been extracted as a function of the incident photon energy E_γ , as discussed in Sec. 9.1.1, and for the final state energy W , as discussed in Sec. 9.1.2.

9.1.1 Incident Photon Energy E_γ

The cross sections as a function of the incident photon energy were extracted for all three reactions, exclusive on the proton σ_p , exclusive on the neutron σ_n , and inclusive σ_{incl} . The total cross sections as a function of the incident photon energy are shown in Fig. 9.1 (a). For the two exclusive reactions, σ_p and σ_n , both decay channels $\eta \rightarrow 2\gamma$ (closed symbols) and $\eta \rightarrow 3\pi^0 \rightarrow 6\gamma$ (open symbols) are shown. The competing background contributions, as well as the systematic uncertainties from the efficiency, and the response to the trigger are completely different for the two decay modes. The cross sections of both decay channels are in good agreement, hence, the background was sufficiently rejected and the efficiency correction was done adequately. Furthermore, the comparison of the inclusive cross section, σ_{incl} , and the sum of the two exclusive cross sections, $\sigma_p + \sigma_n$, allows to check the nucleon detection efficiency correction, since they should be equal. The largest deviations occur at high incident photon energies but they are below 10%, which is within the systematic uncertainties. These deviations are most likely caused by residual background ($\eta\pi$), which is more prominent at high energies and is rejected more efficiently in the exclusive analyses by the cut on the coplanarity angle, as explained in Sec. 7.4.2.

Comparing the proton and neutron cross sections, one sees that for the neutron, the slope on the right side of the $S_{11}(1535)$, around $E_\gamma \sim 1$ GeV, is less steep than for the proton, which was also observed in other deuterium measurements [51, 55]. In contrast to the deuterium cross sections, no distinct structure around $E_\gamma = 1$ GeV is visible. However, this is expected since the much larger Fermi motion in ${}^3\text{He}$ compared to the deuteron smears all narrow structures. The corresponding differential cross sections are presented in Fig. 9.2. Again, both decay channels of the η meson are shown for the proton and neutron cross sections, whereas the inclusive cross section is the weighted average of both channels. The agreement between the two decay channels is good, demonstrating the consistency of the results. All angular distributions show a steep rise at backward angles close to threshold, which is a result of the choice of the cm frame. Fermi momenta with negative z-direction (anti-parallel nucleon and photon momentum) are favoured since they lead to higher cm energies. This means that the boost into the cm system is too strong into the negative z-direction, inducing backward boosted η mesons in the cm frame. In contrast, the angular distributions for the free proton are rather flat close to threshold. At higher incident photon energies, the Fermi momentum causes only a slight smearing of the structures.

Quasi-free inclusive η photoproduction off other nuclei has been intensively studied regarding η -nucleus interactions and in-medium effects in the energy range of the $S_{11}(1535)$ [176, 177]. It was found that for heavier nuclei, the cross sections scale with $A^{2/3}$ (where A is the atomic mass number), indicating strong absorption of the η -meson by nuclei. The cross section data obtained by Mertens *et al.* [177] are compared in Fig. 9.1 (b) to the present results on ${}^3\text{He}$. The cross sections were scaled by $A_{eff} = N_p + (2/3)N_n$, where N_p and N_n are the number of protons and neutrons, respectively. This scaling is motivated by the fact that the cross sections for the proton and neutron scale like $\sigma_p/\sigma_n = 3/2$. Ref. [31] explains this effect as a result of domi-

nant isovector excitation of the $S_{11}(1535)$. As can be seen in the insert in Fig. 9.1 (b), the ^3He data fits nicely to the $A_{\text{eff}}^{2/3}$ scaling of the heavier nuclei. However, the peak of the $S_{11}(1535)$ shifts to higher incident photon energies for heavier nuclei, which is mainly an effect of the higher Fermi momenta in heavier nuclei. For energies above 800 MeV, the cross sections deviate from the $A_{\text{eff}}^{2/3}$ scaling, which is partly caused by residual background from $\eta\pi$ reactions. For heavier nuclei, the separation of η reactions from $\eta\pi$ reactions is more challenging due to the larger Fermi momenta.

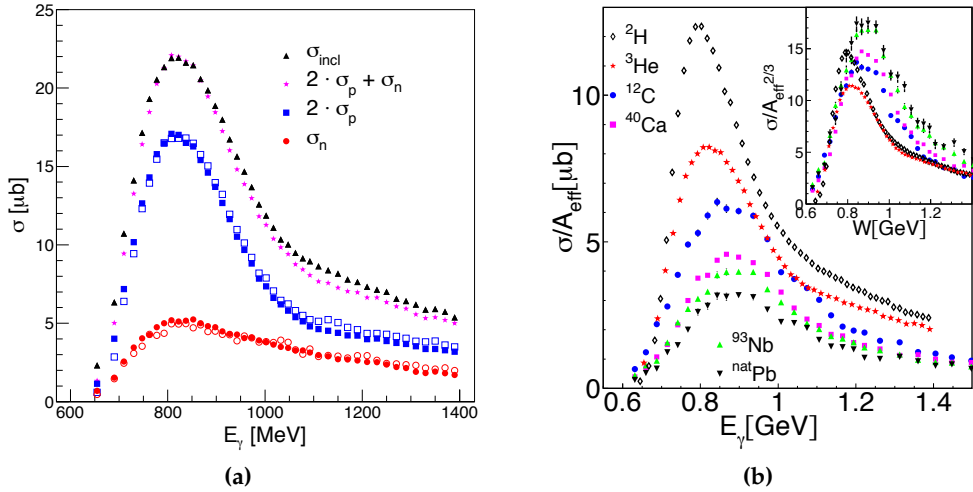


Figure 9.1: (a) Total cross sections as a function of incident photon energy for ^3He . Closed symbols indicate the results for the two-photon decay and open symbols show the results for the six-photon decay. For the inclusive cross section and the sum $\sigma_p + \sigma_n$, only the average of both decay channels is shown. (b) Total inclusive cross section σ_{incl} for different nuclei. The cross sections are scaled by $A_{\text{eff}} = N_p + (2/3)N_n$, in the insert by $A^{2/3}$. The results from this work (^3He) are compared to results on ^2H [55] and other nuclei [177].

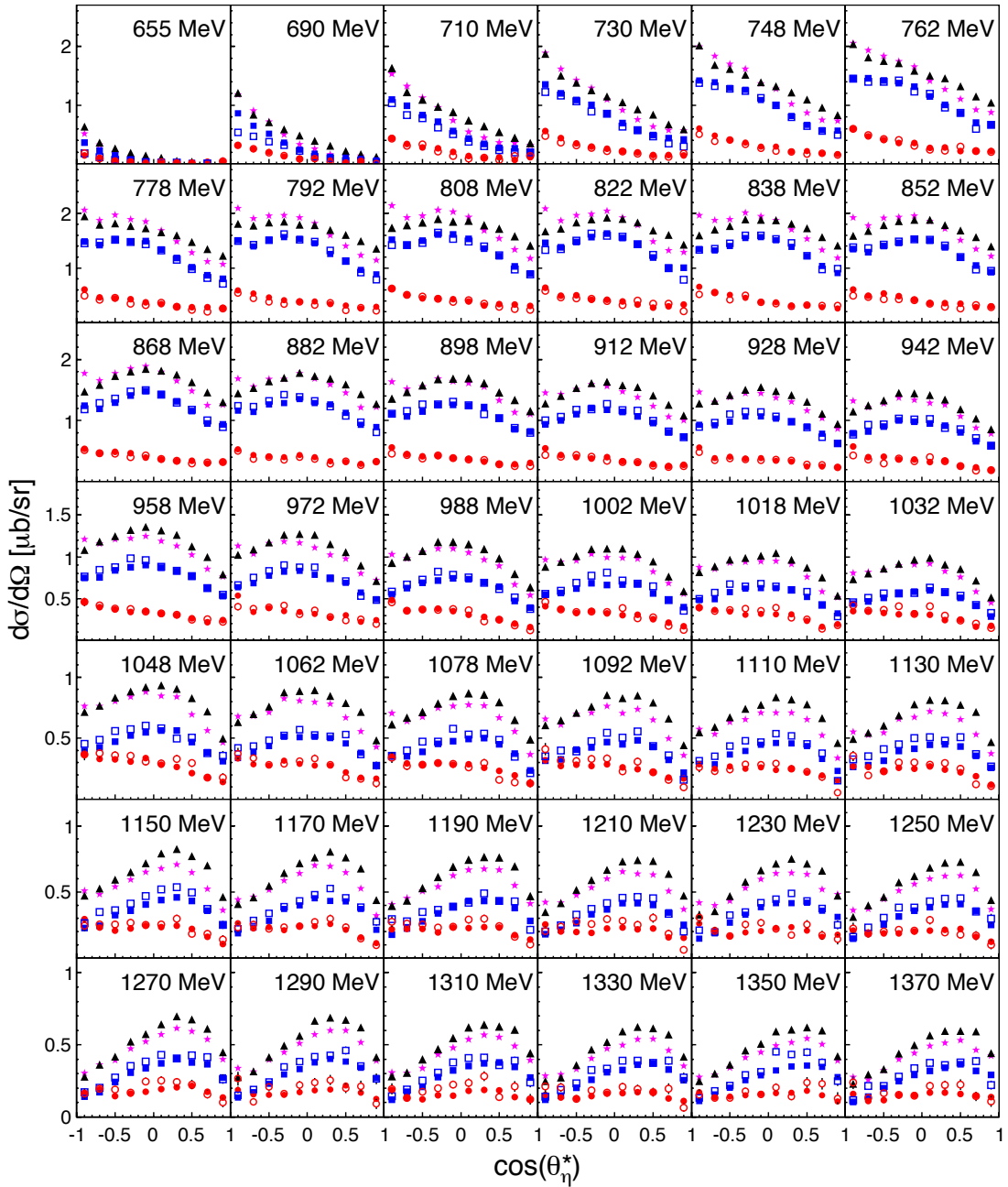


Figure 9.2: Differential cross sections for ${}^3\text{He}$ for different bins of incident photon energy E_γ . Shown are results for the reaction on the neutron σ_n , where the η meson decays into two photons (closed red circles) and into six photons (open red circles). The reaction on the proton σ_p is shown as closed (2γ) and open (6γ) blue squares. The quasi-free inclusive reaction σ_{incl} is indicated by black triangles (average of two- and six-photon decay) and the magenta stars show the reconstructed inclusive $2\sigma_p + \sigma_n$.

9.1.2 Final State Energy W

The cross sections as a function of the final state energy W were reconstructed as explained in Sec. 8.5. Fig. 9.3 (a) shows the total cross section for the proton and neutron, where the recoil nucleon, and hence $W = m(N\eta)$ were reconstructed using a kinematical reconstruction. In contrast, Fig. 9.3 (b), shows the cross section from the TOF reconstruction and thus is limited to the region where the recoil nucleon is detected in the TAPS detector ($\cos(\theta_\eta^*) < -0.4$). In both figures, the cross section on the neutron (red circles) was scaled by a factor of $3/2$ to match the proton cross section (blue squares) in the region of the $S_{11}(1535)$. The results of both reconstruction techniques are in nice agreement and show a bump-like structure around 1.68 GeV. The cross sections were fitted with a sum of three Breit-Wigner curves (solid line). The dash-dotted line shows the Breit-Wigner fit for the $S_{11}(1535)$ resonance, the dashed line shows a Breit-Wigner fit for the narrow structure around 1.68 GeV, and the dotted line represents the Breit-Wigner function for other resonances and non-resonant background contributions. Furthermore, the open circles show the data points when the contribution from the $S_{11}(1535)$ and the broad Breit-Wigner have been subtracted. The corresponding fit parameters are summarised in Table 9.1. The values given in this table are effective quantities, including the experimental resolution of the recoil nucleon. The fit parameters for the narrow structure on the neutron are comparable for both reconstruction methods. However, as seen in Fig 8.1, the TOF reconstruction has a much worse W resolution ($\text{FWHM} \simeq 45 \text{ MeV}$) than the reconstruction via kinematics ($\text{FWHM} \simeq 35 \text{ MeV}$). An approximation for the intrinsic width of the narrow structure in ${}^3\text{He}$ can be found by subtracting quadratically the corresponding experimental resolution from the fitted width. This leads to an intrinsic width of about 40 MeV for the TOF reconstruction and 45 MeV for the extraction via kinematics. Due to the kinematical approximations that have been used (no relative momentum between the two spectator nucleons), the latter value is only an upper limit, as explained in Sec. 7.5.4.

		$W_R \text{ [MeV]}$	$\Gamma \text{ [MeV]}$	$\sqrt{b_\eta} A_{1/2}^n \text{ [10}^{-3}\text{GeV}^{1/2}]$
kin.	narrow state	1675 ± 2	62 ± 8 (46 ± 8)	11.9 ± 1.2
	$S_{11}(1535)$	1536 ± 1	162 ± 4	66 ± 1
TOF	narrow state	1671 ± 2	61 ± 10	-
	$S_{11}(1535)$	1541 ± 2	174 ± 10	-

Table 9.1: Fit parameters of the fits shown in Fig. 9.3. The values for the kinematical reconstruction are indicated with *kin.*, the results for the TOF reconstruction with *TOF*. The position W_R , the width Γ_R , and the electromagnetic coupling $\sqrt{b_\eta} A_{1/2}^n$ are given for the narrow state and the $S_{11}(1535)$ resonance. The width in the parentheses was extracted from a fit, which has been convoluted with experimental resolution. The indicated errors are pure statistical errors.

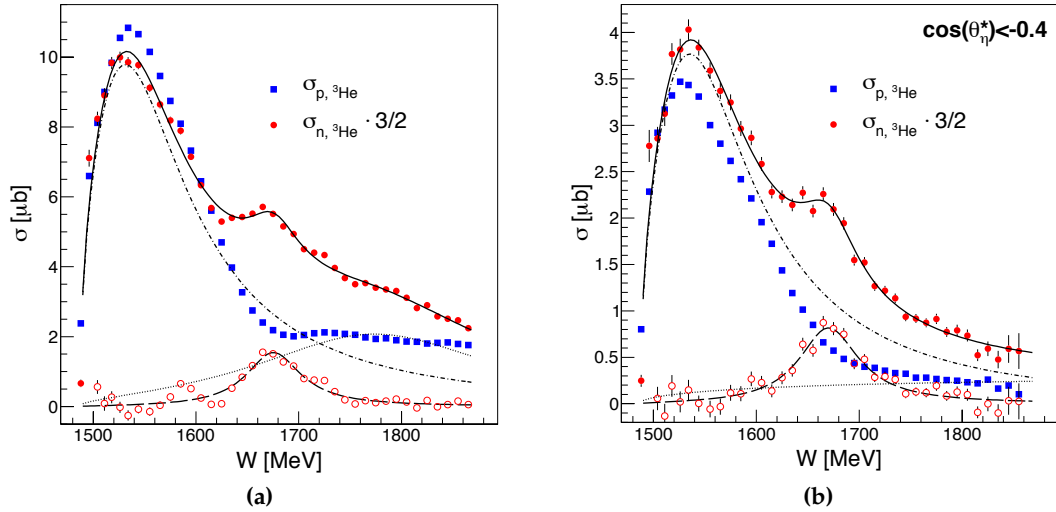


Figure 9.3: Total cross sections as a function of the final state energy W for ${}^3\text{He}$. The results on the proton (blue squares) are compared to the scaled neutron results (red closed circles). A Breit-Wigner fit of the neutron cross section is indicated by the solid black line. The contribution from the $S_{11}(1535)$ is shown as dash-dotted line, the background contribution is shown as dotted line, and the line shape for the narrow structure as a long-dashed line. The red open circles is the neutron cross section after subtraction of S_{11} and background fit. Compared are the results, where (a) the recoil nucleon was reconstructed from kinematics and (b) from TOF measurement for $\cos(\theta_\eta^*) < -0.4$ (b).

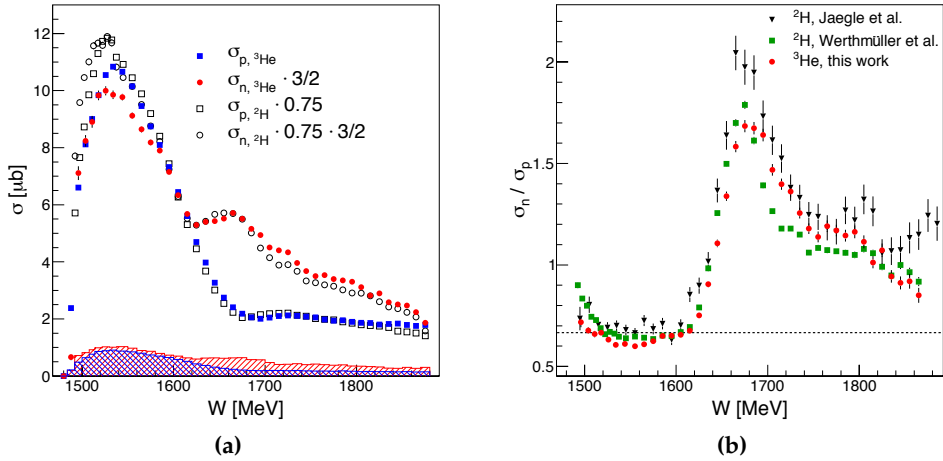


Figure 9.4: (a) Total cross sections as a function of the final state energy W for ${}^3\text{He}$, compared to results from LD₂ by Werthmüller et al. [55]. (b) Ratio of neutron and proton cross section for ${}^3\text{He}$ (red dots) compared to previous results from the LD₂ target from Ref. [55] (green squares) and Ref. [51] (black triangles).

Fig. 9.4 compares the present results from ${}^3\text{He}$ to previous results from the deuteron [56]. The hatched histograms indicate the systematic uncertainty. However, the results on ${}^3\text{He}$ and the deuteron were obtained with an identical setup, such that a large part of the uncertainties cancel when comparing them to each other. The cross section on the neutron $\sigma_{n,{}^3\text{He}}$ was scaled by a factor of $3/2$ to fit the height of the proton. As can be seen, the deuterium cross sections had to be scaled by a factor of 0.75 to agree with the ${}^3\text{He}$ cross sections. However, apart from this 0.75 factor, the cross section in the region of the narrow structure are in agreement with the deuteron data. This factor must originate from different nuclear effects in η photoproduction off ${}^3\text{He}$ and deuteron nuclei. A major part of this factor can likely be attributed to Final State Interaction (FSI). Fig. 9.1 shows that such effects are important for ${}^3\text{He}$ nuclei. A second part of the deviation between deuterium and ${}^3\text{He}$ cross sections can be assigned to the kinematical approximations in the case of ${}^3\text{He}$. The assumption that there is no relative momentum between the two spectator nucleons may decrease the magnitude of the cross sections, since the same approximation was also done for the folding of the photon flux with nuclear Fermi motion. A non-vanishing relative momentum between the two spectator nucleons reduces the available energy in the meson-participant nucleon system and thus suppresses η photoproduction. This leads to an overestimation of the photon flux and hence to smaller cross sections. Figs. 9.5 and 9.6 show the corresponding angular distributions of ${}^3\text{He}$. The results are again compared to the scaled deuterium cross sections. To obtain the total cross sections, the angular distributions were fitted with third order Legendre polynomials (solid lines). The systematic uncertainties, except for 9% overall normalisation, are indicated by the histograms at the bottom. Apart from the overall factor of 0.75, the angular distribution above $W = 1.6$ GeV agree quite well with the deuteron distributions. Deviations may originate from FSI or residual Fermi motion effects, as explained earlier.

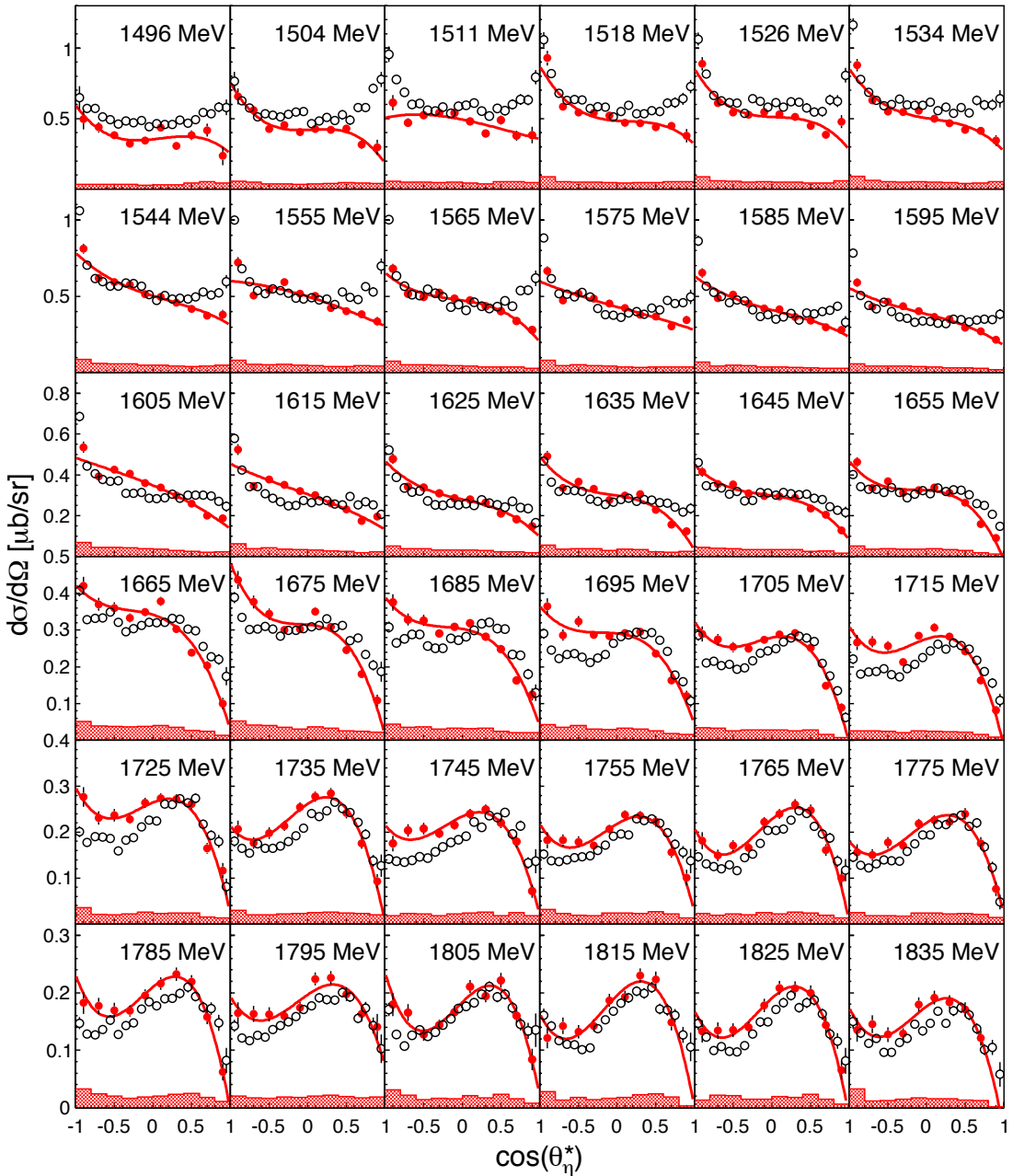


Figure 9.5: Differential cross sections as a function of the final state energy W for $\gamma n \rightarrow \eta n$. Data from present ^3He measurement (red closed circles) are compared to data from the deuterium target [55] scaled down by factor 0.75 (open black circles). The Legendre fits are indicated by solid lines. The systematic uncertainties are indicated by the hatched histograms at the bottom, except for 9% total normalisation uncertainty.

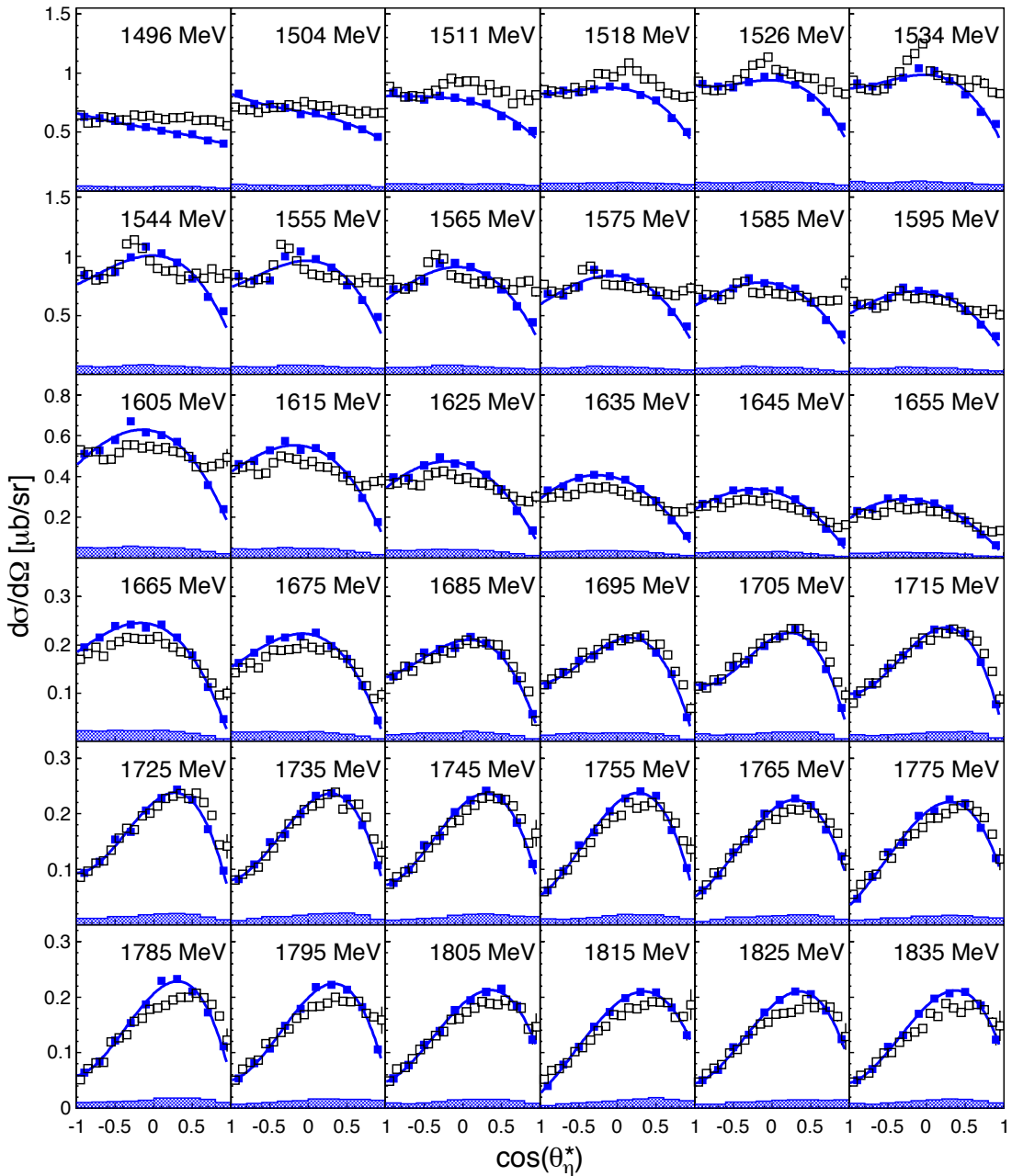


Figure 9.6: Differential cross sections as a function of the final state energy W for $\gamma p \rightarrow \eta p$. Data from present ${}^3\text{He}$ measurement (blue closed squares) are compared to data from the deuterium target [55] scaled down by factor 0.75 (open black squares). The Legendre fits are indicated by solid lines. The systematic uncertainties are indicated by the hatched histograms at the bottom, except for 9% total normalisation uncertainty.

Finally, Fig. 9.7 shows the neutron cross section for different polar angle bins. The data were fitted with a broad background Breit-Wigner and two energy-dependent Breit-Wigner functions for the $S_{11}(1535)$ and the narrow structure. To account for the experimental resolution, the Breit-Wigner distribution was implemented by a convolution with the resolution given in Fig. 8.1. The convolution was realised by a numerical integration, as explained in Ref. [56]. The energy dependent Breit-Wigner function is given by the following equation [178]:

$$\sigma(W) = \frac{q_\eta^*}{q_{\eta R}^*} \cdot \frac{k_R^*}{k^*} \cdot \frac{2m_N \cdot A_{1/2}^2 \cdot W_R \cdot b_\eta \cdot \Gamma_R}{[(W_R^2 - W^2)^2 + W_R^2 \Gamma(W)^2 x^2]} \quad (9.1)$$

where W_R is the resonance position, Γ_R is the energy dependent width, k^* , q_η^* , q_π^* are the cm momenta of incident photon, η meson and pion, respectively, the subscript R refers to the evaluation at the resonance position, $x = b_\eta \frac{q_\eta^*}{q_{\eta R}^*} + b_\pi \frac{q_\pi^*}{q_{\pi R}^*} + b_{\pi\pi}$, and b_η , b_π and $b_{\pi\pi}$ are the branching ratios of the resonance.

The structure around $W = 1.6$ GeV in the cross section is visible for all angular ranges, but is less pronounced for the very forward and backward angles. The non-trivial shape changes across the angular range was also seen by Werthmüller *et al.* [56] in the deuteron data, as shown in Fig. 1.13. A fit of the ${}^3\text{He}$ data using a Breit-Wigner folded with experimental resolution yields a width of (46 ± 8) MeV for the narrow structure, as shown in Table 9.1 in parenthesis.

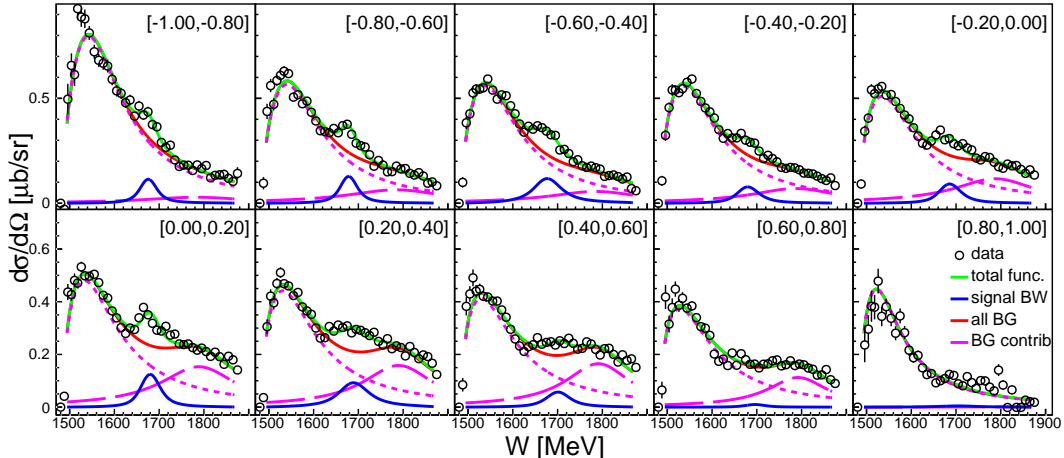


Figure 9.7: Differential cross sections as a function of the final state energy W for different angular bins for ${}^3\text{He}$. The total fit is indicated by the solid green line. The short dashed magenta line is the contribution from the $S_{11}(1535)$, the long dashed magenta line is the phenomenological background, the solid red line is the sum of the latter two. The Breit-Wigner fit for the narrow structure is shown as solid blue line.

9.2 Unpolarised Cross Section from LD₂ (CBELSA/TAPS)

For the CBELSA/TAPS deuterium data, differential and total cross sections were extracted as a function of the incident photon energy E_γ and the final state energy W . Since the reconstruction of the final state energy using the TOF technique has a much worse resolution, and only a very small angular range is covered by MiniTAPS, only the kinematical reconstruction was used to extract $W = m(N\eta)$.

9.2.1 Incident Photon Energy E_γ

Fig. 9.8 summarises the results of the total cross sections for the deuterium data obtained with the CBELSA/TAPS experiment. Shown are the cross sections for the case where the η meson was detected in coincidence with a recoil proton (σ_p) or neutron (σ_n), and the cross section without a condition for the recoil nucleon (σ_{incl}). Furthermore, to check the nucleon identification, the sum of the two exclusive cross sections is shown in magenta. Due to the hardware trigger configuration, only the $\eta \rightarrow 3\pi^0 \rightarrow 6\gamma$ decay was used to extract the results and the $\eta \rightarrow 2\gamma$ decay could not be used. The cross sections are compared to former results on the deuterium target from Ref. [55] (open symbols). It can be seen that all cross sections are in agreement with the previous results. For the neutron, as well as for the sum of the proton and neutron cross sections, a small deviation in the very top of the $S_{11}(1535)$ resonance is visible. This region of the $S_{11}(1535)$ peak is very sensitive to the nucleon detection efficiency. As explained in Sec. 8.8.1, no detection efficiency correction for the neutron could be extracted from hydrogen data as it was done for the proton. Hence, the deviations may originate from a less realistic neutron detection efficiency. However, in the energy region of interest for this work, i.e. above $E_\gamma = 900$ MeV, this effect is no more existent and the cross section agrees with the previous results, and the sum matches the inclusive cross section. This shows the quality of the reconstruction and that the background contributions, as well as trigger efficiencies, are well under control. For a better visibility, the exclusive results are also shown in Fig. 9.9 together with the corresponding systematic uncertainties (indicated at the bottom). In contrast to the ^3He data, the shoulder on the right side of the $S_{11}(1535)$ in the cross section on the neutron is more pronounced due to the smaller Fermi motion of deuterium.

The corresponding differential cross sections are shown in Fig. 9.10. Similar to the ^3He data, close to threshold ($E_\gamma \simeq 630$ MeV), the angular distributions are backward peaking due to the nuclear Fermi motion. Already above $E_\gamma = 800$ MeV, the distributions are rather flat. However, between 800 and 900 MeV, the proton and neutron distributions are slightly curved into opposite directions, which is an effect coming from the interference of the $S_{11}(1535)$ and the $D_{13}(1520)$ resonance. The $A_{3/2}$ helicity coupling for the $D_{13}(1520)$ resonance has a different sign for the proton and the neutron ($A_{3/2}^p \simeq 0.140 \pm 0.010 \text{ GeV}^{-1/2}$, $A_{3/2}^n \simeq -0.115 \pm 0.010 \text{ GeV}^{-1/2}$ [6]). Apart from the energies below 900 MeV the inclusive cross section is in reasonable agreement with the sum of the exclusive angular distributions.

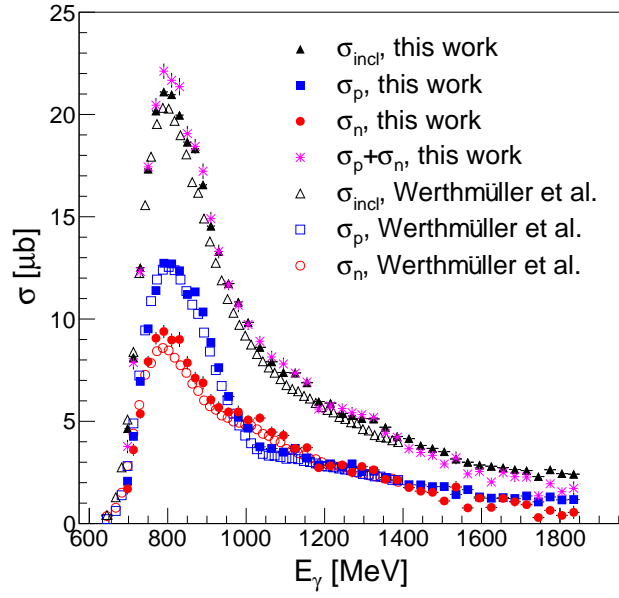


Figure 9.8: Total cross sections as a function of incident photon energy for LD₂. Shown are the results for the neutron σ_n (red circles), for the proton σ_p (blue squares), and for the inclusive reaction σ_{incl} (black triangles). The sum of the proton and neutron is shown as magenta stars. The results from this work (closed symbols) are compared to former results from Ref. [55] (open symbols).

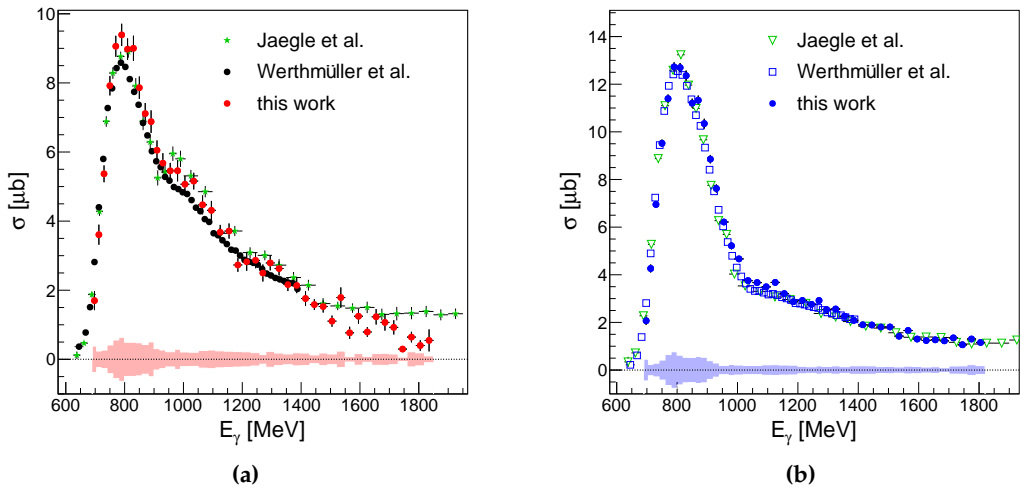


Figure 9.9: Total cross sections as a function of the incident photon energy E_γ for LD₂. The results on the neutron (red circles) are shown in (a), the results on the proton (blue squares) are shown in (b). The systematic uncertainties are indicated at the bottom, not including 10% overall normalisation uncertainty. The results are compared to former results from Ref. [55] (green closed triangles), and from Ref. [51] (black open triangles).

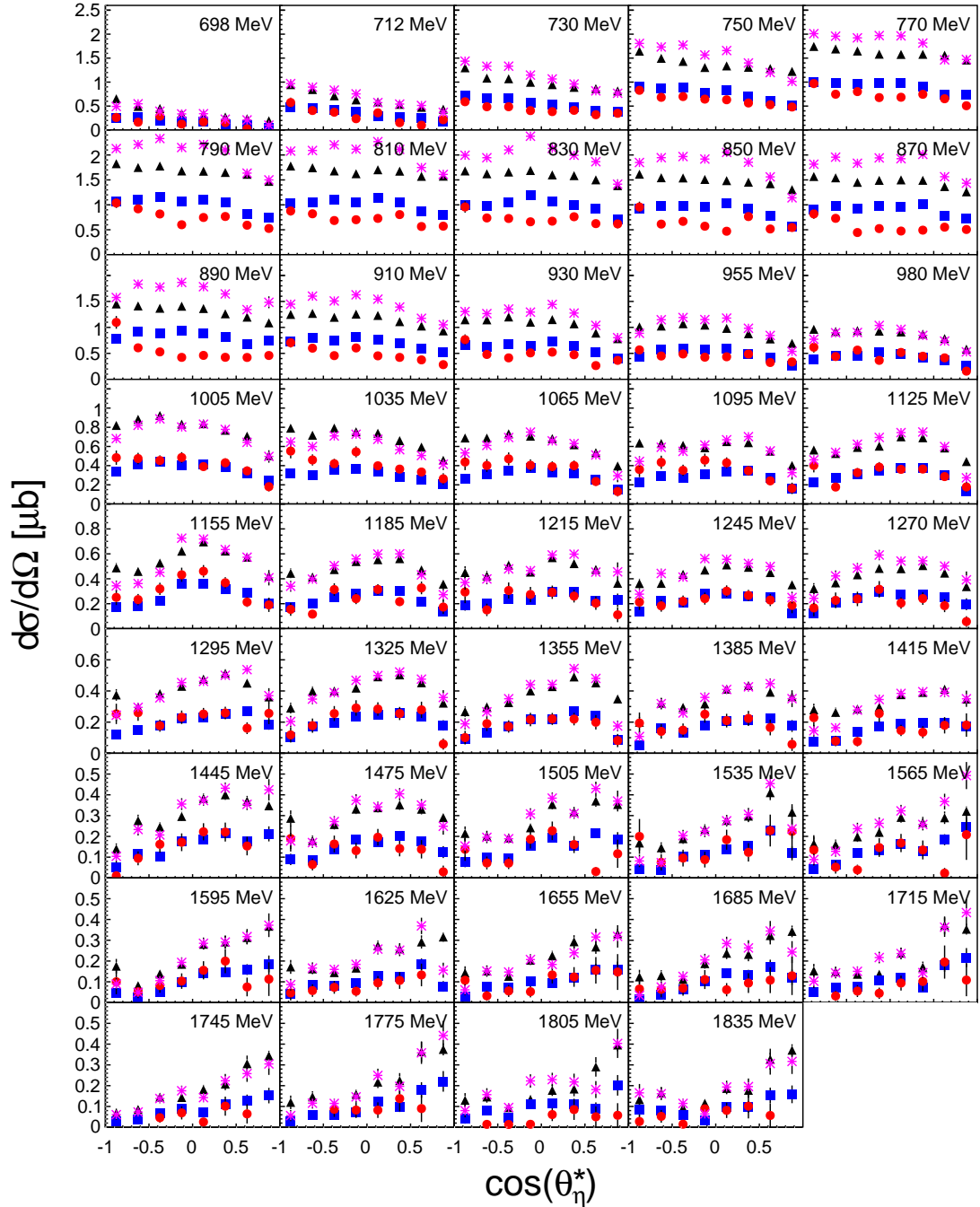


Figure 9.10: Differential cross sections for LD₂ for bins of incident photon energy E_γ . Shown are results for the reaction on the neutron σ_n (red circles) and on the proton σ_p (blue squares). The quasi-free inclusive reaction σ_{incl} is indicated by black triangles and the magenta stars show the reconstructed inclusive $\sigma_p + \sigma_n$ cross sections.

9.2.2 Final State Energy W

Analogous to the ${}^3\text{He}$ data, cross sections were extracted as a function of the final state energy W using the kinematical reconstruction of the recoil nucleon to eliminate effects from Fermi motion. The total cross sections are shown in Fig. 9.11 together with the corresponding systematic uncertainties, and are compared to previous results on the deuteron target from Ref. [51, 55] (open symbols). The total cross sections were extracted from the angular distributions using third order Legendre polynomial fits. Within the statistical and systematic uncertainties, the total cross section on the neutron, shown in Fig. 9.11 (a), agrees with the measurement by Werthmüller *et al.* [55] (open red circles). The narrow structure around 1.68 GeV is clearly beyond statistical fluctuations and in agreement with the results by Werthmüller *et al.* However, both peak structures, the $S_{11}(1535)$ and the narrow bump, are slightly sharper. This may be an effect coming from the better W resolution in the CBELSA/TAPS experiment, as shown in Fig. 8.2. As already mentioned, for the $S_{11}(1535)$, this effect may also be caused by a less realistic neutron detection efficiency. However, in the region of the narrow structure, the nucleon efficiency correction has essentially no influence. In contrast, when comparing the present results to the former results by Jaegle *et al.*, it is quite striking that the whole flank on the right side of the $S_{11}(1535)$ is significantly lower than measured by Jaegle *et al.* [51].

Fig. 9.12 compares the corresponding angular distributions. Apart from the very forward and backward bin, the shape and magnitude of the cross sections is consistent with the angular distributions by Werthmüller *et al.* As seen for the angular distributions of the neutron shown in Fig. 8.13, the most forward and backward bins have a

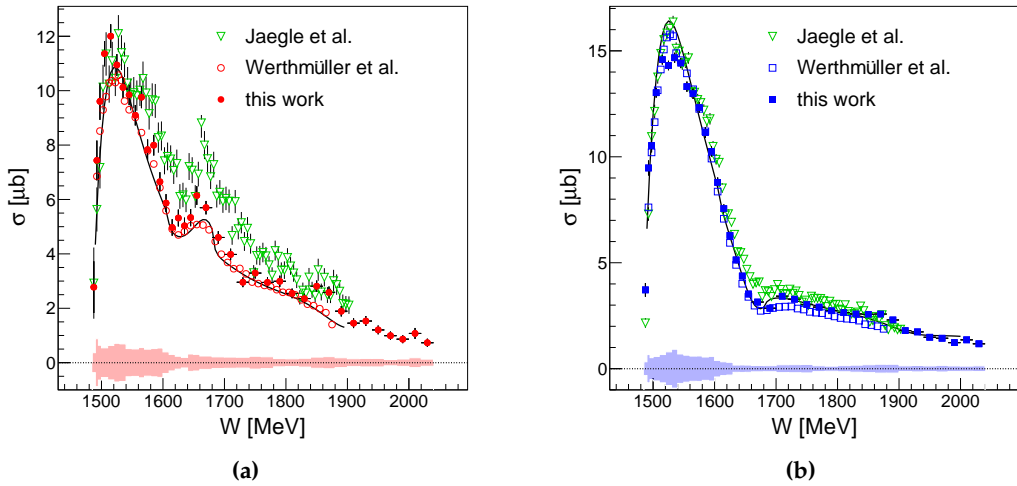


Figure 9.11: Total cross sections as a function of the final state energy W for LD_2 . The results on the neutron (red circles) are shown in (a), the results on the proton (blue squares) are shown in (b). The systematic uncertainties are indicated at the bottom, not including 10% overall normalisation uncertainty. The results are compared to former results from Ref. [55] (green closed triangles), and from Ref. [51] (black open triangles).

very small detection efficiency and are thus very sensitive, leading to a larger systematic uncertainties than the other bins. This is even more apparent in the differential cross sections on the proton, shown in Fig. 9.13. There, for energies between 1515 MeV and 1555 MeV, the most forward bin is always slightly too low, inducing a small deviation in the total cross section in the peak of the $S_{11}(1535)$ resonance, as seen in Fig. 9.11 (b). However, for all other energy ranges the agreement with the former results is almost perfect, demonstrating that the systematic uncertainties are well under control.

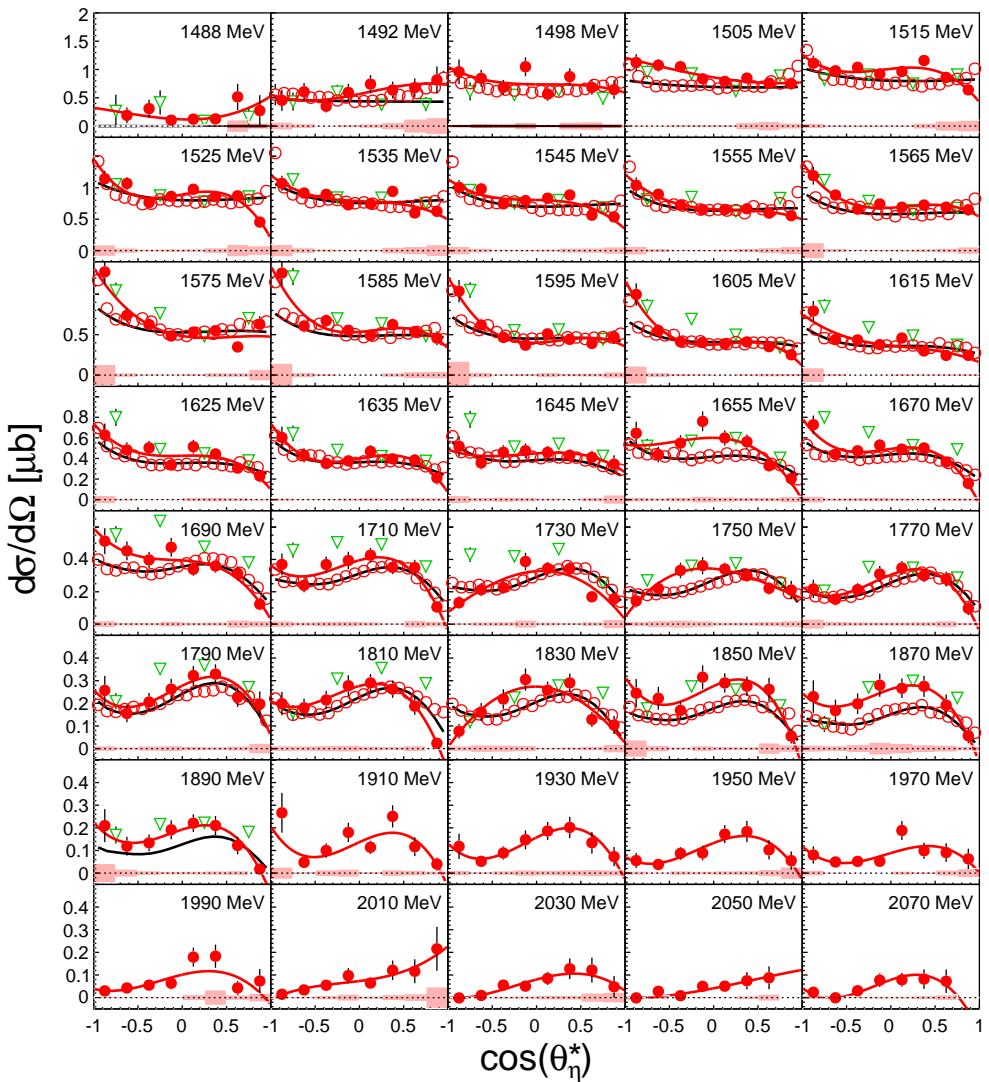


Figure 9.12: Differential cross sections as a function of the final state energy W for $\gamma n \rightarrow \eta n$. Data from present LD₂ measurement (red closed circles) are compared to data from the deuterium target from Ref. [55] (red open circles) and Ref. [51] (green open triangles). The Legendre fits are indicated by solid lines. The systematic uncertainties are indicated at the bottom, not including 10% overall normalisation uncertainty.

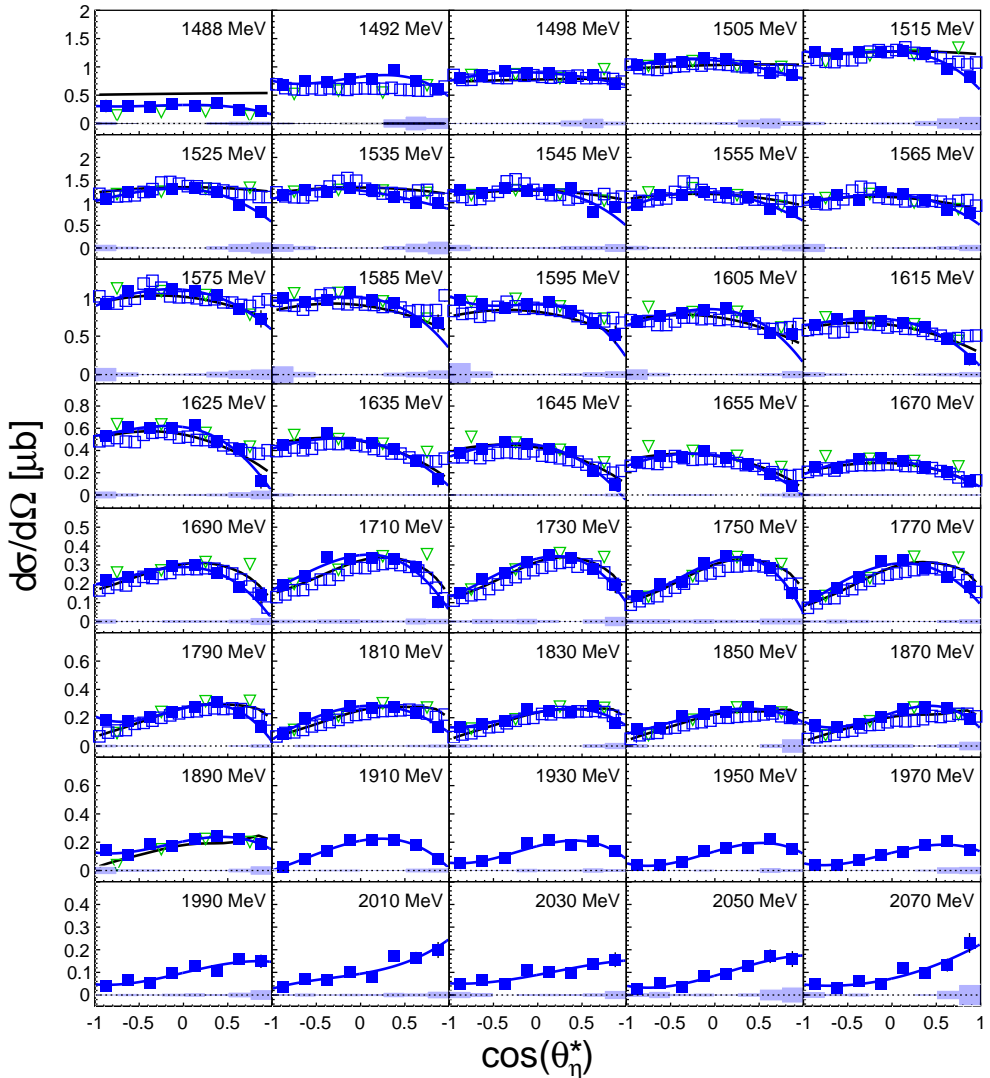


Figure 9.13: Differential cross sections as a function of the final state energy W for $\gamma p \rightarrow \eta p$. Data from present LD₂ measurement (blue closed squares) are compared to data from the deuterium target from Ref. [55] (blue open circles) and Ref. [51] (green open triangles). The Legendre fits are indicated by solid lines. The systematic uncertainties are indicated at the bottom, not including 10% overall normalisation uncertainty.

To further investigate the narrow structure on the neutron, the cross section as a function of the final state energy W was fitted with the same function that was used in Fig. 9.3. The result is compared to the fit of the former deuterium data by Werthmüller *et al.* in Fig. 9.14. Shown are the contributions from the $S_{11}(1535)$ (dash-dotted line) resonance, from the broad background Breit-Wigner (dotted line), and from the Breit-Wigner of the narrow structure (dashed line). The total fit function (solid line) nicely describes the data. The insert shows the ratio of the neutron and proton cross section, and compares it to the former results by Jaegle *et al.* The ratio depicts that the position and width of the structure are in agreement for all measurements. However, the ratio for the results by Jaegle *et al.* is slightly larger, which is caused by the more pronounced

structure in the cross section on the neutron. The fit parameters for the present data and the data by Werthmüller [52] are summarised in Table 9.2. For the present data, the position was determined to be (1667 ± 3) MeV and the width is (35 ± 3) MeV, which is consistent with the former results. Accounting for the experimental resolution in the fit, the width is reduced to only (23 ± 2) MeV.

		W_R [MeV]	Γ [MeV]	$\sqrt{b_\eta} A_{1/2}^n$ [10^{-3} GeV $^{1/2}$]
this work	narrow state	1667 ± 3	35 ± 3 (23 ± 2)	13.4 ± 2
	$S_{11}(1535)$	1525 ± 2	146 ± 13	82 ± 4
Werthmüller <i>et al.</i> [52]	narrow state	1670 ± 1	50 ± 2 (29 ± 3)	12.3 ± 0.8
	$S_{11}(1535)$	1529 ± 1	188 ± 12	90 ± 3

Table 9.2: Fit parameters of the fits shown in Fig. 9.14. The position W_R , the width Γ_R , and the electromagnetic coupling $\sqrt{b_\eta} A_{1/2}^n$ are given for the narrow state and the $S_{11}(1535)$ resonance. The width in the parentheses was extracted from a fit, which has been convoluted with experimental resolution. The indicated errors are pure statistical errors.

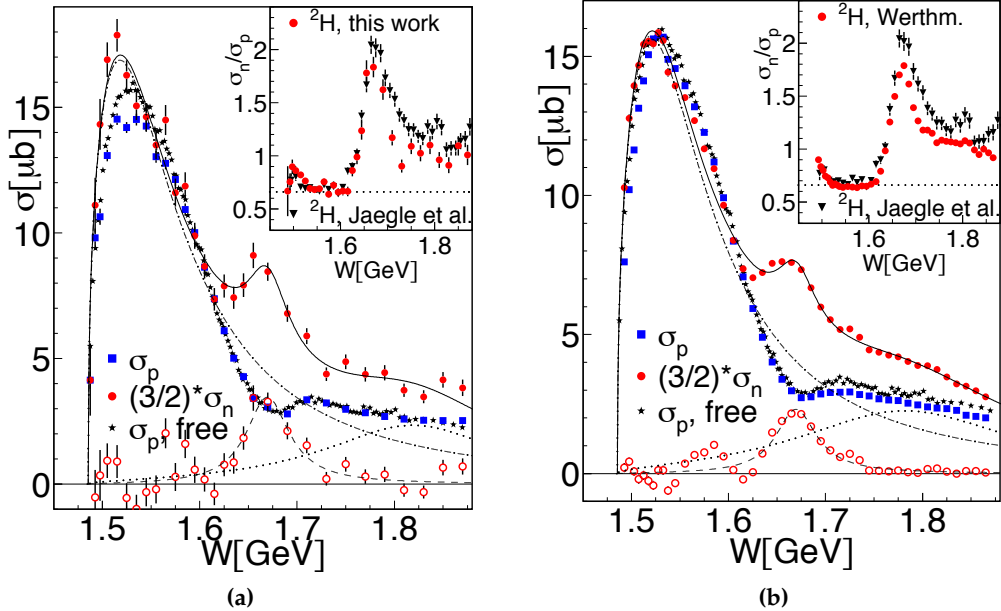


Figure 9.14: Total cross sections as a function of the final state energy W for LD₂. (a) The results from this work are fitted with Breit-Wigner functions. The parameters are given in Table 9.2. The results are compared to previous results on the free proton target [110]. The insert compares the ratio of the neutron and proton cross section to results on LD₂ by Jaegle *et al.* [51] (closed triangles) (b) The same as in (a) for the former results from Ref. [52]. Figure (b) taken from [52].

To investigate the angular dependence of the narrow structure, the cross section

was determined for twelve different bins of polar cm angle and fitted with Breit-Wigner distributions, as shown in Fig. 9.15. The corresponding integrals of the three Breit-Wigner distributions are shown for different angular bins in Fig. 9.16 together with the previous results by Werthmüller *et al.* [55]. The distribution of the integral for the S_{11} and the broad background Breit-Wigner is very similar to the previous results by Werthmüller *et al.* However, the integral of the narrow Breit-Wigner peaks more at backward angles and the distribution is flatter than in the previous results by Werthmüller *et al.*

Figs. 9.15 and 9.16 show that the narrow structure is less pronounced at very forward angles as it was already seen by Werthmüller *et al.* [55]. At backward angles, the structure is still distinct, which is somehow contradictory to the situation observed by Werthmüller *et al.* As mentioned in Sec. 1.4.1, in the new model by the BnGA group, the neutron cross section of Werthmüller *et al.* can be reproduced by an interference of the $S_{11}(1535)$ and the $S_{11}(1650)$ resonances. This interference leads to the effect that the narrow structure at 1.68 GeV almost disappears at very forward and backward angles. Fits with a narrow resonance $N(1685)$ would lead to an anti-symmetric angular distribution with a bump at backward angles and no sign at forward angles (or vice-versa) and hence were ruled out in Ref. [48]. However, the present data is not in contradiction to such a scenario, as can also be seen in Fig. 9.17, where the results of this work are compared to the three different fits by BnGa from Ref. [48]. The fit with the narrow resonance and a positive $A_{1/2}$ coupling (P_{11} , pos, green solid line) reproduces the data quite well, whereas the narrow structure in the fit with the negative $A_{1/2}$ (P_{11} , neg, blue dotted line) coupling is too strong at forward angles. The description of the experimental data with the fit without the narrow resonance (S_{11} , red dashed line) seems do be inferior especially at forward angles.

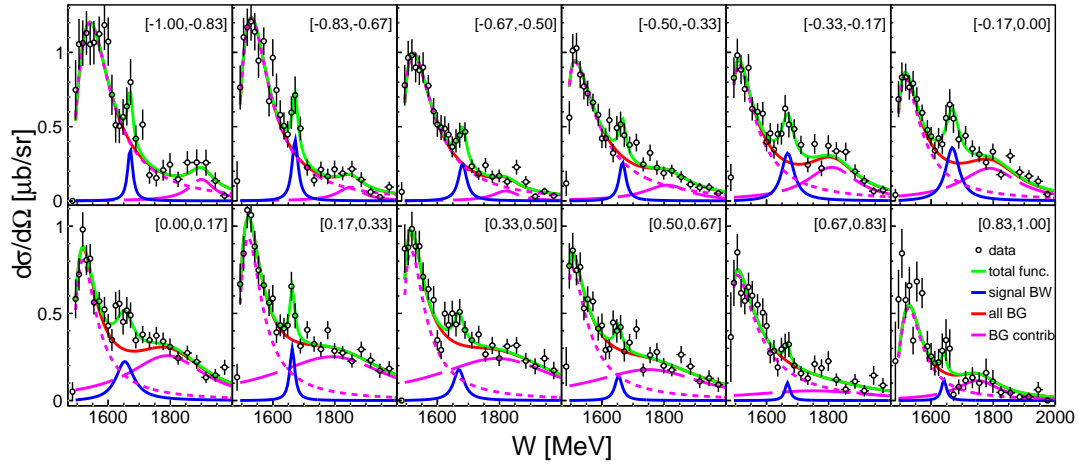


Figure 9.15: Differential cross sections as a function of the final state energy W for different angular bins for LD₂. The total fit is indicated by the solid green line, the short dashed magenta line is the contribution from the $S_{11}(1535)$, the phenomenological background is indicated by the long dashed magenta line, and the red solid line shows the sum of the latter two. The Breit-Wigner fit for the narrow structure is shown as a solid blue line.

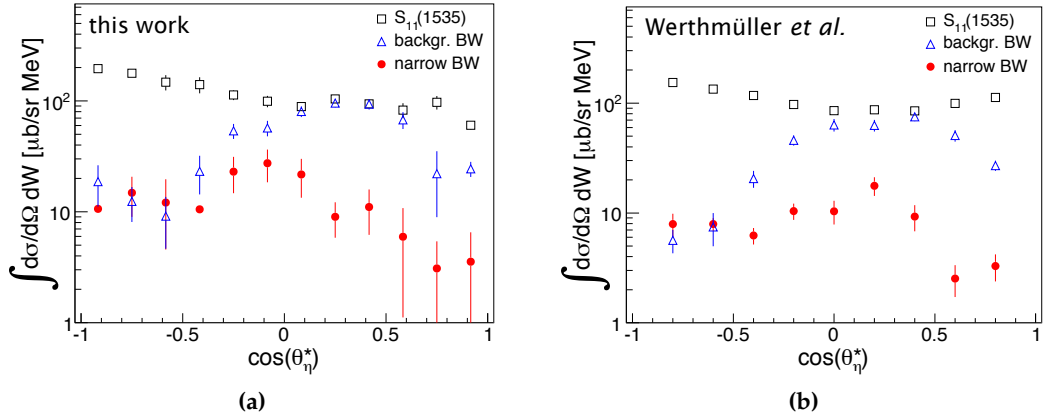


Figure 9.16: Integral of the Breit-Wigner (BW) fits shown in Fig. 9.15 for different angular bins. The integral of the S_{11} BW is shown as open, black squares, the integral of the background function is shown as open, blue triangles, and the integral of the narrow BW is shown as red dots. The fits of the first and fourth angular bins did not converge, hence the errors could not be calculated. The results from this work (a) are compared to previous results by Werthmüller *et al.* (b). Figure (b) taken from [55].

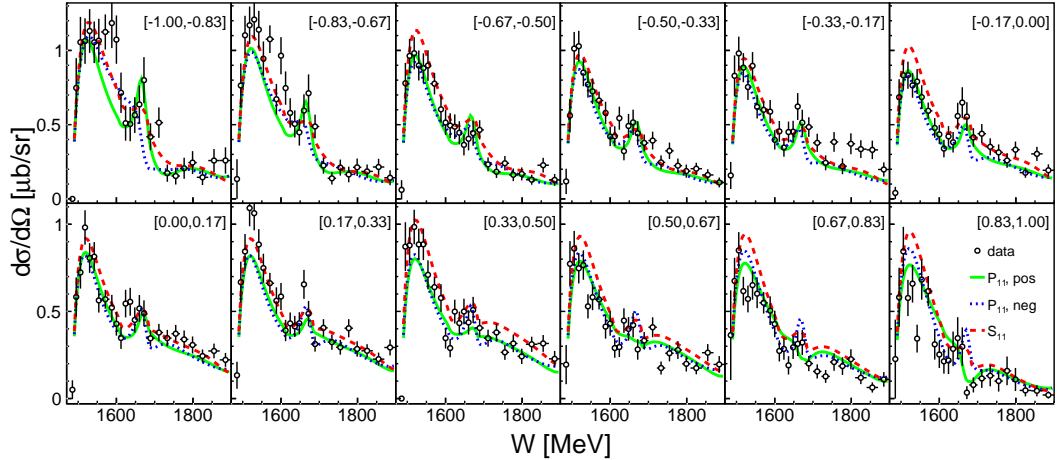


Figure 9.17: Differential cross sections as a function of the final state energy W for different angular bins for LD₂ compared to different BnGa model predictions: fit with a narrow $N(1685)$ resonance with positive (green solid line) or negative (blue dotted line) $A_{1/2}$ coupling, and fit without a narrow resonance (red dashed line).

9.3 Polarisation Observable E from CBELSA/TAPS Data

The double polarisation observable E and the helicity dependent cross sections were extracted for the quasi-free proton and neutron targets using CBELSA/TAPS data. Due to a fire incident in the experimental hall, the experiment had to be aborted. Hence, the available statistics is very limited and allowed only the reaction on the proton to be measured in an exclusive way. The reaction on the neutron was measured inclusively to improve statistics, as mentioned in Sec. 7.1. Since in the inclusive reaction the recoil neutron is not detected, the observables for the neutron could only be determined as a function of the incident photon energy E_γ and not as a function of the final state energy W . Hence, the resulting observables show effects from Fermi motion. However, for the case of the proton, the polarisation observable E , and the helicity dependent cross sections $\sigma_{1/2}$ and $\sigma_{3/2}$ were also extracted as a function of the final state energy and thus are not affected by Fermi motion. The final results are shown in Sec. 9.3.2. First, some consistency checks will be explained in Sec. 9.3.1 to demonstrate the quality of the obtained results.

9.3.1 Consistency Checks

Different consistency checks were performed, namely investigating the inclusive reaction, evaluating the quality of the carbon subtraction, and checking the robustness of the measured asymmetry. The results of these checks will be discussed in this section.

Inclusive Reaction on the Neutron

The inclusive reconstruction of the reaction $\gamma n \rightarrow \eta(n)$, i.e. not requiring the recoil neutron, may lead to additional background, hence the identification had to be thoroughly checked. As explained in Sec. 7.1, the background from charged particles was sufficiently reduced by requiring no hit in the charge sensitive detectors. To verify the final reaction identification, the unpolarised inclusive cross section for η photoproduction off the neutron bound in deuterium was measured and compared to the exclusive results, shown in Fig. 9.18 (a). The corresponding angular distributions are shown in Fig. 9.18 (a). Furthermore, the obtained cross sections are compared to Fermi folded model predictions by BnGa [48]. The systematic uncertainties are indicated by the red shaded areas, not including 10% overall normalisation uncertainty. The inclusive cross section (closed circles) is in agreement with the exclusive measurement (open circles) and the Fermi folded model prediction by BnGa (solid black line). Small deviations appear in the very top of the $S_{11}(1535)$ resonance, which originate from the most forward $\cos(\theta_\eta^*)$ bin in the angular distributions. Overall the angular distributions are much smoother than for the exclusive case, which can be partly assigned to the better statistics, but also to the less sensitive detection efficiency.

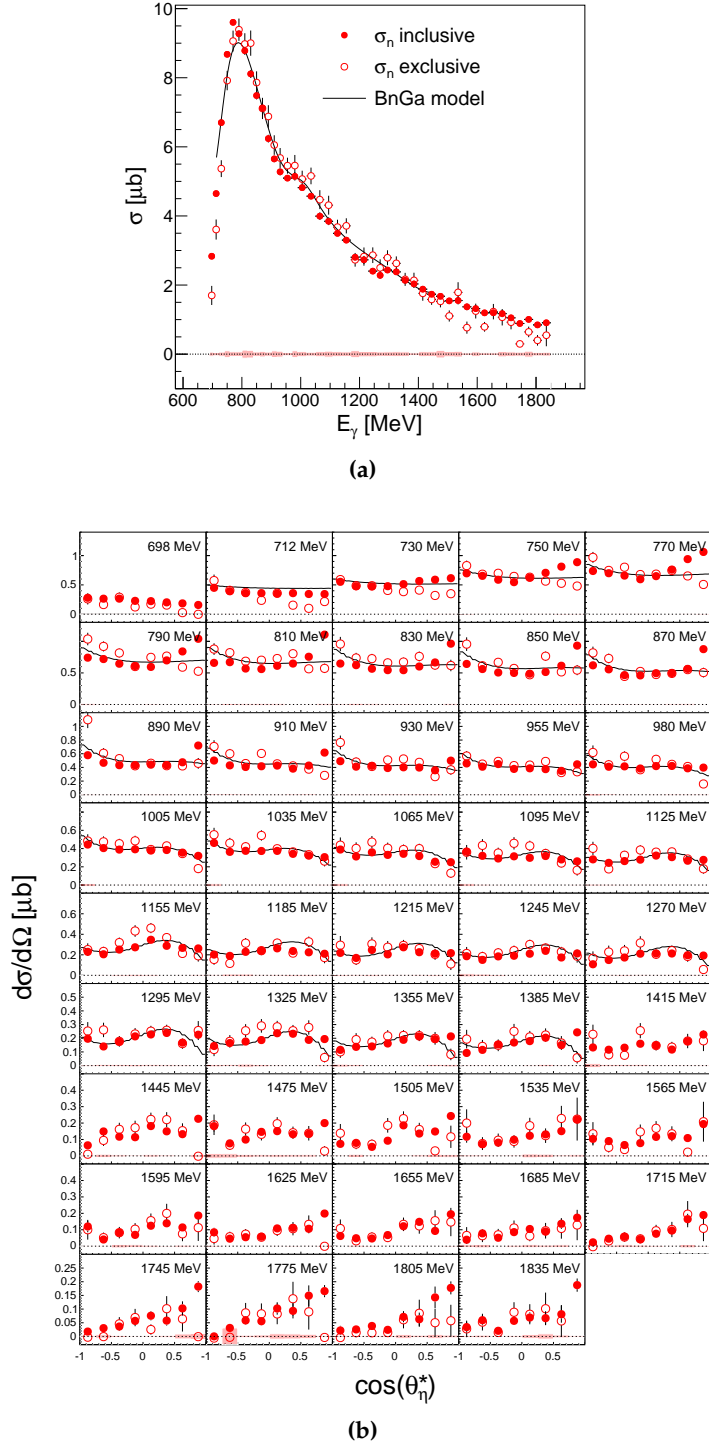


Figure 9.18: Total cross section (a) and angular distributions (b) for inclusive η photoproduction on the neutron for CBELSA/TAPS data (closed circles) for different bins of E_γ . The data are compared to the exclusive analysis (open circles) and BnGA model predictions [48] that were folded with Fermi motion (black line). The systematic uncertainties for the inclusive reaction are indicated at the bottom (very small), not including 10% overall normalisation uncertainty (identical for both data sets).

Carbon Subtraction

As explained in Sec. 8.2 the sum of the two helicity states, $\sigma_{sum} = \sigma_{1/2} + \sigma_{3/2}$, is equal to twice the unpolarised cross section:

$$\sigma_{sum} = 2\sigma \quad (9.2)$$

Eq. 9.2 is only valid if the carbon was properly subtracted previously, as described in Sec. 8.10. Hence, this condition was used to verify the carbon subtraction. Fig. 9.19 compares σ_{sum} after the carbon subtraction to twice the unpolarised cross section on deuterium. The results are shown for the proton (a) and the neutron (b). The flux normalisation factor of 1.6, introduced in Sec. 8.6.2, was used to get a correct normalisation. Within the statistical uncertainties, the results are consistent, which demonstrates the reliability of the carbon subtraction.

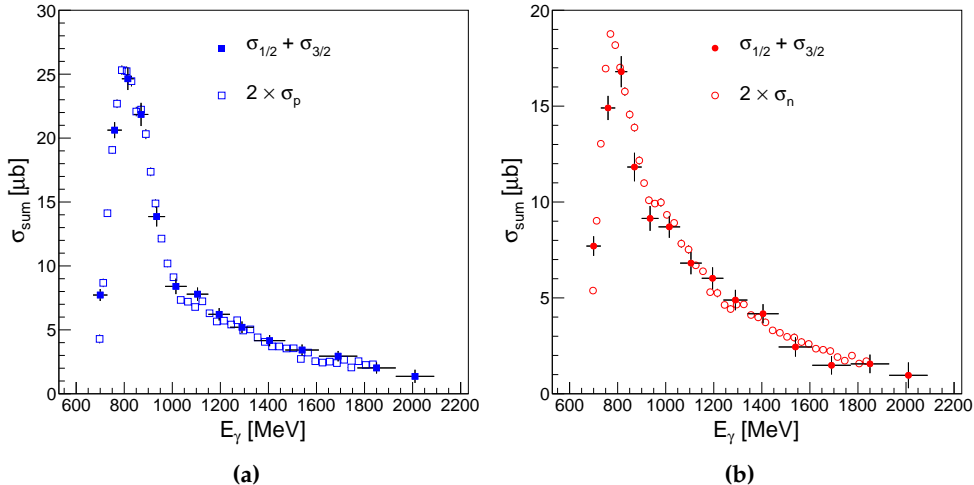


Figure 9.19: The sum of the two helicity states σ_{sum} obtained with the carbon subtraction method (closed symbols) is compared to twice the unpolarised cross section (open symbols). The sum was normalised by a factor of 1.6 to account for the flux normalisation issue mentioned in Sec. 8.6.2. The results are shown for (a) the recoil proton and (b) the recoil neutron.

Positive and Negative Target Polarisation

Experimental data were taken with the target polarisation in the positive and negative z -direction. Hence, there are always two ways to get a parallel $\sigma_{3/2}$ or an anti-parallel $\sigma_{1/2}$ configuration of the nucleon and photon spin. Using correct polarisation values and normalisations, the following two ways should yield identical results:

$$E = \frac{\sigma_{+-} - \sigma_{++}}{\sigma_{+-} + \sigma_{++}} = \frac{\sigma_{-+} - \sigma_{--}}{\sigma_{-+} + \sigma_{--}}, \quad (9.3)$$

where the first of the two signs stands for the z -direction of the target polarisation, and the second sign represents the photon helicity. Hence, σ_{diff} and σ_{sum} should be independent of the target polarisation direction. Fig. 9.20 shows σ_{diff} (a) and σ_{sum} (b) for the reaction on the proton using experimental data with positive (closed symbols) and negative (open symbols) target polarisation direction. Only small deviations can be seen, which are well within the statistical uncertainties. This comparison emphasises that the measured asymmetry is robust against changes of the target polarisation and is stable over time. For the recoil neutron, the check is not very informative due to the poor statistics. However, since the identical polarisation values and the same analysis technique was used, Eq. 9.3 must hold for the case of the neutron as well.

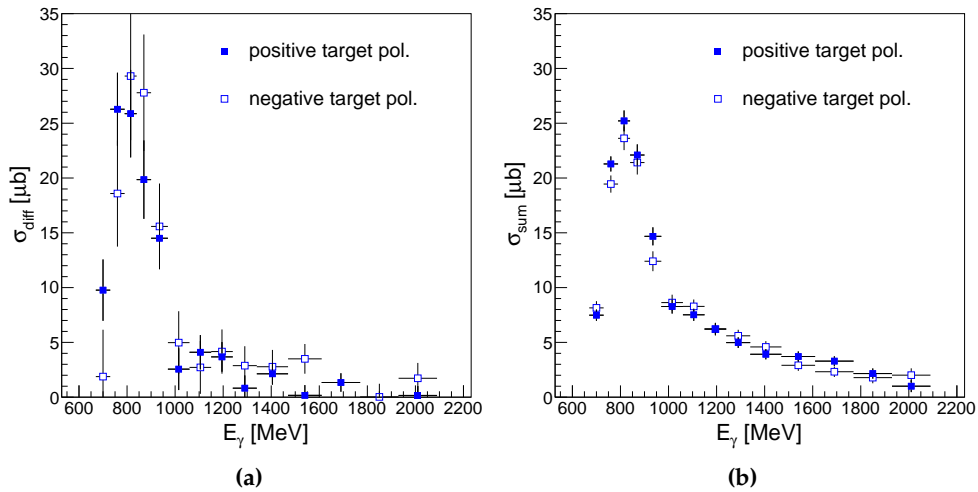


Figure 9.20: (a) σ_{diff} and (b) σ_{sum} for positive (closed squares) and negative (open squares) direction of the target polarisation for quasi-free protons.

9.3.2 Results

As mentioned in Sec. 8.2, the double polarisation observable E was extracted via two different methods, one using the carbon subtraction (*version 1*) and one by normalising with the unpolarised cross section (*version 2*). For the CBELSA/TAPS data, *version 2* could only be used when the flux was corrected with a factor of 1.6, which was explained in Sec. 8.6.2. However, this factor does not play a role in *version 1* since it cancels there. To normalise the asymmetry in *version 2*, the unpolarised cross sections, which were presented in Sec. 9.2, were used.

The results for the double polarisation observable E for both versions as a function of the incident photon energy are shown in Fig. 9.21 together with Fermi folded model predictions by MAID [179] and BnGa [48] (fit without narrow $N(1685)$). For a better visibility, the values of the points from *version 2* were shifted by +5 MeV. The systematic uncertainties were determined as explained in Sec. 8.12.2 and are indicated by the shaded areas.

For both reactions (proton and neutron recoil), the results from the carbon subtrac-

tion (*vers.* 1) and the direct measurement (*vers.* 2) are consistent, which demonstrates that the cross sections were normalised correctly.

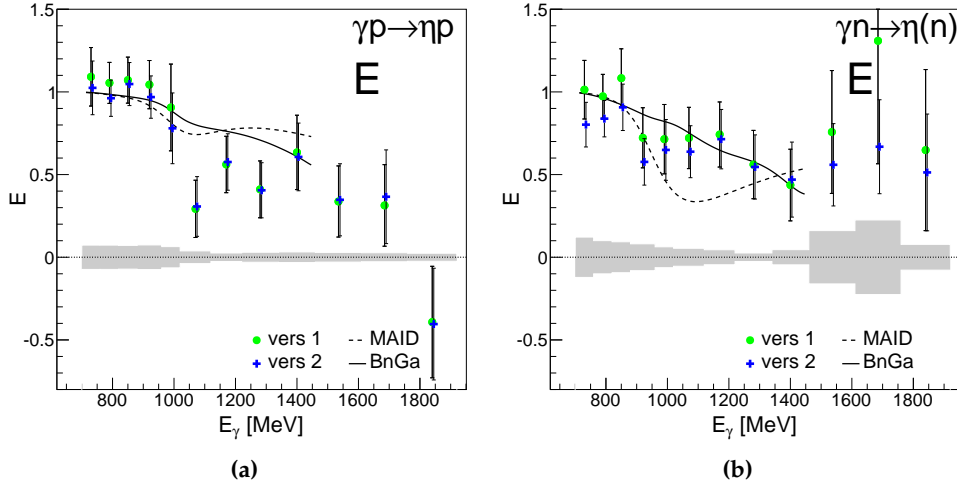


Figure 9.21: Polarisation observable E extracted from CBELSA/TAPS data. The results are shown for the exclusive reaction on the proton (a) and the inclusive reaction on the neutron (b) as a function of the incident photon energy. The results are compared to Fermi folded model predictions by MAID [179] (dashed line) and BnGa [48] (solid line). The systematic uncertainties are indicated by the gray shaded areas. For a better visibility, the points from version 2 (normalisation with the unpolarised cross section) were shifted by +5 MeV with respect to version 1 (carbon subtraction method).

The polarisation observable E for the proton, shown in Fig. 9.21 (a), is unity close to threshold, as predicted by the models due to the dominance of the S_{11} resonances. Both, the $S_{11}(1535)$ and $S_{11}(1650)$ resonance only couple to $\sigma_{1/2}$ due to their spin structure. Hence, over a wide energy range, $\sigma_{1/2}$ is larger than $\sigma_{3/2}$, which is also confirmed by the experimental results shown in Figs. 9.22 (a) and (b). However, above 1 GeV incident photon energy, the measured double polarisation observable E is lower than predicted by the MAID and BnGa models. Around 1.8 GeV photon energy, E becomes negative, and hence $\sigma_{3/2}$ is larger than $\sigma_{1/2}$. The models have no predictions for these high energies.

For the neutron, shown in Fig. 9.21 (b), the measured observable is in agreement with the model predictions by BnGa, which predicts a slow falloff to higher energies. The falloff implies a moderate increase of the $\sigma_{3/2}$ cross section, as seen in Fig. 9.22 (d). The BnGa group has found small contributions from resonances with spin-parity $3/2^+$, $3/2^-$, and $5/2^+$. In contrast, the MAID model predicts a distinct dip for E around an incident photon energy of 1 GeV on the neutron, and a peak in the $\sigma_{3/2}$ cross section, which corresponds to a large contribution of the $D_{15}(1675)$ resonance. According to the PDG [6], the $D_{15}(1675)$ resonance has a larger coupling to the $3/2$ than to the $1/2$

helicity state:

$$A_{1/2}^n = (-0.060 \pm 0.005) \text{ GeV}^{-1/2} \quad (9.4)$$

$$A_{3/2}^n = (-0.085 \pm 0.010) \text{ GeV}^{-1/2} \quad (9.5)$$

Furthermore, the contribution of the $D_{15}(1675)$ to $\sigma_{1/2}$ is much smaller than the con-

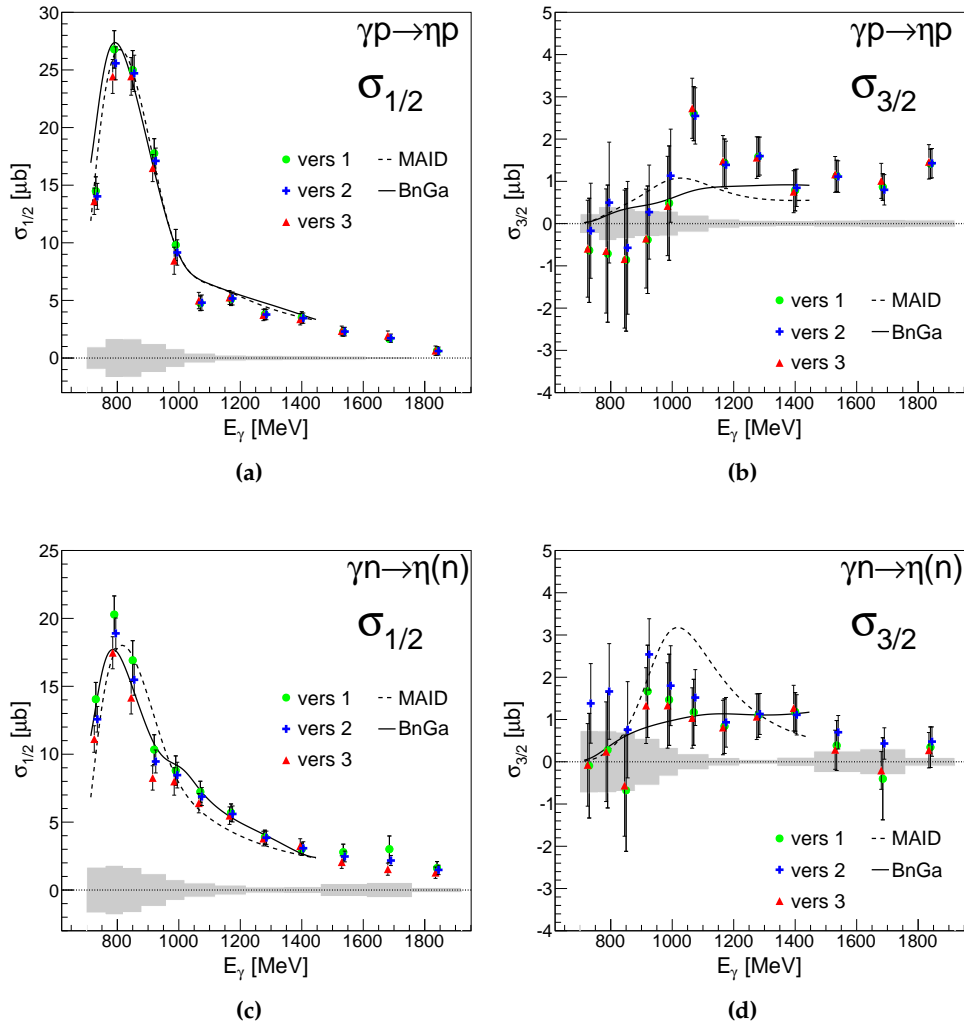


Figure 9.22: Helicity dependent cross sections extracted from CBELSA/TAPS data. The results are shown for the exclusive reaction on the proton (a), (b), and the inclusive reaction on the neutron (c), (d), as a function of the incident photon energy. The results are compared to Fermi folded model predictions by MAID [179] (dashed line) and BnGa [48] (solid line). The systematic uncertainties are indicated by the gray shaded areas. For a better visibility, the points from version 2 (normalisation with the unpolarised cross section) and version 3 (only polarised data) were shifted by ± 5 MeV with respect to version 1 (E via carbon subtraction, helicity dependent cross sections with the unpolarised cross sections, as given in Eqs. 8.15 and 8.16).

tribution of the two strong S_{11} resonances. In the MAID model, the influence of the $D_{15}(1675)$ resonance to the proton cross section is much smaller than to the neutron cross section. However, as mentioned in Sec. 1.4.1, the PDG predicts a branching ratio for ηN of almost zero percent. The results obtained from this work cannot reproduce the peak-like structure in $\sigma_{3/2}$, as seen in Fig. 9.22 (d). However, the interpretation of the experimental results is not straightforward due to the limited statistics.

In addition to the results as a function of the incident photon energy, the observables were extracted as a function of the final state energy W for the proton. The results are shown in Figs. 9.23 and 9.24, and are compared to the model predictions for the free proton. Up to a final state energy of $W = 1.75$ GeV, the results are in agreement with both models. The worse statistical quality of the data for higher energies makes an interpretation of the results more difficult.

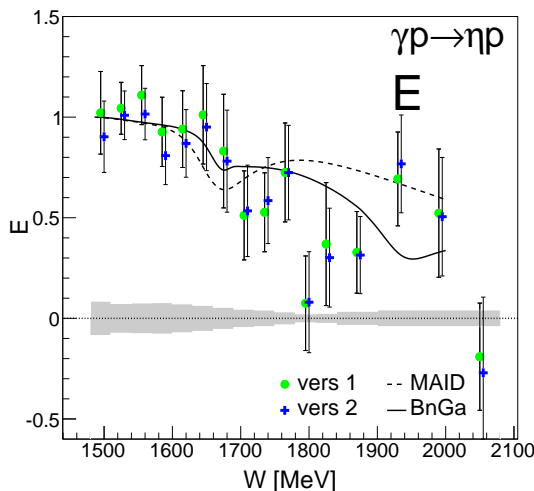


Figure 9.23: Polarisation observable E extracted from CBELSA/TAPS data for the exclusive reaction on the proton as a function of the incident photon energy. The results are compared to model predictions by MAID [179] (dashed line) and BnGa [48] (solid line) for the free proton. The systematic uncertainties are indicated by the gray shaded areas. For a better visibility, the points from version 2 (normalisation with the unpolarised cross section) were shifted by +5 MeV with respect to version 1 (carbon subtraction).

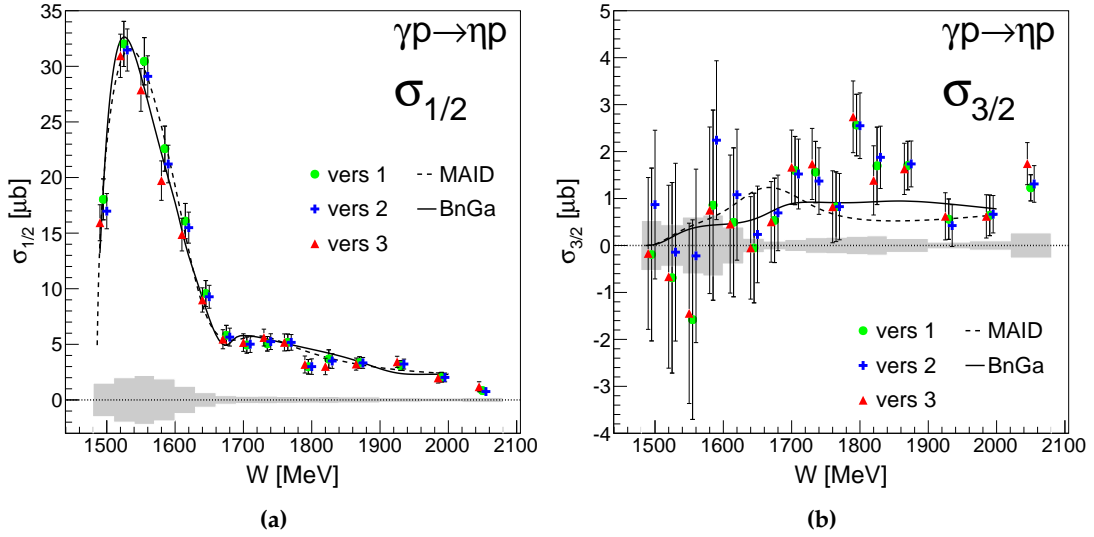


Figure 9.24: Helicity dependent cross sections $\sigma_{1/2}$ (a) and $\sigma_{3/2}$ (b) extracted from CBELSA/TAPS data. The results are shown for the exclusive reaction on the proton as a function of the final state energy. The results are compared to model predictions by MAID [179] (dashed line) and BnGa [48] (solid line) for the free proton. The systematic uncertainties are indicated by the gray shaded areas. For a better visibility, the points from version 2 (normalisation with the unpolarised cross section) and version 3 (only polarised data) were shifted by ± 5 MeV with respect to version 1 (E via carbon subtraction, helicity dependent cross sections with the unpolarised cross sections, as given in Eqs. 8.15 and 8.16).

9.4 Polarisation Observable E from A2 Data

Fig. 9.25 shows the preliminary results obtained by the measurement of the double polarisation observable E with the A2 experiment. As can be seen, the measured double polarisation observable E is missing a factor of ~ 1.5 close to threshold compared to the expected value of $E = 1$ for both, proton and neutron. The small asymmetry E is correlated with a large contribution of the $\sigma_{3/2}$ cross section and a too small $\sigma_{1/2}$ cross section. To find the origin of this issue, consistency checks were performed, which are explained in Sec. 9.4.1. The final results will then be presented in Secs. 9.4.2 and 9.4.3 as a function of the incident photon energy and the final state energy.

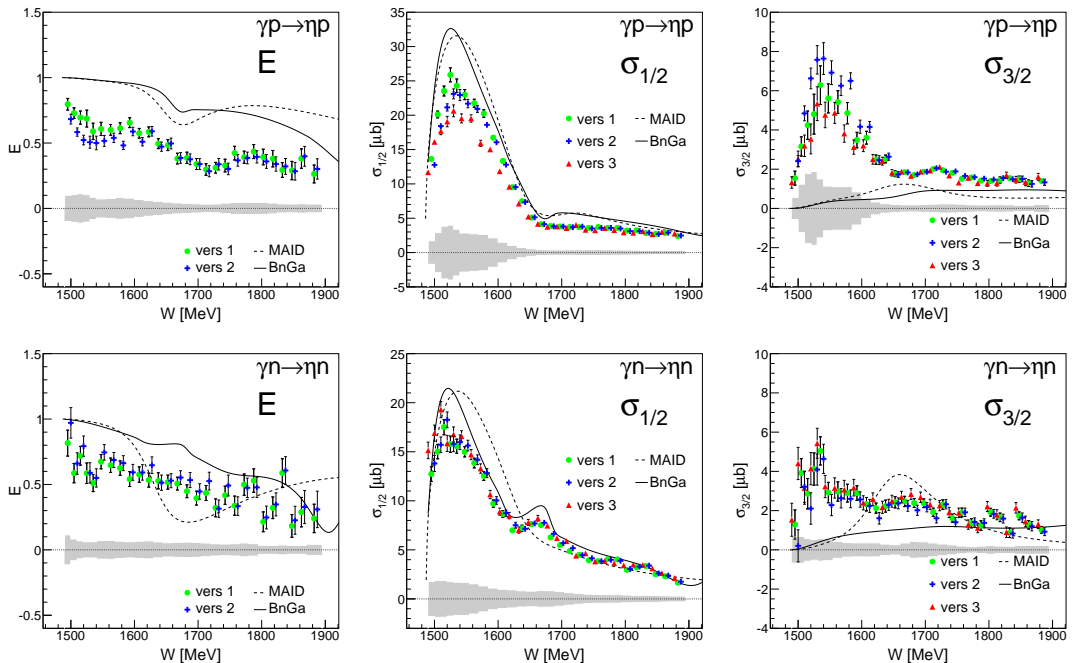


Figure 9.25: Double polarisation observable E and helicity dependent cross sections for the proton (first row) and for the neutron (second row) using the measured target polarisation values. The experimental asymmetry is a factor of ~ 1.5 lower than predicted by the models and seen in the CBELSA/TAPS results. For a better visibility, the points from version 2 and version 3 were shifted by ± 5 MeV with respect to version 1.

9.4.1 Consistency Checks

There are various reasons, which can cause too small double polarisation observable E , which manifests either in the sum of the two helicity states, σ_{sum} , or the difference of the two helicity states, σ_{diff} . Essentially, a too small double polarisation observable E may be caused by a too large σ_{sum} or a too small σ_{diff} or a combination of the latter two.

The carbon subtraction has a large influence on σ_{sum} and hence was checked first. Furthermore, the carbon subtraction was used to verify the overall normalisation.

However, as explained in Sec. 8.2.1, the overall normalisation should not have an influence on the results, which were extracted according to *version 1*.

On the other hand, the magnitude of σ_{diff} depends predominantly on the polarisation degree of the target and the incident photon beam. Whereas there is no possibility to check the target polarisation using the data (except the double polarisation observable E for η photoproduction), the beam polarisation could be checked using the beam helicity asymmetry I^\odot in double pion production.

A third possibility is that an error in the analysis may be the origin of the problem. However, the latter was essentially ruled out by the fact that the CBELSA/TAPS data was processed using the same analysis procedures, and yielded the expected results. Furthermore, for the verification of the analysis, A2 HButanol data was analysed to extract results for the free proton. In addition, the stability of the extracted asymmetry over time was checked.

All these checks will be discussed in detail in the following section.

Carbon Subtraction

As it was done for the CBELSA/TAPS data, the quality of the carbon subtraction in the A2 data was checked by comparing the carbon subtracted sum of the two helicity states, σ_{sum} , to twice the unpolarised cross section. The results are shown in Fig. 9.26 as a function of the final state energy W . Both decay channels of the η meson, $\eta \rightarrow 2\gamma$ and $\eta \rightarrow 6\gamma$, and the weighted average are shown. They are consistent over the whole energy range. For the proton, shown in Fig. 9.26 (a), deviations of σ_{sum} from

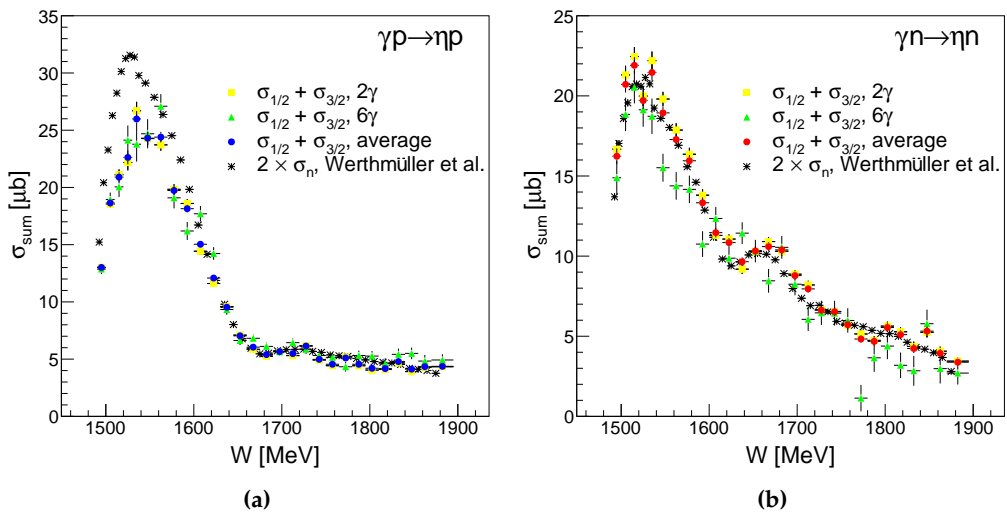


Figure 9.26: σ_{sum} obtained with the carbon subtraction method (coloured symbols), is compared to twice the unpolarised cross section (black stars) of Ref. [55]. The results are shown for both decay channels $\eta \rightarrow 2\gamma$ and $\eta \rightarrow 6\gamma$, and for (a) the recoil proton and (b) the recoil neutron. The deviation for the cross section on the proton must originate from an imperfect proton detection efficiency correction.

twice the unpolarised cross section occur in the maximum of the $S_{11}(1535)$ around $1500 - 1600$ MeV, which can be assigned to an imperfect proton detection efficiency correction. In Sec. 8.8.1, it was shown that the cross section in this energy range is very sensitive to the proton detection efficiency, since the protons in that energy range are low energetic protons. The relative nucleon detection efficiency correction for the dButanol experiment was extracted from a hydrogen measurement of April 2009, as it was done in Ref. [56]. The hydrogen target had a length of 10 cm and a completely different construction than the dButanol target, which may lead to a different proton efficiency. Since this problem with the nucleon detection efficiency is also present in σ_{diff} , it cancels in the double polarisation observable E . Even more, a correction of this effect by fitting the carbon contribution would yield a less correct double polarisation observable E . The systematics of this effect were checked by the different methods used to extract the double polarisation observable E and the helicity dependent cross sections (version 1-3). However, above $W = 1.6$ GeV, σ_{sum} is consistent with the unpolarised cross section, since there, the nucleon efficiency correction has no big influence.

For the neutron, as seen in Fig. 9.26 (b), the nucleon efficiency correction seems to be fine and σ_{sum} is in agreement with twice the unpolarised cross section.

Fig. 9.27 shows σ_{sum} for each dButanol beamtime for the $\eta \rightarrow 2\gamma$ reaction on the proton. As can be seen, the result from all different beamtimes are consistent and all beamtimes are exhibiting the proton efficiency problem mentioned before. This can also be seen in Fig. 9.28, where the angular distributions are shown. The proton efficiency problem is more prominent at forward directions in the cm, which was also seen by Werthmüller *et al.*[56]. The results for the neutron are not shown here for each beamtime, since the statistics was very poor and an interpretation is not possible.

In summary, it was shown that the carbon subtracted sum is consistent with twice the unpolarised cross section on deuterium for the neutron. For the proton, an issue

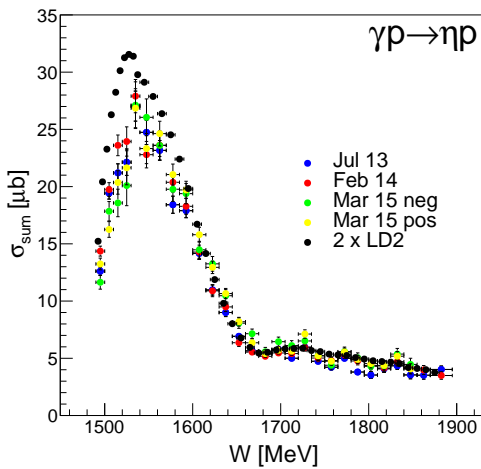


Figure 9.27: σ_{sum} for the $\gamma p \rightarrow \eta p$ reaction, where the η meson decays into two photons. The result for each beamtime is compared to twice the unpolarised cross section of Ref. [55] (black stars).

with the proton efficiency correction was found, which only affects the cross sections up to $W = 1.6$ GeV. This problem does not originate from the carbon subtraction itself. In addition, it was demonstrated that the two decay channels $\eta \rightarrow 2\gamma$ and $\eta \rightarrow 6\gamma$ are in agreement, as well as the cross sections from the different beamtimes.

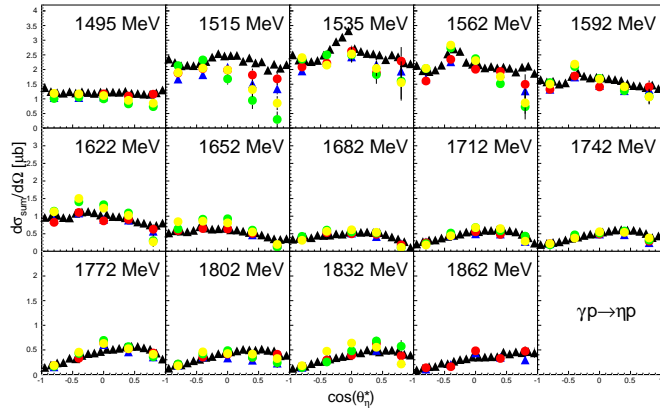


Figure 9.28: Angular distributions for σ_{sum} for the $\gamma p \rightarrow \eta p$ reaction, where the η meson decays into two photons. The result for each beamtime (same colours as in Fig. 9.27) is compared to twice the unpolarised cross section of Ref. [55] (black stars). Only a selection of bins is shown here.

Results from HButanol data

As previously mentioned, to rule out the possibility that the discrepancy in E was caused by an error in the analysis, A2 HButanol data from November 2013 were analysed to verify the analysis procedure. As can be seen from the results in Fig. 9.29, the inconsistency which occurred in the dButanol data could not be found in the HButanol data. The deviations from $E = 1$ close to threshold can be explained by the preliminary analysis (no total normalisation, carbon contribution was fitted) and the fact that also data runs with linear photon polarisation were used to gain enough statistics.

In summary, these results on the free proton, together with the results obtained from CBELSA/TAPS data, show that it is very unlikely that an error in the analysis code is the origin of the problem.

Check of the Photon Polarisation

As mentioned in the beginning of this section, the photon polarisation was checked using the beam helicity asymmetry observable I^\odot for double π^0 photoproduction. The beam helicity asymmetry is given by the following equation:

$$I^\odot(\Phi) = \frac{\sigma^+ - \sigma^-}{\sigma^+ + \sigma^-} = \frac{1}{P_\gamma} \frac{N^+ - N^-}{N^+ + N^-}, \quad (9.6)$$

where σ^\pm are the cross sections for the two photon helicity states, N^\pm are the corresponding yields, P_γ is the degree of circular photon polarisation, and Φ is the angle

between the plane of the incident photon and recoil nucleon, and the plane spanned by the two pions. First, I^\odot was extracted for the deuterium target (black circles in Fig. 9.30) and compared to previous measurements by Oberle *et al.* [180], the results were in good agreement (not shown). Hereby, the analysis procedure was checked. Furthermore, I^\odot was extracted using the dButanol and HButanol data, the corresponding results are shown as blue and green circles in Fig. 9.30. The comparison of the dButanol and Hbutanol data to the results on deuterium is not straightforward due to the

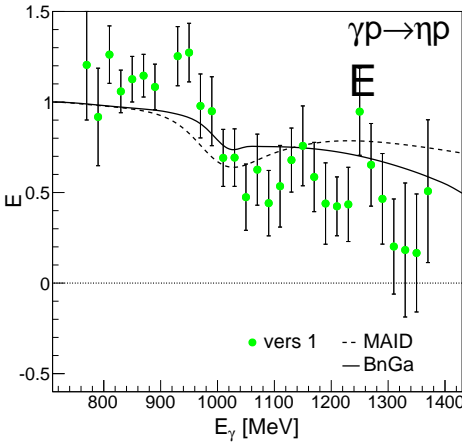


Figure 9.29: Results for the double polarisation observable E for the free proton (green circles). The results are compared to model predictions by MAID [179] (dashed line) and BnGa [48] (solid line).

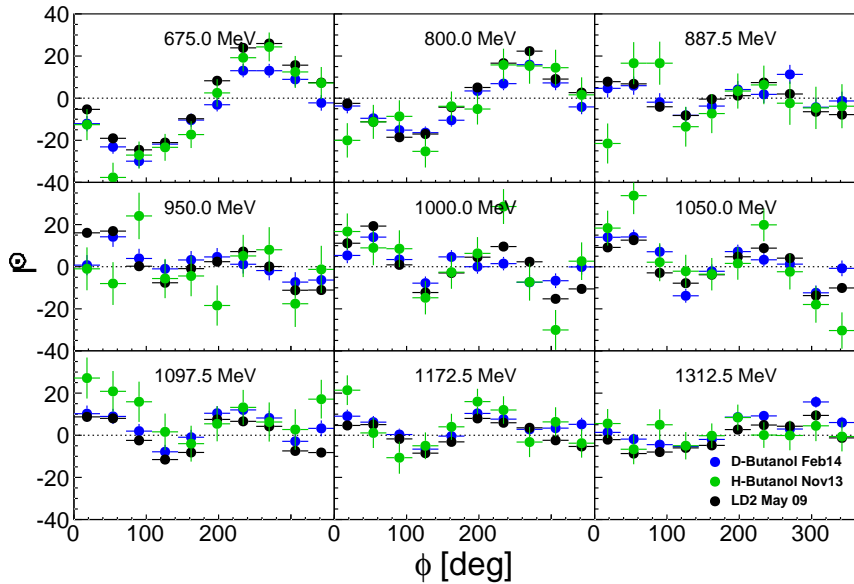


Figure 9.30: Helicity asymmetry I^\odot for $2\pi^0$ photoproduction on the quasi-free proton. Shown are the results for the deuterium target (black), the dButanol (blue) target and the HButanol (green) target.

different Fermi momentum distribution (the carbon contribution was not subtracted to have better statistics). However, the results are consistent and show no sign that the factor of ~ 1.5 may originate from the photon polarisation. This could also be confirmed by the ratio of the asymmetry from dButanol and HButanol, shown in Fig. 9.31, which was integrated over the whole energy range. The average ratio is around unity, hence showing that the beam polarisation of the dButanol and HButanol experiment are in agreement. As explained in the previous section, the HButanol data did not show the same discrepancy in E as the dButanol results. Therefore, it can be concluded that the photon polarisation cannot be the cause of the problem.

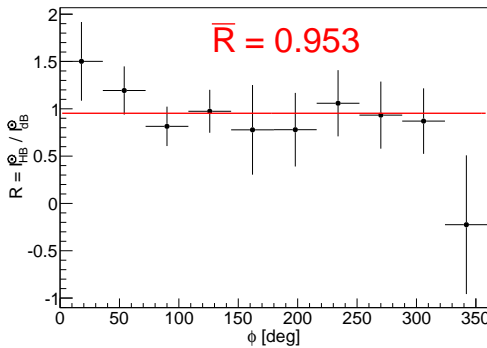


Figure 9.31: Integrated ratio of the helicity asymmetry I^\odot extracted from the HButanol and dButanol target. The average ratio is 0.95 and shows that the measurement on HButanol and dButanol are in agreement.

Stability over Time and Correction of the Target Polarisation

To investigate the problem on E , it was crucial to look at the time dependence of the asymmetry. Since the available statistics for η photoproduction was not sufficient for that purpose, it was done using single π^0 photoproduction by M. Dieterle [181]. The asymmetry

$$A = \frac{1}{p_e p_T} \frac{P - A}{P + A}, \quad (9.7)$$

where P stands for the yields for parallel photon and nucleon spins, A stands for yields for anti-parallel photon and nucleon spins, and p_e, p_T are the polarisation degree of the electron beam and the target, respectively. The polarisation values shown in Figs. 3.3 and 3.8 were used. The asymmetry was integrated over all energies and is shown as a function of the run number in Fig. 9.32. The different beam times, July 2013, February 2014, and March 2015 are colour coded. The March 2015 beamtime is divided into two parts, since the target polarisation direction was flipped after a certain time from negative to positive polarisation. The average and median asymmetry value for each beamtime is indicated in the figure as solid and dashed line, respectively. As can be seen, the average asymmetry of the July 2013 (red) and February 2014 (blue) beamtimes are equal and stable over time (apart from small fluctuations). Hence, it can be excluded that the problem is caused by beam heating, a sudden change of the

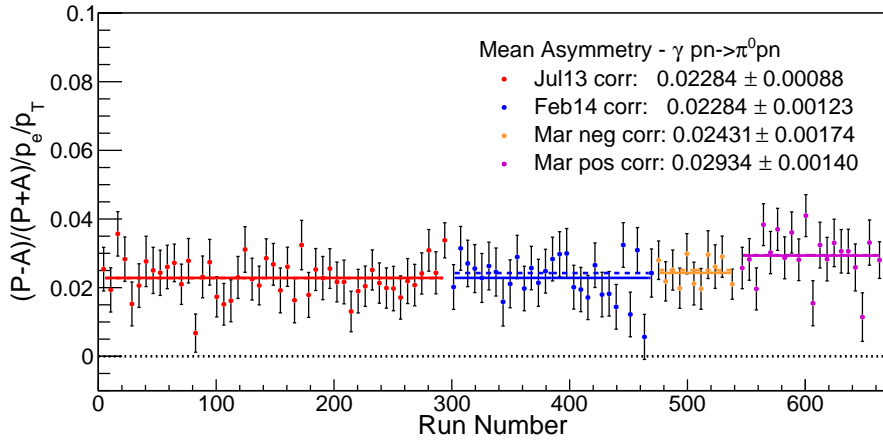


Figure 9.32: Asymmetry as a function of the run number for single π^0 photoproduction. The different beamtimes are colour coded. The target polarisation problem was investigated during the last two blocks (yellow and magenta). The helicity asymmetry from the incident photon beam was already adjusted before. Figure taken from Ref. [181].

polarisation degree during data taking, or effects due to the different direction of the target polarisation (since the target polarisation was positive in July 2013 and negative in February 2014).

As mentioned in Sec. 3.4.2, the March 2015 beamtime was used to perform several target polarisation checks and it was found that the polarisation in the middle of the target was significantly lower than in the outer parts. In this beamtime, the polarisation in the center of the target could be increased by tuning the polarisation frequency. Hence, the measured asymmetry was larger than for the other beamtimes, as seen in Fig. 9.32.

The average asymmetry was $A \simeq 0.02284$ for the July 2013 and February 2014 beamtime, $A \simeq 0.02431$ for the first part of March 2015, and $A \simeq 0.02934$ for the second part. With these asymmetries, the data sets from March 2015 were normalised to the July 2013 and February 2014 data sets. Hence, a factor of $0.02431/0.02284 \simeq 1.06$ was used to normalise the first part of the March 2015 beamtime to the July 2013 and February 2014 beamtimes, and a factor of $0.02934/0.02284 \simeq 1.28$ was necessary to scale the second part of March 2015. The relative target correction factors are summarised in Table 9.3.

beamtime	factor
July 2013:	1.00
February 2014:	1.00
March 2015, negative:	1.06
March 2015, positive:	1.28

Table 9.3: Relative target polarisation correction factors for the different beamtimes. The values were determined using the asymmetry shown in Fig. 9.32.

Having normalised the different data sets relative to each other, the final target polarisation values were found by scaling the double polarisation observable E to unity in the region of the $S_{11}(1535)$ with a factor of 1.5. The normalisation was checked for the reaction from the proton and from the neutron to get consistent results. The relative correction values from Table 9.3 together with the absolute value of 1.5 yielded the following overall correction constants for the target polarisation:

beamtime	factor
July 2013	$1.50/1 = 1.50$
February 2014:	$1.50/1 = 1.50$
March 2015, negative:	$1.50/1.06 \simeq 1.41$
March 2015, positive:	$1.50/1.28 \simeq 1.17$

Table 9.4: Overall target polarisation correction factors for the different beamtimes, which were found by the re-normalisation of the double polarisation observable E for η photoproduction.

Hence, from the experimental extracted double polarisation observable E it was found that the measured (with the surface coil) target polarisation values of the July 2013 and February 2014 experiment were a factor of 1.5 off, whereas the target polarisation values of March 2015 were a factor of 1.41 and 1.17 off for negative and positive target polarisation, respectively. This finding is consistent with the values given in Table 3.2: the measured target polarisation before the start of the March 2015 beamtime (with similar settings as for July 2013 and February 2014) was a factor of 1.4 – 1.47 smaller in the center of the target than on the surface, which is comparable to the factor of 1.5, which was determined from the double polarisation observable and a weighting with the surface coil values. The factor of 1.41 and 1.17 from March 2015 can be explained by the fact that the asymmetry was weighted with the average target polarisation values of the in-beam and the surface coil, hence with a too small polarisation value compared to the in-beam value. Hence, the correction factors for the target polarisation values are consistent with the values determined from the measurement with the two coils. However, it seems that the values measured with the in-beam coil are still higher than the real target polarisation value, which can be explained by the inhomogeneities.

Summary of all Consistency Checks

With the help of all consistency checks and the investigations of the target polarisation of March 2015, the problem in the double polarisation observable E could be attributed to a reduced target polarisation in the center of the target. All other causes such as an error in the analysis, carbon subtraction, overall normalisation, helicity asymmetry of the flux, photon polarisation, and beam heating could be ruled out by the checks explained in this section. A major advantage in the finding of the cause can also be assigned to the parallel analysis of A2 and CBELSA/TAPS data.

An overall correction of the target polarisation was found by a re-normalisation of

the double polarisation observable E to unity in the region of the $S_{11}(1535)$. The values shown in Table 9.4 are consistent with the measured target polarisation values from March 2015 and hence all the results shown in the following sections were obtained using these correction factors.

9.4.2 Results as a Function of the Incident Photon Energy E_γ

The final results for the double polarisation observable E for η photoproduction from the proton and the neutron are shown in Fig. 9.33 for the A2 data as a function of the incident photon energy. The results, which were extracted via the two different methods described in Sec. 8.2, are compared to Fermi folded model predictions by MAID [179] and BnGa [48] (fit without narrow $N(1685)$). Both decay channels of the η meson, $\eta \rightarrow 2\gamma$ and $\eta \rightarrow 6\gamma$, were statistically averaged as mentioned in Sec. 8.11. For a better visibility, the points from *version 2* were shifted by +5 MeV with respect to *version 1*. The indicated systematic errors (gray shaded areas) were determined from the deviation of the two different extraction versions and the uncertainty of the polarisation values, as explained in Sec. 8.12.2.

For the proton, shown in Fig. 9.33 (a), the experimental results from *version 1* are consistent with the model predictions at low energies and start to differ around 1 GeV, where the experimentally determined E is significantly lower than the model predic-

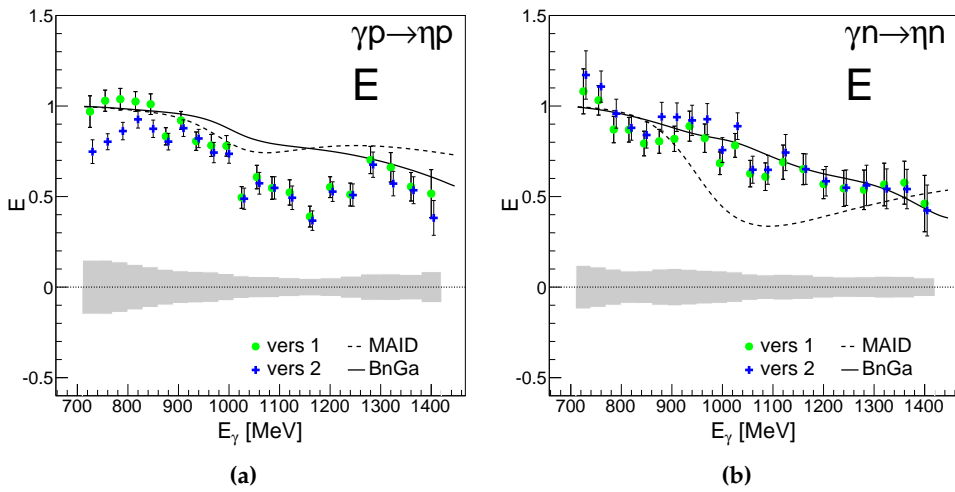


Figure 9.33: Double polarisation observable E extracted from A2 data. The results were averaged over both decay channels $\eta \rightarrow 2\gamma$ and $\eta \rightarrow 6\gamma$ and are shown as a function of the incident photon energy E_γ for the proton (a) and the neutron (b). The results are compared to Fermi folded model calculations by BnGa [48] and MAID [179]. For a better visibility, the points from *version 2* (normalisation with the unpolarised cross section) were shifted by +5 MeV with respect to *version 1* (carbon subtraction method). The systematic uncertainties are indicated by the gray shaded areas. The discrepancy between the different extraction versions at $E_\gamma \leq 850$ MeV for the proton is caused by the unideal nucleon detection efficiency correction.

tions. Extraction *version 2* is slightly lower than unity in the region of the $S_{11}(1535)$, which can be explained by the imperfect nucleon detection efficiency correction, mentioned in Sec. 9.4.1, which cancels only in *version 1*, but not in *version 2*. For the case of the neutron, shown in Fig. 9.33 (b), within statistical and systematic uncertainties, the experimental results from both extraction versions are in agreement with the model predictions by BnGa over the whole energy range. As already seen in the CBELSA/TAPS data in Fig. 9.21, the dip in E seen by the MAID model cannot be reproduced.

Figs. 9.34 and 9.35 show the corresponding helicity dependent cross sections for the proton and neutron, respectively. The three extraction versions introduced in Sec. 8.3 are compared to Fermi folded model predictions by MAID [179] and BnGa [48]. For a better visibility, the points from *version 2* and *version 3* were shifted by ± 5 MeV with respect to *version 1*.

The shape of the $\sigma_{1/2}$ cross section on the proton, shown in Fig. 9.34 (a), is very similar to the model results. However, the overall magnitude of the experimental result is approximately 12% smaller than the models. At least part of this effect is caused by the fact that the unpolarised cross section as a function of E_γ from Ref. [55], which was used for the normalisation of *version 1*, is slightly lower than the Fermi folded model predictions. Extraction *version 2* and *version 3* are even lower, which is mainly due to

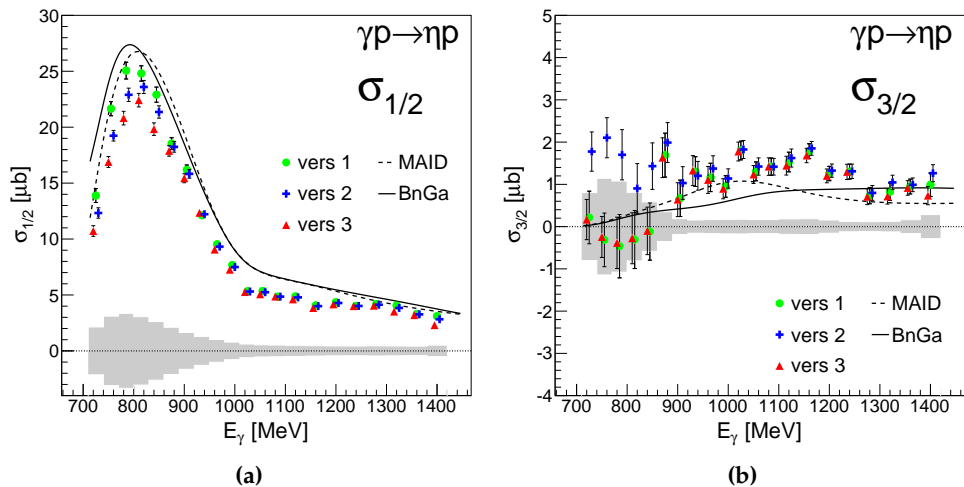


Figure 9.34: Helicity dependent cross sections $\sigma_{1/2}$ (a) and $\sigma_{3/2}$ (b) extracted from A2 data. The results were averaged over both decay channels $\eta \rightarrow 2\gamma$ and $\eta \rightarrow 6\gamma$ and are shown as a function of the incident photon energy E_γ for the proton. The results are compared to Fermi folded model calculations by BnGa [48] and MAID [179]. For a better visibility, the points from *version 2* (normalisation with the unpolarised cross section) and *version 3* (only polarised data) were shifted by ± 5 MeV with respect to *version 1* (E via carbon subtraction, helicity dependent cross sections with the unpolarised cross sections, as given in Eqs. 8.15 and 8.16). The systematic uncertainties are indicated by the gray shaded areas. The discrepancy between the different extraction versions at $E_\gamma \leq 850$ MeV for the proton is caused by the unideal nucleon detection efficiency correction.

the previously mentioned proton efficiency problem. This is also the reason for the deviations at low energies in $\sigma_{3/2}$ and the larger systematic uncertainties in the region of the $S_{11}(1535)$. However, this effect can not fully account for the stronger contribution of the $\sigma_{3/2}$ cross section above 1 GeV incident photon energy than expected from the models, as can be seen in Fig. 9.34 (b).

As shown in Fig. 9.35, the situation for the neutron is similar. The shape of the experimentally measured $\sigma_{1/2}$ cross section is nicely reproduced by the models, which are only marginally higher. Within statistical uncertainties, the $\sigma_{3/2}$ for the neutron is consistent with the model results by BnGa and the large contribution from the $D_{15}(1675)$ resonance in the MAID model can be clearly ruled out. The three different versions for the extraction are in good agreement, demonstrating that the neutron efficiency is well understood.

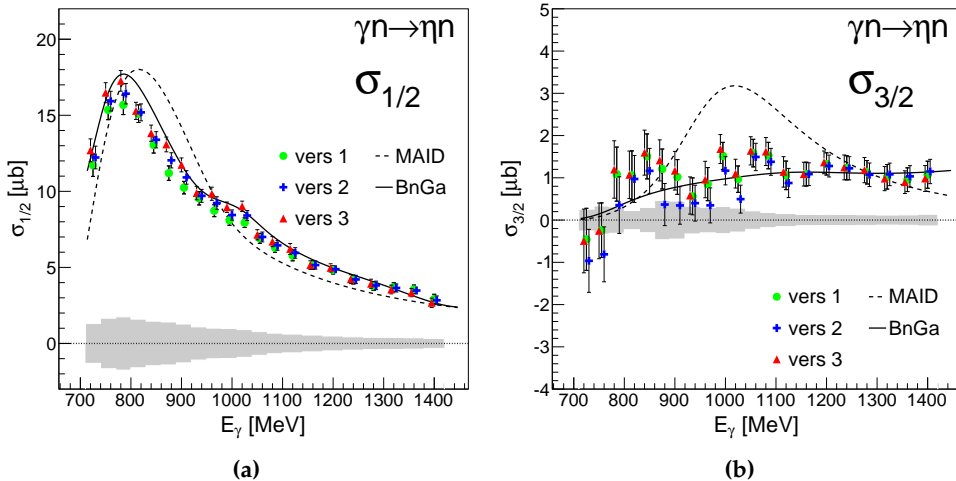


Figure 9.35: Helicity dependent cross sections $\sigma_{1/2}$ (a) and $\sigma_{3/2}$ (b) extracted from A2 data. The results were averaged over both decay channels $\eta \rightarrow 2\gamma$ and $\eta \rightarrow 6\gamma$ and are shown as a function of the incident photon energy E_γ for the neutron. The results are compared to Fermi folded model calculations by BnGa [48] and MAID [179]. For a better visibility, the points from version 2 (normalisation with the unpolarised cross section) and version 3 (only polarised data) were shifted by ± 5 MeV with respect to version 1 (E via carbon subtraction, helicity dependent cross sections with the unpolarised cross sections, as given in Eqs. 8.15 and 8.16). The systematic uncertainties are indicated by the gray shaded areas.

9.4.3 Results as a Function of the Final State Energy W

The double polarisation observable E and the helicity dependent cross sections were also extracted as a function of the final state energy W . The resulting double polarisation observable E is shown in Fig. 9.36 (a) for the proton and in (b) for the neutron. The two different extraction versions are shown by different colours and for a better visibility, the points from *version 2* were shifted by +5 MeV with respect to *version 1*. As for the results as a function of the incident photon energy, the two decay channels

of the η meson, $\eta \rightarrow 2\gamma$ and $\eta \rightarrow 6\gamma$, were statistically averaged as mentioned in Sec. 8.11. The indicated systematic errors (gray shaded areas) were determined from the deviation of the two different extraction versions and the uncertainty of the photon polarisation, as explained in Sec. 8.12.2. The uncertainty of the target polarisation is not included in that calculation. The experimental results are compared to model predictions by MAID [179] and BnGa [48] for the free proton and neutron.

The results for the double polarisation observable E for the proton are very similar to the results as a function of the incident photon energy. Again, extraction *version 2* is slightly lower than *version 1* due to the nucleon efficiency problem, which also leads to a larger systematic uncertainty in this energy range. For both versions, the measured double polarisation observable E is approximately unity close to threshold, as it is also predicted by the models. The observed modulation close to threshold can be partly assigned to the proton efficiency and the quasi-free kinematics. Fermi motion effects might play a role since the calculation of the Fermi folded photon flux close to threshold is very sensitive. Still, in this energy range the deviation from the model predictions are clearly within the systematic uncertainties. Around a final state energy of 1.6 GeV, the measured double polarisation observable E starts to drop and exhibits a dip at $W = 1710$ MeV, which is much more pronounced than in the results as a function of the incident photon energy since there are no effects of Fermi motion.

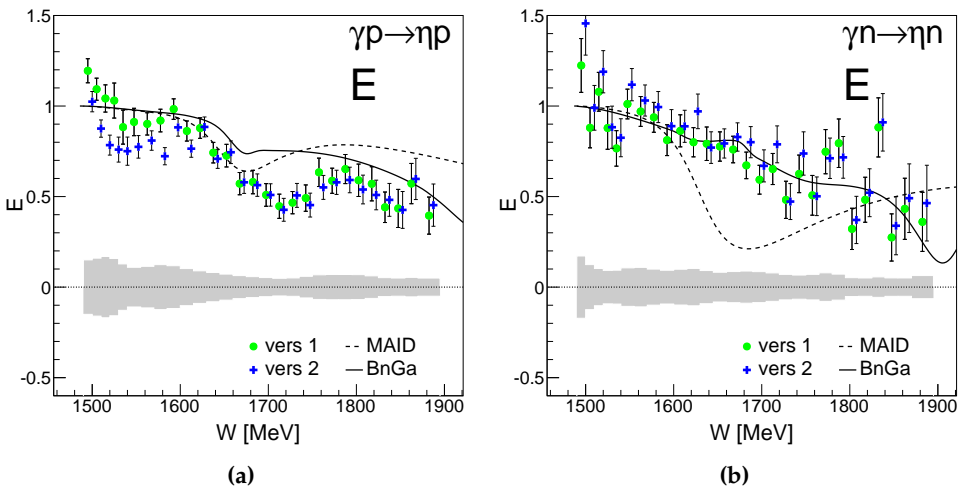


Figure 9.36: Double polarisation observable E extracted from A2 data. The results were averaged over both decay channels $\eta \rightarrow 2\gamma$ and $\eta \rightarrow 6\gamma$ and are shown as a function of the incident photon energy E_γ for the proton (a) and the neutron (b). The results are compared to model calculations by BnGa [48] and MAID [179]. For a better visibility, the points from version 2 (normalisation with the unpolarised cross section) were shifted by +5 MeV with respect to version 1 (carbon subtraction method). The systematic uncertainties are indicated by the gray shaded areas. The discrepancy between the different extraction versions at $W < 1.6$ GeV for the proton is caused by the unideal nucleon detection efficiency correction.

The models also predict a dip structure, however, it is situated at lower energies and is much less distinct. In the BnGa model the dip structure at $W = 1685$ MeV was traced back to the opening of the $K\Sigma$ threshold [48]. On the other hand, the MAID model has contributions from several different resonances in that energy range, the $S_{11}(1650)$, $D_{15}(1675)$, $F_{15}(1680)$, $D_{13}(1700)$, $P_{11}(1710)$, and $P_{13}(1720)$. However, the PDG η branching ratio of the $D_{15}(1675)$, $F_{15}(1680)$, and the $D_{13}(1700)$ resonances is almost zero.

The corresponding helicity dependent cross sections for the proton are shown in Fig. 9.37. As can be seen, the peak of the $S_{11}(1535)$ in $\sigma_{1/2}$ is slightly lower than both model predictions and consequently the $\sigma_{3/2}$ cross section has a larger contribution. The contribution in $\sigma_{3/2}$ is the largest for extraction *version 2* and hence is caused by the proton efficiency. At higher energies, around $W = 1.7$ GeV, the dip structure in $\sigma_{1/2}$ predicted by the models is not seen in the experimental results, but a stronger contribution of $\sigma_{3/2}$ is visible. This dip structure was not perfectly reproduced by the unpolarised cross sections from quasi-free protons by Werthmüller *et al.* [55], however, the dip was nicely seen in the quasi-free proton cross sections from this work using CBELSA/TAPS data, as seen in Fig. 9.11. Resolution effects might play a certain role here, since the resolution is better for the CBELSA/TAPS data than for A2 data. A possible candidate for the enhancement around $W \sim 1720$ in the $\sigma_{3/2}$ cross section is

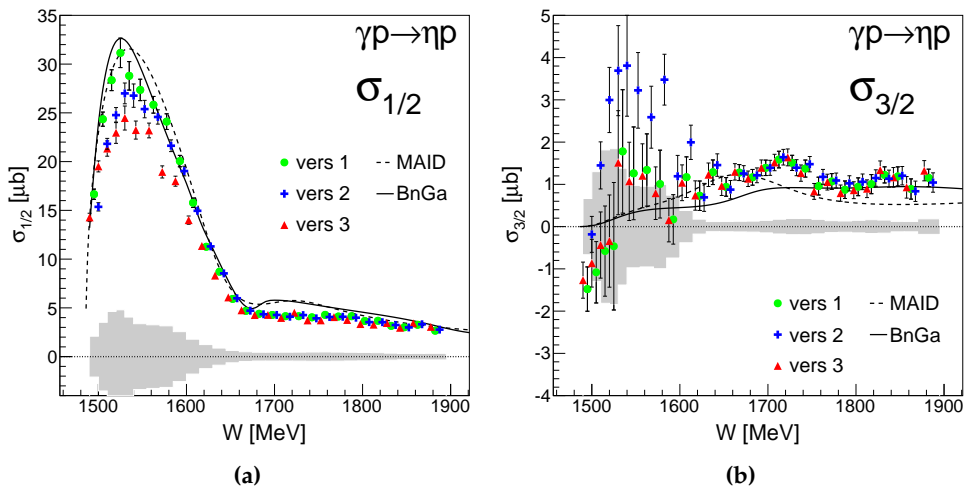


Figure 9.37: Helicity dependent cross sections $\sigma_{1/2}$ (a) and $\sigma_{3/2}$ (b) extracted from A2 data. The results were averaged over both decay channels $\eta \rightarrow 2\gamma$ and $\eta \rightarrow 6\gamma$ and are shown as a function of the incident photon energy E_γ for the proton. The results are compared to model calculations by BnGa [48] and MAID [179]. For a better visibility, the points from version 2 (normalisation with the unpolarised cross section) and version 3 (only polarised data) were shifted by ± 5 MeV with respect to version 1 (E via carbon subtraction, helicity dependent cross sections with the unpolarised cross sections, as given in Eqs. 8.15 and 8.16). The systematic uncertainties are indicated by the gray shaded areas. The discrepancy between the different extraction versions at $W < 1.6$ GeV is caused by the unideal nucleon detection efficiency correction.

the $N(1720)3/2^+$ resonance. The PDG has no prediction for the $A_{3/2}$ coupling of this resonance.

The double polarisation observable E for the neutron as a function of the final state energy W is shown in Fig. 9.36 (b). The results show the same slow falloff as it was already seen in the results as a function of the incident photon energy in Fig. 9.33. For the neutron, both extraction versions are in good agreement and the measured polarisation observable is consistent with the results predicted by the BnGa model. The results are in clear contradiction to the MAID model, which was already seen by the CBELSA/TAPS results, shown in Sec. 9.3.2. Besides the double polarisation observable E , the helicity dependent cross sections were extracted. The results are shown in Fig. 9.38 for the neutron. The results are very interesting, since as seen in Fig. 9.38 (a), the narrow structure around 1.68 GeV is clearly a feature of the $\sigma_{1/2}$ and not of the $\sigma_{3/2}$ cross section. This is also predicted by the BnGa model by the constructive interference of the $S_{11}(1535)$ and the $S_{11}(1650)$ resonance. On the contrary, for the proton, a destructive interference of these resonances was seen by BnGa. The model calculation found the electromagnetic couplings for the two resonances given in Table 9.5. From these couplings one would expect the interference to be constructive for the proton and destructive for the neutron. However, the hadronic phase for the decay of the resonance into $N\eta$ is positive for the $S_{11}(1535)$ and negative for the $S_{11}(1650)$. Hence, the interference of the two resonances is constructive for the neutron and destructive for the proton. [48]

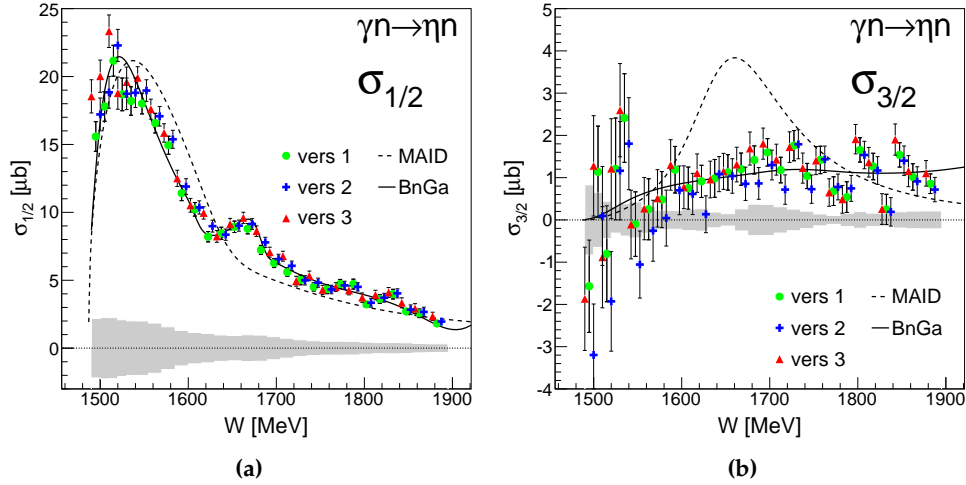


Figure 9.38: Helicity dependent cross sections $\sigma_{1/2}$ (a) and $\sigma_{3/2}$ (b) extracted from A2 data. The results were averaged over both decay channels $\eta \rightarrow 2\gamma$ and $\eta \rightarrow 6\gamma$ and are shown as a function of the incident photon energy E_γ for the neutron. The results are compared to model calculations by BnGa [48] and MAID [179]. For a better visibility, the points from version 2 (normalisation with the unpolarised cross section) and version 3 (only polarised data) were shifted by ± 5 MeV with respect to version 1 (E via carbon subtraction, helicity dependent cross sections with the unpolarised cross sections, as given in Eqs. 8.15 and 8.16). The systematic uncertainties are indicated by the gray shaded areas.

channel	$S_{11}(1535)$ [GeV $^{-1}$]	$S_{11}(1650)$ [GeV $^{-1}$]
p	(0.114 ± 0.008)	(0.032 ± 0.007)
n	(-0.095 ± 0.006)	(0.019 ± 0.006)

Table 9.5: Helicity Breit-Wigner couplings from the BnGa model. Values taken from [48].

In summary, the BnGa model nicely describes the results from the neutron over the whole energy range. The MAID model fails to describe the narrow structure and the overall shape of the double polarisation observable E and the helicity dependent cross sections for the case of the neutron.

9.5 Discussion of the Polarisation Observables

In this section, some additional aspects of the polarised results, i.e. the double polarisation observable E and the helicity dependent cross sections, will be discussed and the results from the CBELSA/TAPS and the A2 experiment will be compared.

9.5.1 Angular Distributions

The results for the helicity dependent cross sections obtained from A2 data, shown in Sec. 9.4, were calculated by fitting the angular distributions with Legendre polynomials of third order, as given by the following equation:

$$\frac{d\sigma}{d\Omega}(W, \cos \theta_\eta^*) = \frac{q^*(W)}{k^*(W)} \sum_{i=0}^3 A_i(E) P_i(\cos \theta_\eta^*), \quad (9.8)$$

where A_i are the Legendre coefficients as already introduced in Eq. 8.5, $P_i(\cos \theta_\eta^*)$ are the Legendre polynomials, $q^*(E)$ and k^* are the momenta of the η meson and the incident photon beam in the cm frame, respectively, and $q^*(E)/k^*$ is the phasespace factor. The extracted Legendre coefficients for extraction *version 1* are shown in Fig. 9.39 for $\sigma_{1/2}$ and $\sigma_{3/2}$. Extraction *version 1* is considered to give the most reliable results, since in the corresponding determination of E almost all systematic effects cancel out and the helicity dependent cross sections were calculated using published cross sections, as mentioned in Secs. 8.2 and 8.3. The experimental results are compared to the model predictions by MAID (dashed green line) and by BnGa. For the neutron, three different BnGa solutions are shown, which show significant differences. Two predictions with a narrow $N(1685)$ resonance are shown, one solution has a positive (dotted line) and one has negative (dash-dotted line) $A_{1/2}$ coupling. The third prediction is the solution without a narrow resonance (solid line), which was favoured in Ref. [48].

For the neutron, the BnGa models describe the experimental data for $\sigma_{1/2}$ better than the MAID model. A distinction between the three different BnGa predictions is not straightforward due to the statistical quality of the experimental data. However, the A_1 coefficient of $\sigma_{1/2}$ has a distinct dip around $W \sim 1685$ MeV, which is also seen

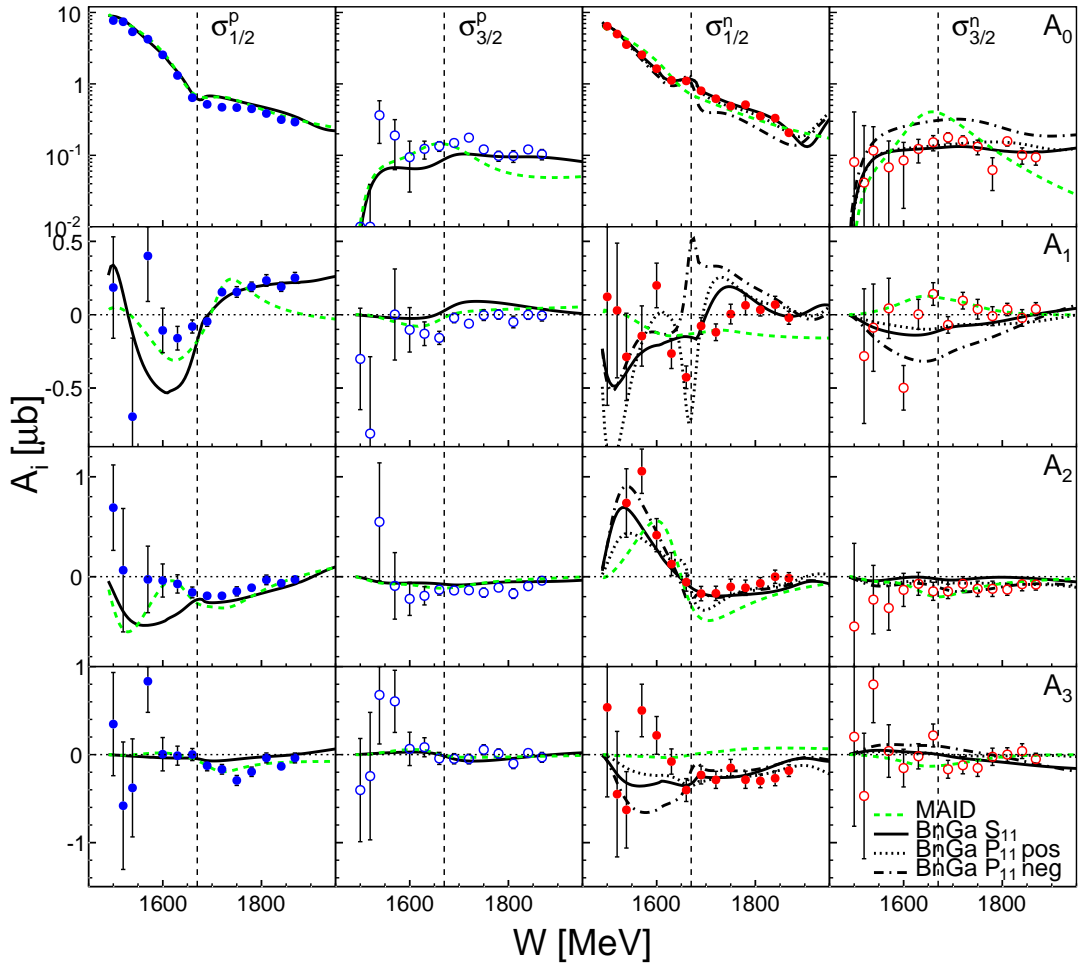


Figure 9.39: Legendre Coefficients $A_0 - A_3$ (rows) as defined in Eq. 9.8, which were extracted from the A_2 data (extraction version 1). First column: coefficients for the $1/2$ helicity state (closed circles) for the reaction on the proton. Second column: coefficients for the $3/2$ helicity state (open circles) for the reaction on the proton. Third and fourth column: same for the reaction on the neutron. The experimental results (blue and red markers) are compared to the coefficients extracted from model predictions by MAID [179] (dashed green line) and BnGa [48]. Three different BnGa models predictions are shown for the neutron: fit with a narrow $N(1685)$ resonance with positive (dotted line) or negative (dash-dotted line) $A_{1/2}$ coupling, and fit without a narrow resonance (solid line). The position of the narrow structure at $W = 1685$ MeV in the neutron cross section is indicated by a dashed vertical line.

in the BnGa model with the narrow $N(1685)$ resonance with the positive helicity coupling (dotted line). The BnGa model without the narrow resonance (solid line) has a step-like structure around the same energy. The BnGa prediction with the negative helicity coupling (dash-dotted line) shows the opposite behaviour in A_1 than seen in the experimental data. An interpretation of the $\sigma_{3/2}$ coefficients for the neutron is not easy due to the error bars, however, the MAID model seems to fit better for $A_1 - A_3$.

For the proton, the MAID model is in better agreement with the experimental data than the BnGa model at energies below $W = 1800$ MeV. At higher energies, the experimental results are closer to the BnGa model, which is most obvious in A_1 of $\sigma_{1/2}$. In A_3 of $\sigma_{1/2}$, the BnGa model is already above $W = 1680$ MeV in better agreement with the experimental data than the MAID model. The discrepancies in $A_1 - A_3$ for the proton below $W = 1650$ MeV can be partly attributed to the issues with the proton efficiency, as it was already seen by D. Werthmüller [56]. The coefficients $\sigma_{3/2}$ for the proton are very small and an interpretation is hard due to the quite large experimental error bars.

The angular distributions for the polarisation observable E , as well as for the helicity dependent cross sections for the proton are shown in Figs. 9.40 – 9.42 and for the neutron in Figs. 9.43 – 9.45. Here, the results are shown for different bins of the final state energy W . The angular distributions for bins of the incident photon energy are shown in App. E. As mentioned before, two different extraction versions were used for the polarisation observable E and three versions for the helicity dependent cross sections. For a better visibility, the points of the angular distributions of *version 2* and *version 3* were shifted by $\Delta \cos(\theta_\eta^*) = \pm 0.05$ with respect to *version 1*. The angular distributions of the $\sigma_{1/2}$ and $\sigma_{3/2}$ cross section from extraction *version 1* were fitted with Legendre polynomials of third order, the function is indicated by a green line. The experimental results are compared to the model predictions by BnGa (only the model without the narrow resonance, solid lines) and MAID (dashed lines). For the experimental data, five $\cos(\theta_\eta^*)$ bins were chosen and the systematic uncertainty is indicated by the gray area.

The angular distributions of the double polarisation observable E for the proton, shown in Fig. 9.40, are flat at low energies up to $W \sim 1620$ MeV. At higher energies, a modulation occurs, which cannot be reproduced by the BnGa model. In the energy region of the dip, around 1700 MeV, the measured asymmetry is forward peaking, whereas the BnGa model is peaking in the backward direction. In that energy range, the experimental data is better reproduced by the MAID model. The angular shape of the corresponding helicity dependent cross section $\sigma_{1/2}$ for the proton, shown in Fig. 9.41, is similar for the BnGa and MAID model, however, the models are slightly higher than the experimental data. The $\sigma_{3/2}$ differential cross section is almost zero, as seen in Fig. 9.42 and hence has quite large statistical and systematic error bars. At medium energies, around 1700 MeV, the angular distributions from the experiment of $\sigma_{3/2}$ show a peak structure, which is neither predicted by the BnGa model nor the MAID model.

The angular distributions for the polarisation observable E for the neutron, shown in Fig. 9.43, are in agreement with the model predictions by BnGa within the statistical and systematic uncertainties. Above 1600 MeV, the MAID model shows a falloff for E to forward angles, which is not seen in the experimental data. Also for the $\sigma_{1/2}$ cross section, shown in Fig. 9.44, the BnGa model describes the experimental data better than the MAID model. The angular modulation is almost identical to the BnGa predictions. The corresponding angular distributions for the helicity dependent cross section $\sigma_{3/2}$, shown in Fig. 9.45, are very small, as it was also seen for the proton, the statistical and systematic errors make an interpretation not straightforward. However,

the MAID model exhibits a large excess between 1700 and 1800 MeV, which is not seen in the experimental results.

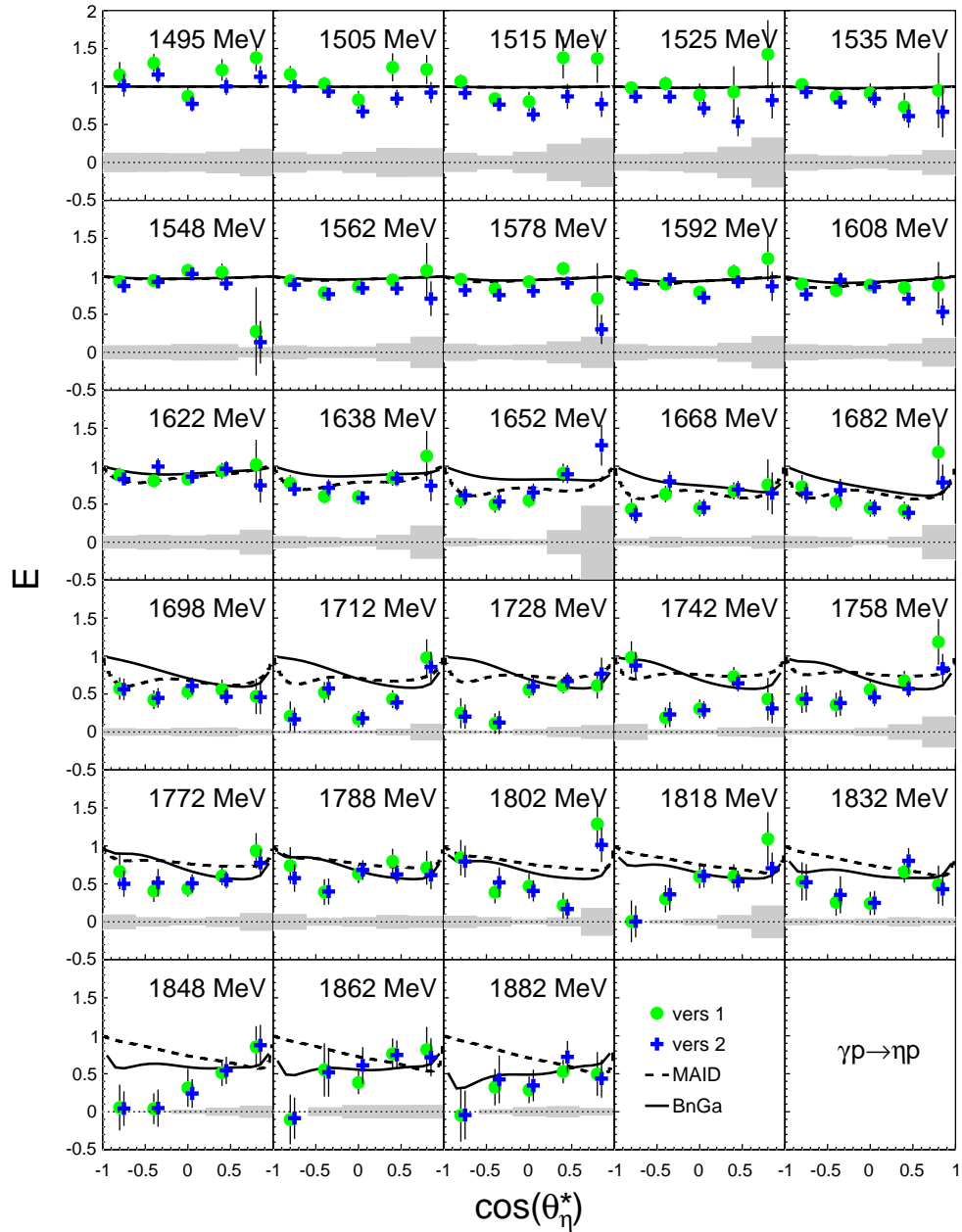


Figure 9.40: Angular distributions for the double polarisation observable E extracted from A2 data for the proton. The results are shown in the cm of the η meson and the final state nucleon. For a better visibility, the points of version 2 (blue) were shifted by $\Delta \cos(\theta_\eta^*) = +0.05$ with respect to version 1 (green). The systematic uncertainties are indicated by the gray shaded areas. The model predictions by BnGa [48] and MAID [179] are indicated as solid and dashed line, respectively.

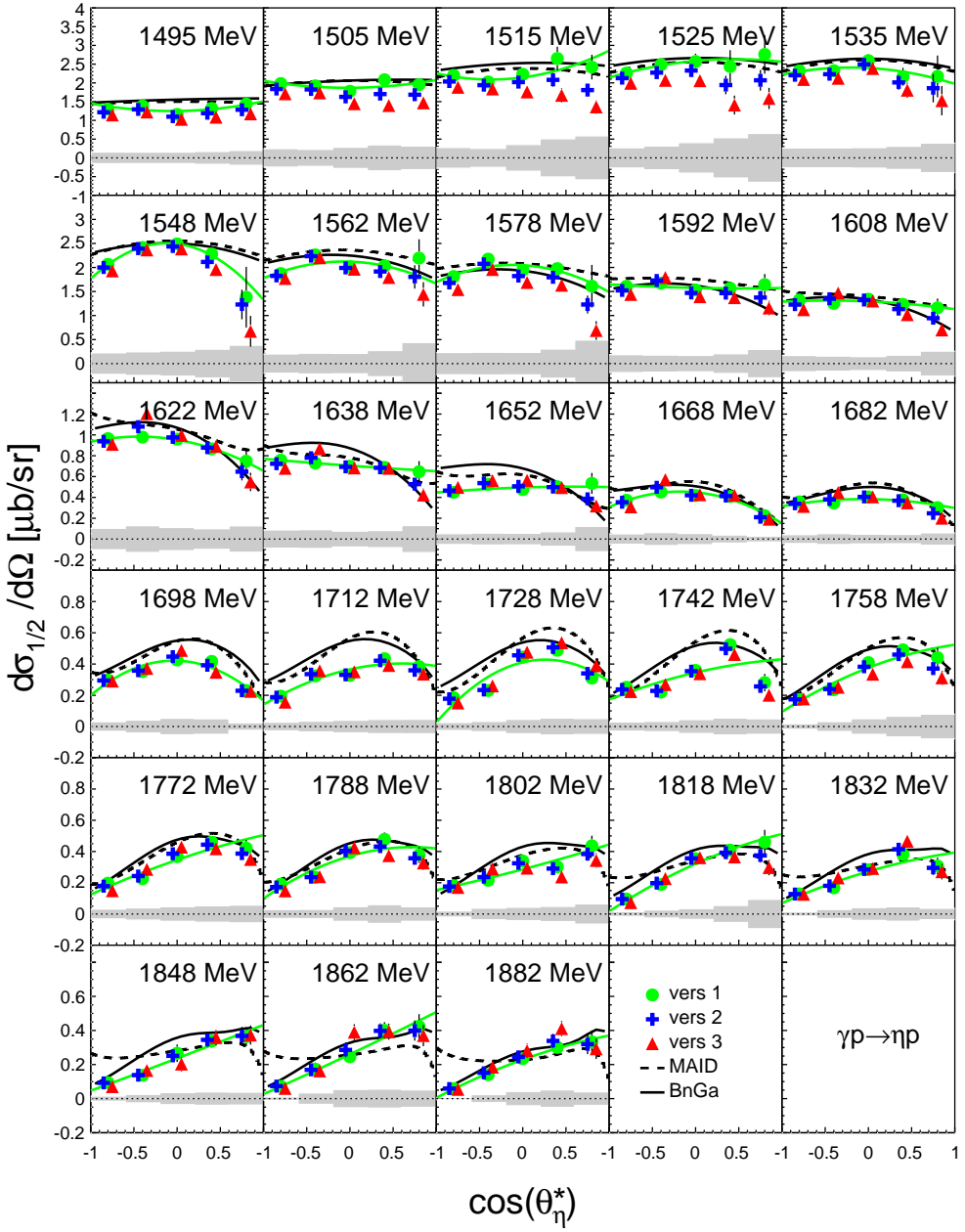


Figure 9.41: Angular distributions for the helicity dependent cross section $\sigma_{1/2}$ extracted from A2 data for the proton. The results are shown in the cm of the η meson and the final state nucleon. For a better visibility, the points of version 2 (blue) and version 3 (red) were shifted by $\Delta \cos(\theta_\eta^*) = \pm 0.05$ with respect to version 1 (green). The systematic uncertainties are indicated by the gray shaded areas. The model predictions by BnGa [48] and MAID [179] are indicated as solid and dashed line, respectively. The Legendre fit for version 1 is shown as a green line.

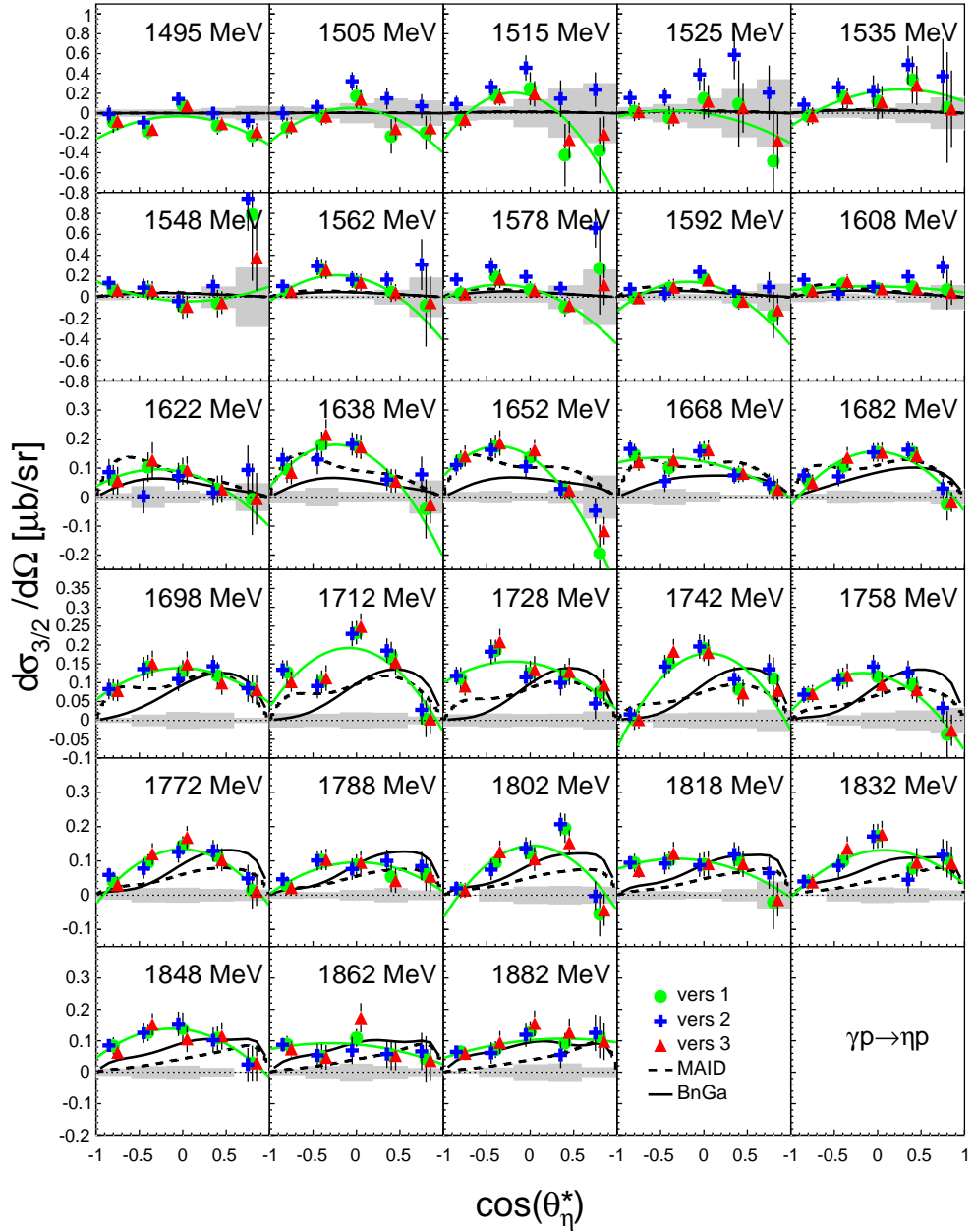


Figure 9.42: Angular distributions for the helicity dependent cross section $\sigma_{3/2}$ extracted from A2 data for the proton. The results are shown in the cm of the η meson and the final state nucleon. For a better visibility, the points of version 2 (blue) and version 3 (red) were shifted by $\Delta \cos(\theta_\eta^*) = \pm 0.05$ with respect to version 1 (green). The systematic uncertainties are indicated by the gray shaded areas. The model predictions by BnGa [48] and MAID [179] are indicated as solid and dashed line, respectively. The Legendre fit for version 1 is shown as a green line.

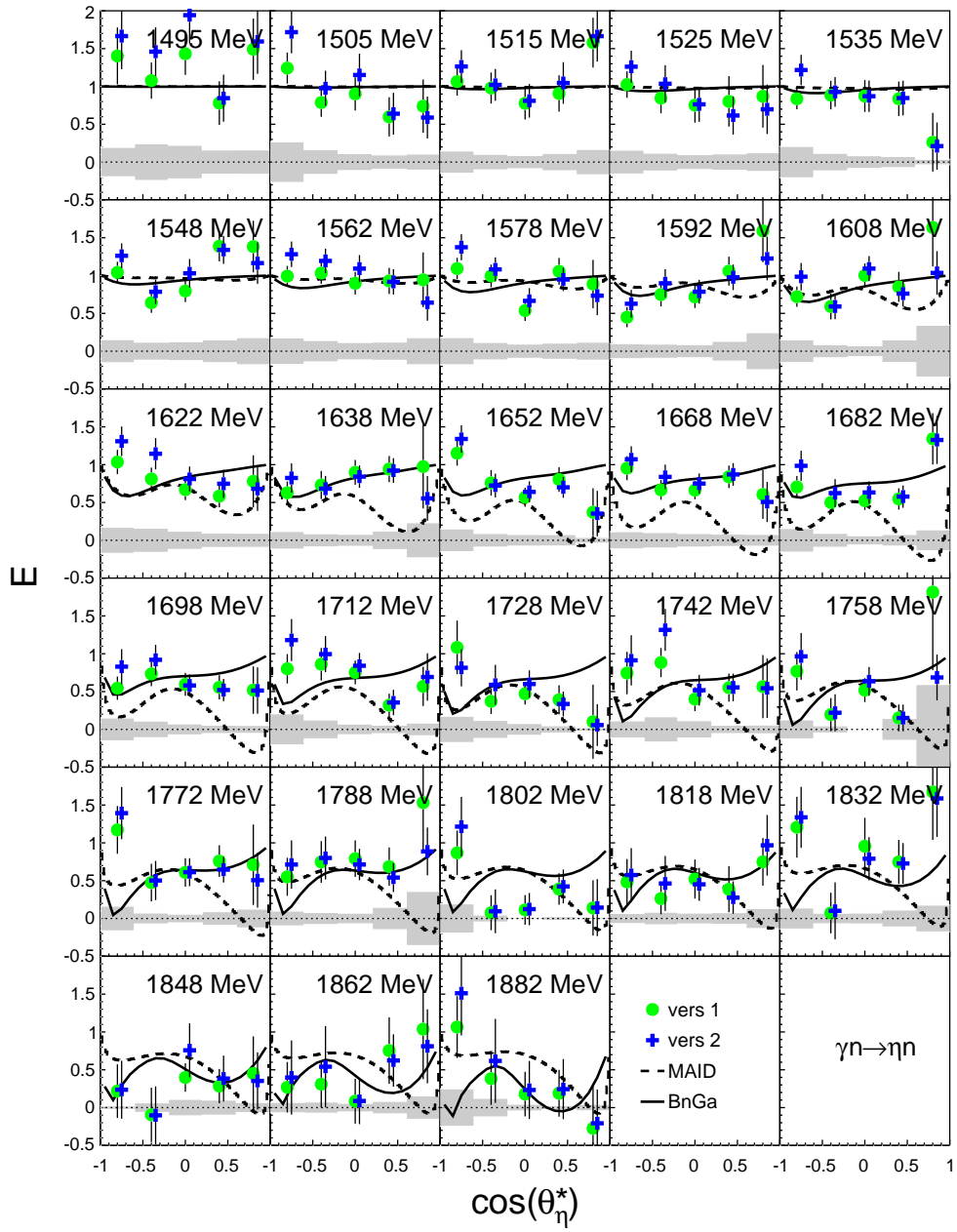


Figure 9.43: Angular distributions for the double polarisation observable E extracted from A2 data for the neutron. The results are shown in the cm of the η meson and the final state nucleon. For a better visibility, the points of version 2 (blue) and version 3 (red) were shifted by $\Delta \cos(\theta_\eta^*) = \pm 0.05$ with respect to version 1 (green). The systematic uncertainties are indicated by the gray shaded areas. The model predictions by BnGa [48] and MAID [179] are indicated as solid and dashed line, respectively.

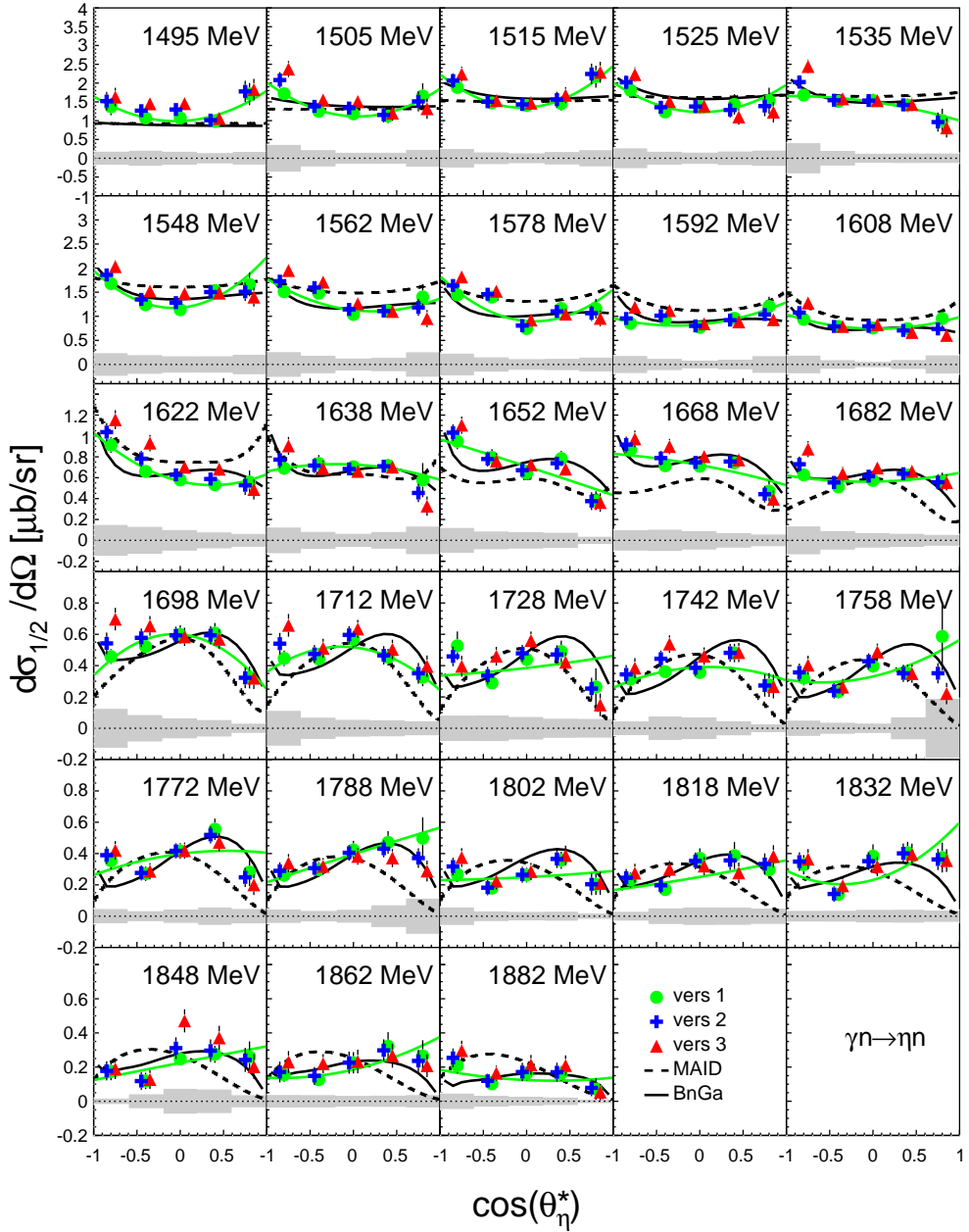


Figure 9.44: Angular distributions for the helicity dependent cross section $\sigma_{1/2}$ extracted from A2 data for the neutron. The results are shown in the cm of the η meson and the final state nucleon. For a better visibility, the points of version 2 (blue) and version 3 (red) were shifted by $\Delta \cos(\theta_\eta^*) = \pm 0.05$ with respect to version 1 (green). The systematic uncertainties are indicated by the gray shaded areas. The model predictions by BnGa [48] and MAID [179] are indicated as solid and dashed line, respectively. The Legendre fit for version 1 is shown as a green line.

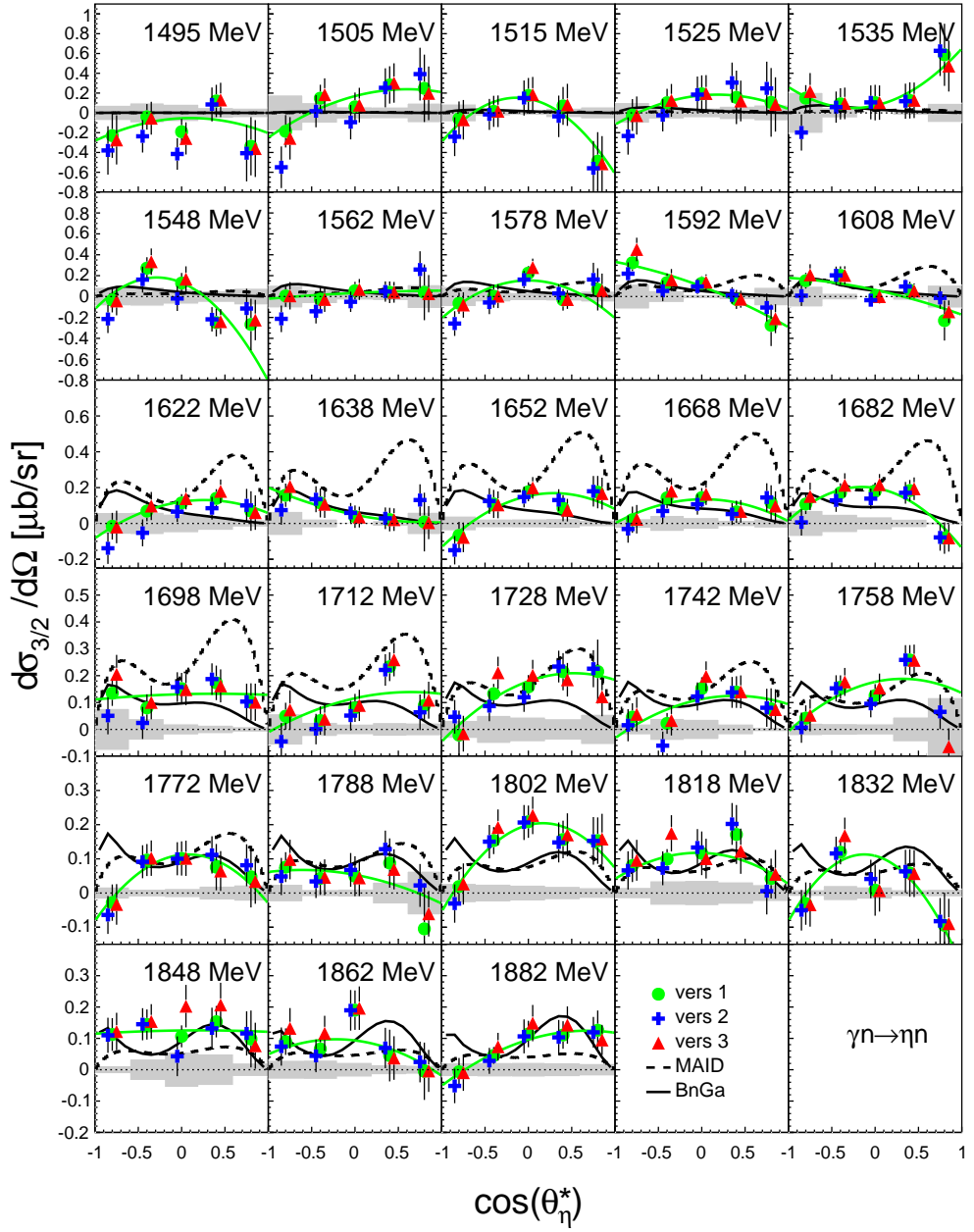


Figure 9.45: Angular distributions for the helicity dependent cross section $\sigma_{3/2}$ extracted from A2 data for the neutron. The results are shown in the cm of the η meson and the final state nucleon. For a better visibility the points of version 2 (blue) and version 3 (red) were shifted by $\Delta \cos(\theta_\eta^*) = \pm 0.05$ with respect to version 1 (green). The systematic uncertainties are indicated by the gray shaded areas. The model predictions by BnGa [48] and MAID [179] are indicated as solid and dashed line, respectively. The Legendre fit for version 1 is shown as a green line.

9.5.2 Cross Sections for Different Polar Angles

Cross sections for five bins of the cm polar angle were extracted and are shown in Fig. 9.46. The first row shows the $\sigma_{1/2}$ results for the proton (blue), the second row shows the $\sigma_{3/2}$ cross sections for the proton (blue), the third and fourth row show the corresponding cross sections for the neutron (red). The results are compared to the BnGa and MAID model predictions. The overall agreement for $\sigma_{1/2}$ and $\sigma_{3/2}$ is quite nice for the proton and the neutron. For the proton, the largest deviations occur in the angular range of $-0.6 < \cos(\theta_\eta^*) < 0.2$. In that range, the $\sigma_{1/2}$ is smaller than the model predictions and hence $\sigma_{3/2}$ is larger. The agreement between experimental and model results for the two most forward bins is striking. As it was already seen in Sec. 9.4, the agreement between BnGa model prediction and experimental data is

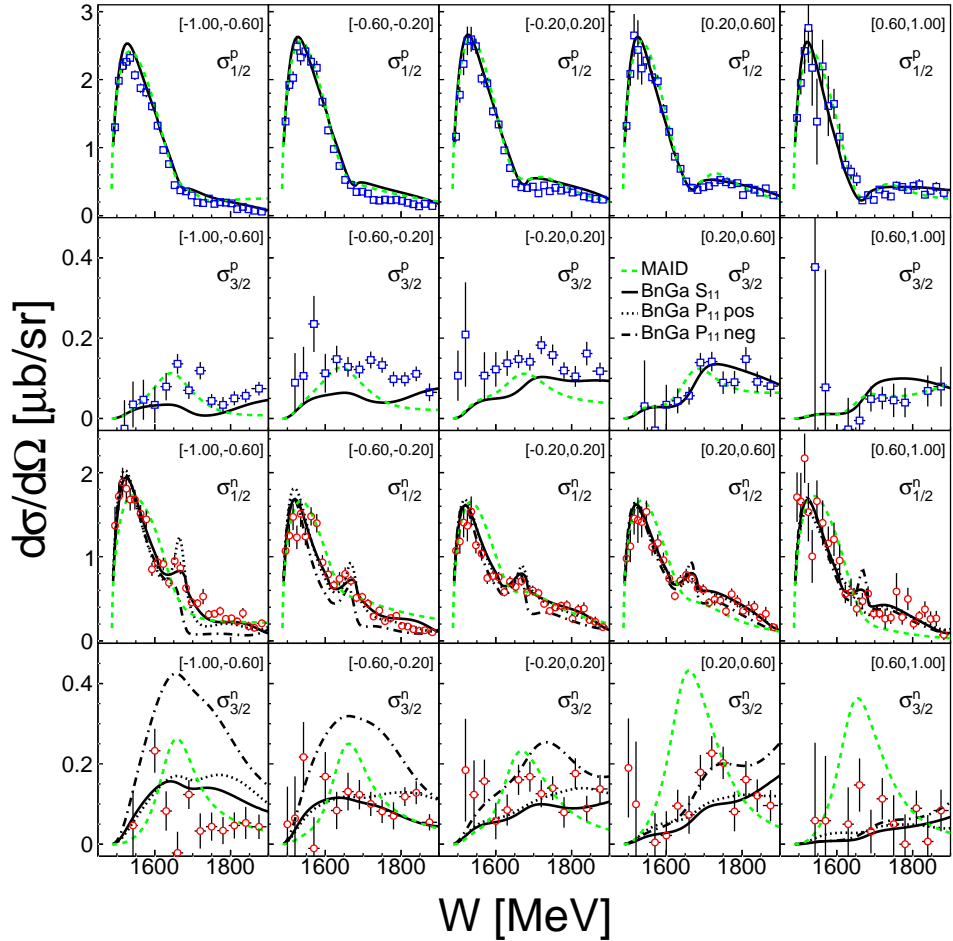


Figure 9.46: Cross sections for the two helicity components (extraction version 1) for the proton (blue) and neutron (red) for five bins of the cm polar angle extracted from A2 data. The experimental results (open circles and squares) are compared to the model predictions by BnGa [48] and MAID [179]. For the neutron three different BnGa solutions are shown: fit with a narrow $N(1685)$ resonance with positive (dotted line) or negative (dash-dotted line) $A_{1/2}$ coupling, and fit without a narrow resonance (solid line).

even better for the neutron. The narrow structure around $W = 1.68$ GeV is visible over the whole angular range in $\sigma_{1/2}$, as predicted by the BnGa model and shown in the third row of Fig. 9.46. However, the structure in the experimental results for $\sigma_{1/2}$ is more pronounced for backward angles. The $\sigma_{3/2}$ cross section is very small in all angular bins. The BnGa solution without the narrow resonance (solid line) seems to fit the best, however, also the solution with narrow $N(1685)$ resonance shows a similar behaviour. The BnGa solution with the negative helicity coupling is inferior and the MAID model completely fails to describe the $\sigma_{1/2}$ and $\sigma_{3/2}$ cross sections for the neutron.

9.5.3 Comparison of A2 and CBELSA/TAPS Results

Finally, the results obtained from the A2 and CBELSA/TAPS data are compared in Fig. 9.47. The results from the CBELSA/TAPS data (open symbols) have of course much inferior statistical quality than the A2 results (closed symbols). However, the CBELSA/TAPS results cover an energy range up to $E_\gamma = 1.85$ GeV, whereas the A2 data are only available up to 1.4 GeV incident photon energy. Over the whole energy

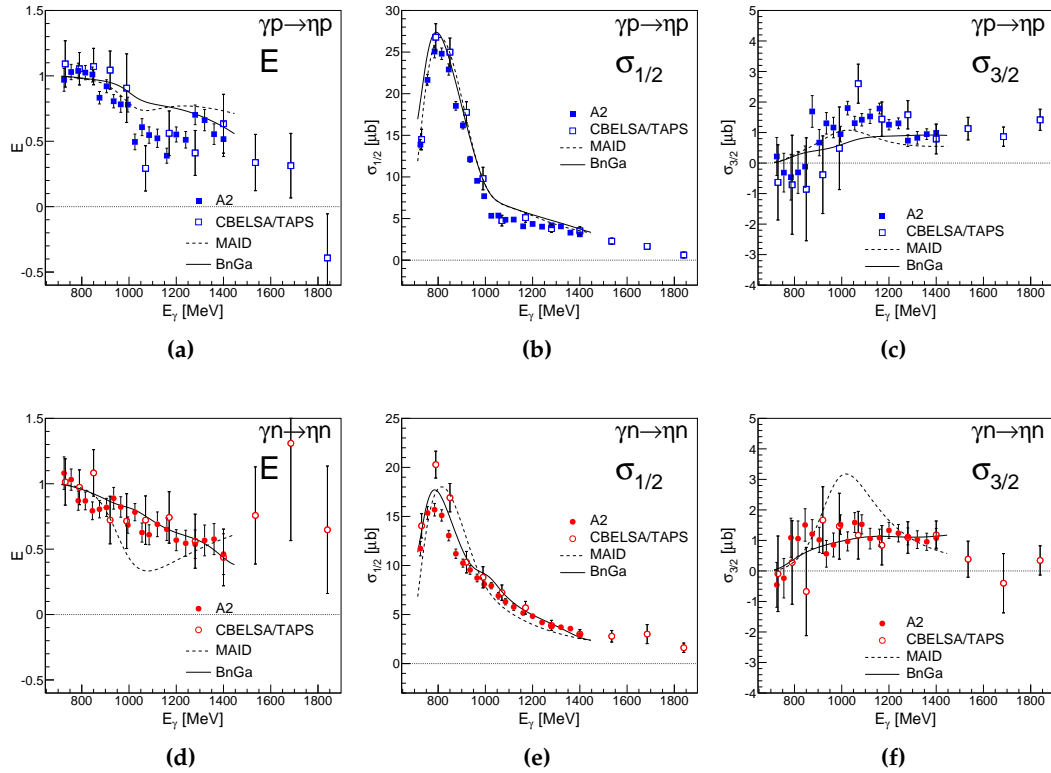


Figure 9.47: Comparison of the polarisation observable E (a,d) and the helicity dependent cross sections $\sigma_{1/2}$ (b,e) and $\sigma_{3/2}$ (c,f) as a function of the incident photon energy from A2 (closed circles) and CBELSA/TAPS data (open circles). The results for the reaction on the proton are shown in (a) – (c) and the results on the neutron are shown in (d) – (f) for extraction version 1.

range, the results from the different experiments are in nearly perfect agreement. This can not only be seen in the polarisation observable E , but also in the helicity dependent cross sections $\sigma_{1/2}$ and $\sigma_{3/2}$. The deviation of the two points in the peak of the $\sigma_{1/2}$ cross section for the neutron is most probably caused by remaining background in the inclusive cross section. As seen in Sec. 9.3.1, this issue is only present for incident photon energies below 850 MeV. The results as a function of the final state energy can only be compared for the proton, since for the CBELSA/TAPS data the neutron could only be extracted inclusively. The results are shown in Fig. 9.48. Also here, the agreement is very good, some small deviations can be assigned to statistical fluctuations.

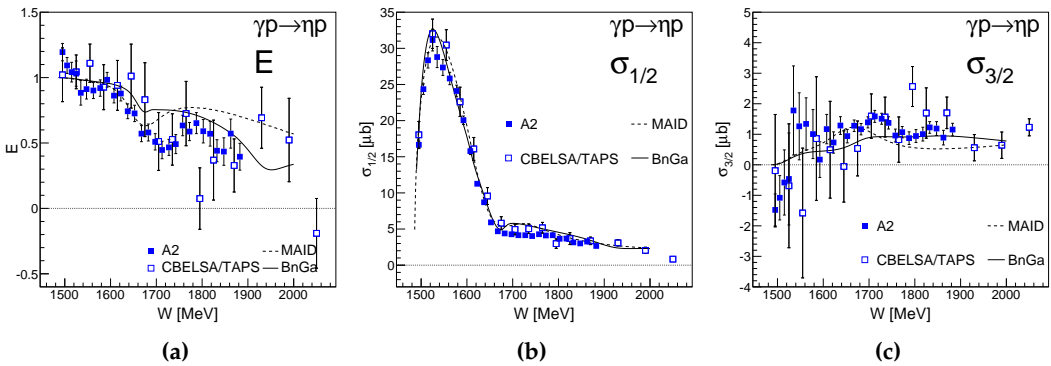


Figure 9.48: Comparison of the double polarisation observable E and the helicity dependent cross sections as a function of the final state energy W from A2 (closed circles) and CBELSA/TAPS data (open circles). The results are shown for the reaction on the proton (the neutron was extracted only as a function of E_γ for CBELSA/TAPS data).

9.6 Conclusions

A precise investigation of the nucleon excitation spectrum is crucial for the understanding of the nucleon structure and the properties of the underlying strong interaction. However, the excitation spectrum is complex, consisting of many broad and overlapping resonances. As a consequence, significant discrepancies between model predictions and experimentally observed states were found. To clarify the situation, a complete set of observables is necessary, which can be used for a model independent partial wave analysis. A complete set of observables consists of the four single polarisations observables and at least four double polarisation observables. The double polarisation observables are sensitive to small contributions from resonances and hence allow to access new information.

In the present work, unpolarised cross sections and the double polarisation observable E was measured for η photoproduction from protons and neutrons. In the last years, η photoproduction has drawn some attention, since previous experiments have shown a narrow structure on the neutron, which is not visible on the proton. The main aim of the present work was to examine the robustness of this structure and restrict its quantum numbers.

For this purpose, unpolarised cross sections were extracted from quasi-free protons and neutrons bound in a ${}^3\text{He}$ and a deuterium target using the A2 and CBELSA/TAPS experiment, respectively. The narrow structure could be confirmed in both measurements. The existence of the structure in two fundamentally different nuclear environments excludes the possibility that the structure is caused by nuclear effects as re-scattering of mesons or FSI. The extracted width and position of the observed structure are consistent with previous results by Werthmüller *et al.* [52] and are given in Table 9.6.

	W_R [MeV]	Γ [MeV]	$\sqrt{b_\eta} A_{1/2}^n$ [$10^{-3}\text{GeV}^{1/2}$]
${}^3\text{He}$, this work	1675 ± 2	62 ± 8 (46 ± 8)	11.9 ± 1.2
LD_2 , this work	1667 ± 3	35 ± 3 (23 ± 2)	13.4 ± 2
LD_2 , Werthmüller [52]	1670 ± 1	50 ± 2 (29 ± 3)	12.3 ± 0.8

Table 9.6: Parameters of the narrow structure from the present work compared to previous results from Ref. [52]. The values in the parentheses were obtained from a fit, which was folded with experimental resolution.

The properties of the narrow structure were further investigated via the double polarisation observable E and the helicity dependent cross sections $\sigma_{1/2}$ and $\sigma_{3/2}$. The helicity dependent cross sections are ideally suited to reveal the spin structure of resonances. In general, resonances with spin $1/2$ couple only to $\sigma_{1/2}$, whereas resonances with spin $\geq 3/2$ couple also to $\sigma_{3/2}$. For this work, double polarisation data were taken with the CBELSA/TAPS and the A2 experiments using a longitudinally polarised dButanol target and a circularly polarised photon beam. The double polarisation observable E obtained in this work are the first available data for the neutron

9.6. CONCLUSIONS

and show that the narrow structure on the neutron is only visible in $\sigma_{1/2}$ and not in $\sigma_{3/2}$, indicating that the structure must be related to S_{11} or P_{11} partial waves. The BnGa model [48] is able to describe this behaviour quite well using the interference of the two well-known resonances $S_{11}(1535)$ and $S_{11}(1650)$. However, this fit induces a sign change of the electromagnetic $A_{1/2}$ coupling of the $S_{11}(1650)$ resonance for the neutron with respect to the current PDG value and is in contradiction with quark model predictions. The BnGa solution with a narrow $N(1685)$ resonance with positive $A_{1/2}$ coupling, which had a worse χ^2 in Ref. [48], shows a similar behaviour and hence cannot be rejected by this work. The MAID model, which predicts the large contribution of the $D_{15}(1675)$ resonance, does not describe the measured asymmetries.

For the proton, currently only the CLAS collaboration has recently published first results on the double polarisation observable E for the free proton [68]. However, the results do not cover the full angular range and have broader energy bins than the results of this work. A comparison of the quasi-free proton results of the current work to model predictions by BnGa and MAID has shown some discrepancies above a final state energy of 1650 MeV, which need further investigations from the theoretical side. The results of this work contribute to the world database on the complete experiment in η photoproduction and give input for new partial wave analyses. Furthermore, the first results on the double polarisation observable E for η photoproduction on the neutron could clarify the origin of the narrow structure on the neutron.

Appendix A

Hadron Multiplets

Hadrons are bound states of quarks. They can be divided into two groups, the mesons with integer spin and the baryons with half-integer spin. According to the quark model, originally proposed by M. Gell-Mann [9, 10] and G. Zweig [11], hadrons with u, d, and s quarks can be organised in flavour $SU(3)$ multiplets. The motivation for this symmetry is that the strong interaction is not depending on the quark flavour (not an exact symmetry since $m_s > m_u \sim m_d$).

A.1 Meson Multiplets

Mesons consist of a quark and an antiquark. If one takes into account the three lightest quark flavours u, d and s, nine combinations are possible. They can be grouped into an octet and a singlet according to the symmetry of the states

$$3 \otimes \bar{3} = 8 \oplus 1 \quad (\text{A.1})$$

Depending on the spin coupling of the quarks one gets the pseudoscalar $J^P = 0^-$ and vector meson $J^P = 1^-$ nonet. Each nonet is composed of one isospin triplet, two doublets and two singlets. The multiplets are shown in meson Figure A.1.

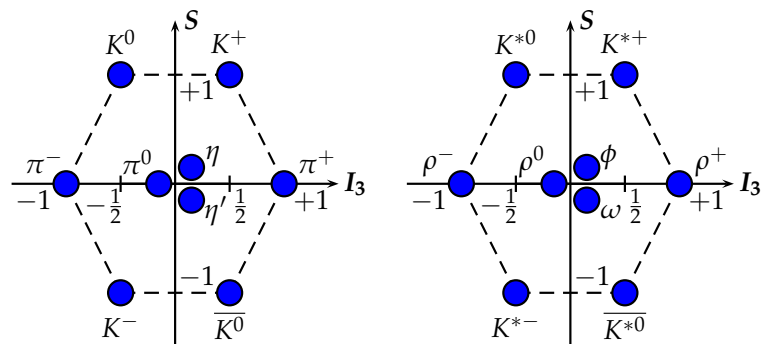


Figure A.1: The nonets of pseudoscalar mesons with $J^P = 0^-$ (left) and vector mesons with $J^P = 1^-$ (right). The third component of the isospin I_3 is plotted on the x-axis, while the y-axis is the strangeness S .

A.2 Baryon Multiplets

With a similar argumentation as for the mesons, the light baryons made of three quarks can be assigned to multiplets:

$$3 \otimes 3 \otimes 3 = 1 \oplus 8 \oplus 8 \oplus 10 \quad (\text{A.2})$$

Protons and neutrons are members of the octet [182]. The weight diagrams for the baryons in shown in Figure A.2 and A.3.

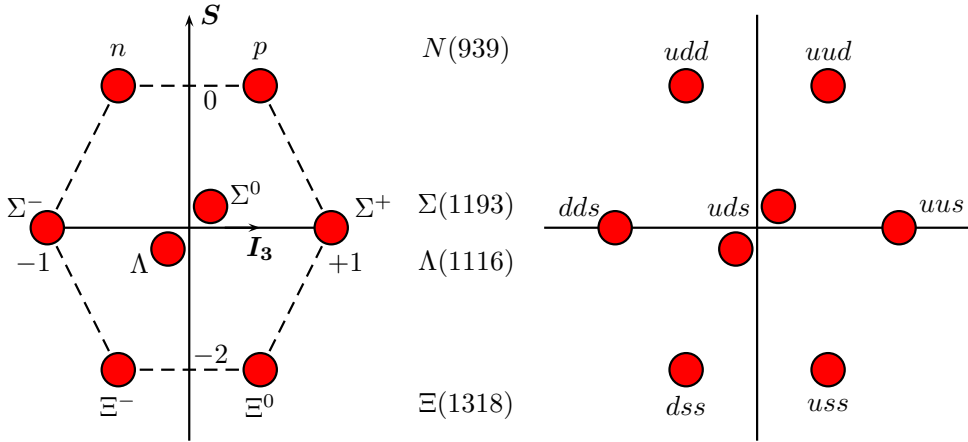


Figure A.2: The mixed symmetric baryon octet of $SU(3)$

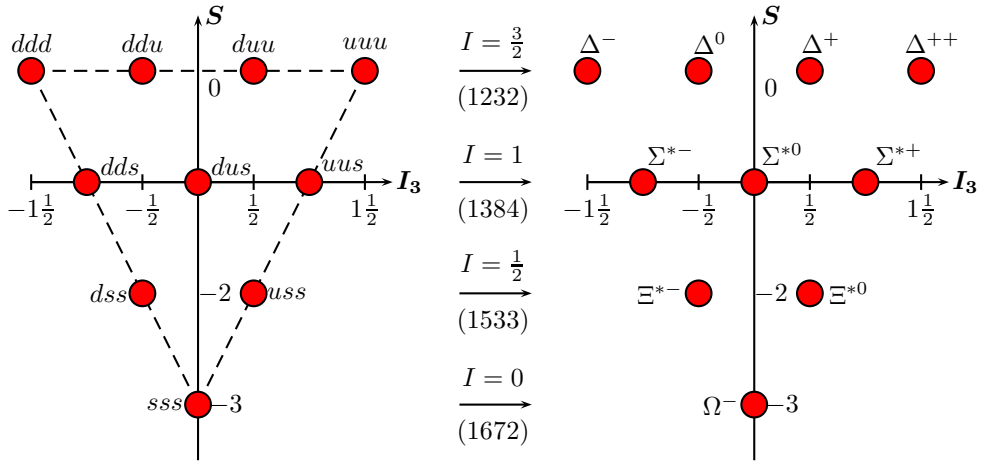


Figure A.3: The symmetric baryon decuplet of $SU(3)$

A.3 Antidecuplet of Pentaquarks

Already in 1964 M. Gell-Mann suggested the existence of a bound state of five quarks. As mentioned in section 1.4.1, χ QSM predicts the existence of the exotic antidecuplet of pentaquarks with $J^P = 1/2^+$. The antidecuplet is shown in Figure A.4. The red

member is the tentative $N(1710)$ state, which is a possible candidate for the narrow structure observed in η photoproduction on the neutron.

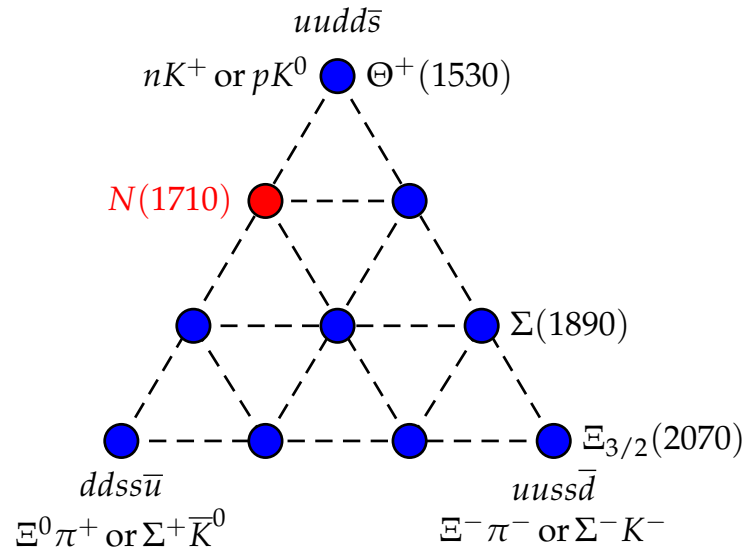


Figure A.4: Baryon antidecuplet of pentaquarks. Red indicated is the non-strange member, which has been assigned to the $N(1710)$.

Appendix B

Polarisation Observables

B.1 General Form of the Cross Section

The most general form of the cross section including higher order terms can be written as follows [183]:

$$\begin{aligned}
d\sigma^{\text{B,T,R}}(\vec{P}^\gamma, \vec{P}^T, \vec{P}^R) = & \frac{1}{2} \left\{ d\sigma_0 \left[1 - P_L^\gamma P_y^T P_y^R \cos(2\phi_\gamma) \right] \right. \\
& + \hat{\Sigma} \left[-P_L^\gamma \cos(2\phi) + P_y^T P_y^R \right] \\
& + \hat{T} \left[P_y^T - P_L^\gamma P_y^R \cos(2\phi_\gamma) \right] \\
& + \hat{P} \left[P_y^R - P_L^\gamma P_y^T \cos(2\phi_\gamma) \right] \\
& + \hat{E} \left[-P_c^\gamma P_z^T + P_L^\gamma P_x^T P_y^R \sin(2\phi_\gamma) \right] \\
& + \hat{G} \left[P_L^\gamma P_z^T \sin(2\phi) + P_c^\gamma P_x^T P_y^R \right] \\
& + \hat{F} \left[P_c^\gamma P_x^T + P_L^\gamma P_z^T P_y^R \sin(2\phi_\gamma) \right] \\
& + \hat{H} \left[P_L^\gamma P_x^T \sin(2\phi) - P_c^\gamma P_z^T P_y^R \right] \\
& + \hat{C}_{x'} \left[P_c^\gamma P_x^R - P_L^\gamma P_y^T P_z^R \sin(2\phi_\gamma) \right] \\
& + \hat{C}_{z'} \left[P_c^\gamma P_z^R + P_L^\gamma P_y^T P_x^R \sin(2\phi_\gamma) \right] \\
& + \hat{O}_{x'} \left[P_L^\gamma P_{x'}^R \sin(2\phi) + P_c^\gamma P_y^T P_z^R \right] \\
& + \hat{O}_{z'} \left[P_L^\gamma P_{z'}^R \sin(2\phi) - P_c^\gamma P_y^T P_{x'}^R \right] \\
& + \hat{L}_{x'} \left[P_z^T P_{x'}^R + P_L^\gamma P_x^T P_z^R \cos(2\phi_\gamma) \right] \\
& + \hat{L}_{z'} \left[P_z^T P_{z'}^R - P_L^\gamma P_x^T P_{x'}^R \cos(2\phi_\gamma) \right] \\
& + \hat{T}_{x'} \left[P_x^T P_{x'}^R - P_L^\gamma P_z^T P_{z'}^R \cos(2\phi_\gamma) \right] \\
& \left. + \hat{T}_{z'} \left[P_x^T P_{z'}^R + P_L^\gamma P_z^T P_{x'}^R \cos(2\phi_\gamma) \right] \right\}. \tag{B.1}
\end{aligned}$$

"Each single polarization observable has another higher order term that depends on two polarization quantities, and each double has another term dependent on three polarizations." [38]

B.2 Complete Set of Observables

The following table summarises all the possible combinations for a set of complete observables as suggested by Chiang and Tabakin [40].

Table B.1: All possible combinations for a complete set of observables needed to unambiguously determine the amplitudes. The 'X' indicate three initially selected measurements, and 'O' indicate the possible choices for fourth observable. [40]

Appendix C

Efficiencies

Fig. C.1 and Fig. C.2 show the angular efficiencies for the A2 deuterium and dButanol target, respectively. The efficiencies were determined for the cm system of the incident photon beam and the target, assuming the nucleon at rest. The reaction on the proton is shown in blue, whereas the reaction on the neutron is shown in red. The $\eta \rightarrow 2\gamma$ decay channels is shown as a solid line, the $\eta \rightarrow 6\gamma$ decay channels is shown as a dashed line.

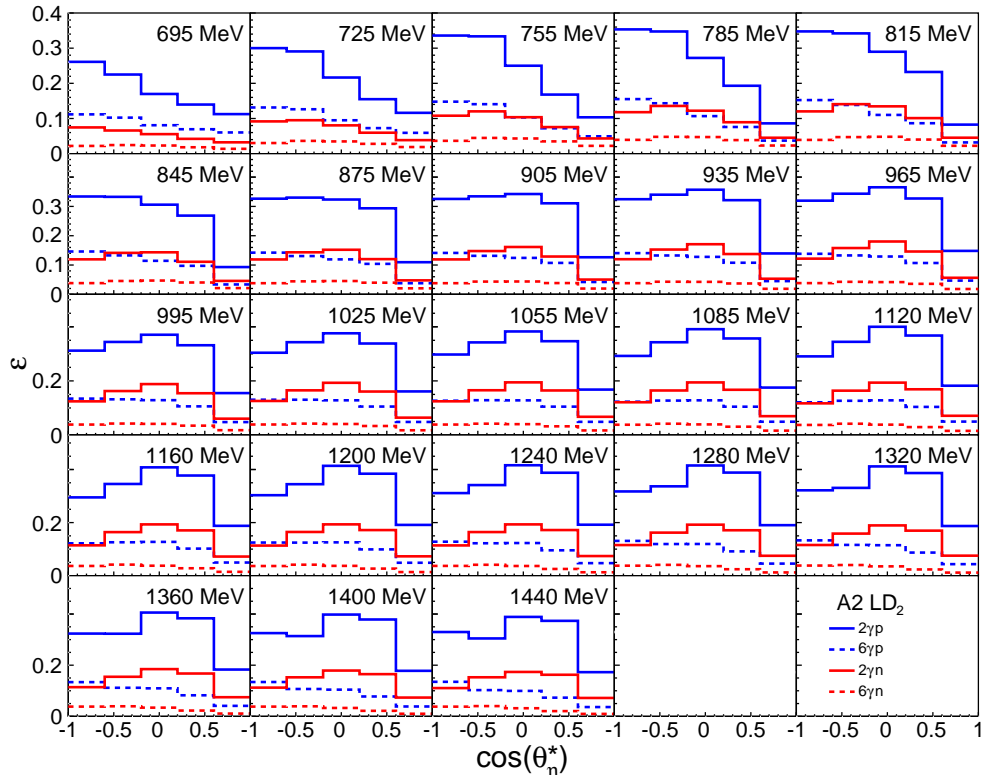


Figure C.1: Detection efficiency for $\gamma p \rightarrow \eta p$ (blue) and $\gamma n \rightarrow \eta n$ (red) for the A2 LD_2 target. The $\cos(\theta_\eta^*)$ distribution is shown as a function of the incident photon energy E_γ for both decay channels, $\eta \rightarrow 2\gamma$ (solid line) and $\eta \rightarrow 6\gamma$ (dashed line).

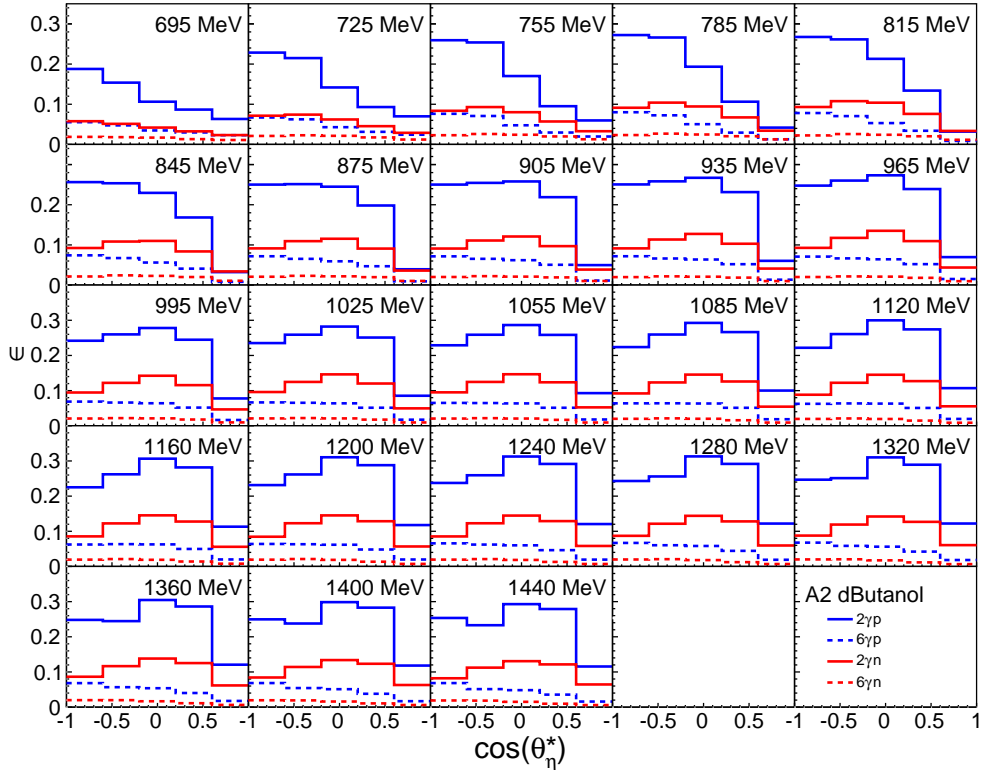


Figure C.2: Detection efficiency for $\gamma p \rightarrow \eta p$ (blue) and $\gamma n \rightarrow \eta n$ (red) for the A2 dButanol target. The $\cos(\theta_\eta^*)$ distribution is shown as a function of the incident photon energy E_γ for both decay channels, $\eta \rightarrow 2\gamma$ (solid line) and $\eta \rightarrow 6\gamma$ (dashed line).

Fig. C.3 shows the angular efficiency in the cm system of the incident photon beam and the target for the CBELSA/TAPS deuterium target. The reaction on the proton is shown in blue, whereas the reaction on the neutron is shown in red.

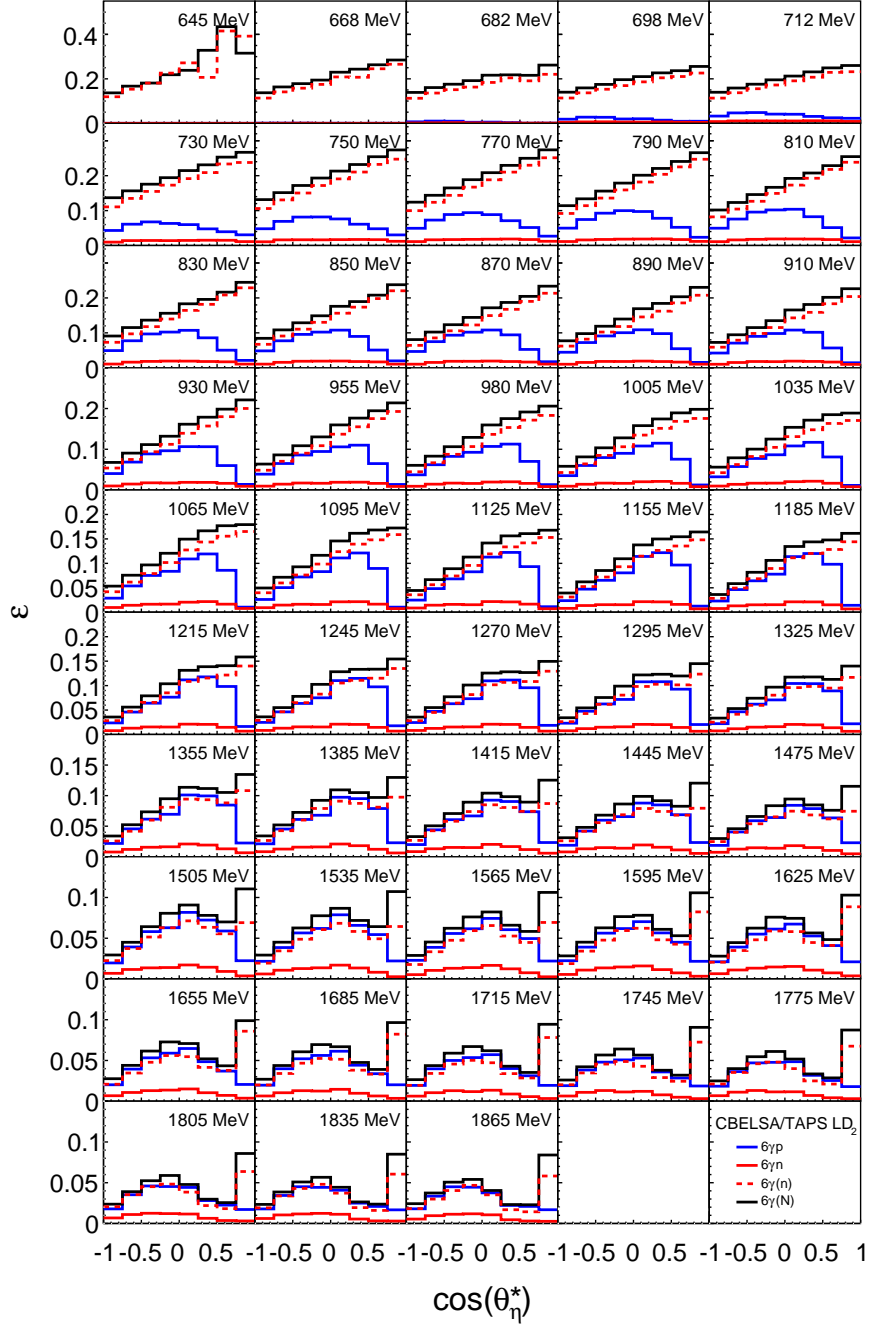


Figure C.3: Detection efficiency for $\gamma p \rightarrow \eta p$ (blue), $\gamma n \rightarrow \eta n$ (red) and $\gamma N \rightarrow \eta(N)$ (black) for the CBELSA/TAPS LD₂ target. The $\cos(\theta_\eta^*)$ distribution is shown as a function of the incident photon energy E_γ .

Appendix D

Systematic Uncertainties for the ${}^3\text{He}$ Cross Sections

Figs. D.1 and D.2 show the relative systematic uncertainties for the ${}^3\text{He}$ cross sections. Shown are the systematic uncertainties from the analysis cuts (blue), the nucleon efficiency (red) and the CB energy sum (green) for the $\gamma + p \rightarrow \eta + p$ and the $\gamma + n \rightarrow \eta + n$ reaction for both decay channels of the η meson. The uncertainties were determined as explained in Sec. 8.12.1. However, the uncertainties from the nucleon detection efficiency were determined using different cut positions in the analysis of the free proton data, as described in Ref. [56].

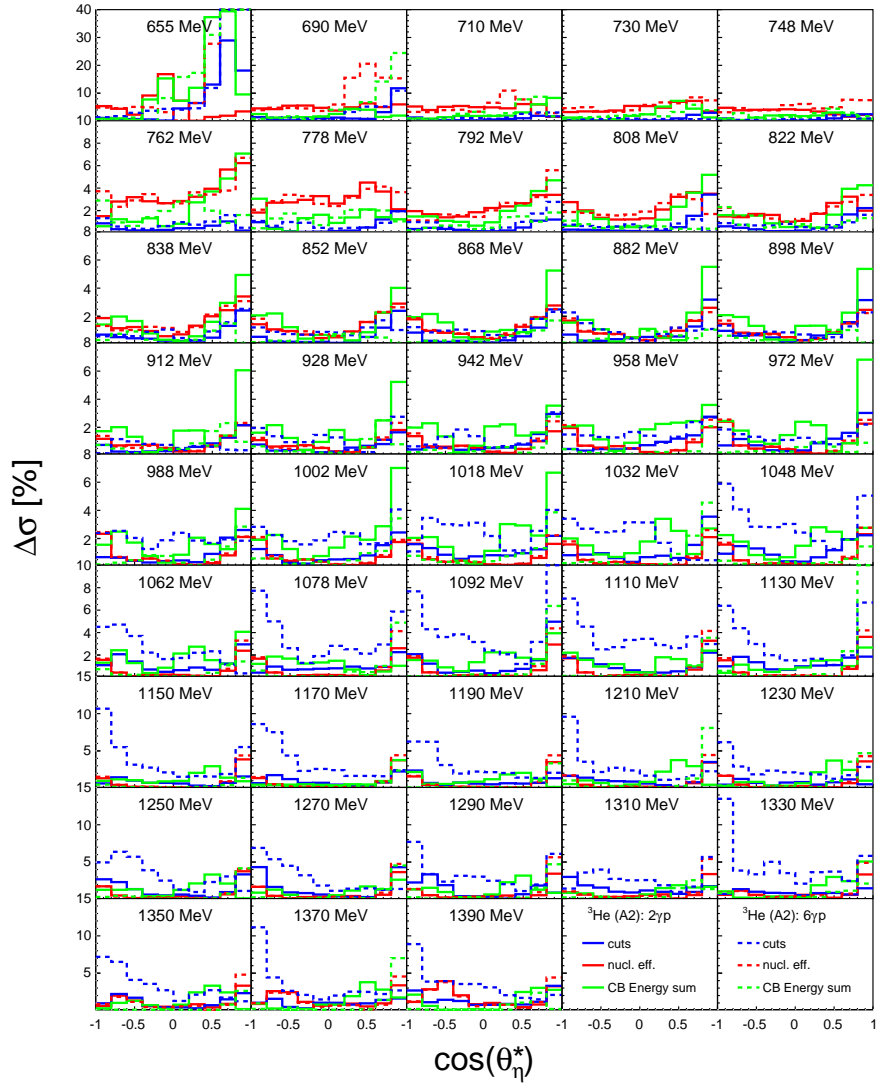


Figure D.1: Relative systematic uncertainties from the analysis cuts (blue), the nucleon efficiency (red), and from the CB energy sum (green) for the $\gamma + p \rightarrow \eta + p$ cross section for the A2 ^3He target. The systematic uncertainties for the $\eta \rightarrow 2\gamma$ decay channel are shown as solid lines, the uncertainties for the $\eta \rightarrow 6\gamma$ decay channel are shown as dashed lines. The systematic uncertainties were determined as described in Sec. 8.12.1. However, the uncertainties from the nucleon detection efficiency were determined using different analysis cuts as described in Ref. [56]. The same variable energy binning as for the cross sections and eight $\cos(\theta_\eta^*)$ -bins were used (mean value indicated).

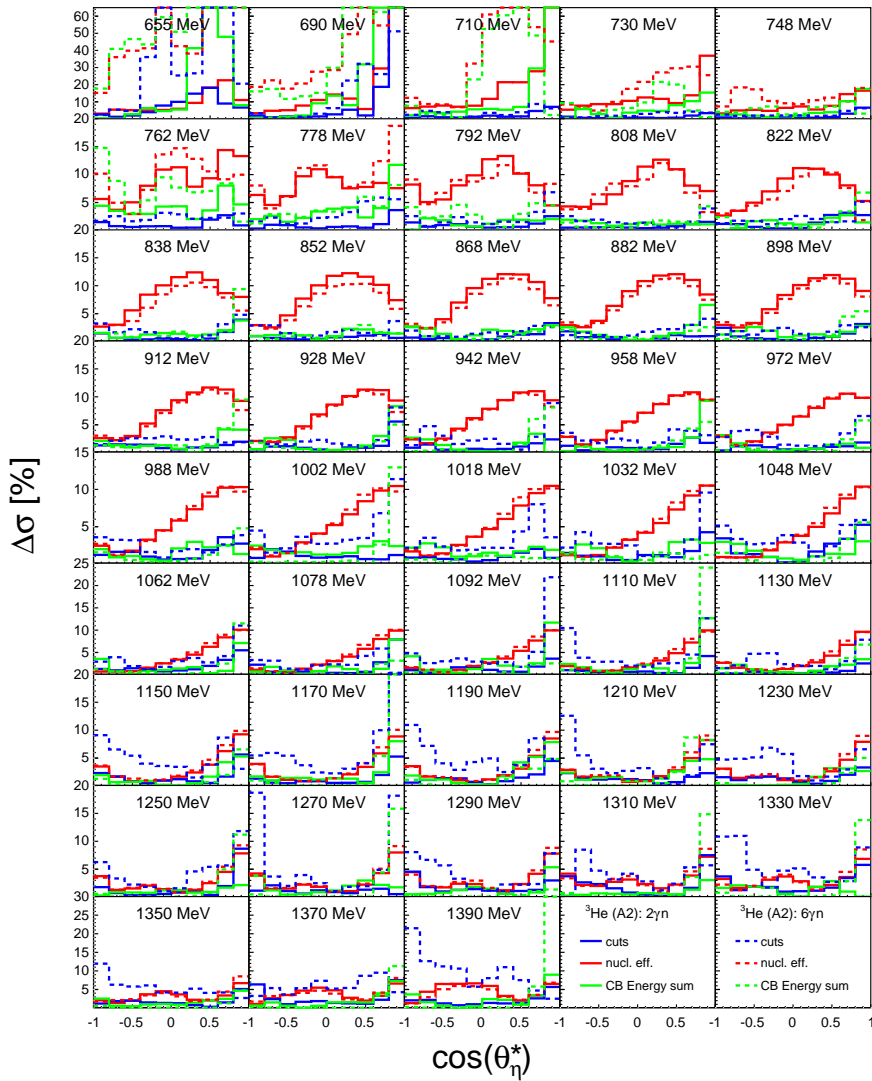


Figure D.2: Relative systematic uncertainties from the analysis cuts (blue), the nucleon efficiency (red), and from the CB energy sum (green) for the $\gamma + n \rightarrow \eta + n$ cross section for the A2 ${}^3\text{He}$ target. The systematic uncertainties for the $\eta \rightarrow 2\gamma$ decay channel are shown as solid lines, the uncertainties for the $\eta \rightarrow 6\gamma$ decay channel are shown as dashed lines. The systematic uncertainties were determined as described in Sec. 8.12.1. However, the uncertainties from the nucleon detection efficiency were determined using different analysis cuts as described in Ref. [56]. The same variable energy binning as for the cross sections and eight $\cos(\theta_\eta^*)$ -bins were used (mean value indicated).

Appendix E

Angular Distributions for the Polarisation Observables

Figs. E.1 – E.6 show the angular distributions in the cm system of the incident photon beam and the target, assuming the nucleon at rest. Figs. E.1, E.1, E.3 show the results for the proton and Figs. E.4, E.5, E.6 show the results for the neutron. All cross sections are shown for different bins of incident photon energy E_γ .

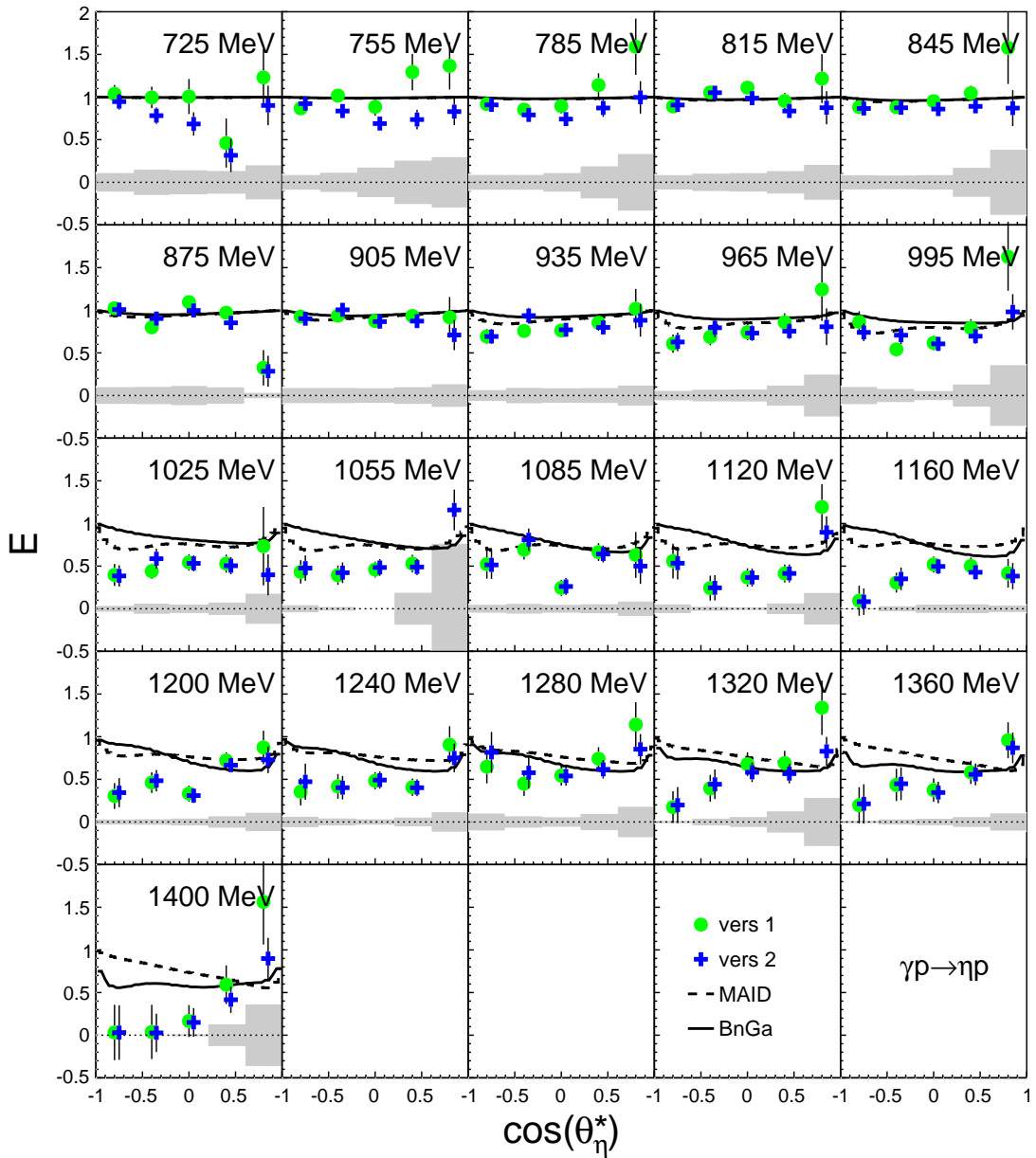


Figure E.1: Angular distributions for the double polarisation observable E for different bins of incident photon energy for the reaction on the proton. The two different extraction versions, explained in Sec. 8.2 are shown. For a better visibility the points of version 2 (blue) were shifted by $\Delta \cos(\theta_{\eta}^*) = +0.05$ with respect to version 1 (green). The systematic uncertainties are indicated by the gray shaded areas. The experimental results are compared to model predictions by BnGa [48] (solid line) and MAID (dashed line) [179].

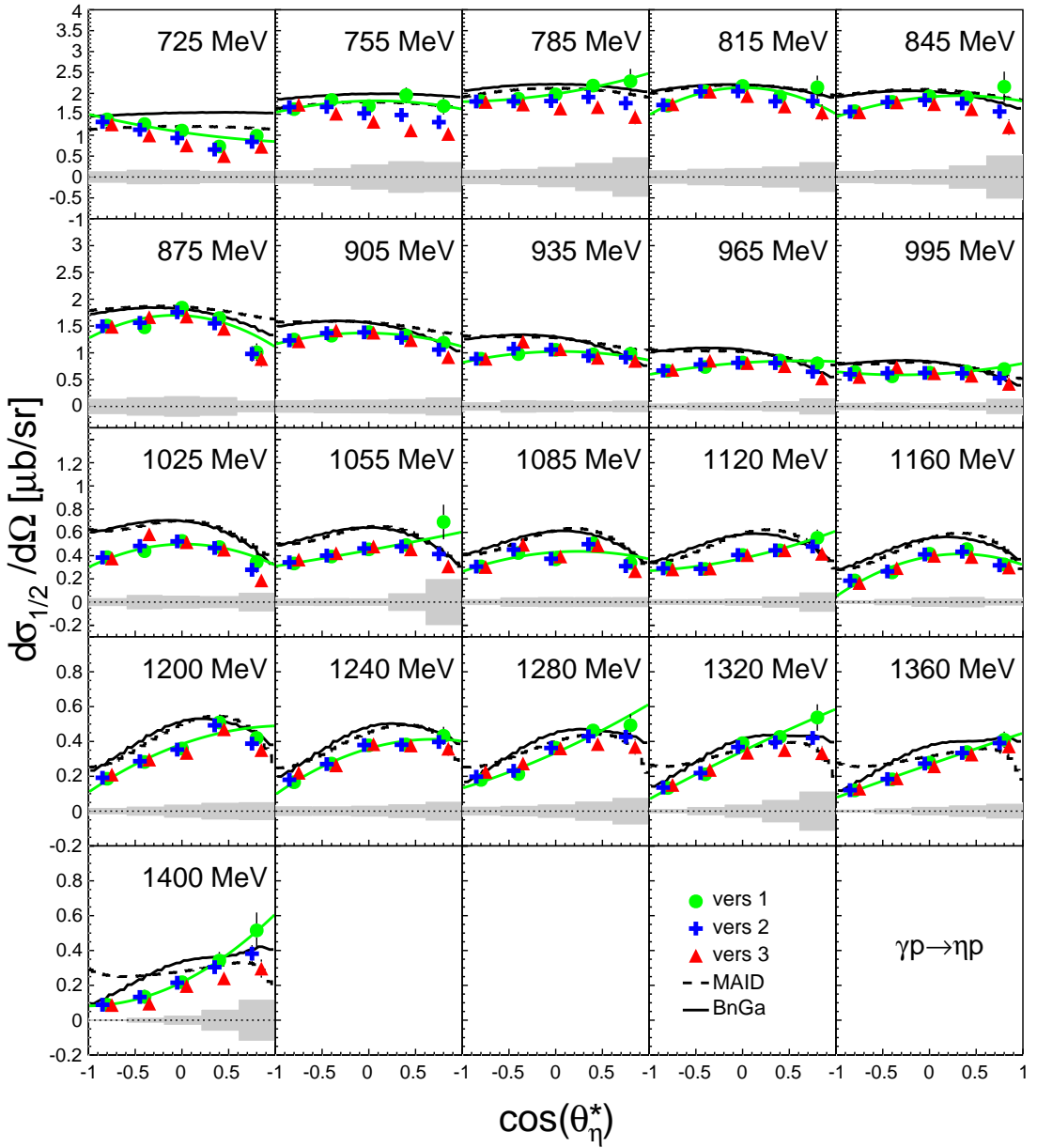


Figure E.2: Angular distributions for the helicity dependent cross section $\sigma_{1/2}$ for different bins of incident photon energy for the reaction on the proton. The two different extraction versions, explained in Sec. 8.2 are shown. For a better visibility the points of version 2 (blue) and version 3 (red) were shifted by $\Delta \cos(\theta_{\eta}^*) = \pm 0.05$ with respect to version 1 (green). The systematic uncertainties are indicated by the gray shaded areas. The experimental results are compared to model predictions by BnGa [48] (solid line) and MAID (dashed line) [179].

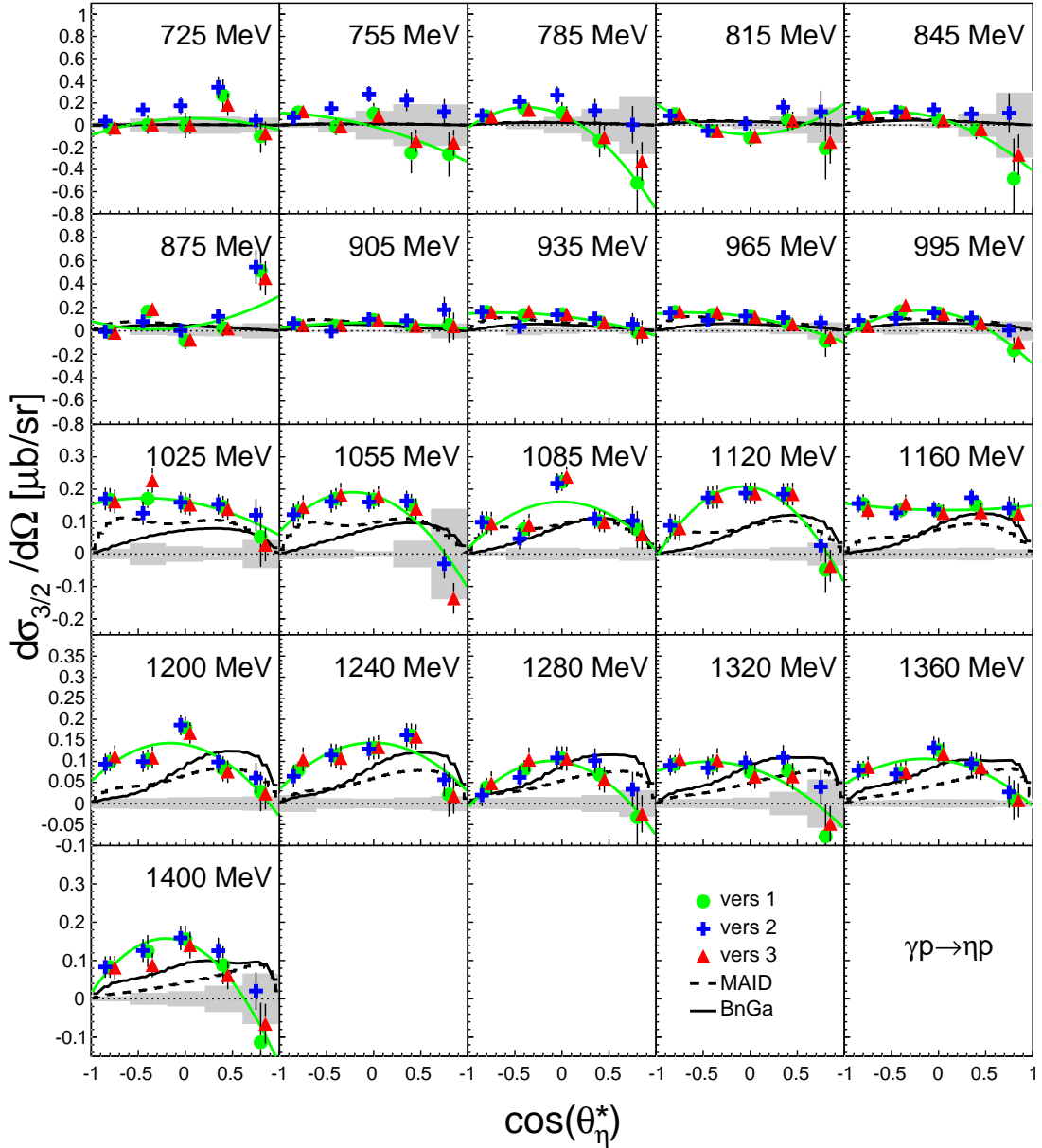


Figure E.3: Angular distributions for the helicity dependent cross section $\sigma_{3/2}$ for different bins of incident photon energy for the reaction on the proton. The two different extraction versions, explained in Sec. 8.2 are shown. For a better visibility the points of version 2 (blue) and version 3 (red) were shifted by $\Delta \cos(\theta_\eta^*) = \pm 0.05$ with respect to version 1 (green). The systematic uncertainties are indicated by the gray shaded areas. The experimental results are compared to model predictions by BnGa [48] (solid line) and MAID (dashed line) [179].

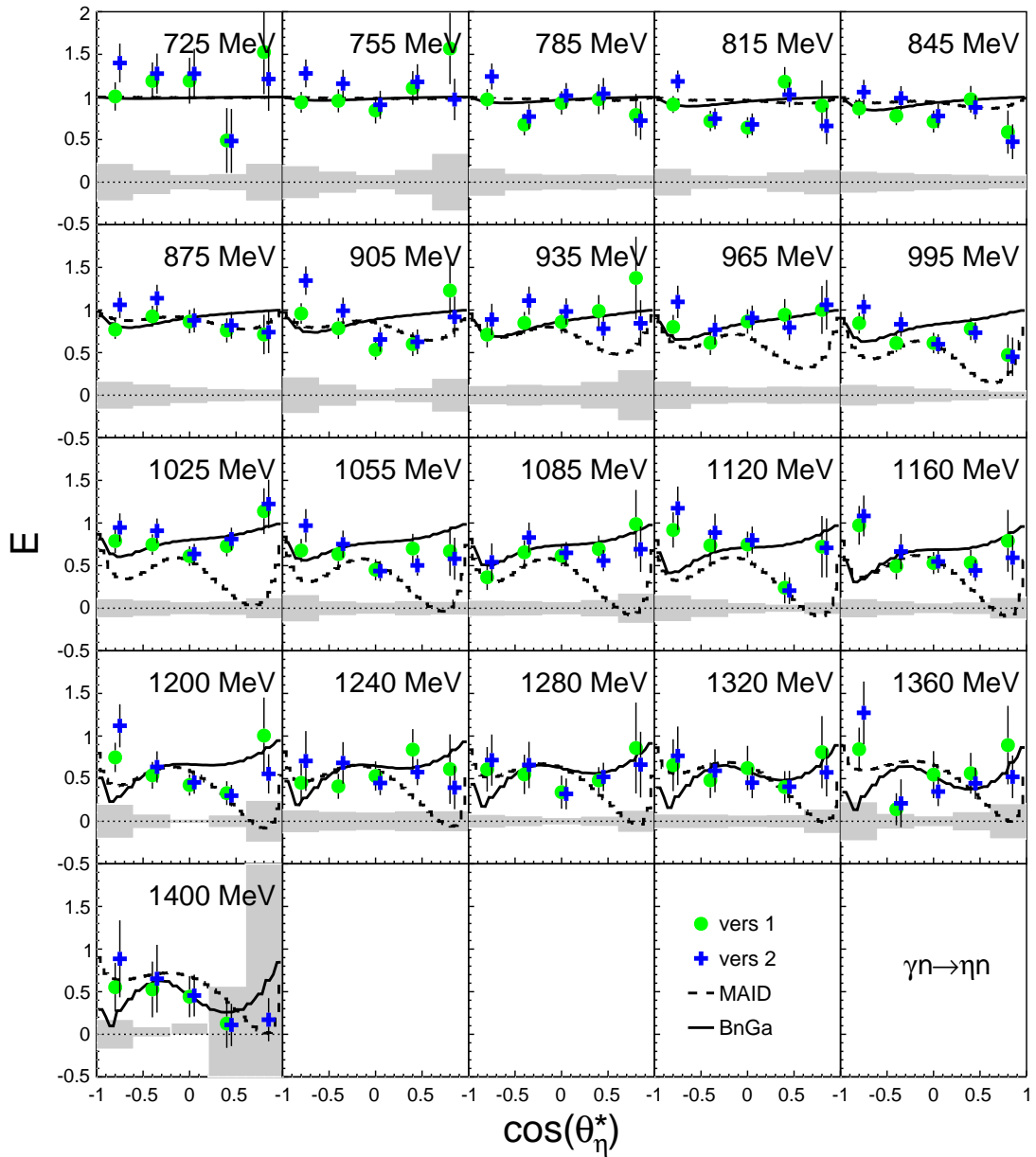


Figure E.4: Angular distributions for the double polarisation observable E for different bins of incident photon energy for the reaction on the proton. The two different extraction versions, explained in Sec. 8.2 are shown. For a better visibility the points of version 2 (blue) were shifted by $\Delta \cos(\theta_\eta^*) = +0.05$ with respect to version 1 (green). The systematic uncertainties are indicated by the gray shaded areas. The experimental results are compared to model predictions by BnGa [48] (solid line) and MAID (dashed line) [179].

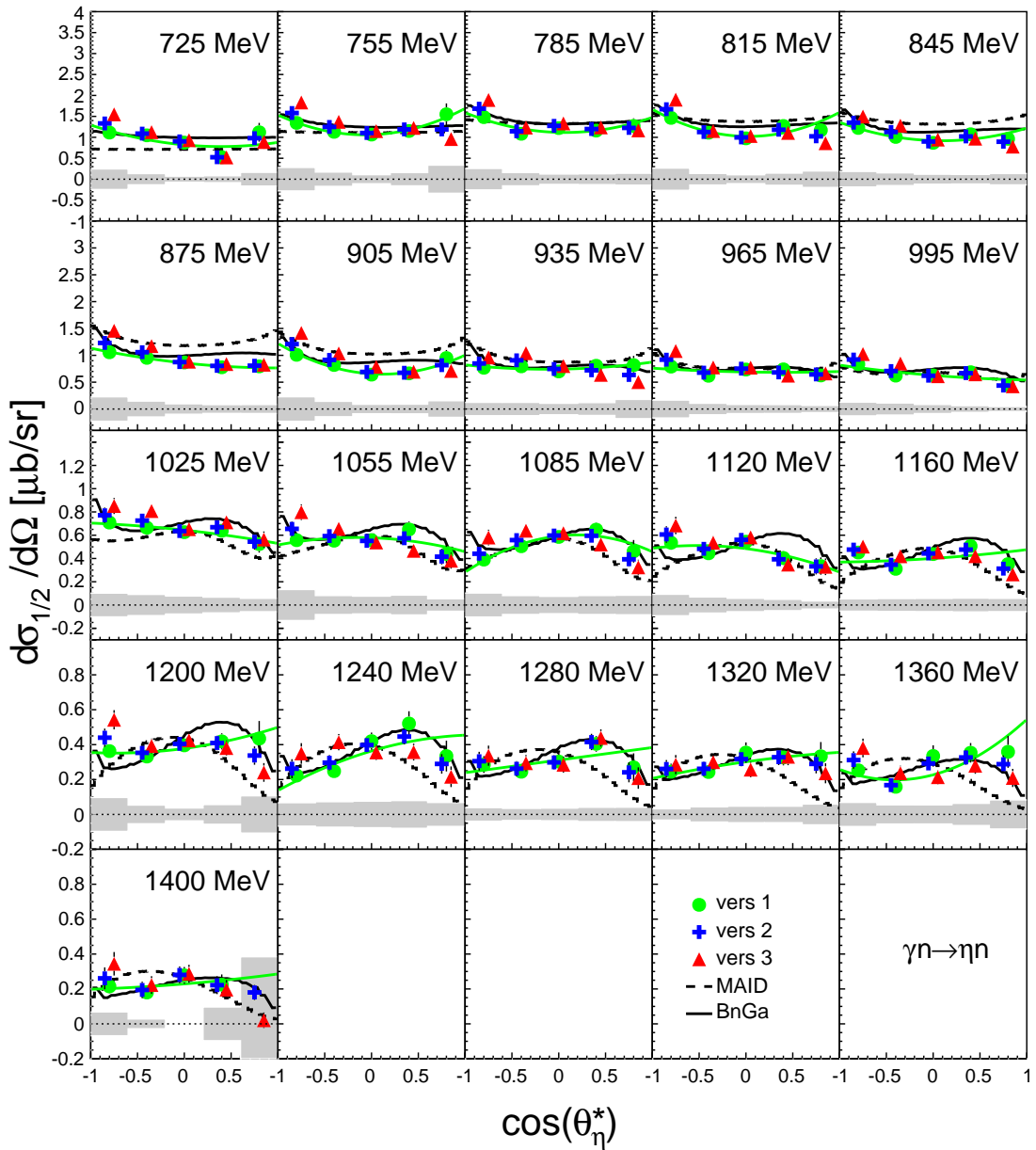


Figure E.5: Angular distributions for the helicity dependent cross section $\sigma_{1/2}$ for different bins of incident photon energy for the reaction on the neutron. The two different extraction versions, explained in Sec. 8.2 are shown. For a better visibility the points of version 2 (blue) were shifted by $\Delta \cos(\theta_\eta^*) = \pm 0.05$ with respect to version 1 (green). The systematic uncertainties are indicated by the gray shaded areas. The experimental results are compared to model predictions by BnGa [48] (solid line) and MAID (dashed line) [179].

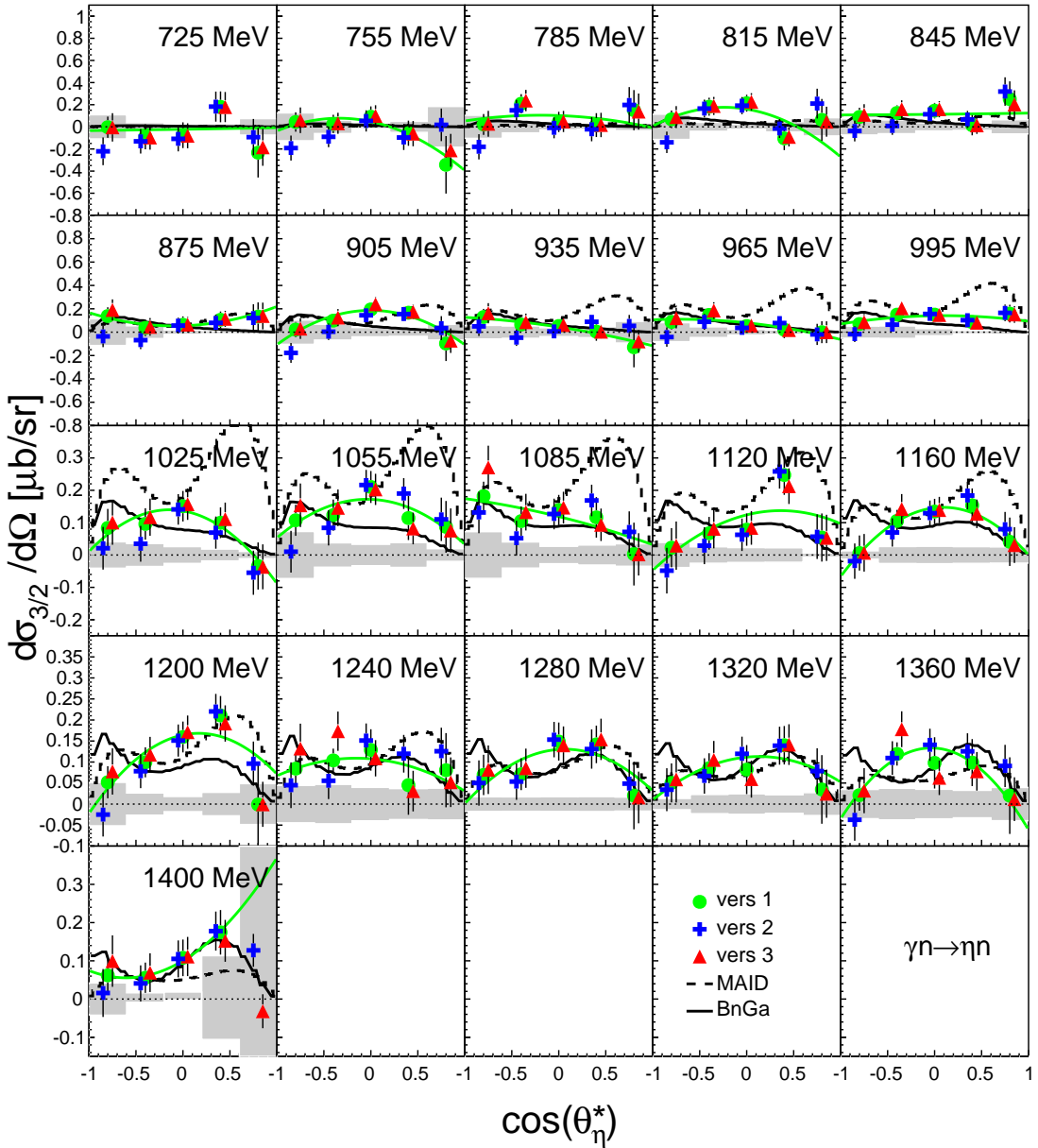


Figure E.6: Angular distributions for the helicity dependent cross section $\sigma_{3/2}$ for different bins of incident photon energy for the reaction on the neutron. The two different extraction versions, explained in Sec. 8.2 are shown. For a better visibility the points of version 2 (blue) and version 3 (red) were shifted by $\Delta \cos(\theta_\eta^*) = \pm 0.05$ with respect to version 1 (green). The systematic uncertainties are indicated by the gray shaded areas. The experimental results are compared to model predictions by BnGa [48] (solid line) and MAID (dashed line) [179].

Appendix F

Data Tables

The following tables contain all measured polarisation observables and cross sections together with the corresponding statistical and systematic uncertainties. Appendix F.1 summarises the data from the differential and total cross sections for η photoproduction for the ${}^3\text{He}$ target (A2 data). Appendix F.2 contains the data from the differential and total cross sections using the LD_2 target of the CBELSA/TAPS collaboration. In Appendix F.3 and F.4, the data of the double polarisation observable E and the helicity dependent cross sections are summarised for CBELSA/TAPS and A2 data, respectively. Only the results from extraction *version 1* (see Sec. 8.2) are given since they are considered as the most reliable results. For the polarised CBELSA/TAPS data, only the total distributions are given since no angular distributions were determined.

F.1 Unpolarised Cross Sections from ${}^3\text{He}$ (A2)

F.1.1 $\gamma N \rightarrow \eta(N)$ as a Function of E_γ

Angular Distributions

$\cos(\theta_\eta^*)$	$E_\gamma = (655.0 \pm 25.0) \text{ MeV}$			$E_\gamma = (690.0 \pm 10.0) \text{ MeV}$			$E_\gamma = (710.0 \pm 10.0) \text{ MeV}$			$E_\gamma = (730.0 \pm 10.0) \text{ MeV}$		
	$d\sigma/d\Omega$			$d\sigma/d\Omega$			$d\sigma/d\Omega$			$d\sigma/d\Omega$		
	$[\mu\text{b}/\text{sr}]$	$[\mu\text{b}/\text{sr}]$	$[\mu\text{b}/\text{sr}]$									
-0.90	0.6388	0.0043	0.0616	1.2074	0.0090	0.1319	1.6309	0.0137	0.1961	1.8741	0.0123	0.2272
-0.70	0.3647	0.0035	0.0397	0.8416	0.0079	0.1039	1.2269	0.0123	0.1592	1.5006	0.0111	0.1972
-0.50	0.2626	0.0032	0.0311	0.7073	0.0074	0.0901	1.0931	0.0119	0.1450	1.3789	0.0108	0.1917
-0.30	0.1927	0.0029	0.0257	0.5870	0.0071	0.0801	0.9768	0.0116	0.1367	1.2523	0.0107	0.1805
-0.10	0.1484	0.0027	0.0231	0.4873	0.0066	0.0710	0.8802	0.0110	0.1264	1.1455	0.0102	0.1679
0.10	0.1038	0.0025	0.0206	0.3938	0.0063	0.0645	0.7386	0.0105	0.1120	1.0501	0.0099	0.1609
0.30	0.0573	0.0022	0.0121	0.3116	0.0059	0.0554	0.6398	0.0101	0.1032	0.9324	0.0095	0.1498
0.50	0.0398	0.0020	0.0082	0.2236	0.0053	0.0422	0.5414	0.0093	0.0893	0.8389	0.0091	0.1336
0.70	0.0240	0.0017	0.0034	0.1676	0.0048	0.0288	0.4488	0.0088	0.0689	0.6727	0.0083	0.0963
0.90	0.0145	0.0015	0.0005	0.1204	0.0043	0.0120	0.3550	0.0079	0.0365	0.5898	0.0078	0.0572
$\cos(\theta_\eta^*)$	$E_\gamma = (747.5 \pm 7.5) \text{ MeV}$			$E_\gamma = (762.5 \pm 7.5) \text{ MeV}$			$E_\gamma = (777.5 \pm 7.5) \text{ MeV}$			$E_\gamma = (792.5 \pm 7.5) \text{ MeV}$		
	$d\sigma/d\Omega$			$d\sigma/d\Omega$			$d\sigma/d\Omega$			$d\sigma/d\Omega$		
	$[\mu\text{b}/\text{sr}]$	$[\mu\text{b}/\text{sr}]$	$[\mu\text{b}/\text{sr}]$									
-0.90	2.0126	0.0143	0.2537	2.0399	0.0168	0.2851	1.9424	0.0169	0.2347	1.8045	0.0167	0.2493
-0.70	1.6864	0.0135	0.2310	1.8130	0.0159	0.2572	1.7911	0.0164	0.2224	1.7781	0.0165	0.2222
-0.50	1.6181	0.0132	0.2283	1.7512	0.0159	0.2502	1.8157	0.0167	0.2401	1.8289	0.0165	0.2135
-0.30	1.5195	0.0131	0.2082	1.7134	0.0157	0.2543	1.7647	0.0165	0.2376	1.8504	0.0165	0.2116
-0.10	1.3911	0.0127	0.1935	1.5831	0.0153	0.2394	1.7287	0.0164	0.2269	1.7892	0.0164	0.2068
0.10	1.3186	0.0124	0.2001	1.5043	0.0149	0.2186	1.6539	0.0160	0.2179	1.7834	0.0163	0.2228
0.30	1.2125	0.0119	0.1929	1.4573	0.0146	0.2314	1.6005	0.0155	0.2179	1.6981	0.0158	0.2303
0.50	1.0984	0.0114	0.1760	1.3212	0.0141	0.2121	1.4783	0.0153	0.2062	1.6065	0.0153	0.2171
0.70	0.9563	0.0108	0.1351	1.1464	0.0132	0.1573	1.3482	0.0145	0.1775	1.4917	0.0146	0.1876
0.90	0.8280	0.0100	0.0759	1.0447	0.0129	0.0950	1.2266	0.0137	0.1329	1.3561	0.0141	0.1472
$\cos(\theta_\eta^*)$	$E_\gamma = (807.5 \pm 7.5) \text{ MeV}$			$E_\gamma = (822.5 \pm 7.5) \text{ MeV}$			$E_\gamma = (837.5 \pm 7.5) \text{ MeV}$			$E_\gamma = (852.5 \pm 7.5) \text{ MeV}$		
	$d\sigma/d\Omega$			$d\sigma/d\Omega$			$d\sigma/d\Omega$			$d\sigma/d\Omega$		
	$[\mu\text{b}/\text{sr}]$	$[\mu\text{b}/\text{sr}]$	$[\mu\text{b}/\text{sr}]$									
-0.90	1.7340	0.0169	0.1843	1.6694	0.0177	0.1557	1.5973	0.0187	0.1574	1.5862	0.0187	0.1200
-0.70	1.7805	0.0173	0.1945	1.7225	0.0180	0.1629	1.7037	0.0187	0.1561	1.6769	0.0188	0.1717
-0.50	1.8304	0.0171	0.2062	1.8300	0.0182	0.1775	1.7693	0.0190	0.1697	1.7837	0.0191	0.1917
-0.30	1.8971	0.0173	0.2109	1.8907	0.0181	0.1864	1.8887	0.0195	0.1864	1.8561	0.0194	0.1732
-0.10	1.8500	0.0167	0.1888	1.9239	0.0183	0.1997	1.8776	0.0191	0.1781	1.8768	0.0190	0.1779
0.10	1.8630	0.0168	0.1886	1.8972	0.0179	0.1960	1.8712	0.0189	0.1895	1.8837	0.0189	0.1914
0.30	1.7824	0.0166	0.1947	1.8293	0.0174	0.1944	1.8091	0.0186	0.1952	1.7858	0.0185	0.1876
0.50	1.7217	0.0163	0.1975	1.6849	0.0157	0.1891	1.7261	0.0181	0.1973	1.6873	0.0180	0.2003
0.70	1.5849	0.0153	0.1810	1.6025	0.0164	0.1867	1.5681	0.0174	0.1859	1.5655	0.0175	0.2019
0.90	1.4126	0.0149	0.1502	1.4285	0.0160	0.1636	1.4142	0.0169	0.1699	1.3909	0.0164	0.1736
$\cos(\theta_\eta^*)$	$E_\gamma = (867.5 \pm 7.5) \text{ MeV}$			$E_\gamma = (882.5 \pm 7.5) \text{ MeV}$			$E_\gamma = (897.5 \pm 7.5) \text{ MeV}$			$E_\gamma = (912.5 \pm 7.5) \text{ MeV}$		
	$d\sigma/d\Omega$			$d\sigma/d\Omega$			$d\sigma/d\Omega$			$d\sigma/d\Omega$		
	$[\mu\text{b}/\text{sr}]$	$[\mu\text{b}/\text{sr}]$	$[\mu\text{b}/\text{sr}]$									
-0.90	1.4755	0.0174	0.1085	1.4482	0.0164	0.1163	1.3557	0.0176	0.0992	1.2763	0.0173	0.1161
-0.70	1.5867	0.0177	0.1486	1.5361	0.0166	0.1365	1.4706	0.0181	0.1197	1.4031	0.0178	0.1287
-0.50	1.7268	0.0178	0.1643	1.6438	0.0171	0.1511	1.5802	0.0187	0.1361	1.5325	0.0184	0.1357
-0.30	1.7985	0.0176	0.1625	1.7011	0.0173	0.1442	1.6807	0.0184	0.1593	1.6155	0.0187	0.1565
-0.10	1.8429	0.0180	0.1633	1.7811	0.0176	0.1597	1.6875	0.0183	0.1656	1.6351	0.0179	0.1573
0.10	1.8177	0.0177	0.1649	1.7328	0.0171	0.1769	1.6937	0.0185	0.1591	1.5770	0.0180	0.1443
0.30	1.7505	0.0173	0.1802	1.6851	0.0161	0.1717	1.6137	0.0176	0.1445	1.5492	0.0179	0.1546
0.50	1.6296	0.0167	0.1850	1.5935	0.0166	0.1660	1.4604	0.0172	0.1496	1.4071	0.0165	0.1470
0.70	1.4582	0.0163	0.1729	1.4289	0.0157	0.1727	1.3398	0.0168	0.1733	1.2569	0.0167	0.1512
0.90	1.3037	0.0155	0.1771	1.2709	0.0153	0.1815	1.1537	0.0160	0.1605	1.0804	0.0158	0.1629

F.1. UNPOLARISED CROSS SECTIONS FROM ${}^3\text{He}$ (A2)

$\cos(\theta_\eta^*)$	$E_\gamma = (927.5 \pm 7.5) \text{ MeV}$			$E_\gamma = (942.5 \pm 7.5) \text{ MeV}$			$E_\gamma = (957.5 \pm 7.5) \text{ MeV}$			$E_\gamma = (972.5 \pm 7.5) \text{ MeV}$								
	$d\sigma/d\Omega$			Δ_{stat}			Δ_{sys}			$d\sigma/d\Omega$			Δ_{stat}			Δ_{sys}		
	$[\mu\text{b}/\text{sr}]$	$[\mu\text{b}/\text{sr}]$	$[\mu\text{b}/\text{sr}]$	$[\mu\text{b}/\text{sr}]$	$[\mu\text{b}/\text{sr}]$	$[\mu\text{b}/\text{sr}]$	$[\mu\text{b}/\text{sr}]$	$[\mu\text{b}/\text{sr}]$										
-0.90	1.2798	0.0166	0.0950	1.1492	0.0165	0.0859	1.0827	0.0174	0.0746	1.0252	0.0155	0.0732						
-0.70	1.3218	0.0170	0.1136	1.2531	0.0166	0.1086	1.1858	0.0175	0.0975	1.0857	0.0157	0.0765						
-0.50	1.4138	0.0172	0.1260	1.3331	0.0168	0.1230	1.2494	0.0180	0.1051	1.1743	0.0161	0.0943						
-0.30	1.5067	0.0168	0.1332	1.4499	0.0173	0.1353	1.3217	0.0183	0.1135	1.2652	0.0161	0.1150						
-0.10	1.5479	0.0172	0.1481	1.4429	0.0171	0.1311	1.3593	0.0183	0.1126	1.2718	0.0161	0.1114						
0.10	1.4825	0.0169	0.1469	1.4144	0.0166	0.1230	1.3180	0.0175	0.1151	1.2637	0.0157	0.1099						
0.30	1.4145	0.0168	0.1416	1.3408	0.0162	0.1284	1.2650	0.0172	0.1181	1.1513	0.0148	0.1088						
0.50	1.3074	0.0156	0.1445	1.1863	0.0160	0.1228	1.1243	0.0165	0.1122	1.0557	0.0148	0.1048						
0.70	1.1133	0.0153	0.1405	1.0329	0.0152	0.1315	0.9991	0.0158	0.1317	0.8974	0.0140	0.1110						
0.90	0.9416	0.0143	0.1537	0.8605	0.0140	0.1412	0.7893	0.0150	0.1282	0.7139	0.0133	0.1194						
<hr/>																		
$\cos(\theta_\eta^*)$	$E_\gamma = (987.5 \pm 7.5) \text{ MeV}$			$E_\gamma = (1002.5 \pm 7.5) \text{ MeV}$			$E_\gamma = (1017.5 \pm 7.5) \text{ MeV}$			$E_\gamma = (1032.5 \pm 7.5) \text{ MeV}$								
	$d\sigma/d\Omega$			Δ_{stat}			Δ_{sys}			$d\sigma/d\Omega$			Δ_{stat}			Δ_{sys}		
	$[\mu\text{b}/\text{sr}]$	$[\mu\text{b}/\text{sr}]$	$[\mu\text{b}/\text{sr}]$	$[\mu\text{b}/\text{sr}]$	$[\mu\text{b}/\text{sr}]$	$[\mu\text{b}/\text{sr}]$	$[\mu\text{b}/\text{sr}]$	$[\mu\text{b}/\text{sr}]$										
-0.90	0.9273	0.0153	0.0643	0.8819	0.0156	0.0697	0.8156	0.0153	0.0522	0.7306	0.0150	0.0568						
-0.70	1.0015	0.0154	0.0762	0.9399	0.0155	0.0718	0.8877	0.0154	0.0648	0.8004	0.0149	0.0555						
-0.50	1.0702	0.0156	0.0932	1.0110	0.0155	0.0842	0.9682	0.0152	0.0812	0.8583	0.0151	0.0671						
-0.30	1.1801	0.0160	0.1153	1.0925	0.0160	0.0970	0.9888	0.0155	0.0879	0.9171	0.0153	0.0760						
-0.10	1.1788	0.0159	0.1073	1.0966	0.0159	0.0883	1.0119	0.0155	0.0858	0.9671	0.0153	0.0857						
0.10	1.1528	0.0155	0.0943	1.1002	0.0156	0.0875	1.0465	0.0154	0.0871	0.9852	0.0154	0.0796						
0.30	1.0958	0.0152	0.1028	1.0372	0.0151	0.0962	0.9676	0.0150	0.0881	0.9067	0.0148	0.0759						
0.50	0.9817	0.0143	0.1134	0.9452	0.0145	0.0990	0.8699	0.0147	0.0861	0.8522	0.0146	0.0908						
0.70	0.7967	0.0141	0.1075	0.7659	0.0146	0.1057	0.7528	0.0141	0.1017	0.7149	0.0141	0.1070						
0.90	0.6371	0.0132	0.1123	0.5883	0.0130	0.1047	0.5362	0.0128	0.1007	0.5133	0.0131	0.0988						
<hr/>																		
$\cos(\theta_\eta^*)$	$E_\gamma = (1047.5 \pm 7.5) \text{ MeV}$			$E_\gamma = (1062.5 \pm 7.5) \text{ MeV}$			$E_\gamma = (1077.5 \pm 7.5) \text{ MeV}$			$E_\gamma = (1092.5 \pm 7.5) \text{ MeV}$								
	$d\sigma/d\Omega$			Δ_{stat}			Δ_{sys}			$d\sigma/d\Omega$			Δ_{stat}			Δ_{sys}		
	$[\mu\text{b}/\text{sr}]$	$[\mu\text{b}/\text{sr}]$	$[\mu\text{b}/\text{sr}]$	$[\mu\text{b}/\text{sr}]$	$[\mu\text{b}/\text{sr}]$	$[\mu\text{b}/\text{sr}]$	$[\mu\text{b}/\text{sr}]$	$[\mu\text{b}/\text{sr}]$										
-0.90	0.7163	0.0156	0.0669	0.6308	0.0148	0.0450	0.6130	0.0147	0.0387	0.6071	0.0161	0.0403						
-0.70	0.7648	0.0154	0.0586	0.6980	0.0145	0.0528	0.6684	0.0145	0.0492	0.6455	0.0154	0.0468						
-0.50	0.8330	0.0156	0.0664	0.7602	0.0148	0.0625	0.7153	0.0144	0.0588	0.7098	0.0152	0.0586						
-0.30	0.8812	0.0157	0.0753	0.8744	0.0154	0.0707	0.7831	0.0146	0.0693	0.7601	0.0156	0.0671						
-0.10	0.9191	0.0157	0.0800	0.8874	0.0153	0.0729	0.8459	0.0148	0.0672	0.8535	0.0158	0.0711						
0.10	0.9347	0.0155	0.0726	0.8933	0.0149	0.0776	0.8674	0.0148	0.0738	0.8264	0.0151	0.0614						
0.30	0.9049	0.0156	0.0693	0.8448	0.0146	0.0881	0.8570	0.0147	0.0928	0.8509	0.0154	0.0646						
0.50	0.8265	0.0147	0.0858	0.7897	0.0144	0.0888	0.7961	0.0142	0.1096	0.7912	0.0151	0.0838						
0.70	0.7176	0.0148	0.1168	0.7156	0.0146	0.1077	0.6502	0.0141	0.1160	0.6621	0.0154	0.1040						
0.90	0.4988	0.0132	0.1040	0.4838	0.0134	0.1087	0.4889	0.0138	0.1152	0.4420	0.0138	0.1026						
<hr/>																		
$\cos(\theta_\eta^*)$	$E_\gamma = (1110.0 \pm 10.0) \text{ MeV}$			$E_\gamma = (1130.0 \pm 10.0) \text{ MeV}$			$E_\gamma = (1150.0 \pm 10.0) \text{ MeV}$			$E_\gamma = (1170.0 \pm 10.0) \text{ MeV}$								
	$d\sigma/d\Omega$			Δ_{stat}			Δ_{sys}			$d\sigma/d\Omega$			Δ_{stat}			Δ_{sys}		
	$[\mu\text{b}/\text{sr}]$	$[\mu\text{b}/\text{sr}]$	$[\mu\text{b}/\text{sr}]$	$[\mu\text{b}/\text{sr}]$	$[\mu\text{b}/\text{sr}]$	$[\mu\text{b}/\text{sr}]$	$[\mu\text{b}/\text{sr}]$	$[\mu\text{b}/\text{sr}]$										
-0.90	0.5486	0.0156	0.0330	0.4944	0.0128	0.0292	0.4723	0.0136	0.0312	0.4080	0.0129	0.0284						
-0.70	0.5932	0.0140	0.0516	0.5465	0.0121	0.0404	0.5271	0.0128	0.0395	0.4580	0.0117	0.0368						
-0.50	0.6735	0.0146	0.0604	0.6020	0.0121	0.0508	0.5936	0.0130	0.0539	0.5455	0.0123	0.0576						
-0.30	0.7418	0.0144	0.0691	0.6872	0.0126	0.0602	0.6493	0.0128	0.0635	0.6450	0.0127	0.0687						
-0.10	0.7744	0.0143	0.0689	0.7755	0.0129	0.0690	0.7185	0.0131	0.0677	0.7166	0.0128	0.0638						
0.10	0.8340	0.0143	0.0739	0.8132	0.0128	0.0751	0.7915	0.0133	0.0799	0.7624	0.0127	0.0694						
0.30	0.8182	0.0143	0.1013	0.8113	0.0127	0.0893	0.8245	0.0135	0.0918	0.8049	0.0129	0.0862						
0.50	0.7787	0.0141	0.1093	0.7741														

APPENDIX F. DATA TABLES

$\cos(\theta_\eta^*)$	$E_\gamma = (1190.0 \pm 10.0) \text{ MeV}$			$E_\gamma = (1210.0 \pm 10.0) \text{ MeV}$			$E_\gamma = (1230.0 \pm 10.0) \text{ MeV}$			$E_\gamma = (1250.0 \pm 10.0) \text{ MeV}$		
	$d\sigma/d\Omega$ [$\mu\text{b}/\text{sr}$]	Δ_{stat} [$\mu\text{b}/\text{sr}$]	Δ_{sys} [$\mu\text{b}/\text{sr}$]	$d\sigma/d\Omega$ [$\mu\text{b}/\text{sr}$]	Δ_{stat} [$\mu\text{b}/\text{sr}$]	Δ_{sys} [$\mu\text{b}/\text{sr}$]	$d\sigma/d\Omega$ [$\mu\text{b}/\text{sr}$]	Δ_{stat} [$\mu\text{b}/\text{sr}$]	Δ_{sys} [$\mu\text{b}/\text{sr}$]	$d\sigma/d\Omega$ [$\mu\text{b}/\text{sr}$]	Δ_{stat} [$\mu\text{b}/\text{sr}$]	Δ_{sys} [$\mu\text{b}/\text{sr}$]
-0.90	0.3940	0.0133	0.0238	0.3491	0.0136	0.0248	0.3293	0.0137	0.0291	0.3124	0.0136	0.0088
-0.70	0.4363	0.0119	0.0356	0.4147	0.0124	0.0293	0.3538	0.0120	0.0340	0.3995	0.0129	0.0241
-0.50	0.5295	0.0127	0.0483	0.5153	0.0133	0.0371	0.4707	0.0132	0.0448	0.4617	0.0136	0.0368
-0.30	0.6147	0.0128	0.0529	0.5895	0.0133	0.0506	0.5780	0.0137	0.0502	0.5721	0.0143	0.0558
-0.10	0.6889	0.0129	0.0633	0.6680	0.0133	0.0592	0.6620	0.0139	0.0579	0.6196	0.0140	0.0677
0.10	0.7441	0.0131	0.0801	0.7305	0.0136	0.0650	0.7133	0.0141	0.0808	0.6835	0.0143	0.0734
0.30	0.7643	0.0131	0.1052	0.7417	0.0136	0.0846	0.7511	0.0144	0.1018	0.7220	0.0149	0.0900
0.50	0.7600	0.0137	0.1266	0.7324	0.0144	0.1060	0.7150	0.0146	0.0996	0.7286	0.0151	0.1059
0.70	0.6951	0.0145	0.1309	0.6371	0.0145	0.1238	0.6591	0.0160	0.1241	0.6515	0.0158	0.1309
0.90	0.4682	0.0127	0.1271	0.4718	0.0133	0.1395	0.4734	0.0146	0.1466	0.4381	0.0145	0.1495
$\cos(\theta_\eta^*)$	$E_\gamma = (1270.0 \pm 10.0) \text{ MeV}$			$E_\gamma = (1290.0 \pm 10.0) \text{ MeV}$			$E_\gamma = (1310.0 \pm 10.0) \text{ MeV}$			$E_\gamma = (1330.0 \pm 10.0) \text{ MeV}$		
	$d\sigma/d\Omega$ [$\mu\text{b}/\text{sr}$]	Δ_{stat} [$\mu\text{b}/\text{sr}$]	Δ_{sys} [$\mu\text{b}/\text{sr}$]	$d\sigma/d\Omega$ [$\mu\text{b}/\text{sr}$]	Δ_{stat} [$\mu\text{b}/\text{sr}$]	Δ_{sys} [$\mu\text{b}/\text{sr}$]	$d\sigma/d\Omega$ [$\mu\text{b}/\text{sr}$]	Δ_{stat} [$\mu\text{b}/\text{sr}$]	Δ_{sys} [$\mu\text{b}/\text{sr}$]	$d\sigma/d\Omega$ [$\mu\text{b}/\text{sr}$]	Δ_{stat} [$\mu\text{b}/\text{sr}$]	Δ_{sys} [$\mu\text{b}/\text{sr}$]
-0.90	0.2785	0.0123	0.0234	0.2764	0.0135	0.0133	0.2825	0.0124	0.0206	0.2487	0.0126	0.0124
-0.70	0.3620	0.0114	0.0369	0.3175	0.0119	0.0269	0.3061	0.0110	0.0218	0.2727	0.0109	0.0228
-0.50	0.4176	0.0121	0.0375	0.4151	0.0134	0.0358	0.3991	0.0119	0.0330	0.3597	0.0121	0.0382
-0.30	0.5212	0.0127	0.0399	0.4933	0.0139	0.0457	0.4687	0.0125	0.0422	0.4672	0.0129	0.0491
-0.10	0.5759	0.0127	0.0505	0.5614	0.0140	0.0578	0.5469	0.0126	0.0575	0.5180	0.0131	0.0557
0.10	0.6413	0.0131	0.0687	0.6662	0.0147	0.0649	0.6208	0.0131	0.0929	0.5940	0.0136	0.0742
0.30	0.6983	0.0134	0.0960	0.6880	0.0149	0.0832	0.6401	0.0130	0.1191	0.6239	0.0140	0.0963
0.50	0.6750	0.0142	0.1099	0.6711	0.0156	0.1099	0.6280	0.0139	0.1262	0.6149	0.0144	0.1194
0.70	0.6118	0.0144	0.1239	0.6189	0.0170	0.1417	0.6051	0.0144	0.1371	0.5716	0.0150	0.1336
0.90	0.4492	0.0136	0.1331	0.4132	0.0164	0.1375	0.4419	0.0148	0.1489	0.4188	0.0144	0.1359
$\cos(\theta_\eta^*)$	$E_\gamma = (1350.0 \pm 10.0) \text{ MeV}$			$E_\gamma = (1370.0 \pm 10.0) \text{ MeV}$			$E_\gamma = (1390.0 \pm 10.0) \text{ MeV}$			$E_\gamma = (1350.0 \pm 10.0) \text{ MeV}$		
	$d\sigma/d\Omega$ [$\mu\text{b}/\text{sr}$]	Δ_{stat} [$\mu\text{b}/\text{sr}$]	Δ_{sys} [$\mu\text{b}/\text{sr}$]	$d\sigma/d\Omega$ [$\mu\text{b}/\text{sr}$]	Δ_{stat} [$\mu\text{b}/\text{sr}$]	Δ_{sys} [$\mu\text{b}/\text{sr}$]	$d\sigma/d\Omega$ [$\mu\text{b}/\text{sr}$]	Δ_{stat} [$\mu\text{b}/\text{sr}$]	Δ_{sys} [$\mu\text{b}/\text{sr}$]	$d\sigma/d\Omega$ [$\mu\text{b}/\text{sr}$]	Δ_{stat} [$\mu\text{b}/\text{sr}$]	Δ_{sys} [$\mu\text{b}/\text{sr}$]
-0.90	0.2494	0.0117	0.0231	0.2291	0.0118	0.0220	0.2418	0.0133	0.0213			
-0.70	0.3013	0.0110	0.0238	0.2938	0.0109	0.0235	0.2781	0.0116	0.0190			
-0.50	0.3637	0.0118	0.0342	0.3300	0.0114	0.0274	0.3065	0.0124	0.0224			
-0.30	0.4617	0.0126	0.0468	0.4397	0.0125	0.0413	0.3934	0.0133	0.0300			
-0.10	0.5058	0.0128	0.0539	0.4967	0.0127	0.0534	0.4706	0.0137	0.0464			
0.10	0.5915	0.0136	0.0770	0.5651	0.0128	0.0737	0.5096	0.0137	0.0840			
0.30	0.6051	0.0137	0.1022	0.5966	0.0132	0.0946	0.5497	0.0144	0.1111			
0.50	0.6210	0.0142	0.1114	0.5956	0.0142	0.1072	0.5525	0.0150	0.1265			
0.70	0.5977	0.0156	0.1384	0.5927	0.0149	0.1470	0.5575	0.0175	0.1544			
0.90	0.4203	0.0142	0.1503	0.4425	0.0140	0.1700	0.4309	0.0174	0.1569			

Total Cross Sections

E_γ [MeV]	ΔE_γ [MeV]	σ [μb]	Δ_{stat} [μb]	Δ_{sys} [μb]
655.0	25.0	2.3138	0.0110	0.2822
690.0	10.0	6.3400	0.0263	0.8536
710.0	10.0	10.7189	0.0431	1.4736
730.0	10.0	14.1124	0.0399	1.9614
747.5	7.5	17.1382	0.0492	2.3797
762.5	7.5	19.3104	0.0595	2.7623
777.5	7.5	20.5361	0.0629	2.6539
792.5	7.5	21.3336	0.0631	2.6485
807.5	7.5	21.9195	0.0657	2.3810
822.5	7.5	21.9360	0.0690	2.2745
837.5	7.5	21.6242	0.0735	2.2417
852.5	7.5	21.4590	0.0732	2.2466
867.5	7.5	20.5722	0.0683	2.0442
882.5	7.5	19.8580	0.0659	1.9813
897.5	7.5	18.8717	0.0704	1.8414
912.5	7.5	17.9866	0.0695	1.8263
927.5	7.5	16.7301	0.0651	1.6866
942.5	7.5	15.6386	0.0645	1.5455
957.5	7.5	14.6733	0.0683	1.3928
972.5	7.5	13.6788	0.0605	1.2857
987.5	7.5	12.5710	0.0599	1.2385
1002.5	7.5	11.8677	0.0602	1.1349
1017.5	7.5	11.0968	0.0592	1.0494
1032.5	7.5	10.3425	0.0586	0.9959
1047.5	7.5	10.0312	0.0603	0.9990
1062.5	7.5	9.4978	0.0583	0.9727
1077.5	7.5	9.1382	0.0575	0.9943
1092.5	7.5	8.9634	0.0607	0.8782
1110.0	10.0	8.6370	0.0568	0.9947
1130.0	10.0	8.3822	0.0501	0.9442
1150.0	10.0	8.1653	0.0522	0.9538
1170.0	10.0	7.7947	0.0504	0.9625
1190.0	10.0	7.6346	0.0519	0.9968
1210.0	10.0	7.3340	0.0538	0.9045
1230.0	10.0	7.1437	0.0557	0.9676
1250.0	10.0	7.0031	0.0569	0.9331
1270.0	10.0	6.5602	0.0517	0.9066
1290.0	10.0	6.4156	0.0579	0.9000
1310.0	10.0	6.1911	0.0516	1.0062
1330.0	10.0	5.8735	0.0530	0.9274
1350.0	10.0	5.9088	0.0524	0.9565
1370.0	10.0	5.7436	0.0512	0.9567
1390.0	10.0	5.3786	0.0569	0.9730

F.1.2 $\gamma p \rightarrow \eta p$ as a Function of E_γ
Angular Distributions

$\cos(\theta_\eta^*)$	$E_\gamma = (655.0 \pm 25.0) \text{ MeV}$			$E_\gamma = (690.0 \pm 10.0) \text{ MeV}$			$E_\gamma = (710.0 \pm 10.0) \text{ MeV}$			$E_\gamma = (730.0 \pm 10.0) \text{ MeV}$		
	$d\sigma/d\Omega$			$d\sigma/d\Omega$			$d\sigma/d\Omega$			$d\sigma/d\Omega$		
	$[\mu\text{b}/\text{sr}]$	Δ_{stat}	Δ_{sys}									
-0.90	0.2477	0.0069	0.0196	0.7091	0.0147	0.0531	1.0738	0.0220	0.0866	1.3102	0.0189	0.1124
-0.70	0.1563	0.0052	0.0114	0.5731	0.0116	0.0380	0.9350	0.0175	0.0692	1.1873	0.0152	0.1029
-0.50	0.1017	0.0044	0.0088	0.4623	0.0102	0.0313	0.8174	0.0158	0.0610	1.0807	0.0141	0.0936
-0.30	0.0651	0.0042	0.0067	0.3465	0.0091	0.0245	0.6838	0.0145	0.0532	0.9674	0.0132	0.0830
-0.10	0.0369	0.0040	0.0040	0.2352	0.0080	0.0185	0.5448	0.0132	0.0447	0.8512	0.0126	0.0756
0.10	0.0255	0.0044	0.0038	0.1531	0.0075	0.0135	0.4142	0.0123	0.0352	0.6800	0.0116	0.0600
0.30	0.0150	0.0046	0.0028	0.1140	0.0077	0.0130	0.3298	0.0123	0.0307	0.5680	0.0115	0.0525
0.50	0.0023	0.0045	0.0009	0.0831	0.0080	0.0093	0.2619	0.0124	0.0281	0.4868	0.0118	0.0468
0.70	-0.0008	0.0042	0.0009	0.0664	0.0084	0.0087	0.2395	0.0135	0.0260	0.4052	0.0121	0.0401
0.90	0.0029	0.0054	0.0012	0.0506	0.0093	0.0134	0.1978	0.0146	0.0192	0.3669	0.0140	0.0347
$\cos(\theta_\eta^*)$	$E_\gamma = (747.5 \pm 7.5) \text{ MeV}$			$E_\gamma = (762.5 \pm 7.5) \text{ MeV}$			$E_\gamma = (777.5 \pm 7.5) \text{ MeV}$			$E_\gamma = (792.5 \pm 7.5) \text{ MeV}$		
	$d\sigma/d\Omega$	Δ_{stat}	Δ_{sys}									
	$[\mu\text{b}/\text{sr}]$	$[\mu\text{b}/\text{sr}]$	$[\mu\text{b}/\text{sr}]$									
-0.90	1.4060	0.0209	0.1217	1.4547	0.0228	0.1224	1.4740	0.0218	0.1204	1.5053	0.0207	0.1217
-0.70	1.3661	0.0173	0.1179	1.4379	0.0189	0.1198	1.4349	0.0179	0.1172	1.4027	0.0163	0.1110
-0.50	1.2891	0.0165	0.1117	1.4152	0.0186	0.1177	1.5217	0.0182	0.1250	1.5124	0.0168	0.1160
-0.30	1.2556	0.0163	0.1093	1.3886	0.0186	0.1162	1.4826	0.0183	0.1199	1.5810	0.0176	0.1205
-0.10	1.0965	0.0154	0.0961	1.2881	0.0181	0.1054	1.4741	0.0185	0.1156	1.5307	0.0176	0.1149
0.10	1.0053	0.0151	0.0874	1.1599	0.0175	0.0986	1.3360	0.0179	0.1049	1.4592	0.0174	0.1093
0.30	0.8083	0.0144	0.0739	0.9913	0.0171	0.0844	1.1770	0.0175	0.0932	1.2719	0.0168	0.0965
0.50	0.6591	0.0144	0.0684	0.8657	0.0176	0.0784	1.0042	0.0178	0.0823	1.1226	0.0174	0.0902
0.70	0.5698	0.0150	0.0620	0.6674	0.0177	0.0641	0.8545	0.0194	0.0759	0.9503	0.0191	0.0854
0.90	0.5432	0.0182	0.0532	0.6632	0.0222	0.0571	0.7749	0.0238	0.0754	0.8498	0.0242	0.0832
$\cos(\theta_\eta^*)$	$E_\gamma = (807.5 \pm 7.5) \text{ MeV}$			$E_\gamma = (822.5 \pm 7.5) \text{ MeV}$			$E_\gamma = (837.5 \pm 7.5) \text{ MeV}$			$E_\gamma = (852.5 \pm 7.5) \text{ MeV}$		
	$d\sigma/d\Omega$	Δ_{stat}	Δ_{sys}									
	$[\mu\text{b}/\text{sr}]$	$[\mu\text{b}/\text{sr}]$	$[\mu\text{b}/\text{sr}]$									
-0.90	1.4833	0.0205	0.1154	1.4166	0.0208	0.1152	1.3421	0.0211	0.1105	1.3568	0.0211	0.1181
-0.70	1.4168	0.0162	0.1066	1.3705	0.0165	0.1049	1.3310	0.0170	0.1059	1.3084	0.0168	0.1057
-0.50	1.4868	0.0164	0.1093	1.4815	0.0169	0.1126	1.4135	0.0172	0.1105	1.4090	0.0171	0.1103
-0.30	1.6223	0.0175	0.1211	1.5830	0.0177	0.1205	1.5618	0.0182	0.1251	1.4629	0.0175	0.1135
-0.10	1.5874	0.0175	0.1164	1.6208	0.0181	0.1207	1.5720	0.0185	0.1236	1.5284	0.0180	0.1180
0.10	1.5207	0.0174	0.1086	1.5532	0.0180	0.1141	1.5133	0.0183	0.1129	1.5039	0.0179	0.1144
0.30	1.3665	0.0170	0.0983	1.4356	0.0178	0.1043	1.4045	0.0181	0.1052	1.3872	0.0177	0.1053
0.50	1.2208	0.0176	0.0931	1.2023	0.0176	0.0921	1.2188	0.0181	0.0954	1.1918	0.0175	0.0960
0.70	1.0154	0.0193	0.0867	1.0057	0.0195	0.0866	1.0180	0.0200	0.0886	1.0285	0.0196	0.0900
0.90	0.8964	0.0255	0.0770	0.9326	0.0277	0.0829	0.9308	0.0293	0.0909	0.9296	0.0293	0.0825
$\cos(\theta_\eta^*)$	$E_\gamma = (867.5 \pm 7.5) \text{ MeV}$			$E_\gamma = (882.5 \pm 7.5) \text{ MeV}$			$E_\gamma = (897.5 \pm 7.5) \text{ MeV}$			$E_\gamma = (912.5 \pm 7.5) \text{ MeV}$		
	$d\sigma/d\Omega$	Δ_{stat}	Δ_{sys}									
	$[\mu\text{b}/\text{sr}]$	$[\mu\text{b}/\text{sr}]$	$[\mu\text{b}/\text{sr}]$									
-0.90	1.2221	0.0189	0.1076	1.1874	0.0180	0.1178	1.1040	0.0189	0.1019	0.9590	0.0178	0.0802
-0.70	1.2202	0.0154	0.1002	1.1643	0.0145	0.0981	1.0927	0.0154	0.0915	1.0181	0.0150	0.0854
-0.50	1.3104	0.0156	0.1059	1.2800	0.0149	0.1044	1.1769	0.0157	0.0969	1.1231	0.0155	0.0927
-0.30	1.4247	0.0163	0.1155	1.3233	0.0151	0.1084	1.2608	0.0162	0.1014	1.2015	0.0159	0.0964
-0.10	1.4890	0.0166	0.1180	1.3584	0.0152	0.1065	1.2694	0.0160	0.1019	1.1997	0.0157	0.0978
0.10	1.4276	0.0163	0.1103	1.2970	0.0149	0.1017	1.2455	0.0159	0.0984	1.1506	0.0153	0.0927
0.30	1.3098	0.0160	0.1008	1.2572	0.0150	0.0997	1.1879	0.0158	0.0928	1.0903	0.0152	0.0911
0.50	1.1624	0.0161	0.0938	1.1147	0.0150	0.0914	1.0399	0.0157	0.0851	0.9696	0.0152	0.0825
0.70	0.9665	0.0175	0.0853	0.9400	0.0163	0.0814	0.8623	0.0167	0.0781	0.8104	0.0161	0.0698
0.90	0.9235	0.0276	0.0813	0.8689	0.0255	0.0732	0.8150	0.0267	0.0742	0.7320	0.0252	0.0607

F.1. UNPOLARISED CROSS SECTIONS FROM ${}^3\text{He}$ (A2)

$\cos(\theta_\eta^*)$	$E_\gamma = (927.5 \pm 7.5) \text{ MeV}$			$E_\gamma = (942.5 \pm 7.5) \text{ MeV}$			$E_\gamma = (957.5 \pm 7.5) \text{ MeV}$			$E_\gamma = (972.5 \pm 7.5) \text{ MeV}$								
	$d\sigma/d\Omega$			Δ_{stat}			Δ_{sys}			$d\sigma/d\Omega$			Δ_{stat}			Δ_{sys}		
	$[\mu\text{b}/\text{sr}]$	$[\mu\text{b}/\text{sr}]$	$[\mu\text{b}/\text{sr}]$	$[\mu\text{b}/\text{sr}]$	$[\mu\text{b}/\text{sr}]$	$[\mu\text{b}/\text{sr}]$	$[\mu\text{b}/\text{sr}]$											
-0.90	0.9199	0.0169	0.0829	0.7838	0.0158	0.0657	0.7551	0.0171	0.0692	0.6432	0.0146	0.0602	0.7051	0.0123	0.0648	0.7899	0.0128	0.0714
-0.70	0.9331	0.0138	0.0790	0.8495	0.0134	0.0717	0.7766	0.0140	0.0699	0.8441	0.0127	0.0738	0.8058	0.0124	0.0725	0.8406	0.0130	0.0752
-0.50	1.0139	0.0143	0.0854	0.9113	0.0137	0.0757	0.8503	0.0145	0.0728	0.7470	0.0122	0.0666	0.6950	0.0123	0.0629	0.7638	0.0141	0.0697
-0.30	1.0887	0.0146	0.0894	1.0106	0.0142	0.0848	0.9000	0.0146	0.0783	0.6290	0.0147	0.0618	0.5608	0.0128	0.0523	0.8045	0.0134	0.0752
-0.10	1.0851	0.0143	0.0890	0.9929	0.0139	0.0832	0.9153	0.0145	0.0807	0.5330	0.0220	0.0524	0.4906	0.0192	0.0501	0.8441	0.0127	0.0738
0.10	1.0385	0.0140	0.0857	0.9678	0.0136	0.0813	0.8756	0.0141	0.0769	0.5003	0.0138	0.0657	0.4587	0.0125	0.0552	0.7899	0.0128	0.0714
0.30	0.9818	0.0138	0.0805	0.9045	0.0134	0.0747	0.8283	0.0140	0.0727	0.4247	0.0116	0.0467	0.3683	0.0111	0.0398	0.5223	0.0114	0.0554
0.50	0.9003	0.0140	0.0740	0.8212	0.0135	0.0713	0.7638	0.0141	0.0697	0.3317	0.0146	0.0331	0.2952	0.0158	0.0302	0.6950	0.0123	0.0629
0.70	0.7675	0.0150	0.0650	0.6743	0.0141	0.0623	0.6290	0.0147	0.0618	0.2596	0.0215	0.0605	0.4163	0.0117	0.0407	0.5608	0.0128	0.0523
0.90	0.6305	0.0222	0.0605	0.5905	0.0215	0.0605	0.5330	0.0220	0.0524	0.4906	0.0192	0.0501	0.4467	0.0135	0.0516	0.5223	0.0114	0.0554
$\cos(\theta_\eta^*)$	$E_\gamma = (987.5 \pm 7.5) \text{ MeV}$			$E_\gamma = (1002.5 \pm 7.5) \text{ MeV}$			$E_\gamma = (1017.5 \pm 7.5) \text{ MeV}$			$E_\gamma = (1032.5 \pm 7.5) \text{ MeV}$								
	$d\sigma/d\Omega$			Δ_{stat}			Δ_{sys}			$d\sigma/d\Omega$			Δ_{stat}			Δ_{sys}		
	$[\mu\text{b}/\text{sr}]$	$[\mu\text{b}/\text{sr}]$	$[\mu\text{b}/\text{sr}]$	$[\mu\text{b}/\text{sr}]$	$[\mu\text{b}/\text{sr}]$	$[\mu\text{b}/\text{sr}]$	$[\mu\text{b}/\text{sr}]$	$[\mu\text{b}/\text{sr}]$										
-0.90	0.5625	0.0140	0.0576	0.5488	0.0143	0.0589	0.4885	0.0138	0.0474	0.4467	0.0135	0.0516	0.5223	0.0114	0.0554	0.5680	0.0115	0.0557
-0.70	0.6385	0.0120	0.0606	0.5745	0.0118	0.0558	0.5134	0.0114	0.0562	0.4796	0.0113	0.0515	0.5805	0.0113	0.0539	0.6054	0.0114	0.0574
-0.50	0.7007	0.0124	0.0644	0.6408	0.0122	0.0601	0.6013	0.0120	0.0644	0.4020	0.0113	0.0406	0.4375	0.0111	0.0472	0.4837	0.0112	0.0503
-0.30	0.7420	0.0125	0.0681	0.7081	0.0125	0.0656	0.6270	0.0119	0.0634	0.4615	0.0107	0.0447	0.4980	0.0113	0.0489	0.5497	0.0113	0.0534
-0.10	0.7528	0.0122	0.0679	0.6944	0.0120	0.0665	0.6374	0.0116	0.0637	0.4300	0.0110	0.0412	0.4763	0.0111	0.0398	0.5173	0.0114	0.0482
0.10	0.7395	0.0121	0.0691	0.6816	0.0119	0.0636	0.6313	0.0115	0.0601	0.4163	0.0117	0.0407	0.4883	0.0112	0.0400	0.5323	0.0113	0.0533
0.30	0.6957	0.0120	0.0647	0.6773	0.0121	0.0621	0.6066	0.0115	0.0560	0.4047	0.0116	0.0407	0.4498	0.0091	0.0371	0.5743	0.0113	0.0534
0.50	0.6353	0.0120	0.0596	0.5826	0.0118	0.0560	0.5323	0.0113	0.0530	0.3683	0.0111	0.0398	0.4300	0.0110	0.0412	0.5173	0.0114	0.0482
0.70	0.4829	0.0121	0.0511	0.4841	0.0124	0.0478	0.4247	0.0116	0.0467	0.3315	0.0112	0.0400	0.3683	0.0111	0.0398	0.4498	0.0091	0.0371
0.90	0.3878	0.0174	0.0418	0.3868	0.0179	0.0452	0.3127	0.0161	0.0351	0.2952	0.0158	0.0302	0.2596	0.0215	0.0605	0.4047	0.0127	0.0738
$\cos(\theta_\eta^*)$	$E_\gamma = (1047.5 \pm 7.5) \text{ MeV}$			$E_\gamma = (1062.5 \pm 7.5) \text{ MeV}$			$E_\gamma = (1077.5 \pm 7.5) \text{ MeV}$			$E_\gamma = (1092.5 \pm 7.5) \text{ MeV}$								
	$d\sigma/d\Omega$			Δ_{stat}			Δ_{sys}			$d\sigma/d\Omega$			Δ_{stat}			Δ_{sys}		
	$[\mu\text{b}/\text{sr}]$	$[\mu\text{b}/\text{sr}]$	$[\mu\text{b}/\text{sr}]$	$[\mu\text{b}/\text{sr}]$	$[\mu\text{b}/\text{sr}]$	$[\mu\text{b}/\text{sr}]$	$[\mu\text{b}/\text{sr}]$											
-0.90	0.4127	0.0137	0.0533	0.3599	0.0129	0.0484	0.3551	0.0130	0.0478	0.3268	0.0137	0.0474	0.3447	0.0111	0.0404	0.4020	0.0113	0.0406
-0.70	0.4398	0.0115	0.0510	0.3996	0.0109	0.0475	0.3631	0.0105	0.0423	0.3447	0.0111	0.0404	0.4597	0.0111	0.0472	0.4980	0.0113	0.0489
-0.50	0.4925	0.0117	0.0532	0.4467	0.0111	0.0468	0.4088	0.0106	0.0425	0.4020	0.0113	0.0406	0.4615	0.0107	0.0447	0.5173	0.0114	0.0482
-0.30	0.5359	0.0117	0.0540	0.5157	0.0113	0.0482	0.4598	0.0107	0.0431	0.4300	0.0110	0.0412	0.4883	0.0112	0.0503	0.5497	0.0113	0.0534
-0.10	0.5604	0.0116	0.0558	0.5228	0.0110	0.0490	0.4986	0.0107	0.0500	0.4615	0.0105	0.0497	0.4980	0.0113	0.0489	0.5743	0.0113	0.0534
0.10	0.5658	0.0115	0.0545	0.5150	0.0108	0.0478	0.5021	0.0105	0.0497	0.4498	0.0109	0.0478	0.4883	0.0112	0.0400	0.5323	0.0113	0.0533
0.30	0.5469	0.0115	0.0501	0.5048	0.0108	0.0483	0.5097	0.0108	0.0509	0.4300	0.0110	0.0412	0.4498	0.0091	0.0371	0.5173	0.0114	0.0482
0.50	0.4761	0.0114	0.0473	0.4709	0.0111	0.0501	0.4590	0.0108	0.0473	0.3683	0.0111	0.0398	0.3315	0.0112	0.0400	0.4047	0.0127	0.0738
0.70	0.3840	0.0116	0.0406	0.3771	0.0113	0.0381	0.4727	0.0097	0.0396	0.3683	0.0111	0.0398	0.3737	0.0101	0.0337	0.4498	0.0091	0.0371
0.90	0.3221	0.0173	0.0333	0.2721	0.0158	0.0267	0.2314	0.0146	0.0331	0.2246	0.0132	0.0260	0.2596	0.0215	0.0605	0.3683	0.0111	0.0398
$\cos(\theta_\eta^*)$	$E_\gamma = (1110.0 \pm 10.0) \text{ MeV}$			$E_\gamma = (1130.0 \pm 10.0) \text{ MeV}$			$E_\gamma = (1150.0 \pm 10.0) \text{ MeV}$			$E_\gamma = (1170.0 \pm 10.0) \text{ MeV}$								
	$d\sigma/d\Omega$			Δ_{stat}			Δ_{sys}			$d\sigma/d\Omega$			Δ_{stat}			Δ_{sys}		
	$[\mu\text{b}/\text{sr}]$	$[\mu\text{b}/\text{sr}]$	$[\mu\text{b}/\text{sr}]$	$[\mu\text{b}/\text{sr}]$	$[\mu\text{b}/\text{sr}]$	$[\mu\text{b}/\text{sr}]$	$[\mu\text{b}/\text{sr}]$	$[\mu\text{b}/\text{sr}]$										
-0.90	0.2987	0.0129	0.0357	0.2813	0.0107	0.0452	0.2381	0.0105	0.0325	0.1955	0.0093	0.0288	0.2442	0.0083	0.0334	0.2953	0.0086	0.0297
-0.70	0.3029	0.0102	0.0327	0.2964	0.0088	0.0349	0.2680	0.0089	0.0355	0.2442	0.0083							

APPENDIX F. DATA TABLES

$\cos(\theta_\eta^*)$	$E_\gamma = (1190.0 \pm 10.0) \text{ MeV}$			$E_\gamma = (1210.0 \pm 10.0) \text{ MeV}$			$E_\gamma = (1230.0 \pm 10.0) \text{ MeV}$			$E_\gamma = (1250.0 \pm 10.0) \text{ MeV}$								
	$d\sigma/d\Omega$			Δ_{stat}			Δ_{sys}			$d\sigma/d\Omega$			Δ_{stat}			Δ_{sys}		
	$[\mu\text{b}/\text{sr}]$	$[\mu\text{b}/\text{sr}]$	$[\mu\text{b}/\text{sr}]$	$[\mu\text{b}/\text{sr}]$	$[\mu\text{b}/\text{sr}]$	$[\mu\text{b}/\text{sr}]$	$[\mu\text{b}/\text{sr}]$	$[\mu\text{b}/\text{sr}]$										
-0.90	0.2021	0.0095	0.0354	0.1874	0.0097	0.0288	0.1613	0.0094	0.0286	0.1515	0.0093	0.0208	0.2005	0.0086	0.0251	0.2652	0.0096	0.0287
-0.70	0.2358	0.0083	0.0339	0.2214	0.0084	0.0242	0.1898	0.0081	0.0206	0.2005	0.0086	0.0251	0.2652	0.0096	0.0287	0.3306	0.0098	0.0311
-0.50	0.2946	0.0088	0.0304	0.2786	0.0091	0.0270	0.2799	0.0095	0.0252	0.3326	0.0095	0.0281	0.3627	0.0096	0.0289	0.4146	0.0101	0.0323
-0.30	0.3457	0.0088	0.0281	0.3412	0.0092	0.0307	0.3927	0.0096	0.0330	0.3937	0.0097	0.0349	0.4180	0.0109	0.0369	0.4335	0.0097	0.0343
-0.10	0.3905	0.0087	0.0303	0.3779	0.0091	0.0316	0.4205	0.0097	0.0349	0.4296	0.0100	0.0355	0.4146	0.0101	0.0323	0.3881	0.0105	0.0343
0.10	0.4287	0.0090	0.0334	0.4241	0.0095	0.0333	0.4216	0.0105	0.0334	0.4180	0.0109	0.0369	0.3602	0.0111	0.0317	0.3578	0.0115	0.0348
0.30	0.4420	0.0093	0.0367	0.4241	0.0096	0.0328	0.3627	0.0096	0.0330	0.3578	0.0115	0.0348	0.2643	0.0146	0.0237	0.2588	0.0161	0.0249
0.50	0.4335	0.0097	0.0350	0.4100	0.0100	0.0324	0.2978	0.0168	0.0248	0.2588	0.0161	0.0249						
$\cos(\theta_\eta^*)$	$E_\gamma = (1270.0 \pm 10.0) \text{ MeV}$			$E_\gamma = (1290.0 \pm 10.0) \text{ MeV}$			$E_\gamma = (1310.0 \pm 10.0) \text{ MeV}$			$E_\gamma = (1330.0 \pm 10.0) \text{ MeV}$								
	$d\sigma/d\Omega$	Δ_{stat}	Δ_{sys}	$d\sigma/d\Omega$	Δ_{stat}	Δ_{sys}	$d\sigma/d\Omega$	Δ_{stat}	Δ_{sys}									
	$[\mu\text{b}/\text{sr}]$	$[\mu\text{b}/\text{sr}]$	$[\mu\text{b}/\text{sr}]$	$[\mu\text{b}/\text{sr}]$	$[\mu\text{b}/\text{sr}]$	$[\mu\text{b}/\text{sr}]$	$[\mu\text{b}/\text{sr}]$	$[\mu\text{b}/\text{sr}]$	$[\mu\text{b}/\text{sr}]$									
-0.90	0.1477	0.0084	0.0221	0.1400	0.0090	0.0243	0.1251	0.0078	0.0120	0.1264	0.0081	0.0278	0.1576	0.0077	0.0205	0.2103	0.0088	0.0201
-0.70	0.1792	0.0076	0.0223	0.1762	0.0084	0.0178	0.1786	0.0078	0.0182	0.3159	0.0090	0.0271	0.3340	0.0089	0.0278	0.3671	0.0096	0.0331
-0.50	0.2502	0.0087	0.0280	0.2341	0.0095	0.0208	0.2181	0.0085	0.0220	0.3716	0.0102	0.0330	0.3927	0.0111	0.0317	0.4146	0.0101	0.0323
-0.30	0.3168	0.0090	0.0287	0.3053	0.0100	0.0288	0.3340	0.0098	0.0278	0.3624	0.0090	0.0314	0.3927	0.0111	0.0317	0.4180	0.0109	0.0343
-0.10	0.3482	0.0087	0.0275	0.3433	0.0098	0.0303	0.3578	0.0115	0.0348	0.3602	0.0111	0.0317	0.3578	0.0115	0.0348	0.3881	0.0105	0.0343
0.10	0.3815	0.0089	0.0296	0.3859	0.0101	0.0319	0.3624	0.0109	0.0314	0.3927	0.0111	0.0317	0.4146	0.0101	0.0323	0.4335	0.0097	0.0343
0.30	0.4057	0.0093	0.0305	0.4081	0.0106	0.0323	0.3795	0.0094	0.0317	0.3927	0.0111	0.0317	0.4180	0.0109	0.0343	0.4335	0.0097	0.0343
0.50	0.3852	0.0097	0.0308	0.3956	0.0110	0.0328	0.3729	0.0099	0.0290	0.3674	0.0101	0.0311	0.3578	0.0113	0.0306	0.3881	0.0105	0.0343
0.70	0.3749	0.0109	0.0318	0.3428	0.0118	0.0309	0.3543	0.0112	0.0311	0.3602	0.0111	0.0317	0.3578	0.0115	0.0348	0.3881	0.0105	0.0343
0.90	0.2705	0.0153	0.0258	0.2697	0.0171	0.0294	0.2643	0.0157	0.0273	0.2588	0.0160	0.0249						
$\cos(\theta_\eta^*)$	$E_\gamma = (1350.0 \pm 10.0) \text{ MeV}$			$E_\gamma = (1370.0 \pm 10.0) \text{ MeV}$			$E_\gamma = (1390.0 \pm 10.0) \text{ MeV}$											
	$d\sigma/d\Omega$	Δ_{stat}	Δ_{sys}	$d\sigma/d\Omega$	Δ_{stat}	Δ_{sys}	$d\sigma/d\Omega$	Δ_{stat}	Δ_{sys}									
	$[\mu\text{b}/\text{sr}]$	$[\mu\text{b}/\text{sr}]$	$[\mu\text{b}/\text{sr}]$	$[\mu\text{b}/\text{sr}]$	$[\mu\text{b}/\text{sr}]$	$[\mu\text{b}/\text{sr}]$	$[\mu\text{b}/\text{sr}]$	$[\mu\text{b}/\text{sr}]$	$[\mu\text{b}/\text{sr}]$									
-0.90	0.1159	0.0077	0.0159	0.1071	0.0073	0.0229	0.1084	0.0081	0.0182	0.1442	0.0079	0.0170	0.1953	0.0095	0.0237	0.2413	0.0093	0.0255
-0.70	0.1634	0.0078	0.0210	0.1584	0.0075	0.0224	0.2938	0.0088	0.0187	0.3096	0.0095	0.0278	0.3671	0.0102	0.0330	0.4146	0.0108	0.0279
-0.50	0.2054	0.0087	0.0190	0.2029	0.0087	0.0187	0.2625	0.0090	0.0217	0.3427	0.0092	0.0301	0.3632	0.0095	0.0315	0.3695	0.0103	0.0317
-0.30	0.2625	0.0090	0.0217	0.2562	0.0087	0.0215	0.2938	0.0088	0.0250	0.3427	0.0101	0.0311	0.3632	0.0109	0.0315	0.3674	0.0101	0.0311
-0.10	0.2938	0.0088	0.0241	0.3002	0.0088	0.0250	0.3427	0.0111	0.0326	0.3674	0.0111	0.0326	0.3695	0.0117	0.0296	0.3749	0.0117	0.0296
0.10	0.3427	0.0092	0.0301	0.3278	0.0088	0.0287	0.3632	0.0111	0.0326	0.3674	0.0101	0.0311	0.3695	0.0117	0.0296	0.3749	0.0117	0.0296
0.30	0.3632	0.0095	0.0315	0.3434	0.0091	0.0293	0.3674	0.0111	0.0326	0.3632	0.0111	0.0326	0.3695	0.0117	0.0296	0.3749	0.0117	0.0296
0.50	0.3695	0.0103	0.0317	0.3674	0.0101	0.0311	0.3674	0.0111	0.0326	0.3674	0.0111	0.0326	0.3749	0.0117	0.0296	0.3881	0.0105	0.0343
0.70	0.3530	0.0117	0.0296	0.3293	0.0111	0.0326	0.3530	0.0111	0.0326	0.3530	0.0111	0.0326	0.3674	0.0117	0.0296	0.3749	0.0117	0.0296
0.90	0.2706	0.0162	0.0227	0.2740	0.0161	0.0253	0.2706	0.0161	0.0253	0.2706	0.0161	0.0253	0.2740	0.0178	0.0274			

Total Cross Sections

E_γ [MeV]	ΔE_γ [MeV]	σ [μb]	Δ_{stat} [μb]	Δ_{sys} [μb]
655.0	25.0	0.8184	0.0192	0.0748
690.0	10.0	3.5211	0.0386	0.2807
710.0	10.0	6.9163	0.0601	0.5705
730.0	10.0	9.9293	0.0543	0.8818
747.5	7.5	12.5382	0.0653	1.1327
762.5	7.5	14.1966	0.0753	1.2094
777.5	7.5	15.6877	0.0761	1.2901
792.5	7.5	16.4644	0.0731	1.3111
807.5	7.5	16.9974	0.0736	1.2904
822.5	7.5	16.9347	0.0758	1.3131
837.5	7.5	16.5816	0.0779	1.3316
852.5	7.5	16.3332	0.0766	1.3152
867.5	7.5	15.4992	0.0701	1.2695
882.5	7.5	14.7167	0.0655	1.2267
897.5	7.5	13.7759	0.0688	1.1509
912.5	7.5	12.8142	0.0665	1.0636
927.5	7.5	11.7158	0.0609	0.9891
942.5	7.5	10.6352	0.0585	0.9145
957.5	7.5	9.7923	0.0611	0.8826
972.5	7.5	8.9107	0.0534	0.8128
987.5	7.5	7.9337	0.0511	0.7581
1002.5	7.5	7.4765	0.0513	0.7260
1017.5	7.5	6.7264	0.0487	0.6865
1032.5	7.5	6.2706	0.0479	0.6246
1047.5	7.5	5.9129	0.0490	0.6178
1062.5	7.5	5.4925	0.0465	0.5666
1077.5	7.5	5.2045	0.0451	0.5588
1092.5	7.5	4.9003	0.0465	0.5444
1110.0	10.0	4.7385	0.0435	0.4806
1130.0	10.0	4.6734	0.0388	0.4791
1150.0	10.0	4.5244	0.0400	0.4411
1170.0	10.0	4.3347	0.0379	0.4089
1190.0	10.0	4.3004	0.0391	0.4054
1210.0	10.0	4.0640	0.0399	0.3718
1230.0	10.0	4.1004	0.0419	0.3685
1250.0	10.0	3.9554	0.0424	0.3711
1270.0	10.0	3.8355	0.0390	0.3484
1290.0	10.0	3.7550	0.0433	0.3479
1310.0	10.0	3.6046	0.0394	0.3186
1330.0	10.0	3.4544	0.0401	0.3468
1350.0	10.0	3.4432	0.0403	0.3118
1370.0	10.0	3.3480	0.0391	0.3248
1390.0	10.0	3.2528	0.0429	0.3118

F.1.3 $\gamma n \rightarrow \eta n$ as a Function of E_γ

Angular Distributions

$\cos(\theta_\eta^*)$	$E_\gamma = (655.0 \pm 25.0) \text{ MeV}$			$E_\gamma = (690.0 \pm 10.0) \text{ MeV}$			$E_\gamma = (710.0 \pm 10.0) \text{ MeV}$			$E_\gamma = (730.0 \pm 10.0) \text{ MeV}$		
	$d\sigma/d\Omega$			$d\sigma/d\Omega$			$d\sigma/d\Omega$			$d\sigma/d\Omega$		
	$[\mu\text{b}/\text{sr}]$	$[\mu\text{b}/\text{sr}]$	$[\mu\text{b}/\text{sr}]$									
-0.90	0.1516	0.0111	0.0160	0.3196	0.0184	0.0319	0.4366	0.0255	0.0424	0.5341	0.0217	0.0511
-0.70	0.0982	0.0086	0.0109	0.2547	0.0144	0.0203	0.3337	0.0185	0.0310	0.4133	0.0158	0.0395
-0.50	0.0580	0.0070	0.0060	0.2021	0.0125	0.0151	0.2930	0.0167	0.0290	0.3375	0.0133	0.0329
-0.30	0.0364	0.0064	0.0105	0.1350	0.0108	0.0120	0.2457	0.0153	0.0212	0.2903	0.0121	0.0286
-0.10	0.0079	0.0050	0.0011	0.0900	0.0097	0.0099	0.1784	0.0135	0.0159	0.2439	0.0113	0.0242
0.10	0.0350	0.0080	0.0093	0.0813	0.0106	0.0127	0.1160	0.0122	0.0126	0.2166	0.0114	0.0238
0.30	0.0201	0.0081	0.0056	0.0389	0.0106	0.0075	0.1032	0.0141	0.0119	0.1869	0.0119	0.0216
0.50	0.0099	0.0086	0.0062	0.0190	0.0114	0.0051	0.0912	0.0157	0.0109	0.1424	0.0123	0.0174
0.70	0.0004	0.0055	0.0098	0.0500	0.0151	0.0132	0.0899	0.0187	0.0176	0.1398	0.0145	0.0182
0.90	0.0431	0.0140	0.0198	0.0050	0.0160	0.0040	0.1238	0.0286	0.0155	0.1545	0.0214	0.0202
$\cos(\theta_\eta^*)$	$E_\gamma = (747.5 \pm 7.5) \text{ MeV}$			$E_\gamma = (762.5 \pm 7.5) \text{ MeV}$			$E_\gamma = (777.5 \pm 7.5) \text{ MeV}$			$E_\gamma = (792.5 \pm 7.5) \text{ MeV}$		
	$d\sigma/d\Omega$			$d\sigma/d\Omega$			$d\sigma/d\Omega$			$d\sigma/d\Omega$		
	$[\mu\text{b}/\text{sr}]$	$[\mu\text{b}/\text{sr}]$	$[\mu\text{b}/\text{sr}]$									
-0.90	0.5738	0.0243	0.0561	0.5991	0.0270	0.0584	0.5714	0.0257	0.0524	0.5767	0.0241	0.0567
-0.70	0.4509	0.0176	0.0437	0.4761	0.0195	0.0490	0.4522	0.0183	0.0439	0.5094	0.0181	0.0449
-0.50	0.4066	0.0153	0.0414	0.4136	0.0165	0.0417	0.4481	0.0163	0.0432	0.4403	0.0151	0.0391
-0.30	0.3556	0.0139	0.0354	0.3688	0.0150	0.0385	0.4027	0.0147	0.0363	0.3935	0.0134	0.0359
-0.10	0.2844	0.0124	0.0280	0.3446	0.0142	0.0331	0.3592	0.0134	0.0332	0.3895	0.0129	0.0359
0.10	0.2673	0.0126	0.0259	0.2660	0.0129	0.0260	0.3471	0.0135	0.0338	0.3693	0.0127	0.0318
0.30	0.2098	0.0122	0.0217	0.2613	0.0138	0.0256	0.3020	0.0135	0.0301	0.3458	0.0130	0.0321
0.50	0.2000	0.0138	0.0218	0.2387	0.0151	0.0281	0.2684	0.0146	0.0293	0.2836	0.0134	0.0254
0.70	0.1767	0.0161	0.0238	0.2199	0.0181	0.0250	0.2516	0.0174	0.0301	0.2682	0.0161	0.0304
0.90	0.1606	0.0215	0.0221	0.2130	0.0249	0.0234	0.2623	0.0254	0.0339	0.2615	0.0233	0.0327
$\cos(\theta_\eta^*)$	$E_\gamma = (807.5 \pm 7.5) \text{ MeV}$			$E_\gamma = (822.5 \pm 7.5) \text{ MeV}$			$E_\gamma = (837.5 \pm 7.5) \text{ MeV}$			$E_\gamma = (852.5 \pm 7.5) \text{ MeV}$		
	$d\sigma/d\Omega$			$d\sigma/d\Omega$			$d\sigma/d\Omega$			$d\sigma/d\Omega$		
	$[\mu\text{b}/\text{sr}]$	$[\mu\text{b}/\text{sr}]$	$[\mu\text{b}/\text{sr}]$									
-0.90	0.6258	0.0246	0.0641	0.6225	0.0253	0.0599	0.6149	0.0263	0.0631	0.5752	0.0254	0.0587
-0.70	0.5024	0.0177	0.0475	0.4873	0.0181	0.0453	0.5491	0.0202	0.0539	0.4888	0.0189	0.0493
-0.50	0.4554	0.0152	0.0437	0.4854	0.0164	0.0439	0.4869	0.0171	0.0454	0.5076	0.0174	0.0454
-0.30	0.4475	0.0140	0.0409	0.4240	0.0141	0.0394	0.4669	0.0155	0.0471	0.4750	0.0156	0.0426
-0.10	0.4165	0.0131	0.0361	0.4128	0.0133	0.0377	0.3796	0.0133	0.0345	0.4192	0.0138	0.0391
0.10	0.3960	0.0127	0.0358	0.3719	0.0126	0.0325	0.3704	0.0130	0.0327	0.3554	0.0126	0.0329
0.30	0.3264	0.0121	0.0294	0.3473	0.0128	0.0338	0.3152	0.0125	0.0281	0.3384	0.0126	0.0299
0.50	0.3272	0.0138	0.0283	0.2923	0.0131	0.0293	0.3193	0.0140	0.0302	0.3203	0.0136	0.0289
0.70	0.3025	0.0163	0.0290	0.3178	0.0170	0.0342	0.2921	0.0165	0.0327	0.2931	0.0160	0.0307
0.90	0.2758	0.0232	0.0324	0.2798	0.0237	0.0326	0.2747	0.0242	0.0344	0.2953	0.0242	0.0335
$\cos(\theta_\eta^*)$	$E_\gamma = (867.5 \pm 7.5) \text{ MeV}$			$E_\gamma = (882.5 \pm 7.5) \text{ MeV}$			$E_\gamma = (897.5 \pm 7.5) \text{ MeV}$			$E_\gamma = (912.5 \pm 7.5) \text{ MeV}$		
	$d\sigma/d\Omega$			$d\sigma/d\Omega$			$d\sigma/d\Omega$			$d\sigma/d\Omega$		
	$[\mu\text{b}/\text{sr}]$	$[\mu\text{b}/\text{sr}]$	$[\mu\text{b}/\text{sr}]$									
-0.90	0.5306	0.0232	0.0562	0.5251	0.0221	0.0533	0.5327	0.0242	0.0532	0.5158	0.0241	0.0500
-0.70	0.4598	0.0173	0.0447	0.4174	0.0157	0.0392	0.4495	0.0177	0.0449	0.4303	0.0175	0.0420
-0.50	0.4803	0.0160	0.0450	0.4118	0.0142	0.0392	0.4053	0.0154	0.0381	0.4063	0.0154	0.0420
-0.30	0.4473	0.0143	0.0405	0.3911	0.0127	0.0359	0.4257	0.0145	0.0420	0.3828	0.0137	0.0390
-0.10	0.4021	0.0127	0.0400	0.4254	0.0126	0.0395	0.3867	0.0130	0.0379	0.3859	0.0132	0.0361
0.10	0.3661	0.0119	0.0354	0.3950	0.0119	0.0372	0.3708	0.0125	0.0351	0.3299	0.0118	0.0319
0.30	0.3382	0.0118	0.0322	0.3212	0.0110	0.0305	0.3339	0.0121	0.0330	0.3111	0.0118	0.0316
0.50	0.3269	0.0128	0.0310	0.3249	0.0121	0.0333	0.2882	0.0124	0.0288	0.2762	0.0122	0.0286
0.70	0.3005	0.0150	0.0322	0.2843	0.0139	0.0302	0.2748	0.0148	0.0296	0.2521	0.0142	0.0263
0.90	0.3192	0.0238	0.0332	0.3272	0.0234	0.0371	0.2857	0.0237	0.0292	0.2667	0.0230	0.0272

F.1. UNPOLARISED CROSS SECTIONS FROM ${}^3\text{He}$ (A2)

$\cos(\theta_\eta^*)$	$E_\gamma = (927.5 \pm 7.5) \text{ MeV}$			$E_\gamma = (942.5 \pm 7.5) \text{ MeV}$			$E_\gamma = (957.5 \pm 7.5) \text{ MeV}$			$E_\gamma = (972.5 \pm 7.5) \text{ MeV}$								
	$d\sigma/d\Omega$			Δ_{stat}			Δ_{sys}			$d\sigma/d\Omega$			Δ_{stat}			Δ_{sys}		
	$[\mu\text{b}/\text{sr}]$	$[\mu\text{b}/\text{sr}]$	$[\mu\text{b}/\text{sr}]$	$[\mu\text{b}/\text{sr}]$	$[\mu\text{b}/\text{sr}]$	$[\mu\text{b}/\text{sr}]$	$[\mu\text{b}/\text{sr}]$											
-0.90	0.5365	0.0237	0.0532	0.5321	0.0238	0.0494	0.4602	0.0239	0.0517	0.4970	0.0229	0.0499						
-0.70	0.3769	0.0158	0.0359	0.3893	0.0161	0.0395	0.4026	0.0177	0.0421	0.3492	0.0151	0.0399						
-0.50	0.3984	0.0145	0.0380	0.3797	0.0142	0.0346	0.3719	0.0152	0.0373	0.3876	0.0142	0.0432						
-0.30	0.3771	0.0130	0.0361	0.3688	0.0129	0.0361	0.3466	0.0135	0.0361	0.3639	0.0127	0.0412						
-0.10	0.3762	0.0124	0.0351	0.3548	0.0121	0.0338	0.3495	0.0130	0.0352	0.3356	0.0115	0.0328						
0.10	0.3442	0.0115	0.0342	0.3352	0.0114	0.0365	0.3180	0.0120	0.0320	0.3247	0.0111	0.0345						
0.30	0.3295	0.0116	0.0333	0.3429	0.0119	0.0336	0.3056	0.0122	0.0317	0.2739	0.0106	0.0286						
0.50	0.2561	0.0112	0.0264	0.2566	0.0113	0.0253	0.2609	0.0123	0.0290	0.2864	0.0118	0.0282						
0.70	0.2546	0.0137	0.0275	0.2146	0.0126	0.0224	0.2236	0.0139	0.0276	0.2316	0.0130	0.0280						
0.90	0.2307	0.0206	0.0302	0.1909	0.0189	0.0271	0.2353	0.0229	0.0255	0.2286	0.0208	0.0287						
<hr/>																		
$\cos(\theta_\eta^*)$	$E_\gamma = (987.5 \pm 7.5) \text{ MeV}$			$E_\gamma = (1002.5 \pm 7.5) \text{ MeV}$			$E_\gamma = (1017.5 \pm 7.5) \text{ MeV}$			$E_\gamma = (1032.5 \pm 7.5) \text{ MeV}$								
	$d\sigma/d\Omega$			Δ_{stat}			Δ_{sys}			$d\sigma/d\Omega$			Δ_{stat}			Δ_{sys}		
	$[\mu\text{b}/\text{sr}]$	$[\mu\text{b}/\text{sr}]$	$[\mu\text{b}/\text{sr}]$	$[\mu\text{b}/\text{sr}]$	$[\mu\text{b}/\text{sr}]$	$[\mu\text{b}/\text{sr}]$	$[\mu\text{b}/\text{sr}]$	$[\mu\text{b}/\text{sr}]$										
-0.90	0.4772	0.0228	0.0550	0.4216	0.0221	0.0553	0.3923	0.0214	0.0443	0.3645	0.0208	0.0460						
-0.70	0.3562	0.0156	0.0384	0.3743	0.0166	0.0395	0.3621	0.0165	0.0413	0.3486	0.0164	0.0432						
-0.50	0.3657	0.0141	0.0392	0.3328	0.0139	0.0353	0.3501	0.0144	0.0397	0.3386	0.0143	0.0407						
-0.30	0.3793	0.0131	0.0384	0.3486	0.0130	0.0369	0.3186	0.0126	0.0379	0.3302	0.0130	0.0411						
-0.10	0.3561	0.0120	0.0369	0.3282	0.0119	0.0350	0.3231	0.0119	0.0363	0.3239	0.0121	0.0339						
0.10	0.3155	0.0112	0.0351	0.3152	0.0115	0.0368	0.3256	0.0118	0.0386	0.3195	0.0119	0.0379						
0.30	0.2711	0.0108	0.0266	0.2994	0.0116	0.0301	0.3037	0.0117	0.0309	0.2535	0.0109	0.0290						
0.50	0.2500	0.0111	0.0268	0.2572	0.0117	0.0292	0.2391	0.0113	0.0291	0.2487	0.0116	0.0262						
0.70	0.1974	0.0121	0.0225	0.2012	0.0125	0.0246	0.1575	0.0111	0.0215	0.1716	0.0117	0.0219						
0.90	0.1491	0.0171	0.0183	0.1565	0.0183	0.0239	0.1934	0.0201	0.0233	0.1673	0.0188	0.0237						
<hr/>																		
$\cos(\theta_\eta^*)$	$E_\gamma = (1047.5 \pm 7.5) \text{ MeV}$			$E_\gamma = (1062.5 \pm 7.5) \text{ MeV}$			$E_\gamma = (1077.5 \pm 7.5) \text{ MeV}$			$E_\gamma = (1092.5 \pm 7.5) \text{ MeV}$								
	$d\sigma/d\Omega$			Δ_{stat}			Δ_{sys}			$d\sigma/d\Omega$			Δ_{stat}			Δ_{sys}		
	$[\mu\text{b}/\text{sr}]$	$[\mu\text{b}/\text{sr}]$	$[\mu\text{b}/\text{sr}]$	$[\mu\text{b}/\text{sr}]$	$[\mu\text{b}/\text{sr}]$	$[\mu\text{b}/\text{sr}]$	$[\mu\text{b}/\text{sr}]$	$[\mu\text{b}/\text{sr}]$										
-0.90	0.3666	0.0223	0.0470	0.3416	0.0214	0.0441	0.3484	0.0214	0.0413	0.3389	0.0228	0.0498						
-0.70	0.3401	0.0170	0.0422	0.2957	0.0157	0.0382	0.2897	0.0154	0.0322	0.2812	0.0163	0.0338						
-0.50	0.3325	0.0149	0.0390	0.2784	0.0136	0.0304	0.2845	0.0137	0.0301	0.2905	0.0146	0.0337						
-0.30	0.3165	0.0133	0.0369	0.3107	0.0129	0.0315	0.2945	0.0125	0.0312	0.2811	0.0129	0.0352						
-0.10	0.3319	0.0128	0.0357	0.2954	0.0119	0.0318	0.2845	0.0116	0.0311	0.2954	0.0125	0.0350						
0.10	0.2847	0.0117	0.0316	0.2853	0.0115	0.0332	0.2807	0.0113	0.0294	0.2539	0.0114	0.0260						
0.30	0.2749	0.0118	0.0319	0.2785	0.0117	0.0311	0.2626	0.0113	0.0306	0.2547	0.0118	0.0311						
0.50	0.2244	0.0115	0.0295	0.2130	0.0110	0.0225	0.2153	0.0110	0.0228	0.2229	0.0117	0.0247						
0.70	0.1785	0.0125	0.0234	0.1753	0.0121	0.0222	0.1820	0.0121	0.0217	0.1742	0.0124	0.0230						
0.90	0.1514	0.0190	0.0184	0.1588	0.0188	0.0234	0.1307	0.0169	0.0156	0.1431	0.0185	0.0299						
<hr/>																		
$\cos(\theta_\eta^*)$	$E_\gamma = (1110.0 \pm 10.0) \text{ MeV}$			$E_\gamma = (1130.0 \pm 10.0) \text{ MeV}$			$E_\gamma = (1150.0 \pm 10.0) \text{ MeV}$			$E_\gamma = (1170.0 \pm 10.0) \text{ MeV}$								
	$d\sigma/d\Omega$			Δ_{stat}			Δ_{sys}			$d\sigma/d\Omega$			Δ_{stat}			Δ_{sys}		
	$[\mu\text{b}/\text{sr}]$	$[\mu\text{b}/\text{sr}]$	$[\mu\text{b}/\text{sr}]$	$[\mu\text{b}/\text{sr}]$	$[\mu\text{b}/\text{sr}]$	$[\mu\text{b}/\text{sr}]$	$[\mu\text{b}/\text{sr}]$	$[\mu\text{b}/\text{sr}]$										
-0.90	0.2816	0.0202	0.0387	0.2848	0.0181	0.0379	0.2813	0.0193	0.0352	0.2562	0.0183	0.0314						
-0.70	0.2451	0.0145	0.0272	0.2465	0.0129	0.0253	0.2367	0.0134	0.0337	0.2294	0.0129	0.0314						
-0.50	0.2639	0.0133	0.0274	0.2282	0.0110	0.0265	0.2159	0.0111	0.0301	0.2328	0.0112	0.0261						
-0.30	0.2558	0.0116	0.0287	0.2644	0.0106	0.0325	0.2325	0.0105	0.0286	0.2144	0.0098	0.0233						
-0.10	0.2638	0.0111	0.0288	0.2587	0.0099	0.0301	0.2456	0.0101	0.0268	0.2424	0.0098	0.0244						
0.10	0.2458	0.0104	0.0286	0.2709	0.0099	0.0301	0.2380	0.0097	0.0265	0.2457	0.0097	0.0258						
0.30	0.2514	0.0109	0.0274	0.2514	0.0098	0.0296	0.2498	0.0102	0.0289	0.2617	0.0101	0.0287						
0.50	0.2198	0.0110	0.0246	0.2247	0.0100	0.0259	0.2156	0.0102	0.0227	0.2158	0.0099	0.0248						
0.70	0.1920	0.0122	0.0236	0.1729	0.0104</													

APPENDIX F. DATA TABLES

$\cos(\theta_\eta^*)$	$E_\gamma = (1190.0 \pm 10.0) \text{ MeV}$			$E_\gamma = (1210.0 \pm 10.0) \text{ MeV}$			$E_\gamma = (1230.0 \pm 10.0) \text{ MeV}$			$E_\gamma = (1250.0 \pm 10.0) \text{ MeV}$								
	$d\sigma/d\Omega$			Δ_{stat}			Δ_{sys}			$d\sigma/d\Omega$			Δ_{stat}			Δ_{sys}		
	$[\mu\text{b}/\text{sr}]$	$[\mu\text{b}/\text{sr}]$	$[\mu\text{b}/\text{sr}]$	$[\mu\text{b}/\text{sr}]$	$[\mu\text{b}/\text{sr}]$	$[\mu\text{b}/\text{sr}]$	$[\mu\text{b}/\text{sr}]$	$[\mu\text{b}/\text{sr}]$										
-0.90	0.2291	0.0182	0.0458	0.2399	0.0196	0.0366	0.2717	0.0215	0.0410	0.2128	0.0205	0.0328						
-0.70	0.2295	0.0133	0.0360	0.2073	0.0135	0.0275	0.2128	0.0142	0.0261	0.1827	0.0137	0.0196						
-0.50	0.2264	0.0113	0.0271	0.2110	0.0116	0.0254	0.1647	0.0107	0.0179	0.1910	0.0118	0.0183						
-0.30	0.1992	0.0097	0.0208	0.2015	0.0102	0.0213	0.2023	0.0106	0.0250	0.1930	0.0108	0.0183						
-0.10	0.2323	0.0098	0.0228	0.2333	0.0104	0.0239	0.2126	0.0103	0.0247	0.2017	0.0103	0.0176						
0.10	0.2343	0.0096	0.0264	0.2357	0.0102	0.0230	0.2266	0.0104	0.0195	0.2147	0.0105	0.0217						
0.30	0.2414	0.0099	0.0260	0.2212	0.0101	0.0202	0.2260	0.0106	0.0169	0.2119	0.0107	0.0198						
0.50	0.2332	0.0105	0.0245	0.2310	0.0111	0.0223	0.2132	0.0111	0.0200	0.2140	0.0116	0.0211						
0.70	0.1721	0.0109	0.0219	0.1602	0.0111	0.0168	0.1634	0.0116	0.0165	0.1621	0.0120	0.0201						
0.90	0.1298	0.0152	0.0147	0.1175	0.0152	0.0155	0.1684	0.0189	0.0174	0.1197	0.0166	0.0172						
$\cos(\theta_\eta^*)$	$E_\gamma = (1270.0 \pm 10.0) \text{ MeV}$			$E_\gamma = (1290.0 \pm 10.0) \text{ MeV}$			$E_\gamma = (1310.0 \pm 10.0) \text{ MeV}$			$E_\gamma = (1330.0 \pm 10.0) \text{ MeV}$								
	$d\sigma/d\Omega$			Δ_{stat}			Δ_{sys}			$d\sigma/d\Omega$			Δ_{stat}			Δ_{sys}		
	$[\mu\text{b}/\text{sr}]$	$[\mu\text{b}/\text{sr}]$	$[\mu\text{b}/\text{sr}]$	$[\mu\text{b}/\text{sr}]$	$[\mu\text{b}/\text{sr}]$	$[\mu\text{b}/\text{sr}]$	$[\mu\text{b}/\text{sr}]$	$[\mu\text{b}/\text{sr}]$										
-0.90	0.1651	0.0173	0.0347	0.2026	0.0212	0.0434	0.1887	0.0186	0.0200	0.1643	0.0186	0.0378						
-0.70	0.1917	0.0131	0.0225	0.1401	0.0128	0.0156	0.1313	0.0115	0.0181	0.1470	0.0125	0.0333						
-0.50	0.1515	0.0100	0.0175	0.1631	0.0116	0.0224	0.1297	0.0096	0.0174	0.1276	0.0101	0.0142						
-0.30	0.1650	0.0094	0.0171	0.1549	0.0102	0.0169	0.1574	0.0096	0.0178	0.1502	0.0097	0.0160						
-0.10	0.1836	0.0092	0.0201	0.1780	0.0102	0.0194	0.1555	0.0089	0.0198	0.1626	0.0095	0.0171						
0.10	0.1992	0.0095	0.0205	0.1915	0.0105	0.0207	0.1860	0.0096	0.0217	0.1710	0.0094	0.0196						
0.30	0.2091	0.0099	0.0207	0.1965	0.0109	0.0224	0.1945	0.0100	0.0238	0.1743	0.0098	0.0189						
0.50	0.2158	0.0109	0.0206	0.2158	0.0123	0.0210	0.1762	0.0103	0.0162	0.1711	0.0106	0.0172						
0.70	0.1725	0.0115	0.0182	0.1748	0.0131	0.0211	0.1448	0.0111	0.0215	0.1335	0.0112	0.0172						
0.90	0.1272	0.0161	0.0221	0.1172	0.0172	0.0132	0.1199	0.0161	0.0148	0.0976	0.0152	0.0115						
$\cos(\theta_\eta^*)$	$E_\gamma = (1350.0 \pm 10.0) \text{ MeV}$			$E_\gamma = (1370.0 \pm 10.0) \text{ MeV}$			$E_\gamma = (1390.0 \pm 10.0) \text{ MeV}$											
	$d\sigma/d\Omega$			Δ_{stat}			Δ_{sys}			$d\sigma/d\Omega$			Δ_{stat}			Δ_{sys}		
	$[\mu\text{b}/\text{sr}]$	$[\mu\text{b}/\text{sr}]$	$[\mu\text{b}/\text{sr}]$	$[\mu\text{b}/\text{sr}]$	$[\mu\text{b}/\text{sr}]$	$[\mu\text{b}/\text{sr}]$	$[\mu\text{b}/\text{sr}]$	$[\mu\text{b}/\text{sr}]$										
-0.90	0.1663	0.0191	0.0254		0.1736	0.0194	0.0291		0.1810	0.0213	0.0460							
-0.70	0.1339	0.0119	0.0172		0.1149	0.0110	0.0167		0.1243	0.0125	0.0228							
-0.50	0.1393	0.0105	0.0147		0.1235	0.0096	0.0155		0.1171	0.0101	0.0231							
-0.30	0.1557	0.0099	0.0168		0.1505	0.0095	0.0158		0.1240	0.0095	0.0181							
-0.10	0.1600	0.0094	0.0156		0.1500	0.0090	0.0160		0.1451	0.0097	0.0153							
0.10	0.1708	0.0094	0.0192		0.1724	0.0093	0.0206		0.1519	0.0095	0.0209							
0.30	0.1646	0.0095	0.0157		0.1729	0.0095	0.0210		0.1561	0.0100	0.0180							
0.50	0.1863	0.0111	0.0208		0.1661	0.0103	0.0232		0.1450	0.0107	0.0174							
0.70	0.1561	0.0122	0.0200		0.1459	0.0116	0.0196		0.1537	0.0131	0.0175							
0.90	0.1111	0.0163	0.0131		0.1319	0.0176	0.0144		0.1055	0.0173	0.0127							

Total Cross Sections

E_γ [MeV]	ΔE_γ [MeV]	σ [μb]	Δ_{stat} [μb]	Δ_{sys} [μb]
655.0	25.0	0.5182	0.0309	0.1109
690.0	10.0	1.4985	0.0526	0.1635
710.0	10.0	2.5230	0.0732	0.2630
730.0	10.0	3.3251	0.0592	0.3471
747.5	7.5	3.8720	0.0652	0.4023
762.5	7.5	4.2650	0.0724	0.4394
777.5	7.5	4.5803	0.0703	0.4591
792.5	7.5	4.8025	0.0659	0.4556
807.5	7.5	5.0959	0.0663	0.4834
822.5	7.5	5.0530	0.0679	0.4863
837.5	7.5	5.1170	0.0707	0.5059
852.5	7.5	5.1021	0.0693	0.4905
867.5	7.5	4.9763	0.0647	0.4887
882.5	7.5	4.7347	0.0604	0.4645
897.5	7.5	4.6767	0.0650	0.4643
912.5	7.5	4.4370	0.0637	0.4440
927.5	7.5	4.3072	0.0598	0.4319
942.5	7.5	4.1728	0.0587	0.4181
957.5	7.5	4.0829	0.0635	0.4359
972.5	7.5	4.0701	0.0581	0.4435
987.5	7.5	3.8789	0.0567	0.4191
1002.5	7.5	3.7955	0.0580	0.4314
1017.5	7.5	3.6558	0.0573	0.4259
1032.5	7.5	3.5731	0.0572	0.4289
1047.5	7.5	3.4996	0.0594	0.4215
1062.5	7.5	3.2675	0.0566	0.3823
1077.5	7.5	3.2122	0.0555	0.3570
1092.5	7.5	3.1638	0.0587	0.3986
1110.0	10.0	2.9164	0.0529	0.3394
1130.0	10.0	2.8929	0.0470	0.3397
1150.0	10.0	2.7408	0.0484	0.3460
1170.0	10.0	2.6995	0.0466	0.3281
1190.0	10.0	2.6677	0.0480	0.3343
1210.0	10.0	2.5716	0.0498	0.2903
1230.0	10.0	2.5375	0.0523	0.2755
1250.0	10.0	2.3844	0.0520	0.2571
1270.0	10.0	2.2379	0.0474	0.2657
1290.0	10.0	2.1685	0.0527	0.2657
1310.0	10.0	1.9624	0.0465	0.2395
1330.0	10.0	1.8749	0.0472	0.2551
1350.0	10.0	1.9329	0.0484	0.2234
1370.0	10.0	1.8522	0.0469	0.2391
1390.0	10.0	1.7458	0.0503	0.2621

F.1.4 $\gamma p \rightarrow \eta p$ as a Function of W

Angular Distributions

$\cos(\theta_\eta^*)$	W=(1488.0±4.0) MeV			W=(1496.0±4.0) MeV			W=(1504.0±4.0) MeV			W=(1511.0±3.0) MeV		
	$d\sigma/d\Omega$			$d\sigma/d\Omega$			$d\sigma/d\Omega$			$d\sigma/d\Omega$		
	$[\mu\text{b}/\text{sr}]$	Δ_{stat}	Δ_{sys}									
-0.90	0.4858	0.0502	0.0455	1.2565	0.0476	0.0937	1.6477	0.0406	0.1183	1.6655	0.0379	0.1300
-0.70	0.3951	0.0216	0.0300	1.2327	0.0253	0.0792	1.4752	0.0227	0.1046	1.5930	0.0235	0.1255
-0.50	0.4255	0.0179	0.0280	1.1900	0.0214	0.0746	1.4664	0.0206	0.1039	1.5530	0.0222	0.1236
-0.30	0.4048	0.0161	0.0288	1.0956	0.0197	0.0750	1.4105	0.0202	0.1012	1.6150	0.0236	0.1285
-0.10	0.3826	0.0152	0.0303	1.0881	0.0195	0.0785	1.3037	0.0201	0.0951	1.5795	0.0248	0.1242
0.10	0.3869	0.0154	0.0359	1.0251	0.0194	0.0804	1.3191	0.0211	0.0985	1.5218	0.0259	0.1238
0.30	0.3846	0.0159	0.0423	0.9666	0.0196	0.0859	1.2724	0.0217	0.1068	1.4773	0.0272	0.1305
0.50	0.3597	0.0165	0.0379	0.9628	0.0208	0.0832	1.1020	0.0215	0.1073	1.2757	0.0271	0.1261
0.70	0.3167	0.0178	0.0324	0.8614	0.0220	0.0682	1.0451	0.0228	0.1035	1.1007	0.0272	0.1123
0.90	0.2717	0.0281	0.0401	0.8031	0.0317	0.0548	0.9186	0.0291	0.0772	1.0205	0.0336	0.0969
$\cos(\theta_\eta^*)$	W=(1518.0±4.0) MeV			W=(1526.0±4.0) MeV			W=(1534.0±4.0) MeV			W=(1544.0±6.0) MeV		
	$d\sigma/d\Omega$	Δ_{stat}	Δ_{sys}									
	$[\mu\text{b}/\text{sr}]$											
-0.90	1.6432	0.0312	0.1364	1.8185	0.0311	0.1472	1.8236	0.0300	0.1654	1.6816	0.0235	0.1444
-0.70	1.7051	0.0212	0.1383	1.7692	0.0210	0.1452	1.7709	0.0208	0.1421	1.6713	0.0168	0.1333
-0.50	1.6755	0.0206	0.1365	1.7518	0.0210	0.1452	1.7972	0.0213	0.1425	1.7366	0.0176	0.1413
-0.30	1.7267	0.0224	0.1412	1.8483	0.0235	0.1515	1.9185	0.0243	0.1573	1.9832	0.0209	0.1586
-0.10	1.7704	0.0246	0.1433	1.9400	0.0261	0.1549	2.0805	0.0267	0.1697	2.1672	0.0219	0.1676
0.10	1.7642	0.0260	0.1470	1.9256	0.0268	0.1544	2.0329	0.0262	0.1589	2.0528	0.0204	0.1570
0.30	1.6249	0.0266	0.1397	1.8020	0.0270	0.1478	1.8593	0.0254	0.1460	1.8907	0.0197	0.1446
0.50	1.5377	0.0281	0.1376	1.5857	0.0279	0.1406	1.6342	0.0264	0.1407	1.6231	0.0200	0.1335
0.70	1.2337	0.0280	0.1302	1.3374	0.0302	0.1279	1.3443	0.0298	0.1237	1.3149	0.0231	0.1165
0.90	1.0043	0.0320	0.1155	1.0890	0.0352	0.1032	1.1406	0.0384	0.1109	1.0707	0.0331	0.1064
$\cos(\theta_\eta^*)$	W=(1555.0±5.0) MeV			W=(1565.0±5.0) MeV			W=(1575.0±5.0) MeV			W=(1585.0±5.0) MeV		
	$d\sigma/d\Omega$	Δ_{stat}	Δ_{sys}									
	$[\mu\text{b}/\text{sr}]$											
-0.90	1.6578	0.0243	0.1366	1.4411	0.0224	0.1220	1.3681	0.0217	0.1148	1.2905	0.0211	0.1098
-0.70	1.5957	0.0175	0.1278	1.4801	0.0169	0.1234	1.3402	0.0162	0.1119	1.3122	0.0162	0.1146
-0.50	1.5959	0.0183	0.1311	1.5789	0.0185	0.1316	1.4877	0.0184	0.1240	1.4555	0.0185	0.1268
-0.30	1.9980	0.0225	0.1623	1.8774	0.0216	0.1581	1.7713	0.0207	0.1475	1.6296	0.0195	0.1423
-0.10	2.0817	0.0218	0.1633	1.8839	0.0197	0.1586	1.7075	0.0181	0.1418	1.5444	0.0168	0.1342
0.10	1.9515	0.0200	0.1514	1.8206	0.0184	0.1453	1.6455	0.0171	0.1330	1.4930	0.0161	0.1257
0.30	1.8104	0.0193	0.1412	1.6766	0.0179	0.1330	1.5730	0.0170	0.1257	1.4586	0.0163	0.1215
0.50	1.5134	0.0192	0.1244	1.4391	0.0178	0.1188	1.3358	0.0166	0.1102	1.2210	0.0156	0.1018
0.70	1.2631	0.0224	0.1237	1.1580	0.0201	0.1052	1.0582	0.0183	0.0950	0.9192	0.0165	0.0789
0.90	0.9773	0.0349	0.1077	0.8845	0.0333	0.0950	0.8137	0.0315	0.0817	0.6817	0.0280	0.0572
$\cos(\theta_\eta^*)$	W=(1595.0±5.0) MeV			W=(1605.0±5.0) MeV			W=(1615.0±5.0) MeV			W=(1625.0±5.0) MeV		
	$d\sigma/d\Omega$	Δ_{stat}	Δ_{sys}									
	$[\mu\text{b}/\text{sr}]$											
-0.90	1.1796	0.0202	0.1098	1.0229	0.0189	0.1050	0.9243	0.0180	0.0890	0.7903	0.0168	0.0771
-0.70	1.1642	0.0154	0.1015	1.0563	0.0148	0.0988	0.9520	0.0142	0.0883	0.7883	0.0132	0.0738
-0.50	1.2881	0.0177	0.1115	1.1586	0.0171	0.1047	1.0573	0.0166	0.0952	0.9094	0.0156	0.0802
-0.30	1.4749	0.0181	0.1285	1.3434	0.0169	0.1183	1.1494	0.0154	0.1038	0.9876	0.0140	0.0884
-0.10	1.4170	0.0157	0.1216	1.2331	0.0146	0.1085	1.0620	0.0135	0.0961	0.9247	0.0126	0.0816
0.10	1.3694	0.0154	0.1161	1.2074	0.0145	0.1042	1.0794	0.0138	0.0945	0.9103	0.0128	0.0831
0.30	1.3210	0.0155	0.1157	1.1416	0.0144	0.0992	1.0006	0.0135	0.0886	0.8151	0.0123	0.0720
0.50	1.0770	0.0146	0.0947	0.9759	0.0138	0.0850	0.8157	0.0127	0.0722	0.6740	0.0116	0.0602
0.70	0.8433	0.0154	0.0777	0.7152	0.0139	0.0643	0.5891	0.0125	0.0559	0.4625	0.0110	0.0419
0.90	0.6486	0.0264	0.0630	0.4819	0.0220	0.0430	0.3522	0.0181	0.0359	0.2705	0.0152	0.0259

F.1. UNPOLARISED CROSS SECTIONS FROM ${}^3\text{He}$ (A2)

$\cos(\theta_\eta^*)$	W=(1635.0±5.0) MeV			W=(1645.0±5.0) MeV			W=(1655.0±5.0) MeV			W=(1665.0±5.0) MeV			W=(1675.0±5.0) MeV			W=(1685.0±5.0) MeV			W=(1695.0±5.0) MeV			W=(1705.0±5.0) MeV																																																																																																																																																																																																																																																																																																																																																																																																																																																																																																																																																																																																																																																																																																																																																																																																																																								
	$d\sigma/d\Omega$			Δ_{stat}			Δ_{sys}			$d\sigma/d\Omega$			Δ_{stat}			Δ_{sys}			$d\sigma/d\Omega$			Δ_{stat}			Δ_{sys}																																																																																																																																																																																																																																																																																																																																																																																																																																																																																																																																																																																																																																																																																																																																																																																																																																					
	$[\mu\text{b}/\text{sr}]$																																																																																																																																																																																																																																																																																																																																																																																																																																																																																																																																																																																																																																																																																																																																																																																																																																																													
-0.90	0.6625	0.0156	0.0602	0.5347	0.0142	0.0506	0.4642	0.0134	0.0488	0.3910	0.0124	0.0442	-0.90	0.3261	0.0113	0.0383	0.2709	0.0104	0.0281	0.2332	0.0097	0.0257	0.2288	0.0096	0.0318	-0.90	0.1968	0.0090	0.0273	0.1873	0.0087	0.0226	0.1648	0.0082	0.0161	0.1510	0.0079	0.0176	-0.90	0.1242	0.0073	0.0209	0.1239	0.0073	0.0123	0.0941	0.0065	0.0163	0.1277	0.0075	0.0208	-0.90	0.1938	0.0078	0.0195	0.1771	0.0075	0.0199	0.1721	0.0075	0.0198	0.1690	0.0075	0.0220	-0.90	0.2865	0.0106	0.0238	0.2608	0.0103	0.0276	0.2613	0.0105	0.0256	0.2438	0.0104	0.0240	-0.90	0.3323	0.0087	0.0268	0.3094	0.0085	0.0278	0.2970	0.0085	0.0242	0.3063	0.0088	0.0247	-0.90	0.4081	0.0098	0.0321	0.3998	0.0098	0.0307	0.3920	0.0100	0.0309	0.3729	0.0100	0.0292	-0.90	0.4542	0.0100	0.0375	0.4317	0.0099	0.0327	0.4095	0.0099	0.0317	0.4580	0.0106	0.0365	-0.90	0.4806	0.0105	0.0360	0.4552	0.0104	0.0364	0.4512	0.0105	0.0345	0.4654	0.0108	0.0373	-0.90	0.4639	0.0107	0.0355	0.4306	0.0105	0.0364	0.4372	0.0107	0.0328	0.4203	0.0108	0.0361	-0.90	0.3406	0.0104	0.0289	0.3425	0.0106	0.0308	0.3490	0.0110	0.0286	0.3452	0.0112	0.0318	-0.90	0.2047	0.0142	0.0209	0.2458	0.0159	0.0197	0.2401	0.0161	0.0244	0.2236	0.0161	0.0213	-0.90	0.7868	0.0148	0.0709	0.6637	0.0137	0.0620	0.5837	0.0130	0.0565	0.4795	0.0119	0.0460	-0.90	0.8169	0.0126	0.0736	0.6603	0.0113	0.0610	0.5837	0.0106	0.0561	0.4847	0.0097	0.0452	-0.90	0.8060	0.0119	0.0723	0.6532	0.0108	0.0611	0.5534	0.0101	0.0524	0.4717	0.0094	0.0447	-0.90	0.7674	0.0119	0.0705	0.6641	0.0111	0.0639	0.5367	0.0101	0.0519	0.4841	0.0096	0.0456	-0.90	0.6751	0.0112	0.0632	0.5786	0.0104	0.0542	0.4864	0.0095	0.0470	0.4298	0.0090	0.0406	-0.90	0.5579	0.0105	0.0524	0.4625	0.0096	0.0439	0.3688	0.0086	0.0361	0.3563	0.0085	0.0328	-0.90	0.3698	0.0097	0.0370	0.2864	0.0085	0.0298	0.2302	0.0076	0.0223	0.2248	0.0075	0.0240	-0.90	0.2189	0.0131	0.0251	0.1608	0.0107	0.0153	0.1269	0.0090	0.0145	0.0922	0.0074	0.0120	-0.90	0.4513	0.0094	0.0406	0.4326	0.0092	0.0427	0.4256	0.0092	0.0356	0.4337	0.0094	0.0393	-0.90	0.3957	0.0087	0.0350	0.4060	0.0090	0.0365	0.4303	0.0093	0.0362	0.4651	0.0097	0.0399	-0.90	0.3416	0.0084	0.0300	0.3574	0.0087	0.0320	0.3686	0.0089	0.0314	0.4131	0.0095	0.0387	-0.90	0.2318	0.0077	0.0233	0.2542	0.0081	0.0237	0.2795	0.0086	0.0240	0.3003	0.0090	0.0296	-0.90	0.0864	0.0071	0.0117	0.1120	0.0082	0.0109	0.0996	0.0081	0.0089	0.1385	0.0100	0.0117	-0.90	0.4081	0.0098	0.0321	0.3998	0.0101	0.0404	0.4747	0.0101	0.0411	0.4814	0.0103	0.0399	-0.90	0.4663	0.0098	0.0390	0.4873	0.0101	0.0404	0.4747	0.0101	0.0411	0.4530	0.0105	0.0359	-0.90	0.4500	0.0100	0.0414	0.4499	0.0101	0.0376	0.4546	0.0104	0.0421	0.4530	0.0105	0.0359	-0.90	0.3288	0.0096	0.0340	0.3438	0.0099	0.0282	0.3593	0.0103	0.0360	0.3683	0.0106	0.0314	-0.90	0.1539	0.0109	0.0151	0.1950	0.0128	0.0191	0.2141	0.0138	0.0207	0.2186	0.0143	0.0299	-0.90	0.4542	0.0100	0.0375	0.4317	0.0099	0.0327	0.4095	0.0099	0.0317	0.4580	0.0106	0.0365	-0.90	0.4806	0.0105	0.0360	0.4552	0.0104	0.0364	0.4512	0.0105	0.0345	0.4654	0.0108	0.0373	-0.90	0.4639	0.0107	0.0355	0.4306	0.0105	0.0364	0.4372	0.0107	0.0328	0.4203	0.0108	0.0361	-0.90	0.3406	0.0104	0.0289	0.3425	0.0106	0.0308	0.3490	0.0110	0.0286	0.3452	0.0112	0.0318	-0.90	0.2047	0.0142	0.0209	0.2458	0.0159	0.0197	0.2401	0.0161	0.0244	0.2236	0.0161	0.0213	-0.90	0.4513	0.0094	0.0406	0.4326	0.0092	0.0427	0.4256	0.0092	0.0356	0.4337	0.0094	0.0393	-0.90	0.3957	0.0087	0.0350	0.4060	0.0090	0.0365	0.4303	0.0093	0.0362	0.4651	0.0097	0.0399	-0.90	0.3416	0.0084	0.0300	0.3574	0.0087	0.0320	0.3686	0.0089	0.0314	0.4131	0.0095	0.0387	-0.90	0.2318	0.0077	0.0233	0.2542	0.0081	0.0237	0.2795	0.0086	0.0240	0.3003	0.0090	0.0296	-0.90	0.0864	0.0071	0.0117	0.1120	0.0082	0.0109	0.0996	0.0081	0.0089	0.1385	0.0100	0.0117	-0.90	0.4542	0.0100	0.0375	0.4317	0.0099	0.0327	0.4095	0.0099	0.0317	0.4580	0.0106	0.0365	-0.90	0.4806	0.0105	0.0360	0.4552	0.0104	0.0364	0.4512	0.0105	0.0345	0.4654	0.0108	0.0373	-0.90	0.4639	0.0107	0.0355	0.4306	0.0105	0.0364	0.4372	0.0107	0.0328	0.4203	0.0108	0.0361	-0.90	0.3406	0.0104	0.0289	0.3425	0.0106	0.0308	0.3490	0.0110	0.0286	0.3452	0.0112	0.0318	-0.90	0.2047	0.0142	0.0209	0.2458	0.0159	0.0197	0.2401	0.0161	0.0244	0.2236	0.0161	0.0213	-0.90	0.4513	0.0094	0.0406	0.4326	0.0092	0.0427	0.4256	0.0092	0.0356	0.4337	0.0094	0.0393	-0.90	0.3957	0.0087	0.0350	0.4060	0.0090	0.0365	0.4303	0.0093	0.0362	0.4651	0.0097	0.0399	-0.90	0.3416	0.0084	0.0300	0.3574	0.0087	0.0320	0.3686	0.0089	0.0314	0.4131	0.0095	0.0387	-0.90	0.2318	0.0077	0.0233	0.2542	0.0081	0.0237	0.2795	0.0086	0.0240	0.3003	0.0090	0.0296	-0.90	0.0864	0.0071	0.0117	0.1120	0.0082	0.0109	0.0996	0.0081	0.0089	0.1385	0.0100	0.0117	-0.90	0.4542	0.0100	0.0375	0.4317	0.0099	0.0327	0.4095	0.0099	0.0317	0.4580	0.0106	0.0365	-0.90	0.4806	0.0105	0.0360	0.4552	0.0104	0.0364	0.4512	0.0105	0.0345	0.4654	0.0108	0.0373	-0.90	0.4639	0.0107	0.0355	0.4306	0.0105	0.0364	0.4372	0.0107	0.0328	0.4203	0.0108	0.0361	-0.90	0.3406	0.0104	0.0289	0.3425	0.0106	0.0308	0.3490	0.0110	0.0286	0.3452	0.0112	0.0318	-0.90	0.2047	0.0142	0.0209	0.2458	0.0159	0.0197	0.2401	0.0161	0.0244	0.2236	0.0161	0.0213	-0.90	0.4513	0.0094	0.0406	0.4326	0.0092	0.0427	0.4256	0.0092	0.0356	0.4337	0.0094	0.0393	-0.90	0.3957	0.0087	0.0350	0.4060	0.0090	0.0365	0.4303	0.0093	0.0362	0.4651	0.0097	0.0399	-0.90	0.3416	0.0084	0.0300	0.3574	0.0087	0.0320	0.3686	0.0089	0.0314	0.4131	0.0095	0.0387	-0.90	0.2318	0.0077	0.0233	0.2542	0.0081	0.0237	0.2795	0.0086	0.0240	0.3003	0.0090	0.0296	-0.90	0.0864	0.0071	0.0117	0.1120	0.0082	0.0109	0.0996	0.0081	0.0089	0.1385	0.0100	0.0117	-0.90	0.4542	0.0100	0.0375	0.4317	0.0099	0.0327	0.4095	0.0099	0.0317	0.4580	0.0106	0.0365	-0.90	0.4806	0.0105	0.0360	0.4552	0.0104	0.0364	0.4512	0.0105	0.0345	0.4654	0.0108	0.0373	-0.90	0.4639	0.0107	0.0355	0.4306	0.0105	0.0364	0.4372	0.0107	0.0328	0.4203	0.01

APPENDIX F. DATA TABLES

$\cos(\theta_\eta^*)$	W=(1795.0±5.0) MeV			W=(1805.0±5.0) MeV			W=(1815.0±5.0) MeV			W=(1825.0±5.0) MeV					
	$d\sigma/d\Omega$			Δ_{stat}			Δ_{sys}			$d\sigma/d\Omega$			Δ_{stat}		
	$[\mu\text{b}/\text{sr}]$														
-0.90	0.1079	0.0071	0.0135	0.1069	0.0072	0.0188	0.0802	0.0065	0.0095	0.1011	0.0074	0.0141			
-0.70	0.1626	0.0076	0.0178	0.1548	0.0076	0.0160	0.1564	0.0080	0.0163	0.1374	0.0079	0.0146			
-0.50	0.2141	0.0101	0.0213	0.2280	0.0107	0.0186	0.2218	0.0112	0.0192	0.2198	0.0118	0.0223			
-0.30	0.2959	0.0089	0.0252	0.2779	0.0089	0.0240	0.2932	0.0094	0.0230	0.2643	0.0094	0.0221			
-0.10	0.3573	0.0101	0.0279	0.3527	0.0103	0.0297	0.3471	0.0107	0.0259	0.3441	0.0113	0.0254			
0.10	0.4360	0.0106	0.0339	0.3882	0.0104	0.0312	0.3962	0.0108	0.0295	0.3900	0.0111	0.0287			
0.30	0.4447	0.0108	0.0331	0.4194	0.0108	0.0316	0.4193	0.0113	0.0342	0.4194	0.0119	0.0298			
0.50	0.4268	0.0112	0.0317	0.4291	0.0116	0.0322	0.4173	0.0118	0.0379	0.4107	0.0121	0.0297			
0.70	0.3646	0.0119	0.0324	0.3668	0.0123	0.0269	0.3626	0.0127	0.0314	0.3510	0.0131	0.0288			
0.90	0.2114	0.0163	0.0279	0.2477	0.0183	0.0182	0.2629	0.0198	0.0277	0.2488	0.0205	0.0307			
$\cos(\theta_\eta^*)$	W=(1835.0±5.0) MeV			W=(1845.0±5.0) MeV			W=(1855.0±5.0) MeV			W=(1865.0±5.0) MeV					
	$d\sigma/d\Omega$			Δ_{stat}			Δ_{sys}			$d\sigma/d\Omega$			Δ_{stat}		
	$[\mu\text{b}/\text{sr}]$														
-0.90	0.1006	0.0077	0.0175	0.1011	0.0082	0.0092	0.0817	0.0082	0.0148	0.0898	0.0097	0.0115			
-0.70	0.1412	0.0085	0.0149	0.1378	0.0089	0.0130	0.1356	0.0097	0.0175	0.1684	0.0125	0.0167			
-0.50	0.2206	0.0123	0.0183	0.2307	0.0133	0.0193	0.2218	0.0143	0.0186	0.1982	0.0149	0.0148			
-0.30	0.2626	0.0099	0.0216	0.2542	0.0106	0.0196	0.2546	0.0117	0.0201	0.2531	0.0132	0.0192			
-0.10	0.3406	0.0119	0.0274	0.3667	0.0133	0.0269	0.3550	0.0142	0.0283	0.3581	0.0156	0.0268			
0.10	0.3946	0.0117	0.0308	0.3697	0.0121	0.0284	0.3654	0.0132	0.0293	0.3695	0.0149	0.0290			
0.30	0.4144	0.0125	0.0333	0.4458	0.0139	0.0341	0.4241	0.0144	0.0340	0.4157	0.0153	0.0317			
0.50	0.4189	0.0127	0.0322	0.3941	0.0130	0.0308	0.3883	0.0140	0.0278	0.4051	0.0158	0.0269			
0.70	0.3711	0.0144	0.0273	0.3774	0.0157	0.0285	0.3845	0.0175	0.0281	0.3451	0.0186	0.0262			
0.90	0.2477	0.0220	0.0188	0.2783	0.0253	0.0218	0.2566	0.0271	0.0231	0.1965	0.0278	0.0185			

Total Cross Sections

W [MeV]	ΔW [MeV]	σ [μb]	Δ_{stat} [μb]	Δ_{sys} [μb]
1488.0	4.0	4.7547	0.0860	0.4294
1496.0	4.0	13.1980	0.0997	0.9698
1504.0	4.0	16.2321	0.0959	1.2839
1511.0	3.0	18.0035	0.1083	1.5351
1518.0	4.0	19.6756	0.1038	1.7152
1526.0	4.0	21.0948	0.1075	1.7787
1534.0	4.0	21.6793	0.1069	1.8112
1544.0	6.0	21.3175	0.0858	1.7402
1555.0	5.0	20.2986	0.0868	1.6938
1565.0	5.0	18.9221	0.0816	1.6010
1575.0	5.0	17.4883	0.0772	1.4710
1585.0	5.0	16.1914	0.0729	1.3874
1595.0	5.0	14.6425	0.0688	1.2916
1605.0	5.0	12.8928	0.0636	1.1617
1615.0	5.0	11.2136	0.0587	1.0242
1625.0	5.0	9.3933	0.0535	0.8534
1635.0	5.0	7.9533	0.0492	0.7371
1645.0	5.0	6.5408	0.0446	0.6256
1655.0	5.0	5.4968	0.0410	0.5383
1665.0	5.0	4.8094	0.0383	0.4723
1675.0	5.0	4.3647	0.0366	0.4221
1685.0	5.0	4.1053	0.0360	0.3889
1695.0	5.0	4.0151	0.0359	0.3707
1705.0	5.0	4.0916	0.0369	0.3913
1715.0	5.0	4.1984	0.0378	0.3900
1725.0	5.0	4.2458	0.0388	0.3813
1735.0	5.0	4.2111	0.0394	0.3917
1745.0	5.0	4.1615	0.0398	0.3676
1755.0	5.0	4.1041	0.0399	0.3522
1765.0	5.0	3.9602	0.0404	0.3448
1775.0	5.0	3.8744	0.0408	0.3353
1785.0	5.0	3.9059	0.0416	0.3559
1795.0	5.0	3.7902	0.0423	0.3322
1805.0	5.0	3.7248	0.0439	0.3092
1815.0	5.0	3.7122	0.0458	0.3206
1825.0	5.0	3.6029	0.0472	0.3061
1835.0	5.0	3.6471	0.0505	0.3022
1845.0	5.0	3.6698	0.0548	0.2886
1855.0	5.0	3.5830	0.0594	0.3009
1865.0	5.0	3.5125	0.0648	0.2764

F.1.5 $\gamma n \rightarrow \eta n$ as a Function of W

Angular Distributions

$\cos(\theta_\eta^*)$	W=(1488.0±4.0) MeV			W=(1496.0±4.0) MeV			W=(1504.0±4.0) MeV			W=(1511.0±3.0) MeV		
	$d\sigma/d\Omega$			$d\sigma/d\Omega$			$d\sigma/d\Omega$			$d\sigma/d\Omega$		
	$[\mu\text{b}/\text{sr}]$	Δ_{stat}	Δ_{sys}									
-0.90	-0.0288	0.0076	-0.0006	0.4961	0.0732	0.0359	0.6569	0.0578	0.0560	0.6130	0.0539	0.0553
-0.70	0.0953	0.0296	0.0120	0.4377	0.0366	0.0341	0.5607	0.0312	0.0507	0.4717	0.0292	0.0502
-0.50	0.0994	0.0247	0.0106	0.3835	0.0296	0.0348	0.4264	0.0245	0.0379	0.5257	0.0279	0.0515
-0.30	0.1070	0.0236	0.0140	0.3235	0.0261	0.0362	0.4560	0.0246	0.0370	0.5399	0.0276	0.0476
-0.10	0.0916	0.0215	0.0123	0.3434	0.0266	0.0283	0.4060	0.0234	0.0344	0.5405	0.0275	0.0497
0.10	0.0413	0.0161	0.0116	0.4367	0.0306	0.0325	0.4275	0.0246	0.0365	0.4809	0.0265	0.0436
0.30	0.0362	0.0162	0.0117	0.3054	0.0279	0.0326	0.4212	0.0262	0.0413	0.3959	0.0257	0.0366
0.50	0.0847	0.0257	0.0271	0.3825	0.0345	0.0439	0.4296	0.0295	0.0478	0.4907	0.0319	0.0522
0.70	0.0648	0.0319	0.0162	0.4180	0.0458	0.0534	0.3151	0.0322	0.0452	0.3781	0.0348	0.0534
0.90	-0.0521	0.0081	0.0098	0.2359	0.0654	0.0436	0.2961	0.0534	0.0399	0.3828	0.0590	0.0460
$\cos(\theta_\eta^*)$	W=(1518.0±4.0) MeV			W=(1526.0±4.0) MeV			W=(1534.0±4.0) MeV			W=(1544.0±6.0) MeV		
	$d\sigma/d\Omega$	Δ_{stat}	Δ_{sys}									
	$[\mu\text{b}/\text{sr}]$											
-0.90	0.9277	0.0511	0.0877	0.8878	0.0466	0.0876	0.8795	0.0442	0.0903	0.8117	0.0332	0.0885
-0.70	0.5853	0.0260	0.0533	0.6096	0.0253	0.0615	0.6290	0.0251	0.0618	0.6181	0.0201	0.0633
-0.50	0.5441	0.0230	0.0504	0.5443	0.0219	0.0584	0.5505	0.0215	0.0528	0.5922	0.0180	0.0592
-0.30	0.5396	0.0223	0.0512	0.5269	0.0207	0.0497	0.5460	0.0201	0.0519	0.5766	0.0163	0.0608
-0.10	0.5228	0.0216	0.0472	0.5454	0.0204	0.0528	0.5570	0.0190	0.0543	0.5154	0.0140	0.0503
0.10	0.4710	0.0206	0.0443	0.5322	0.0197	0.0492	0.4986	0.0174	0.0498	0.4970	0.0132	0.0493
0.30	0.4691	0.0216	0.0460	0.5106	0.0202	0.0497	0.4685	0.0175	0.0466	0.4599	0.0130	0.0460
0.50	0.4402	0.0236	0.0458	0.4471	0.0213	0.0448	0.4207	0.0185	0.0415	0.4181	0.0138	0.0417
0.70	0.4479	0.0290	0.0546	0.3863	0.0248	0.0433	0.4132	0.0232	0.0451	0.3756	0.0167	0.0435
0.90	0.3793	0.0464	0.0546	0.4783	0.0468	0.0593	0.3446	0.0373	0.0522	0.3813	0.0299	0.0515
$\cos(\theta_\eta^*)$	W=(1555.0±5.0) MeV			W=(1565.0±5.0) MeV			W=(1575.0±5.0) MeV			W=(1585.0±5.0) MeV		
	$d\sigma/d\Omega$	Δ_{stat}	Δ_{sys}									
	$[\mu\text{b}/\text{sr}]$											
-0.90	0.7223	0.0332	0.0841	0.6814	0.0316	0.0770	0.6675	0.0311	0.0819	0.6543	0.0306	0.0721
-0.70	0.5060	0.0197	0.0564	0.5173	0.0197	0.0543	0.4744	0.0191	0.0480	0.4869	0.0195	0.0453
-0.50	0.5396	0.0188	0.0537	0.4962	0.0181	0.0522	0.5167	0.0187	0.0524	0.5126	0.0187	0.0511
-0.30	0.5923	0.0177	0.0579	0.5232	0.0163	0.0506	0.4853	0.0154	0.0483	0.4542	0.0147	0.0465
-0.10	0.5183	0.0147	0.0505	0.4849	0.0137	0.0484	0.4519	0.0128	0.0435	0.4207	0.0122	0.0403
0.10	0.5042	0.0138	0.0485	0.4726	0.0128	0.0459	0.4244	0.0120	0.0385	0.4140	0.0118	0.0385
0.30	0.4234	0.0130	0.0405	0.4353	0.0128	0.0400	0.3805	0.0118	0.0369	0.3650	0.0115	0.0364
0.50	0.4026	0.0142	0.0405	0.4024	0.0137	0.0392	0.3690	0.0129	0.0383	0.3412	0.0123	0.0341
0.70	0.3840	0.0176	0.0482	0.3396	0.0161	0.0376	0.3056	0.0150	0.0386	0.2996	0.0146	0.0315
0.90	0.3371	0.0300	0.0439	0.2804	0.0268	0.0315	0.3461	0.0283	0.0387	0.2825	0.0252	0.0311
$\cos(\theta_\eta^*)$	W=(1595.0±5.0) MeV			W=(1605.0±5.0) MeV			W=(1615.0±5.0) MeV			W=(1625.0±5.0) MeV		
	$d\sigma/d\Omega$	Δ_{stat}	Δ_{sys}									
	$[\mu\text{b}/\text{sr}]$											
-0.90	0.5909	0.0286	0.0586	0.5358	0.0270	0.0697	0.5240	0.0266	0.0638	0.4794	0.0254	0.0521
-0.70	0.4337	0.0184	0.0445	0.3922	0.0174	0.0458	0.3456	0.0163	0.0387	0.3419	0.0162	0.0381
-0.50	0.4648	0.0179	0.0454	0.4267	0.0169	0.0451	0.3780	0.0157	0.0431	0.3388	0.0151	0.0386
-0.30	0.4357	0.0141	0.0440	0.4062	0.0131	0.0428	0.3511	0.0119	0.0368	0.3097	0.0112	0.0332
-0.10	0.4021	0.0118	0.0412	0.3598	0.0109	0.0382	0.3205	0.0101	0.0334	0.2856	0.0096	0.0314
0.10	0.3650	0.0111	0.0380	0.3387	0.0105	0.0364	0.3018	0.0098	0.0313	0.2795	0.0095	0.0314
0.30	0.3523	0.0112	0.0334	0.3002	0.0102	0.0293	0.2619	0.0095	0.0288	0.2634	0.0096	0.0291
0.50	0.2952	0.0113	0.0318	0.2587	0.0103	0.0250	0.2322	0.0098	0.0256	0.2114	0.0094	0.0244
0.70	0.2723	0.0136	0.0304	0.2015	0.0115	0.0212	0.1737	0.0105	0.0201	0.1824	0.0108	0.0226
0.90	0.2162	0.0216	0.0207	0.1874	0.0193	0.0227	0.1963	0.0190	0.0227	0.1492	0.0169	0.0182

F.1. UNPOLARISED CROSS SECTIONS FROM ${}^3\text{He}$ (A2)

$\cos(\theta_\eta^*)$	W=(1635.0±5.0) MeV			W=(1645.0±5.0) MeV			W=(1655.0±5.0) MeV			W=(1665.0±5.0) MeV		
	$d\sigma/d\Omega$ [$\mu\text{b}/\text{sr}$]	Δ_{stat} [$\mu\text{b}/\text{sr}$]	Δ_{sys} [$\mu\text{b}/\text{sr}$]	$d\sigma/d\Omega$ [$\mu\text{b}/\text{sr}$]	Δ_{stat} [$\mu\text{b}/\text{sr}$]	Δ_{sys} [$\mu\text{b}/\text{sr}$]	$d\sigma/d\Omega$ [$\mu\text{b}/\text{sr}$]	Δ_{stat} [$\mu\text{b}/\text{sr}$]	Δ_{sys} [$\mu\text{b}/\text{sr}$]	$d\sigma/d\Omega$ [$\mu\text{b}/\text{sr}$]	Δ_{stat} [$\mu\text{b}/\text{sr}$]	Δ_{sys} [$\mu\text{b}/\text{sr}$]
-0.90	0.4920	0.0254	0.0564	0.4151	0.0234	0.0454	0.4632	0.0248	0.0514	0.4206	0.0240	0.0506
-0.70	0.3358	0.0162	0.0359	0.3565	0.0167	0.0416	0.3360	0.0164	0.0366	0.3700	0.0174	0.0392
-0.50	0.3670	0.0159	0.0389	0.3529	0.0156	0.0398	0.3694	0.0159	0.0396	0.3603	0.0158	0.0382
-0.30	0.3324	0.0117	0.0391	0.3111	0.0114	0.0353	0.3113	0.0115	0.0369	0.3331	0.0119	0.0364
-0.10	0.2771	0.0097	0.0307	0.2974	0.0104	0.0340	0.3252	0.0110	0.0366	0.3488	0.0115	0.0383
0.10	0.3002	0.0102	0.0359	0.2947	0.0104	0.0353	0.3391	0.0114	0.0396	0.3786	0.0121	0.0400
0.30	0.3061	0.0105	0.0354	0.2884	0.0106	0.0349	0.3116	0.0112	0.0345	0.3022	0.0111	0.0348
0.50	0.2293	0.0099	0.0245	0.2365	0.0103	0.0266	0.2637	0.0111	0.0297	0.2386	0.0107	0.0266
0.70	0.1577	0.0103	0.0212	0.2056	0.0119	0.0274	0.1590	0.0106	0.0196	0.2027	0.0120	0.0240
0.90	0.1233	0.0163	0.0252	0.1275	0.0166	0.0168	0.0921	0.0143	0.0115	0.1002	0.0150	0.0133
<hr/>												
$\cos(\theta_\eta^*)$	W=(1675.0±5.0) MeV			W=(1685.0±5.0) MeV			W=(1695.0±5.0) MeV			W=(1705.0±5.0) MeV		
	$d\sigma/d\Omega$ [$\mu\text{b}/\text{sr}$]	Δ_{stat} [$\mu\text{b}/\text{sr}$]	Δ_{sys} [$\mu\text{b}/\text{sr}$]	$d\sigma/d\Omega$ [$\mu\text{b}/\text{sr}$]	Δ_{stat} [$\mu\text{b}/\text{sr}$]	Δ_{sys} [$\mu\text{b}/\text{sr}$]	$d\sigma/d\Omega$ [$\mu\text{b}/\text{sr}$]	Δ_{stat} [$\mu\text{b}/\text{sr}$]	Δ_{sys} [$\mu\text{b}/\text{sr}$]	$d\sigma/d\Omega$ [$\mu\text{b}/\text{sr}$]	Δ_{stat} [$\mu\text{b}/\text{sr}$]	Δ_{sys} [$\mu\text{b}/\text{sr}$]
-0.90	0.4359	0.0243	0.0526	0.3753	0.0226	0.0434	0.3645	0.0225	0.0428	0.2899	0.0207	0.0337
-0.70	0.3766	0.0175	0.0415	0.3286	0.0163	0.0350	0.2862	0.0154	0.0360	0.2747	0.0154	0.0328
-0.50	0.3438	0.0153	0.0409	0.3263	0.0149	0.0363	0.3235	0.0149	0.0406	0.2536	0.0136	0.0255
-0.30	0.3005	0.0112	0.0351	0.2907	0.0109	0.0306	0.2868	0.0108	0.0306	0.2487	0.0102	0.0276
-0.10	0.3023	0.0108	0.0304	0.3084	0.0110	0.0330	0.2836	0.0105	0.0289	0.2735	0.0104	0.0277
0.10	0.3504	0.0117	0.0368	0.3182	0.0112	0.0320	0.2921	0.0108	0.0330	0.2887	0.0108	0.0280
0.30	0.3085	0.0113	0.0334	0.2818	0.0109	0.0327	0.2950	0.0113	0.0306	0.2915	0.0113	0.0260
0.50	0.2456	0.0110	0.0259	0.2481	0.0111	0.0247	0.2356	0.0109	0.0263	0.2517	0.0113	0.0277
0.70	0.1802	0.0115	0.0244	0.1625	0.0110	0.0211	0.1636	0.0108	0.0188	0.1487	0.0104	0.0155
0.90	0.1085	0.0162	0.0219	0.1244	0.0166	0.0213	0.1205	0.0149	0.0163	0.0886	0.0126	0.0080
<hr/>												
$\cos(\theta_\eta^*)$	W=(1715.0±5.0) MeV			W=(1725.0±5.0) MeV			W=(1735.0±5.0) MeV			W=(1745.0±5.0) MeV		
	$d\sigma/d\Omega$ [$\mu\text{b}/\text{sr}$]	Δ_{stat} [$\mu\text{b}/\text{sr}$]	Δ_{sys} [$\mu\text{b}/\text{sr}$]	$d\sigma/d\Omega$ [$\mu\text{b}/\text{sr}$]	Δ_{stat} [$\mu\text{b}/\text{sr}$]	Δ_{sys} [$\mu\text{b}/\text{sr}$]	$d\sigma/d\Omega$ [$\mu\text{b}/\text{sr}$]	Δ_{stat} [$\mu\text{b}/\text{sr}$]	Δ_{sys} [$\mu\text{b}/\text{sr}$]	$d\sigma/d\Omega$ [$\mu\text{b}/\text{sr}$]	Δ_{stat} [$\mu\text{b}/\text{sr}$]	Δ_{sys} [$\mu\text{b}/\text{sr}$]
-0.90	0.2662	0.0202	0.0258	0.2766	0.0211	0.0356	0.2064	0.0184	0.0295	0.1751	0.0168	0.0176
-0.70	0.2680	0.0155	0.0255	0.2312	0.0146	0.0208	0.1765	0.0130	0.0201	0.2039	0.0139	0.0229
-0.50	0.2567	0.0138	0.0239	0.2371	0.0135	0.0200	0.1979	0.0124	0.0195	0.2074	0.0128	0.0215
-0.30	0.2134	0.0096	0.0209	0.2285	0.0102	0.0221	0.2131	0.0099	0.0218	0.1972	0.0095	0.0182
-0.10	0.2841	0.0108	0.0255	0.2637	0.0107	0.0254	0.2541	0.0107	0.0233	0.2155	0.0098	0.0217
0.10	0.3068	0.0113	0.0249	0.2732	0.0110	0.0230	0.2772	0.0111	0.0250	0.2399	0.0104	0.0241
0.30	0.2824	0.0112	0.0237	0.2715	0.0113	0.0235	0.2840	0.0117	0.0256	0.2494	0.0109	0.0258
0.50	0.2414	0.0113	0.0224	0.2614	0.0121	0.0234	0.2420	0.0117	0.0238	0.2199	0.0112	0.0183
0.70	0.1630	0.0112	0.0161	0.1644	0.0116	0.0147	0.1759	0.0122	0.0227	0.1792	0.0124	0.0253
0.90	0.0810	0.0131	0.0082	0.1159	0.0167	0.0128	0.0932	0.0156	0.0204	0.0711	0.0142	0.0176
<hr/>												
$\cos(\theta_\eta^*)$	W=(1755.0±5.0) MeV			W=(1765.0±5.0) MeV			W=(1775.0±5.0) MeV			W=(1785.0±5.0) MeV		
	$d\sigma/d\Omega$ [$\mu\text{b}/\text{sr}$]	Δ_{stat} [$\mu\text{b}/\text{sr}$]	Δ_{sys} [$\mu\text{b}/\text{sr}$]	$d\sigma/d\Omega$ [$\mu\text{b}/\text{sr}$]	Δ_{stat} [$\mu\text{b}/\text{sr}$]	Δ_{sys} [$\mu\text{b}/\text{sr}$]	$d\sigma/d\Omega$ [$\mu\text{b}/\text{sr}$]	Δ_{stat} [$\mu\text{b}/\text{sr}$]	Δ_{sys} [$\mu\text{b}/\text{sr}$]	$d\sigma/d\Omega$ [$\mu\text{b}/\text{sr}$]	Δ_{stat} [$\mu\text{b}/\text{sr}$]	Δ_{sys} [$\mu\text{b}/\text{sr}$]
-0.90	0.1821	0.0176	0.0315	0.1812	0.0182	0.0224	0.1561	0.0175	0.0245	0.1826	0.0191	0.0328
-0.70	0.1819	0.0135	0.0224	0.1494	0.0126	0.0193	0.1505	0.0127	0.0179	0.1770	0.0141	0.0236
-0.50	0.1785	0.0121	0.0188	0.1705	0.0120	0.0214	0.1771	0.0125	0.0182	0.1697	0.0128	0.0204
-0.30	0.1706	0.0090	0.0178	0.1660	0.0091	0.0195	0.1707	0.0093	0.0168	0.1684	0.0095	0.0161
-0.10	0.2063	0.0098	0.0237	0.2224	0.0105	0.0252	0.2183	0.0106	0.0235	0.1955	0.0103	0.0188
0.10	0.2374	0.0105	0.0237	0.2399	0.0109	0.0222	0.2258	0.0109	0.0234	0.2162	0.0107	0.0198
0.30	0.2362	0.0108	0.0231	0.2598	0.0117	0.0262	0.2218	0.0112	0.0218	0.2326	0.0114	0.0233
0.50	0.2230	0.0114	0.0269	0.2478	0.0124	0.0239	0.2397	0.0125	0.0229	0.2190	0.0121	0.0252
0.70	0.1565	0.0118	0.0221	0.1609	0.0123	0.0192	0.1758	0.0131	0.0208	0.1578	0.0126	0.0178
0.90	0.1008	0.0171	0.0130	0.0994	0.0168	0.0132	0.0763	0.0151	0.0136	0.0618	0.0144	0.0110

APPENDIX F. DATA TABLES

$\cos(\theta_\eta^*)$	W=(1795.0±5.0) MeV			W=(1805.0±5.0) MeV			W=(1815.0±5.0) MeV			W=(1825.0±5.0) MeV					
	$d\sigma/d\Omega$			Δ_{stat}			Δ_{sys}			$d\sigma/d\Omega$			Δ_{stat}		
	$[\mu\text{b}/\text{sr}]$														
-0.90	0.1650	0.0186	0.0202	0.1800	0.0202	0.0311	0.1211	0.0176	0.0278	0.1329	0.0192	0.0134	0.1343	0.0145	0.0217
-0.70	0.1633	0.0142	0.0171	0.1654	0.0146	0.0216	0.1424	0.0143	0.0132	0.1349	0.0123	0.0208	0.1396	0.0095	0.0149
-0.50	0.1625	0.0128	0.0161	0.1278	0.0113	0.0142	0.1319	0.0116	0.0179	0.1780	0.0116	0.0149	0.2241	0.0112	0.0203
-0.30	0.1595	0.0094	0.0186	0.1439	0.0092	0.0162	0.1426	0.0093	0.0141	0.2086	0.0122	0.0195	0.2263	0.0115	0.0217
-0.10	0.1739	0.0100	0.0176	0.1667	0.0103	0.0155	0.1867	0.0113	0.0163	0.2073	0.0125	0.0175	0.1978	0.0118	0.0196
0.10	0.2241	0.0112	0.0203	0.2109	0.0114	0.0213	0.1926	0.0114	0.0176	0.2000	0.0133	0.0234	0.1636	0.0133	0.0171
0.30	0.2263	0.0115	0.0217	0.1944	0.0112	0.0172	0.2302	0.0128	0.0229	0.1485	0.0139	0.0187	0.1437	0.0140	0.0146
0.50	0.1978	0.0118	0.0196	0.2218	0.0131	0.0235	0.2233	0.0138	0.0237	-0.0013	0.0004	0.0031	0.0655	0.0164	0.0060
0.70	0.1636	0.0133	0.0171	0.1605	0.0138	0.0151	0.1485	0.0139	0.0187	0.0655	0.0164	0.0060			
0.90	0.1405	0.0227	0.0182	0.0838	0.0186	0.0077	-0.0013	0.0004	0.0031						

$\cos(\theta_\eta^*)$	W=(1835.0±5.0) MeV			W=(1845.0±5.0) MeV			W=(1855.0±5.0) MeV			W=(1865.0±5.0) MeV					
	$d\sigma/d\Omega$			Δ_{stat}			Δ_{sys}			$d\sigma/d\Omega$			Δ_{stat}		
	$[\mu\text{b}/\text{sr}]$														
-0.90	0.1353	0.0206	0.0325	0.1375	0.0221	0.0172	0.1184	0.0216	0.0302	0.1038	0.0220	0.0189	0.1457	0.0155	0.0119
-0.70	0.1272	0.0127	0.0126	0.1152	0.0127	0.0103	0.1248	0.0131	0.0166	0.0955	0.0141	0.0122	0.1272	0.0127	0.0126
-0.50	0.1290	0.0095	0.0146	0.1172	0.0096	0.0100	0.1084	0.0101	0.0107	0.1207	0.0114	0.0108	0.1799	0.0121	0.0167
-0.30	0.1799	0.0121	0.0167	0.1614	0.0122	0.0164	0.1425	0.0125	0.0148	0.1590	0.0141	0.0179	0.1914	0.0120	0.0154
-0.10	0.1914	0.0120	0.0154	0.1626	0.0116	0.0150	0.1931	0.0138	0.0197	0.1794	0.0142	0.0207	0.1839	0.0121	0.0152
0.10	0.1711	0.0125	0.0134	0.1987	0.0142	0.0162	0.1773	0.0145	0.0166	0.1664	0.0135	0.0158	0.1214	0.0135	0.0125
0.30	0.1214	0.0135	0.0125	0.1222	0.0145	0.0163	0.1427	0.0170	0.0152	0.1040	0.0158	0.0100	-0.0008	0.0005	0.0016
0.50	-0.0008	0.0005	0.0016	-0.0011	0.0005	0.0015	0.0266	0.0142	0.0098	0.0209	0.0138	0.0041			

Total Cross Sections

W [MeV]	ΔW [MeV]	σ [μb]	Δ_{stat} [μb]	Δ_{sys} [μb]
1488.0	4.0	0.4412	0.0718	0.1310
1496.0	4.0	4.7383	0.1620	0.4795
1504.0	4.0	5.4933	0.1320	0.5435
1511.0	3.0	5.9360	0.1374	0.6135
1518.0	4.0	6.5552	0.1145	0.6586
1526.0	4.0	6.6620	0.1068	0.6810
1534.0	4.0	6.5681	0.0988	0.6705
1544.0	6.0	6.5143	0.0766	0.6849
1555.0	5.0	6.0798	0.0781	0.6486
1565.0	5.0	5.7620	0.0742	0.5934
1575.0	5.0	5.4566	0.0724	0.5755
1585.0	5.0	5.2636	0.0705	0.5290
1595.0	5.0	4.7672	0.0659	0.4857
1605.0	5.0	4.2241	0.0607	0.4642
1615.0	5.0	3.7877	0.0574	0.4223
1625.0	5.0	3.5291	0.0555	0.3974
1635.0	5.0	3.6000	0.0560	0.4200
1645.0	5.0	3.6173	0.0566	0.4228
1655.0	5.0	3.6791	0.0566	0.4166
1665.0	5.0	3.8068	0.0581	0.4253
1675.0	5.0	3.6747	0.0579	0.4270
1685.0	5.0	3.4358	0.0556	0.3849
1695.0	5.0	3.2923	0.0541	0.3777
1705.0	5.0	3.0042	0.0516	0.3168
1715.0	5.0	2.9339	0.0520	0.2711
1725.0	5.0	2.8900	0.0537	0.2738
1735.0	5.0	2.6428	0.0509	0.2894
1745.0	5.0	2.4530	0.0493	0.2663
1755.0	5.0	2.3353	0.0499	0.2799
1765.0	5.0	2.3570	0.0509	0.2656
1775.0	5.0	2.2659	0.0505	0.2538
1785.0	5.0	2.2346	0.0515	0.2622
1795.0	5.0	2.2036	0.0547	0.2322
1805.0	5.0	2.0746	0.0544	0.2295
1815.0	5.0	1.8787	0.0487	0.2180
1825.0	5.0	1.9320	0.0547	0.2108
1835.0	5.0	1.7202	0.0513	0.1829
1845.0	5.0	1.6721	0.0538	0.1776
1855.0	5.0	1.6468	0.0583	0.2035
1865.0	5.0	1.4935	0.0585	0.1809

F.2 Unpolarised Cross Sections from LD₂ (CBELSA/TAPS)

F.2.1 $\gamma N \rightarrow \eta(N)$ as a Function of E_γ

Angular Distributions

$\cos(\theta_\eta^*)$	$E_\gamma = (697.5 \pm 7.5) \text{ MeV}$			$E_\gamma = (712.5 \pm 7.5) \text{ MeV}$			$E_\gamma = (730.0 \pm 10.0) \text{ MeV}$			$E_\gamma = (750.0 \pm 10.0) \text{ MeV}$		
	$d\sigma/d\Omega$ [$\mu\text{b}/\text{sr}$]	Δ_{stat} [$\mu\text{b}/\text{sr}$]	Δ_{sys} [$\mu\text{b}/\text{sr}$]	$d\sigma/d\Omega$ [$\mu\text{b}/\text{sr}$]	Δ_{stat} [$\mu\text{b}/\text{sr}$]	Δ_{sys} [$\mu\text{b}/\text{sr}$]	$d\sigma/d\Omega$ [$\mu\text{b}/\text{sr}$]	Δ_{stat} [$\mu\text{b}/\text{sr}$]	Δ_{sys} [$\mu\text{b}/\text{sr}$]	$d\sigma/d\Omega$ [$\mu\text{b}/\text{sr}$]	Δ_{stat} [$\mu\text{b}/\text{sr}$]	Δ_{sys} [$\mu\text{b}/\text{sr}$]
-0.88	0.6527	0.0271	0.0120	0.9473	0.0305	0.0086	1.2989	0.0293	0.0077	1.6450	0.0339	0.0081
-0.62	0.4932	0.0222	0.0078	0.8452	0.0271	0.0084	1.0830	0.0250	0.0122	1.4962	0.0302	0.0099
-0.38	0.4497	0.0203	0.0075	0.7145	0.0238	0.0067	1.0703	0.0235	0.0131	1.4321	0.0277	0.0090
-0.12	0.3389	0.0169	0.0044	0.6291	0.0213	0.0072	0.9969	0.0216	0.0091	1.3049	0.0250	0.0088
0.12	0.3215	0.0159	0.0020	0.5877	0.0198	0.0080	0.9476	0.0201	0.0040	1.3380	0.0241	0.0096
0.38	0.2713	0.0143	0.0017	0.5364	0.0182	0.0052	0.8910	0.0188	0.0007	1.3095	0.0229	0.0075
0.62	0.2361	0.0132	0.0035	0.4750	0.0166	0.0030	0.8645	0.0177	0.0013	1.2832	0.0216	0.0064
0.88	0.1935	0.0117	0.0049	0.4362	0.0156	0.0038	0.8158	0.0168	0.0046	1.2237	0.0204	0.0087
<hr/>												
$\cos(\theta_\eta^*)$	$E_\gamma = (770.0 \pm 10.0) \text{ MeV}$			$E_\gamma = (790.0 \pm 10.0) \text{ MeV}$			$E_\gamma = (810.0 \pm 10.0) \text{ MeV}$			$E_\gamma = (830.0 \pm 10.0) \text{ MeV}$		
	$d\sigma/d\Omega$ [$\mu\text{b}/\text{sr}$]	Δ_{stat} [$\mu\text{b}/\text{sr}$]	Δ_{sys} [$\mu\text{b}/\text{sr}$]	$d\sigma/d\Omega$ [$\mu\text{b}/\text{sr}$]	Δ_{stat} [$\mu\text{b}/\text{sr}$]	Δ_{sys} [$\mu\text{b}/\text{sr}$]	$d\sigma/d\Omega$ [$\mu\text{b}/\text{sr}$]	Δ_{stat} [$\mu\text{b}/\text{sr}$]	Δ_{sys} [$\mu\text{b}/\text{sr}$]	$d\sigma/d\Omega$ [$\mu\text{b}/\text{sr}$]	Δ_{stat} [$\mu\text{b}/\text{sr}$]	Δ_{sys} [$\mu\text{b}/\text{sr}$]
-0.88	1.7439	0.0369	0.0089	1.8256	0.0413	0.0331	1.7789	0.0428	0.0201	1.6800	0.0506	0.0239
-0.62	1.6915	0.0338	0.0108	1.7492	0.0374	0.0139	1.7439	0.0384	0.0154	1.6229	0.0442	0.0164
-0.38	1.6481	0.0312	0.0149	1.7785	0.0349	0.0075	1.6800	0.0347	0.0132	1.6583	0.0410	0.0170
-0.12	1.5825	0.0286	0.0155	1.6799	0.0316	0.0087	1.6243	0.0319	0.0082	1.6887	0.0386	0.0195
0.12	1.5778	0.0271	0.0113	1.6749	0.0298	0.0104	1.7037	0.0304	0.0075	1.6003	0.0347	0.0199
0.38	1.5801	0.0259	0.0084	1.6499	0.0282	0.0127	1.6757	0.0290	0.0138	1.5858	0.0334	0.0264
0.62	1.5607	0.0247	0.0072	1.6128	0.0267	0.0139	1.5717	0.0267	0.0177	1.5017	0.0309	0.0244
0.88	1.4608	0.0228	0.0043	1.4709	0.0243	0.0078	1.5750	0.0253	0.0188	1.3847	0.0279	0.0046
<hr/>												
$\cos(\theta_\eta^*)$	$E_\gamma = (850.0 \pm 10.0) \text{ MeV}$			$E_\gamma = (870.0 \pm 10.0) \text{ MeV}$			$E_\gamma = (890.0 \pm 10.0) \text{ MeV}$			$E_\gamma = (910.0 \pm 10.0) \text{ MeV}$		
	$d\sigma/d\Omega$ [$\mu\text{b}/\text{sr}$]	Δ_{stat} [$\mu\text{b}/\text{sr}$]	Δ_{sys} [$\mu\text{b}/\text{sr}$]	$d\sigma/d\Omega$ [$\mu\text{b}/\text{sr}$]	Δ_{stat} [$\mu\text{b}/\text{sr}$]	Δ_{sys} [$\mu\text{b}/\text{sr}$]	$d\sigma/d\Omega$ [$\mu\text{b}/\text{sr}$]	Δ_{stat} [$\mu\text{b}/\text{sr}$]	Δ_{sys} [$\mu\text{b}/\text{sr}$]	$d\sigma/d\Omega$ [$\mu\text{b}/\text{sr}$]	Δ_{stat} [$\mu\text{b}/\text{sr}$]	Δ_{sys} [$\mu\text{b}/\text{sr}$]
-0.88	1.6145	0.0486	0.0280	1.5684	0.0481	0.0334	1.4518	0.0504	0.0299	1.2502	0.0455	0.0197
-0.62	1.5436	0.0418	0.0143	1.5421	0.0423	0.0155	1.4135	0.0441	0.0241	1.2698	0.0400	0.0220
-0.38	1.5396	0.0382	0.0101	1.4515	0.0373	0.0092	1.3690	0.0393	0.0170	1.1949	0.0351	0.0171
-0.12	1.5097	0.0352	0.0126	1.4913	0.0349	0.0108	1.4082	0.0367	0.0143	1.2557	0.0331	0.0139
0.12	1.4858	0.0321	0.0122	1.5007	0.0320	0.0130	1.3637	0.0328	0.0127	1.2305	0.0296	0.0159
0.38	1.4545	0.0306	0.0092	1.4924	0.0306	0.0172	1.2621	0.0302	0.0104	1.1112	0.0269	0.0216
0.62	1.4239	0.0289	0.0102	1.3668	0.0280	0.0161	1.1978	0.0280	0.0097	1.0268	0.0245	0.0235
0.88	1.3052	0.0258	0.0129	1.2608	0.0252	0.0072	1.0877	0.0251	0.0100	0.9327	0.0220	0.0171
<hr/>												
$\cos(\theta_\eta^*)$	$E_\gamma = (930.0 \pm 10.0) \text{ MeV}$			$E_\gamma = (955.0 \pm 15.0) \text{ MeV}$			$E_\gamma = (980.0 \pm 10.0) \text{ MeV}$			$E_\gamma = (1005.0 \pm 15.0) \text{ MeV}$		
	$d\sigma/d\Omega$ [$\mu\text{b}/\text{sr}$]	Δ_{stat} [$\mu\text{b}/\text{sr}$]	Δ_{sys} [$\mu\text{b}/\text{sr}$]	$d\sigma/d\Omega$ [$\mu\text{b}/\text{sr}$]	Δ_{stat} [$\mu\text{b}/\text{sr}$]	Δ_{sys} [$\mu\text{b}/\text{sr}$]	$d\sigma/d\Omega$ [$\mu\text{b}/\text{sr}$]	Δ_{stat} [$\mu\text{b}/\text{sr}$]	Δ_{sys} [$\mu\text{b}/\text{sr}$]	$d\sigma/d\Omega$ [$\mu\text{b}/\text{sr}$]	Δ_{stat} [$\mu\text{b}/\text{sr}$]	Δ_{sys} [$\mu\text{b}/\text{sr}$]
-0.88	1.1474	0.0468	0.0387	1.0107	0.0369	0.0342	0.9641	0.0490	0.0416	0.8195	0.0378	0.0467
-0.62	1.1459	0.0402	0.0312	1.0265	0.0318	0.0225	0.9222	0.0407	0.0197	0.8835	0.0329	0.0271
-0.38	1.2012	0.0370	0.0208	1.0709	0.0288	0.0186	0.9394	0.0361	0.0145	0.9228	0.0296	0.0164
-0.12	1.1002	0.0325	0.0136	1.0443	0.0259	0.0154	0.9274	0.0325	0.0163	0.8330	0.0252	0.0136
0.12	1.1508	0.0300	0.0157	0.9818	0.0226	0.0117	0.9124	0.0289	0.0157	0.8375	0.0227	0.0169
0.38	1.0689	0.0274	0.0197	0.8788	0.0204	0.0112	0.8710	0.0269	0.0147	0.7692	0.0207	0.0180
0.62	0.8906	0.0238	0.0195	0.7781	0.0183	0.0136	0.7855	0.0245	0.0182	0.7074	0.0191	0.0178
0.88	0.7831	0.0212	0.0142	0.6925	0.0165	0.0164	0.5819	0.0204	0.0223	0.5041	0.0158	0.0148

F.2. UNPOLARISED CROSS SECTIONS FROM LD₂ (CBELSA/TAPS)

$\cos(\theta_\eta^*)$	$E_\gamma = (1035.0 \pm 15.0) \text{ MeV}$			$E_\gamma = (1065.0 \pm 15.0) \text{ MeV}$			$E_\gamma = (1095.0 \pm 15.0) \text{ MeV}$			$E_\gamma = (1125.0 \pm 15.0) \text{ MeV}$		
	$d\sigma/d\Omega$	Δ_{stat}	Δ_{sys}									
	[$\mu\text{b}/\text{sr}$]	[$\mu\text{b}/\text{sr}$]	[$\mu\text{b}/\text{sr}$]	[$\mu\text{b}/\text{sr}$]	[$\mu\text{b}/\text{sr}$]	[$\mu\text{b}/\text{sr}$]	[$\mu\text{b}/\text{sr}$]	[$\mu\text{b}/\text{sr}$]	[$\mu\text{b}/\text{sr}$]	[$\mu\text{b}/\text{sr}$]	[$\mu\text{b}/\text{sr}$]	[$\mu\text{b}/\text{sr}$]
-0.88	0.7908	0.0370	0.0362	0.6884	0.0439	0.0133	0.6359	0.0448	0.0533	0.5631	0.0376	0.0500
-0.62	0.7172	0.0295	0.0248	0.6875	0.0366	0.0236	0.6312	0.0367	0.0298	0.5266	0.0294	0.0301
-0.38	0.7919	0.0273	0.0211	0.7322	0.0331	0.0243	0.6120	0.0315	0.0148	0.5903	0.0267	0.0200
-0.12	0.7531	0.0238	0.0148	0.7071	0.0290	0.0172	0.5867	0.0275	0.0082	0.6031	0.0238	0.0122
0.12	0.7380	0.0212	0.0103	0.6822	0.0256	0.0119	0.6510	0.0258	0.0069	0.7007	0.0229	0.0117
0.38	0.6607	0.0190	0.0097	0.6180	0.0231	0.0081	0.6399	0.0243	0.0099	0.6909	0.0216	0.0141
0.62	0.5934	0.0173	0.0124	0.5356	0.0209	0.0078	0.5510	0.0221	0.0132	0.5844	0.0196	0.0139
0.88	0.4561	0.0151	0.0118	0.3963	0.0179	0.0096	0.4012	0.0187	0.0106	0.4428	0.0168	0.0105
<hr/>												
$\cos(\theta_\eta^*)$	$E_\gamma = (1155.0 \pm 15.0) \text{ MeV}$			$E_\gamma = (1185.0 \pm 15.0) \text{ MeV}$			$E_\gamma = (1215.0 \pm 15.0) \text{ MeV}$			$E_\gamma = (1245.0 \pm 15.0) \text{ MeV}$		
	$d\sigma/d\Omega$	Δ_{stat}	Δ_{sys}									
	[$\mu\text{b}/\text{sr}$]	[$\mu\text{b}/\text{sr}$]	[$\mu\text{b}/\text{sr}$]	[$\mu\text{b}/\text{sr}$]	[$\mu\text{b}/\text{sr}$]	[$\mu\text{b}/\text{sr}$]	[$\mu\text{b}/\text{sr}$]	[$\mu\text{b}/\text{sr}$]	[$\mu\text{b}/\text{sr}$]	[$\mu\text{b}/\text{sr}$]	[$\mu\text{b}/\text{sr}$]	[$\mu\text{b}/\text{sr}$]
-0.88	0.4877	0.0377	0.0315	0.4441	0.0388	0.0285	0.4504	0.0507	0.0098	0.3618	0.0387	0.0284
-0.62	0.4591	0.0286	0.0208	0.4144	0.0289	0.0286	0.4231	0.0388	0.0148	0.3633	0.0309	0.0200
-0.38	0.5262	0.0259	0.0196	0.4739	0.0259	0.0242	0.5094	0.0354	0.0195	0.4362	0.0281	0.0152
-0.12	0.6214	0.0247	0.0195	0.5384	0.0241	0.0138	0.4537	0.0291	0.0142	0.4699	0.0253	0.0108
0.12	0.6959	0.0232	0.0156	0.5532	0.0217	0.0084	0.5696	0.0289	0.0137	0.5114	0.0236	0.0116
0.38	0.6224	0.0211	0.0105	0.5614	0.0211	0.0081	0.5217	0.0269	0.0120	0.4922	0.0227	0.0120
0.62	0.5735	0.0199	0.0121	0.4715	0.0191	0.0095	0.4754	0.0255	0.0133	0.4499	0.0217	0.0112
0.88	0.4208	0.0166	0.0150	0.3572	0.0160	0.0139	0.3639	0.0211	0.0125	0.3517	0.0179	0.0109
<hr/>												
$\cos(\theta_\eta^*)$	$E_\gamma = (1270.0 \pm 10.0) \text{ MeV}$			$E_\gamma = (1295.0 \pm 15.0) \text{ MeV}$			$E_\gamma = (1325.0 \pm 15.0) \text{ MeV}$			$E_\gamma = (1355.0 \pm 15.0) \text{ MeV}$		
	$d\sigma/d\Omega$	Δ_{stat}	Δ_{sys}									
	[$\mu\text{b}/\text{sr}$]	[$\mu\text{b}/\text{sr}$]	[$\mu\text{b}/\text{sr}$]	[$\mu\text{b}/\text{sr}$]	[$\mu\text{b}/\text{sr}$]	[$\mu\text{b}/\text{sr}$]	[$\mu\text{b}/\text{sr}$]	[$\mu\text{b}/\text{sr}$]	[$\mu\text{b}/\text{sr}$]	[$\mu\text{b}/\text{sr}$]	[$\mu\text{b}/\text{sr}$]	[$\mu\text{b}/\text{sr}$]
-0.88	0.3214	0.0438	0.0439	0.3746	0.0372	0.0261	0.2903	0.0345	0.0258	0.2672	0.0333	0.0152
-0.62	0.3675	0.0369	0.0227	0.2970	0.0260	0.0135	0.3982	0.0313	0.0203	0.2975	0.0278	0.0214
-0.38	0.4320	0.0336	0.0162	0.3828	0.0247	0.0138	0.4001	0.0264	0.0162	0.3252	0.0244	0.0171
-0.12	0.4828	0.0309	0.0151	0.4300	0.0229	0.0152	0.4185	0.0236	0.0145	0.4001	0.0237	0.0099
0.12	0.4808	0.0276	0.0110	0.4763	0.0216	0.0160	0.4910	0.0232	0.0116	0.4281	0.0223	0.0064
0.38	0.5059	0.0280	0.0075	0.5133	0.0223	0.0176	0.5032	0.0234	0.0094	0.4899	0.0241	0.0092
0.62	0.4456	0.0264	0.0059	0.4504	0.0212	0.0142	0.4527	0.0227	0.0104	0.4519	0.0238	0.0134
0.88	0.3371	0.0212	0.0102	0.3619	0.0173	0.0069	0.3220	0.0172	0.0106	0.3487	0.0186	0.0156
<hr/>												
$\cos(\theta_\eta^*)$	$E_\gamma = (1385.0 \pm 15.0) \text{ MeV}$			$E_\gamma = (1415.0 \pm 15.0) \text{ MeV}$			$E_\gamma = (1445.0 \pm 15.0) \text{ MeV}$			$E_\gamma = (1475.0 \pm 15.0) \text{ MeV}$		
	$d\sigma/d\Omega$	Δ_{stat}	Δ_{sys}									
	[$\mu\text{b}/\text{sr}$]	[$\mu\text{b}/\text{sr}$]	[$\mu\text{b}/\text{sr}$]	[$\mu\text{b}/\text{sr}$]	[$\mu\text{b}/\text{sr}$]	[$\mu\text{b}/\text{sr}$]	[$\mu\text{b}/\text{sr}$]	[$\mu\text{b}/\text{sr}$]	[$\mu\text{b}/\text{sr}$]	[$\mu\text{b}/\text{sr}$]	[$\mu\text{b}/\text{sr}$]	[$\mu\text{b}/\text{sr}$]
-0.88	0.1994	0.0340	0.0140	0.2792	0.0391	0.0291	0.1393	0.0270	0.0134	0.2871	0.0381	0.0313
-0.62	0.3217	0.0336	0.0122	0.2625	0.0301	0.0162	0.2759	0.0287	0.0182	0.1800	0.0243	0.0170
-0.38	0.2947	0.0271	0.0074	0.2841	0.0264	0.0127	0.2453	0.0226	0.0087	0.2571	0.0238	0.0172
-0.12	0.3170	0.0248	0.0071	0.2961	0.0238	0.0120	0.2958	0.0219	0.0057	0.3313	0.0238	0.0149
0.12	0.4118	0.0260	0.0107	0.3763	0.0248	0.0112	0.3829	0.0232	0.0076	0.3380	0.0226	0.0124
0.38	0.4346	0.0272	0.0133	0.3906	0.0260	0.0070	0.4003	0.0246	0.0092	0.3518	0.0243	0.0099
0.62	0.3919	0.0268	0.0120	0.4111	0.0279	0.0046	0.3700	0.0249	0.0084	0.3308	0.0249	0.0057
0.88	0.3631	0.0223	0.0119	0.3482	0.0217	0.0017	0.3474	0.0200	0.0083	0.2905	0.0190	0.0033
<hr/>												
$\cos(\theta_\eta^*)$	$E_\gamma = (1505.0 \pm 15.0) \text{ MeV}$			$E_\gamma = (1535.0 \pm 15.0) \text{ MeV}$			$E_\gamma = (1565.0 \pm 15.0) \text{ MeV}$			$E_\gamma = (1595.0 \pm 15.0) \text{ MeV}$		
	$d\sigma/d\Omega$	Δ_{stat}	Δ_{sys}									
	[$\mu\text{b}/\text{sr}$]	[$\mu\text{b}/\text{sr}$]	[$\mu\text{b}/\text{sr}$]	[$\mu\text{b}/\text{sr}$]	[$\mu\text{b}/\text{sr}$]	[$\mu\text{b}/\text{sr}$]	[$\mu\text{b}/\text{sr}$]	[$\mu\text{b}/\text{sr}$]	[$\mu\text{b}/\text{sr}$]	[$\mu\text{b}/\text{sr}$]	[$\mu\text{b}/\text{sr}$]	[$\mu\text{b}/\text{sr}$]
-0.88	0.2144	0.0337	0.0228	0.1682	0.0359	0.0325	0.1642	0.0337	0.0194	0.1752	0.0351	0.0116
-0.62	0.2010	0.0259	0.0157	0.1450	0.0264	0.0106	0.1590	0.0257	0.0112	0.0813	0.0190	0.0095
-0.38	0.1924	0.0210	0.0081	0.1889	0.0250	0.0124	0.1978	0.0243	0.0080	0.1379	0.0203	0.0157
-0.12	0.2414	0.0209	0.0045	0.2335	0.0248	0.0212	0.2194	0.0230	0.0044	0.1844	0.0211	0.0123
0.12	0.3538	0.0238	0.0047	0.2768	0.0255	0.0198	0.2915	0.0254	0.0048	0.2808	0.0256	0.0075
0.38	0.3181	0.0243	0.0065	0.2977	0.0290	0.0122	0.2668	0.0271	0.0080	0.2918	0.0296	0.0070
0.62	0.3704	0.0276	0.0142	0.4105	0.0359	0.0117	0.2897	0.0300	0.0122	0.3131	0.0328	0.0099
0.88	0.3535	0.0215	0.0206	0.3162	0.0244	0.0101	0.3207	0.0234	0.0154	0.3674	0.0251	0.0068

APPENDIX F. DATA TABLES

$\cos(\theta_\eta^*)$	$E_\gamma = (1625.0 \pm 15.0) \text{ MeV}$			$E_\gamma = (1655.0 \pm 15.0) \text{ MeV}$			$E_\gamma = (1685.0 \pm 15.0) \text{ MeV}$			$E_\gamma = (1715.0 \pm 15.0) \text{ MeV}$								
	$d\sigma/d\Omega$			Δ_{stat}			Δ_{sys}			$d\sigma/d\Omega$			Δ_{stat}			Δ_{sys}		
	$[\mu\text{b}/\text{sr}]$	$[\mu\text{b}/\text{sr}]$	$[\mu\text{b}/\text{sr}]$	$[\mu\text{b}/\text{sr}]$	$[\mu\text{b}/\text{sr}]$	$[\mu\text{b}/\text{sr}]$	$[\mu\text{b}/\text{sr}]$	$[\mu\text{b}/\text{sr}]$										
-0.88	0.1717	0.0334	0.0111	0.1425	0.0321	0.0144	0.1236	0.0341	0.0194	0.1526	0.0338	0.0191	0.1484	0.0250	0.0144	0.1363	0.0206	0.0132
-0.62	0.1620	0.0250	0.0083	0.1523	0.0253	0.0085	0.1299	0.0261	0.0102	0.1654	0.0285	0.0109	0.1362	0.0192	0.0109	0.1326	0.0206	0.0132
-0.38	0.1443	0.0199	0.0066	0.1264	0.0194	0.0072	0.1115	0.0205	0.0047	0.1374	0.0280	0.0085	0.2382	0.0262	0.0117	0.2352	0.0267	0.0066
-0.12	0.1660	0.0192	0.0078	0.2041	0.0224	0.0107	0.1876	0.0245	0.0072	0.1705	0.0267	0.0114	0.3714	0.0432	0.0114	0.3684	0.0432	0.0114
0.12	0.2735	0.0247	0.0089	0.2252	0.0238	0.0071	0.2374	0.0280	0.0085	0.3226	0.0426	0.0088	0.3531	0.0258	0.0032	0.3501	0.0258	0.0032
0.38	0.2585	0.0276	0.0041	0.2928	0.0315	0.0082	0.2318	0.0328	0.0062	0.3714	0.0432	0.0114	0.3531	0.0258	0.0032	0.3501	0.0258	0.0032
0.62	0.2918	0.0316	0.0069	0.2676	0.0330	0.0081	0.3427	0.0279	0.0135	0.3531	0.0258	0.0032	0.3501	0.0258	0.0032	0.3501	0.0258	0.0032
0.88	0.3156	0.0225	0.0145	0.3309	0.0243	0.0062	0.3427	0.0279	0.0135	0.3531	0.0258	0.0032	0.3501	0.0258	0.0032	0.3501	0.0258	0.0032

$\cos(\theta_\eta^*)$	$E_\gamma = (1745.0 \pm 15.0) \text{ MeV}$			$E_\gamma = (1775.0 \pm 15.0) \text{ MeV}$			$E_\gamma = (1805.0 \pm 15.0) \text{ MeV}$			$E_\gamma = (1835.0 \pm 15.0) \text{ MeV}$								
	$d\sigma/d\Omega$			Δ_{stat}			Δ_{sys}			$d\sigma/d\Omega$			Δ_{stat}			Δ_{sys}		
	$[\mu\text{b}/\text{sr}]$	$[\mu\text{b}/\text{sr}]$	$[\mu\text{b}/\text{sr}]$	$[\mu\text{b}/\text{sr}]$	$[\mu\text{b}/\text{sr}]$	$[\mu\text{b}/\text{sr}]$	$[\mu\text{b}/\text{sr}]$	$[\mu\text{b}/\text{sr}]$										
-0.88	0.0679	0.0227	0.0165	0.1197	0.0326	0.0155	0.1299	0.0345	0.0173	0.1327	0.0342	0.0131	0.1654	0.0285	0.0109	0.1626	0.0285	0.0109
-0.62	0.0857	0.0187	0.0095	0.1463	0.0271	0.0098	0.1459	0.0274	0.0077	0.1654	0.0285	0.0109	0.1626	0.0285	0.0109	0.1626	0.0285	0.0109
-0.38	0.1450	0.0204	0.0056	0.0968	0.0189	0.0041	0.0946	0.0191	0.0017	0.0928	0.0187	0.0076	0.1153	0.0197	0.0084	0.1153	0.0197	0.0084
-0.12	0.1431	0.0191	0.0027	0.1585	0.0226	0.0097	0.1338	0.0212	0.0035	0.1868	0.0280	0.0071	0.1868	0.0280	0.0071	0.1868	0.0280	0.0071
0.12	0.1811	0.0228	0.0040	0.2172	0.0287	0.0184	0.1776	0.0270	0.0093	0.1776	0.0354	0.0054	0.1776	0.0354	0.0054	0.1776	0.0354	0.0054
0.38	0.2080	0.0296	0.0071	0.2245	0.0362	0.0150	0.1840	0.0348	0.0128	0.1776	0.0354	0.0054	0.3273	0.0507	0.0129	0.3273	0.0507	0.0129
0.62	0.3057	0.0391	0.0128	0.3634	0.0496	0.0107	0.2905	0.0469	0.0172	0.3709	0.0285	0.0186	0.3709	0.0285	0.0186	0.3709	0.0285	0.0186
0.88	0.3436	0.0246	0.0124	0.3747	0.0288	0.0058	0.3959	0.0300	0.0101	0.3709	0.0285	0.0186	0.3709	0.0285	0.0186	0.3709	0.0285	0.0186

Total Cross Sections

E_{γ} [MeV]	ΔE_{γ} [MeV]	σ [μ b]	Δ_{stat} [μ b]	Δ_{sys} [μ b]
697.5	7.5	4.6450	0.0817	0.0689
712.5	7.5	8.1289	0.0987	0.0795
730.0	10.0	12.5152	0.0977	0.0828
750.0	10.0	17.3357	0.1160	0.1068
770.0	10.0	20.1768	0.1300	0.1271
790.0	10.0	21.1064	0.1433	0.1705
810.0	10.0	20.9700	0.1463	0.1813
830.0	10.0	19.9676	0.1703	0.2385
850.0	10.0	18.6510	0.1595	0.1727
870.0	10.0	18.3278	0.1582	0.1932
890.0	10.0	16.5653	0.1634	0.2018
910.0	10.0	14.5460	0.1466	0.2377
930.0	10.0	13.3079	0.1483	0.2737
955.0	15.0	11.7378	0.1157	0.2263
980.0	10.0	10.8311	0.1493	0.2568
1005.0	15.0	9.8362	0.1176	0.2706
1035.0	15.0	8.6183	0.1100	0.2222
1065.0	15.0	7.9124	0.1332	0.1817
1095.0	15.0	7.3872	0.1337	0.2326
1125.0	15.0	7.3654	0.1136	0.2567
1155.0	15.0	6.8872	0.1130	0.2260
1185.0	15.0	5.9670	0.1126	0.2136
1215.0	15.0	5.8910	0.1480	0.1718
1245.0	15.0	5.3830	0.1193	0.1894
1270.0	10.0	5.2804	0.1412	0.2095
1295.0	15.0	5.1358	0.1100	0.1925
1325.0	15.0	5.1184	0.1146	0.1875
1355.0	15.0	4.7118	0.1115	0.1695
1385.0	15.0	4.2606	0.1240	0.1386
1415.0	15.0	4.1541	0.1243	0.1492
1445.0	15.0	3.8189	0.1069	0.1219
1475.0	15.0	3.6756	0.1134	0.1732
1505.0	15.0	3.5180	0.1120	0.1534
1535.0	15.0	3.1604	0.1266	0.2067
1565.0	15.0	3.0007	0.1191	0.1318
1595.0	15.0	2.8648	0.1178	0.1222
1625.0	15.0	2.8026	0.1151	0.1089
1655.0	15.0	2.7377	0.1190	0.1108
1685.0	15.0	2.6432	0.1324	0.1257
1715.0	15.0	2.5926	0.1220	0.1376
1745.0	15.0	2.2985	0.1087	0.1087
1775.0	15.0	2.6346	0.1360	0.1428
1805.0	15.0	2.4451	0.1348	0.1233
1835.0	15.0	2.4169	0.1350	0.1329

F.2.2 $\gamma p \rightarrow \eta p$ as a Function of E_γ

Angular Distributions

$\cos(\theta_\eta^*)$	$E_\gamma = (697.5 \pm 7.5) \text{ MeV}$			$E_\gamma = (712.5 \pm 7.5) \text{ MeV}$			$E_\gamma = (730.0 \pm 10.0) \text{ MeV}$			$E_\gamma = (750.0 \pm 10.0) \text{ MeV}$		
	$d\sigma/d\Omega$			$d\sigma/d\Omega$			$d\sigma/d\Omega$			$d\sigma/d\Omega$		
	$[\mu\text{b}/\text{sr}]$	$[\mu\text{b}/\text{sr}]$	$[\mu\text{b}/\text{sr}]$									
-0.88	0.2461	0.0469	0.0781	0.4847	0.0463	0.0165	0.7187	0.0394	0.0142	0.9036	0.0422	0.0255
-0.62	0.2738	0.0405	0.0475	0.4481	0.0371	0.0097	0.6660	0.0319	0.0092	0.8664	0.0344	0.0083
-0.38	0.1962	0.0348	0.0178	0.4165	0.0352	0.0079	0.6663	0.0303	0.0138	0.8867	0.0320	0.0166
-0.12	0.1683	0.0380	0.0203	0.3774	0.0362	0.0067	0.5733	0.0291	0.0164	0.7830	0.0300	0.0213
0.12	0.1707	0.0373	0.0231	0.2865	0.0319	0.0057	0.5329	0.0288	0.0152	0.8289	0.0321	0.0156
0.38	0.1129	0.0364	0.0256	0.2710	0.0354	0.0227	0.4805	0.0307	0.0348	0.6997	0.0329	0.0280
0.62	0.1055	0.0437	0.0487	0.2562	0.0385	0.0518	0.4087	0.0311	0.0527	0.5995	0.0344	0.0680
0.88	0.0514	0.0302	0.0317	0.1844	0.0342	0.0338	0.3833	0.0341	0.0255	0.5072	0.0397	0.0808
$\cos(\theta_\eta^*)$	$E_\gamma = (770.0 \pm 10.0) \text{ MeV}$			$E_\gamma = (790.0 \pm 10.0) \text{ MeV}$			$E_\gamma = (810.0 \pm 10.0) \text{ MeV}$			$E_\gamma = (830.0 \pm 10.0) \text{ MeV}$		
	$d\sigma/d\Omega$	Δ_{stat}	Δ_{sys}									
	$[\mu\text{b}/\text{sr}]$	$[\mu\text{b}/\text{sr}]$	$[\mu\text{b}/\text{sr}]$									
-0.88	1.0054	0.0451	0.0800	1.0640	0.0483	0.0924	1.0390	0.0474	0.0681	0.9973	0.0535	0.1036
-0.62	0.9789	0.0366	0.0290	1.1052	0.0402	0.0523	1.0451	0.0384	0.0334	0.9726	0.0421	0.0195
-0.38	0.9614	0.0329	0.0182	1.1648	0.0370	0.0306	1.1018	0.0350	0.0249	1.0506	0.0391	0.0125
-0.12	0.9856	0.0323	0.0194	1.0745	0.0342	0.0228	1.0582	0.0333	0.0286	1.1879	0.0403	0.0275
0.12	0.9822	0.0332	0.0141	1.1053	0.0351	0.0228	1.1339	0.0341	0.0345	1.0664	0.0373	0.0306
0.38	0.9073	0.0356	0.0352	1.0508	0.0382	0.0502	1.0561	0.0369	0.0464	0.9970	0.0404	0.0393
0.62	0.7319	0.0376	0.0849	0.8181	0.0413	0.0949	0.8740	0.0426	0.0692	0.9325	0.0509	0.0499
0.88	0.7363	0.0523	0.1275	0.7502	0.0589	0.1136	0.8051	0.0629	0.0909	0.7072	0.0689	0.0638
$\cos(\theta_\eta^*)$	$E_\gamma = (850.0 \pm 10.0) \text{ MeV}$			$E_\gamma = (870.0 \pm 10.0) \text{ MeV}$			$E_\gamma = (890.0 \pm 10.0) \text{ MeV}$			$E_\gamma = (910.0 \pm 10.0) \text{ MeV}$		
	$d\sigma/d\Omega$	Δ_{stat}	Δ_{sys}									
	$[\mu\text{b}/\text{sr}]$	$[\mu\text{b}/\text{sr}]$	$[\mu\text{b}/\text{sr}]$									
-0.88	0.9244	0.0489	0.0958	0.9076	0.0485	0.1064	0.7878	0.0494	0.1277	0.7234	0.0458	0.0819
-0.62	0.9729	0.0396	0.0266	0.9780	0.0396	0.0402	0.9162	0.0416	0.0418	0.8010	0.0370	0.0334
-0.38	0.9842	0.0358	0.0170	0.9171	0.0344	0.0196	0.8887	0.0364	0.0149	0.7544	0.0318	0.0137
-0.12	0.9592	0.0341	0.0159	0.9706	0.0337	0.0177	0.9330	0.0355	0.0227	0.8139	0.0316	0.0187
0.12	1.0260	0.0343	0.0225	0.9626	0.0326	0.0181	0.8919	0.0333	0.0156	0.7719	0.0293	0.0125
0.38	0.9268	0.0357	0.0420	1.0057	0.0356	0.0372	0.8222	0.0337	0.0229	0.6961	0.0286	0.0169
0.62	0.7802	0.0437	0.0540	0.7818	0.0421	0.0548	0.6712	0.0408	0.0437	0.5879	0.0352	0.0349
0.88	0.5703	0.0603	0.0600	0.7168	0.0705	0.0638	0.7417	0.0810	0.0570	0.5252	0.0670	0.0378
$\cos(\theta_\eta^*)$	$E_\gamma = (930.0 \pm 10.0) \text{ MeV}$			$E_\gamma = (955.0 \pm 15.0) \text{ MeV}$			$E_\gamma = (980.0 \pm 10.0) \text{ MeV}$			$E_\gamma = (1005.0 \pm 15.0) \text{ MeV}$		
	$d\sigma/d\Omega$	Δ_{stat}	Δ_{sys}									
	$[\mu\text{b}/\text{sr}]$	$[\mu\text{b}/\text{sr}]$	$[\mu\text{b}/\text{sr}]$									
-0.88	0.6528	0.0460	0.0442	0.4433	0.0316	0.0136	0.3862	0.0403	0.0124	0.3410	0.0321	0.0159
-0.62	0.6329	0.0347	0.0209	0.5738	0.0275	0.0128	0.4484	0.0333	0.0168	0.4102	0.0266	0.0129
-0.38	0.6771	0.0314	0.0123	0.5950	0.0243	0.0121	0.4512	0.0289	0.0174	0.4437	0.0239	0.0153
-0.12	0.6471	0.0294	0.0131	0.5753	0.0227	0.0142	0.5190	0.0291	0.0196	0.4013	0.0213	0.0144
0.12	0.7212	0.0295	0.0168	0.5897	0.0217	0.0131	0.4819	0.0261	0.0145	0.4162	0.0198	0.0147
0.38	0.6380	0.0277	0.0233	0.4917	0.0194	0.0133	0.4230	0.0237	0.0087	0.3890	0.0185	0.0102
0.62	0.5195	0.0334	0.0297	0.4226	0.0234	0.0198	0.3682	0.0281	0.0196	0.3215	0.0207	0.0175
0.88	0.4012	0.0618	0.0275	0.2689	0.0416	0.0249	0.2644	0.0557	0.0429	0.2479	0.0458	0.0354
$\cos(\theta_\eta^*)$	$E_\gamma = (1035.0 \pm 15.0) \text{ MeV}$			$E_\gamma = (1065.0 \pm 15.0) \text{ MeV}$			$E_\gamma = (1095.0 \pm 15.0) \text{ MeV}$			$E_\gamma = (1125.0 \pm 15.0) \text{ MeV}$		
	$d\sigma/d\Omega$	Δ_{stat}	Δ_{sys}									
	$[\mu\text{b}/\text{sr}]$	$[\mu\text{b}/\text{sr}]$	$[\mu\text{b}/\text{sr}]$									
-0.88	0.3232	0.0321	0.0298	0.2662	0.0388	0.0158	0.2220	0.0379	0.0225	0.2301	0.0333	0.0246
-0.62	0.2996	0.0230	0.0157	0.3052	0.0300	0.0126	0.2956	0.0309	0.0205	0.2696	0.0254	0.0209
-0.38	0.3549	0.0214	0.0129	0.3465	0.0268	0.0122	0.2744	0.0247	0.0134	0.3118	0.0228	0.0157
-0.12	0.3636	0.0204	0.0130	0.3750	0.0263	0.0155	0.3077	0.0242	0.0167	0.3470	0.0218	0.0213
0.12	0.3372	0.0175	0.0117	0.3289	0.0216	0.0114	0.3350	0.0218	0.0129	0.3722	0.0193	0.0128
0.38	0.2829	0.0154	0.0110	0.3153	0.0201	0.0111	0.3511	0.0213	0.0084	0.3755	0.0185	0.0028
0.62	0.2527	0.0175	0.0138	0.2555	0.0214	0.0193	0.2770	0.0221	0.0181	0.2997	0.0190	0.0186
0.88	0.2077	0.0432	0.0173	0.1475	0.0476	0.0239	0.1634	0.0512	0.0271	0.1364	0.0377	0.0249

F.2. UNPOLARISED CROSS SECTIONS FROM LD₂ (CBELSA/TAPS)

$\cos(\theta_\eta^*)$	$E_\gamma = (1155.0 \pm 15.0) \text{ MeV}$			$E_\gamma = (1185.0 \pm 15.0) \text{ MeV}$			$E_\gamma = (1215.0 \pm 15.0) \text{ MeV}$			$E_\gamma = (1245.0 \pm 15.0) \text{ MeV}$		
	$d\sigma/d\Omega$	Δ_{stat}	Δ_{sys}									
	[$\mu\text{b}/\text{sr}$]	[$\mu\text{b}/\text{sr}$]	[$\mu\text{b}/\text{sr}$]	[$\mu\text{b}/\text{sr}$]	[$\mu\text{b}/\text{sr}$]	[$\mu\text{b}/\text{sr}$]	[$\mu\text{b}/\text{sr}$]	[$\mu\text{b}/\text{sr}$]	[$\mu\text{b}/\text{sr}$]	[$\mu\text{b}/\text{sr}$]	[$\mu\text{b}/\text{sr}$]	[$\mu\text{b}/\text{sr}$]
-0.88	0.1717	0.0297	0.0255	0.1701	0.0310	0.0208	0.1850	0.0409	0.0129	0.1383	0.0296	0.0125
-0.62	0.1808	0.0212	0.0179	0.1984	0.0233	0.0232	0.1994	0.0302	0.0197	0.2214	0.0269	0.0100
-0.38	0.2258	0.0200	0.0131	0.2529	0.0221	0.0179	0.2397	0.0279	0.0139	0.2066	0.0222	0.0066
-0.12	0.3630	0.0226	0.0203	0.2798	0.0211	0.0131	0.2326	0.0251	0.0067	0.2807	0.0236	0.0099
0.12	0.3595	0.0189	0.0123	0.2991	0.0180	0.0118	0.2956	0.0233	0.0057	0.2782	0.0194	0.0080
0.38	0.3173	0.0172	0.0090	0.3001	0.0175	0.0137	0.2988	0.0228	0.0061	0.2618	0.0184	0.0035
0.62	0.2865	0.0183	0.0182	0.2158	0.0164	0.0144	0.2268	0.0218	0.0112	0.2494	0.0195	0.0139
0.88	0.2041	0.0435	0.0193	0.1362	0.0349	0.0123	0.2277	0.0537	0.0208	0.1249	0.0330	0.0252
<hr/>												
$\cos(\theta_\eta^*)$	$E_\gamma = (1270.0 \pm 10.0) \text{ MeV}$			$E_\gamma = (1295.0 \pm 15.0) \text{ MeV}$			$E_\gamma = (1325.0 \pm 15.0) \text{ MeV}$			$E_\gamma = (1355.0 \pm 15.0) \text{ MeV}$		
	$d\sigma/d\Omega$	Δ_{stat}	Δ_{sys}									
	[$\mu\text{b}/\text{sr}$]	[$\mu\text{b}/\text{sr}$]	[$\mu\text{b}/\text{sr}$]	[$\mu\text{b}/\text{sr}$]	[$\mu\text{b}/\text{sr}$]	[$\mu\text{b}/\text{sr}$]	[$\mu\text{b}/\text{sr}$]	[$\mu\text{b}/\text{sr}$]	[$\mu\text{b}/\text{sr}$]	[$\mu\text{b}/\text{sr}$]	[$\mu\text{b}/\text{sr}$]	[$\mu\text{b}/\text{sr}$]
-0.88	0.1215	0.0332	0.0115	0.1221	0.0264	0.0102	0.1020	0.0256	0.0171	0.0945	0.0252	0.0173
-0.62	0.2114	0.0310	0.0145	0.1473	0.0201	0.0155	0.1738	0.0228	0.0147	0.1331	0.0204	0.0078
-0.38	0.2429	0.0289	0.0126	0.1778	0.0191	0.0111	0.1946	0.0207	0.0081	0.1751	0.0201	0.0039
-0.12	0.2953	0.0294	0.0142	0.2268	0.0201	0.0076	0.2341	0.0213	0.0105	0.2203	0.0211	0.0086
0.12	0.2711	0.0229	0.0106	0.2306	0.0165	0.0062	0.2496	0.0180	0.0110	0.2212	0.0175	0.0059
0.38	0.2722	0.0228	0.0081	0.2502	0.0171	0.0083	0.2610	0.0184	0.0080	0.2719	0.0195	0.0048
0.62	0.2511	0.0236	0.0141	0.2684	0.0191	0.0165	0.2379	0.0190	0.0140	0.2401	0.0199	0.0176
0.88	0.1957	0.0475	0.0253	0.1849	0.0340	0.0177	0.1790	0.0333	0.0285	0.0876	0.0236	0.0240
<hr/>												
$\cos(\theta_\eta^*)$	$E_\gamma = (1385.0 \pm 15.0) \text{ MeV}$			$E_\gamma = (1415.0 \pm 15.0) \text{ MeV}$			$E_\gamma = (1445.0 \pm 15.0) \text{ MeV}$			$E_\gamma = (1475.0 \pm 15.0) \text{ MeV}$		
	$d\sigma/d\Omega$	Δ_{stat}	Δ_{sys}									
	[$\mu\text{b}/\text{sr}$]	[$\mu\text{b}/\text{sr}$]	[$\mu\text{b}/\text{sr}$]	[$\mu\text{b}/\text{sr}$]	[$\mu\text{b}/\text{sr}$]	[$\mu\text{b}/\text{sr}$]	[$\mu\text{b}/\text{sr}$]	[$\mu\text{b}/\text{sr}$]	[$\mu\text{b}/\text{sr}$]	[$\mu\text{b}/\text{sr}$]	[$\mu\text{b}/\text{sr}$]	[$\mu\text{b}/\text{sr}$]
-0.88	0.0539	0.0233	0.0062	0.0721	0.0263	0.0080	0.0520	0.0215	0.0147	0.0891	0.0274	0.0082
-0.62	0.1591	0.0259	0.0140	0.0820	0.0186	0.0126	0.1165	0.0203	0.0175	0.0851	0.0181	0.0083
-0.38	0.1294	0.0202	0.0113	0.1385	0.0203	0.0175	0.1034	0.0160	0.0068	0.1357	0.0187	0.0102
-0.12	0.1793	0.0224	0.0180	0.1724	0.0215	0.0205	0.1778	0.0199	0.0089	0.1868	0.0209	0.0100
0.12	0.2047	0.0199	0.0134	0.1922	0.0192	0.0165	0.1863	0.0175	0.0078	0.1711	0.0174	0.0046
0.38	0.2132	0.0206	0.0073	0.1977	0.0197	0.0117	0.2159	0.0192	0.0076	0.2024	0.0196	0.0049
0.62	0.2234	0.0231	0.0142	0.1957	0.0217	0.0138	0.1771	0.0193	0.0136	0.1755	0.0203	0.0172
0.88	0.1753	0.0381	0.0318	0.1749	0.0367	0.0158	0.2121	0.0362	0.0387	0.1244	0.0287	0.0301
<hr/>												
$\cos(\theta_\eta^*)$	$E_\gamma = (1505.0 \pm 15.0) \text{ MeV}$			$E_\gamma = (1535.0 \pm 15.0) \text{ MeV}$			$E_\gamma = (1565.0 \pm 15.0) \text{ MeV}$			$E_\gamma = (1595.0 \pm 15.0) \text{ MeV}$		
	$d\sigma/d\Omega$	Δ_{stat}	Δ_{sys}									
	[$\mu\text{b}/\text{sr}$]	[$\mu\text{b}/\text{sr}$]	[$\mu\text{b}/\text{sr}$]	[$\mu\text{b}/\text{sr}$]	[$\mu\text{b}/\text{sr}$]	[$\mu\text{b}/\text{sr}$]	[$\mu\text{b}/\text{sr}$]	[$\mu\text{b}/\text{sr}$]	[$\mu\text{b}/\text{sr}$]	[$\mu\text{b}/\text{sr}$]	[$\mu\text{b}/\text{sr}$]	[$\mu\text{b}/\text{sr}$]
-0.88	0.0769	0.0254	0.0040	0.0409	0.0212	0.0055	0.0442	0.0202	0.0098	0.0447	0.0204	0.0061
-0.62	0.0976	0.0199	0.0087	0.0367	0.0151	0.0058	0.0641	0.0182	0.0097	0.0247	0.0117	0.0047
-0.38	0.0943	0.0160	0.0088	0.1018	0.0195	0.0122	0.1184	0.0203	0.0117	0.0527	0.0137	0.0068
-0.12	0.1539	0.0194	0.0153	0.1120	0.0196	0.0117	0.1314	0.0203	0.0077	0.0967	0.0173	0.0052
0.12	0.1920	0.0189	0.0121	0.1375	0.0191	0.0110	0.1614	0.0205	0.0062	0.1426	0.0196	0.0061
0.38	0.1551	0.0181	0.0086	0.1529	0.0220	0.0099	0.1287	0.0202	0.0093	0.1457	0.0221	0.0096
0.62	0.2151	0.0235	0.0225	0.2270	0.0294	0.0194	0.1838	0.0266	0.0221	0.1589	0.0258	0.0218
0.88	0.1850	0.0355	0.0188	0.1180	0.0334	0.0107	0.2464	0.0461	0.0245	0.1862	0.0403	0.0378
<hr/>												
$\cos(\theta_\eta^*)$	$E_\gamma = (1625.0 \pm 15.0) \text{ MeV}$			$E_\gamma = (1655.0 \pm 15.0) \text{ MeV}$			$E_\gamma = (1685.0 \pm 15.0) \text{ MeV}$			$E_\gamma = (1715.0 \pm 15.0) \text{ MeV}$		
	$d\sigma/d\Omega$	Δ_{stat}	Δ_{sys}									
	[$\mu\text{b}/\text{sr}$]	[$\mu\text{b}/\text{sr}$]	[$\mu\text{b}/\text{sr}$]	[$\mu\text{b}/\text{sr}$]	[$\mu\text{b}/\text{sr}$]	[$\mu\text{b}/\text{sr}$]	[$\mu\text{b}/\text{sr}$]	[$\mu\text{b}/\text{sr}$]	[$\mu\text{b}/\text{sr}$]	[$\mu\text{b}/\text{sr}$]	[$\mu\text{b}/\text{sr}$]	[$\mu\text{b}/\text{sr}$]
-0.88	0.0432	0.0197	0.0090	0.0306	0.0183	0.0058	0.0173	0.0163	0.0067	0.0514	0.0235	0.0167
-0.62	0.0830	0.0194	0.0070	0.0758	0.0193	0.0097	0.0374	0.0151	0.0066	0.0714	0.0187	0.0140
-0.38	0.0798	0.0160	0.0027	0.0735	0.0163	0.0057	0.0629	0.0169	0.0043	0.0751	0.0170	0.0064
-0.12	0.0920	0.0162	0.0059	0.1035	0.0183	0.0108	0.1028	0.0206	0.0060	0.1084	0.0196	0.0071
0.12	0.1287	0.0182	0.0100	0.0918	0.0164	0.0101	0.1421	0.0231	0.0098	0.1180	0.0198	0.0125
0.38	0.1261	0.0203	0.0075	0.1197	0.0216	0.0089	0.1315	0.0262	0.0073	0.0720	0.0185	0.0077
0.62	0.1846	0.0278	0.0185	0.1578	0.0283	0.0120	0.1723	0.0342	0.0099	0.1814	0.0331	0.0174
0.88	0.0779	0.0255	0.0209	0.1593	0.0381	0.0270	0.1215	0.0373	0.0119	0.2166	0.0458	0.0295

$\cos(\theta_\eta^*)$	$E_\gamma = (1745.0 \pm 15.0) \text{ MeV}$			$E_\gamma = (1775.0 \pm 15.0) \text{ MeV}$			$E_\gamma = (1805.0 \pm 15.0) \text{ MeV}$			$E_\gamma = (1835.0 \pm 15.0) \text{ MeV}$		
	$d\sigma/d\Omega$ [$\mu\text{b}/\text{sr}$]	Δ_{stat} [$\mu\text{b}/\text{sr}$]	Δ_{sys} [$\mu\text{b}/\text{sr}$]	$d\sigma/d\Omega$ [$\mu\text{b}/\text{sr}$]	Δ_{stat} [$\mu\text{b}/\text{sr}$]	Δ_{sys} [$\mu\text{b}/\text{sr}$]	$d\sigma/d\Omega$ [$\mu\text{b}/\text{sr}$]	Δ_{stat} [$\mu\text{b}/\text{sr}$]	Δ_{sys} [$\mu\text{b}/\text{sr}$]	$d\sigma/d\Omega$ [$\mu\text{b}/\text{sr}$]	Δ_{stat} [$\mu\text{b}/\text{sr}$]	Δ_{sys} [$\mu\text{b}/\text{sr}$]
-0.88	0.0301	0.0178	0.0118	0.0280	0.0187	0.0122	0.0400	0.0230	0.0132	0.0827	0.0302	0.0135
-0.62	0.0366	0.0133	0.0104	0.0579	0.0182	0.0185	0.0785	0.0218	0.0189	0.0806	0.0215	0.0110
-0.38	0.0691	0.0158	0.0089	0.0573	0.0158	0.0114	0.0474	0.0148	0.0084	0.0573	0.0158	0.0071
-0.12	0.0877	0.0174	0.0074	0.0730	0.0177	0.0070	0.1114	0.0227	0.0076	0.0320	0.0122	0.0029
0.12	0.0712	0.0154	0.0086	0.1247	0.0229	0.0070	0.1146	0.0233	0.0051	0.0968	0.0214	0.0067
0.38	0.1118	0.0231	0.0112	0.0984	0.0251	0.0071	0.1089	0.0284	0.0086	0.0979	0.0275	0.0096
0.62	0.1290	0.0280	0.0178	0.1790	0.0376	0.0300	0.0907	0.0289	0.0173	0.1531	0.0376	0.0297
0.88	0.1524	0.0374	0.0352	0.2207	0.0497	0.0512	0.2017	0.0495	0.0417	0.1583	0.0426	0.0428

Total Cross Sections

E_γ [MeV]	ΔE_γ [MeV]	σ [μb]	Δ_{stat} [μb]	Δ_{sys} [μb]
697.5	7.5	2.0691	0.1712	0.4555
712.5	7.5	4.2640	0.1646	0.2395
730.0	10.0	6.9520	0.1429	0.2879
750.0	10.0	9.5205	0.1556	0.4197
770.0	10.0	11.3921	0.1723	0.6500
790.0	10.0	12.7261	0.1885	0.7672
810.0	10.0	12.6950	0.1883	0.6242
830.0	10.0	12.3574	0.2121	0.5356
850.0	10.0	11.2018	0.1892	0.5263
870.0	10.0	11.3272	0.1935	0.5661
890.0	10.0	10.3450	0.2020	0.5375
910.0	10.0	8.8545	0.1754	0.3928
930.0	10.0	7.6226	0.1673	0.2971
955.0	15.0	6.2153	0.1206	0.1949
980.0	10.0	5.2178	0.1503	0.2338
1005.0	15.0	4.6665	0.1185	0.2092
1035.0	15.0	3.7540	0.1069	0.1929
1065.0	15.0	3.6720	0.1311	0.1927
1095.0	15.0	3.4939	0.1320	0.2194
1125.0	15.0	3.6791	0.1113	0.2245
1155.0	15.0	3.2074	0.1055	0.2110
1185.0	15.0	2.8693	0.1029	0.2058
1215.0	15.0	2.9191	0.1369	0.1587
1245.0	15.0	2.7603	0.1084	0.1399
1270.0	10.0	2.9199	0.1348	0.1737
1295.0	15.0	2.5379	0.0972	0.1533
1325.0	15.0	2.5625	0.1007	0.1739
1355.0	15.0	2.2569	0.0932	0.1415
1385.0	15.0	2.0886	0.1094	0.1783
1415.0	15.0	1.8998	0.1028	0.1792
1445.0	15.0	1.8916	0.0953	0.1754
1475.0	15.0	1.8066	0.0951	0.1459
1505.0	15.0	1.8090	0.1005	0.1537
1535.0	15.0	1.4225	0.1020	0.1314
1565.0	15.0	1.6600	0.1119	0.1634
1595.0	15.0	1.3026	0.0997	0.1538
1625.0	15.0	1.2418	0.0916	0.1270
1655.0	15.0	1.2688	0.1035	0.1406
1685.0	15.0	1.2268	0.1110	0.0981
1715.0	15.0	1.3496	0.1153	0.1716
1745.0	15.0	1.0601	0.0990	0.1761
1775.0	15.0	1.3030	0.1251	0.2276
1805.0	15.0	1.1590	0.1221	0.1865
1835.0	15.0	1.1740	0.1246	0.1936

F.2.3 $\gamma n \rightarrow \eta n$ as a Function of E_γ

Angular Distributions

$\cos(\theta_\eta^*)$	$E_\gamma = (697.5 \pm 7.5) \text{ MeV}$			$E_\gamma = (712.5 \pm 7.5) \text{ MeV}$			$E_\gamma = (730.0 \pm 10.0) \text{ MeV}$			$E_\gamma = (750.0 \pm 10.0) \text{ MeV}$		
	$d\sigma/d\Omega$			$d\sigma/d\Omega$			$d\sigma/d\Omega$			$d\sigma/d\Omega$		
	$[\mu\text{b}/\text{sr}]$	Δ_{stat}	Δ_{sys}									
-0.88	0.2615	0.0956	0.0895	0.5737	0.1025	0.0360	0.5908	0.0745	0.0121	0.8288	0.0852	0.0297
-0.62	0.1645	0.0650	0.0326	0.4071	0.0749	0.0129	0.4860	0.0563	0.0099	0.6826	0.0630	0.0146
-0.38	0.2896	0.0821	0.0367	0.3721	0.0705	0.0076	0.4863	0.0557	0.0148	0.6985	0.0632	0.0208
-0.12	0.1239	0.0590	0.0162	0.2365	0.0566	0.0040	0.4054	0.0515	0.0154	0.6449	0.0608	0.0246
0.12	0.1716	0.0723	0.0226	0.3589	0.0703	0.0105	0.3846	0.0493	0.0133	0.6318	0.0593	0.0158
0.38	0.1557	0.0640	0.0484	0.1539	0.0444	0.0191	0.4110	0.0500	0.0312	0.5644	0.0554	0.0224
0.62	0.0266	0.0317	0.0161	0.1003	0.0369	0.0243	0.3197	0.0443	0.0428	0.5274	0.0543	0.0596
0.88	-0.0016	0.0012	0.0011	0.2157	0.0605	0.0407	0.3496	0.0535	0.0278	0.4806	0.0610	0.0769
<hr/>												
$\cos(\theta_\eta^*)$	$E_\gamma = (770.0 \pm 10.0) \text{ MeV}$			$E_\gamma = (790.0 \pm 10.0) \text{ MeV}$			$E_\gamma = (810.0 \pm 10.0) \text{ MeV}$			$E_\gamma = (830.0 \pm 10.0) \text{ MeV}$		
	$d\sigma/d\Omega$			$d\sigma/d\Omega$			$d\sigma/d\Omega$			$d\sigma/d\Omega$		
	$[\mu\text{b}/\text{sr}]$	Δ_{stat}	Δ_{sys}									
-0.88	0.9695	0.0925	0.0776	1.0369	0.0993	0.0902	0.8774	0.0922	0.0578	0.9574	0.1133	0.1002
-0.62	0.7473	0.0674	0.0262	0.9199	0.0791	0.0435	0.8204	0.0738	0.0324	0.7370	0.0808	0.0201
-0.38	0.8019	0.0684	0.0193	0.8164	0.0714	0.0245	0.6853	0.0643	0.0248	0.7263	0.0752	0.0282
-0.12	0.6771	0.0618	0.0139	0.6009	0.0598	0.0193	0.7017	0.0630	0.0238	0.6597	0.0697	0.0305
0.12	0.6840	0.0613	0.0148	0.7464	0.0660	0.0250	0.7279	0.0643	0.0233	0.6723	0.0706	0.0232
0.38	0.7453	0.0630	0.0365	0.7664	0.0661	0.0460	0.8044	0.0681	0.0367	0.7612	0.0772	0.0291
0.62	0.6525	0.0614	0.0775	0.5912	0.0613	0.0722	0.5653	0.0595	0.0473	0.6232	0.0717	0.0322
0.88	0.5071	0.0645	0.0880	0.5265	0.0695	0.0796	0.5721	0.0741	0.0680	0.6178	0.0911	0.0592
<hr/>												
$\cos(\theta_\eta^*)$	$E_\gamma = (850.0 \pm 10.0) \text{ MeV}$			$E_\gamma = (870.0 \pm 10.0) \text{ MeV}$			$E_\gamma = (890.0 \pm 10.0) \text{ MeV}$			$E_\gamma = (910.0 \pm 10.0) \text{ MeV}$		
	$d\sigma/d\Omega$			$d\sigma/d\Omega$			$d\sigma/d\Omega$			$d\sigma/d\Omega$		
	$[\mu\text{b}/\text{sr}]$	Δ_{stat}	Δ_{sys}									
-0.88	0.9561	0.1077	0.0997	0.8176	0.0988	0.0973	1.0970	0.1221	0.1798	0.7051	0.0928	0.0811
-0.62	0.6135	0.0704	0.0197	0.7293	0.0762	0.0317	0.6071	0.0742	0.0290	0.6001	0.0700	0.0255
-0.38	0.6682	0.0670	0.0194	0.4447	0.0541	0.0116	0.5285	0.0634	0.0106	0.4568	0.0559	0.0094
-0.12	0.5711	0.0613	0.0209	0.5235	0.0584	0.0133	0.4230	0.0569	0.0138	0.6043	0.0647	0.0157
0.12	0.4704	0.0556	0.0200	0.4745	0.0547	0.0121	0.4613	0.0577	0.0169	0.4526	0.0539	0.0100
0.38	0.7648	0.0730	0.0391	0.4922	0.0575	0.0210	0.4244	0.0573	0.0176	0.4226	0.0531	0.0128
0.62	0.5160	0.0621	0.0365	0.5519	0.0637	0.0407	0.4215	0.0595	0.0300	0.3747	0.0527	0.0235
0.88	0.5451	0.0807	0.0602	0.5056	0.0763	0.0446	0.4594	0.0785	0.0395	0.2832	0.0599	0.0212
<hr/>												
$\cos(\theta_\eta^*)$	$E_\gamma = (930.0 \pm 10.0) \text{ MeV}$			$E_\gamma = (955.0 \pm 15.0) \text{ MeV}$			$E_\gamma = (980.0 \pm 10.0) \text{ MeV}$			$E_\gamma = (1005.0 \pm 15.0) \text{ MeV}$		
	$d\sigma/d\Omega$			$d\sigma/d\Omega$			$d\sigma/d\Omega$			$d\sigma/d\Omega$		
	$[\mu\text{b}/\text{sr}]$	Δ_{stat}	Δ_{sys}									
-0.88	0.7645	0.1012	0.0482	0.5669	0.0723	0.0223	0.6182	0.1031	0.0417	0.4830	0.0743	0.0200
-0.62	0.4790	0.0658	0.0189	0.4492	0.0524	0.0114	0.4392	0.0695	0.0298	0.4740	0.0595	0.0154
-0.38	0.4133	0.0556	0.0130	0.4883	0.0496	0.0164	0.5627	0.0718	0.0278	0.4536	0.0533	0.0161
-0.12	0.5093	0.0623	0.0143	0.4266	0.0472	0.0209	0.3654	0.0597	0.0139	0.4849	0.0557	0.0173
0.12	0.5239	0.0601	0.0156	0.4345	0.0443	0.0180	0.5184	0.0640	0.0161	0.3901	0.0450	0.0140
0.38	0.4742	0.0574	0.0252	0.4874	0.0466	0.0162	0.4451	0.0585	0.0086	0.4296	0.0462	0.0142
0.62	0.2651	0.0460	0.0208	0.3243	0.0414	0.0145	0.4137	0.0627	0.0214	0.3449	0.0467	0.0190
0.88	0.3652	0.0723	0.0193	0.3355	0.0576	0.0245	0.1578	0.0544	0.0281	0.1805	0.0490	0.0197
<hr/>												
$\cos(\theta_\eta^*)$	$E_\gamma = (1035.0 \pm 15.0) \text{ MeV}$			$E_\gamma = (1065.0 \pm 15.0) \text{ MeV}$			$E_\gamma = (1095.0 \pm 15.0) \text{ MeV}$			$E_\gamma = (1125.0 \pm 15.0) \text{ MeV}$		
	$d\sigma/d\Omega$			$d\sigma/d\Omega$			$d\sigma/d\Omega$			$d\sigma/d\Omega$		
	$[\mu\text{b}/\text{sr}]$	Δ_{stat}	Δ_{sys}									
-0.88	0.5519	0.0759	0.0165	0.4375	0.0845	0.0300	0.3597	0.0797	0.0208	0.4022	0.0725	0.0234
-0.62	0.4593	0.0579	0.0116	0.4017	0.0668	0.0226	0.4348	0.0688	0.0281	0.1767	0.0380	0.0145
-0.38	0.4201	0.0504	0.0146	0.4707	0.0670	0.0225	0.3511	0.0587	0.0230	0.3269	0.0479	0.0199
-0.12	0.5438	0.0570	0.0210	0.4041	0.0614	0.0193	0.4575	0.0678	0.0289	0.3843	0.0529	0.0238
0.12	0.3984	0.0442	0.0145	0.3897	0.0544	0.0152	0.4294	0.0565	0.0185	0.3611	0.0431	0.0129
0.38	0.3639	0.0412	0.0139	0.3998	0.0533	0.0158	0.3466	0.0505	0.0099	0.3642	0.0438	0.0151
0.62	0.3333	0.0448	0.0179	0.2346	0.0470	0.0181	0.2410	0.0480	0.0168	0.2858	0.0439	0.0254
0.88	0.2626	0.0579	0.0237	0.1303	0.0522	0.0189	0.1631	0.0592	0.0283	0.1779	0.0528	0.0281

APPENDIX F. DATA TABLES

$\cos(\theta_\eta^*)$	$E_\gamma = (1155.0 \pm 15.0) \text{ MeV}$			$E_\gamma = (1185.0 \pm 15.0) \text{ MeV}$			$E_\gamma = (1215.0 \pm 15.0) \text{ MeV}$			$E_\gamma = (1245.0 \pm 15.0) \text{ MeV}$		
	$d\sigma/d\Omega$ [$\mu\text{b}/\text{sr}$]	Δ_{stat} [$\mu\text{b}/\text{sr}$]	Δ_{sys} [$\mu\text{b}/\text{sr}$]	$d\sigma/d\Omega$ [$\mu\text{b}/\text{sr}$]	Δ_{stat} [$\mu\text{b}/\text{sr}$]	Δ_{sys} [$\mu\text{b}/\text{sr}$]	$d\sigma/d\Omega$ [$\mu\text{b}/\text{sr}$]	Δ_{stat} [$\mu\text{b}/\text{sr}$]	Δ_{sys} [$\mu\text{b}/\text{sr}$]	$d\sigma/d\Omega$ [$\mu\text{b}/\text{sr}$]	Δ_{stat} [$\mu\text{b}/\text{sr}$]	Δ_{sys} [$\mu\text{b}/\text{sr}$]
-0.88	0.2507	0.0616	0.0262	0.1546	0.0518	0.0214	0.2939	0.0896	0.0214	0.2132	0.0633	0.0257
-0.62	0.2330	0.0451	0.0203	0.1163	0.0341	0.0154	0.1503	0.0496	0.0201	0.1829	0.0468	0.0176
-0.38	0.3192	0.0490	0.0183	0.3135	0.0502	0.0261	0.3059	0.0645	0.0340	0.2195	0.0460	0.0125
-0.12	0.4322	0.0568	0.0246	0.2404	0.0438	0.0120	0.2740	0.0608	0.0175	0.2409	0.0486	0.0092
0.12	0.4605	0.0494	0.0171	0.3145	0.0423	0.0132	0.2918	0.0535	0.0123	0.3008	0.0461	0.0110
0.38	0.3680	0.0446	0.0136	0.2165	0.0352	0.0118	0.2608	0.0509	0.0128	0.2671	0.0439	0.0117
0.62	0.2133	0.0391	0.0150	0.3267	0.0509	0.0273	0.2045	0.0535	0.0143	0.2292	0.0482	0.0137
0.88	0.1903	0.0564	0.0185	0.1731	0.0556	0.0226	0.1110	0.0594	0.0106	0.1867	0.0631	0.0218
<hr/>												
$\cos(\theta_\eta^*)$	$E_\gamma = (1270.0 \pm 10.0) \text{ MeV}$			$E_\gamma = (1295.0 \pm 15.0) \text{ MeV}$			$E_\gamma = (1325.0 \pm 15.0) \text{ MeV}$			$E_\gamma = (1355.0 \pm 15.0) \text{ MeV}$		
	$d\sigma/d\Omega$ [$\mu\text{b}/\text{sr}$]	Δ_{stat} [$\mu\text{b}/\text{sr}$]	Δ_{sys} [$\mu\text{b}/\text{sr}$]	$d\sigma/d\Omega$ [$\mu\text{b}/\text{sr}$]	Δ_{stat} [$\mu\text{b}/\text{sr}$]	Δ_{sys} [$\mu\text{b}/\text{sr}$]	$d\sigma/d\Omega$ [$\mu\text{b}/\text{sr}$]	Δ_{stat} [$\mu\text{b}/\text{sr}$]	Δ_{sys} [$\mu\text{b}/\text{sr}$]	$d\sigma/d\Omega$ [$\mu\text{b}/\text{sr}$]	Δ_{stat} [$\mu\text{b}/\text{sr}$]	Δ_{sys} [$\mu\text{b}/\text{sr}$]
-0.88	0.1664	0.0671	0.0133	0.2529	0.0653	0.0262	0.1178	0.0485	0.0170	0.1005	0.0436	0.0164
-0.62	0.2271	0.0627	0.0139	0.2609	0.0526	0.0341	0.1774	0.0458	0.0172	0.1901	0.0474	0.0138
-0.38	0.2383	0.0580	0.0115	0.1773	0.0390	0.0156	0.2550	0.0482	0.0155	0.1720	0.0396	0.0066
-0.12	0.3156	0.0658	0.0158	0.2313	0.0431	0.0131	0.2906	0.0498	0.0127	0.2166	0.0431	0.0089
0.12	0.2051	0.0458	0.0088	0.2518	0.0392	0.0100	0.2840	0.0433	0.0095	0.2205	0.0385	0.0072
0.38	0.2409	0.0499	0.0088	0.2587	0.0402	0.0089	0.2553	0.0420	0.0095	0.2194	0.0400	0.0068
0.62	0.1843	0.0518	0.0122	0.1607	0.0374	0.0106	0.2788	0.0524	0.0255	0.1991	0.0463	0.0172
0.88	0.0568	0.0430	0.0077	0.2563	0.0695	0.0307	0.0591	0.0355	0.0138	0.0817	0.0423	0.0237
<hr/>												
$\cos(\theta_\eta^*)$	$E_\gamma = (1385.0 \pm 15.0) \text{ MeV}$			$E_\gamma = (1415.0 \pm 15.0) \text{ MeV}$			$E_\gamma = (1445.0 \pm 15.0) \text{ MeV}$			$E_\gamma = (1475.0 \pm 15.0) \text{ MeV}$		
	$d\sigma/d\Omega$ [$\mu\text{b}/\text{sr}$]	Δ_{stat} [$\mu\text{b}/\text{sr}$]	Δ_{sys} [$\mu\text{b}/\text{sr}$]	$d\sigma/d\Omega$ [$\mu\text{b}/\text{sr}$]	Δ_{stat} [$\mu\text{b}/\text{sr}$]	Δ_{sys} [$\mu\text{b}/\text{sr}$]	$d\sigma/d\Omega$ [$\mu\text{b}/\text{sr}$]	Δ_{stat} [$\mu\text{b}/\text{sr}$]	Δ_{sys} [$\mu\text{b}/\text{sr}$]	$d\sigma/d\Omega$ [$\mu\text{b}/\text{sr}$]	Δ_{stat} [$\mu\text{b}/\text{sr}$]	Δ_{sys} [$\mu\text{b}/\text{sr}$]
-0.88	0.1939	0.0679	0.0169	0.2287	0.0705	0.0231	0.0102	0.0184	0.0022	0.1895	0.0623	0.0213
-0.62	0.1407	0.0469	0.0127	0.0788	0.0335	0.0117	0.0943	0.0335	0.0148	0.0647	0.0283	0.0132
-0.38	0.1485	0.0428	0.0145	0.0755	0.0309	0.0095	0.1618	0.0401	0.0158	0.1633	0.0406	0.0262
-0.12	0.2506	0.0543	0.0274	0.2554	0.0555	0.0314	0.1716	0.0427	0.0143	0.1314	0.0373	0.0142
0.12	0.2097	0.0438	0.0163	0.1467	0.0362	0.0144	0.2222	0.0411	0.0139	0.1959	0.0400	0.0125
0.38	0.2238	0.0483	0.0130	0.1352	0.0385	0.0107	0.2208	0.0456	0.0107	0.1412	0.0372	0.0035
0.62	0.1655	0.0505	0.0138	0.1797	0.0525	0.0156	0.1536	0.0449	0.0132	0.1379	0.0442	0.0217
0.88	0.0576	0.0425	0.0113	0.1812	0.0750	0.0185	-0.0019	0.0010	0.0004	0.0293	0.0300	0.0162
<hr/>												
$\cos(\theta_\eta^*)$	$E_\gamma = (1505.0 \pm 15.0) \text{ MeV}$			$E_\gamma = (1535.0 \pm 15.0) \text{ MeV}$			$E_\gamma = (1565.0 \pm 15.0) \text{ MeV}$			$E_\gamma = (1595.0 \pm 15.0) \text{ MeV}$		
	$d\sigma/d\Omega$ [$\mu\text{b}/\text{sr}$]	Δ_{stat} [$\mu\text{b}/\text{sr}$]	Δ_{sys} [$\mu\text{b}/\text{sr}$]	$d\sigma/d\Omega$ [$\mu\text{b}/\text{sr}$]	Δ_{stat} [$\mu\text{b}/\text{sr}$]	Δ_{sys} [$\mu\text{b}/\text{sr}$]	$d\sigma/d\Omega$ [$\mu\text{b}/\text{sr}$]	Δ_{stat} [$\mu\text{b}/\text{sr}$]	Δ_{sys} [$\mu\text{b}/\text{sr}$]	$d\sigma/d\Omega$ [$\mu\text{b}/\text{sr}$]	Δ_{stat} [$\mu\text{b}/\text{sr}$]	Δ_{sys} [$\mu\text{b}/\text{sr}$]
-0.88	0.1381	0.0562	0.0215	0.1997	0.0840	0.0268	0.1346	0.0711	0.0117	0.1001	0.0601	0.0139
-0.62	0.0720	0.0309	0.0157	0.0750	0.0392	0.0115	0.0519	0.0311	0.0070	0.0521	0.0307	0.0057
-0.38	0.0711	0.0286	0.0111	0.0956	0.0405	0.0137	0.0387	0.0249	0.0044	0.0823	0.0349	0.0108
-0.12	0.1862	0.0446	0.0197	0.0881	0.0377	0.0130	0.1463	0.0449	0.0106	0.1034	0.0372	0.0146
0.12	0.2269	0.0445	0.0138	0.1840	0.0481	0.0226	0.1680	0.0439	0.0078	0.1555	0.0437	0.0125
0.38	0.1606	0.0408	0.0087	0.1232	0.0442	0.0114	0.1347	0.0456	0.0102	0.1997	0.0584	0.0121
0.62	0.0307	0.0225	0.0042	0.2281	0.0767	0.0265	0.0230	0.0249	0.0030	0.0751	0.0449	0.0119
0.88	0.1163	0.0678	0.0345	0.2241	0.1307	0.0416	0.2082	0.1214	0.0245	0.1128	0.0810	0.0389
<hr/>												
$\cos(\theta_\eta^*)$	$E_\gamma = (1625.0 \pm 15.0) \text{ MeV}$			$E_\gamma = (1655.0 \pm 15.0) \text{ MeV}$			$E_\gamma = (1685.0 \pm 15.0) \text{ MeV}$			$E_\gamma = (1715.0 \pm 15.0) \text{ MeV}$		
	$d\sigma/d\Omega$ [$\mu\text{b}/\text{sr}$]	Δ_{stat} [$\mu\text{b}/\text{sr}$]	Δ_{sys} [$\mu\text{b}/\text{sr}$]	$d\sigma/d\Omega$ [$\mu\text{b}/\text{sr}$]	Δ_{stat} [$\mu\text{b}/\text{sr}$]	Δ_{sys} [$\mu\text{b}/\text{sr}$]	$d\sigma/d\Omega$ [$\mu\text{b}/\text{sr}$]	Δ_{stat} [$\mu\text{b}/\text{sr}$]	Δ_{sys} [$\mu\text{b}/\text{sr}$]	$d\sigma/d\Omega$ [$\mu\text{b}/\text{sr}$]	Δ_{stat} [$\mu\text{b}/\text{sr}$]	Δ_{sys} [$\mu\text{b}/\text{sr}$]
-0.88	0.0465	0.0364	0.0093	0.1075	0.0553	0.0190	0.0651	0.0511	0.0223	-0.0032	0.0014	0.0012
-0.62	0.0577	0.0302	0.0080	0.0325	0.0246	0.0046	0.0636	0.0387	0.0102	0.0318	0.0249	0.0084
-0.38	0.0733	0.0307	0.0077	0.0559	0.0287	0.0068	0.0693	0.0360	0.0054	0.0553	0.0285	0.0085
-0.12	0.0546	0.0253	0.0049	0.0524	0.0273	0.0069	0.1109	0.0456	0.0091	0.0448	0.0271	0.0056
0.12	0.0950	0.0325	0.0083	0.1331	0.0411	0.0144	0.0619	0.0318	0.0050	0.0939	0.0361	0.0153
0.38	0.1066	0.0405	0.0085	0.1234	0.0473	0.0097	0.0940	0.0476	0.0083	0.1016	0.0465	0.0185
0.62	0.1329	0.0545	0.0162	0.1553	0.0638	0.0174	0.1081	0.0624	0.0182	0.1950	0.0798	0.0328
0.88	-0.0007	0.0007	0.0002	0.1471	0.0862	0.0375	0.1289	0.0926	0.0354	0.1084	0.0779	0.0154

$\cos(\theta_\eta^*)$	$E_\gamma = (1745.0 \pm 15.0) \text{ MeV}$			$E_\gamma = (1775.0 \pm 15.0) \text{ MeV}$			$E_\gamma = (1805.0 \pm 15.0) \text{ MeV}$			$E_\gamma = (1835.0 \pm 15.0) \text{ MeV}$			$d\sigma/d\Omega$			Δ_{stat}			Δ_{sys}		
	$d\sigma/d\Omega$			Δ_{stat}			Δ_{sys}			$d\sigma/d\Omega$			Δ_{stat}			Δ_{sys}					
	[$\mu\text{b}/\text{sr}$]			[$\mu\text{b}/\text{sr}$]			[$\mu\text{b}/\text{sr}$]			[$\mu\text{b}/\text{sr}$]			[$\mu\text{b}/\text{sr}$]			[$\mu\text{b}/\text{sr}$]					
-0.88	-0.0027	0.0012	0.0029	-0.0060	0.0019	0.0024	-0.0041	0.0015	0.0014	0.0277	0.0303	0.0046									
-0.62	-0.0006	0.0005	0.0004	-0.0030	0.0011	0.0009	0.0138	0.0165	0.0033	0.0523	0.0306	0.0074									
-0.38	0.0460	0.0246	0.0118	0.0862	0.0363	0.0174	0.0132	0.0145	0.0047	0.0145	0.0159	0.0018									
-0.12	0.0691	0.0317	0.0091	0.0827	0.0380	0.0098	0.0141	0.0150	0.0077	0.0885	0.0367	0.0085									
0.12	0.0254	0.0188	0.0048	0.0823	0.0376	0.0123	0.0609	0.0313	0.0198	0.0812	0.0367	0.0097									
0.38	0.1014	0.0460	0.0212	0.1379	0.0619	0.0685	0.0848	0.0495	0.0049	0.1013	0.0589	0.0155									
0.62	0.0642	0.0463	0.0138	0.0900	0.0648	0.0841	0.0503	0.0503	0.0150	0.0566	0.0584	0.0116									
0.88	-0.0008	0.0008	0.0002	-0.0036	0.0021	0.0037	0.0575	0.0583	0.0567	0.0000	0.0000	0.0000									

Total Cross Sections

E_γ [MeV]	ΔE_γ [MeV]	σ [μb]	Δ_{stat} [μb]	Δ_{sys} [μb]
697.5	7.5	1.6994	0.2761	0.3841
712.5	7.5	3.6071	0.2908	0.2400
730.0	10.0	5.3689	0.2436	0.2685
750.0	10.0	7.9181	0.2807	0.4161
770.0	10.0	9.0612	0.3029	0.5599
790.0	10.0	9.3901	0.3226	0.6367
810.0	10.0	8.9755	0.3129	0.4953
830.0	10.0	9.0013	0.3650	0.4947
850.0	10.0	7.8609	0.3248	0.4789
870.0	10.0	7.1116	0.3072	0.4303
890.0	10.0	6.8787	0.3266	0.5044
910.0	10.0	6.0518	0.2834	0.3093
930.0	10.0	5.6777	0.2884	0.2704
955.0	15.0	5.4550	0.2303	0.2201
980.0	10.0	5.4580	0.3069	0.2924
1005.0	15.0	5.0675	0.2419	0.2124
1035.0	15.0	5.1579	0.2411	0.2053
1065.0	15.0	4.4718	0.2742	0.2548
1095.0	15.0	4.3115	0.2731	0.2700
1125.0	15.0	3.6764	0.2141	0.2463
1155.0	15.0	3.7135	0.2193	0.2355
1185.0	15.0	2.7311	0.1980	0.2247
1215.0	15.0	2.8243	0.2634	0.2182
1245.0	15.0	2.8638	0.2265	0.1941
1270.0	10.0	2.4986	0.2466	0.1405
1295.0	15.0	2.7899	0.2161	0.2302
1325.0	15.0	2.6282	0.2012	0.1819
1355.0	15.0	2.1647	0.1886	0.1572
1385.0	15.0	2.1361	0.2209	0.1897
1415.0	15.0	1.7603	0.2142	0.1821
1445.0	15.0	1.5840	0.1574	0.1269
1475.0	15.0	1.5286	0.1745	0.1833
1505.0	15.0	1.1050	0.1612	0.1546
1535.0	15.0	1.7878	0.2943	0.2391
1565.0	15.0	0.7676	0.1753	0.0772
1595.0	15.0	1.2469	0.2146	0.1692
1625.0	15.0	0.7919	0.1405	0.0865
1655.0	15.0	1.2304	0.2230	0.1724
1685.0	15.0	1.0682	0.2376	0.1753
1715.0	15.0	0.9250	0.2067	0.1543
1745.0	15.0	0.2968	0.0920	0.0642
1775.0	15.0	0.6436	0.1530	0.2203
1805.0	15.0	0.4001	0.1527	0.1894
1835.0	15.0	0.5474	0.3188	0.0990

F.2.4 $\gamma n \rightarrow \eta(n)$ as a Function of E_γ
Angular Distributions

$\cos(\theta_\eta^*)$	$E_\gamma = (697.5 \pm 7.5) \text{ MeV}$			$E_\gamma = (712.5 \pm 7.5) \text{ MeV}$			$E_\gamma = (730.0 \pm 10.0) \text{ MeV}$			$E_\gamma = (750.0 \pm 10.0) \text{ MeV}$		
	$d\sigma/d\Omega$			$d\sigma/d\Omega$			$d\sigma/d\Omega$			$d\sigma/d\Omega$		
	$[\mu\text{b}/\text{sr}]$	$[\mu\text{b}/\text{sr}]$	$[\mu\text{b}/\text{sr}]$									
-0.88	0.2802	0.0196	0.0068	0.4502	0.0232	0.0046	0.5527	0.0211	0.0027	0.6975	0.0245	0.0119
-0.62	0.2647	0.0174	0.0061	0.3914	0.0197	0.0061	0.4770	0.0178	0.0045	0.6544	0.0214	0.0057
-0.38	0.2654	0.0164	0.0062	0.3587	0.0178	0.0046	0.4726	0.0165	0.0042	0.5881	0.0189	0.0045
-0.12	0.2277	0.0145	0.0038	0.3595	0.0169	0.0036	0.4779	0.0157	0.0048	0.5468	0.0170	0.0061
0.12	0.2230	0.0137	0.0016	0.3505	0.0159	0.0034	0.5129	0.0155	0.0028	0.6245	0.0172	0.0064
0.38	0.2023	0.0126	0.0020	0.3591	0.0154	0.0039	0.5663	0.0156	0.0028	0.7059	0.0175	0.0071
0.62	0.1846	0.0120	0.0045	0.3448	0.0144	0.0028	0.5885	0.0150	0.0075	0.8112	0.0178	0.0110
0.88	0.1578	0.0108	0.0061	0.3435	0.0144	0.0012	0.6146	0.0153	0.0085	0.8874	0.0181	0.0102
<hr/>												
$\cos(\theta_\eta^*)$	$E_\gamma = (770.0 \pm 10.0) \text{ MeV}$			$E_\gamma = (790.0 \pm 10.0) \text{ MeV}$			$E_\gamma = (810.0 \pm 10.0) \text{ MeV}$			$E_\gamma = (830.0 \pm 10.0) \text{ MeV}$		
	$d\sigma/d\Omega$			$d\sigma/d\Omega$			$d\sigma/d\Omega$			$d\sigma/d\Omega$		
	$[\mu\text{b}/\text{sr}]$	$[\mu\text{b}/\text{sr}]$	$[\mu\text{b}/\text{sr}]$									
-0.88	0.7372	0.0267	0.0035	0.7416	0.0292	0.0114	0.6590	0.0290	0.0078	0.6480	0.0350	0.0085
-0.62	0.6994	0.0233	0.0045	0.7197	0.0259	0.0062	0.6704	0.0258	0.0156	0.6230	0.0297	0.0175
-0.38	0.6587	0.0210	0.0061	0.6456	0.0224	0.0014	0.5693	0.0216	0.0109	0.5661	0.0257	0.0109
-0.12	0.5963	0.0185	0.0065	0.6083	0.0201	0.0043	0.5609	0.0197	0.0123	0.5438	0.0231	0.0073
0.12	0.6492	0.0182	0.0032	0.5951	0.0186	0.0075	0.6129	0.0191	0.0111	0.5433	0.0213	0.0075
0.38	0.7611	0.0187	0.0021	0.6983	0.0190	0.0043	0.6484	0.0186	0.0035	0.6016	0.0212	0.0056
0.62	0.9398	0.0198	0.0079	0.8404	0.0198	0.0025	0.7562	0.0189	0.0041	0.6659	0.0209	0.0030
0.88	1.0619	0.0201	0.0106	1.0405	0.0210	0.0057	1.1065	0.0218	0.0107	0.9635	0.0239	0.0106
<hr/>												
$\cos(\theta_\eta^*)$	$E_\gamma = (850.0 \pm 10.0) \text{ MeV}$			$E_\gamma = (870.0 \pm 10.0) \text{ MeV}$			$E_\gamma = (890.0 \pm 10.0) \text{ MeV}$			$E_\gamma = (910.0 \pm 10.0) \text{ MeV}$		
	$d\sigma/d\Omega$			$d\sigma/d\Omega$			$d\sigma/d\Omega$			$d\sigma/d\Omega$		
	$[\mu\text{b}/\text{sr}]$	$[\mu\text{b}/\text{sr}]$	$[\mu\text{b}/\text{sr}]$									
-0.88	0.6424	0.0343	0.0031	0.6205	0.0339	0.0054	0.5785	0.0354	0.0062	0.5005	0.0320	0.0101
-0.62	0.5615	0.0275	0.0030	0.5566	0.0278	0.0062	0.4676	0.0277	0.0041	0.4300	0.0255	0.0105
-0.38	0.5064	0.0236	0.0066	0.4652	0.0228	0.0072	0.4325	0.0238	0.0043	0.4063	0.0222	0.0084
-0.12	0.4997	0.0216	0.0070	0.4605	0.0210	0.0064	0.4322	0.0221	0.0048	0.4169	0.0207	0.0043
0.12	0.4877	0.0195	0.0051	0.4957	0.0197	0.0055	0.4401	0.0200	0.0067	0.4269	0.0187	0.0050
0.38	0.5147	0.0189	0.0048	0.4977	0.0186	0.0085	0.4330	0.0188	0.0064	0.3822	0.0168	0.0090
0.62	0.6137	0.0193	0.0037	0.5641	0.0186	0.0095	0.4751	0.0184	0.0027	0.4268	0.0165	0.0102
0.88	0.9318	0.0225	0.0077	0.8767	0.0218	0.0025	0.7200	0.0214	0.0038	0.6166	0.0188	0.0028
<hr/>												
$\cos(\theta_\eta^*)$	$E_\gamma = (930.0 \pm 10.0) \text{ MeV}$			$E_\gamma = (955.0 \pm 15.0) \text{ MeV}$			$E_\gamma = (980.0 \pm 10.0) \text{ MeV}$			$E_\gamma = (1005.0 \pm 15.0) \text{ MeV}$		
	$d\sigma/d\Omega$			$d\sigma/d\Omega$			$d\sigma/d\Omega$			$d\sigma/d\Omega$		
	$[\mu\text{b}/\text{sr}]$	$[\mu\text{b}/\text{sr}]$	$[\mu\text{b}/\text{sr}]$									
-0.88	0.4913	0.0343	0.0061	0.4581	0.0287	0.0023	0.4449	0.0393	0.0181	0.4441	0.0328	0.0167
-0.62	0.4111	0.0265	0.0070	0.4102	0.0224	0.0038	0.4099	0.0306	0.0104	0.4053	0.0255	0.0060
-0.38	0.4232	0.0239	0.0066	0.4490	0.0205	0.0038	0.4152	0.0268	0.0045	0.3889	0.0216	0.0055
-0.12	0.3909	0.0210	0.0089	0.3780	0.0172	0.0040	0.3838	0.0233	0.0026	0.3923	0.0194	0.0034
0.12	0.4016	0.0190	0.0088	0.3867	0.0154	0.0049	0.4192	0.0215	0.0047	0.3784	0.0169	0.0014
0.38	0.3980	0.0178	0.0085	0.3748	0.0143	0.0037	0.4215	0.0203	0.0080	0.3842	0.0160	0.0042
0.62	0.3582	0.0158	0.0081	0.3494	0.0130	0.0033	0.3868	0.0184	0.0073	0.3556	0.0146	0.0057
0.88	0.4990	0.0177	0.0006	0.4452	0.0139	0.0039	0.3972	0.0180	0.0074	0.3201	0.0136	0.0036
<hr/>												
$\cos(\theta_\eta^*)$	$E_\gamma = (1035.0 \pm 15.0) \text{ MeV}$			$E_\gamma = (1065.0 \pm 15.0) \text{ MeV}$			$E_\gamma = (1095.0 \pm 15.0) \text{ MeV}$			$E_\gamma = (1125.0 \pm 15.0) \text{ MeV}$		
	$d\sigma/d\Omega$			$d\sigma/d\Omega$			$d\sigma/d\Omega$			$d\sigma/d\Omega$		
	$[\mu\text{b}/\text{sr}]$	$[\mu\text{b}/\text{sr}]$	$[\mu\text{b}/\text{sr}]$									
-0.88	0.4616	0.0331	0.0140	0.3895	0.0380	0.0147	0.3668	0.0388	0.0147	0.2817	0.0301	0.0098
-0.62	0.3640	0.0241	0.0039	0.3133	0.0280	0.0071	0.3205	0.0293	0.0089	0.2433	0.0222	0.0085
-0.38	0.3755	0.0213	0.0019	0.3587	0.0263	0.0038	0.2912	0.0247	0.0069	0.2628	0.0199	0.0071
-0.12	0.3736	0.0187	0.0020	0.3307	0.0221	0.0036	0.3149	0.0225	0.0061	0.2786	0.0179	0.0030
0.12	0.3747	0.0167	0.0015	0.3427	0.0201	0.0048	0.2987	0.0195	0.0037	0.3232	0.0173	0.0026
0.38	0.3422	0.0151	0.0015	0.3180	0.0183	0.0060	0.3184	0.0190	0.0029	0.3060	0.0159	0.0042
0.62	0.3229	0.0139	0.0034	0.2556	0.0157	0.0040	0.2808	0.0172	0.0045	0.2668	0.0144	0.0049
0.88	0.3060	0.0132	0.0077	0.2506	0.0151	0.0028	0.2599	0.0160	0.0073	0.2757	0.0141	0.0057

F.2. UNPOLARISED CROSS SECTIONS FROM LD₂ (CBELSA/TAPS)

$\cos(\theta_\eta^*)$	$E_\gamma = (1155.0 \pm 15.0) \text{ MeV}$			$E_\gamma = (1185.0 \pm 15.0) \text{ MeV}$			$E_\gamma = (1215.0 \pm 15.0) \text{ MeV}$			$E_\gamma = (1245.0 \pm 15.0) \text{ MeV}$		
	$d\sigma/d\Omega$	Δ_{stat}	Δ_{sys}									
	[$\mu\text{b}/\text{sr}$]	[$\mu\text{b}/\text{sr}$]	[$\mu\text{b}/\text{sr}$]	[$\mu\text{b}/\text{sr}$]	[$\mu\text{b}/\text{sr}$]	[$\mu\text{b}/\text{sr}$]	[$\mu\text{b}/\text{sr}$]	[$\mu\text{b}/\text{sr}$]	[$\mu\text{b}/\text{sr}$]	[$\mu\text{b}/\text{sr}$]	[$\mu\text{b}/\text{sr}$]	[$\mu\text{b}/\text{sr}$]
-0.88	0.2292	0.0297	0.0022	0.2025	0.0302	0.0054	0.2189	0.0407	0.0082	0.1863	0.0316	0.0146
-0.62	0.2052	0.0213	0.0039	0.1896	0.0218	0.0121	0.1695	0.0273	0.0065	0.1505	0.0222	0.0117
-0.38	0.2512	0.0199	0.0075	0.2291	0.0201	0.0121	0.2474	0.0277	0.0089	0.1845	0.0205	0.0082
-0.12	0.2732	0.0181	0.0096	0.2394	0.0179	0.0052	0.2042	0.0220	0.0053	0.1909	0.0184	0.0036
0.12	0.3467	0.0184	0.0072	0.2630	0.0168	0.0067	0.2734	0.0225	0.0044	0.2107	0.0171	0.0032
0.38	0.2878	0.0159	0.0028	0.2369	0.0153	0.0087	0.2255	0.0198	0.0058	0.2387	0.0177	0.0035
0.62	0.2675	0.0148	0.0035	0.2245	0.0144	0.0076	0.2113	0.0186	0.0078	0.1739	0.0148	0.0026
0.88	0.2622	0.0140	0.0062	0.2103	0.0131	0.0056	0.2164	0.0176	0.0019	0.2134	0.0151	0.0010
<hr/>												
$\cos(\theta_\eta^*)$	$E_\gamma = (1270.0 \pm 10.0) \text{ MeV}$			$E_\gamma = (1295.0 \pm 15.0) \text{ MeV}$			$E_\gamma = (1325.0 \pm 15.0) \text{ MeV}$			$E_\gamma = (1355.0 \pm 15.0) \text{ MeV}$		
	$d\sigma/d\Omega$	Δ_{stat}	Δ_{sys}									
	[$\mu\text{b}/\text{sr}$]	[$\mu\text{b}/\text{sr}$]	[$\mu\text{b}/\text{sr}$]	[$\mu\text{b}/\text{sr}$]	[$\mu\text{b}/\text{sr}$]	[$\mu\text{b}/\text{sr}$]	[$\mu\text{b}/\text{sr}$]	[$\mu\text{b}/\text{sr}$]	[$\mu\text{b}/\text{sr}$]	[$\mu\text{b}/\text{sr}$]	[$\mu\text{b}/\text{sr}$]	[$\mu\text{b}/\text{sr}$]
-0.88	0.1079	0.0297	0.0022	0.1966	0.0313	0.0041	0.1433	0.0285	0.0083	0.1149	0.0257	0.0103
-0.62	0.1493	0.0266	0.0055	0.1399	0.0206	0.0069	0.1650	0.0233	0.0064	0.1371	0.0215	0.0075
-0.38	0.1736	0.0238	0.0075	0.1752	0.0189	0.0071	0.1758	0.0199	0.0108	0.1399	0.0181	0.0022
-0.12	0.2112	0.0232	0.0054	0.2137	0.0182	0.0081	0.1868	0.0176	0.0083	0.1617	0.0166	0.0008
0.12	0.2129	0.0208	0.0042	0.2277	0.0170	0.0059	0.2368	0.0182	0.0033	0.1886	0.0166	0.0014
0.38	0.2127	0.0203	0.0048	0.2387	0.0170	0.0049	0.2330	0.0178	0.0014	0.2128	0.0177	0.0034
0.62	0.1958	0.0193	0.0053	0.1678	0.0143	0.0040	0.1881	0.0162	0.0016	0.1935	0.0173	0.0070
0.88	0.1929	0.0175	0.0059	0.2259	0.0150	0.0015	0.1941	0.0149	0.0048	0.2135	0.0164	0.0088
<hr/>												
$\cos(\theta_\eta^*)$	$E_\gamma = (1385.0 \pm 15.0) \text{ MeV}$			$E_\gamma = (1415.0 \pm 15.0) \text{ MeV}$			$E_\gamma = (1445.0 \pm 15.0) \text{ MeV}$			$E_\gamma = (1475.0 \pm 15.0) \text{ MeV}$		
	$d\sigma/d\Omega$	Δ_{stat}	Δ_{sys}									
	[$\mu\text{b}/\text{sr}$]	[$\mu\text{b}/\text{sr}$]	[$\mu\text{b}/\text{sr}$]	[$\mu\text{b}/\text{sr}$]	[$\mu\text{b}/\text{sr}$]	[$\mu\text{b}/\text{sr}$]	[$\mu\text{b}/\text{sr}$]	[$\mu\text{b}/\text{sr}$]	[$\mu\text{b}/\text{sr}$]	[$\mu\text{b}/\text{sr}$]	[$\mu\text{b}/\text{sr}$]	[$\mu\text{b}/\text{sr}$]
-0.88	0.0926	0.0269	0.0030	0.1327	0.0302	0.0144	0.0645	0.0202	0.0030	0.1813	0.0333	0.0140
-0.62	0.1150	0.0229	0.0028	0.1162	0.0222	0.0072	0.1489	0.0229	0.0101	0.0764	0.0172	0.0131
-0.38	0.1548	0.0222	0.0022	0.1311	0.0201	0.0070	0.1169	0.0175	0.0060	0.0994	0.0166	0.0092
-0.12	0.1689	0.0201	0.0006	0.1599	0.0195	0.0062	0.1138	0.0155	0.0041	0.1464	0.0181	0.0069
0.12	0.1792	0.0193	0.0032	0.1486	0.0176	0.0030	0.1816	0.0182	0.0068	0.1507	0.0172	0.0079
0.38	0.2040	0.0209	0.0072	0.1173	0.0160	0.0027	0.1497	0.0170	0.0049	0.1319	0.0168	0.0071
0.62	0.1497	0.0186	0.0030	0.1788	0.0205	0.0029	0.1324	0.0167	0.0029	0.1344	0.0178	0.0070
0.88	0.2432	0.0216	0.0020	0.2274	0.0213	0.0030	0.2260	0.0201	0.0092	0.1999	0.0197	0.0031
<hr/>												
$\cos(\theta_\eta^*)$	$E_\gamma = (1505.0 \pm 15.0) \text{ MeV}$			$E_\gamma = (1535.0 \pm 15.0) \text{ MeV}$			$E_\gamma = (1565.0 \pm 15.0) \text{ MeV}$			$E_\gamma = (1595.0 \pm 15.0) \text{ MeV}$		
	$d\sigma/d\Omega$	Δ_{stat}	Δ_{sys}									
	[$\mu\text{b}/\text{sr}$]	[$\mu\text{b}/\text{sr}$]	[$\mu\text{b}/\text{sr}$]	[$\mu\text{b}/\text{sr}$]	[$\mu\text{b}/\text{sr}$]	[$\mu\text{b}/\text{sr}$]	[$\mu\text{b}/\text{sr}$]	[$\mu\text{b}/\text{sr}$]	[$\mu\text{b}/\text{sr}$]	[$\mu\text{b}/\text{sr}$]	[$\mu\text{b}/\text{sr}$]	[$\mu\text{b}/\text{sr}$]
-0.88	0.0733	0.0230	0.0034	0.1167	0.0364	0.0055	0.1038	0.0343	0.0012	0.1200	0.0353	0.0027
-0.62	0.0791	0.0180	0.0098	0.0717	0.0214	0.0053	0.0903	0.0227	0.0062	0.0406	0.0152	0.0032
-0.38	0.0549	0.0128	0.0044	0.0806	0.0187	0.0034	0.0661	0.0164	0.0037	0.0826	0.0181	0.0104
-0.12	0.0925	0.0148	0.0025	0.0987	0.0185	0.0043	0.0779	0.0158	0.0018	0.0688	0.0149	0.0084
0.12	0.1859	0.0195	0.0039	0.1227	0.0194	0.0114	0.1157	0.0182	0.0021	0.1245	0.0194	0.0059
0.38	0.1361	0.0177	0.0058	0.1310	0.0216	0.0104	0.1203	0.0206	0.0032	0.1394	0.0233	0.0041
0.62	0.1487	0.0197	0.0096	0.1508	0.0252	0.0051	0.1086	0.0213	0.0020	0.1142	0.0224	0.0061
0.88	0.2429	0.0226	0.0081	0.2222	0.0267	0.0066	0.1938	0.0228	0.0018	0.1864	0.0205	0.0032
<hr/>												
$\cos(\theta_\eta^*)$	$E_\gamma = (1625.0 \pm 15.0) \text{ MeV}$			$E_\gamma = (1655.0 \pm 15.0) \text{ MeV}$			$E_\gamma = (1685.0 \pm 15.0) \text{ MeV}$			$E_\gamma = (1715.0 \pm 15.0) \text{ MeV}$		
	$d\sigma/d\Omega$	Δ_{stat}	Δ_{sys}									
	[$\mu\text{b}/\text{sr}$]	[$\mu\text{b}/\text{sr}$]	[$\mu\text{b}/\text{sr}$]	[$\mu\text{b}/\text{sr}$]	[$\mu\text{b}/\text{sr}$]	[$\mu\text{b}/\text{sr}$]	[$\mu\text{b}/\text{sr}$]	[$\mu\text{b}/\text{sr}$]	[$\mu\text{b}/\text{sr}$]	[$\mu\text{b}/\text{sr}$]	[$\mu\text{b}/\text{sr}$]	[$\mu\text{b}/\text{sr}$]
-0.88	0.0847	0.0273	0.0050	0.0620	0.0241	0.0018	0.0392	0.0230	0.0081	0.0234	0.0163	0.0024
-0.62	0.0457	0.0153	0.0019	0.0484	0.0162	0.0056	0.0779	0.0233	0.0101	0.0455	0.0161	0.0063
-0.38	0.0546	0.0141	0.0019	0.0467	0.0134	0.0042	0.0512	0.0163	0.0030	0.0576	0.0155	0.0085
-0.12	0.0578	0.0132	0.0016	0.0677	0.0149	0.0019	0.0857	0.0195	0.0060	0.0422	0.0126	0.0062
0.12	0.1082	0.0179	0.0030	0.1213	0.0200	0.0018	0.1046	0.0218	0.0089	0.0757	0.0173	0.0049
0.38	0.1118	0.0207	0.0039	0.1481	0.0253	0.0024	0.0888	0.0233	0.0067	0.0951	0.0229	0.0025
0.62	0.1060	0.0209	0.0026	0.0929	0.0210	0.0015	0.1364	0.0308	0.0079	0.1646	0.0326	0.0101
0.88	0.1988	0.0196	0.0051	0.1945	0.0202	0.0045	0.1737	0.0221	0.0018	0.1895	0.0212	0.0042

$\cos(\theta_\eta^*)$	$E_\gamma = (1745.0 \pm 15.0) \text{ MeV}$			$E_\gamma = (1775.0 \pm 15.0) \text{ MeV}$			$E_\gamma = (1805.0 \pm 15.0) \text{ MeV}$			$E_\gamma = (1835.0 \pm 15.0) \text{ MeV}$		
	$d\sigma/d\Omega$ [$\mu\text{b}/\text{sr}$]	Δ_{stat} [$\mu\text{b}/\text{sr}$]	Δ_{sys} [$\mu\text{b}/\text{sr}$]	$d\sigma/d\Omega$ [$\mu\text{b}/\text{sr}$]	Δ_{stat} [$\mu\text{b}/\text{sr}$]	Δ_{sys} [$\mu\text{b}/\text{sr}$]	$d\sigma/d\Omega$ [$\mu\text{b}/\text{sr}$]	Δ_{stat} [$\mu\text{b}/\text{sr}$]	Δ_{sys} [$\mu\text{b}/\text{sr}$]	$d\sigma/d\Omega$ [$\mu\text{b}/\text{sr}$]	Δ_{stat} [$\mu\text{b}/\text{sr}$]	Δ_{sys} [$\mu\text{b}/\text{sr}$]
-0.88	0.0179	0.0136	0.0022	0.0002	0.0095	0.0002	0.0219	0.0169	0.0031	0.0342	0.0196	0.0037
-0.62	0.0304	0.0121	0.0063	0.0311	0.0138	0.0311	0.0257	0.0127	0.0015	0.0594	0.0184	0.0046
-0.38	0.0363	0.0115	0.0037	0.0585	0.0161	0.0044	0.0383	0.0133	0.0028	0.0207	0.0098	0.0013
-0.12	0.0568	0.0138	0.0013	0.0557	0.0154	0.0053	0.0242	0.0102	0.0031	0.0571	0.0151	0.0025
0.12	0.0757	0.0169	0.0018	0.1023	0.0227	0.0098	0.0715	0.0195	0.0068	0.0692	0.0189	0.0070
0.38	0.0579	0.0181	0.0028	0.0935	0.0275	0.0093	0.0630	0.0242	0.0044	0.0668	0.0255	0.0096
0.62	0.1025	0.0259	0.0090	0.1491	0.0376	0.0080	0.1427	0.0398	0.0067	0.0813	0.0310	0.0051
0.88	0.1822	0.0200	0.0110	0.1657	0.0221	0.0027	0.1775	0.0237	0.0048	0.1877	0.0242	0.0021

Total Cross Sections

E_γ [MeV]	ΔE_γ [MeV]	σ [μb]	Δ_{stat} [μb]	Δ_{sys} [μb]
697.5	7.5	2.8342	0.0662	0.0586
712.5	7.5	4.6475	0.0777	0.0474
730.0	10.0	6.7011	0.0743	0.0599
750.0	10.0	8.6778	0.0855	0.0994
770.0	10.0	9.6030	0.0935	0.0699
790.0	10.0	9.2728	0.0994	0.0684
810.0	10.0	8.7825	0.0985	0.1185
830.0	10.0	8.1115	0.1138	0.1115
850.0	10.0	7.4842	0.1066	0.0637
870.0	10.0	7.1252	0.1050	0.0814
890.0	10.0	6.2390	0.1071	0.0605
910.0	10.0	5.6509	0.0977	0.0967
930.0	10.0	5.2768	0.1011	0.0859
955.0	15.0	5.0951	0.0840	0.0466
980.0	10.0	5.1457	0.1145	0.0999
1005.0	15.0	4.8187	0.0934	0.0736
1035.0	15.0	4.5717	0.0910	0.0561
1065.0	15.0	3.9938	0.1068	0.0735
1095.0	15.0	3.8455	0.1088	0.0867
1125.0	15.0	3.4963	0.0871	0.0728
1155.0	15.0	3.3002	0.0868	0.0653
1185.0	15.0	2.8049	0.0861	0.1014
1215.0	15.0	2.7302	0.1125	0.0769
1245.0	15.0	2.4030	0.0901	0.0770
1270.0	10.0	2.2815	0.1022	0.0638
1295.0	15.0	2.4351	0.0867	0.0668
1325.0	15.0	2.3815	0.0890	0.0706
1355.0	15.0	2.1369	0.0846	0.0658
1385.0	15.0	2.0323	0.0963	0.0369
1415.0	15.0	1.8810	0.0945	0.0722
1445.0	15.0	1.7352	0.0821	0.0703
1475.0	15.0	1.6756	0.0876	0.1105
1505.0	15.0	1.5419	0.0831	0.0755
1535.0	15.0	1.5520	0.1070	0.0825
1565.0	15.0	1.3699	0.0991	0.0353
1595.0	15.0	1.3177	0.0950	0.0639
1625.0	15.0	1.1952	0.0849	0.0389
1655.0	15.0	1.1985	0.0875	0.0368
1685.0	15.0	1.1724	0.0993	0.0784
1715.0	15.0	1.0511	0.0845	0.0648
1745.0	15.0	0.8875	0.0745	0.0579
1775.0	15.0	1.0054	0.0921	0.0861
1805.0	15.0	0.8468	0.0886	0.0510
1835.0	15.0	0.9078	0.0921	0.0540

F.2.5 $\gamma p \rightarrow \eta p$ as a Function of W

Angular Distributions

$\cos(\theta_\eta^*)$	W=(1487.5±2.5) MeV			W=(1492.5±2.5) MeV			W=(1497.5±2.5) MeV			W=(1505.0±5.0) MeV		
	$d\sigma/d\Omega$			$d\sigma/d\Omega$			$d\sigma/d\Omega$			$d\sigma/d\Omega$		
	$[\mu\text{b}/\text{sr}]$	Δ_{stat}	Δ_{sys}									
-0.88	0.3084	0.1101	0.0401	0.6874	0.1013	0.0241	0.7958	0.0861	0.0180	1.0340	0.0606	0.0161
-0.62	0.3076	0.0759	0.0163	0.7426	0.0771	0.0161	0.8527	0.0694	0.0231	1.1325	0.0522	0.0200
-0.38	0.2910	0.0624	0.0075	0.7314	0.0708	0.0154	0.9187	0.0688	0.0220	1.0783	0.0473	0.0236
-0.12	0.3499	0.0656	0.0086	0.7863	0.0748	0.0119	0.8971	0.0687	0.0237	1.1504	0.0483	0.0286
0.12	0.3075	0.0578	0.0087	0.7906	0.0741	0.0123	0.8925	0.0682	0.0327	1.1338	0.0478	0.0377
0.38	0.3605	0.0644	0.0340	0.9467	0.0782	0.0858	0.8070	0.0643	0.0648	1.0178	0.0468	0.0800
0.62	0.2438	0.0581	0.0451	0.7433	0.0726	0.1340	0.8547	0.0714	0.0972	0.9000	0.0504	0.1015
0.88	0.2293	0.0770	0.0433	0.6130	0.0814	0.1108	0.6995	0.0747	0.0452	0.8655	0.0584	0.0556
<hr/>												
$\cos(\theta_\eta^*)$	W=(1515.0±5.0) MeV			W=(1525.0±5.0) MeV			W=(1535.0±5.0) MeV			W=(1545.0±5.0) MeV		
	$d\sigma/d\Omega$			$d\sigma/d\Omega$			$d\sigma/d\Omega$			$d\sigma/d\Omega$		
	$[\mu\text{b}/\text{sr}]$	Δ_{stat}	Δ_{sys}									
-0.88	1.2648	0.0618	0.0408	1.0824	0.0557	0.0863	1.1704	0.0584	0.1024	1.2913	0.0627	0.0857
-0.62	1.2198	0.0513	0.0166	1.2403	0.0493	0.0432	1.2719	0.0486	0.0617	1.2105	0.0475	0.0413
-0.38	1.2610	0.0465	0.0212	1.2321	0.0441	0.0257	1.2295	0.0439	0.0327	1.3271	0.0453	0.0293
-0.12	1.2568	0.0452	0.0269	1.2951	0.0427	0.0232	1.3352	0.0424	0.0255	1.2569	0.0417	0.0311
0.12	1.2801	0.0451	0.0252	1.3282	0.0430	0.0201	1.2787	0.0418	0.0273	1.2727	0.0420	0.0382
0.38	1.2455	0.0470	0.0578	1.2280	0.0445	0.0546	1.1221	0.0428	0.0599	1.3153	0.0471	0.0602
0.62	0.9654	0.0496	0.1025	0.9460	0.0479	0.1046	0.9921	0.0511	0.1097	0.7852	0.0488	0.0610
0.88	0.8186	0.0613	0.1294	0.8013	0.0673	0.1389	0.9980	0.0824	0.1545	0.8973	0.0857	0.1027
<hr/>												
$\cos(\theta_\eta^*)$	W=(1555.0±5.0) MeV			W=(1565.0±5.0) MeV			W=(1575.0±5.0) MeV			W=(1585.0±5.0) MeV		
	$d\sigma/d\Omega$			$d\sigma/d\Omega$			$d\sigma/d\Omega$			$d\sigma/d\Omega$		
	$[\mu\text{b}/\text{sr}]$	Δ_{stat}	Δ_{sys}									
-0.88	0.9536	0.0553	0.0635	1.0162	0.0585	0.1053	0.9236	0.0569	0.0961	0.9981	0.0603	0.1171
-0.62	1.1680	0.0471	0.0393	1.1769	0.0482	0.0338	1.0913	0.0473	0.0376	0.9494	0.0449	0.0448
-0.38	1.1706	0.0419	0.0255	1.0523	0.0397	0.0101	1.0528	0.0402	0.0155	0.9728	0.0394	0.0176
-0.12	1.2409	0.0423	0.0305	1.2354	0.0427	0.0250	1.1183	0.0403	0.0202	1.0709	0.0394	0.0150
0.12	1.2048	0.0406	0.0369	1.2005	0.0409	0.0351	1.0860	0.0399	0.0262	0.9676	0.0392	0.0174
0.38	1.1318	0.0446	0.0528	1.0606	0.0447	0.0404	1.0311	0.0448	0.0467	0.9298	0.0419	0.0345
0.62	0.8606	0.0545	0.0666	0.8440	0.0575	0.0552	0.8505	0.0602	0.0632	0.6792	0.0537	0.0451
0.88	0.7935	0.0902	0.0896	0.7838	0.1038	0.0851	0.7247	0.1127	0.0762	0.6661	0.1168	0.0631
<hr/>												
$\cos(\theta_\eta^*)$	W=(1595.0±5.0) MeV			W=(1605.0±5.0) MeV			W=(1615.0±5.0) MeV			W=(1625.0±5.0) MeV		
	$d\sigma/d\Omega$			$d\sigma/d\Omega$			$d\sigma/d\Omega$			$d\sigma/d\Omega$		
	$[\mu\text{b}/\text{sr}]$	Δ_{stat}	Δ_{sys}									
-0.88	0.9719	0.0609	0.1595	0.6878	0.0528	0.0773	0.6391	0.0508	0.0408	0.5330	0.0470	0.0375
-0.62	0.9139	0.0442	0.0508	0.7568	0.0408	0.0325	0.7214	0.0400	0.0244	0.6109	0.0376	0.0207
-0.38	0.8621	0.0379	0.0181	0.8022	0.0378	0.0145	0.7602	0.0372	0.0148	0.6055	0.0340	0.0112
-0.12	0.9236	0.0367	0.0181	0.8457	0.0359	0.0173	0.6962	0.0329	0.0117	0.6021	0.0315	0.0110
0.12	0.9440	0.0398	0.0172	0.8630	0.0386	0.0162	0.6769	0.0337	0.0163	0.6257	0.0318	0.0158
0.38	0.8275	0.0377	0.0256	0.7679	0.0345	0.0210	0.6236	0.0296	0.0240	0.4864	0.0258	0.0185
0.62	0.6660	0.0507	0.0406	0.5353	0.0437	0.0290	0.4657	0.0386	0.0312	0.4161	0.0346	0.0320
0.88	0.5201	0.1160	0.0524	0.5250	0.1285	0.0560	0.2008	0.0826	0.0432	0.1236	0.0661	0.0452
<hr/>												
$\cos(\theta_\eta^*)$	W=(1635.0±5.0) MeV			W=(1645.0±5.0) MeV			W=(1655.0±5.0) MeV			W=(1670.0±10.0) MeV		
	$d\sigma/d\Omega$			$d\sigma/d\Omega$			$d\sigma/d\Omega$			$d\sigma/d\Omega$		
	$[\mu\text{b}/\text{sr}]$	Δ_{stat}	Δ_{sys}									
-0.88	0.4460	0.0438	0.0201	0.3816	0.0413	0.0145	0.2933	0.0379	0.0026	0.2483	0.0265	0.0177
-0.62	0.4644	0.0336	0.0121	0.4133	0.0327	0.0139	0.3550	0.0312	0.0128	0.2471	0.0194	0.0114
-0.38	0.5579	0.0330	0.0134	0.4770	0.0309	0.0157	0.3448	0.0267	0.0143	0.3278	0.0192	0.0131
-0.12	0.4708	0.0290	0.0128	0.4542	0.0299	0.0144	0.3948	0.0290	0.0138	0.3312	0.0197	0.0131
0.12	0.4642	0.0268	0.0110	0.4100	0.0247	0.0119	0.3355	0.0220	0.0089	0.3027	0.0150	0.0113
0.38	0.4120	0.0237	0.0112	0.3826	0.0227	0.0080	0.2818	0.0194	0.0059	0.2480	0.0131	0.0076
0.62	0.3067	0.0280	0.0142	0.2148	0.0222	0.0138	0.1857	0.0198	0.0179	0.2026	0.0145	0.0101
0.88	0.1416	0.0727	0.0139	0.0917	0.0568	0.0194	0.0852	0.0535	0.0284	0.1243	0.0417	0.0132

APPENDIX F. DATA TABLES

$\cos(\theta_\eta^*)$	W=(1690.0±10.0) MeV			W=(1710.0±10.0) MeV			W=(1730.0±10.0) MeV			W=(1750.0±10.0) MeV			W=(1770.0±10.0) MeV			W=(1790.0±10.0) MeV									
	$d\sigma/d\Omega$			Δ_{stat}			Δ_{sys}			$d\sigma/d\Omega$			Δ_{stat}			Δ_{sys}									
	$[\mu\text{b}/\text{sr}]$																								
-0.88	0.2200	0.0272	0.0151	0.1931	0.0268	0.0136	0.1502	0.0238	0.0104	0.1331	0.0229	0.0163	-0.88	0.1343	0.0238	0.0103	0.1804	0.0284	0.0142	0.0831	0.0203	0.0055	0.1315	0.0272	0.0182
-0.62	0.2333	0.0204	0.0067	0.2421	0.0223	0.0125	0.2248	0.0218	0.0171	0.1967	0.0209	0.0166	-0.62	0.1777	0.0207	0.0143	0.1762	0.0212	0.0087	0.1983	0.0228	0.0134	0.1582	0.0211	0.0128
-0.38	0.2521	0.0180	0.0068	0.3422	0.0219	0.0149	0.2551	0.0191	0.0154	0.2110	0.0179	0.0134	-0.38	0.2563	0.0139	0.0095	0.3288	0.0163	0.0091	0.3377	0.0164	0.0046	0.3244	0.0165	0.0119
-0.12	0.2957	0.0198	0.0110	0.3332	0.0220	0.0159	0.3175	0.0214	0.0179	0.3126	0.0217	0.0162	0.12	0.2989	0.0157	0.0108	0.3351	0.0172	0.0124	0.3520	0.0176	0.0119	0.3455	0.0177	0.0132
0.38	0.2563	0.0139	0.0095	0.3288	0.0163	0.0091	0.3377	0.0164	0.0046	0.3244	0.0165	0.0119	0.62	0.1838	0.0140	0.0137	0.2864	0.0177	0.0196	0.2805	0.0171	0.0152	0.2813	0.0172	0.0192
0.88	0.1382	0.0421	0.0224	0.1043	0.0338	0.0177	0.1918	0.0405	0.0286	0.1490	0.0330	0.0195	-0.88	0.1382	0.0421	0.0224	0.1043	0.0338	0.0177	0.1918	0.0405	0.0286	0.1490	0.0330	0.0195
<hr/>																									
$\cos(\theta_\eta^*)$	W=(1770.0±10.0) MeV			W=(1790.0±10.0) MeV			W=(1810.0±10.0) MeV			W=(1830.0±10.0) MeV			W=(1850.0±10.0) MeV			W=(1870.0±10.0) MeV			W=(1890.0±10.0) MeV						
	$d\sigma/d\Omega$			Δ_{stat}			Δ_{sys}			$d\sigma/d\Omega$			$d\sigma/d\Omega$			Δ_{stat}			Δ_{sys}						
	$[\mu\text{b}/\text{sr}]$																								
-0.88	0.1343	0.0238	0.0103	0.1804	0.0284	0.0142	0.0831	0.0203	0.0055	0.1315	0.0272	0.0182	-0.88	0.1777	0.0207	0.0143	0.1762	0.0212	0.0087	0.1983	0.0228	0.0134	0.1582	0.0211	0.0128
-0.62	0.2363	0.0198	0.0124	0.2049	0.0191	0.0069	0.2222	0.0201	0.0118	0.1741	0.0182	0.0077	-0.38	0.2197	0.0227	0.0079	0.2420	0.0204	0.0078	0.2811	0.0221	0.0134	0.2590	0.0217	0.0078
-0.12	0.3197	0.0227	0.0079	0.2420	0.0204	0.0078	0.2677	0.0170	0.0100	0.2441	0.0167	0.0066	0.12	0.3281	0.0180	0.0044	0.2724	0.0169	0.0070	0.2441	0.0167	0.0066	0.2424	0.0164	0.0068
0.38	0.2821	0.0162	0.0063	0.3082	0.0175	0.0050	0.2779	0.0170	0.0083	0.2796	0.0190	0.0181	0.62	0.2344	0.0162	0.0117	0.2356	0.0166	0.0102	0.2342	0.0168	0.0132	0.2796	0.0190	0.0181
0.88	0.1852	0.0356	0.0158	0.1315	0.0287	0.0176	0.1328	0.0275	0.0158	0.1646	0.0293	0.0270	-0.88	0.1852	0.0356	0.0158	0.1315	0.0287	0.0176	0.1328	0.0275	0.0158	0.1646	0.0293	0.0270
<hr/>																									
$\cos(\theta_\eta^*)$	W=(1850.0±10.0) MeV			W=(1870.0±10.0) MeV			W=(1890.0±10.0) MeV			W=(1910.0±10.0) MeV			W=(1930.0±10.0) MeV			W=(1950.0±10.0) MeV			W=(1970.0±10.0) MeV						
	$d\sigma/d\Omega$			Δ_{stat}			Δ_{sys}			$d\sigma/d\Omega$			$d\sigma/d\Omega$			Δ_{stat}			Δ_{sys}						
	$[\mu\text{b}/\text{sr}]$																								
-0.88	0.1182	0.0294	0.0182	0.1469	0.0373	0.0104	0.1460	0.0407	0.0303	0.0280	0.0167	0.0042	-0.88	0.1239	0.0201	0.0076	0.1331	0.0223	0.0130	0.1064	0.0204	0.0143	0.0849	0.0173	0.0085
-0.62	0.2119	0.0212	0.0071	0.1578	0.0194	0.0140	0.1882	0.0216	0.0135	0.1367	0.0178	0.0102	-0.38	0.2284	0.0214	0.0073	0.2070	0.0210	0.0187	0.1748	0.0196	0.0077	0.2161	0.0227	0.0115
-0.12	0.2436	0.0177	0.0056	0.2634	0.0196	0.0168	0.2198	0.0187	0.0079	0.2132	0.0190	0.0067	0.12	0.2436	0.0177	0.0056	0.2776	0.0203	0.0097	0.2438	0.0202	0.0088	0.2179	0.0202	0.0073
0.38	0.2732	0.0186	0.0050	0.2776	0.0203	0.0097	0.2438	0.0202	0.0088	0.2179	0.0202	0.0073	0.62	0.2466	0.0190	0.0192	0.2676	0.0213	0.0183	0.2227	0.0208	0.0180	0.1790	0.0199	0.0182
0.88	0.2065	0.0328	0.0528	0.1942	0.0323	0.0353	0.1905	0.0323	0.0349	0.0839	0.0213	0.0195	-0.88	0.2065	0.0328	0.0528	0.1942	0.0323	0.0353	0.1445	0.0286	0.0307	0.1488	0.0295	0.0246
<hr/>																									
$\cos(\theta_\eta^*)$	W=(2010.0±10.0) MeV			W=(2030.0±10.0) MeV			W=(2050.0±10.0) MeV			W=(2070.0±10.0) MeV			W=(2010.0±10.0) MeV			W=(2030.0±10.0) MeV			W=(2050.0±10.0) MeV						
	$d\sigma/d\Omega$			Δ_{stat}			Δ_{sys}			$d\sigma/d\Omega$			$d\sigma/d\Omega$			Δ_{stat}			Δ_{sys}						
	$[\mu\text{b}/\text{sr}]$																								
-0.88	0.0362	0.0147	0.0071	0.0492	0.0179	0.0170	0.0286	0.0141	0.0117	0.0502	0.0184	0.0163	-0.88	0.0695	0.0158	0.0098	0.0652	0.0155	0.0119	0.0541	0.0145	0.0170	0.0327	0.0120	0.0079
-0.62	0.0681	0.0133	0.0059	0.0481	0.0114	0.0037	0.0370	0.0104	0.0081	0.0598	0.0136	0.0098	-0.38	0.1005	0.0165	0.0085	0.1119	0.0177	0.0070	0.0842	0.0162	0.0093	0.0508	0.0135	0.0040
-0.12	0.0802	0.0139	0.0077	0.1034	0.0162	0.0082	0.0950	0.0167	0.0054	0.1211	0.0210	0.0035	0.12	0.1734	0.0244	0.0128	0.0992	0.0196	0.0073	0.1272	0.0240	0.0104	0.0989	0.0230	0.0065
0.38	0.1645	0.0260	0.0102	0.1359	0.0251	0.0106	0.1714	0.0302	0.0269	0.1322	0.0285	0.0216	0.62	0.1988	0.0355										

Total Cross Sections

W [MeV]	ΔW [MeV]	σ [μ b]	Δ_{stat} [μ b]	Δ_{sys} [μ b]
1487.5	2.5	3.7192	0.3231	0.3258
1492.5	2.5	9.4732	0.3518	0.6662
1497.5	2.5	10.5304	0.3185	0.5193
1505.0	5.0	13.0238	0.2302	0.5785
1515.0	5.0	14.5841	0.2289	0.6678
1525.0	5.0	14.3083	0.2222	0.7933
1535.0	5.0	14.6743	0.2348	0.9174
1545.0	5.0	14.4249	0.2386	0.6946
1555.0	5.0	13.3088	0.2401	0.6368
1565.0	5.0	12.9830	0.2541	0.5950
1575.0	5.0	12.3308	0.2617	0.6003
1585.0	5.0	11.1468	0.2539	0.5504
1595.0	5.0	10.2587	0.2458	0.5806
1605.0	5.0	8.7909	0.2336	0.3905
1615.0	5.0	7.5543	0.1980	0.3258
1625.0	5.0	6.2886	0.1758	0.3011
1635.0	5.0	5.1323	0.1639	0.1710
1645.0	5.0	4.3735	0.1453	0.1760
1655.0	5.0	3.5244	0.1330	0.1707
1670.0	10.0	3.1449	0.0933	0.1481
1690.0	10.0	2.8545	0.0934	0.1418
1710.0	10.0	3.4219	0.1000	0.1844
1730.0	10.0	3.2807	0.0990	0.1891
1750.0	10.0	3.0339	0.0933	0.2000
1770.0	10.0	2.9060	0.0956	0.1372
1790.0	10.0	2.7352	0.0943	0.1203
1810.0	10.0	2.6505	0.0914	0.1443
1830.0	10.0	2.5839	0.0950	0.1655
1850.0	10.0	2.5664	0.1004	0.1859
1870.0	10.0	2.5792	0.1089	0.2078
1890.0	10.0	2.2988	0.1084	0.2070
1910.0	10.0	1.7963	0.0857	0.1349
1930.0	10.0	1.7367	0.0894	0.1508
1950.0	10.0	1.4847	0.0846	0.1305
1970.0	10.0	1.4383	0.0861	0.1551
1990.0	10.0	1.2286	0.0835	0.1300
2010.0	10.0	1.3615	0.0942	0.1223
2030.0	10.0	1.1745	0.0906	0.1339
2050.0	10.0	1.1662	0.0966	0.1931
2070.0	10.0	1.1785	0.1049	0.1818

F.2.6 $\gamma n \rightarrow \eta n$ as a Function of W
Angular Distributions

$\cos(\theta_\eta^*)$	W=(1487.5±2.5) MeV			W=(1492.5±2.5) MeV			W=(1497.5±2.5) MeV			W=(1505.0±5.0) MeV		
	$d\sigma/d\Omega$			$d\sigma/d\Omega$			$d\sigma/d\Omega$			$d\sigma/d\Omega$		
	$[\mu\text{b}/\text{sr}]$	Δ_{stat}	Δ_{sys}									
-0.88	0.0000	0.0000	0.0000	0.4551	0.1865	0.0712	0.9602	0.2168	0.0332	1.1235	0.1466	0.0239
-0.62	0.1896	0.1386	0.0068	0.6067	0.1538	0.0446	0.8442	0.1514	0.0453	1.0752	0.1101	0.0215
-0.38	0.3089	0.1561	0.0162	0.3505	0.1089	0.0175	0.6846	0.1310	0.0430	1.0491	0.1052	0.0310
-0.12	0.1050	0.0750	0.0080	0.5953	0.1504	0.0307	1.0488	0.1666	0.0677	0.8352	0.0915	0.0292
0.12	0.1238	0.0912	0.0173	0.7420	0.1624	0.0426	0.5653	0.1181	0.0315	0.7891	0.0874	0.0280
0.38	0.1272	0.0899	0.0242	0.6372	0.1483	0.0683	0.8736	0.1459	0.0717	0.8483	0.0909	0.0666
0.62	0.5165	0.2310	0.1126	0.6800	0.1628	0.1271	0.6832	0.1286	0.0780	0.7587	0.0857	0.0864
0.88	0.2735	0.2735	0.0566	0.8155	0.2383	0.1525	0.6441	0.1641	0.0423	0.7490	0.1076	0.0547
<hr/>												
$\cos(\theta_\eta^*)$	W=(1515.0±5.0) MeV			W=(1525.0±5.0) MeV			W=(1535.0±5.0) MeV			W=(1545.0±5.0) MeV		
	$d\sigma/d\Omega$			$d\sigma/d\Omega$			$d\sigma/d\Omega$			$d\sigma/d\Omega$		
	$[\mu\text{b}/\text{sr}]$	Δ_{stat}	Δ_{sys}									
-0.88	1.1113	0.1327	0.0478	1.1436	0.1265	0.0934	1.0703	0.1198	0.0996	1.0045	0.1173	0.0698
-0.62	0.9773	0.0993	0.0253	1.0680	0.1007	0.0441	0.9151	0.0932	0.0477	0.9807	0.0967	0.0393
-0.38	1.0389	0.0951	0.0252	0.7649	0.0773	0.0258	0.8953	0.0849	0.0280	0.7433	0.0789	0.0228
-0.12	0.9219	0.0901	0.0257	0.8616	0.0828	0.0293	0.7277	0.0726	0.0214	0.7947	0.0756	0.0240
0.12	0.9648	0.0903	0.0242	0.9756	0.0857	0.0299	0.7441	0.0723	0.0243	0.8334	0.0758	0.0272
0.38	1.1589	0.0987	0.0540	0.8592	0.0802	0.0474	0.9416	0.0817	0.0552	0.8844	0.0807	0.0418
0.62	0.8606	0.0867	0.0916	0.8720	0.0831	0.1011	0.5980	0.0673	0.0672	0.5628	0.0659	0.0442
0.88	0.6398	0.0893	0.1050	0.4535	0.0718	0.0785	0.6247	0.0843	0.0952	0.5352	0.0789	0.0610
<hr/>												
$\cos(\theta_\eta^*)$	W=(1555.0±5.0) MeV			W=(1565.0±5.0) MeV			W=(1575.0±5.0) MeV			W=(1585.0±5.0) MeV		
	$d\sigma/d\Omega$			$d\sigma/d\Omega$			$d\sigma/d\Omega$			$d\sigma/d\Omega$		
	$[\mu\text{b}/\text{sr}]$	Δ_{stat}	Δ_{sys}									
-0.88	1.0391	0.1237	0.0706	1.1914	0.1416	0.1277	1.2766	0.1526	0.1329	1.2617	0.1510	0.1482
-0.62	0.8959	0.0928	0.0349	0.8830	0.0932	0.0349	0.7399	0.0863	0.0283	0.6076	0.0787	0.0335
-0.38	0.7252	0.0773	0.0192	0.6596	0.0735	0.0188	0.6254	0.0717	0.0161	0.6747	0.0746	0.0196
-0.12	0.6519	0.0699	0.0188	0.7413	0.0753	0.0232	0.4840	0.0610	0.0144	0.5548	0.0651	0.0090
0.12	0.6535	0.0681	0.0255	0.6896	0.0715	0.0247	0.5315	0.0632	0.0192	0.4907	0.0621	0.0099
0.38	0.6652	0.0724	0.0359	0.7247	0.0761	0.0304	0.5495	0.0666	0.0303	0.6250	0.0729	0.0290
0.62	0.5965	0.0702	0.0489	0.6910	0.0784	0.0405	0.3478	0.0568	0.0291	0.5388	0.0704	0.0446
0.88	0.5553	0.0833	0.0659	0.6489	0.0963	0.0603	0.6297	0.0986	0.0728	0.4570	0.0859	0.0478
<hr/>												
$\cos(\theta_\eta^*)$	W=(1595.0±5.0) MeV			W=(1605.0±5.0) MeV			W=(1615.0±5.0) MeV			W=(1625.0±5.0) MeV		
	$d\sigma/d\Omega$			$d\sigma/d\Omega$			$d\sigma/d\Omega$			$d\sigma/d\Omega$		
	$[\mu\text{b}/\text{sr}]$	Δ_{stat}	Δ_{sys}									
-0.88	1.0383	0.1376	0.1733	0.9972	0.1379	0.1138	0.7929	0.1239	0.0926	0.6286	0.1098	0.0408
-0.62	0.6182	0.0796	0.0358	0.5512	0.0765	0.0324	0.4396	0.0709	0.0206	0.4821	0.0738	0.0149
-0.38	0.4660	0.0623	0.0157	0.4133	0.0587	0.0209	0.4349	0.0620	0.0103	0.5031	0.0672	0.0096
-0.12	0.3703	0.0531	0.0213	0.4030	0.0555	0.0164	0.3765	0.0559	0.0115	0.3357	0.0543	0.0103
0.12	0.5101	0.0657	0.0322	0.3871	0.0578	0.0122	0.4583	0.0628	0.0188	0.5139	0.0671	0.0213
0.38	0.4423	0.0621	0.0224	0.4103	0.0570	0.0175	0.2984	0.0468	0.0161	0.4440	0.0565	0.0229
0.62	0.3913	0.0611	0.0256	0.3515	0.0566	0.0241	0.2436	0.0467	0.0173	0.3061	0.0526	0.0192
0.88	0.4713	0.0855	0.0406	0.2513	0.0603	0.0216	0.2447	0.0600	0.0192	0.2294	0.0616	0.0141
<hr/>												
$\cos(\theta_\eta^*)$	W=(1635.0±5.0) MeV			W=(1645.0±5.0) MeV			W=(1655.0±5.0) MeV			W=(1670.0±10.0) MeV		
	$d\sigma/d\Omega$			$d\sigma/d\Omega$			$d\sigma/d\Omega$			$d\sigma/d\Omega$		
	$[\mu\text{b}/\text{sr}]$	Δ_{stat}	Δ_{sys}									
-0.88	0.6037	0.1051	0.0177	0.5183	0.0973	0.0405	0.6454	0.1110	0.0234	0.7279	0.0893	0.0340
-0.62	0.4302	0.0677	0.0116	0.3573	0.0635	0.0230	0.4371	0.0744	0.0190	0.4405	0.0559	0.0181
-0.38	0.3507	0.0565	0.0117	0.4603	0.0677	0.0263	0.5490	0.0768	0.0235	0.4744	0.0522	0.0205
-0.12	0.3764	0.0590	0.0151	0.4749	0.0708	0.0230	0.7605	0.0966	0.0329	0.5297	0.0599	0.0227
0.12	0.4691	0.0628	0.0186	0.4587	0.0628	0.0157	0.5985	0.0735	0.0262	0.4907	0.0472	0.0167
0.38	0.3959	0.0543	0.0138	0.4305	0.0593	0.0115	0.5620	0.0699	0.0227	0.5020	0.0472	0.0132
0.62	0.3845	0.0599	0.0190	0.4110	0.0635	0.0228	0.3297	0.0577	0.0226	0.3652	0.0440	0.0176
0.88	0.2113	0.0642	0.0183	0.3446	0.0857	0.0465	0.2041	0.0645	0.0314	0.1568	0.0395	0.0177

F.2. UNPOLARISED CROSS SECTIONS FROM LD₂ (CBELSA/TAPS)

$\cos(\theta_\eta^*)$	W=(1690.0±10.0) MeV			W=(1710.0±10.0) MeV			W=(1730.0±10.0) MeV			W=(1750.0±10.0) MeV		
	$d\sigma/d\Omega$	Δ_{stat}	Δ_{sys}									
	[$\mu\text{b}/\text{sr}$]											
-0.88	0.5128	0.0801	0.0215	0.3691	0.0672	0.0211	0.1326	0.0382	0.0096	0.1435	0.0410	0.0166
-0.62	0.4529	0.0583	0.0126	0.2401	0.0431	0.0140	0.2128	0.0403	0.0142	0.2202	0.0420	0.0217
-0.38	0.3972	0.0497	0.0119	0.3683	0.0492	0.0181	0.2255	0.0386	0.0152	0.3320	0.0477	0.0254
-0.12	0.4753	0.0578	0.0187	0.3935	0.0541	0.0186	0.3872	0.0537	0.0254	0.3617	0.0527	0.0208
0.12	0.3390	0.0394	0.0126	0.4261	0.0450	0.0145	0.3441	0.0401	0.0131	0.3402	0.0403	0.0132
0.38	0.3592	0.0404	0.0140	0.3508	0.0410	0.0080	0.3430	0.0400	0.0103	0.2999	0.0381	0.0136
0.62	0.3142	0.0430	0.0257	0.3502	0.0474	0.0239	0.1690	0.0325	0.0151	0.2214	0.0380	0.0171
0.88	0.1234	0.0368	0.0216	0.1061	0.0363	0.0185	0.1562	0.0464	0.0292	0.2110	0.0573	0.0213
<hr/>												
$\cos(\theta_\eta^*)$	W=(1770.0±10.0) MeV			W=(1790.0±10.0) MeV			W=(1810.0±10.0) MeV			W=(1830.0±10.0) MeV		
	$d\sigma/d\Omega$	Δ_{stat}	Δ_{sys}									
	[$\mu\text{b}/\text{sr}$]											
-0.88	0.2178	0.0566	0.0318	0.2570	0.0645	0.0130	0.1985	0.0515	0.0131	0.0769	0.0322	0.0125
-0.62	0.1539	0.0370	0.0169	0.1552	0.0383	0.0076	0.1803	0.0406	0.0124	0.1615	0.0397	0.0173
-0.38	0.2134	0.0397	0.0147	0.2058	0.0398	0.0121	0.2148	0.0408	0.0139	0.2191	0.0430	0.0163
-0.12	0.3100	0.0494	0.0132	0.2629	0.0455	0.0134	0.2778	0.0461	0.0153	0.3051	0.0492	0.0142
0.12	0.3474	0.0427	0.0137	0.3228	0.0421	0.0104	0.2902	0.0392	0.0117	0.2579	0.0381	0.0063
0.38	0.3002	0.0404	0.0152	0.3292	0.0434	0.0089	0.2627	0.0381	0.0094	0.2904	0.0412	0.0076
0.62	0.2790	0.0458	0.0214	0.2270	0.0427	0.0118	0.1874	0.0379	0.0133	0.1286	0.0327	0.0098
0.88	0.0975	0.0412	0.0121	0.1970	0.0556	0.0239	0.0238	0.0186	0.0034	0.1044	0.0401	0.0192
<hr/>												
$\cos(\theta_\eta^*)$	W=(1850.0±10.0) MeV			W=(1870.0±10.0) MeV			W=(1890.0±10.0) MeV			W=(1910.0±10.0) MeV		
	$d\sigma/d\Omega$	Δ_{stat}	Δ_{sys}									
	[$\mu\text{b}/\text{sr}$]											
-0.88	0.2447	0.0626	0.0386	0.2298	0.0719	0.0160	0.2100	0.0730	0.0429	0.2665	0.0877	0.0274
-0.62	0.2225	0.0501	0.0148	0.1676	0.0481	0.0134	0.1189	0.0415	0.0184	0.0476	0.0255	0.0075
-0.38	0.1689	0.0402	0.0077	0.1979	0.0455	0.0184	0.1336	0.0367	0.0111	0.0999	0.0314	0.0156
-0.12	0.3156	0.0521	0.0130	0.2801	0.0512	0.0290	0.1915	0.0420	0.0087	0.1798	0.0421	0.0182
0.12	0.2901	0.0425	0.0095	0.2666	0.0430	0.0237	0.2206	0.0389	0.0089	0.1142	0.0295	0.0072
0.38	0.2757	0.0432	0.0086	0.2751	0.0465	0.0177	0.2104	0.0420	0.0102	0.2507	0.0489	0.0155
0.62	0.2617	0.0509	0.0257	0.1919	0.0473	0.0157	0.1221	0.0389	0.0113	0.1166	0.0416	0.0131
0.88	0.0555	0.0328	0.0168	0.0569	0.0333	0.0110	0.0181	0.0184	0.0034	0.0401	0.0290	0.0095
<hr/>												
$\cos(\theta_\eta^*)$	W=(1930.0±10.0) MeV			W=(1950.0±10.0) MeV			W=(1970.0±10.0) MeV			W=(1990.0±10.0) MeV		
	$d\sigma/d\Omega$	Δ_{stat}	Δ_{sys}									
	[$\mu\text{b}/\text{sr}$]											
-0.88	0.1182	0.0557	0.0124	0.0553	0.0334	0.0097	0.0802	0.0376	0.0132	0.0299	0.0243	0.0058
-0.62	0.0521	0.0245	0.0069	0.0382	0.0202	0.0053	0.0493	0.0228	0.0053	0.0428	0.0224	0.0047
-0.38	0.0890	0.0290	0.0109	0.0873	0.0282	0.0104	0.0518	0.0218	0.0039	0.0552	0.0230	0.0051
-0.12	0.1474	0.0414	0.0147	0.0887	0.0323	0.0086	0.0522	0.0244	0.0032	0.0638	0.0271	0.0048
0.12	0.1861	0.0396	0.0130	0.1723	0.0395	0.0104	0.1882	0.0418	0.0097	0.1788	0.0418	0.0138
0.38	0.2018	0.0471	0.0144	0.1838	0.0468	0.0112	0.0990	0.0357	0.0067	0.1830	0.0511	0.0344
0.62	0.1341	0.0476	0.0161	0.1028	0.0425	0.0167	0.0907	0.0412	0.0139	0.0427	0.0304	0.0126
0.88	0.0730	0.0424	0.0144	0.0553	0.0403	0.0281	0.0631	0.0449	0.0203	0.0734	0.0531	0.0197
<hr/>												
$\cos(\theta_\eta^*)$	W=(2010.0±10.0) MeV			W=(2030.0±10.0) MeV			W=(2050.0±10.0) MeV			W=(2070.0±10.0) MeV		
	$d\sigma/d\Omega$	Δ_{stat}	Δ_{sys}									
	[$\mu\text{b}/\text{sr}$]											
-0.88	0.0148	0.0184	0.0029	-0.0013	0.0008	0.0004	-0.0010	0.0007	0.0004	0.0238	0.0255	0.0077
-0.62	0.0342	0.0211	0.0062	0.0098	0.0127	0.0019	0.0277	0.0200	0.0085	-0.0006	0.0004	0.0001
-0.38	0.0546	0.0234	0.0104	0.0551	0.0234	0.0074	0.0085	0.0103	0.0016	0.0304	0.0182	0.0049
-0.12	0.0972	0.0333	0.0160	0.0507	0.0234	0.0075	0.0499	0.0237	0.0050	0.0771	0.0299	0.0066
0.12	0.0645	0.0259	0.0081	0.0849	0.0290	0.0107	0.0506	0.0231	0.0041	0.0788	0.0303	0.0063
0.38	0.1208	0.0430	0.0140	0.1278	0.0459	0.0110	0.0746	0.0379	0.0091	0.0819	0.0432	0.0093
0.62	0.1165	0.0529	0.0175	0.1218	0.0550	0.0210	0.0876	0.0506	0.0160	0.0725	0.0522	0.0127
0.88	0.2155	0.0973	0.0480	0.0480	0.0480	0.0242	0.0000	0.0000	0.0000	0.0000	0.0000	0.0000

Total Cross Sections

W [MeV]	ΔW [MeV]	σ [μ b]	Δ_{stat} [μ b]	Δ_{sys} [μ b]
1487.5	2.5	2.7765	0.9496	0.3673
1492.5	2.5	7.4351	0.7300	0.8797
1497.5	2.5	9.6066	0.6778	0.6402
1505.0	5.0	11.3608	0.4654	0.5452
1515.0	5.0	12.0046	0.4383	0.6337
1525.0	5.0	10.9450	0.4001	0.7112
1535.0	5.0	10.1202	0.3807	0.6906
1545.0	5.0	9.8454	0.3769	0.5179
1555.0	5.0	9.0962	0.3748	0.5050
1565.0	5.0	9.7613	0.4030	0.5563
1575.0	5.0	7.8313	0.3756	0.4962
1585.0	5.0	7.9952	0.3778	0.5192
1595.0	5.0	6.6517	0.3496	0.5396
1605.0	5.0	5.8682	0.3283	0.3964
1615.0	5.0	4.9715	0.3027	0.3037
1625.0	5.0	5.3194	0.3082	0.2363
1635.0	5.0	5.0304	0.2995	0.1943
1645.0	5.0	5.3339	0.3161	0.3196
1655.0	5.0	6.1457	0.3431	0.3053
1670.0	10.0	5.6992	0.2460	0.2457
1690.0	10.0	4.6034	0.2303	0.2125
1710.0	10.0	3.9796	0.2114	0.2055
1730.0	10.0	2.9573	0.1796	0.1998
1750.0	10.0	3.2939	0.1978	0.2354
1770.0	10.0	2.9492	0.1940	0.2167
1790.0	10.0	2.9921	0.2053	0.1522
1810.0	10.0	2.5463	0.1766	0.1425
1830.0	10.0	2.3579	0.1747	0.1613
1850.0	10.0	2.8103	0.2084	0.2054
1870.0	10.0	2.5814	0.2177	0.2222
1890.0	10.0	1.8928	0.1921	0.1800
1910.0	10.0	1.4527	0.1801	0.1455
1930.0	10.0	1.5314	0.1821	0.1561
1950.0	10.0	1.2044	0.1602	0.1558
1970.0	10.0	0.9926	0.1528	0.1168
1990.0	10.0	0.8645	0.1470	0.1355
2010.0	10.0	1.0753	0.2007	0.1811
2030.0	10.0	0.7331	0.1485	0.1317
2050.0	10.0	0.6012	0.2619	0.1189
2070.0	10.0	0.4353	0.2507	0.0628

F.3 Polarisation Observable E and Helicity Dependent Cross Sections from CBELSA/TAPS Data

F.3.1 E for $\gamma p \rightarrow \eta p$ as a Function of E_γ

Total Distributions for E

E_γ [MeV]	ΔE_γ [MeV]	E	Δ_{stat}	Δ_{sys}
730.0	30.0	1.0914	0.1770	0.0735
790.0	30.0	1.0545	0.1240	0.0734
850.0	30.0	1.0712	0.1392	0.0718
920.0	40.0	1.0440	0.1458	0.0744
990.0	30.0	0.9059	0.2623	0.0643
1070.0	50.0	0.2927	0.1731	0.0385
1170.0	50.0	0.5610	0.1705	0.0259
1280.0	60.0	0.4107	0.1719	0.0302
1400.0	60.0	0.6341	0.2248	0.0320
1535.0	75.0	0.3373	0.2151	0.0292
1685.0	75.0	0.3134	0.2466	0.0272
1840.0	80.0	-0.3919	0.3372	0.0243

F.3.2 Helicity Dependent Cross Sections for $\gamma p \rightarrow \eta p$ as a Function of E_γ

Total Cross Sections $\sigma_{1/2}$ and $\sigma_{3/2}$

E_γ [MeV]	ΔE_γ [MeV]	$\sigma_{1/2}$ [μb]	Δ_{stat} [μb]	Δ_{sys} [μb]	E_γ [MeV]	ΔE_γ [MeV]	$\sigma_{3/2}$ [μb]	Δ_{stat} [μb]	Δ_{sys} [μb]
730.0	30.0	14.4944	1.2324	0.9767	730.0	30.0	-0.6333	1.2324	0.2350
790.0	30.0	26.7853	1.6229	1.6899	790.0	30.0	-0.7111	1.6229	0.4030
850.0	30.0	24.9936	1.6867	1.6733	850.0	30.0	-0.8589	1.6867	0.3552
920.0	40.0	17.7623	1.2721	1.2577	920.0	40.0	-0.3824	1.2721	0.3075
990.0	30.0	9.8079	1.3534	0.8147	990.0	30.0	0.4842	1.3534	0.2955
1070.0	50.0	4.7536	0.6391	0.4340	1070.0	50.0	2.6010	0.6391	0.2027
1170.0	50.0	5.1172	0.5622	0.2615	1170.0	50.0	1.4390	0.5622	0.1104
1280.0	60.0	3.7891	0.4642	0.2359	1280.0	60.0	1.5829	0.4642	0.0795
1400.0	60.0	3.5222	0.4877	0.2062	1400.0	60.0	0.7886	0.4877	0.0722
1535.0	75.0	2.2789	0.3693	0.1746	1535.0	75.0	1.1293	0.3693	0.0830
1685.0	75.0	1.6563	0.3143	0.1336	1685.0	75.0	0.8658	0.3143	0.0993
1840.0	80.0	0.6190	0.3464	0.0404	1840.0	80.0	1.4170	0.3464	0.0879

F.3.3 E for $\gamma n \rightarrow \eta(n)$ as a Function of E_γ

Total Distributions for E

E_γ [MeV]	ΔE_γ [MeV]	E	Δ_{stat}	Δ_{sys}
730.0	30.0	1.0134	0.1772	0.1219
790.0	30.0	0.9732	0.1329	0.1004
850.0	30.0	1.0830	0.1777	0.0935
920.0	40.0	0.7225	0.1818	0.0812
990.0	30.0	0.7143	0.2097	0.0631
1070.0	50.0	0.7214	0.1853	0.0544
1170.0	50.0	0.7423	0.1968	0.0453
1280.0	60.0	0.5606	0.2067	0.0259
1400.0	60.0	0.4367	0.2166	0.0459
1535.0	75.0	0.7575	0.3716	0.1612
1685.0	75.0	1.3090	0.7436	0.2256
1840.0	80.0	0.6480	0.4872	0.0779

F.3.4 Helicity Dependent Cross Sections for $\gamma n \rightarrow \eta(n)$ as a Function of E_γ

Total Cross Sections $\sigma_{1/2}$ and $\sigma_{3/2}$

E_γ [MeV]	ΔE_γ [MeV]	$\sigma_{1/2}$ [μb]	Δ_{stat} [μb]	Δ_{sys} [μb]	E_γ [MeV]	ΔE_γ [MeV]	$\sigma_{3/2}$ [μb]	Δ_{stat} [μb]	Δ_{sys} [μb]
730.0	30.0	14.0482	1.2377	1.6902	730.0	30.0	-0.0935	1.2377	0.7374
790.0	30.0	20.2843	1.3691	1.8253	790.0	30.0	0.2760	1.3691	0.7337
850.0	30.0	16.9132	1.4458	1.6645	850.0	30.0	-0.6740	1.4458	0.7046
920.0	40.0	10.3397	1.0931	1.2070	920.0	40.0	1.6658	1.0931	0.5558
990.0	30.0	8.7975	1.0787	0.7670	990.0	30.0	1.4664	1.0787	0.3408
1070.0	50.0	7.2303	0.7806	0.5280	1070.0	50.0	1.1702	0.7806	0.1915
1170.0	50.0	5.6924	0.6456	0.3692	1170.0	50.0	0.8418	0.6456	0.1028
1280.0	60.0	3.8888	0.5170	0.2311	1280.0	60.0	1.0949	0.5170	0.0579
1400.0	60.0	3.0089	0.4562	0.2504	1400.0	60.0	1.1797	0.4562	0.1095
1535.0	75.0	2.7853	0.5910	0.4789	1535.0	75.0	0.3843	0.5910	0.2565
1685.0	75.0	3.0086	0.9713	0.5616	1685.0	75.0	-0.4027	0.9713	0.3068
1840.0	80.0	1.6147	0.4798	0.1941	1840.0	80.0	0.3449	0.4798	0.1041

F.3.5 E for $\gamma p \rightarrow \eta p$ as a Function of W

Total Distributions for E

W [MeV]	ΔW [MeV]	E	Δ_{stat}	Δ_{sys}
1495.0	15.0	1.0215	0.2054	0.0855
1525.0	15.0	1.0439	0.1290	0.0738
1555.0	15.0	1.1094	0.1466	0.0765
1585.0	15.0	0.9268	0.1721	0.0782
1615.0	15.0	0.9405	0.1907	0.0720
1645.0	15.0	1.0114	0.2445	0.0649
1675.0	15.0	0.8312	0.2824	0.0550
1705.0	15.0	0.5116	0.2212	0.0457
1735.0	15.0	0.5271	0.1962	0.0414
1765.0	15.0	0.7251	0.2459	0.0325
1795.0	15.0	0.0751	0.2350	0.0226
1825.0	15.0	0.3691	0.3055	0.0249
1870.0	30.0	0.3280	0.2028	0.0351
1930.0	30.0	0.6929	0.2333	0.0416
1990.0	30.0	0.5228	0.3189	0.0415
2050.0	30.0	-0.1907	0.2664	0.0416

F.3.6 Helicity Dependent Cross Sections for $\gamma p \rightarrow \eta p$ as a Function of W

Total Cross Sections $\sigma_{1/2}$ and $\sigma_{3/2}$

W [MeV]	ΔW [MeV]	$\sigma_{1/2}$ [μb]	Δ_{stat} [μb]	Δ_{sys} [μb]	W [MeV]	ΔW [MeV]	$\sigma_{3/2}$ [μb]	Δ_{stat} [μb]	Δ_{sys} [μb]
1495.0	15.0	18.0379	1.8404	1.5093	1495.0	15.0	-0.1921	1.8404	0.5317
1525.0	15.0	32.0138	2.0293	1.9970	1525.0	15.0	-0.6881	2.0293	0.4430
1555.0	15.0	30.4562	2.1254	2.1989	1555.0	15.0	-1.5794	2.1254	0.6064
1585.0	15.0	22.5978	2.0251	1.8892	1585.0	15.0	0.8591	2.0251	0.6499
1615.0	15.0	16.0824	1.5863	1.2276	1615.0	15.0	0.4934	1.5863	0.3943
1645.0	15.0	9.5658	1.1676	0.6575	1645.0	15.0	-0.0543	1.1676	0.1542
1675.0	15.0	5.8077	0.8992	0.3857	1675.0	15.0	0.5352	0.8992	0.0936
1705.0	15.0	4.9392	0.7266	0.3327	1705.0	15.0	1.5959	0.7266	0.1289
1735.0	15.0	5.0506	0.6532	0.3425	1735.0	15.0	1.5641	0.6532	0.1668
1765.0	15.0	5.1772	0.7424	0.3080	1765.0	15.0	0.8252	0.7424	0.1761
1795.0	15.0	2.9814	0.6551	0.2872	1795.0	15.0	2.5650	0.6551	0.1960
1825.0	15.0	3.6809	0.8247	0.3064	1825.0	15.0	1.6961	0.8247	0.2061
1870.0	30.0	3.3645	0.5169	0.2758	1870.0	30.0	1.7024	0.5169	0.1482
1930.0	30.0	3.0902	0.4302	0.2025	1930.0	30.0	0.5606	0.4302	0.0724
1990.0	30.0	2.0477	0.4321	0.1742	1990.0	30.0	0.6417	0.4321	0.0992
2050.0	30.0	0.8348	0.2787	0.2221	2050.0	30.0	1.2282	0.2787	0.2679

F.4 Polarisation Observable E and Helicity Dependent Cross Sections from A2 Data

F.4.1 E for $\gamma p \rightarrow \eta p$ as a Function of E_γ

Angular Distributions for E

$\cos(\theta_\eta^*)$	$E_\gamma = (725.0 \pm 15.0) \text{ MeV}$			$E_\gamma = (755.0 \pm 15.0) \text{ MeV}$			$E_\gamma = (785.0 \pm 15.0) \text{ MeV}$			$E_\gamma = (815.0 \pm 15.0) \text{ MeV}$		
	E	Δ_{stat}	Δ_{sys}									
-0.80	1.0369	0.1048	0.1166	0.8668	0.0651	0.0940	0.9173	0.0682	0.0951	0.8895	0.0604	0.0925
-0.40	0.9955	0.1261	0.1486	1.0172	0.0801	0.1390	0.8529	0.0698	0.0937	1.0539	0.0608	0.1092
0.00	1.0058	0.2054	0.1916	0.8844	0.1031	0.1339	0.8940	0.0898	0.1201	1.1099	0.0730	0.1304
0.40	0.4610	0.2877	0.0866	1.2922	0.2133	0.3087	1.1400	0.1388	0.1788	0.9533	0.0939	0.1148
0.80	1.2303	0.3311	0.2081	1.3657	0.2773	0.3032	1.5898	0.3301	0.3395	1.2164	0.2862	0.2123
$\cos(\theta_\eta^*)$	$E_\gamma = (845.0 \pm 15.0) \text{ MeV}$			$E_\gamma = (875.0 \pm 15.0) \text{ MeV}$			$E_\gamma = (905.0 \pm 15.0) \text{ MeV}$			$E_\gamma = (935.0 \pm 15.0) \text{ MeV}$		
	E	Δ_{stat}	Δ_{sys}									
-0.80	0.8816	0.0674	0.0917	1.0227	0.0729	0.1062	0.9253	0.0805	0.0966	0.6925	0.0901	0.0717
-0.40	0.8807	0.0647	0.0913	0.7994	0.0636	0.0976	0.9357	0.0773	0.1030	0.7574	0.0756	0.1194
0.00	0.9522	0.0709	0.1091	1.0959	0.0725	0.1238	0.8737	0.0707	0.0906	0.7626	0.0776	0.0791
0.40	1.0458	0.0862	0.1333	0.9707	0.0780	0.1167	0.9331	0.0804	0.1012	0.8542	0.0940	0.0927
0.80	1.5773	0.4233	0.3894	0.3257	0.2078	0.0394	0.9168	0.2386	0.1405	1.0184	0.2320	0.1255
$\cos(\theta_\eta^*)$	$E_\gamma = (965.0 \pm 15.0) \text{ MeV}$			$E_\gamma = (995.0 \pm 15.0) \text{ MeV}$			$E_\gamma = (1025.0 \pm 15.0) \text{ MeV}$			$E_\gamma = (1055.0 \pm 15.0) \text{ MeV}$		
	E	Δ_{stat}	Δ_{sys}									
-0.80	0.6085	0.1075	0.0638	0.8633	0.1246	0.1085	0.3966	0.1293	0.0415	0.4327	0.1367	0.0499
-0.40	0.6866	0.0971	0.0894	0.5417	0.0801	0.0999	0.4403	0.0891	0.0862	0.3936	0.1135	0.0433
0.00	0.7421	0.0944	0.0770	0.6174	0.0872	0.0642	0.5435	0.0960	0.0566	0.4591	0.0934	0.0492
0.40	0.8588	0.1059	0.1031	0.7926	0.1037	0.0953	0.5294	0.1059	0.0562	0.5293	0.1033	0.0583
0.80	1.2433	0.3684	0.2536	1.6264	0.3979	0.3641	0.7340	0.4596	0.1845	2.6008	0.7603	0.7699
$\cos(\theta_\eta^*)$	$E_\gamma = (1085.0 \pm 15.0) \text{ MeV}$			$E_\gamma = (1120.0 \pm 20.0) \text{ MeV}$			$E_\gamma = (1160.0 \pm 20.0) \text{ MeV}$			$E_\gamma = (1200.0 \pm 20.0) \text{ MeV}$		
	E	Δ_{stat}	Δ_{sys}									
-0.80	0.5227	0.1702	0.0543	0.5594	0.2040	0.0593	0.0944	0.1760	0.0112	0.3045	0.1518	0.0372
-0.40	0.6924	0.1153	0.0925	0.2420	0.1462	0.0251	0.3061	0.1160	0.0387	0.4614	0.1210	0.0491
0.00	0.2448	0.0938	0.0267	0.3676	0.1072	0.0381	0.5187	0.0942	0.0549	0.3327	0.0934	0.0364
0.40	0.6644	0.1047	0.0697	0.4138	0.1056	0.0429	0.5019	0.0995	0.0639	0.7217	0.0946	0.0797
0.80	0.6312	0.2691	0.0925	1.1934	0.2678	0.1931	0.4161	0.1678	0.0462	0.8738	0.1960	0.1158
$\cos(\theta_\eta^*)$	$E_\gamma = (1240.0 \pm 20.0) \text{ MeV}$			$E_\gamma = (1280.0 \pm 20.0) \text{ MeV}$			$E_\gamma = (1320.0 \pm 20.0) \text{ MeV}$			$E_\gamma = (1360.0 \pm 20.0) \text{ MeV}$		
	E	Δ_{stat}	Δ_{sys}									
-0.80	0.3554	0.1609	0.0691	0.6485	0.1959	0.1074	0.1748	0.1860	0.0216	0.1964	0.2121	0.0220
-0.40	0.4174	0.1447	0.0439	0.4493	0.1438	0.0792	0.3952	0.1566	0.0472	0.4346	0.1888	0.0455
0.00	0.4833	0.1004	0.0502	0.5440	0.1168	0.0564	0.6784	0.1382	0.0851	0.3738	0.1376	0.0413
0.40	0.4076	0.1019	0.0423	0.7420	0.1347	0.0991	0.6896	0.1450	0.0942	0.5820	0.1368	0.0615
0.80	0.9061	0.2168	0.1218	1.1420	0.2632	0.1866	1.3393	0.3192	0.2905	0.9583	0.2107	0.1088

$\cos(\theta_\eta^*)$	$E_\gamma = (1400.0 \pm 20.0) \text{ MeV}$		
	E	Δ_{stat}	Δ_{sys}
-0.80	0.0315	0.3245	0.0033
-0.40	0.0384	0.3180	0.0069
0.00	0.1664	0.1872	0.0191
0.40	0.5917	0.2265	0.1073
0.80	1.5634	0.5000	0.3697

Total Distributions for E

E_γ [MeV]	ΔE_γ [MeV]	E	Δ_{stat}	Δ_{sys}
725.0	15.0	0.9694	0.0872	0.1494
755.0	15.0	1.0294	0.0584	0.1497
785.0	15.0	1.0377	0.0597	0.1398
815.0	15.0	1.0249	0.0546	0.1260
845.0	15.0	1.0103	0.0570	0.1127
875.0	15.0	0.8328	0.0476	0.0992
905.0	15.0	0.9206	0.0495	0.0906
935.0	15.0	0.8060	0.0508	0.0873
965.0	15.0	0.7824	0.0611	0.0844
995.0	15.0	0.7801	0.0568	0.0751
1025.0	15.0	0.4950	0.0600	0.0628
1055.0	15.0	0.6079	0.0649	0.0590
1085.0	15.0	0.5474	0.0627	0.0584
1120.0	20.0	0.5228	0.0698	0.0525
1160.0	20.0	0.3896	0.0575	0.0485
1200.0	20.0	0.5520	0.0575	0.0516
1240.0	20.0	0.5112	0.0632	0.0611
1280.0	20.0	0.7019	0.0751	0.0730
1320.0	20.0	0.6616	0.0814	0.0735
1360.0	20.0	0.5543	0.0788	0.0706
1400.0	20.0	0.5162	0.1327	0.0858

F.4.2 Helicity Dependent Cross Sections for $\gamma p \rightarrow \eta p$ as a Function of E_γ
Angular Cross Sections $\sigma_{1/2}$

$\cos(\theta_\eta^*)$	$E_\gamma = (725.0 \pm 15.0) \text{ MeV}$			$E_\gamma = (755.0 \pm 15.0) \text{ MeV}$			$E_\gamma = (785.0 \pm 15.0) \text{ MeV}$			$E_\gamma = (815.0 \pm 15.0) \text{ MeV}$		
	$d\sigma_{1/2}/d\Omega$ [$\mu\text{b}/\text{sr}$]	Δ_{stat} [$\mu\text{b}/\text{sr}$]	Δ_{sys} [$\mu\text{b}/\text{sr}$]	$d\sigma_{1/2}/d\Omega$ [$\mu\text{b}/\text{sr}$]	Δ_{stat} [$\mu\text{b}/\text{sr}$]	Δ_{sys} [$\mu\text{b}/\text{sr}$]	$d\sigma_{1/2}/d\Omega$ [$\mu\text{b}/\text{sr}$]	Δ_{stat} [$\mu\text{b}/\text{sr}$]	Δ_{sys} [$\mu\text{b}/\text{sr}$]	$d\sigma_{1/2}/d\Omega$ [$\mu\text{b}/\text{sr}$]	Δ_{stat} [$\mu\text{b}/\text{sr}$]	Δ_{sys} [$\mu\text{b}/\text{sr}$]
-0.80	1.3783	0.0725	0.1550	1.6237	0.0582	0.1761	1.8156	0.0662	0.1883	1.7070	0.0563	0.1776
-0.40	1.2667	0.0815	0.1891	1.8423	0.0749	0.2517	1.8722	0.0733	0.2058	2.0465	0.0648	0.2120
0.00	1.1102	0.1150	0.2115	1.6962	0.0958	0.2569	1.9760	0.0968	0.2654	2.1778	0.0798	0.2559
0.40	0.7291	0.1443	0.1369	1.9582	0.1843	0.4678	2.1864	0.1456	0.3429	1.9240	0.0962	0.2318
0.80	0.9863	0.1479	0.1668	1.6965	0.2010	0.3766	2.2913	0.2954	0.4893	2.1450	0.2807	0.3743
<hr/>												
$\cos(\theta_\eta^*)$	$E_\gamma = (845.0 \pm 15.0) \text{ MeV}$			$E_\gamma = (875.0 \pm 15.0) \text{ MeV}$			$E_\gamma = (905.0 \pm 15.0) \text{ MeV}$			$E_\gamma = (935.0 \pm 15.0) \text{ MeV}$		
	$d\sigma_{1/2}/d\Omega$ [$\mu\text{b}/\text{sr}$]	Δ_{stat} [$\mu\text{b}/\text{sr}$]	Δ_{sys} [$\mu\text{b}/\text{sr}$]	$d\sigma_{1/2}/d\Omega$ [$\mu\text{b}/\text{sr}$]	Δ_{stat} [$\mu\text{b}/\text{sr}$]	Δ_{sys} [$\mu\text{b}/\text{sr}$]	$d\sigma_{1/2}/d\Omega$ [$\mu\text{b}/\text{sr}$]	Δ_{stat} [$\mu\text{b}/\text{sr}$]	Δ_{sys} [$\mu\text{b}/\text{sr}$]	$d\sigma_{1/2}/d\Omega$ [$\mu\text{b}/\text{sr}$]	Δ_{stat} [$\mu\text{b}/\text{sr}$]	Δ_{sys} [$\mu\text{b}/\text{sr}$]
-0.80	1.5752	0.0586	0.1638	1.5074	0.0590	0.1565	1.2481	0.0537	0.1303	0.8895	0.0485	0.0921
-0.40	1.7982	0.0663	0.1864	1.4756	0.0589	0.1801	1.3196	0.0547	0.1453	0.9768	0.0438	0.1539
0.00	1.9323	0.0748	0.2214	1.8425	0.0722	0.2081	1.3874	0.0546	0.1438	1.0554	0.0484	0.1095
0.40	1.9055	0.0853	0.2429	1.6487	0.0716	0.1981	1.3224	0.0571	0.1435	0.9709	0.0510	0.1054
0.80	2.1588	0.3619	0.5329	1.0109	0.1649	0.1223	1.1880	0.1508	0.1821	0.9805	0.1158	0.1209
<hr/>												
$\cos(\theta_\eta^*)$	$E_\gamma = (965.0 \pm 15.0) \text{ MeV}$			$E_\gamma = (995.0 \pm 15.0) \text{ MeV}$			$E_\gamma = (1025.0 \pm 15.0) \text{ MeV}$			$E_\gamma = (1055.0 \pm 15.0) \text{ MeV}$		
	$d\sigma_{1/2}/d\Omega$ [$\mu\text{b}/\text{sr}$]	Δ_{stat} [$\mu\text{b}/\text{sr}$]	Δ_{sys} [$\mu\text{b}/\text{sr}$]	$d\sigma_{1/2}/d\Omega$ [$\mu\text{b}/\text{sr}$]	Δ_{stat} [$\mu\text{b}/\text{sr}$]	Δ_{sys} [$\mu\text{b}/\text{sr}$]	$d\sigma_{1/2}/d\Omega$ [$\mu\text{b}/\text{sr}$]	Δ_{stat} [$\mu\text{b}/\text{sr}$]	Δ_{sys} [$\mu\text{b}/\text{sr}$]	$d\sigma_{1/2}/d\Omega$ [$\mu\text{b}/\text{sr}$]	Δ_{stat} [$\mu\text{b}/\text{sr}$]	Δ_{sys} [$\mu\text{b}/\text{sr}$]
-0.80	0.6618	0.0453	0.0694	0.6414	0.0443	0.0806	0.3867	0.0367	0.0405	0.3323	0.0326	0.0383
-0.40	0.7359	0.0437	0.0958	0.5615	0.0307	0.1036	0.4385	0.0284	0.0858	0.3921	0.0330	0.0431
0.00	0.8195	0.0458	0.0851	0.6302	0.0355	0.0655	0.5265	0.0341	0.0548	0.4539	0.0303	0.0486
0.40	0.8566	0.0503	0.1029	0.6520	0.0393	0.0784	0.4736	0.0340	0.0503	0.4909	0.0345	0.0541
0.80	0.8035	0.1341	0.1639	0.6979	0.1087	0.1562	0.3448	0.0926	0.0867	0.6898	0.1491	0.2042
<hr/>												
$\cos(\theta_\eta^*)$	$E_\gamma = (1085.0 \pm 15.0) \text{ MeV}$			$E_\gamma = (1120.0 \pm 20.0) \text{ MeV}$			$E_\gamma = (1160.0 \pm 20.0) \text{ MeV}$			$E_\gamma = (1200.0 \pm 20.0) \text{ MeV}$		
	$d\sigma_{1/2}/d\Omega$ [$\mu\text{b}/\text{sr}$]	Δ_{stat} [$\mu\text{b}/\text{sr}$]	Δ_{sys} [$\mu\text{b}/\text{sr}$]	$d\sigma_{1/2}/d\Omega$ [$\mu\text{b}/\text{sr}$]	Δ_{stat} [$\mu\text{b}/\text{sr}$]	Δ_{sys} [$\mu\text{b}/\text{sr}$]	$d\sigma_{1/2}/d\Omega$ [$\mu\text{b}/\text{sr}$]	Δ_{stat} [$\mu\text{b}/\text{sr}$]	Δ_{sys} [$\mu\text{b}/\text{sr}$]	$d\sigma_{1/2}/d\Omega$ [$\mu\text{b}/\text{sr}$]	Δ_{stat} [$\mu\text{b}/\text{sr}$]	Δ_{sys} [$\mu\text{b}/\text{sr}$]
-0.80	0.3075	0.0351	0.0320	0.2952	0.0395	0.0313	0.1861	0.0306	0.0221	0.1858	0.0224	0.0227
-0.40	0.4222	0.0301	0.0564	0.2853	0.0345	0.0296	0.2554	0.0237	0.0323	0.2822	0.0245	0.0300
0.00	0.3679	0.0288	0.0401	0.4056	0.0330	0.0420	0.4164	0.0271	0.0441	0.3594	0.0264	0.0393
0.40	0.5052	0.0333	0.0530	0.4455	0.0347	0.0461	0.4559	0.0316	0.0580	0.5089	0.0298	0.0562
0.80	0.3364	0.0572	0.0493	0.5533	0.0710	0.0895	0.3242	0.0404	0.0360	0.4199	0.0465	0.0557
<hr/>												
$\cos(\theta_\eta^*)$	$E_\gamma = (1240.0 \pm 20.0) \text{ MeV}$			$E_\gamma = (1280.0 \pm 20.0) \text{ MeV}$			$E_\gamma = (1320.0 \pm 20.0) \text{ MeV}$			$E_\gamma = (1360.0 \pm 20.0) \text{ MeV}$		
	$d\sigma_{1/2}/d\Omega$ [$\mu\text{b}/\text{sr}$]	Δ_{stat} [$\mu\text{b}/\text{sr}$]	Δ_{sys} [$\mu\text{b}/\text{sr}$]	$d\sigma_{1/2}/d\Omega$ [$\mu\text{b}/\text{sr}$]	Δ_{stat} [$\mu\text{b}/\text{sr}$]	Δ_{sys} [$\mu\text{b}/\text{sr}$]	$d\sigma_{1/2}/d\Omega$ [$\mu\text{b}/\text{sr}$]	Δ_{stat} [$\mu\text{b}/\text{sr}$]	Δ_{sys} [$\mu\text{b}/\text{sr}$]	$d\sigma_{1/2}/d\Omega$ [$\mu\text{b}/\text{sr}$]	Δ_{stat} [$\mu\text{b}/\text{sr}$]	Δ_{sys} [$\mu\text{b}/\text{sr}$]
-0.80	0.1659	0.0206	0.0322	0.1793	0.0221	0.0297	0.1328	0.0217	0.0164	0.1189	0.0217	0.0133
-0.40	0.2730	0.0290	0.0287	0.2129	0.0221	0.0375	0.2116	0.0247	0.0253	0.1825	0.0249	0.0191
0.00	0.3774	0.0270	0.0392	0.3636	0.0286	0.0377	0.3903	0.0332	0.0489	0.2786	0.0288	0.0308
0.40	0.3827	0.0293	0.0397	0.4629	0.0371	0.0618	0.4263	0.0378	0.0583	0.3391	0.0306	0.0358
0.80	0.4322	0.0519	0.0581	0.4929	0.0629	0.0806	0.5376	0.0757	0.1166	0.4097	0.0466	0.0465
<hr/>												
$\cos(\theta_\eta^*)$	$E_\gamma = (1400.0 \pm 20.0) \text{ MeV}$											
	$d\sigma_{1/2}/d\Omega$ [$\mu\text{b}/\text{sr}$]	Δ_{stat} [$\mu\text{b}/\text{sr}$]	Δ_{sys} [$\mu\text{b}/\text{sr}$]									
-0.80	0.0884	0.0283	0.0092									
-0.40	0.1346	0.0418	0.0242									
0.00	0.2181	0.0357	0.0251									
0.40	0.3420	0.0496	0.0620									
0.80	0.5154	0.1028	0.1219									

Angular Cross Sections $\sigma_{3/2}$

$\cos(\theta_\eta^*)$	$E_\gamma = (725.0 \pm 15.0) \text{ MeV}$			$E_\gamma = (755.0 \pm 15.0) \text{ MeV}$			$E_\gamma = (785.0 \pm 15.0) \text{ MeV}$			$E_\gamma = (815.0 \pm 15.0) \text{ MeV}$		
	$d\sigma_{3/2}/d\Omega$ [$\mu\text{b}/\text{sr}$]	Δ_{stat} [$\mu\text{b}/\text{sr}$]	Δ_{sys} [$\mu\text{b}/\text{sr}$]	$d\sigma_{3/2}/d\Omega$ [$\mu\text{b}/\text{sr}$]	Δ_{stat} [$\mu\text{b}/\text{sr}$]	Δ_{sys} [$\mu\text{b}/\text{sr}$]	$d\sigma_{3/2}/d\Omega$ [$\mu\text{b}/\text{sr}$]	Δ_{stat} [$\mu\text{b}/\text{sr}$]	Δ_{sys} [$\mu\text{b}/\text{sr}$]	$d\sigma_{3/2}/d\Omega$ [$\mu\text{b}/\text{sr}$]	Δ_{stat} [$\mu\text{b}/\text{sr}$]	Δ_{sys} [$\mu\text{b}/\text{sr}$]
-0.80	-0.0250	0.0725	0.0308	0.1159	0.0582	0.0304	0.0783	0.0662	0.0095	0.0999	0.0563	0.0135
-0.40	0.0028	0.0815	0.0682	-0.0157	0.0749	0.0828	0.1486	0.0733	0.0402	-0.0537	0.0648	0.0058
0.00	-0.0032	0.1150	0.0890	0.1041	0.0958	0.1000	0.1106	0.0968	0.0899	-0.1135	0.0798	0.0646
0.40	0.2690	0.1443	0.0830	-0.2497	0.1843	0.2391	-0.1431	0.1456	0.1380	0.0460	0.0962	0.0608
0.80	-0.1018	0.1479	0.0735	-0.2623	0.2010	0.1942	-0.5218	0.2954	0.2682	-0.2094	0.2807	0.1667
$\cos(\theta_\eta^*)$	$E_\gamma = (845.0 \pm 15.0) \text{ MeV}$			$E_\gamma = (875.0 \pm 15.0) \text{ MeV}$			$E_\gamma = (905.0 \pm 15.0) \text{ MeV}$			$E_\gamma = (935.0 \pm 15.0) \text{ MeV}$		
	$d\sigma_{3/2}/d\Omega$ [$\mu\text{b}/\text{sr}$]	Δ_{stat} [$\mu\text{b}/\text{sr}$]	Δ_{sys} [$\mu\text{b}/\text{sr}$]	$d\sigma_{3/2}/d\Omega$ [$\mu\text{b}/\text{sr}$]	Δ_{stat} [$\mu\text{b}/\text{sr}$]	Δ_{sys} [$\mu\text{b}/\text{sr}$]	$d\sigma_{3/2}/d\Omega$ [$\mu\text{b}/\text{sr}$]	Δ_{stat} [$\mu\text{b}/\text{sr}$]	Δ_{sys} [$\mu\text{b}/\text{sr}$]	$d\sigma_{3/2}/d\Omega$ [$\mu\text{b}/\text{sr}$]	Δ_{stat} [$\mu\text{b}/\text{sr}$]	Δ_{sys} [$\mu\text{b}/\text{sr}$]
-0.80	0.0991	0.0586	0.0128	-0.0170	0.0590	0.0057	0.0484	0.0537	0.0099	0.1616	0.0485	0.0167
-0.40	0.1141	0.0663	0.0124	0.1645	0.0589	0.0557	0.0439	0.0547	0.0258	0.1349	0.0438	0.0675
0.00	0.0473	0.0748	0.0488	-0.0843	0.0722	0.0442	0.0935	0.0546	0.0102	0.1422	0.0484	0.0151
0.40	-0.0427	0.0853	0.0725	0.0245	0.0716	0.0511	0.0458	0.0571	0.0226	0.0763	0.0510	0.0187
0.80	-0.4836	0.3619	0.3003	0.5142	0.1649	0.0715	0.0516	0.1508	0.0702	-0.0090	0.1158	0.0331
$\cos(\theta_\eta^*)$	$E_\gamma = (965.0 \pm 15.0) \text{ MeV}$			$E_\gamma = (995.0 \pm 15.0) \text{ MeV}$			$E_\gamma = (1025.0 \pm 15.0) \text{ MeV}$			$E_\gamma = (1055.0 \pm 15.0) \text{ MeV}$		
	$d\sigma_{3/2}/d\Omega$ [$\mu\text{b}/\text{sr}$]	Δ_{stat} [$\mu\text{b}/\text{sr}$]	Δ_{sys} [$\mu\text{b}/\text{sr}$]	$d\sigma_{3/2}/d\Omega$ [$\mu\text{b}/\text{sr}$]	Δ_{stat} [$\mu\text{b}/\text{sr}$]	Δ_{sys} [$\mu\text{b}/\text{sr}$]	$d\sigma_{3/2}/d\Omega$ [$\mu\text{b}/\text{sr}$]	Δ_{stat} [$\mu\text{b}/\text{sr}$]	Δ_{sys} [$\mu\text{b}/\text{sr}$]	$d\sigma_{3/2}/d\Omega$ [$\mu\text{b}/\text{sr}$]	Δ_{stat} [$\mu\text{b}/\text{sr}$]	Δ_{sys} [$\mu\text{b}/\text{sr}$]
-0.80	0.1611	0.0453	0.0179	0.0471	0.0443	0.0250	0.1671	0.0367	0.0178	0.1316	0.0326	0.0180
-0.40	0.1367	0.0437	0.0372	0.1669	0.0307	0.0582	0.1704	0.0284	0.0536	0.1706	0.0330	0.0205
0.00	0.1213	0.0458	0.0130	0.1491	0.0355	0.0159	0.1557	0.0341	0.0165	0.1683	0.0303	0.0194
0.40	0.0651	0.0503	0.0288	0.0754	0.0393	0.0236	0.1457	0.0340	0.0168	0.1511	0.0345	0.0198
0.80	-0.0872	0.1341	0.0788	-0.1664	0.1087	0.0875	0.0529	0.0926	0.0459	-0.3066	0.1491	0.1418
$\cos(\theta_\eta^*)$	$E_\gamma = (1085.0 \pm 15.0) \text{ MeV}$			$E_\gamma = (1120.0 \pm 20.0) \text{ MeV}$			$E_\gamma = (1160.0 \pm 20.0) \text{ MeV}$			$E_\gamma = (1200.0 \pm 20.0) \text{ MeV}$		
	$d\sigma_{3/2}/d\Omega$ [$\mu\text{b}/\text{sr}$]	Δ_{stat} [$\mu\text{b}/\text{sr}$]	Δ_{sys} [$\mu\text{b}/\text{sr}$]	$d\sigma_{3/2}/d\Omega$ [$\mu\text{b}/\text{sr}$]	Δ_{stat} [$\mu\text{b}/\text{sr}$]	Δ_{sys} [$\mu\text{b}/\text{sr}$]	$d\sigma_{3/2}/d\Omega$ [$\mu\text{b}/\text{sr}$]	Δ_{stat} [$\mu\text{b}/\text{sr}$]	Δ_{sys} [$\mu\text{b}/\text{sr}$]	$d\sigma_{3/2}/d\Omega$ [$\mu\text{b}/\text{sr}$]	Δ_{stat} [$\mu\text{b}/\text{sr}$]	Δ_{sys} [$\mu\text{b}/\text{sr}$]
-0.80	0.0964	0.0351	0.0101	0.0834	0.0395	0.0096	0.1540	0.0306	0.0188	0.0991	0.0224	0.0138
-0.40	0.0767	0.0301	0.0225	0.1742	0.0345	0.0181	0.1357	0.0237	0.0200	0.1040	0.0245	0.0118
0.00	0.2232	0.0288	0.0252	0.1876	0.0330	0.0194	0.1319	0.0271	0.0149	0.1800	0.0264	0.0209
0.40	0.1018	0.0333	0.0117	0.1847	0.0347	0.0191	0.1512	0.0316	0.0274	0.0822	0.0298	0.0142
0.80	0.0761	0.0572	0.0228	-0.0488	0.0710	0.0378	0.1337	0.0404	0.0166	0.0283	0.0465	0.0188
$\cos(\theta_\eta^*)$	$E_\gamma = (1240.0 \pm 20.0) \text{ MeV}$			$E_\gamma = (1280.0 \pm 20.0) \text{ MeV}$			$E_\gamma = (1320.0 \pm 20.0) \text{ MeV}$			$E_\gamma = (1360.0 \pm 20.0) \text{ MeV}$		
	$d\sigma_{3/2}/d\Omega$ [$\mu\text{b}/\text{sr}$]	Δ_{stat} [$\mu\text{b}/\text{sr}$]	Δ_{sys} [$\mu\text{b}/\text{sr}$]	$d\sigma_{3/2}/d\Omega$ [$\mu\text{b}/\text{sr}$]	Δ_{stat} [$\mu\text{b}/\text{sr}$]	Δ_{sys} [$\mu\text{b}/\text{sr}$]	$d\sigma_{3/2}/d\Omega$ [$\mu\text{b}/\text{sr}$]	Δ_{stat} [$\mu\text{b}/\text{sr}$]	Δ_{sys} [$\mu\text{b}/\text{sr}$]	$d\sigma_{3/2}/d\Omega$ [$\mu\text{b}/\text{sr}$]	Δ_{stat} [$\mu\text{b}/\text{sr}$]	Δ_{sys} [$\mu\text{b}/\text{sr}$]
-0.80	0.0789	0.0206	0.0217	0.0382	0.0221	0.0146	0.0933	0.0217	0.0123	0.0799	0.0217	0.0093
-0.40	0.1122	0.0290	0.0122	0.0809	0.0221	0.0226	0.0917	0.0247	0.0131	0.0719	0.0249	0.0077
0.00	0.1315	0.0270	0.0138	0.1074	0.0286	0.0112	0.0748	0.0332	0.0182	0.1270	0.0288	0.0153
0.40	0.1611	0.0293	0.0168	0.0686	0.0371	0.0235	0.0783	0.0378	0.0239	0.0896	0.0306	0.0103
0.80	0.0213	0.0519	0.0195	-0.0327	0.0629	0.0334	-0.0780	0.0757	0.0592	0.0087	0.0466	0.0098
$\cos(\theta_\eta^*)$	$E_\gamma = (1400.0 \pm 20.0) \text{ MeV}$											
	$d\sigma_{3/2}/d\Omega$ [$\mu\text{b}/\text{sr}$]	Δ_{stat} [$\mu\text{b}/\text{sr}$]	Δ_{sys} [$\mu\text{b}/\text{sr}$]									
-0.80	0.0830	0.0283	0.0086									
-0.40	0.1246	0.0418	0.0230									
0.00	0.1559	0.0357	0.0187									
0.40	0.0878	0.0496	0.0332									
0.80	-0.1133	0.1028	0.0678									

Total Cross Sections $\sigma_{1/2}$ and $\sigma_{3/2}$

E_γ [MeV]	ΔE_γ [MeV]	$\sigma_{1/2}$ [μb]	Δ_{stat} [μb]	Δ_{sys} [μb]	E_γ [MeV]	ΔE_γ [MeV]	$\sigma_{3/2}$ [μb]	Δ_{stat} [μb]	Δ_{sys} [μb]
725.0	15.0	13.8889	0.6220	2.1406	725.0	15.0	0.2160	0.6220	0.8052
755.0	15.0	21.6555	0.6344	3.1074	755.0	15.0	-0.3140	0.6344	1.1439
785.0	15.0	25.0595	0.7492	3.3501	785.0	15.0	-0.4634	0.7492	1.0784
815.0	15.0	24.8033	0.6869	3.0577	815.0	15.0	-0.3054	0.6869	0.8110
845.0	15.0	22.9087	0.6764	2.6213	845.0	15.0	-0.1169	0.6764	0.5849
875.0	15.0	18.5370	0.5197	2.1125	875.0	15.0	1.6910	0.5197	0.3531
905.0	15.0	16.1912	0.4307	1.6430	905.0	15.0	0.6695	0.4307	0.1882
935.0	15.0	12.1207	0.3522	1.2933	935.0	15.0	1.3022	0.3522	0.1568
965.0	15.0	9.5331	0.3355	1.0171	965.0	15.0	1.1639	0.3355	0.1658
995.0	15.0	7.6865	0.2550	0.7849	995.0	15.0	0.9493	0.2550	0.1709
1025.0	15.0	5.3322	0.2211	0.6126	1025.0	15.0	1.8012	0.2211	0.1733
1055.0	15.0	5.3603	0.2235	0.5385	1055.0	15.0	1.3073	0.2235	0.1673
1085.0	15.0	4.8509	0.2040	0.5220	1085.0	15.0	1.4188	0.2040	0.1671
1120.0	20.0	4.8781	0.2319	0.4967	1120.0	20.0	1.5286	0.2319	0.1834
1160.0	20.0	4.0659	0.1756	0.4637	1160.0	20.0	1.7859	0.1756	0.1872
1200.0	20.0	4.3523	0.1698	0.4387	1200.0	20.0	1.2564	0.1698	0.1568
1240.0	20.0	4.0251	0.1771	0.4341	1240.0	20.0	1.3020	0.1771	0.1223
1280.0	20.0	4.1906	0.1925	0.4519	1280.0	20.0	0.7339	0.1925	0.1173
1320.0	20.0	4.0615	0.2061	0.4385	1320.0	20.0	0.8271	0.2061	0.1247
1360.0	20.0	3.3080	0.1747	0.4253	1360.0	20.0	0.9485	0.1747	0.1634
1400.0	20.0	3.1020	0.2764	0.5154	1400.0	20.0	0.9898	0.2764	0.2849

F.4.3 E for $\gamma n \rightarrow \eta n$ as a Function of E_γ

 Angular Distributions for E

$\cos(\theta_\eta^*)$	$E_\gamma = (725.0 \pm 15.0) \text{ MeV}$			$E_\gamma = (755.0 \pm 15.0) \text{ MeV}$			$E_\gamma = (785.0 \pm 15.0) \text{ MeV}$			$E_\gamma = (815.0 \pm 15.0) \text{ MeV}$				
	E	Δ_{stat}	Δ_{sys}											
-0.80	1.0061	0.1663	0.2222	0.9371	0.1220	0.1954	0.9714	0.1215	0.1679	0.9115	0.0992	0.1653		
-0.40	1.1879	0.2173	0.1304	0.9545	0.1349	0.1411	0.6770	0.1283	0.0840	0.7182	0.1194	0.0756		
0.00	1.1903	0.2692	0.1300	0.8423	0.1537	0.0932	0.9299	0.1376	0.1052	0.6409	0.1217	0.0689		
0.40	0.4891	0.3804	0.0507	1.1058	0.1975	0.1199	0.9734	0.1751	0.1058	1.1791	0.1720	0.1442		
0.80	1.5268	0.4940	0.2238	1.5686	0.4180	0.3404	0.7885	0.2473	0.0882	0.8979	0.2967	0.1512		
<hr/>														
$\cos(\theta_\eta^*)$	$E_\gamma = (845.0 \pm 15.0) \text{ MeV}$			$E_\gamma = (875.0 \pm 15.0) \text{ MeV}$			$E_\gamma = (905.0 \pm 15.0) \text{ MeV}$			$E_\gamma = (935.0 \pm 15.0) \text{ MeV}$				
	E	Δ_{stat}	Δ_{sys}											
-0.80	0.8645	0.1183	0.1314	0.7692	0.1081	0.1660	0.9583	0.1209	0.2171	0.7110	0.1498	0.1155		
-0.40	0.7787	0.1106	0.1314	0.9254	0.1234	0.1431	0.7854	0.1240	0.1312	0.8483	0.1287	0.1574		
0.00	0.7118	0.1293	0.0804	0.8641	0.1368	0.0898	0.5337	0.1185	0.0817	0.8595	0.1375	0.1083		
0.40	0.9729	0.1569	0.1115	0.7601	0.1414	0.0841	0.5993	0.1399	0.0636	0.9879	0.1877	0.1456		
0.80	0.5875	0.2531	0.0831	0.7123	0.2318	0.0751	1.2283	0.3388	0.2006	1.3756	0.4852	0.3018		
<hr/>														
$\cos(\theta_\eta^*)$	$E_\gamma = (965.0 \pm 15.0) \text{ MeV}$			$E_\gamma = (995.0 \pm 15.0) \text{ MeV}$			$E_\gamma = (1025.0 \pm 15.0) \text{ MeV}$			$E_\gamma = (1055.0 \pm 15.0) \text{ MeV}$				
	E	Δ_{stat}	Δ_{sys}											
-0.80	0.8006	0.1418	0.1690	0.8453	0.1234	0.1297	0.7887	0.1413	0.1138	0.6770	0.1370	0.1621		
-0.40	0.6141	0.1429	0.1000	0.6115	0.1063	0.1277	0.7474	0.1208	0.1118	0.6354	0.1361	0.0879		
0.00	0.8656	0.1430	0.0920	0.6125	0.1202	0.0639	0.6116	0.1153	0.0646	0.4520	0.1236	0.0475		
0.40	0.9439	0.1847	0.1230	0.7779	0.1319	0.0836	0.7296	0.1206	0.0861	0.7007	0.1724	0.1228		
0.80	1.0008	0.2817	0.1079	0.4726	0.2376	0.0501	1.1390	0.2687	0.1253	0.6688	0.2888	0.0821		
<hr/>														
$\cos(\theta_\eta^*)$	$E_\gamma = (1085.0 \pm 15.0) \text{ MeV}$			$E_\gamma = (1120.0 \pm 20.0) \text{ MeV}$			$E_\gamma = (1160.0 \pm 20.0) \text{ MeV}$			$E_\gamma = (1200.0 \pm 20.0) \text{ MeV}$				
	E	Δ_{stat}	Δ_{sys}											
-0.80	0.3636	0.1491	0.0962	0.9186	0.2071	0.1590	0.9731	0.2276	0.1148	0.7494	0.1720	0.2011		
-0.40	0.6563	0.1412	0.1102	0.7373	0.1893	0.1070	0.4935	0.1552	0.1000	0.5392	0.1571	0.0744		
0.00	0.6161	0.1230	0.0660	0.7480	0.1518	0.0816	0.5301	0.1298	0.0557	0.4255	0.1246	0.0466		
0.40	0.6954	0.1577	0.0994	0.2405	0.1830	0.0300	0.5344	0.1515	0.0718	0.3302	0.1397	0.0374		
0.80	0.9877	0.4009	0.1796	0.7219	0.3604	0.0751	0.7911	0.3629	0.1286	1.0050	0.4469	0.2473		
<hr/>														
$\cos(\theta_\eta^*)$	$E_\gamma = (1240.0 \pm 20.0) \text{ MeV}$			$E_\gamma = (1280.0 \pm 20.0) \text{ MeV}$			$E_\gamma = (1320.0 \pm 20.0) \text{ MeV}$			$E_\gamma = (1360.0 \pm 20.0) \text{ MeV}$				
	E	Δ_{stat}	Δ_{sys}											
-0.80	0.4512	0.2269	0.1364	0.6095	0.2616	0.0832	0.6581	0.3042	0.0876	0.8453	0.2533	0.2308		
-0.40	0.4101	0.1469	0.1437	0.5502	0.2312	0.0794	0.4808	0.2075	0.0749	0.1410	0.1884	0.0378		
0.00	0.5308	0.1722	0.0685	0.3415	0.1945	0.0368	0.6241	0.2611	0.1075	0.5472	0.2761	0.1142		
0.40	0.8409	0.2405	0.1581	0.4802	0.1552	0.0537	0.4006	0.1879	0.0416	0.5634	0.2394	0.0831		
0.80	0.6118	0.4080	0.1256	0.8597	0.5336	0.1322	0.8107	0.4236	0.1452	0.8937	0.4610	0.2080		
<hr/>														
$\cos(\theta_\eta^*)$	$E_\gamma = (1400.0 \pm 20.0) \text{ MeV}$													
	E	Δ_{stat}	Δ_{sys}											
-0.80	0.5523	0.2864	0.1762											
-0.40	0.5263	0.3269	0.0832											
0.00	0.4410	0.2406	0.0462											
0.40	0.1260	0.2850	0.0153											
0.80	-4.771619.9323	2.5204												

Total Distributions for E

E_γ [MeV]	ΔE_γ [MeV]	E	Δ_{stat}	Δ_{sys}
725.0	15.0	1.0810	0.1242	0.1207
755.0	15.0	1.0315	0.0814	0.1120
785.0	15.0	0.8703	0.0730	0.1001
815.0	15.0	0.8690	0.0681	0.0897
845.0	15.0	0.7930	0.0680	0.0907
875.0	15.0	0.8051	0.0660	0.1003
905.0	15.0	0.8189	0.0697	0.1036
935.0	15.0	0.8889	0.0830	0.0988
965.0	15.0	0.8223	0.0784	0.0932
995.0	15.0	0.6840	0.0625	0.0900
1025.0	15.0	0.7827	0.0657	0.0844
1055.0	15.0	0.6268	0.0731	0.0732
1085.0	15.0	0.6098	0.0763	0.0682
1120.0	20.0	0.6899	0.0945	0.0712
1160.0	20.0	0.6516	0.0859	0.0684
1200.0	20.0	0.5687	0.0803	0.0605
1240.0	20.0	0.5448	0.0996	0.0564
1280.0	20.0	0.5373	0.1091	0.0574
1320.0	20.0	0.5667	0.1177	0.0605
1360.0	20.0	0.5767	0.1187	0.0597
1400.0	20.0	0.4615	0.1557	0.0515

F.4.4 Helicity Dependent Cross Sections for $\gamma n \rightarrow \eta n$ as a Function of E_γ

 Angular Cross Sections $\sigma_{1/2}$

$\cos(\theta_\eta^*)$	$E_\gamma = (725.0 \pm 15.0) \text{ MeV}$			$E_\gamma = (755.0 \pm 15.0) \text{ MeV}$			$E_\gamma = (785.0 \pm 15.0) \text{ MeV}$			$E_\gamma = (815.0 \pm 15.0) \text{ MeV}$		
	$d\sigma_{1/2}/d\Omega$ [$\mu\text{b}/\text{sr}$]	Δ_{stat} [$\mu\text{b}/\text{sr}$]	Δ_{sys} [$\mu\text{b}/\text{sr}$]	$d\sigma_{1/2}/d\Omega$ [$\mu\text{b}/\text{sr}$]	Δ_{stat} [$\mu\text{b}/\text{sr}$]	Δ_{sys} [$\mu\text{b}/\text{sr}$]	$d\sigma_{1/2}/d\Omega$ [$\mu\text{b}/\text{sr}$]	Δ_{stat} [$\mu\text{b}/\text{sr}$]	Δ_{sys} [$\mu\text{b}/\text{sr}$]	$d\sigma_{1/2}/d\Omega$ [$\mu\text{b}/\text{sr}$]	Δ_{stat} [$\mu\text{b}/\text{sr}$]	Δ_{sys} [$\mu\text{b}/\text{sr}$]
-0.80	1.1133	0.0958	0.2459	1.3448	0.0877	0.2805	1.4818	0.0944	0.2561	1.4638	0.0795	0.2654
-0.40	1.0472	0.1132	0.1149	1.1311	0.0827	0.1673	1.0845	0.0865	0.1346	1.1098	0.0812	0.1167
0.00	0.8707	0.1163	0.0951	1.0656	0.0933	0.1179	1.2208	0.0917	0.1380	0.9755	0.0762	0.1049
0.40	0.5266	0.1393	0.0546	1.1510	0.1137	0.1248	1.1604	0.1079	0.1261	1.2705	0.1060	0.1554
0.80	1.1200	0.2243	0.1642	1.5499	0.2599	0.3363	1.2718	0.1818	0.1422	1.1704	0.1891	0.1971
<hr/>												
$\cos(\theta_\eta^*)$	$E_\gamma = (845.0 \pm 15.0) \text{ MeV}$			$E_\gamma = (875.0 \pm 15.0) \text{ MeV}$			$E_\gamma = (905.0 \pm 15.0) \text{ MeV}$			$E_\gamma = (935.0 \pm 15.0) \text{ MeV}$		
	$d\sigma_{1/2}/d\Omega$ [$\mu\text{b}/\text{sr}$]	Δ_{stat} [$\mu\text{b}/\text{sr}$]	Δ_{sys} [$\mu\text{b}/\text{sr}$]	$d\sigma_{1/2}/d\Omega$ [$\mu\text{b}/\text{sr}$]	Δ_{stat} [$\mu\text{b}/\text{sr}$]	Δ_{sys} [$\mu\text{b}/\text{sr}$]	$d\sigma_{1/2}/d\Omega$ [$\mu\text{b}/\text{sr}$]	Δ_{stat} [$\mu\text{b}/\text{sr}$]	Δ_{sys} [$\mu\text{b}/\text{sr}$]	$d\sigma_{1/2}/d\Omega$ [$\mu\text{b}/\text{sr}$]	Δ_{stat} [$\mu\text{b}/\text{sr}$]	Δ_{sys} [$\mu\text{b}/\text{sr}$]
-0.80	1.2238	0.0832	0.1860	1.0572	0.0754	0.2282	1.0097	0.0657	0.2288	0.7682	0.0696	0.1248
-0.40	1.0091	0.0685	0.1702	0.9529	0.0712	0.1474	0.8202	0.0594	0.1370	0.7950	0.0580	0.1475
0.00	0.8677	0.0701	0.0980	0.8673	0.0718	0.0901	0.6406	0.0514	0.0981	0.6999	0.0542	0.0882
0.40	1.0730	0.0913	0.1229	0.7773	0.0711	0.0860	0.6640	0.0602	0.0704	0.8053	0.0785	0.1187
0.80	0.9632	0.1606	0.1362	0.7941	0.1214	0.0837	0.9494	0.1497	0.1550	0.8175	0.1717	0.1793
<hr/>												
$\cos(\theta_\eta^*)$	$E_\gamma = (965.0 \pm 15.0) \text{ MeV}$			$E_\gamma = (995.0 \pm 15.0) \text{ MeV}$			$E_\gamma = (1025.0 \pm 15.0) \text{ MeV}$			$E_\gamma = (1055.0 \pm 15.0) \text{ MeV}$		
	$d\sigma_{1/2}/d\Omega$ [$\mu\text{b}/\text{sr}$]	Δ_{stat} [$\mu\text{b}/\text{sr}$]	Δ_{sys} [$\mu\text{b}/\text{sr}$]	$d\sigma_{1/2}/d\Omega$ [$\mu\text{b}/\text{sr}$]	Δ_{stat} [$\mu\text{b}/\text{sr}$]	Δ_{sys} [$\mu\text{b}/\text{sr}$]	$d\sigma_{1/2}/d\Omega$ [$\mu\text{b}/\text{sr}$]	Δ_{stat} [$\mu\text{b}/\text{sr}$]	Δ_{sys} [$\mu\text{b}/\text{sr}$]	$d\sigma_{1/2}/d\Omega$ [$\mu\text{b}/\text{sr}$]	Δ_{stat} [$\mu\text{b}/\text{sr}$]	Δ_{sys} [$\mu\text{b}/\text{sr}$]
-0.80	0.7900	0.0649	0.1668	0.8349	0.0593	0.1281	0.7087	0.0588	0.1022	0.5574	0.0480	0.1335
-0.40	0.6189	0.0566	0.1008	0.6219	0.0437	0.1299	0.6643	0.0486	0.0994	0.5529	0.0482	0.0765
0.00	0.7356	0.0586	0.0782	0.6258	0.0490	0.0652	0.6260	0.0471	0.0661	0.5572	0.0494	0.0585
0.40	0.7385	0.0724	0.0962	0.6855	0.0537	0.0736	0.6382	0.0474	0.0753	0.6495	0.0680	0.1138
0.80	0.6254	0.0937	0.0675	0.4436	0.0759	0.0470	0.5239	0.0728	0.0576	0.4388	0.0800	0.0539
<hr/>												
$\cos(\theta_\eta^*)$	$E_\gamma = (1085.0 \pm 15.0) \text{ MeV}$			$E_\gamma = (1120.0 \pm 20.0) \text{ MeV}$			$E_\gamma = (1160.0 \pm 20.0) \text{ MeV}$			$E_\gamma = (1200.0 \pm 20.0) \text{ MeV}$		
	$d\sigma_{1/2}/d\Omega$ [$\mu\text{b}/\text{sr}$]	Δ_{stat} [$\mu\text{b}/\text{sr}$]	Δ_{sys} [$\mu\text{b}/\text{sr}$]	$d\sigma_{1/2}/d\Omega$ [$\mu\text{b}/\text{sr}$]	Δ_{stat} [$\mu\text{b}/\text{sr}$]	Δ_{sys} [$\mu\text{b}/\text{sr}$]	$d\sigma_{1/2}/d\Omega$ [$\mu\text{b}/\text{sr}$]	Δ_{stat} [$\mu\text{b}/\text{sr}$]	Δ_{sys} [$\mu\text{b}/\text{sr}$]	$d\sigma_{1/2}/d\Omega$ [$\mu\text{b}/\text{sr}$]	Δ_{stat} [$\mu\text{b}/\text{sr}$]	Δ_{sys} [$\mu\text{b}/\text{sr}$]
-0.80	0.3902	0.0446	0.1032	0.5352	0.0605	0.0926	0.4513	0.0542	0.0532	0.3628	0.0382	0.0974
-0.40	0.5052	0.0452	0.0848	0.4446	0.0505	0.0645	0.3109	0.0340	0.0630	0.3318	0.0357	0.0458
0.00	0.5851	0.0468	0.0627	0.5442	0.0498	0.0594	0.4377	0.0392	0.0460	0.3959	0.0367	0.0434
0.40	0.6476	0.0626	0.0925	0.4040	0.0614	0.0505	0.5064	0.0522	0.0680	0.4187	0.0461	0.0474
0.80	0.4617	0.0971	0.0840	0.3349	0.0744	0.0348	0.3514	0.0748	0.0571	0.4347	0.1008	0.1070
<hr/>												
$\cos(\theta_\eta^*)$	$E_\gamma = (1240.0 \pm 20.0) \text{ MeV}$			$E_\gamma = (1280.0 \pm 20.0) \text{ MeV}$			$E_\gamma = (1320.0 \pm 20.0) \text{ MeV}$			$E_\gamma = (1360.0 \pm 20.0) \text{ MeV}$		
	$d\sigma_{1/2}/d\Omega$ [$\mu\text{b}/\text{sr}$]	Δ_{stat} [$\mu\text{b}/\text{sr}$]	Δ_{sys} [$\mu\text{b}/\text{sr}$]	$d\sigma_{1/2}/d\Omega$ [$\mu\text{b}/\text{sr}$]	Δ_{stat} [$\mu\text{b}/\text{sr}$]	Δ_{sys} [$\mu\text{b}/\text{sr}$]	$d\sigma_{1/2}/d\Omega$ [$\mu\text{b}/\text{sr}$]	Δ_{stat} [$\mu\text{b}/\text{sr}$]	Δ_{sys} [$\mu\text{b}/\text{sr}$]	$d\sigma_{1/2}/d\Omega$ [$\mu\text{b}/\text{sr}$]	Δ_{stat} [$\mu\text{b}/\text{sr}$]	Δ_{sys} [$\mu\text{b}/\text{sr}$]
-0.80	0.2228	0.0366	0.0674	0.2859	0.0479	0.0390	0.2446	0.0463	0.0326	0.2530	0.0369	0.0691
-0.40	0.2481	0.0280	0.0870	0.2446	0.0378	0.0353	0.2431	0.0356	0.0379	0.1583	0.0276	0.0424
0.00	0.4200	0.0492	0.0542	0.3029	0.0453	0.0327	0.3544	0.0583	0.0610	0.3349	0.0610	0.0699
0.40	0.5209	0.0704	0.0980	0.4042	0.0447	0.0452	0.3269	0.0457	0.0339	0.3533	0.0559	0.0521
0.80	0.3346	0.0882	0.0687	0.2697	0.0804	0.0415	0.3332	0.0816	0.0597	0.3586	0.0911	0.0834
<hr/>												
$\cos(\theta_\eta^*)$	$E_\gamma = (1400.0 \pm 20.0) \text{ MeV}$											
	$d\sigma_{1/2}/d\Omega$ [$\mu\text{b}/\text{sr}$]	Δ_{stat} [$\mu\text{b}/\text{sr}$]	Δ_{sys} [$\mu\text{b}/\text{sr}$]									
-0.80	0.2147	0.0414	0.0685									
-0.40	0.1796	0.0397	0.0284									
0.00	0.2779	0.0479	0.0291									
0.40	0.2249	0.0583	0.0274									
0.80	-0.5798	3.0653	0.3846									

Angular Cross Sections $\sigma_{3/2}$

$\cos(\theta_\eta^*)$	$E_\gamma = (725.0 \pm 15.0) \text{ MeV}$			$E_\gamma = (755.0 \pm 15.0) \text{ MeV}$			$E_\gamma = (785.0 \pm 15.0) \text{ MeV}$			$E_\gamma = (815.0 \pm 15.0) \text{ MeV}$		
	$d\sigma_{3/2}/d\Omega$ [$\mu\text{b}/\text{sr}$]	Δ_{stat} [$\mu\text{b}/\text{sr}$]	Δ_{sys} [$\mu\text{b}/\text{sr}$]	$d\sigma_{3/2}/d\Omega$ [$\mu\text{b}/\text{sr}$]	Δ_{stat} [$\mu\text{b}/\text{sr}$]	Δ_{sys} [$\mu\text{b}/\text{sr}$]	$d\sigma_{3/2}/d\Omega$ [$\mu\text{b}/\text{sr}$]	Δ_{stat} [$\mu\text{b}/\text{sr}$]	Δ_{sys} [$\mu\text{b}/\text{sr}$]	$d\sigma_{3/2}/d\Omega$ [$\mu\text{b}/\text{sr}$]	Δ_{stat} [$\mu\text{b}/\text{sr}$]	Δ_{sys} [$\mu\text{b}/\text{sr}$]
-0.80	-0.0034	0.0958	1.5524	0.0437	0.0877	1.7722	0.0215	0.0944	1.8643	0.0678	0.0795	1.8115
-0.40	-0.0899	0.1132	1.2196	0.0263	0.0827	1.3380	0.2089	0.0865	0.9955	0.1820	0.0812	0.9619
0.00	-0.0756	0.1163	1.0121	0.0912	0.0933	1.0500	0.0443	0.0917	1.2832	0.2135	0.0762	0.8061
0.40	0.1807	0.1393	0.3419	-0.0578	0.1137	1.2863	0.0156	0.1079	1.2200	-0.1044	0.1060	1.1962
0.80	-0.2335	0.2243	1.0727	-0.3431	0.2599	1.1710	0.1504	0.1818	1.0271	0.0630	0.1891	0.8134
<hr/>												
$\cos(\theta_\eta^*)$	$E_\gamma = (845.0 \pm 15.0) \text{ MeV}$			$E_\gamma = (875.0 \pm 15.0) \text{ MeV}$			$E_\gamma = (905.0 \pm 15.0) \text{ MeV}$			$E_\gamma = (935.0 \pm 15.0) \text{ MeV}$		
	$d\sigma_{3/2}/d\Omega$ [$\mu\text{b}/\text{sr}$]	Δ_{stat} [$\mu\text{b}/\text{sr}$]	Δ_{sys} [$\mu\text{b}/\text{sr}$]	$d\sigma_{3/2}/d\Omega$ [$\mu\text{b}/\text{sr}$]	Δ_{stat} [$\mu\text{b}/\text{sr}$]	Δ_{sys} [$\mu\text{b}/\text{sr}$]	$d\sigma_{3/2}/d\Omega$ [$\mu\text{b}/\text{sr}$]	Δ_{stat} [$\mu\text{b}/\text{sr}$]	Δ_{sys} [$\mu\text{b}/\text{sr}$]	$d\sigma_{3/2}/d\Omega$ [$\mu\text{b}/\text{sr}$]	Δ_{stat} [$\mu\text{b}/\text{sr}$]	Δ_{sys} [$\mu\text{b}/\text{sr}$]
-0.80	0.0889	0.0832	1.3873	0.1379	0.0754	1.2674	0.0215	0.0657	1.3865	0.1298	0.0696	0.7983
-0.40	0.1255	0.0685	1.1188	0.0369	0.0712	1.1264	0.0986	0.0594	0.9107	0.0653	0.0580	0.9544
0.00	0.1461	0.0701	0.7867	0.0632	0.0718	0.8175	0.1948	0.0514	0.5464	0.0529	0.0542	0.7398
0.40	0.0147	0.0913	0.9547	0.1059	0.0711	0.7236	0.1664	0.0602	0.5204	0.0049	0.0785	0.6325
0.80	0.2503	0.1606	0.5756	0.1334	0.1214	0.6863	-0.0973	0.1497	0.7824	-0.1293	0.1717	0.5806
<hr/>												
$\cos(\theta_\eta^*)$	$E_\gamma = (965.0 \pm 15.0) \text{ MeV}$			$E_\gamma = (995.0 \pm 15.0) \text{ MeV}$			$E_\gamma = (1025.0 \pm 15.0) \text{ MeV}$			$E_\gamma = (1055.0 \pm 15.0) \text{ MeV}$		
	$d\sigma_{3/2}/d\Omega$ [$\mu\text{b}/\text{sr}$]	Δ_{stat} [$\mu\text{b}/\text{sr}$]	Δ_{sys} [$\mu\text{b}/\text{sr}$]	$d\sigma_{3/2}/d\Omega$ [$\mu\text{b}/\text{sr}$]	Δ_{stat} [$\mu\text{b}/\text{sr}$]	Δ_{sys} [$\mu\text{b}/\text{sr}$]	$d\sigma_{3/2}/d\Omega$ [$\mu\text{b}/\text{sr}$]	Δ_{stat} [$\mu\text{b}/\text{sr}$]	Δ_{sys} [$\mu\text{b}/\text{sr}$]	$d\sigma_{3/2}/d\Omega$ [$\mu\text{b}/\text{sr}$]	Δ_{stat} [$\mu\text{b}/\text{sr}$]	Δ_{sys} [$\mu\text{b}/\text{sr}$]
-0.80	0.0875	0.0649	0.9609	0.0700	0.0593	0.9380	0.0837	0.0588	0.7505	0.1074	0.0480	0.6444
-0.40	0.1480	0.0566	0.5894	0.1500	0.0437	0.6432	0.0961	0.0486	0.6910	0.1233	0.0482	0.5085
0.00	0.0530	0.0586	0.7154	0.1504	0.0490	0.4642	0.1509	0.0471	0.4948	0.2103	0.0494	0.3347
0.40	0.0213	0.0724	0.6038	0.0856	0.0537	0.5657	0.0998	0.0474	0.5994	0.1143	0.0680	0.3838
0.80	-0.0002	0.0937	0.6632	0.1589	0.0759	0.2718	-0.0340	0.0728	0.5993	0.0871	0.0800	0.3053
<hr/>												
$\cos(\theta_\eta^*)$	$E_\gamma = (1085.0 \pm 15.0) \text{ MeV}$			$E_\gamma = (1120.0 \pm 20.0) \text{ MeV}$			$E_\gamma = (1160.0 \pm 20.0) \text{ MeV}$			$E_\gamma = (1200.0 \pm 20.0) \text{ MeV}$		
	$d\sigma_{3/2}/d\Omega$ [$\mu\text{b}/\text{sr}$]	Δ_{stat} [$\mu\text{b}/\text{sr}$]	Δ_{sys} [$\mu\text{b}/\text{sr}$]	$d\sigma_{3/2}/d\Omega$ [$\mu\text{b}/\text{sr}$]	Δ_{stat} [$\mu\text{b}/\text{sr}$]	Δ_{sys} [$\mu\text{b}/\text{sr}$]	$d\sigma_{3/2}/d\Omega$ [$\mu\text{b}/\text{sr}$]	Δ_{stat} [$\mu\text{b}/\text{sr}$]	Δ_{sys} [$\mu\text{b}/\text{sr}$]	$d\sigma_{3/2}/d\Omega$ [$\mu\text{b}/\text{sr}$]	Δ_{stat} [$\mu\text{b}/\text{sr}$]	Δ_{sys} [$\mu\text{b}/\text{sr}$]
-0.80	0.1821	0.0446	0.3094	0.0227	0.0605	0.6546	0.0062	0.0542	0.4954	0.0520	0.0382	0.4648
-0.40	0.1048	0.0452	0.5062	0.0672	0.0505	0.4541	0.1054	0.0340	0.2770	0.0993	0.0357	0.2748
0.00	0.1390	0.0468	0.4705	0.0785	0.0498	0.4976	0.1344	0.0392	0.3137	0.1596	0.0367	0.2533
0.40	0.1163	0.0626	0.4267	0.2474	0.0614	0.1347	0.1537	0.0522	0.2924	0.2108	0.0461	0.1890
0.80	0.0029	0.0971	0.3217	0.0541	0.0744	0.2755	0.0410	0.0748	0.2325	-0.0011	0.1008	0.2413
<hr/>												
$\cos(\theta_\eta^*)$	$E_\gamma = (1240.0 \pm 20.0) \text{ MeV}$			$E_\gamma = (1280.0 \pm 20.0) \text{ MeV}$			$E_\gamma = (1320.0 \pm 20.0) \text{ MeV}$			$E_\gamma = (1360.0 \pm 20.0) \text{ MeV}$		
	$d\sigma_{3/2}/d\Omega$ [$\mu\text{b}/\text{sr}$]	Δ_{stat} [$\mu\text{b}/\text{sr}$]	Δ_{sys} [$\mu\text{b}/\text{sr}$]	$d\sigma_{3/2}/d\Omega$ [$\mu\text{b}/\text{sr}$]	Δ_{stat} [$\mu\text{b}/\text{sr}$]	Δ_{sys} [$\mu\text{b}/\text{sr}$]	$d\sigma_{3/2}/d\Omega$ [$\mu\text{b}/\text{sr}$]	Δ_{stat} [$\mu\text{b}/\text{sr}$]	Δ_{sys} [$\mu\text{b}/\text{sr}$]	$d\sigma_{3/2}/d\Omega$ [$\mu\text{b}/\text{sr}$]	Δ_{stat} [$\mu\text{b}/\text{sr}$]	Δ_{sys} [$\mu\text{b}/\text{sr}$]
-0.80	0.0843	0.0366	0.2172	0.0693	0.0479	0.2550	0.0504	0.0463	0.2266	0.0212	0.0369	0.3489
-0.40	0.1038	0.0280	0.2409	0.0710	0.0378	0.2085	0.0852	0.0356	0.1946	0.1192	0.0276	0.0584
0.00	0.1287	0.0492	0.2464	0.1487	0.0453	0.1450	0.0820	0.0583	0.1974	0.0980	0.0610	0.1511
0.40	0.0450	0.0704	0.3265	0.1420	0.0447	0.2844	0.1399	0.0457	0.1891	0.0987	0.0559	0.2011
0.80	0.0806	0.0882	0.1639	0.0203	0.0804	0.1927	0.0348	0.0816	0.2112	0.0201	0.0911	0.1974
<hr/>												
$\cos(\theta_\eta^*)$	$E_\gamma = (1400.0 \pm 20.0) \text{ MeV}$			$d\sigma_{3/2}/d\Omega$ [$\mu\text{b}/\text{sr}$]			Δ_{stat} [$\mu\text{b}/\text{sr}$]			Δ_{sys} [$\mu\text{b}/\text{sr}$]		
	-0.80	0.0619	0.0414	0.2450	0.0557	0.0397	0.1534	0.1078	0.0479	0.1755	0.1745	0.0583
-0.40	0.0557	0.0397	0.1534	0.08872	0.0653	0.0527	0.08872	0.0653	0.0527	0.08872	0.0653	0.0527

Total Cross Sections $\sigma_{1/2}$ and $\sigma_{3/2}$

E_γ [MeV]	ΔE_γ [MeV]	$\sigma_{1/2}$ [μb]	Δ_{stat} [μb]	Δ_{sys} [μb]	E_γ [MeV]	ΔE_γ [MeV]	$\sigma_{3/2}$ [μb]	Δ_{stat} [μb]	Δ_{sys} [μb]
725.0	15.0	11.7165	0.7346	1.3085	725.0	15.0	-0.4562	0.7346	0.2586
755.0	15.0	15.3567	0.6454	1.6610	755.0	15.0	-0.2382	0.6454	0.3332
785.0	15.0	15.6863	0.6397	1.7514	785.0	15.0	1.0878	0.6397	0.3128
815.0	15.0	15.1062	0.5794	1.5986	815.0	15.0	1.0584	0.5794	0.2271
845.0	15.0	13.0489	0.5321	1.4648	845.0	15.0	1.5065	0.5321	0.2986
875.0	15.0	11.1973	0.4723	1.4139	875.0	15.0	1.2088	0.4723	0.4650
905.0	15.0	10.2427	0.4112	1.2770	905.0	15.0	1.0197	0.4112	0.4495
935.0	15.0	9.5436	0.4372	1.0906	935.0	15.0	0.5615	0.4372	0.3283
965.0	15.0	8.7278	0.3923	1.0077	965.0	15.0	0.8510	0.3923	0.3018
995.0	15.0	8.0928	0.3199	0.9876	995.0	15.0	1.5188	0.3199	0.3207
1025.0	15.0	7.9393	0.3122	0.9122	1025.0	15.0	0.9679	0.3122	0.2837
1055.0	15.0	6.9098	0.3260	0.7790	1055.0	15.0	1.5850	0.3260	0.2185
1085.0	15.0	6.2999	0.3131	0.6769	1085.0	15.0	1.5269	0.3131	0.1797
1120.0	20.0	5.7698	0.3383	0.6172	1120.0	20.0	1.0586	0.3383	0.1543
1160.0	20.0	5.1537	0.2820	0.5526	1160.0	20.0	1.0871	0.2820	0.1324
1200.0	20.0	4.8325	0.2627	0.4890	1200.0	20.0	1.3288	0.2627	0.1297
1240.0	20.0	4.1975	0.2856	0.4373	1240.0	20.0	1.2368	0.2856	0.1319
1280.0	20.0	3.7583	0.2778	0.4033	1280.0	20.0	1.1313	0.2778	0.1256
1320.0	20.0	3.7054	0.2903	0.3923	1320.0	20.0	1.0248	0.2903	0.1192
1360.0	20.0	3.5588	0.2807	0.3736	1360.0	20.0	0.9554	0.2807	0.1227
1400.0	20.0	2.9125	0.3203	0.3249	1400.0	20.0	1.0733	0.3203	0.1385

F.4.5 E for $\gamma p \rightarrow \eta p$ as a Function of W

Angular Distributions for E

$\cos(\theta_\eta^*)$	W=(1495.0±5.0) MeV			W=(1505.0±5.0) MeV			W=(1515.0±5.0) MeV			W=(1525.0±5.0) MeV		
	E	Δ_{stat}	Δ_{sys}									
-0.80	1.1519	0.1708	0.1376	1.1607	0.1088	0.1444	1.0675	0.0932	0.1348	0.9839	0.0848	0.1178
-0.40	1.3086	0.1201	0.1555	1.0349	0.0902	0.1185	0.8388	0.0836	0.0951	1.0385	0.0918	0.1385
0.00	0.8700	0.1156	0.1029	0.8246	0.1171	0.1151	0.8009	0.1292	0.1186	0.8907	0.1494	0.1280
0.40	1.2171	0.1414	0.1662	1.2529	0.1848	0.2441	1.3794	0.2758	0.2926	0.9262	0.3411	0.2175
0.80	1.3794	0.1782	0.1904	1.2249	0.1909	0.1982	1.3675	0.3197	0.3316	1.4249	0.4490	0.3371
$\cos(\theta_\eta^*)$	W=(1535.0±5.0) MeV			W=(1547.5±7.5) MeV			W=(1562.5±7.5) MeV			W=(1577.5±7.5) MeV		
	E	Δ_{stat}	Δ_{sys}									
-0.80	1.0261	0.0813	0.1176	0.9337	0.0652	0.1015	0.9418	0.0688	0.1009	0.9615	0.0778	0.1230
-0.40	0.8669	0.0884	0.0974	0.9464	0.0723	0.0985	0.7859	0.0722	0.0821	0.8359	0.0829	0.0960
0.00	0.9111	0.1296	0.1013	1.0768	0.0913	0.1138	0.8655	0.0754	0.0903	0.9290	0.0768	0.1142
0.40	0.7321	0.1859	0.0971	1.0547	0.1140	0.1324	0.9529	0.0871	0.1139	1.1028	0.0899	0.1495
0.80	0.9490	0.4963	0.1721	0.2740	0.5806	0.0759	1.0751	0.3664	0.2156	0.7068	0.4658	0.2152
$\cos(\theta_\eta^*)$	W=(1592.5±7.5) MeV			W=(1607.5±7.5) MeV			W=(1622.5±7.5) MeV			W=(1637.5±7.5) MeV		
	E	Δ_{stat}	Δ_{sys}									
-0.80	1.0087	0.0794	0.1172	0.8983	0.0870	0.1155	0.8828	0.0970	0.0949	0.7766	0.1061	0.0899
-0.40	0.8999	0.0862	0.0983	0.8151	0.0863	0.1093	0.8090	0.0904	0.1253	0.6020	0.0935	0.0844
0.00	0.7911	0.0758	0.0897	0.8857	0.0771	0.0926	0.8301	0.0864	0.0875	0.5963	0.0938	0.0622
0.40	1.0590	0.0947	0.1280	0.8508	0.0987	0.1149	0.9397	0.1030	0.0982	0.8488	0.1061	0.0881
0.80	1.2337	0.2964	0.2228	0.8826	0.3086	0.1975	1.0204	0.3280	0.1727	1.1344	0.3317	0.2286
$\cos(\theta_\eta^*)$	W=(1652.5±7.5) MeV			W=(1667.5±7.5) MeV			W=(1682.5±7.5) MeV			W=(1697.5±7.5) MeV		
	E	Δ_{stat}	Δ_{sys}									
-0.80	0.5568	0.1106	0.0648	0.4353	0.1388	0.0584	0.7294	0.1556	0.0877	0.5732	0.1464	0.0597
-0.40	0.5011	0.1119	0.0546	0.6330	0.1072	0.1064	0.5307	0.1172	0.0942	0.4236	0.1239	0.0456
0.00	0.5522	0.0991	0.0769	0.4466	0.1103	0.0464	0.4483	0.1128	0.0464	0.5305	0.1013	0.0669
0.40	0.9085	0.1255	0.0944	0.6743	0.1138	0.0705	0.4185	0.1143	0.0463	0.5571	0.1323	0.0742
0.80	2.1474	0.5757	0.4892	0.7557	0.3347	0.0965	1.1846	0.3855	0.2342	0.4700	0.2320	0.0490
$\cos(\theta_\eta^*)$	W=(1712.5±7.5) MeV			W=(1727.5±7.5) MeV			W=(1742.5±7.5) MeV			W=(1757.5±7.5) MeV		
	E	Δ_{stat}	Δ_{sys}									
-0.80	0.2078	0.1940	0.0298	0.2483	0.1980	0.0344	0.9818	0.2121	0.1149	0.4261	0.1752	0.0444
-0.40	0.5212	0.1386	0.0600	0.1104	0.1359	0.0134	0.1890	0.1345	0.0285	0.3577	0.1602	0.0389
0.00	0.1691	0.1082	0.0185	0.5596	0.1129	0.0612	0.3053	0.1242	0.0329	0.5580	0.1469	0.0769
0.40	0.4330	0.1178	0.0498	0.6108	0.1034	0.0701	0.7286	0.1274	0.0872	0.6731	0.1316	0.0871
0.80	0.9787	0.2416	0.1184	0.6114	0.1709	0.1006	0.4336	0.2802	0.0767	1.1856	0.3007	0.2131
$\cos(\theta_\eta^*)$	W=(1772.5±7.5) MeV			W=(1787.5±7.5) MeV			W=(1802.5±7.5) MeV			W=(1817.5±7.5) MeV		
	E	Δ_{stat}	Δ_{sys}									
-0.80	0.6634	0.2340	0.1064	0.7415	0.2425	0.1129	0.8449	0.2334	0.0910	0.0062	0.2753	0.0010
-0.40	0.4069	0.1445	0.0686	0.3926	0.1698	0.0408	0.3900	0.1474	0.0766	0.3019	0.1788	0.0434
0.00	0.4352	0.1047	0.0577	0.6325	0.1238	0.0702	0.4703	0.1635	0.0581	0.5942	0.1547	0.0618
0.40	0.6035	0.1225	0.0683	0.7974	0.1655	0.1200	0.2152	0.1694	0.0322	0.5989	0.1599	0.0698
0.80	0.9367	0.2330	0.1260	0.7118	0.2227	0.0880	1.2895	0.3281	0.1921	1.0923	0.3522	0.2237

$\cos(\theta_\eta^*)$	W=(1832.5±7.5) MeV			W=(1847.5±7.5) MeV			W=(1862.5±7.5) MeV			W=(1882.5±12.5) MeV		
	E	Δ_{stat}	Δ_{sys}	E	Δ_{stat}	Δ_{sys}	E	Δ_{stat}	Δ_{sys}	E	Δ_{stat}	Δ_{sys}
-0.80	0.5330	0.2511	0.0555	0.0553	0.3015	0.0089	-0.1023	-0.3277	0.0137	-0.0468	-0.3483	0.0052
-0.40	0.2568	0.1772	0.0556	0.0393	0.2025	0.0058	0.5509	0.3498	0.0592	0.3230	0.2404	0.0610
0.00	0.2423	0.1531	0.0253	0.3145	0.2503	0.0496	0.3843	0.1531	0.1198	0.2884	0.1743	0.0414
0.40	0.6584	0.1409	0.0997	0.5132	0.1731	0.0554	0.7622	0.2028	0.0793	0.5282	0.1551	0.1111
0.80	0.4883	0.2526	0.0583	0.8539	0.2730	0.0891	0.8190	0.2978	0.0992	0.4967	0.2888	0.0597

Total Distributions for E

W [MeV]	ΔW [MeV]	E	Δ_{stat}	Δ_{sys}
1495.0	5.0	1.1948	0.0665	0.1503
1505.0	5.0	1.0929	0.0610	0.1600
1515.0	5.0	1.0417	0.0752	0.1692
1525.0	5.0	1.0303	0.0967	0.1582
1535.0	5.0	0.8836	0.0940	0.1281
1547.5	7.5	0.9119	0.0756	0.1096
1562.5	7.5	0.9014	0.0615	0.1147
1577.5	7.5	0.9198	0.0626	0.1241
1592.5	7.5	0.9832	0.0565	0.1182
1607.5	7.5	0.8620	0.0555	0.1025
1622.5	7.5	0.8782	0.0567	0.0899
1637.5	7.5	0.7425	0.0567	0.0809
1652.5	7.5	0.7261	0.0625	0.0719
1667.5	7.5	0.5714	0.0614	0.0637
1682.5	7.5	0.5803	0.0648	0.0578
1697.5	7.5	0.5090	0.0625	0.0528
1712.5	7.5	0.4465	0.0668	0.0487
1727.5	7.5	0.4664	0.0614	0.0507
1742.5	7.5	0.4915	0.0728	0.0597
1757.5	7.5	0.6339	0.0784	0.0679
1772.5	7.5	0.5874	0.0694	0.0698
1787.5	7.5	0.6520	0.0804	0.0697
1802.5	7.5	0.5899	0.0894	0.0689
1817.5	7.5	0.5705	0.0943	0.0622
1832.5	7.5	0.4409	0.0842	0.0522
1847.5	7.5	0.4345	0.1052	0.0501
1862.5	7.5	0.5718	0.1112	0.0538
1882.5	12.5	0.3949	0.1024	0.0501

F.4.6 Helicity Dependent Cross Sections for $\gamma p \rightarrow \eta p$ as a Function of W
Angular Cross Sections $\sigma_{1/2}$

$\cos(\theta_\eta^*)$	W=(1495.0±5.0) MeV			W=(1505.0±5.0) MeV			W=(1515.0±5.0) MeV			W=(1525.0±5.0) MeV		
	$d\sigma_{1/2}/d\Omega$ [$\mu\text{b}/\text{sr}$]	Δ_{stat} [$\mu\text{b}/\text{sr}$]	Δ_{sys} [$\mu\text{b}/\text{sr}$]	$d\sigma_{1/2}/d\Omega$ [$\mu\text{b}/\text{sr}$]	Δ_{stat} [$\mu\text{b}/\text{sr}$]	Δ_{sys} [$\mu\text{b}/\text{sr}$]	$d\sigma_{1/2}/d\Omega$ [$\mu\text{b}/\text{sr}$]	Δ_{stat} [$\mu\text{b}/\text{sr}$]	Δ_{sys} [$\mu\text{b}/\text{sr}$]	$d\sigma_{1/2}/d\Omega$ [$\mu\text{b}/\text{sr}$]	Δ_{stat} [$\mu\text{b}/\text{sr}$]	Δ_{sys} [$\mu\text{b}/\text{sr}$]
-0.80	1.3001	0.1068	0.1553	1.9828	0.1027	0.2467	2.2001	0.1018	0.2777	2.2610	0.0991	0.2706
-0.40	1.3845	0.0755	0.1645	1.9211	0.0880	0.2200	2.0252	0.0947	0.2297	2.4861	0.1174	0.3315
0.00	1.1608	0.0740	0.1373	1.7769	0.1166	0.2481	2.2309	0.1657	0.3305	2.5699	0.2096	0.3693
0.40	1.3199	0.0870	0.1802	2.0839	0.1740	0.4060	2.6497	0.3144	0.5621	2.4365	0.4361	0.5722
0.80	1.4363	0.1127	0.1982	1.9520	0.1707	0.3159	2.4212	0.3302	0.5872	2.7590	0.5149	0.6528
$\cos(\theta_\eta^*)$	W=(1535.0±5.0) MeV			W=(1547.5±7.5) MeV			W=(1562.5±7.5) MeV			W=(1577.5±7.5) MeV		
	$d\sigma_{1/2}/d\Omega$ [$\mu\text{b}/\text{sr}$]	Δ_{stat} [$\mu\text{b}/\text{sr}$]	Δ_{sys} [$\mu\text{b}/\text{sr}$]	$d\sigma_{1/2}/d\Omega$ [$\mu\text{b}/\text{sr}$]	Δ_{stat} [$\mu\text{b}/\text{sr}$]	Δ_{sys} [$\mu\text{b}/\text{sr}$]	$d\sigma_{1/2}/d\Omega$ [$\mu\text{b}/\text{sr}$]	Δ_{stat} [$\mu\text{b}/\text{sr}$]	Δ_{sys} [$\mu\text{b}/\text{sr}$]	$d\sigma_{1/2}/d\Omega$ [$\mu\text{b}/\text{sr}$]	Δ_{stat} [$\mu\text{b}/\text{sr}$]	Δ_{sys} [$\mu\text{b}/\text{sr}$]
-0.80	2.3192	0.0957	0.2659	2.0652	0.0711	0.2245	1.8746	0.0680	0.2009	1.8116	0.0734	0.2317
-0.40	2.3255	0.1150	0.2612	2.4159	0.0933	0.2515	2.2624	0.0957	0.2363	2.1733	0.1024	0.2495
0.00	2.5934	0.1828	0.2883	2.4906	0.1134	0.2632	2.0141	0.0843	0.2102	1.9450	0.0806	0.2390
0.40	2.1635	0.2374	0.2870	2.2809	0.1301	0.2862	2.0347	0.0941	0.2433	1.9766	0.0868	0.2679
0.80	2.1732	0.5573	0.3942	1.3822	0.6312	0.3828	2.1944	0.3919	0.4400	1.6115	0.4418	0.4908
$\cos(\theta_\eta^*)$	W=(1592.5±7.5) MeV			W=(1607.5±7.5) MeV			W=(1622.5±7.5) MeV			W=(1637.5±7.5) MeV		
	$d\sigma_{1/2}/d\Omega$ [$\mu\text{b}/\text{sr}$]	Δ_{stat} [$\mu\text{b}/\text{sr}$]	Δ_{sys} [$\mu\text{b}/\text{sr}$]	$d\sigma_{1/2}/d\Omega$ [$\mu\text{b}/\text{sr}$]	Δ_{stat} [$\mu\text{b}/\text{sr}$]	Δ_{sys} [$\mu\text{b}/\text{sr}$]	$d\sigma_{1/2}/d\Omega$ [$\mu\text{b}/\text{sr}$]	Δ_{stat} [$\mu\text{b}/\text{sr}$]	Δ_{sys} [$\mu\text{b}/\text{sr}$]	$d\sigma_{1/2}/d\Omega$ [$\mu\text{b}/\text{sr}$]	Δ_{stat} [$\mu\text{b}/\text{sr}$]	Δ_{sys} [$\mu\text{b}/\text{sr}$]
-0.80	1.6081	0.0652	0.1869	1.3226	0.0620	0.1700	0.9645	0.0509	0.1037	0.7576	0.0463	0.0877
-0.40	1.6743	0.0782	0.1828	1.2532	0.0616	0.1680	0.9788	0.0509	0.1516	0.7293	0.0442	0.1022
0.00	1.5329	0.0665	0.1738	1.3406	0.0565	0.1402	0.9592	0.0466	0.1011	0.6995	0.0421	0.0729
0.40	1.5669	0.0739	0.1894	1.2317	0.0670	0.1663	0.8662	0.0474	0.0905	0.6883	0.0407	0.0714
0.80	1.6433	0.2216	0.2968	1.1607	0.1923	0.2598	0.7483	0.1232	0.1266	0.6461	0.1022	0.1302
$\cos(\theta_\eta^*)$	W=(1652.5±7.5) MeV			W=(1667.5±7.5) MeV			W=(1682.5±7.5) MeV			W=(1697.5±7.5) MeV		
	$d\sigma_{1/2}/d\Omega$ [$\mu\text{b}/\text{sr}$]	Δ_{stat} [$\mu\text{b}/\text{sr}$]	Δ_{sys} [$\mu\text{b}/\text{sr}$]	$d\sigma_{1/2}/d\Omega$ [$\mu\text{b}/\text{sr}$]	Δ_{stat} [$\mu\text{b}/\text{sr}$]	Δ_{sys} [$\mu\text{b}/\text{sr}$]	$d\sigma_{1/2}/d\Omega$ [$\mu\text{b}/\text{sr}$]	Δ_{stat} [$\mu\text{b}/\text{sr}$]	Δ_{sys} [$\mu\text{b}/\text{sr}$]	$d\sigma_{1/2}/d\Omega$ [$\mu\text{b}/\text{sr}$]	Δ_{stat} [$\mu\text{b}/\text{sr}$]	Δ_{sys} [$\mu\text{b}/\text{sr}$]
-0.80	0.4485	0.0328	0.0522	0.3727	0.0368	0.0500	0.3573	0.0330	0.0430	0.2971	0.0283	0.0309
-0.40	0.5254	0.0404	0.0572	0.4509	0.0311	0.0758	0.3464	0.0278	0.0615	0.3515	0.0316	0.0379
0.00	0.4749	0.0313	0.0662	0.4183	0.0327	0.0435	0.4047	0.0324	0.0419	0.4262	0.0291	0.0537
0.40	0.5026	0.0342	0.0522	0.4087	0.0287	0.0427	0.3770	0.0313	0.0417	0.4171	0.0363	0.0555
0.80	0.5349	0.0999	0.1218	0.2242	0.0437	0.0286	0.3022	0.0548	0.0597	0.2308	0.0376	0.0241
$\cos(\theta_\eta^*)$	W=(1712.5±7.5) MeV			W=(1727.5±7.5) MeV			W=(1742.5±7.5) MeV			W=(1757.5±7.5) MeV		
	$d\sigma_{1/2}/d\Omega$ [$\mu\text{b}/\text{sr}$]	Δ_{stat} [$\mu\text{b}/\text{sr}$]	Δ_{sys} [$\mu\text{b}/\text{sr}$]	$d\sigma_{1/2}/d\Omega$ [$\mu\text{b}/\text{sr}$]	Δ_{stat} [$\mu\text{b}/\text{sr}$]	Δ_{sys} [$\mu\text{b}/\text{sr}$]	$d\sigma_{1/2}/d\Omega$ [$\mu\text{b}/\text{sr}$]	Δ_{stat} [$\mu\text{b}/\text{sr}$]	Δ_{sys} [$\mu\text{b}/\text{sr}$]	$d\sigma_{1/2}/d\Omega$ [$\mu\text{b}/\text{sr}$]	Δ_{stat} [$\mu\text{b}/\text{sr}$]	Δ_{sys} [$\mu\text{b}/\text{sr}$]
-0.80	0.1947	0.0317	0.0279	0.1847	0.0297	0.0256	0.2510	0.0276	0.0294	0.1727	0.0218	0.0180
-0.40	0.3243	0.0305	0.0373	0.2311	0.0291	0.0280	0.2205	0.0257	0.0332	0.2358	0.0286	0.0257
0.00	0.3276	0.0310	0.0358	0.4446	0.0331	0.0486	0.3592	0.0349	0.0387	0.4092	0.0393	0.0564
0.40	0.4345	0.0366	0.0500	0.4881	0.0325	0.0560	0.5244	0.0397	0.0628	0.4910	0.0396	0.0636
0.80	0.3836	0.0487	0.0464	0.3100	0.0347	0.0510	0.2811	0.0559	0.0497	0.4413	0.0625	0.0793
$\cos(\theta_\eta^*)$	W=(1772.5±7.5) MeV			W=(1787.5±7.5) MeV			W=(1802.5±7.5) MeV			W=(1817.5±7.5) MeV		
	$d\sigma_{1/2}/d\Omega$ [$\mu\text{b}/\text{sr}$]	Δ_{stat} [$\mu\text{b}/\text{sr}$]	Δ_{sys} [$\mu\text{b}/\text{sr}$]	$d\sigma_{1/2}/d\Omega$ [$\mu\text{b}/\text{sr}$]	Δ_{stat} [$\mu\text{b}/\text{sr}$]	Δ_{sys} [$\mu\text{b}/\text{sr}$]	$d\sigma_{1/2}/d\Omega$ [$\mu\text{b}/\text{sr}$]	Δ_{stat} [$\mu\text{b}/\text{sr}$]	Δ_{sys} [$\mu\text{b}/\text{sr}$]	$d\sigma_{1/2}/d\Omega$ [$\mu\text{b}/\text{sr}$]	Δ_{stat} [$\mu\text{b}/\text{sr}$]	Δ_{sys} [$\mu\text{b}/\text{sr}$]
-0.80	0.1974	0.0283	0.0317	0.1907	0.0271	0.0290	0.1809	0.0235	0.0195	0.0956	0.0265	0.0152
-0.40	0.2257	0.0241	0.0380	0.2347	0.0294	0.0244	0.2159	0.0238	0.0424	0.1891	0.0267	0.0272
0.00	0.3673	0.0277	0.0487	0.3929	0.0307	0.0436	0.3392	0.0384	0.0419	0.3540	0.0352	0.0368
0.40	0.4596	0.0362	0.0520	0.4779	0.0450	0.0719	0.3023	0.0428	0.0452	0.4088	0.0418	0.0476
0.80	0.4217	0.0526	0.0567	0.3780	0.0508	0.0467	0.4365	0.0646	0.0650	0.4597	0.0790	0.0941

$\cos(\theta_\eta^*)$	W=(1832.5±7.5) MeV			W=(1847.5±7.5) MeV			W=(1862.5±7.5) MeV			W=(1882.5±12.5) MeV		
	$d\sigma_{1/2}/d\Omega$ [$\mu\text{b}/\text{sr}$]	Δ_{stat} [$\mu\text{b}/\text{sr}$]	Δ_{sys} [$\mu\text{b}/\text{sr}$]	$d\sigma_{1/2}/d\Omega$ [$\mu\text{b}/\text{sr}$]	Δ_{stat} [$\mu\text{b}/\text{sr}$]	Δ_{sys} [$\mu\text{b}/\text{sr}$]	$d\sigma_{1/2}/d\Omega$ [$\mu\text{b}/\text{sr}$]	Δ_{stat} [$\mu\text{b}/\text{sr}$]	Δ_{sys} [$\mu\text{b}/\text{sr}$]	$d\sigma_{1/2}/d\Omega$ [$\mu\text{b}/\text{sr}$]	Δ_{stat} [$\mu\text{b}/\text{sr}$]	Δ_{sys} [$\mu\text{b}/\text{sr}$]
-0.80	0.1288	0.0217	0.0134	0.0936	0.0272	0.0151	0.0722	0.0268	0.0101	0.0588	0.0221	0.0065
-0.40	0.1674	0.0245	0.0362	0.1368	0.0274	0.0201	0.1725	0.0397	0.0185	0.1406	0.0266	0.0265
0.00	0.2833	0.0357	0.0296	0.2662	0.0512	0.0420	0.2457	0.0283	0.0766	0.2346	0.0330	0.0337
0.40	0.3812	0.0337	0.0577	0.3379	0.0397	0.0365	0.4010	0.0476	0.0417	0.3008	0.0324	0.0633
0.80	0.3072	0.0537	0.0367	0.3636	0.0558	0.0380	0.4234	0.0722	0.0513	0.3329	0.0673	0.0400

Angular Cross Sections $\sigma_{3/2}$

$\cos(\theta_\eta^*)$	W=(1495.0±5.0) MeV			W=(1505.0±5.0) MeV			W=(1515.0±5.0) MeV			W=(1525.0±5.0) MeV		
	$d\sigma_{3/2}/d\Omega$ [$\mu\text{b}/\text{sr}$]	Δ_{stat} [$\mu\text{b}/\text{sr}$]	Δ_{sys} [$\mu\text{b}/\text{sr}$]	$d\sigma_{3/2}/d\Omega$ [$\mu\text{b}/\text{sr}$]	Δ_{stat} [$\mu\text{b}/\text{sr}$]	Δ_{sys} [$\mu\text{b}/\text{sr}$]	$d\sigma_{3/2}/d\Omega$ [$\mu\text{b}/\text{sr}$]	Δ_{stat} [$\mu\text{b}/\text{sr}$]	Δ_{sys} [$\mu\text{b}/\text{sr}$]	$d\sigma_{3/2}/d\Omega$ [$\mu\text{b}/\text{sr}$]	Δ_{stat} [$\mu\text{b}/\text{sr}$]	Δ_{sys} [$\mu\text{b}/\text{sr}$]
-0.80	-0.0918	0.1068	0.0425	-0.1474	0.1027	0.0749	-0.0719	0.1018	0.0823	0.0184	0.0991	0.0684
-0.40	-0.1850	0.0755	0.0496	-0.0329	0.0880	0.0478	0.1776	0.0947	0.0541	-0.0470	0.1174	0.1065
0.00	0.0807	0.0740	0.0364	0.1709	0.1166	0.0929	0.2467	0.1657	0.1336	0.1486	0.2096	0.1363
0.40	-0.1293	0.0870	0.0658	-0.2339	0.1740	0.1928	-0.4225	0.3144	0.2877	0.0933	0.4361	0.2668
0.80	-0.2290	0.1127	0.0796	-0.1973	0.1707	0.1352	-0.3758	0.3302	0.3091	-0.4835	0.5149	0.3485

$\cos(\theta_\eta^*)$	W=(1535.0±5.0) MeV			W=(1547.5±7.5) MeV			W=(1562.5±7.5) MeV			W=(1577.5±7.5) MeV		
	$d\sigma_{3/2}/d\Omega$ [$\mu\text{b}/\text{sr}$]	Δ_{stat} [$\mu\text{b}/\text{sr}$]	Δ_{sys} [$\mu\text{b}/\text{sr}$]	$d\sigma_{3/2}/d\Omega$ [$\mu\text{b}/\text{sr}$]	Δ_{stat} [$\mu\text{b}/\text{sr}$]	Δ_{sys} [$\mu\text{b}/\text{sr}$]	$d\sigma_{3/2}/d\Omega$ [$\mu\text{b}/\text{sr}$]	Δ_{stat} [$\mu\text{b}/\text{sr}$]	Δ_{sys} [$\mu\text{b}/\text{sr}$]	$d\sigma_{3/2}/d\Omega$ [$\mu\text{b}/\text{sr}$]	Δ_{stat} [$\mu\text{b}/\text{sr}$]	Δ_{sys} [$\mu\text{b}/\text{sr}$]
-0.80	-0.0299	0.0957	0.0578	0.0708	0.0711	0.0359	0.0562	0.0680	0.0272	0.0356	0.0734	0.0694
-0.40	0.1658	0.1150	0.0568	0.0665	0.0933	0.0147	0.2712	0.0957	0.0329	0.1943	0.1024	0.0620
0.00	0.1207	0.1828	0.0562	-0.0922	0.1134	0.0288	0.1452	0.0843	0.0203	0.0716	0.0806	0.0671
0.40	0.3346	0.2374	0.1092	-0.0608	0.1301	0.0832	0.0490	0.0941	0.0624	-0.0967	0.0868	0.0912
0.80	0.0569	0.5573	0.1662	0.7877	0.6312	0.2903	-0.0794	0.3919	0.1954	0.2769	0.4418	0.2719

$\cos(\theta_\eta^*)$	W=(1592.5±7.5) MeV			W=(1607.5±7.5) MeV			W=(1622.5±7.5) MeV			W=(1637.5±7.5) MeV		
	$d\sigma_{3/2}/d\Omega$ [$\mu\text{b}/\text{sr}$]	Δ_{stat} [$\mu\text{b}/\text{sr}$]	Δ_{sys} [$\mu\text{b}/\text{sr}$]	$d\sigma_{3/2}/d\Omega$ [$\mu\text{b}/\text{sr}$]	Δ_{stat} [$\mu\text{b}/\text{sr}$]	Δ_{sys} [$\mu\text{b}/\text{sr}$]	$d\sigma_{3/2}/d\Omega$ [$\mu\text{b}/\text{sr}$]	Δ_{stat} [$\mu\text{b}/\text{sr}$]	Δ_{sys} [$\mu\text{b}/\text{sr}$]	$d\sigma_{3/2}/d\Omega$ [$\mu\text{b}/\text{sr}$]	Δ_{stat} [$\mu\text{b}/\text{sr}$]	Δ_{sys} [$\mu\text{b}/\text{sr}$]
-0.80	-0.0070	0.0652	0.0426	0.0708	0.0620	0.0536	0.0601	0.0509	0.0159	0.0952	0.0463	0.0242
-0.40	0.0882	0.0782	0.0318	0.1277	0.0616	0.0603	0.1033	0.0509	0.0632	0.1812	0.0442	0.0469
0.00	0.1788	0.0665	0.0436	0.0813	0.0565	0.0131	0.0891	0.0466	0.0137	0.1769	0.0421	0.0191
0.40	-0.0449	0.0739	0.0504	0.0993	0.0670	0.0585	0.0269	0.0474	0.0067	0.0563	0.0407	0.0063
0.80	-0.1719	0.2216	0.1355	0.0724	0.1923	0.1226	-0.0076	0.1232	0.0506	-0.0407	0.1022	0.0595

$\cos(\theta_\eta^*)$	W=(1652.5±7.5) MeV			W=(1667.5±7.5) MeV			W=(1682.5±7.5) MeV			W=(1697.5±7.5) MeV		
	$d\sigma_{3/2}/d\Omega$ [$\mu\text{b}/\text{sr}$]	Δ_{stat} [$\mu\text{b}/\text{sr}$]	Δ_{sys} [$\mu\text{b}/\text{sr}$]	$d\sigma_{3/2}/d\Omega$ [$\mu\text{b}/\text{sr}$]	Δ_{stat} [$\mu\text{b}/\text{sr}$]	Δ_{sys} [$\mu\text{b}/\text{sr}$]	$d\sigma_{3/2}/d\Omega$ [$\mu\text{b}/\text{sr}$]	Δ_{stat} [$\mu\text{b}/\text{sr}$]	Δ_{sys} [$\mu\text{b}/\text{sr}$]	$d\sigma_{3/2}/d\Omega$ [$\mu\text{b}/\text{sr}$]	Δ_{stat} [$\mu\text{b}/\text{sr}$]	Δ_{sys} [$\mu\text{b}/\text{sr}$]
-0.80	0.1277	0.0328	0.0202	0.1466	0.0368	0.0268	0.0559	0.0330	0.0139	0.0806	0.0283	0.0086
-0.40	0.1746	0.0404	0.0216	0.1014	0.0311	0.0381	0.1062	0.0278	0.0344	0.1423	0.0316	0.0165
0.00	0.1370	0.0313	0.0318	0.1600	0.0327	0.0168	0.1542	0.0324	0.0160	0.1307	0.0291	0.0241
0.40	0.0241	0.0342	0.0033	0.0795	0.0287	0.0089	0.1546	0.0313	0.0190	0.1186	0.0363	0.0256
0.80	-0.1950	0.0999	0.0767	0.0312	0.0437	0.0101	-0.0255	0.0548	0.0277	0.0832	0.0376	0.0088

$\cos(\theta_\eta^*)$	W=(1712.5±7.5) MeV			W=(1727.5±7.5) MeV			W=(1742.5±7.5) MeV			W=(1757.5±7.5) MeV		
$d\sigma_{3/2}/d\Omega$ [$\mu\text{b}/\text{sr}$]	Δ_{stat} [$\mu\text{b}/\text{sr}$]	Δ_{sys} [$\mu\text{b}/\text{sr}$]	$d\sigma_{3/2$									

APPENDIX F. DATA TABLES

$\cos(\theta_\eta^*)$	W=(1772.5±7.5) MeV			W=(1787.5±7.5) MeV			W=(1802.5±7.5) MeV			W=(1817.5±7.5) MeV		
	$d\sigma_{3/2}/d\Omega$ [$\mu\text{b}/\text{sr}$]	Δ_{stat} [$\mu\text{b}/\text{sr}$]	Δ_{sys} [$\mu\text{b}/\text{sr}$]	$d\sigma_{3/2}/d\Omega$ [$\mu\text{b}/\text{sr}$]	Δ_{stat} [$\mu\text{b}/\text{sr}$]	Δ_{sys} [$\mu\text{b}/\text{sr}$]	$d\sigma_{3/2}/d\Omega$ [$\mu\text{b}/\text{sr}$]	Δ_{stat} [$\mu\text{b}/\text{sr}$]	Δ_{sys} [$\mu\text{b}/\text{sr}$]	$d\sigma_{3/2}/d\Omega$ [$\mu\text{b}/\text{sr}$]	Δ_{stat} [$\mu\text{b}/\text{sr}$]	Δ_{sys} [$\mu\text{b}/\text{sr}$]
-0.80	0.0400	0.0283	0.0151	0.0283	0.0271	0.0126	0.0152	0.0235	0.0033	0.0945	0.0265	0.0151
-0.40	0.0951	0.0241	0.0235	0.1024	0.0294	0.0107	0.0948	0.0238	0.0277	0.1014	0.0267	0.0179
0.00	0.1446	0.0277	0.0259	0.0884	0.0307	0.0133	0.1222	0.0384	0.0200	0.0901	0.0352	0.0095
0.40	0.1136	0.0362	0.0176	0.0539	0.0450	0.0296	0.1953	0.0428	0.0336	0.1026	0.0418	0.0173
0.80	0.0138	0.0526	0.0187	0.0636	0.0508	0.0163	-0.0552	0.0646	0.0269	-0.0203	0.0790	0.0425

$\cos(\theta_\eta^*)$	W=(1832.5±7.5) MeV			W=(1847.5±7.5) MeV			W=(1862.5±7.5) MeV			W=(1882.5±12.5) MeV		
	$d\sigma_{3/2}/d\Omega$ [$\mu\text{b}/\text{sr}$]	Δ_{stat} [$\mu\text{b}/\text{sr}$]	Δ_{sys} [$\mu\text{b}/\text{sr}$]	$d\sigma_{3/2}/d\Omega$ [$\mu\text{b}/\text{sr}$]	Δ_{stat} [$\mu\text{b}/\text{sr}$]	Δ_{sys} [$\mu\text{b}/\text{sr}$]	$d\sigma_{3/2}/d\Omega$ [$\mu\text{b}/\text{sr}$]	Δ_{stat} [$\mu\text{b}/\text{sr}$]	Δ_{sys} [$\mu\text{b}/\text{sr}$]	$d\sigma_{3/2}/d\Omega$ [$\mu\text{b}/\text{sr}$]	Δ_{stat} [$\mu\text{b}/\text{sr}$]	Δ_{sys} [$\mu\text{b}/\text{sr}$]
-0.80	0.0392	0.0217	0.0042	0.0838	0.0272	0.0140	0.0886	0.0268	0.0118	0.0646	0.0221	0.0071
-0.40	0.0990	0.0245	0.0273	0.1264	0.0274	0.0189	0.0500	0.0397	0.0061	0.0720	0.0266	0.0184
0.00	0.1728	0.0357	0.0182	0.1388	0.0512	0.0281	0.1093	0.0283	0.0534	0.1296	0.0330	0.0225
0.40	0.0785	0.0337	0.0267	0.1087	0.0397	0.0131	0.0541	0.0476	0.0060	0.0929	0.0324	0.0373
0.80	0.1056	0.0537	0.0164	0.0287	0.0558	0.0039	0.0421	0.0722	0.0153	0.1119	0.0673	0.0178

Total Cross Sections $\sigma_{1/2}$ and $\sigma_{3/2}$

W [MeV]	ΔW [MeV]	$\sigma_{1/2}$ [μb]	Δ_{stat} [μb]	Δ_{sys} [μb]	W [MeV]	ΔW [MeV]	$\sigma_{3/2}$ [μb]	Δ_{stat} [μb]	Δ_{sys} [μb]
1495.0	5.0	16.6555	0.5242	2.0954	1495.0	5.0	-1.4783	0.5242	0.6653
1505.0	5.0	24.3533	0.7261	3.5198	1505.0	5.0	-1.0809	0.7261	1.3007
1515.0	5.0	28.3466	1.0673	4.6315	1515.0	5.0	-0.5794	1.0673	1.8147
1525.0	5.0	31.1512	1.5087	4.7996	1525.0	5.0	-0.4645	1.5087	1.8441
1535.0	5.0	28.7961	1.4600	4.0577	1535.0	5.0	1.7802	1.4600	1.3824
1547.5	7.5	27.3513	1.0979	3.3763	1547.5	7.5	1.2607	1.0979	0.9750
1562.5	7.5	25.8278	0.8548	3.2629	1562.5	7.5	1.3400	0.8548	0.9546
1577.5	7.5	24.0998	0.8027	3.1581	1577.5	7.5	1.0062	0.8027	0.9956
1592.5	7.5	20.0534	0.5845	2.5604	1592.5	7.5	0.1701	0.5845	0.7433
1607.5	7.5	15.7801	0.4809	1.7876	1607.5	7.5	1.1698	0.4809	0.3823
1622.5	7.5	11.2658	0.3488	1.2347	1622.5	7.5	0.7306	0.3488	0.1767
1637.5	7.5	8.7058	0.2910	0.8778	1637.5	7.5	1.2863	0.2910	0.1199
1652.5	7.5	5.9202	0.2206	0.6332	1652.5	7.5	0.9395	0.2206	0.1225
1667.5	7.5	4.6903	0.1889	0.4955	1667.5	7.5	1.2792	0.1889	0.1257
1682.5	7.5	4.3925	0.1859	0.4516	1682.5	7.5	1.1667	0.1859	0.1298
1697.5	7.5	4.2755	0.1825	0.4503	1697.5	7.5	1.3910	0.1825	0.1482
1712.5	7.5	4.1470	0.1967	0.4522	1712.5	7.5	1.5867	0.1967	0.1740
1727.5	7.5	4.1448	0.1793	0.4575	1727.5	7.5	1.5083	0.1793	0.1913
1742.5	7.5	4.0299	0.2015	0.4717	1742.5	7.5	1.3738	0.2015	0.1919
1757.5	7.5	4.2811	0.2107	0.4778	1757.5	7.5	0.9592	0.2107	0.1714
1772.5	7.5	4.1116	0.1858	0.4627	1772.5	7.5	1.0688	0.1858	0.1410
1787.5	7.5	4.1422	0.2073	0.4446	1787.5	7.5	0.8726	0.2073	0.1329
1802.5	7.5	3.6558	0.2108	0.4318	1802.5	7.5	0.9429	0.2108	0.1485
1817.5	7.5	3.6750	0.2259	0.4042	1817.5	7.5	1.0049	0.2259	0.1634
1832.5	7.5	3.1541	0.1906	0.3566	1832.5	7.5	1.2239	0.1906	0.1547
1847.5	7.5	3.0125	0.2265	0.3272	1847.5	7.5	1.1876	0.2265	0.1235
1862.5	7.5	3.2665	0.2396	0.3316	1862.5	7.5	0.8899	0.2396	0.1227
1882.5	12.5	2.6599	0.2059	0.3374	1882.5	12.5	1.1538	0.2059	0.1838

F.4.7 E for $\gamma p n \rightarrow \eta n$ as a Function of W

 Angular Distributions for E

$\cos(\theta_\eta^*)$	W=(1495.0±5.0) MeV			W=(1505.0±5.0) MeV			W=(1515.0±5.0) MeV			W=(1525.0±5.0) MeV		
	E	Δ_{stat}	Δ_{sys}									
-0.80	1.4033	0.3764	0.1957	1.2430	0.2053	0.2700	1.0640	0.1849	0.1487	1.0244	0.1751	0.1590
-0.40	1.0771	0.2390	0.2214	0.7876	0.1885	0.1246	0.9789	0.2052	0.1035	0.8454	0.2010	0.1293
0.00	1.4320	0.2797	0.2952	0.9014	0.2196	0.1561	0.7771	0.2143	0.0822	0.7526	0.2304	0.0781
0.40	0.7804	0.2886	0.0871	0.5983	0.2593	0.0653	0.9075	0.2404	0.1167	0.8029	0.3333	0.1253
0.80	1.4920	0.4049	0.1628	0.7395	0.3523	0.1075	1.5795	0.3293	0.1691	0.8702	0.4148	0.1247
$\cos(\theta_\eta^*)$	W=(1535.0±5.0) MeV			W=(1547.5±7.5) MeV			W=(1562.5±7.5) MeV			W=(1577.5±7.5) MeV		
	E	Δ_{stat}	Δ_{sys}									
-0.80	0.8374	0.1388	0.2087	1.0420	0.1393	0.1540	0.9926	0.1337	0.1773	1.0927	0.1415	0.1807
-0.40	0.8859	0.1889	0.0941	0.6405	0.1332	0.0984	1.0328	0.1422	0.1338	0.9951	0.1496	0.1117
0.00	0.8734	0.2104	0.0905	0.7959	0.1473	0.1430	0.8980	0.1492	0.1343	0.5372	0.1372	0.0849
0.40	0.8367	0.2282	0.0868	1.3872	0.1992	0.1457	0.9289	0.1726	0.0964	1.0556	0.1772	0.1219
0.80	0.2622	0.3879	0.0372	1.3832	0.3413	0.1802	0.9438	0.3618	0.1799	0.8881	0.3191	0.1199
$\cos(\theta_\eta^*)$	W=(1592.5±7.5) MeV			W=(1607.5±7.5) MeV			W=(1622.5±7.5) MeV			W=(1637.5±7.5) MeV		
	E	Δ_{stat}	Δ_{sys}									
-0.80	0.4495	0.1322	0.1003	0.7207	0.1342	0.1517	1.0349	0.1605	0.1740	0.6287	0.1487	0.1175
-0.40	0.7492	0.1576	0.1075	0.5912	0.1705	0.0612	0.8112	0.1498	0.1865	0.7310	0.1855	0.0795
0.00	0.7177	0.1460	0.0819	1.0011	0.1580	0.1132	0.6698	0.1384	0.0988	0.8984	0.1645	0.0973
0.40	1.0586	0.1912	0.1170	0.8501	0.1973	0.0987	0.5839	0.1481	0.1018	0.9418	0.1731	0.0980
0.80	1.5904	0.4137	0.2459	1.6354	0.5148	0.3447	0.7799	0.3434	0.0949	0.9740	0.5531	0.2332
$\cos(\theta_\eta^*)$	W=(1652.5±7.5) MeV			W=(1667.5±7.5) MeV			W=(1682.5±7.5) MeV			W=(1697.5±7.5) MeV		
	E	Δ_{stat}	Δ_{sys}									
-0.80	1.1516	0.1643	0.1519	0.9530	0.1591	0.1150	0.7056	0.1452	0.1574	0.5450	0.1537	0.1529
-0.40	0.7593	0.1692	0.0806	0.6662	0.1302	0.1103	0.4998	0.1498	0.0807	0.7337	0.1616	0.1202
0.00	0.5688	0.1255	0.0688	0.6625	0.1200	0.0814	0.5239	0.1239	0.0768	0.5957	0.1519	0.0622
0.40	0.8042	0.1635	0.0982	0.8394	0.1484	0.0883	0.5469	0.1412	0.0587	0.5565	0.1601	0.0604
0.80	0.3705	0.3176	0.0394	0.6057	0.3220	0.0798	1.3417	0.3396	0.1392	0.5198	0.3132	0.0539
$\cos(\theta_\eta^*)$	W=(1712.5±7.5) MeV			W=(1727.5±7.5) MeV			W=(1742.5±7.5) MeV			W=(1757.5±7.5) MeV		
	E	Δ_{stat}	Δ_{sys}									
-0.80	0.8013	0.1943	0.2071	1.0840	0.3543	0.1752	0.7454	0.2803	0.1140	0.7687	0.2541	0.1265
-0.40	0.8614	0.2153	0.1115	0.3713	0.1670	0.1157	0.8836	0.1925	0.2345	0.1958	0.2187	0.0236
0.00	0.7529	0.1562	0.0896	0.4710	0.1427	0.0808	0.4000	0.1585	0.0720	0.5188	0.1578	0.0794
0.40	0.3203	0.1520	0.0376	0.3910	0.1927	0.0488	0.5515	0.1853	0.0572	0.1519	0.1773	0.0157
0.80	0.5691	0.2599	0.0855	0.1017	0.4902	0.0245	0.5656	0.4174	0.0596	1.8160	1.0334	0.5952
$\cos(\theta_\eta^*)$	W=(1772.5±7.5) MeV			W=(1787.5±7.5) MeV			W=(1802.5±7.5) MeV			W=(1817.5±7.5) MeV		
	E	Δ_{stat}	Δ_{sys}									
-0.80	1.1719	0.3151	0.1643	0.5511	0.2511	0.0992	0.8679	0.2942	0.1953	0.4830	0.3032	0.0679
-0.40	0.4751	0.2489	0.0511	0.7473	0.2765	0.0818	0.0763	0.2315	0.0124	0.2632	0.2072	0.1036
0.00	0.6092	0.1881	0.0631	0.7912	0.2418	0.0906	0.1139	0.1959	0.0128	0.5216	0.2580	0.0643
0.40	0.7597	0.2090	0.0971	0.6860	0.2529	0.1015	0.3900	0.2083	0.0438	0.3867	0.3044	0.0682
0.80	0.7108	0.5313	0.1261	1.5321	0.6537	0.3595	0.1397	0.3656	0.0146	0.7492	0.3145	0.1340

APPENDIX F. DATA TABLES

$\cos(\theta_\eta^*)$	W=(1832.5±7.5) MeV			W=(1847.5±7.5) MeV			W=(1862.5±7.5) MeV			W=(1882.5±12.5) MeV		
	E	Δ_{stat}	Δ_{sys}	E	Δ_{stat}	Δ_{sys}	E	Δ_{stat}	Δ_{sys}	E	Δ_{stat}	Δ_{sys}
-0.80	1.2071	0.4022	0.1410	0.2181	0.3551	0.0243	0.2693	0.3334	0.0699	1.0649	0.4084	0.2491
-0.40	0.0723	0.2677	0.0164	-0.0956	-0.3588	0.0104	0.3095	0.3093	0.1200	0.3836	0.3471	0.1236
0.00	0.9564	0.3748	0.1292	0.3981	0.1885	0.1846	0.0847	0.2965	0.0089	0.1786	0.2944	0.0330
0.40	0.7478	0.2912	0.0781	0.2845	0.2261	0.0578	0.7540	0.4401	0.1020	0.1896	0.3094	0.0336
0.80	1.6737	0.6342	0.1786	0.4518	0.4894	0.0681	1.0374	0.6613	0.1561	-0.2746	-0.5931	0.0441

Total Distributions for E

W [MeV]	ΔW [MeV]	E	Δ_{stat}	Δ_{sys}
1495.0	5.0	1.2240	0.1486	0.1719
1505.0	5.0	0.8799	0.1107	0.1244
1515.0	5.0	1.0787	0.1072	0.1028
1525.0	5.0	0.8787	0.1174	0.0924
1535.0	5.0	0.7660	0.0980	0.0935
1547.5	7.5	1.0111	0.0821	0.1063
1562.5	7.5	0.9701	0.0823	0.1091
1577.5	7.5	0.9376	0.0825	0.0995
1592.5	7.5	0.8115	0.0852	0.0932
1607.5	7.5	0.8631	0.0885	0.0988
1622.5	7.5	0.7999	0.0806	0.1031
1637.5	7.5	0.7918	0.0924	0.0916
1652.5	7.5	0.7765	0.0810	0.0821
1667.5	7.5	0.7598	0.0733	0.0860
1682.5	7.5	0.6722	0.0734	0.0887
1697.5	7.5	0.5931	0.0796	0.0855
1712.5	7.5	0.6523	0.0858	0.0785
1727.5	7.5	0.4820	0.1027	0.0703
1742.5	7.5	0.6254	0.1038	0.0667
1757.5	7.5	0.5070	0.1097	0.0705
1772.5	7.5	0.7479	0.1220	0.0789
1787.5	7.5	0.7946	0.1340	0.0717
1802.5	7.5	0.3216	0.1139	0.0522
1817.5	7.5	0.4825	0.1243	0.0505
1832.5	7.5	0.8819	0.1633	0.0564
1847.5	7.5	0.2742	0.1303	0.0508
1862.5	7.5	0.4325	0.1687	0.0506
1882.5	12.5	0.3604	0.1631	0.0638

F.4.8 Helicity Dependent Cross Sections for $\gamma n \rightarrow \eta n$ as a Function of W

 Angular Cross Sections $\sigma_{1/2}$

W=(1495.0±5.0) MeV				W=(1505.0±5.0) MeV				W=(1515.0±5.0) MeV				W=(1525.0±5.0) MeV			
$\cos(\theta_\eta^*)$	$d\sigma_{1/2}/d\Omega$ [$\mu\text{b}/\text{sr}$]	Δ_{stat} [$\mu\text{b}/\text{sr}$]	Δ_{sys} [$\mu\text{b}/\text{sr}$]	$d\sigma_{1/2}/d\Omega$ [$\mu\text{b}/\text{sr}$]	Δ_{stat} [$\mu\text{b}/\text{sr}$]	Δ_{sys} [$\mu\text{b}/\text{sr}$]	$d\sigma_{1/2}/d\Omega$ [$\mu\text{b}/\text{sr}$]	Δ_{stat} [$\mu\text{b}/\text{sr}$]	Δ_{sys} [$\mu\text{b}/\text{sr}$]	$d\sigma_{1/2}/d\Omega$ [$\mu\text{b}/\text{sr}$]	Δ_{stat} [$\mu\text{b}/\text{sr}$]	Δ_{sys} [$\mu\text{b}/\text{sr}$]	$d\sigma_{1/2}/d\Omega$ [$\mu\text{b}/\text{sr}$]	Δ_{stat} [$\mu\text{b}/\text{sr}$]	Δ_{sys} [$\mu\text{b}/\text{sr}$]
-0.80	1.3707	0.2245	0.1912	1.7173	0.1636	0.3730	1.8841	0.1738	0.2634	1.8086	0.1611	0.2808			
-0.40	1.0691	0.1292	0.2198	1.2498	0.1358	0.1977	1.4730	0.1570	0.1558	1.2304	0.1402	0.1882			
0.00	1.0714	0.1299	0.2209	1.1803	0.1444	0.2044	1.4064	0.1763	0.1488	1.3681	0.1858	0.1421			
0.40	0.9781	0.1630	0.1091	1.1237	0.1886	0.1227	1.4545	0.1915	0.1871	1.4336	0.2702	0.2236			
0.80	1.7078	0.2943	0.1864	1.6568	0.3405	0.2408	2.1706	0.2928	0.2324	1.5296	0.3469	0.2193			
W=(1535.0±5.0) MeV				W=(1547.5±7.5) MeV				W=(1562.5±7.5) MeV				W=(1577.5±7.5) MeV			
$\cos(\theta_\eta^*)$	$d\sigma_{1/2}/d\Omega$ [$\mu\text{b}/\text{sr}$]	Δ_{stat} [$\mu\text{b}/\text{sr}$]	Δ_{sys} [$\mu\text{b}/\text{sr}$]	$d\sigma_{1/2}/d\Omega$ [$\mu\text{b}/\text{sr}$]	Δ_{stat} [$\mu\text{b}/\text{sr}$]	Δ_{sys} [$\mu\text{b}/\text{sr}$]	$d\sigma_{1/2}/d\Omega$ [$\mu\text{b}/\text{sr}$]	Δ_{stat} [$\mu\text{b}/\text{sr}$]	Δ_{sys} [$\mu\text{b}/\text{sr}$]	$d\sigma_{1/2}/d\Omega$ [$\mu\text{b}/\text{sr}$]	Δ_{stat} [$\mu\text{b}/\text{sr}$]	Δ_{sys} [$\mu\text{b}/\text{sr}$]	$d\sigma_{1/2}/d\Omega$ [$\mu\text{b}/\text{sr}$]	Δ_{stat} [$\mu\text{b}/\text{sr}$]	Δ_{sys} [$\mu\text{b}/\text{sr}$]
-0.80	1.6800	0.1316	0.4188	1.6777	0.1173	0.2479	1.5100	0.1044	0.2697	1.4444	0.1010	0.2388			
-0.40	1.5106	0.1579	0.1604	1.2409	0.1045	0.1906	1.4791	0.1091	0.1916	1.3982	0.1105	0.1570			
0.00	1.5372	0.1795	0.1592	1.1361	0.0968	0.2041	1.0370	0.0849	0.1551	0.7454	0.0692	0.1177			
0.40	1.4130	0.1824	0.1466	1.5341	0.1333	0.1611	1.1152	0.1037	0.1157	1.1636	0.1028	0.1343			
0.80	1.0034	0.3137	0.1423	1.6605	0.2465	0.2163	1.4018	0.2669	0.2672	1.1579	0.2020	0.1564			
W=(1592.5±7.5) MeV				W=(1607.5±7.5) MeV				W=(1622.5±7.5) MeV				W=(1637.5±7.5) MeV			
$\cos(\theta_\eta^*)$	$d\sigma_{1/2}/d\Omega$ [$\mu\text{b}/\text{sr}$]	Δ_{stat} [$\mu\text{b}/\text{sr}$]	Δ_{sys} [$\mu\text{b}/\text{sr}$]	$d\sigma_{1/2}/d\Omega$ [$\mu\text{b}/\text{sr}$]	Δ_{stat} [$\mu\text{b}/\text{sr}$]	Δ_{sys} [$\mu\text{b}/\text{sr}$]	$d\sigma_{1/2}/d\Omega$ [$\mu\text{b}/\text{sr}$]	Δ_{stat} [$\mu\text{b}/\text{sr}$]	Δ_{sys} [$\mu\text{b}/\text{sr}$]	$d\sigma_{1/2}/d\Omega$ [$\mu\text{b}/\text{sr}$]	Δ_{stat} [$\mu\text{b}/\text{sr}$]	Δ_{sys} [$\mu\text{b}/\text{sr}$]	$d\sigma_{1/2}/d\Omega$ [$\mu\text{b}/\text{sr}$]	Δ_{stat} [$\mu\text{b}/\text{sr}$]	Δ_{sys} [$\mu\text{b}/\text{sr}$]
-0.80	0.8509	0.0796	0.1898	0.9342	0.0753	0.1966	0.9135	0.0745	0.1536	0.6904	0.0650	0.1290			
-0.40	0.9329	0.0864	0.1339	0.7891	0.0863	0.0817	0.6604	0.0568	0.1519	0.7369	0.0807	0.0801			
0.00	0.7701	0.0670	0.0879	0.7569	0.0616	0.0856	0.5787	0.0493	0.0854	0.7050	0.0626	0.0763			
0.40	0.9584	0.0912	0.1059	0.7424	0.0808	0.0862	0.5327	0.0514	0.0929	0.7171	0.0658	0.0746			
0.80	1.2071	0.1985	0.1866	0.9546	0.1909	0.2012	0.5589	0.1105	0.0680	0.5770	0.1638	0.1382			
W=(1652.5±7.5) MeV				W=(1667.5±7.5) MeV				W=(1682.5±7.5) MeV				W=(1697.5±7.5) MeV			
$\cos(\theta_\eta^*)$	$d\sigma_{1/2}/d\Omega$ [$\mu\text{b}/\text{sr}$]	Δ_{stat} [$\mu\text{b}/\text{sr}$]	Δ_{sys} [$\mu\text{b}/\text{sr}$]	$d\sigma_{1/2}/d\Omega$ [$\mu\text{b}/\text{sr}$]	Δ_{stat} [$\mu\text{b}/\text{sr}$]	Δ_{sys} [$\mu\text{b}/\text{sr}$]	$d\sigma_{1/2}/d\Omega$ [$\mu\text{b}/\text{sr}$]	Δ_{stat} [$\mu\text{b}/\text{sr}$]	Δ_{sys} [$\mu\text{b}/\text{sr}$]	$d\sigma_{1/2}/d\Omega$ [$\mu\text{b}/\text{sr}$]	Δ_{stat} [$\mu\text{b}/\text{sr}$]	Δ_{sys} [$\mu\text{b}/\text{sr}$]	$d\sigma_{1/2}/d\Omega$ [$\mu\text{b}/\text{sr}$]	Δ_{stat} [$\mu\text{b}/\text{sr}$]	Δ_{sys} [$\mu\text{b}/\text{sr}$]
-0.80	0.9484	0.0755	0.1251	0.8648	0.0732	0.1043	0.6267	0.0557	0.1398	0.4579	0.0473	0.1285			
-0.40	0.7952	0.0786	0.0844	0.7145	0.0584	0.1183	0.5122	0.0530	0.0827	0.5216	0.0504	0.0854			
0.00	0.6427	0.0530	0.0777	0.7095	0.0531	0.0872	0.5739	0.0485	0.0841	0.5990	0.0585	0.0625			
0.40	0.7838	0.0729	0.0957	0.7427	0.0621	0.0782	0.6258	0.0592	0.0672	0.6079	0.0642	0.0660			
0.80	0.3804	0.0904	0.0404	0.4711	0.0973	0.0621	0.5608	0.0876	0.0582	0.3238	0.0693	0.0336			
W=(1712.5±7.5) MeV				W=(1727.5±7.5) MeV				W=(1742.5±7.5) MeV				W=(1757.5±7.5) MeV			
$\cos(\theta_\eta^*)$	$d\sigma_{1/2}/d\Omega$ [$\mu\text{b}/\text{sr}$]	Δ_{stat} [$\mu\text{b}/\text{sr}$]	Δ_{sys} [$\mu\text{b}/\text{sr}$]	$d\sigma_{1/2}/d\Omega$ [$\mu\text{b}/\text{sr}$]	Δ_{stat} [$\mu\text{b}/\text{sr}$]	Δ_{sys} [$\mu\text{b}/\text{sr}$]	$d\sigma_{1/2}/d\Omega$ [$\mu\text{b}/\text{sr}$]	Δ_{stat} [$\mu\text{b}/\text{sr}$]	Δ_{sys} [$\mu\text{b}/\text{sr}$]	$d\sigma_{1/2}/d\Omega$ [$\mu\text{b}/\text{sr}$]	Δ_{stat} [$\mu\text{b}/\text{sr}$]	Δ_{sys} [$\mu\text{b}/\text{sr}$]	$d\sigma_{1/2}/d\Omega$ [$\mu\text{b}/\text{sr}$]	Δ_{stat} [$\mu\text{b}/\text{sr}$]	Δ_{sys} [$\mu\text{b}/\text{sr}$]
-0.80	0.4462	0.0500	0.1153	0.5269	0.0910	0.0852	0.3139	0.0516	0.0480	0.3210	0.0475	0.0528			
-0.40	0.4427	0.0528	0.0573	0.2898	0.0367	0.0903	0.3612	0.0387	0.0959	0.2341	0.0438	0.0282			
0.00	0.5676	0.0522	0.0676	0.4400	0.0441	0.0755	0.3558	0.0415	0.0641	0.3974	0.0426	0.0608			
0.40	0.4535	0.0537	0.0533	0.4904	0.0693	0.0612	0.4805	0.0589	0.0498	0.3510	0.0553	0.0364			
0.80	0.3253	0.0573	0.0489	0.2641	0.1190	0.0637	0.2767	0.0762	0.0291	0.5866	0.2186	0.1923			
W=(1772.5±7.5) MeV				W=(1787.5±7.5) MeV				W=(1802.5±7.5) MeV				W=(1817.5±7.5) MeV			
$\cos(\theta_\eta^*)$	$d\sigma_{1/2}/d\Omega$ [$\mu\text{b}/\text{sr}$]	Δ_{stat} [$\mu\text{b}/\text{sr}$]	Δ_{sys} [$\mu\text{b}/\text{sr}$]	$d\sigma_{1/2}/d\Omega$ [$\mu\text{b}/\text{sr}$]	Δ_{stat} [$\mu\text{b}/\text{sr}$]	Δ_{sys} [$\mu\text{b}/\text{sr}$]	$d\sigma_{1/2}/d\Omega$ [$\mu\text{b}/\text{sr}$]	Δ_{stat} [$\mu\text{b}/\text{sr}$]	Δ_{sys} [$\mu\text{b}/\text{sr}$]	$d\sigma_{1/2}/d\Omega$ [$\mu\text{b}/\text{sr}$]	Δ_{stat} [$\mu\text{b}/\text{sr}$]	Δ_{sys} [$\mu\text{b}/\text{sr}$]	$d\sigma_{1/2}/d\Omega$ [$\mu\text{b}/\text{sr}$]	Δ_{stat} [$\mu\text{b}/\text{sr}$]	Δ_{sys} [$\mu\text{b}/\text{sr}$]
-0.80	0.3536	0.0531	0.0496	0.2620	0.0437	0.0471	0.2676	0.0438	0.0602	0.2310	0.0484	0.0325			
-0.40	0.2713	0.0468	0.0292	0.2975	0.0483	0.0326	0.1787	0.0395	0.0291	0.1703	0.0291	0.0670			
0.00	0.4165	0.0500	0.0432	0.4231	0.0584	0.0485	0.2623	0.0472	0.0296	0.3697	0.0638	0.0456			
0.40	0.5551	0.0677	0.0709	0.4712	0.0721	0.0697	0.3569	0.0550	0.0401	0.3872	0.0861	0.0683			
0.80	0.2815	0.0897	0.0499	0.4980	0.1329	0.1169	0.2031	0.0678	0.0213	0.2962	0.0582	0.0530			

APPENDIX F. DATA TABLES

$\cos(\theta_\eta^*)$	W=(1832.5±7.5) MeV			W=(1847.5±7.5) MeV			W=(1862.5±7.5) MeV			W=(1882.5±12.5) MeV		
	$d\sigma_{1/2}/d\Omega$ [$\mu\text{b}/\text{sr}$]	Δ_{stat} [$\mu\text{b}/\text{sr}$]	Δ_{sys} [$\mu\text{b}/\text{sr}$]	$d\sigma_{1/2}/d\Omega$ [$\mu\text{b}/\text{sr}$]	Δ_{stat} [$\mu\text{b}/\text{sr}$]	Δ_{sys} [$\mu\text{b}/\text{sr}$]	$d\sigma_{1/2}/d\Omega$ [$\mu\text{b}/\text{sr}$]	Δ_{stat} [$\mu\text{b}/\text{sr}$]	Δ_{sys} [$\mu\text{b}/\text{sr}$]	$d\sigma_{1/2}/d\Omega$ [$\mu\text{b}/\text{sr}$]	Δ_{stat} [$\mu\text{b}/\text{sr}$]	Δ_{sys} [$\mu\text{b}/\text{sr}$]
-0.80	0.3289	0.0619	0.0384	0.1752	0.0521	0.0196	0.1555	0.0423	0.0404	0.2088	0.0440	0.0488
-0.40	0.1381	0.0354	0.0314	0.1191	0.0481	0.0131	0.1260	0.0309	0.0489	0.1022	0.0267	0.0329
0.00	0.3838	0.0748	0.0519	0.2473	0.0350	0.1147	0.2253	0.0628	0.0236	0.1634	0.0422	0.0302
0.40	0.4060	0.0693	0.0424	0.2750	0.0501	0.0558	0.3222	0.0824	0.0436	0.1626	0.0439	0.0288
0.80	0.3746	0.0955	0.0400	0.2597	0.0908	0.0391	0.2659	0.0914	0.0400	0.0717	0.0629	0.0142

Angular Cross Sections $\sigma_{3/2}$

$\cos(\theta_\eta^*)$	W=(1495.0±5.0) MeV			W=(1505.0±5.0) MeV			W=(1515.0±5.0) MeV			W=(1525.0±5.0) MeV		
	$d\sigma_{3/2}/d\Omega$ [$\mu\text{b}/\text{sr}$]	Δ_{stat} [$\mu\text{b}/\text{sr}$]	Δ_{sys} [$\mu\text{b}/\text{sr}$]	$d\sigma_{3/2}/d\Omega$ [$\mu\text{b}/\text{sr}$]	Δ_{stat} [$\mu\text{b}/\text{sr}$]	Δ_{sys} [$\mu\text{b}/\text{sr}$]	$d\sigma_{3/2}/d\Omega$ [$\mu\text{b}/\text{sr}$]	Δ_{stat} [$\mu\text{b}/\text{sr}$]	Δ_{sys} [$\mu\text{b}/\text{sr}$]	$d\sigma_{3/2}/d\Omega$ [$\mu\text{b}/\text{sr}$]	Δ_{stat} [$\mu\text{b}/\text{sr}$]	Δ_{sys} [$\mu\text{b}/\text{sr}$]
-0.80	-0.2300	0.2245	0.0785	-0.1860	0.1636	0.1827	-0.0584	0.1738	0.0914	-0.0218	0.1611	0.1058
-0.40	-0.0397	0.1292	0.0985	0.1485	0.1358	0.0850	0.0157	0.1570	0.0160	0.1031	0.1402	0.0758
0.00	-0.1903	0.1299	0.1142	0.0612	0.1444	0.0864	0.1764	0.1763	0.0249	0.1931	0.1858	0.0208
0.40	0.1206	0.1630	0.0260	0.2824	0.1886	0.0380	0.0705	0.1915	0.0586	0.1567	0.2702	0.0942
0.80	-0.3372	0.2943	0.0495	0.2481	0.3405	0.1004	-0.4876	0.2928	0.0620	0.1062	0.3469	0.0818

$\cos(\theta_\eta^*)$	W=(1535.0±5.0) MeV			W=(1547.5±7.5) MeV			W=(1562.5±7.5) MeV			W=(1577.5±7.5) MeV		
	$d\sigma_{3/2}/d\Omega$ [$\mu\text{b}/\text{sr}$]	Δ_{stat} [$\mu\text{b}/\text{sr}$]	Δ_{sys} [$\mu\text{b}/\text{sr}$]	$d\sigma_{3/2}/d\Omega$ [$\mu\text{b}/\text{sr}$]	Δ_{stat} [$\mu\text{b}/\text{sr}$]	Δ_{sys} [$\mu\text{b}/\text{sr}$]	$d\sigma_{3/2}/d\Omega$ [$\mu\text{b}/\text{sr}$]	Δ_{stat} [$\mu\text{b}/\text{sr}$]	Δ_{sys} [$\mu\text{b}/\text{sr}$]	$d\sigma_{3/2}/d\Omega$ [$\mu\text{b}/\text{sr}$]	Δ_{stat} [$\mu\text{b}/\text{sr}$]	Δ_{sys} [$\mu\text{b}/\text{sr}$]
-0.80	0.1487	0.1316	0.2079	-0.0345	0.1173	0.0903	0.0056	0.1044	0.1103	-0.0640	0.1010	0.0974
-0.40	0.0914	0.1579	0.0211	0.2719	0.1045	0.0903	-0.0239	0.1091	0.0585	0.0035	0.1105	0.0303
0.00	0.1039	0.1795	0.0108	0.1291	0.0968	0.0938	0.0557	0.0849	0.0593	0.2244	0.0692	0.0623
0.40	0.1256	0.1824	0.0138	-0.2488	0.1333	0.0300	0.0411	0.1037	0.0057	-0.0315	0.1028	0.0307
0.80	0.5865	0.3137	0.0981	-0.2670	0.2465	0.0810	0.0405	0.2669	0.1155	0.0686	0.2020	0.0536

$\cos(\theta_\eta^*)$	W=(1592.5±7.5) MeV			W=(1607.5±7.5) MeV			W=(1622.5±7.5) MeV			W=(1637.5±7.5) MeV		
	$d\sigma_{3/2}/d\Omega$ [$\mu\text{b}/\text{sr}$]	Δ_{stat} [$\mu\text{b}/\text{sr}$]	Δ_{sys} [$\mu\text{b}/\text{sr}$]	$d\sigma_{3/2}/d\Omega$ [$\mu\text{b}/\text{sr}$]	Δ_{stat} [$\mu\text{b}/\text{sr}$]	Δ_{sys} [$\mu\text{b}/\text{sr}$]	$d\sigma_{3/2}/d\Omega$ [$\mu\text{b}/\text{sr}$]	Δ_{stat} [$\mu\text{b}/\text{sr}$]	Δ_{sys} [$\mu\text{b}/\text{sr}$]	$d\sigma_{3/2}/d\Omega$ [$\mu\text{b}/\text{sr}$]	Δ_{stat} [$\mu\text{b}/\text{sr}$]	Δ_{sys} [$\mu\text{b}/\text{sr}$]
-0.80	0.3231	0.0796	0.1207	0.1516	0.0753	0.1007	-0.0157	0.0745	0.0616	0.1574	0.0650	0.0679
-0.40	0.1338	0.0864	0.0547	0.2028	0.0863	0.0210	0.0688	0.0568	0.0752	0.1145	0.0807	0.0184
0.00	0.1266	0.0670	0.0252	-0.0004	0.0616	0.0172	0.1144	0.0493	0.0383	0.0377	0.0626	0.0123
0.40	-0.0273	0.0912	0.0192	0.0601	0.0808	0.0219	0.1400	0.0514	0.0493	0.0215	0.0658	0.0044
0.80	-0.2751	0.1985	0.0897	-0.2301	0.1909	0.1113	0.0691	0.1105	0.0213	0.0076	0.1638	0.0631

$\cos(\theta_\eta^*)$	W=(1652.5±7.5) MeV			W=(1667.5±7.5) MeV			W=(1682.5±7.5) MeV			W=(1697.5±7.5) MeV		
	$d\sigma_{3/2}/d\Omega$ [$\mu\text{b}/\text{sr}$]	Δ_{stat} [$\mu\text{b}/\text{sr}$]	Δ_{sys} [$\mu\text{b}/\text{sr}$]	$d\sigma_{3/2}/d\Omega$ [$\mu\text{b}/\text{sr}$]	Δ_{stat} [$\mu\text{b}/\text{sr}$]	Δ_{sys} [$\mu\text{b}/\text{sr}$]	$d\sigma_{3/2}/d\Omega$ [$\mu\text{b}/\text{sr}$]	Δ_{stat} [$\mu\text{b}/\text{sr}$]	Δ_{sys} [$\mu\text{b}/\text{sr}$]	$d\sigma_{3/2}/d\Omega$ [$\mu\text{b}/\text{sr}$]	Δ_{stat} [$\mu\text{b}/\text{sr}$]	Δ_{sys} [$\mu\text{b}/\text{sr}$]
-0.80	-0.0668	0.0755	0.0420	0.0208	0.0732	0.0275	0.1082	0.0557	0.0735	0.1348	0.0473	0.0785
-0.40	0.1088	0.0786	0.0154	0.1431	0.0584	0.0573	0.1708	0.0530	0.0458	0.0801	0.0504	0.0391
0.00	0.1767	0.0530	0.0315	0.1440	0.0531	0.0319	0.1793	0.0485	0.0432	0.1518	0.0585	0.0164
0.40	0.0850	0.0729	0.0295	0.0648	0.0621	0.0101	0.1833	0.0592	0.0222	0.1732	0.0642	0.0219
0.80	0.1747	0.0904	0.0192	0.1157	0.0973	0.0267	-0.0818	0.0876	0.0087	0.1023	0.0693	0.0107

$\cos(\theta_\eta^*)$	W=(1712.5±7.5) MeV			W=(1727.5±7.5) MeV			W=(1742.5±7.5) MeV			W=(1757.5±7.5) MeV		
$d\sigma_{3/2}/d\Omega$ [$\mu\text{b}/\text{sr}$]	Δ_{stat} [$\mu\text{b}/\text{sr}$]	Δ_{sys} [$\mu\text{b}/\text{sr}$]	$d\sigma_{3/2}/d\Omega$ [<math									

$\cos(\theta_\eta^*)$	W=(1772.5±7.5) MeV			W=(1787.5±7.5) MeV			W=(1802.5±7.5) MeV			W=(1817.5±7.5) MeV		
	$d\sigma_{3/2}/d\Omega$ [$\mu\text{b}/\text{sr}$]	Δ_{stat} [$\mu\text{b}/\text{sr}$]	Δ_{sys} [$\mu\text{b}/\text{sr}$]	$d\sigma_{3/2}/d\Omega$ [$\mu\text{b}/\text{sr}$]	Δ_{stat} [$\mu\text{b}/\text{sr}$]	Δ_{sys} [$\mu\text{b}/\text{sr}$]	$d\sigma_{3/2}/d\Omega$ [$\mu\text{b}/\text{sr}$]	Δ_{stat} [$\mu\text{b}/\text{sr}$]	Δ_{sys} [$\mu\text{b}/\text{sr}$]	$d\sigma_{3/2}/d\Omega$ [$\mu\text{b}/\text{sr}$]	Δ_{stat} [$\mu\text{b}/\text{sr}$]	Δ_{sys} [$\mu\text{b}/\text{sr}$]
-0.80	-0.0280	0.0531	0.0182	0.0758	0.0437	0.0261	0.0189	0.0438	0.0287	0.0805	0.0484	0.0170
-0.40	0.0966	0.0468	0.0113	0.0430	0.0483	0.0075	0.1534	0.0395	0.0262	0.0993	0.0291	0.0522
0.00	0.1011	0.0500	0.0105	0.0493	0.0584	0.0126	0.2087	0.0472	0.0240	0.1162	0.0638	0.0202
0.40	0.0758	0.0677	0.0249	0.0877	0.0721	0.0309	0.1566	0.0550	0.0197	0.1713	0.0861	0.0437
0.80	0.0476	0.0897	0.0242	-0.1046	0.1329	0.0644	0.1533	0.0678	0.0161	0.0425	0.0582	0.0251
$\cos(\theta_\eta^*)$	W=(1832.5±7.5) MeV			W=(1847.5±7.5) MeV			W=(1862.5±7.5) MeV			W=(1882.5±12.5) MeV		
	$d\sigma_{3/2}/d\Omega$ [$\mu\text{b}/\text{sr}$]	Δ_{stat} [$\mu\text{b}/\text{sr}$]	Δ_{sys} [$\mu\text{b}/\text{sr}$]	$d\sigma_{3/2}/d\Omega$ [$\mu\text{b}/\text{sr}$]	Δ_{stat} [$\mu\text{b}/\text{sr}$]	Δ_{sys} [$\mu\text{b}/\text{sr}$]	$d\sigma_{3/2}/d\Omega$ [$\mu\text{b}/\text{sr}$]	Δ_{stat} [$\mu\text{b}/\text{sr}$]	Δ_{sys} [$\mu\text{b}/\text{sr}$]	$d\sigma_{3/2}/d\Omega$ [$\mu\text{b}/\text{sr}$]	Δ_{stat} [$\mu\text{b}/\text{sr}$]	Δ_{sys} [$\mu\text{b}/\text{sr}$]
-0.80	-0.0309	0.0619	0.0102	0.1124	0.0521	0.0131	0.0895	0.0423	0.0306	-0.0066	0.0440	0.0226
-0.40	0.1195	0.0354	0.0289	0.1442	0.0481	0.0157	0.0665	0.0309	0.0366	0.0455	0.0267	0.0230
0.00	0.0086	0.0748	0.0171	0.1065	0.0350	0.0807	0.1901	0.0628	0.0200	0.1139	0.0422	0.0242
0.40	0.0586	0.0693	0.0069	0.1532	0.0501	0.0406	0.0452	0.0824	0.0166	0.1107	0.0439	0.0227
0.80	-0.0944	0.0955	0.0115	0.0981	0.0908	0.0221	-0.0049	0.0914	0.0148	0.1259	0.0629	0.0202

Total Cross Sections $\sigma_{1/2}$ and $\sigma_{3/2}$

W [MeV]	ΔW [MeV]	$\sigma_{1/2}$ [μb]	Δ_{stat} [μb]	Δ_{sys} [μb]	W [MeV]	ΔW [MeV]	$\sigma_{3/2}$ [μb]	Δ_{stat} [μb]	Δ_{sys} [μb]
1495.0	5.0	15.5842	1.0923	2.1889	1495.0	5.0	-1.5699	1.0923	0.8297
1505.0	5.0	17.7952	1.0831	2.2608	1505.0	5.0	1.1368	1.0831	0.6507
1515.0	5.0	21.1650	1.1352	2.2450	1515.0	5.0	-0.8015	1.1352	0.4411
1525.0	5.0	18.6868	1.2050	2.0912	1525.0	5.0	1.2066	1.2050	0.3123
1535.0	5.0	18.1985	1.0486	2.0157	1535.0	5.0	2.4111	1.0486	0.3815
1547.5	7.5	18.0120	0.7633	2.0057	1547.5	7.5	-0.0995	0.7633	0.4270
1562.5	7.5	16.5680	0.7222	1.8492	1562.5	7.5	0.2516	0.7222	0.3158
1577.5	7.5	14.9428	0.6633	1.5748	1577.5	7.5	0.4812	0.6633	0.2301
1592.5	7.5	11.4132	0.5514	1.3070	1592.5	7.5	1.1877	0.5514	0.2219
1607.5	7.5	10.2233	0.4995	1.1569	1607.5	7.5	0.7514	0.4995	0.2509
1622.5	7.5	8.2069	0.3803	1.0824	1622.5	7.5	0.9122	0.3803	0.2647
1637.5	7.5	8.4573	0.4476	0.9718	1637.5	7.5	0.9827	0.4476	0.1864
1652.5	7.5	8.9360	0.4206	0.9316	1652.5	7.5	1.1244	0.4206	0.1464
1667.5	7.5	8.7981	0.3815	0.9859	1667.5	7.5	1.2006	0.3815	0.2624
1682.5	7.5	7.2353	0.3323	0.9638	1682.5	7.5	1.4184	0.3323	0.3729
1697.5	7.5	6.2607	0.3239	0.8511	1697.5	7.5	1.5990	0.3239	0.3685
1712.5	7.5	5.6044	0.3029	0.7282	1712.5	7.5	1.1795	0.3029	0.3108
1727.5	7.5	5.0273	0.3578	0.6187	1727.5	7.5	1.7571	0.3578	0.2559
1742.5	7.5	4.5094	0.2979	0.5427	1742.5	7.5	1.0394	0.2979	0.2066
1757.5	7.5	4.3377	0.3252	0.5069	1757.5	7.5	1.4191	0.3252	0.1412
1772.5	7.5	4.7226	0.3397	0.5100	1772.5	7.5	0.6813	0.3397	0.1065
1787.5	7.5	4.7185	0.3631	0.5010	1787.5	7.5	0.5401	0.3631	0.1554
1802.5	7.5	3.2270	0.2876	0.4423	1802.5	7.5	1.6564	0.2876	0.1978
1817.5	7.5	3.6199	0.3136	0.4062	1817.5	7.5	1.2637	0.3136	0.1590
1832.5	7.5	3.9761	0.3571	0.4156	1832.5	7.5	0.2495	0.3571	0.1470
1847.5	7.5	2.7018	0.2876	0.3970	1847.5	7.5	1.5389	0.2876	0.1930
1862.5	7.5	2.5653	0.3136	0.3476	1862.5	7.5	1.0163	0.3136	0.2089
1882.5	12.5	1.8212	0.2326	0.3225	1882.5	12.5	0.8563	0.2326	0.2117

References

- [1] R. Frisch and O. Stern, "Über die magnetische Ablenkung von Wasserstoffmolekülen und das magnetische Moment des Protons. I", *Zeitschrift für Physik* **85**, 4–16 (1933) 10.1007/BF01330773.
- [2] P. J. Mohrm, B. N. Taylor, and D. B. Newell, *The 2014 CODATA Recommended Values of the Fundamental Physical Constants* (Web Version 7.0), <http://physics.nist.gov/Constants>, Accessed: 10.07.2015.
- [3] R. W. McAllister and R. Hofstadter, "Elastic Scattering of 188-Mev Electrons From the Proton and the α Particle", *Phys. Rev.* **102**, 851–856 (1956) 10.1103/PhysRev.102.851.
- [4] H. L. Anderson et al., "Total Cross Sections of Positive Pions in Hydrogen", *Phys. Rev.* **85**, 936–936 (1952) 10.1103/PhysRev.85.936.
- [5] S. Schadmand, *Double Pion Photoproduction* (Proceedings to the sixth Workshop on Electromagnetic Induced Two-Hadron Emission, Pavia, 2004), ISBN: 88-85159-20-6.
- [6] K. A. Olive, "Review of Particle Physics", *Chinese Physics C* **38**, 090001 (2014) 10.1088/1674-1137/38/9/090001.
- [7] B. Krusche, "Photoproduction of mesons off nuclei", *The European Physical Journal Special Topics* **198**, 199–238 (2011) 10.1140/epjst/e2011-01491-2.
- [8] S. Bethke, "Experimental tests of asymptotic freedom", *Progress in Particle and Nuclear Physics* **58**, 351–386 (2007) 10.1016/j.ppnp.2006.06.001.
- [9] M. Gell-Mann, "Symmetries of Baryons and Mesons", *Phys. Rev.* **125**, 1067–1084 (1962) 10.1103/PhysRev.125.1067.
- [10] M. Gell-Mann, "A schematic model of baryons and mesons", *Physics Letters* **8**, 214–215 (1964) 10.1016/S0031-9163(64)92001-3.
- [11] G. Zweig, "An SU(3) model for strong interaction symmetry and its breaking. Version 2", in *Developments in the quark theory of hadrons. vol. 1. 1964 - 1978*, edited by D. B. Lichtenberg and S. P. Rosen (1964), pp. 22–101, <http://inspirehep.net/record/4674/files/cern-th-412.pdf>.
- [12] O. W. Greenberg, "Spin and Unitary-Spin Independence in a Paraquark Model of Baryons and Mesons", *Physical Review Letters* **13**, 598–602 (1964) 10.1103/PhysRevLett.13.598.

- [13] M. Y. Han and Y. Nambu, "Three-Triplet Model with Double SU(3) Symmetry", *Phys. Rev.* **139**, B1006–B1010 (1965) 10.1103/PhysRev.139.B1006.
- [14] O. W. Greenberg, "Color Charge Degree of Freedom in Particle Physics", in *Compendium of quantum physics* (Springer Berlin Heidelberg, Berlin, Heidelberg, 2009), pp. 109–111, ISBN: 978-3-540-70622-9, 10.1007/978-3-540-70626-7_32.
- [15] R. P. Feynman, "Very High-Energy Collisions of Hadrons", *Physical Review Letters* **23**, 1415–1417 (1969) 10.1103/PhysRevLett.23.1415.
- [16] J. D. Bjorken and E. A. Paschos, "Inelastic Electron-Proton and γ -Proton Scattering and the Structure of the Nucleon", *Phys. Rev.* **185**, 1975–1982 (1969) 10.1103/PhysRev.185.1975.
- [17] H. Fritzsch, M. Gell-Mann, and H. Leutwyler, "Advantages of the color octet gluon picture", *Physics Letters B* **47**, 365–368 (1973) 10.1016/0370-2693(73)90625-4.
- [18] D. J. Gross and F. Wilczek, "Ultraviolet Behavior of Non-Abelian Gauge Theories", *Physical Review Letters* **30**, 1343–1346 (1973) 10.1103/PhysRevLett.30.1343.
- [19] H. D. Politzer, "Reliable Perturbative Results for Strong Interactions?", *Physical Review Letters* **30**, 1346–1349 (1973) 10.1103/PhysRevLett.30.1346.
- [20] R. H. Dalitz, "Hadron Spectroscopy", in *Hawaii topical conferences in particle physics* (WORLD SCIENTIFIC, 1983), pp. 45–159, ISBN: 978-9971-950-36-1, 10.1142/9789814542500_0002.
- [21] D. Faiman and A. W. Hendry, "Harmonic-Oscillator Model for Baryons", *Phys. Rev.* **173**, 1720–1729 (1968) 10.1103/PhysRev.173.1720.
- [22] A. De Rújula, H. Georgi, and S. L. Glashow, "Hadron masses in a gauge theory", *Physical Review D* **12**, 147–162 (1975) 10.1103/PhysRevD.12.147.
- [23] M. V. N. Murthy et al., "Spin-orbit splitting in the N- Δ spectra and the deformed baryon model", *Zeitschrift für Physik C Particles and Fields* **29**, 385–396 (1985) 10.1007/BF01565186.
- [24] N. Isgur and G. Karl, "P-wave baryons in the quark model", *Physical Review D* **18**, 4187–4205 (1978) 10.1103/PhysRevD.18.4187.
- [25] U. Loering, B. C. Metsch, and H. R. Petry, "The light-baryon spectrum in a relativistic quark model with instanton-induced quark forces", *European Physical Journal A* **10**, 395–446 (2001) 10.1007/s100500170105.
- [26] N. Isgur and J. Paton, "Flux-tube model for hadrons in QCD", *Physical Review D* **31**, 2910–2929 (1985) 10.1103/PhysRevD.31.2910.
- [27] F. Iachello, N. C. Mukhopadhyay, and L. Zhang, "Spectrum generating algebra for string-like hadrons. Mass formula for mesons", *Physics Letters B* **256**, 295–300 (1991) 10.1016/0370-2693(91)91764-M.
- [28] M. Anselmino et al., "Diquarks", *Reviews of Modern Physics* **65**, 1199–1233 (1993) 10.1103/RevModPhys.65.1199.

- [29] D. B. Leinweber, "Do quarks really form diquark clusters in the nucleon?", *Physical Review D* **47**, 5096–5103 (1993) 10.1103/PhysRevD.47.5096.
- [30] R. G. Edwards et al., "Excited state baryon spectroscopy from lattice QCD", *Physical Review D* **84**, 074508–29 (2011) 10.1103/PhysRevD.84.074508.
- [31] B. Krusche and S. Schadmand, "Study of Non-Strange Baryon Resonances with Meson Photoproduction", *Prog. Part. Nucl. Phys.* **51**, 399–485 (2003) 10.1016/S0146-6410(03)90005-6.
- [32] M. Benmerrouche, N. C. Mukhopadhyay, and J. F. Zhang, "Effective Lagrangian approach to the theory of η photoproduction in the $N^*(1535)$ region", *Physical Review D* **51**, 3237–3266 (1995) 10.1103/PhysRevD.51.3237.
- [33] W.-T. Chiang et al., "An isobar model for η photo- and electroproduction on the nucleon", *Nuclear Physics A* **700**, 429–453 (2002) 10.1016/S0375-9474(01)01325-2.
- [34] R. L. Walker, "Phenomenological Analysis of Single-Pion Photoproduction", *Phys. Rev.* **182**, 1729–1748 (1969) 10.1103/PhysRev.182.1729.
- [35] G. F. Chew et al., "Relativistic Dispersion Relation Approach to Photomeson Production", *Phys. Rev.* **106**, 1345–1355 (1957) 10.1103/PhysRev.106.1345.
- [36] B. Krusche, "Photoproduction of Mesons off Nuclei - The Photonuclear Programs at ELSA and MAMI", *J.Phys.Conf.Ser.* **349**, 012003 (2012) 10.1088/1742-6596/349/1/012003.
- [37] I. S. Barker, A. Donnachie, and J. K. Storrow, "Complete Experiments in Pseudoscalar Photoproduction", *Nuclear Physics B* **B95**, 347–356 (1975) 10.1016/0550-3213(75)90049-8.
- [38] A. M. Sandorfi et al., "Calculations of Polarization Observables in Pseudoscalar Meson Photo-production Reactions", *arXiv.org* (2009), <http://arxiv.org/abs/0912.3505>.
- [39] G. Keaton and R. Workman, "Amplitude ambiguities in pseudoscalar meson photoproduction", *Physical Review C* **53**, 1434–1436 (1996) 10.1103/PhysRevC.53.1434.
- [40] W.-T. Chiang and F. Tabakin, "Completeness Rules for Spin Observables in Pseudoscalar Meson Photoproduction", *Phys. Rev.* **55**, 2054–2066 (1997) 10.1103/PhysRevC.55.2054.
- [41] I. Strakovsky et al., *SAID solution SP06*, <http://gwdac.phys.gwu.edu>, Accessed: 01.09.2011.
- [42] L. Tiator et al., *MAID*, <http://portal.kph.uni-mainz.de/MAID>, Accessed: 16.07.2015.
- [43] V. Nikonov et al., *Bonn-Gatchina Partial Wave Analysis*, <http://pwa.hiskp.uni-bonn.de>, Accessed: 16.07.2015.
- [44] R. A. Arndt et al., "Extended Partial-Wave Analysis of πN Scattering Data", *Physical Review C* **74**, 045205 (2006) 10.1103/PhysRevC.74.045205.

- [45] W.-T. Chiang et al., "Reggeized model for η and η' photoproduction", *Physical Review C* **68**, 045202 (2003) 10.1103/PhysRevC.68.045202.
- [46] A. Fix, L. Tiator, and M. V. Polyakov, "Photoproduction of η -mesons on the deuteron above $S_{11}(1535)$ in the presence of a narrow $P_{11}(1670)$ -resonance", *The European Physical Journal A* **32**, 311–319 (2007) 10.1140/epja/i2007-10385-6.
- [47] A. V. Anisovich et al., "Photoproduction of pions and properties of baryon resonances from a Bonn-Gatchina partial-wave analysis", *The European Physical Journal A* **44**, 203–220 (2010) 10.1140/epja/i2010-10950-x.
- [48] A. V. Anisovich et al., "Interference phenomena in the $J^P = 1/2^-$ wave in η photoproduction", *The European Physical Journal A* **51**, 72 (2015) 10.1140/epja/i2015-15072-5.
- [49] V. Kuznetsov et al., "Evidence for a narrow structure at $W \sim 1.68$ GeV in η photoproduction off the neutron", *Physics Letters B* **647**, 23–29 (2007) 10.1016/j.physletb.2007.01.041.
- [50] V. Kuznetsov et al., "Evidence for Narrow $N^*(1685)$ Resonance in Quasifree Compton Scattering on the Neutron", *Physical Review C* **83**, 022201 (2011) 10.1103/PhysRevC.83.022201.
- [51] I. Jaegle et al., "Quasi-free photoproduction of η -mesons off the deuteron", *The European Physical Journal A* **47**, 89 (2011) 10.1140/epja/i2011-11089-0.
- [52] D. Werthmüller et al., "A narrow structure in the excitation function of eta-photoproduction off the neutron", *Physical Review Letters*, 232001 (2013) 10.1103/PhysRevLett.111.232001.
- [53] A. Fantini et al., "First measurement of the Σ beam asymmetry in η photoproduction on the neutron", *Physical Review C* **78**, 015203 (2008) 10.1103/PhysRevC.78.015203.
- [54] T. Nakabayashi et al., "Photoproduction of η mesons off protons for $E_\gamma \leq 1.15$ GeV", *Physical Review C* **74**, 035202 (2006) 10.1103/PhysRevC.74.035202.
- [55] D. Werthmüller et al., "Quasifree photoproduction of η mesons off protons and neutrons", *Physical Review C* **90**, 015205 (2014) 10.1103/PhysRevC.90.015205.
- [56] D. Werthmüller, "Experimental study of nucleon resonance contributions to η -photoproduction on the neutron", PhD thesis (Universität Basel, Basel, 2014), 10.5451/unibas-006230854.
- [57] R. G. Moorhouse, "Photoproduction of N^* Resonances in the Quark Model", *Physical Review Letters* **16**, 772–774 (1966) 10.1103/PhysRevLett.16.772.
- [58] Q. Zhao and F. E. Close, "Selection rules and quark correlations in the N^* resonance spectrum", in *Nstar 2007* (Springer Berlin Heidelberg, Berlin, Heidelberg, 2008), pp. 196–198, ISBN: 978-3-540-85143-1, 10.1007/978-3-540-85144-8_40.

- [59] V. Shklyar, H. Lenske, and U. Mosel, “ η photoproduction in the resonance energy region”, Physics Letters B **650**, 172–178 (2007) 10.1016/j.physletb.2007.05.005.
- [60] X.-H. Zhong and Q. Zhao, “ η photoproduction on quasifree nucleons in the chiral quark model”, Physical Review C **84**, 045207 (2011) 10.1103/PhysRevC.84.045207.
- [61] A. V. Anisovich et al., “Photoproduction of η -mesons off neutrons from a deuteron target”, The European Physical Journal A **41**, 13–24 (2009) 10.1140/epja/i2009-10766-9.
- [62] M. Döring and K. Nakayama, “On the cross section ratio σ_n/σ_p in η photoproduction”, Physics Letters B **683**, 145–149 (2010) 10.1016/j.physletb.2009.12.029.
- [63] D. Diakonov, V. Petrov, and M. Polyakov, “Exotic anti-decuplet of baryons: prediction from chiral solitons”, Zeitschrift für Physik A **359**, 305–314 (1997) 10.1007/s002180050406.
- [64] R. A. Arndt et al., “Nonstrange and other flavor partners of the exotic Θ^+ baryon”, Physical Review C **69**, 035208 (2004) 10.1103/PhysRevC.69.035208.
- [65] M. V. Polyakov and A. Rathke, “On photoexcitation of baryon antidecuplet”, arXiv **18**, 691–695 (2003) 10.1140/epja/i2003-10029-y.
- [66] M. V. Polyakov, “Notes on New Narrow N^* ”, arXiv.org (2011), <http://arxiv.org/pdf/1108.4524.pdf>.
- [67] T. Ledwig, “Anti-Decuplet Pentaquarks in the Chiral the Chiral Quark-Soliton Model ”, PhD thesis (Ruhr Universität Bochum, Bochum, Dec. 2007).
- [68] I. Senderovich et al., “First measurement of the helicity asymmetry E in η photoproduction on the proton”, arXiv.org (2015), <http://arxiv.org/pdf/1507.00325.pdf>.
- [69] H. Kamano et al., “Nucleon resonances within a dynamical coupled-channels model of πN and γN reactions”, Physical Review C **88**, 035209 (2013) 10.1103/PhysRevC.88.035209.
- [70] D. Rönchen et al., “Eta photoproduction in a combined analysis of pion- and photon-induced reactions”, The European Physical Journal A **51**, 70 (2015) 10.1140/epja/i2015-15070-7.
- [71] K. H. Kaiser et al., “The 1.5 GeV harmonic double-sided microtron at Mainz University”, Nuclear Instruments and Methods in Physics Research Section A: Accelerators, Spectrometers, Detectors and Associated Equipment **593**, 159–170 (2008) 10.1016/j.nima.2008.05.018.
- [72] K. Aulenbacher et al., “The MAMI source of polarized electrons”, Nuclear Instruments and Methods in Physics Research Section A: Accelerators, Spectrometers, Detectors and Associated Equipment **391**, 498–506 (1997) 10.1016/S0168-9002(97)00528-7.

- [73] C. Nachtigall et al., "The new polarized beam injection at MAMI", in Particle accelerator. proceedings, 6th european conference, epac'98, stockholm, sweden, june 22-26, 1998. vol. 1-3 (1998), pp. 1430–1432, <http://cds.cern.ch/record/859140>.
- [74] K. Aulenbacher, "Polarized beams for electron accelerators", The European Physical Journal Special Topics **198**, 361–380 (2011) [10.1140/epjst/e2011-01499-6](https://doi.org/10.1140/epjst/e2011-01499-6).
- [75] V. Bargmann, L. Michel, and V. L. Telegdi, "Precession of the polarization of particles moving in a homogeneous electromagnetic field", Physical Review Letters **2**, 435–436 (1959) [10.1103/PhysRevLett.2.435](https://doi.org/10.1103/PhysRevLett.2.435).
- [76] V. Tioukine and K. Aulenbacher, "Operation of the MAMI accelerator with a Wien filter based spin rotation system", Nuclear Instruments and Methods in Physics Research Section A: Accelerators, Spectrometers, Detectors and Associated Equipment **568**, 537–542 (2006) [10.1016/j.nima.2006.08.022](https://doi.org/10.1016/j.nima.2006.08.022).
- [77] F. Frommberger, *Elektronen-stretcher-anlage*, <http://www-elsa.physik.uni-bonn.de>, Accessed: 07.01.2015.
- [78] W. Hillert, "Erzeugung eines Nutzstrahls spinpolarisierter Elektronen an der Beschleunigeranlage ELSA.", Habilitationsschrift (Rheinische Friedrich-Wilhelms-Universität Bonn, Bonn, 2000).
- [79] W. Hillert, "The Bonn electron stretcher accelerator ELSA: Past and future", The European Physical Journal A **28**, 139–148 (2006) [10.1140/epja/i2006-09-015-4](https://doi.org/10.1140/epja/i2006-09-015-4).
- [80] W. Heitler, *The Quantum Theory of Radiation*, Third Edition (Dover Pubn Inc, New York), ISBN: 978-0486645582, <http://www.worldcat.org/title/quantum-theory-of-radiation/oclc/9394435>.
- [81] S. Kammer, "Strahlpolarimetrie am CBELSA/TAPS Experiment", PhD thesis (Rheinische Friedrich-Wilhelms-Universität Bonn, Bonn, Oct. 2009).
- [82] C. Schmidt, *Logos and Images*, <http://www1.cb.uni-bonn.de>, Accessed: 08.01.2015.
- [83] K. Fornet-Ponse, "Die Photonmarkierungsanlage für das Crystal-Barrel/TAPS Experiment an ELSA", PhD thesis (Rheinische Friedrich-Wilhelms-Universität Bonn, Bonn, Nov. 2009), <http://hss.ulb.uni-bonn.de/2010/1998/1998.pdf>.
- [84] H. Olsen and L. C. Maximon, "Photon and Electron Polarization in High-Energy Bremsstrahlung and Pair Production with Screening", Phys. Rev. **114**, 887–904 (1959) [10.1103/PhysRev.114.887](https://doi.org/10.1103/PhysRev.114.887).
- [85] D. Elsner et al., "Linearly polarised photon beams at ELSA and measurement of the beam asymmetry in π^0 photoproduction off the proton", The European Physical Journal A **39** (2009) [10.1140/epja/i2008-10708-1](https://doi.org/10.1140/epja/i2008-10708-1).

- [86] P.-B. Otte, "Aufbau und Test eines Møllerpolarimeters für das Crystal-Ball-Experiment an MAMI-C", Diploma thesis (Johannes Gutenberg-Universität Mainz, Mainz, Oct. 2008).
- [87] U. Timm, "Coherent bremsstrahlung of electrons in crystals", *Fortsch.Phys.* **17**, 765–808 (1969) 10.1002/prop.19690171202.
- [88] A. Thomas, "Recent result from the A2 real photon facility at MAMI", *Chin.Phys. C* **33**, 1120–1126 (2009) 10.1088/1674-1137/33/12/012.
- [89] J. C. McGeorge et al., "Upgrade of the Glasgow photon tagging spectrometer for Mainz MAMI-C", *The European Physical Journal A* **37**, 129–137 (2008) 10.1140/epja/i2007-10606-0.
- [90] C. Hammann, "Aufbau eines Flüssigwasserstofftargets zur Durchführung von Kalibrationsmessungen am Crystal-Barrel Experiment an ELSA", Diploma thesis (Rheinischen Friedrich-Wilhelms-Universität Bonn, Bonn, Mar. 2009).
- [91] A. Thomas, *Crystal Ball Hydrogen (Deuterium) Target manual* (May 2013).
- [92] A. Thomas, "Review on the last developments on polarized targets at Mainz", Annual Meeting of the GDR PH-QCD, 1–40 (2013), <https://indico.in2p3.fr/event/9046/session/3/contribution/27/material/0/0.pdf>.
- [93] F. Pheron, " η Photoproduction off ${}^3\text{He}$ and Search for η -Mesic Nuclei", PhD thesis (Universität Basel, Basel, 2012), 10.5451/unibas-006041333.
- [94] R. Kondratiev and C. Carasco, *Target cell construction* (Apr. 2005).
- [95] A. Thomas, personal communication, 2011.
- [96] C. Rohlof, "Entwicklung polarisierter Targets zur Messung der Gerasimov-Drell-Hearn-Summenregel an ELSA", PhD thesis (Rheinischen Friedrich-Wilhelms-Universität Bonn, Bonn, 2003).
- [97] M. Schiemann, "Polarisationsmessungen an mit Trityl-Radikalen dotiertem D-Butanol", Diploma thesis (Ruhr-Universität Bochum, Bochum, Sept. 2006).
- [98] C. Bradtke et al., "A new frozen-spin target for 4π particle detection", *Nucl. Instrum. Methods Phys. Res., A* **436**, 430–442 (1999) 10.1016/S0168-9002(99)00383-6.
- [99] M. Martínez Fabregat, "Setup and test of a 70 GHz microwave apparatus for a polarized target", Diploma thesis (Johannes Gutenberg Universität Mainz, Mainz, 2003).
- [100] S. Schrauf, "Aufbau eines cw-NMR-Moduls für die Polarisationsmessung in Festkörpertargets", Diploma thesis (Ruhr-Universität Bochum, Bochum, 2010).
- [101] H. G. Ortega Spina, "Design of Superconducting Holding Magnet for a Polarized Solid Target", Diploma thesis (Johannes Gutenberg Universität Mainz, Mainz, 2009).
- [102] A. Thomas, <http://www.a2.kph.uni-mainz.de/internalpages/detectors-and-setup/target/95-frozen-spin-target.html>, Accessed: 08.01.2015.

- [103] H. Dutz, personal communication, 2013.
- [104] H. Dutz, "The Bonn Frozen Spin Target", in Eu fp spinmap (Universität Bonn, Dec. 2011), pp. 1–35, http://www.polarisiertes-target.physik.uni-bonn.de/pub/EU_FP7_Linz_Dutz.pdf.
- [105] A. Starostin et al., "Measurement of $K^- p \rightarrow \eta \Lambda$ near threshold", Physical Review C **64**, 055205 (2001) 10.1103/PhysRevC.64.055205.
- [106] D. Watts, "The Crystal Ball and TAPS Detectors at the MAMI Electron Beam Facility", in Calorimetry in particle physics - the eleventh international conference (2005), pp. 116–123, ISBN: 9789812562722, 10.1142/9789812701978_0015.
- [107] R. Novotny, "The electromagnetic calorimeter TAPS", in Calorimetry in high-energy physics. proceedings, 6th international conference (1996), pp. 683–692.
- [108] A. R. Gabler et al., "Response of TAPS to monochromatic photons with energies between 45 and 790 MeV", Nuclear Instruments and Methods **346**, 168–176 (1994) 10.1016/0168-9002(94)90701-3.
- [109] L. Withauer et al., "Quasi-free photoproduction of η -mesons off ^3He nuclei", The European Physical Journal A **49**, 154 (2013) 10.1140/epja/i2013-13154-0.
- [110] E. F. McNicoll et al., "Experimental study of the $\gamma p \rightarrow \eta p$ reaction with the Crystal Ball detector at the Mainz Microtron (MAMI-C)", Physical Review C **82**, 035208 (2010) 10.1103/PhysRevC.82.035208.
- [111] *School of Physics, The University of Edinburgh*, <http://www2.ph.ed.ac.uk/nuclear/mami/welcome.html>, Accessed: 02.02.2015.
- [112] M. Oreglia, "A Study of the Reactions $\psi' \rightarrow \gamma\gamma\psi$ ", PhD thesis (Stanford University, 1980), <http://www.slac.stanford.edu/cgi-wrap/getdoc/slac-r-236.pdf>.
- [113] D. Watts, "Crystal Ball at MAMI", in Nstar (2005), <http://www2.ph.ed.ac.uk/~dwatts1/WattsNstar2005.pdf>.
- [114] P. Drexler, "Entwicklung und Aufbau der neuen TAPS-Elektronik", PhD thesis (Justus-Liebig-Universität Gießen, Gießen, 2004).
- [115] P. Drexler et al., *The new read-out electronics for the BaF₂-calorimeter TAPS*, Vol. 1 (IEEE, Nov. 2002), ISBN: 0-7803-7636-6, 10.1109/NSSMIC.2002.1239381.
- [116] E. Aker et al., "The Crystal Barrel spectrometer at LEAR", Nucl. Instrum. Methods Phys. Res., A **A321**, 69–108 (1992) 10.1016/0168-9002(92)90379-I.
- [117] C. Wendel, "The Crystal-Barrel/TAPS experiment at ELSA Current status of the CsI(Tl) calorimeters", J.Phys.Conf.Ser. **160**, 012006 (2009) 10.1088/1742-6596/160/1/012006.
- [118] H. Flemming, "Entwurf und Aufbau eines Zellularlogik-Triggers für das Crystal Barrel-Experiment an der Elektronenbeschleunigeranlage ELSA", PhD thesis (Ruhr-Universität Bochum, Bochum, Sept. 2001).

- [119] A. Thiel, "Bestimmung der Doppelpolarisationsobservablen G in π^0 -Photoproduktion", PhD thesis (Rheinische Friedrich-Wilhelms- Universität Bonn, Bonn, 2012).
- [120] C. Wendel, "Entwicklung eines Szintillations-Detektors zur Identifikation geladener Teilchen im Crystal-Barrel Vorwärtsdetektor", Diploma thesis (Rheinischen Friedrich-Wilhelms-Universität Bonn, Bonn, June 2004).
- [121] G. Suft et al., "A scintillating fibre detector for the Crystal Barrel experiment at ELSA", Nuclear Instruments and Methods in Physics Research Section A: Accelerators, Spectrometers, Detectors and Associated Equipment **538**, 416–424 (2005) 10.1016/j.nima.2004.09.029.
- [122] M. Grüner, "Modifikation und Test des Innendetektors für das Crystal Barrel Experiment", Diploma thesis (Rheinischen Friedrich-Wilhelms- Universität Bonn, Bonn, May 2006).
- [123] V. M. Hennen, *MiniTAPS*, <http://www1.cb.uni-bonn.de/>, Accessed: 30.01.2015.
- [124] D. Kaiser, "Aufbau und Test des Gas-Cerenkov-Detektors für den Crystal-Barrel-Aufbau an ELSA", Diploma thesis (Rheinische Friedrich-Wilhelms-Universität Bonn, Bonn, 2007).
- [125] J. Hartmann, "Zeitkalibrierung und Photonenflussbestimmung für das Crystal-Barrel-Experiment an ELSA", Diploma thesis (Rheinischen Friedrich-Wilhelms-Universität Bonn, Bonn, Dec. 2008).
- [126] P.-B. Otte, personal communication, 2013.
- [127] A. Winnebeck, "Entwicklung und Implementierung eines universellen, FPGA basierten Triggermoduls für das Crystal-Barrel-Experiment an ELSA", Diploma thesis (Rheinischen Friedrich-Wilhelms-Universität Bonn, Bonn, Dec. 2006).
- [128] C. Funke, "Analyse der Triggerfähigkeiten zur Selektion hadronischer Ereignisse und Entwicklung eines Hochgeschwindigkeits-Triggers für den Vorwärtskonus des Crystal-Barrel-Detektors", PhD thesis (Rheinischen Friedrich-Wilhelms- Universität Bonn, Bonn, June 2008).
- [129] L. Witthauer, " η -Photoproduction off ${}^3\text{He}$ ", MA thesis (Universität Basel, Basel, Jan. 2010).
- [130] dab, "Uni: ELSAs Trafo fängt Feuer", General-Anzeiger, Accessed: 08.02.2015 (2010), <http://www.general-anzeiger-bonn.de/lokales/bonn/Uni-ELSAs-Trafo-faengt-Feuer-article43202.html>.
- [131] V. Tioukine, K. Aulenbacher, and E. Riehn, "A Mott polarimeter operating at MeV electron beam energies", Review of Scientific Instruments **82**, 033303 (2011) 10.1063/1.3556593.
- [132] M. Gowin, "Optimierung der laserinduzierten Photoemission zur Erzeugung polarisierter Elektronenstrahlen an der 50 keV-Quelle der Bonner Beschleunigeranlage ELSA", PhD thesis (Universität Bonn, 2001).

- [133] V. Tioukine and K. Aulenbacher, "Polarimetry at MAMI", AIP Conf. Proc. **1563**, 276–279, ISSN: 0094-243X (2013) 10.1063/1.4829428.
- [134] P.-B. Otte, "Erste Messung der π^0 -Photoproduktion an transversal polarisierten Protonen nahe der Schwelle", PhD thesis (Johannes Gutenberg-Universität Mainz, Mainz, Apr. 2015).
- [135] V. Tioukine, "Mott polarimeter at MAMI", in Istituto nazionale di fisica nucleare, xiiith international workshop on polarized sources, targets and polarimetry. (Sept. 9), <http://web.fe.infn.it/PST2009/body/talks/tioukine.pdf>.
- [136] D. Heiliger, "Erzeugung intensiver spinpolarisierter Elektronenstrahlen an der Beschleuigneranlage ELSA", PhD thesis (Rheinische Friedrich-Wilhelms- Universität Bonn, 2014).
- [137] H. Eberhardt, "Messung der Targetpolarisation und Detektorstudie für das Møllerpolarimeter des Crystal-Barrel-Aufbaus an ELSA", Diploma thesis (Rheinischen Friedrich-Wilhelms- Universität Bonn, Dec. 2006).
- [138] T. Speckner et al., "The GDH-Møller-Polarimeter at ELSA", Nuclear Instruments and Methods in Physics Research Section A: Accelerators, Spectrometers, Detectors and Associated Equipment **519**, 518–531 (2004) 10.1016/j.nima.2003.11.016.
- [139] J. Arrington et al., "A variable energy Møller polarimeter at the MIT-Bates Linear Accelerator Center", Nuclear Instruments and Methods in Physics Research Section A: Accelerators, Spectrometers, Detectors and Associated Equipment **311**, 39–48 (1992) 10.1016/0168-9002(92)90849-Y.
- [140] S. Costanza, *Report on the Moeller analysis of the Jan/Feb 2014 beamtime*, tech. rep. (2010), https://www.a2.kph.uni-mainz.de/intern/daqwiki/_media/experiment/analysis/beamtimes/moellerreport.pdf.
- [141] M. Hoffmann, "Beschleunigung polarisierter Elektronen in der Bonner Elektronen-Beschleunigeranlage ELSA", PhD thesis (Rheinischen Friedrich-Wilhelms- Universität Bonn, 2001).
- [142] O. Rondon, "Corrections to nucleon spin structure asymmetries measured on nuclear polarized targets", Physical Review C **60**, 035201 (1999) 10.1103/PhysRevC.60.035201.
- [143] H. Rochholz, "Entwicklungsarbeiten für einen Freie-Elektronen-Laser auf der Basis des Smith-Purcell-Effektes im infraroten Spektralbereich", Diploma thesis (Johannes Gutenberg Universität Mainz, Mainz, 2002).
- [144] A. Thomas, "Frozen Spin Target", in 26th a2 collaboration meeting (Mar. 2015).
- [145] E. Rickert, "Untersuchung der Ortsabhängigkeit der Polarisation des Mainzer Frozen-Spin-Targets", BA thesis (Johannes Gutenberg-Universität Mainz, Mainz, June 2015), <https://mail.unibas.ch/owa/>.

- [146] R. Brun and F. Rademakers, "ROOT: An object oriented data analysis framework", *Nucl.Instrum.Meth.* **A389**, 81–86 (1997) 10 . 1016 / S0168 – 9002(97) 00048–X.
- [147] J. R. M. Annand, *Data Analysis within an AcquRoot Framework*, <http://www.nuclear.gla.ac.uk/~acqusys/doc/AcquRoot.11.08.pdf>, Accessed: 25.07.2015.
- [148] L. Zana, D. Watts, and D. Glazier, *A2 Geant4 Simulation*, <http://www2.ph.ed.ac.uk/nuclear/G4/>, Accessed: 25.07.2015.
- [149] S. Agostinelli et al., "GEANT4: A Simulation toolkit", *Nucl.Instrum.Meth.* **A506**, 250–303 (2003) 10 . 1016/S0168-9002(03)01368-8.
- [150] *Geant4, Reference Physics Lists*, http://geant4.cern.ch/support/proc_mod_catalog/physics_lists/referencePL.shtml, Accessed: 11.02.2015.
- [151] I. Froehlich et al., "Pluto: A Monte Carlo Simulation Tool for Hadronic Physics", in Proceedings, 11th international workshop on advanced computing and analysis techniques in physics research acat (Aug. 2007), <http://arxiv.org/abs/0708.2382v2>.
- [152] M. Lacombe et al., "Parametrization of the deuteron wave function of the Paris n-n potential", *Phys.Lett.* **B101**, 139–140 (1981) 10 . 1016/0370-2693(81)90659-6.
- [153] J. Arrington et al., "Hard probes of short-range nucleon-nucleon correlations", *Progress in Particle and Nuclear Physics* **67**, 898–938 (2012) 10 . 1016/j.ppnp.2012.04.002.
- [154] K. Nakamura et al., "The reaction $^{12}\text{C}(\text{e}, \text{e}'\text{p})$ at 700 MeV and DWIA analysis", *Nuclear Physics A* **268**, 381–407 (1976) 10 . 1016/0375-9474(76)90539-X.
- [155] C. Schmidt, *EXPLORA*, Helmholtz-Institut für Strahlen- und Kernphysik, Bonn.
- [156] V. Credé, *CBGEANT 1.08/01*, CB-Note 002, 2001.
- [157] *GEANT 3.15 User's Guide* (Jan. 1993), <http://www.desy.de/~golubkov/manuals/geant.ps.gz>.
- [158] C. Zeitnitz, *GCALOR*, <http://www.atlas.uni-wuppertal.de/zeitnitz/gcalor>, Accessed: 10.02.2015.
- [159] K. Molenaar, "Performance of TAPS in the Tagged Photon Beam of MAMI", Diploma thesis (Rijksuniversiteit Groningen, Groningen, 1992).
- [160] V. Hejny, "Photoproduktion von η -Mesonen an Helium 4", PhD thesis (Justus-Liebig-Universität Gießen, Gießen, Oct. 1998).
- [161] J. Müller, "Bestimmung einer Energiekorrekturfunktion für das Kalorimeter des Crystal-Barrel-Experiments an ELSA", Diploma thesis (Rheinische Friedrich-Wilhelms-Universität Bonn, Bonn, 2007).
- [162] T. Seifen, "Verbesserung der Rekonstruktion und Entwicklung eines First-Level-Triggerschemas für das Crystal-Barrel-Kalorimeter", Diploma thesis (Rheinische Friedrich-Wilhelms-Universität Bonn, Bonn, Sept. 2009).

[163] J. Junkersfeld, "Kalibration des Crystal-Barrel-ELSA Detektors mit Hilfe der Reaktion $\gamma p \rightarrow p\pi^0$ ", PhD thesis (Rheinischen Friedrich-Wilhelms-Universität Bonn, Bonn, 2000).

[164] R. Castelijns, "Photoproduction of strange mesons and hyperons on the proton", PhD thesis (Rijksuniversiteit Groningen, Groningen, 2006).

[165] T. Dahlke, "Bestimmung einer winkelabhängigen Energiekorrekturfunktion für das TAPS-Kalorimeter des Crystal-Barrel/TAPS-Experimentes an ELSA", Diploma thesis (Rheinische Friedrich-Wilhelms-Universität Bonn, Bonn, 2008).

[166] M. Unverzagt, "Energie-Eichung des Crystal Ball-Detektors am MAMI", Diploma thesis (Johannes Gutenberg–Universität Mainz, Mainz, 2004).

[167] B. Povh et al., *Teilchen und Kerne, Eine Einführung in die physikalischen Konzepte* (Springer Berlin Heidelberg, Berlin, Heidelberg, 2009), ISBN: 978-3-540-68075-8, 10.1007/978-3-540-68080-2.

[168] M. E. Röbig, "Eichung des TAPS-Detektorsystems mit Höhenstrahlung", Diploma thesis (Universität Gießen, Gießen, 1991).

[169] T. Jude, "Strangeness Photoproduction off the Proton at Threshold Energies", PhD thesis (University of Edinburgh, Edinburgh, 2010).

[170] S. Böse, "Modifikation und Test des Lichtpulsersystems für den Crystal Barrel Aufbau an ELSA", Diploma thesis (Rheinische Friedrich-Wilhelms-Universität Bonn, June 2006).

[171] S. Brandt, *Data analysis: Using statistical methods and computer programs* (Spektrum Akademischer Verlag, 1999), ISBN: 978-3827401588.

[172] M. Dieterle, "Comparison of the Experimental Resolution in Case of Using a 1.76 or 4.76 cm LD₂ Target", Master Project thesis (Universität Basel, 2009).

[173] O. Hen et al., "Momentum sharing in imbalanced Fermi systems", *Science* **346**, 614–617 (2014) 10.1126/science.1256785.

[174] U. S. of Commerce on behalf of the United States of America., *NIST Chemistry WebBook*, <http://webbook.nist.gov/chemistry>, Accessed: 27.08.2015.

[175] H. Dutz, personal communication, 22.06.2015.

[176] M. Roebig-Landau et al., "Near threshold photoproduction of η mesons from complex nuclei", *Phys.Lett.* **B373**, 45–50 (1996) 10.1016/0370-2693(96)00125-6.

[177] T. Mertens et al., "Photoproduction of η -mesons off nuclei for $E_\gamma \leq 2.2$ GeV", *arXiv* **38**, 195–207 (2008) 10.1140/epja/i2007-10667-y.

[178] B. Krusche et al., "Constraining N*(1535) parameters from the eta photoproduction", *Phys.Lett.* **B397**, 171–176 (1997) 10.1016/S0370-2693(97)00160-3.

[179] L. Tiator et al., *MAID 2000*, <http://portal.kph.uni-mainz.de/MAID//eta/etamaid.html>, Accessed: 08.08.2015.

- [180] M. Oberle et al., “Measurement of the beam-helicity asymmetry I^\odot in the photoproduction of $\pi^0 \pi^\pm$ pairs off protons and off neutrons”, *The European Physical Journal A* **50**, 54 (2014) 10.1140/epja/i2014-14054-5.
- [181] M. Dieterle, “Measurement of Polarization Observables in π^0 and $\pi^0\pi^0$ Photoproduction from Protons and Neutrons at MAMI and ELSA”, PhD thesis (Universität Basel, Basel, in preparation).
- [182] V. Crede and W. Roberts, “Progress towards understanding baryon resonances”, *Reports on Progress in Physics* **76**, 076301 (2013) 10.1088/0034-4885/76/7/076301.
- [183] A. M. Sandorfi et al., “Determining pseudoscalar meson photoproduction amplitudes from complete experiments”, *Journal of Physics G: Nuclear and Particle Physics* **38**, 053001 (2011) 10.1088/0954-3899/38/5/053001.